

Ernesto Anoz Carbonell

Molecular and dynamic  
mechanisms of prokaryotic and  
eukaryotic flavoenzymes: insights  
into their implication in human  
metabolism and health

Director/es

Medina Trullenque, Milagros  
Aínsa Claver, José Antonio

<http://zaguan.unizar.es/collection/Tesis>

© Universidad de Zaragoza  
Servicio de Publicaciones

ISSN 2254-7606

Tesis Doctoral

MOLECULAR AND DYNAMIC MECHANISMS OF  
PROKARYOTIC AND EUKARYOTIC  
FLAVOENZYMES: INSIGHTS INTO THEIR  
IMPLICATION IN HUMAN METABOLISM AND  
HEALTH

Autor

Ernesto Anoz Carbonell

Director/es

Medina Trullenque, Milagros  
Aínsa Claver, José Antonio

**UNIVERSIDAD DE ZARAGOZA**  
**Escuela de Doctorado**

Programa de Doctorado en Bioquímica y Biología Molecular

2021



## Tesis Doctoral

Molecular and dynamic mechanisms of prokaryotic and eukaryotic flavoenzymes: insights into their implication in human metabolism and health

Autor

Ernesto Anoz Carbonell

Director/es

Milagros Medina Trullenque  
José Antonio Aínsa Claver

**UNIVERSIDAD DE ZARAGOZA**

Facultad de Ciencias

2020



Dña. MILAGROS MEDINA TRULLENQUE, Catedrática del Departamento de Bioquímica y Biología Molecular y Celular de la Universidad de Zaragoza,

D. JOSÉ ANTONIO AÍNSA CLAVER, Profesor titular del Departamento de Microbiología, Pediatría, Radiología y Salud Pública de la Universidad de Zaragoza,

CERTIFICAN:

Que la Tesis Doctoral **“Molecular and dynamic mechanisms of prokaryotic and eukaryotic flavoenzymes: insights into their implication in human metabolism and health”** ha sido realizada por el graduado ERNESTO ANOZ CARBONELL en el Departamento de Bioquímica y Biología Molecular y Celular (Facultad de Ciencias), y en el Departamento de Microbiología, Pediatría, Radiología y Salud Pública (Facultad de Medicina), y en el Instituto de Biocomputación y Física de Sistemas Complejos (BIFI), de la Universidad de Zaragoza bajo su dirección, y que reúne, a su juicio, las condiciones requeridas para optar al Grado de Doctor por la Universidad de Zaragoza y a la mención de Doctorado Internacional.

Zaragoza, Octubre de 2020

Fdo.: Milagros Medina Trullenque

Fdo.: José Antonio Aínsa Claver





# Index



|  |            |
|--|------------|
| <b>Abstract</b>  | <b>1</b>   |
| <b>Resumen</b>   | <b>5</b>   |
| <b>Introduction</b>  | <b>9</b>   |
| I.    Flavins  | 11         |
| II.   Synthesis of the riboflavin precursor  | 17         |
| III.  Biosynthesis of the flavin cofactors   | 21         |
| IV.  Flavoproteins   | 44         |
| <br>   |            |
| <b>Objetives</b>   | <b>55</b>  |
| <br>   |            |
| <b>Publication I.</b>  | <b>59</b>  |
| Human riboflavin kinase: species-specific traits in the biosynthesis of the FMN cofactor.  |            |
| <br>   |            |
| <b>Publication II.</b>   | <b>85</b>  |
| Mutation of aspartate 238 in FAD synthase isoform 6 increases the specific activity by weakening the FAD binding                                 |            |
| <br>   |            |
| <b>Publication III.</b>  | <b>109</b> |
| The catalytic cycle of the antioxidant and cancer-associated NQO1 enzyme: hydride transfer, conformational dynamics and functional cooperativity |            |
| <br>   |            |
| <b>Publication IV.</b>   | <b>133</b> |
| Discovery of antimicrobial compounds targeting bacterial type FAD synthase   |            |
| <br>   |            |
| <b>Publication V.</b>  | <b>157</b> |
| In silico discovery and biological validation of ligands of FAD synthase, a promising new antimicrobial target.                                  |            |
| <br>   |            |
| <b>General discussion</b>  | <b>197</b> |
| <b>Conclusions</b>   | <b>205</b> |
| <b>Conclusiones</b>  | <b>209</b> |
| <b>Participation in other related publications</b>   | <b>215</b> |
| <b>Bibliography</b>  | <b>255</b> |
| <b>Abbreviations</b>   | <b>277</b> |



# Abstract



Flavoenzymes and flavoproteins are versatile and diverse biomolecules that are implicated in the energetic metabolism and other cellular processes such as signalling, nucleotide synthesis, protein folding or defense against oxidative stress. These proteins have as cofactors the riboflavin (RF, vitamin B2) derivatives flavin mononucleotide (FMN) and/or flavin adenine dinucleotide (FAD), which confer them their unique and versatile properties. All organisms contain key flavoproteins and flavoenzymes, and many of them are becoming interesting as therapeutic targets or biotechnological tools.

In the present thesis, we have delved into the molecular mechanisms of flavoenzymes with key metabolic functions in prokaryotes and eukaryotes, such as the human RF kinase (**Publication I**) and FAD synthase (FADS) (**Publication II**), human NAD(P)H:quinone oxidoreductase 1 (**Publication III**), and prokaryotic FADS (**Publications IV and V**). The detailed characterization of these enzymes contributes to the better understanding of their associated pathologies, and provides a framework to novel therapeutic strategies and to the design of compounds targeting them. For instance, here we show a first approximation for identification of inhibitors of the prokaryotic FADS that might contribute to exploit them as pharmacological antimicrobial drugs (**Publications IV and V**).

This Doctoral Thesis, presented in the form of a *compendium* of publications, comprises the following publications:

- **Publication I.** Anoz-Carbonell E, Ribero M, Polo V, Velázquez-Campoy A, Medina M. 2020. Human riboflavin kinase: species-specific traits in the biosynthesis of the FMN cofactor. *The FASEB Journal*, 34:10871–10886.

JCR Impact Factor 2019: 4.966. Rank: Q1 (57/297) Biochemistry and Molecular Biology; D1 (9/93) Biology; Q2 (58/195) Cell Biology.

- **Publication II.** Leone P, Galluccio M, Quarta S, Anoz-Carbonell E, Medina M, Indiveri C, Barile M. 2019. Mutation of aspartate 238 in FAD synthase isoform 6 increases the specific activity by weakening the FAD binding. *International Journal of Molecular Sciences*, 20(24):6203.

JCR Impact Factor 2019: 4.556. Rank: Q1 (74/297) Biochemistry and Molecular Biology; Q2 (48/177) Chemistry (multidisciplinary).

- **Publication III.** Anoz-Carbonell E, Timson DJ, Pey AL, Medina M. 2020. The catalytic cycle of the antioxidant and cancer-associated human NQO1 enzyme: hydride transfer, conformational dynamics and functional cooperativity. *Antioxidants*, 9(9):E772.

JCR Impact Factor 2019: 5.014. Rank: Q1 (56/297) Biochemistry and Molecular Biology; Q1 (7/61) Medicinal Chemistry; D1 (10/139) Food Science & Technology.

- **Publication IV.** Sebastián M, Anoz-Carbonell E, Gracia B, Cossio P, Aínsa JA, Lans I, Medina M. 2018. Discovery of antimicrobial compounds targeting bacterial type FAD synthetases. *Journal of Enzyme Inhibition and Medicinal Chemistry*, 33:1, 241-254.

JCR Impact Factor 2018: 4.027. Rank: Q1 (10/61) Medicinal Chemistry; Q2 (84/299) Biochemistry and Molecular Biology.

- **Publication V.** Lans I, Anoz-Carbonell E, Palacio-Rodríguez K, Aínsa JA, Medina M, Cossio P. 2020. In silico discovery and biological validation of ligands FAD synthase, a promising new antimicrobial target. *PLOS Computational Biology*, 16(8):e1007898.

JCR Impact Factor 2019: 4.700. Rank: Q1 (9/77) Biochemical Research Methods; Q1 (6/59) Mathematical & Computational Biology.



# Resumen



Las flavoenzimas y flavoproteínas son biomoléculas versátiles y diversas que están implicadas en el metabolismo energético y otros procesos celulares como la transducción de señales, la síntesis de nucleótidos, el plegamiento de proteínas o la defensa frente al estrés oxidativo. Estas proteínas tienen como cofactores los derivados de riboflavina (RF, vitamina B2), mononucleótido de flavina (FMN) y/o dinucleótido de flavina y adenina (FAD), que les confieren propiedades únicas y versátiles. Todos los organismos contienen flavoproteínas y flavoenzimas clave, y muchas de ellas se han convertido en interesantes dianas terapéuticas o herramientas biotecnológicas.

En esta tesis, se ha indagado en los mecanismos moleculares de flavoenzimas y flavoproteínas con funciones metabólicas clave en procariotas y eucariotas, como las enzimas humanas RF quinasa (**Publicación I**), FAD sintetasa (FADS) (**Publicación II**) o NAD(P)H:quinona oxidoreductasa 1 (**Publicación III**), o las FADS procariotas (**Publicaciones IV y V**). La caracterización detallada de estas enzimas contribuye a la mejor comprensión de sus patologías asociadas, y sienta las bases de nuevas estrategias terapéuticas y del diseño de compuestos dirigidos a estas dianas. Por ejemplo, aquí presentamos una primera aproximación a la búsqueda de inhibidores de las FADS procariotas que puede contribuir a su explotación farmacológica como potencial agentes antimicrobianos (**Publicaciones IV y V**).

Esta Tesis Doctoral, presentada en la modalidad de compendio de publicaciones, incluye las siguientes publicaciones:

- **Publicación I.** Anoz-Carbonell E, Ribero M, Polo V, Velázquez-Campoy A, Medina M. 2020. Human riboflavin kinase: species-specific traits in the biosynthesis of the FMN cofactor. *The FASEB Journal*, 34:10871–10886.

JCR Impact Factor 2019: 4.966. Rank: Q1 (57/297) Biochemistry and Molecular Biology; D1 (9/93) Biology; Q2 (58/195) Cell Biology.

- **Publicación II.** Leone P, Galluccio M, Quarta S, Anoz-Carbonell E, Medina M, Indiveri C, Barile M. 2019. Mutation of aspartate 238 in FAD synthase isoform 6 increases the specific activity by weakening the FAD binding. *International Journal of Molecular Sciences*, 20(24):6203.

JCR Impact Factor 2019: 4.556. Rank: Q1 (74/297) Biochemistry and Molecular Biology; Q2 (48/177) Chemistry (multidisciplinary).

- **Publicación III.** Anoz-Carbonell E, Timson DJ, Pey AL, Medina M. 2020. The catalytic cycle of the antioxidant and cancer-associated human NQO1 enzyme: hydride transfer, conformational dynamics and functional cooperativity. *Antioxidants*, 9(9):E772.

JCR Impact Factor 2019: 5.014. Rank: Q1 (56/297) Biochemistry and Molecular Biology; Q1 (7/61) Medicinal Chemistry; D1 (10/139) Food Science & Technology.

- **Publicación IV.** Sebastián M, Anoz-Carbonell E, Gracia B, Cossio P, Aínsa JA, Lans I, Medina M. 2018. Discovery of antimicrobial compounds targeting bacterial type FAD synthetases. *Journal of Enzyme Inhibition and Medicinal Chemistry*, 33:1, 241-254.

JCR Impact Factor 2018: 4.027. Rank: Q1 (10/61) Medicinal Chemistry; Q2 (84/299) Biochemistry and Molecular Biology.

- **Publicación V.** Lans I, Anoz-Carbonell E, Palacio-Rodríguez K, Aínsa JA, Medina M, Cossio P. 2020. In silico discovery and biological validation of ligands FAD synthase, a promising new antimicrobial target. *PLOS Computational Biology*, 16(8):e1007898.

JCR Impact Factor 2019: 4.700. Rank: Q1 (9/77) Biochemical Research Methods; Q1 (6/59) Mathematical & Computational Biology.

# Introduction



## I. FLAVINS

Biological cofactors extend the catalytic repertoire of proteins by increasing the limited chemical space of the aminoacyl side chains of peptides. Some of these cofactors catalyze a small but nevertheless essential set of biological reactions, such as biotin or thiamine pyrophosphate. In contrast, other cofactors are far more versatile contributing to very different chemical reactions, as for example flavin and pyridoxine-derived cofactors (Leys and Scrutton, 2016).

Flavin cofactors are a family of heterocyclic compounds with the basic structure of 7,8-dimethyl-10-alkylisoalloxazine (**FIG I.1**), also referred as lumichrome. The term is derived from the Latin word *flavus*, due to their characteristic yellow color in the oxidized state.

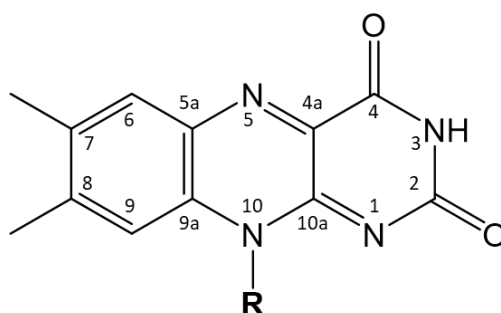


**Figure I.1.** Chemical structure and atomic numbering of the 7,8-dimethyl-isoalloxazine ring. **R** determines the nature of the flavin: R=CH<sub>3</sub>, lumiflavin; R=ribityl, riboflavin (RF); R=ribityl-5'-phosphate, flavin mononucleotide (FMN); R=ribityl-(9-adenosyl)-pyrophosphate, flavin adenine dinucleotide (FAD).

Another non-technical but widely extended terminology is the designation of the two faces of the isoalloxazine ring as *re* and *si* faces. If the isoalloxazine ring is oriented with the N(10) in the lower part of the molecule, the *re* face is the one in which the benzene is located at the left side, as shown in FIG I.2.



**Figure I.2.** *Re* and *Si* faces of the isoalloxazine ring of FMN.

In general, the flavins with higher biological relevance are riboflavin (RF) and their active derivatives flavin mononucleotide (FMN, also termed riboflavin 5'-phosphate) and flavin adenine dinucleotide (FAD) (**FIG I.3**), as well as the inactive products of their photodegradation, lumiflavin and lumichrome.

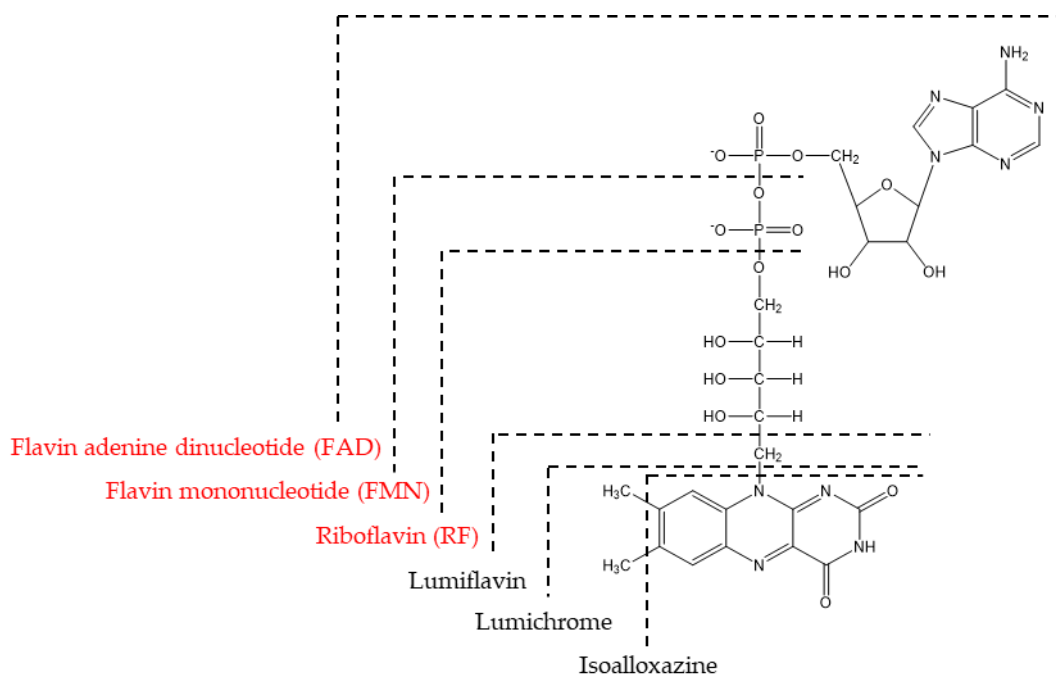


**Figure I.3.** Chemical structure of oxidized isoalloxazine ring and its most biologically relevant derivatives (in red): RF (with a ribityl chain attached to the N(10)), FMN (formed through the addition of a phosphate group to the 5' carbon of the RF ribityl chain) and FAD (formed by condensation of FMN with a molecule of AMP).

Despite flavins are usually referred as nucleotides, this term is not strictly correct since the bond established between the ribityl chain and the isoalloxazine is a carbon-nitrogen bond, susceptible to hydrolysis, and not a glycosidic bond. Therefore, the nomenclature of FMN and FAD would be incorrect, but it is traditionally accepted.

### *Flavins are not only riboflavin-derivatives*

Flavins are ubiquitous in the three-domains of life (Archaea, Bacteria and Eukarya) (Macheroux *et al.*, 2011). In general, RF is not used in any enzyme as a cofactor, but it seems to be the preferred storage form in some organisms (e.g. archaea dodecins, riboflavin-binding protein in chicken eggs) (Gringer *et al.*,



2009; Monaco, 1997). Furthermore, all organisms use RF as the precursor of FMN and FAD. On the contrary, FMN and FAD are used as cofactors of a wide plethora of flavoproteins and flavoenzymes (Fraaije and Mattevi, 2000). In addition, some other flavins with modifications in the ribityl chain and/or in the isoalloxazine ring, have been found in nature, but in general they are restricted to few species or genus. Examples of flavins modified at the ribityl chain would include schizoflavins (2,3,4-trihydroxy-4-carboxybutyl)isoalloxazine and 7,8-dimethyl-10-(2,3,4-trihydroxy-4-formylbutyl)isoalloxazine) from *Schizophillum commune* (Tachibana and Murakami, 1975) and the glycosylated or phosphorylated flavin derivatives (apart from FMN). Some examples of flavins with modifications at the isoalloxazine moiety are roseoflavin (8-dimethylaminoriboflavin) produced from *Streptomyces davawensis* (Lee *et al.*, 2009), 8-hydroxy-5-deazaflavin (constituent of cofactor F<sub>420</sub>) produced by some Actinobacteria (Daniels *et al.*, 1985), or neko-flavin (8 $\alpha$ -hydroxyriboflavin) and 7 $\alpha$ -hydroxyriboflavin produced in some mammals (Matsui, 1965). Furthermore, flavin cofactors covalently linked to their corresponding flavoproteins could be also included within this later group (Piano *et al.*, 2017). Recently, a prenylated FMN has been found as cofactor of yeast ferulic acid decarboxylases Fdc1 and prokaryotic UbiD (de)carboxylases (Payne *et al.*, 2015), but only when co-expressed with the corresponding flavin prenyltransferases Pad10 or UbiX, respectively. This unexpected discovery opens the door to new flavin-derived cofactors broadening the chemical space and catalytic repertoire of flavoproteins.

Additionally, it has been extensively reported the presence of 6- or 8-hydroxy-flavins when isolating and purifying some flavoproteins, such as electron-transferring flavoprotein of *Peptostreptococcus elsdenii*, pig liver glycolate oxidase, the D-aspartate oxidase from *Bos taurus* or *Octopus vulgaris*, cellobiose dehydrogenase from *Humicola insolens* or the human apoptosis factor (Igarashi *et al.*, 1999; Marshall *et al.*, 2005; Mayhew and Ludwig, 1975; Muller and Edmondson, 2018; Negri *et al.*, 1987; Tedeschi *et al.*, 1994). The biological role of these derivatives is still unknown, and they are probably generated as result of the oxidation of flavoproteins during the protein production and/or purification processes (Bertagnolli and Hager, 1993; Gong *et al.*, 2007; Negri *et al.*, 1987). This is further supported by the fact that proteins loaded with these cofactors are less active than with FMN or FAD, and there is not a characterized biosynthetic route for the modified cofactor.

*Flavin redox properties explain their ubiquity in nature*

Flavins, and thus flavoproteins, have always been the apple of enzymologists' eyes due to their distinctive redox and spectroscopic properties. Henceforth, flavins have the potential to undergo redox reactions through both one-electron and two-electron transfer processes. These redox reactions proceed in a thermodynamically and kinetically fully reversible manner. The part of the molecule actively involved in the redox process is the isoalloxazine ring. However, the ribityl chain (or the adenine nucleotide in the case of FAD) is not only merely structural but also can regulate catalytically-relevant amino acid residues (Murthy and Massey, 1997).

The free isoalloxazine ring (not bound to a protein) can exist in three different redox states: oxidized (flavoquinone, ox), one-electron reduced (flavosemiquinone, sq), and two-electron reduced (flavoquinone, rd) (Müller, 1991). Moreover, due to the amphoteric nature of the flavin ring, each redox state can be found in three different protonation states depending the pH: anionic, neutral or cationic species (**FIG I.4**). From the nine forms shown in **FIG I.4**, at least six are physiologically possible based on their pK<sub>a</sub> values. Each redox and protonation species has differential characteristic properties.

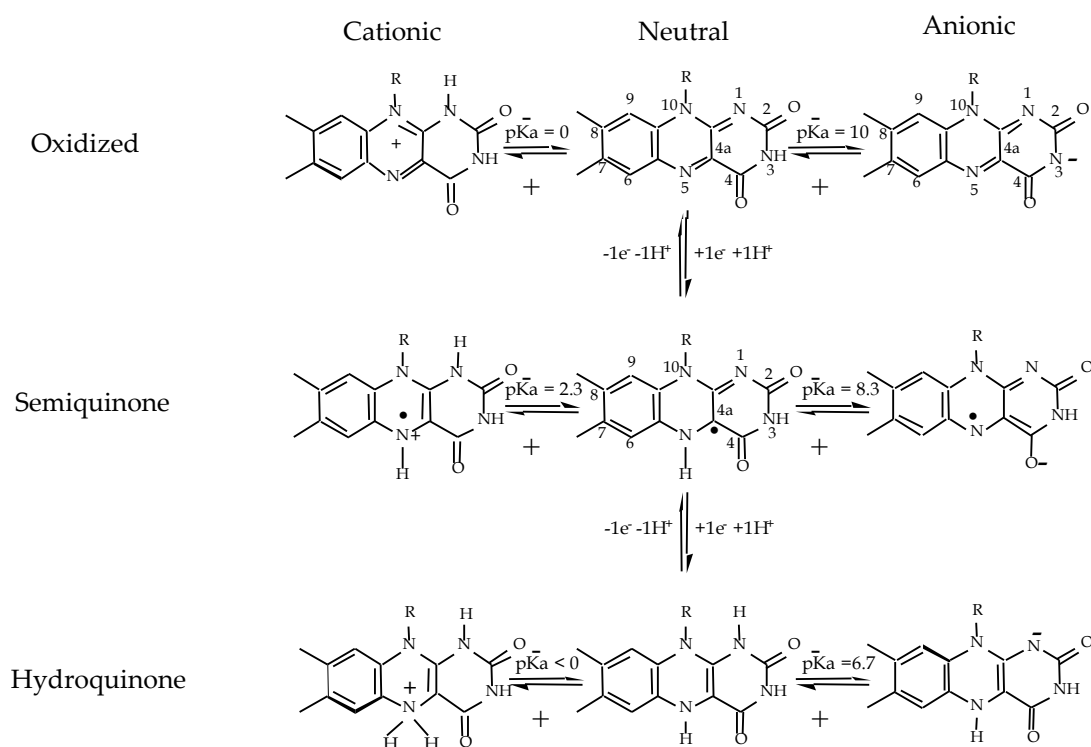


**Figure I.4.** Redox states and acid-base equilibrium of the isoalloxazine ring. Figure modified from (Edwards, 2006).

The oxidized flavoquinone form is stable toward molecular oxygen, independently of the substituent at N(10). At pH values between 1 and 9, the oxidized flavin is in the neutral form. The proton at N(3) dissociates with a pK<sub>a</sub> value of about 10. The cationic specie is formed at pH < 0. Protonation occurs at the N(1) atom, which is the most basic nitrogen atom in the isoalloxazine ring. A dicationic form can also be found in extreme acidic conditions due to the additional protonation at N(5). The semiquinone form, first discovered by Michaelis in 1936 (Michaelis and Schwarzenbach, 1938), incorporates an electron over the oxidized form. Depending on the pH (pK<sub>a</sub> ~8.3), it can be found in the red-colored anionic form or in the blue/green-colored neutral form (color depends of the tautomeric form stabilized, and it varies with the solvent polarity). The cationic flavosemiquinone, observed at pH < 2.3, is rather stable against oxygen compared to the other semiquinone species. The fully reduced flavin incorporates an electron over the semiquinone state. In the hydroquinone state, the pyrimidine ring is rich in electronic density and harbors negative charge at neutral pH (pK<sub>a</sub> ~6.5). Neutral flavohydroquinone incorporates a proton at N(1), the least basic position in this redox state, and at N(5) in the cationic form (at pH < 0).

In aqueous solution, an equimolar mixture of oxidized and reduced flavin reaches an equilibrium with only a small percentage of flavin in the semiquinone form (less than the 1% at pH 8.0) (Mayhew, 1999a). This is caused by the high thermodynamically instability of the semiquinone form, also reflected in the redox potential of the half-reactions or reduction by a single electron:  $E_{ox/sq}$  is more negative than  $E_{sq/rd}$ . At pH 7.0, the redox potential for the two-electron reduction of the free flavin is about  $E_m = -200$  mV (-219 mV for FAD, -205 mV for FMN, and -200 mV for RF) (Clark and Lowe, 1956). Reduction potential values for FMN at pH 7.0 and 20°C are  $E_{ox/sq} = -313$  mV and  $E_{sq/rd} = -101$  mV (Mayhew, 1999b).

### *Spectroscopic properties of flavins*

Spectroscopic properties of flavins depend on the redox and protonation state, due to their different distribution of electronic density along the isoalloxazine ring. In aqueous solvents, all oxidized flavins exhibit strong absorption in the ultraviolet and visible region, with four characteristic peaks at 220, 265, 375 (band II) and 445 nm (band I) (FIG I.5). The UV-visible absorption spectra is almost

independent of the substituent in N(10). However, there are subtle differences for FAD in the intensity of bands I and II, and in the position of band I (hypochromic displacement to 450 nm), due to the formation of an intramolecular complex between the isoalloxazine moiety and the adenine moieties (van den Berg *et al.*, 2001; Weber, 1950). The neutral semiquinone has a characteristic blue or green color (depending of the solvent) because it has a band of absorption around 500-600 nm (with a maximum at 580-600 nm) (**FIG I.5**). The anionic semiquinone shows red color and has low absorbance above 550 nm and has two maxima at 370 and 490 nm. The reduced flavins show a low absorption at the band I and II, and a shoulder around 290 nm (van den Berg *et al.*, 2002; Weber, 1950).

The neutral oxidized forms of flavins exhibit an intense yellow-green fluorescence, being the maxima of absorption and emission around 440-450 and 525-530 nm respectively (Sun *et al.*, 1972). For the free flavins, at neutral pH, the quantum yield of RF and FMN is 10-times higher than that of FAD, result of the interaction of the isoalloxazine ring and the adenine group of the nucleotide (which quenches the fluorescence of the isoalloxazine ring) (van den Berg *et al.*, 2002; Weber, 1950). Flavin fluorescence is highly dependent on solvent polarity, pH, temperature and position and nature of substituents in the isoalloxazine ring (Ghisla and Hemmerich, 1971; Sun *et al.*, 1972; Walker *et al.*, 1972). The fluorescent quantum yield of reduced flavins is very small.

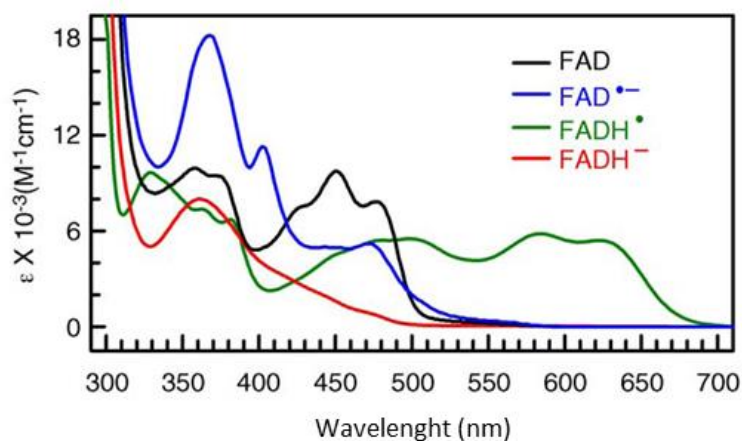


**Figure I.5.** UV-visible absorption spectra of the oxidized (black), reduced (red), anionic semiquinone (blue) and neutral semiquinone (green) of some FAD-dependent flavoproteins. Adapted from (Liu *et al.*, 2010)

The flavosemiquinone state has radical character (unpaired electron spin) and can also be studied by electron paramagnetic resonance (EPR) related methods. Those studies demonstrate that the spin density is mostly located in pyrazine rings (mainly at N(5)) and benzene (predominantly at CH<sub>3</sub>(8)), with lower density at the pyrimidine ring (Garcia *et al.*, 2002; Martínez *et al.*, 2016)

## II. SYNTHESIS OF THE RIBOFLAVIN PRECURSOR

### *De novo riboflavin biosynthesis*

Bacteria, fungi and plants have the ability to synthesize RF *de novo* (Barile *et al.*, 2016; Fischer and Bacher, 2006; García-Angulo, 2017). With a few variations in some reaction steps, the biosynthetic pathways are similar across kingdoms but they are surprisingly identical in eubacteria and plants. In all cases, each molecule of RF is synthesized from a molecule of guanosine 5'-phosphate (GTP) and two molecules of ribulose 5-phosphate (derived from glucose through the pentose phosphate pathway) (FIG I.6).

In a first step, GTP cyclohydrolase II (EC 3.5.4.25) catalyzes the hydrolytic opening of GTP imidazole ring producing 2,5-diamino-6-ribosylamino-4(3H)-pyrimidinone 5'-phosphate. GTP cyclohydrolase II can be found as a monofunctional enzyme (yeast and some bacteria) or as part of a bifunctional enzyme with 3,4-dihydroxy-2-butanone-4-phosphate synthase activity (EC 4.1.99.12) (some bacteria and plants). In archaea and some bacteria, this reaction is carried out by the sequential action of GTP cyclohydrolase III and formamide hydrolase. The product of GTP hydrolysis is converted to 5-amino-6-ribitylamino-2,4(1H,3H)-pyrimidinedione 5'-phosphate by two reaction steps, involving the hydrolytic cleavage of the position 2 amino group of the heterocyclic ring (EC 3.5.4.26) and the reduction of the ribosyl side chain (EC 1.1.1.193). The sequential order of these steps varies in different organisms. Whereas in bacteria the product is firstly deaminated and then reduced (catalyzed by a single bifunctional deaminase/reductase enzyme); in yeast and fungi, the reduction precedes the deamination. The final product, 5-amino-6-ribitylamino-2,4(1H,3H) pyrimidinedione 5'-phosphate, is dephosphorylated by a mechanism still unknown.

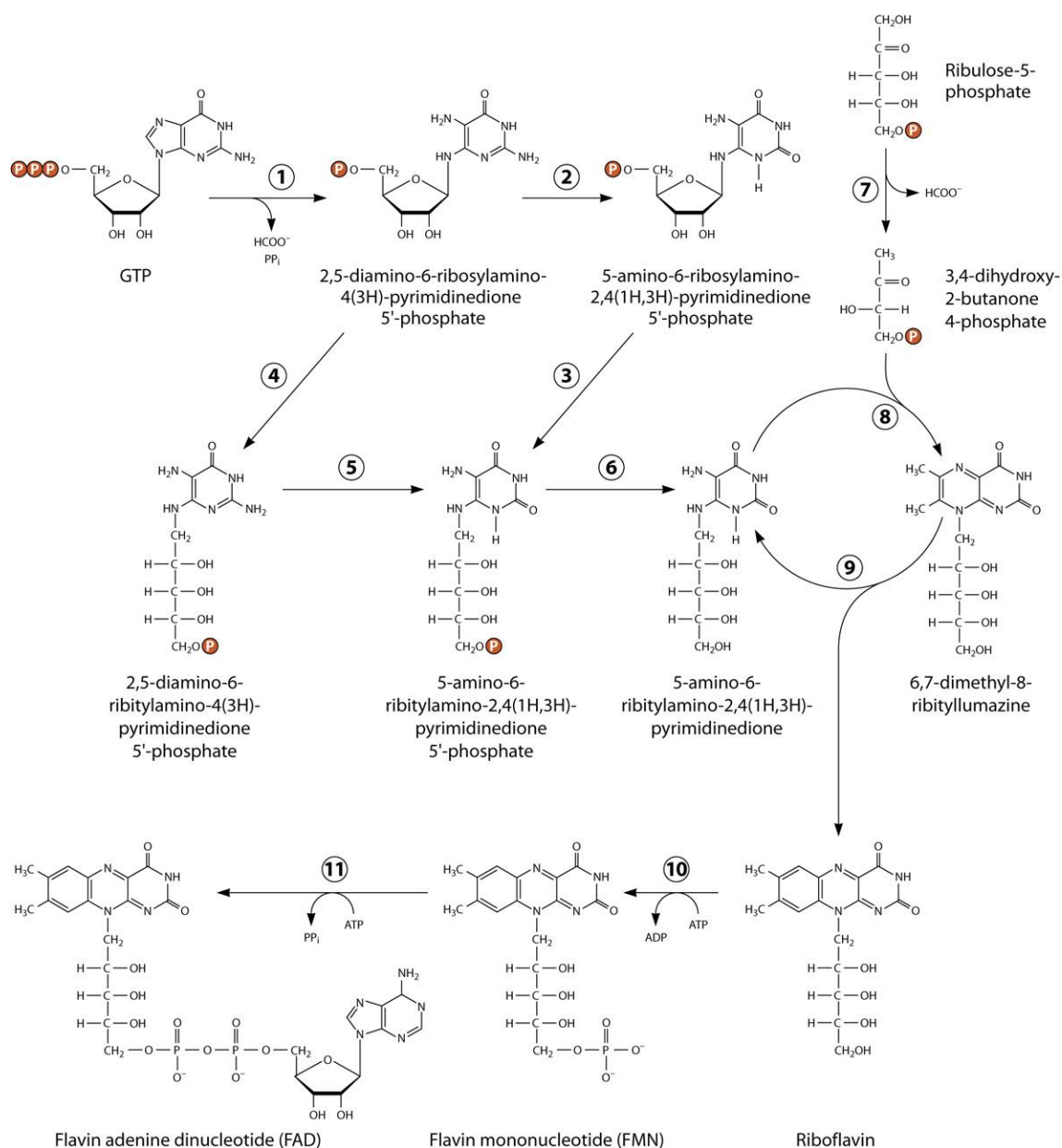


**Figure I.6.** Pathway for FAD biosynthesis in prokaryotes. The enzymes involved in the metabolic route are: GTP cyclohydrolase II (1), 2,5-diamino-6-ribosylamino-4(3H)-pyrimidinedione 5'-phosphate deaminase (2), 5-amino-6-ribosylamino-2,4(1H,3H)-pyrimidinedione 5'-phosphate reductase (3), 2,5-diamino-6-ribosylamino-4(3H)-pyrimidinedione 5'-phosphate reductase (4), 2,5-diamino-6-ribitylamino-4(3H)-pyrimidinedione 5'-phosphate deaminase (5), hypothetical phosphatase (6), 3,4-dihydroxy-2-butanone 4-phosphate synthase (7), 6,7-dimethyl-8-ribityllumazine synthase (8), riboflavin synthase (9), riboflavin kinase (10), and FAD synthase (11). Eubacteria and plants produce RF through (2) and (3) while yeasts utilize path through (4) and (5). Figure from (Abbas and Sibirny, 2011).

Formerly, the lumazine synthase (EC 2.5.1.78) catalyzes the condensation of 5-amino-6-ribitylamino-2,4(1H,3H) pyrimidinedione with 3,4-dihydroxy-2-butanone-4-phosphate (product of dihydroxy-2-butanone-4-phosphate synthase (EC 4.1.99.12) with ribulose 5-phosphate as substrate). The final step, catalyzed by the RF synthase (EC 2.5.1.9), comprises the dismutation of two molecules of 6,7-dimethyl-8-ribityllumazine (lumazine) into RF and 5-amino-6-ribitylamino-2,4(1H,3H) pyrimidinedione. The reaction produces RF and recycles the substrate of the lumazine synthase reaction. In some eubacteria, both lumazine and RF synthases form oligomeric assemblies that could favor substrate channeling and thus the enzymatic reaction.

In eubacteria, the enzymes performing the aforementioned steps are encoded by *rib* genes (with the exception of the dephosphorylation step, probably accomplished by low specificity hydrolases). It is noteworthy to highlight that the *rib* genes nomenclature is different between *Escherichia coli* and some Gram-positive bacteria, such as *Bacillus subtilis*. The latter organisms is used for RF industrial production (Duan *et al.*, 2010) and for this reason its *rib* operon has been so extensively characterized.

### ***Riboflavin transport***

Although most bacteria can synthesize RF, some species rely on external sources of RF and harbor specialized flavin transport systems. Nine different families of bacterial riboflavin transport system have been described, the energy-coupling factor (ECF)-RibU, PnuC/RibM, RibN, RfuABCD, ImpX, RibXYZ, RfnT, RibZ and RibV (Gutiérrez-Preciado *et al.*, 2015). Some bacterial species conserve both uptake genes (generally, expressed constitutively) and RF biosynthetic genes, only expressed when there is not an external RF source available. Moreover, it has also been reported that some bacterial strains can secrete flavins to the extracellular media (Marsili *et al.*, 2008; Mehta-Kolte and Bond, 2012; Yurgel *et al.*, 2014).

In eukaryotic organisms, sub-cellular compartmentalization entails an additional level of complexity and regulation in flavin metabolism and transport. Hence, there probably exist specific systems involved in flavin trafficking to the different organelles or cellular compartments (mitochondria, chloroplast, vacuoles, nucleus...) (Barile *et al.*, 2016; Gudipati *et al.*, 2014).

In addition to *de novo* biosynthesis, yeast species are capable of RF uptake. For example, to date, five RF transporters have been described in the yeast *Saccharomyces cerevisiae*: plasma membrane transporter MCH5 (flavin import from the extracellular media), flavin-antiporter Flx1p (exchange of mitochondrial-matrix FMN by cytosolic FAD) and three putative FLC transporters (transport of FAD to the endoplasmic reticulum).

Nonetheless, higher organisms have lost the ability to synthesize RF and they need to acquire it from the diet or to a lesser extent from its intestinal microflora's production. For instance, in the case of human nutrition, the daily recommended allowance for RF is 1.1-1.3 mg/day, which is mainly supplied by the consumption of vegetables, milk, eggs and cereals. In mammals, flavins from diet are transformed into RF by non-specific hydrolases and absorbed at the small and large intestine via carrier-mediated processes. Recently, five flavin transporters have been discovered: mitochondrial riboflavin transporter (mRF), mitochondrial FAD transporter and three plasma membrane transporters (hRFTV1, hRFTV2 and hRFTV3) (Spaan *et al.*, 2005; Yonezawa and Inui, 2013). These proteins have different subcellular and tissue-specific expression profiles, as well as functional and kinetic properties.

To date, data on RF transport mechanisms in archaea, fungi and plants, are still quite limited on the literature.

### ***Riboflavin supply pathways are tightly regulated***

The transcriptional organization of RF biosynthesis genes is highly variable among bacteria species. In the simplest cases, all *rib* genes are encoded by a single operon, as observed in *Bacillus* or *Mycobacteria* genomes (García-Angulo, 2017). This seems to allow the coordinated expression of all *rib* genes. However, genes can also be dispersed along the chromosome, such as in *E. coli*. Hence, each gene can be independently regulated to satisfy cellular requirements. Additionally, many bacteria have redundant duplications or incomplete RF biosynthetic genes.

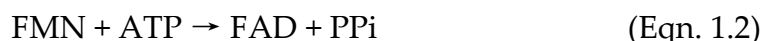
Both the *de novo* biosynthesis and the uptake of riboflavin is energetically costly for the microorganisms, consequently both processes are tightly regulated. As in other anabolic pathways, the first step of the pathway (GTP hydrolysis) is rate-limiting and could be inhibited by the product RF, at least in *B. subtilis* (Hümbelin *et al.*, 1999). Also, it has been reported the feedback inhibition of 6,7-dimethyl-8-ribityllumazine synthase from *Pichia guilliermondii* by RF



(Logvinenko *et al.*, 1973). Furthermore, apart from the regulation at the protein level, RF synthesis is regulated at the transcriptional and translational level. The most widely distributed regulatory factor is the FMN riboswitch (also termed RFN element), a sequence in the 5'-UTR that adopts a characteristic metabolite-dependent secondary structure (García-Angulo, 2017). FMN binding to the riboswitch avoids the transcription and/or translation by forming a terminator and by hiding the ribosome binding site (Winkler *et al.*, 2002). Therefore, this mechanisms couple RF needs with the expression of the genes required to produce it, avoiding waste of metabolic energy when intracellular flavin levels are sufficient. In some species (from bacteria to yeast and plants), a link between iron and RF metabolisms has been observed, since iron starvation induces *rib* gene expression and the replacement of iron-dependent enzymes by flavin-dependent enzymes (Crossley *et al.*, 2007; Fedorovich *et al.*, 1999; Sepúlveda Cisternas *et al.*, 2018; Welkie and Miller, 1960). Nonetheless, regulatory mechanisms are neither present in all organisms or genes (García-Angulo, 2017; Vitreschak *et al.*, 2002), or remain still uncharacterized.

### III. BIOSYNTHESIS OF THE FLAVIN COFACTORS

Independently on the endogenous or exogenous origin of RF, all the organisms transform RF into FMN and FAD through two sequential reactions. Firstly, a riboflavin kinase (RFK, ATP:riboflavin 5'phosphotransferase, EC 2.7.1.26) phosphorylates RF into FMN by transferring the  $\gamma$ -phosphate group from ATP to the C5' ribityl chain (Eqn. 1.1; reaction **(10)** in **FIG I.6**). After the phosphorylation step, an ATP:FMN adenylyltransferase (FMNAT, EC 2.7.7.2) activity converts FMN into FAD (Eqn. 1.2; reaction **(11)** in **FIG I.6**).



Although all organisms synthesize FMN and FAD from RF, they utilize different enzymes for that purpose.

In most of prokaryotes, both enzymatic reactions RFK and FMNAT are catalyzed by a single bifunctional enzyme, the type-I FAD synthase (FADS) (FIG I.7) (Herguedas *et al.*, 2010; Krupa *et al.*, 2003; Sebastián *et al.*, 2017a; Wang *et al.*, 2003, 2004). Its C-terminus RFK module is homologous to monofunctional eukaryotic RFKs. However, its N-terminus FMNAT module belongs to the *nucleotidyl-transferase* superfamily and differs from mammalian eukaryotic FMNATs. In addition to these type-I FADS bifunctional enzymes, some bacterial species own monofunctional enzymes with RFK and/or FMNAT activities (Solovieva *et al.*, 1999; Yruela *et al.*, 2010), and bifunctional enzymes different from type-I FADS. These latter enzymes show a N-terminus FMNAT module and a C-terminal module of unknown function, and are designated type-II FADS (Sebastián *et al.*, 2019; Yruela *et al.*, 2010).

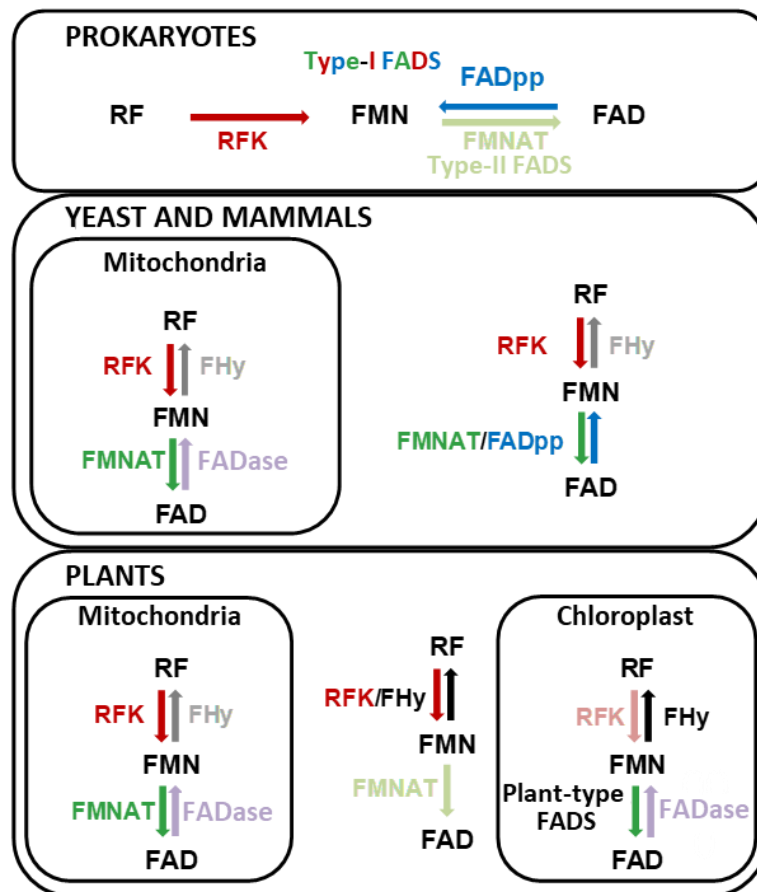


**Figure I.7.** Distribution of the activities related to FMN and FAD synthesis in the subcellular locations of different organisms. Enzymes in solid color have been purified and characterized biochemically. Enzymes shown with transparency have been predicted by bioinformatical analysis even though they have not been found experimentally. RFK (riboflavin kinase), FMNAT (FMN adenylyltransferase), FADase (FAD hydrolase), FADpp (FAD pyrophosphorilase), FHy (FMN hydrolase). Figure modified from (Medina, 2012).

Contrary to prokaryotes, two independent monofunctional enzymes catalyzing RFK and FMNAT activities are present in yeast, animals and, in general, non-photosynthetic eukaryotes (**FIG I.7**) (Barile *et al.*, 2000; Kasai *et al.*, 1990; Merrill Jr. and McCormick, 1980; Santos *et al.*, 2000). Monofunctional RFKs are ATP-dependent, and sequence analyses revealed a highly conserved PTAN motif and a glutamic residue that acts as catalytic base (Bauer *et al.*, 2003b; Karthikeyan *et al.*, 2003a, 2003b). Likewise, eukaryotic FMNATs are currently classified as member of the 3'-phosphoadenosine 5'-phosphosulfate (PAPS) reductase-like family, belonging to the adenine nucleotide  $\alpha$ -hydroxylase-like superfamily (Huerta *et al.*, 2009; Leulliot *et al.*, 2010; Santos *et al.*, 2000). Both proteins can present different isoforms with different sub-cellular location (mitochondria, nucleus, cytosol...) (Brizio *et al.*, 2006; Giancaspero *et al.*, 2013; Leone *et al.*, 2018; Miccolis *et al.*, 2012; Torchetti *et al.*, 2010).

In addition to the enzymes involved in FMN and FAD biosynthesis, eukaryotic cells harbor enzymes that hydrolyze FMN (FHy) in the cytosol and the intermembrane space (**FIG I.7**) (Barile *et al.*, 1997; Fischer and Bacher, 2006; Fuchs *et al.*, 1992; Granjeiro *et al.*, 1997; Lee and Ford, 1997; Sandoval *et al.*, 2008). Moreover, in *S. cerevisiae*, FAD pyrophosphatase (FADase) (EC 3.6.1.18) and FHy (EC 3.1.3.102) have also been reported in the mitochondrial inner membrane and in the matrix, respectively (Pallotta, 2011).

In plants, the situation is even more intricate, since additionally to the monofunctional RFKs and FMNATs, two different bifunctional enzymes can be found (**FIG I.7**) (Yruela *et al.*, 2010). One of them presents RFK activity in its C-terminus module, and hydrolase activity in its N-terminus one (Sandoval and Roje, 2005). The other bifunctional enzyme shows a N-terminus module similar to prokaryotic FMNATs, and a shorter C-terminal of unknown function (shorter than eukaryotic RFKs and without the PTAN motif) (Sandoval *et al.*, 2008). These plant bifunctional enzymes have been named as FADSs-type II and plant-like FADSs, respectively (Yruela *et al.*, 2010). The monofunctional RFKs and FMNATs have been found in multiple sub-cellular localizations (mainly mitochondria and cytosol but also in chloroplast) (Mitsuda *et al.*, 1970). However, the location of bifunctional enzymes is still not clear, but they might be located in mitochondrion and/or chloroplast, since they have location sequences for these organelles (Giancaspero *et al.*, 2009; Sandoval and Roje, 2005; Sandoval *et al.*, 2008).

Archaea possess two monofunctional proteins that are phylogenetically different from the eukaryotic counterparts. The archaeal RFKs use exclusively CTP as substrate (instead of ATP in eukaryotic RFKs) (Ammelburg *et al.*, 2007). The FMNATs belong to the *nucleotidyl-transferase* superfamily, although they do not show some of its characteristic motifs (Mashhadi *et al.*, 2008), and either ATP or CTP can be used as substrates.

### *Eukaryotic riboflavin kinases*

Monofunctional RFKs have been purified and characterized from yeasts (Santos *et al.*, 2000) and diverse mammal tissues (Kasai *et al.*, 1990; Kashchenko and Shavlovsky, 1976; McCormick *et al.*, 1997; Schrecker and Kornberg, 1950; Yamada *et al.*, 1990). Additionally, the crystallographic structures of the RFKs of *Schizosaccharomyces pombe* (*SpRFK*) and *Homo sapiens* (*HsRFK*) have been resolved (Bauer *et al.*, 2003b; Karthikeyan *et al.*, 2003a, 2003b).

In general, RFKs are cytosolic enzymes of 18-24 kDa (Merrill and McCormick, 1980; Yamada *et al.*, 1990) and their expression levels are particularly high in brain, placenta, bladder, liver and intestine of higher organisms. However, mitochondrial isoforms have also been identified in yeast and other eukaryotic organisms, including plants and animals (Barile *et al.*, 2000; Giancaspero *et al.*, 2009; Mitsuda *et al.*, 1970; Sandoval *et al.*, 2008; Santos *et al.*, 2000).

RFKs catalyze the phosphorylation of RF into FMN, using exclusively ATP as phosphate donor (Merrill and McCormick, 1980; Yamada *et al.*, 1990). However, some RFKs show moderate activity using other nucleotides as substrates (as GTP) (Kashchenko and Shavlovsky, 1976). Apart from RF, eukaryotic RFKs can also phosphorylate a wide variety of RF-analogs (Kashchenko and Shavlovsky, 1976; Kearney, 1952; McCormick and Butler, 1962), being the determinants of specificity the length of 4-6 C-atoms of the N(10) substituent, the substitution in positions 7 and 8, and the absence of substituents in N(3) and N(5) (McCormick and Butler, 1962). The RFK activity also requires of the presence of a divalent cation, such as Zn<sup>2+</sup> or Mg<sup>2+</sup> (Nakano and McCormick, 1991).

Nowadays, the tridimensional structures of the RFKs of *S. pombe* (PDB entries 1N05, 1N06, 1N07 and 1N08) (Bauer *et al.*, 2003b) and *H. sapiens* (PDB entries 1NB0, 1NB9, 1P4M and 1Q9S) (Karthikeyan *et al.*, 2003a, 2003b) are available, both free and/or in complex with their ligands (substrates and products of the RFK reaction). Both RFKs fold into a six-stranded antiparallel  $\beta$ -barrel core with

Greek key topology and some segments of  $\alpha$ -helix located mainly at the C-terminal end (**FIG I.8**). The adenine nucleotide is located between a glycine-rich loop, a short  $3_{10}$ -helix, and a reverse turn leading to a short  $\beta$ -strand that contains the most conserved PTAN sequence motif (Bauer *et al.*, 2003b; Karthikeyan *et al.*, 2003a). This motif is implicated in the coordination of the divalent cation and the binding of the triphosphate moiety of ATP. In contrast, the flavin binds in a pocket between the surface of the  $\beta$ -barrel and an  $\alpha$ -helix, with the ribityl moiety extended to the nucleotide binding site. This folding represented a new fold in the kinase family with a novel nucleotide binding motif never previously described (Cheek *et al.*, 2005; Karthikeyan *et al.*, 2003a).

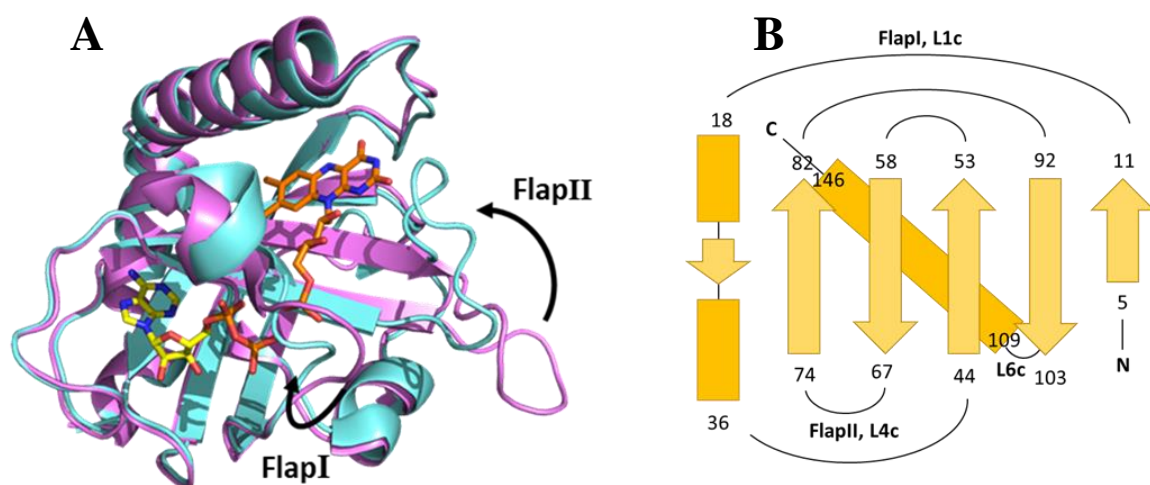


**Figure I.8.** Structural properties of *HsRFK*. **(A)** Crystallographic structures of *HsRFK* in complex with FMN and ADP showing the FlapII loop in either open (PDB ID 1P4M, in purple) or closed conformation (PDB ID 1Q9S, in blue). FMN and ADP ligands are shown as CPK colored sticks colored with carbons in orange and yellow, respectively. **(B)** Topology of *HsRFK*, with  $\alpha$ -helices as dark rectangles and  $\beta$ -strands as light arrows. Numbers indicate residue positions.

Despite the overall structural identity among the RFK available structures, differences are found in the conformation of the loops constituting the adenine and flavin binding sites, termed FlapI and FlapII (**FIG I.8A**) (Karthikeyan *et al.*, 2003a, 2003b). These variations regarding the apo-RFK and in complex with different combinations of ligands (ADP, RF:ADP and FMN:ADP) point to drastic conformational changes upon substrate binding and catalysis.

The structure of the apo-form has only been resolved for *Sp*RFK (PDB entry 1N05). However, high sequence identity between eukaryotic RFKs suggest that *Sp*RFK structure is a representative model of the whole family (Bauer *et al.*, 2003b; Karthikeyan *et al.*, 2003b). In this structure, FlapI collapses onto the  $\beta$ -barrel and blocks the adenine binding site, hampering ATP binding; whereas FlapII is disordered (not observed in the crystallographic structure), leaving the flavin pocket accessible to RF. Hence, this structure suggests that the RFK activity occurs through a sequential ordered bi-bi mechanism in which the preferred pathway is for RF to bind to the enzyme first followed by ATP. Binding of RF might induce a conformational change both in FlapII, that encloses the flavin into the protein, and in FlapI, opening the adenine binding site to ATP, as observed in the crystallographic structures of RFK in complex with ADP and RF/FMN. After the catalysis, the FMN is blocked by FlapII, whereas ADP is completely solvent exposed, favoring its release. Finally, both protein loops might acquire the initial conformation, in which the flavin binding site is open for FMN product dissociation.

### *Eukaryotic FMN adenylyltransferases*

FMN adenylyltransferases (FMNAT, but also referred as FAD synthases, FADS) have been purified and characterized from yeast (Huerta *et al.*, 2009; Wu *et al.*, 1995), rat liver (Gomes and McCormick, 1983; McCormick *et al.*, 1997), and *Homo sapiens* (Brizio *et al.*, 2006; Galluccio *et al.*, 2007). The crystallographic structure has been resolved for the FADS from the yeasts *Saccharomyces cerevisiae* (ScFMNAT) and *Candida glabrata* (CgFMNAT) (Huerta *et al.*, 2009; Leulliot *et al.*, 2010), but not for the human protein (*h*FADS).

In yeast and fungi, FMNATs are monofunctional enzymes with a *PAPS reductase-like* domain, which has conserved motifs different from those of *nucleotidyl-transferases* (FMNAT modules of bifunctional prokaryotic FADS). Nonetheless, an additional domain is found at the N-terminus of FMNATs of higher eukaryotes, including *H. sapiens*. This module resembles *molybdopterin-binding* (MPTb) domain and harbors FAD pyrophosphatase activity (Cialabrini *et al.*, 2013; Giancaspero *et al.*, 2015a). Therefore, these latter enzymes are bifunctional FMNAT/FADases that can both synthesize and hydrolyze FAD in response to the physiological state of the cell.

Eukaryotic FMNATs are enzymes of 30-40 kDa (monofunctional fungi FMNATs) or 50-60 kDa (bifunctional FMNAT/FADases), and their subcellular location is still controversial since both FMNAT and FADase activities are detected in almost all cellular compartments (Bafunno *et al.*, 2004; Giancaspero *et al.*, 2013; Torchetti *et al.*, 2010, 2011). Furthermore, these enzymes are constitutively expressed in all tissues, but their expression levels are particularly high in brain, placenta, bladder, liver and gastrointestinal tract of higher organisms (Expression Atlas, <http://www.ebi.ac.uk/gxa>) (Papatheodorou *et al.*, 2018).

FMNATs catalyze the adenylation of FMN into FAD, using exclusively ATP as adenylyl donor (Bowers-Komro *et al.*, 1989; Schrecker and Kornberg, 1950). Hence, no enzymatic activity is detected when using AMP, ADP, dATP, TTP, UTP, CTP or GTP as nucleotide donors. Nonetheless, although these enzymes show higher enzymatic activity with FMN as substrate, a wide variety of FMN-analogs can be adenylated. The determinants of specificity are the absence of substitutions in the pyrimidine portion of the isoalloxazine ring (CO and NH groups at positions 2 and 3), and the length of 5-6 C-atoms of the N(10) substituent (Bowers-Komro *et al.*, 1989). Additionally, the FMNAT activity has a strict requirement of Mg<sup>2+</sup>, although other divalent cations as Co<sup>2+</sup>, Mn<sup>2+</sup>, Ca<sup>2+</sup> and Zn<sup>2+</sup> can be used with less efficiency (Bowers-Komro *et al.*, 1989; McCormick *et al.*, 1997; Torchetti *et al.*, 2011).

The FMNAT activity follows an sequential ordered bi-bi mechanism in which ATP binds first to the enzyme followed by FMN, and product pyrophosphate (PPi) is released first followed by the release of FAD (Giancaspero *et al.*, 2015a; Huerta *et al.*, 2009; Oka and McCormick, 1987; Yamada *et al.*, 1990). Both products of the forward reaction (FAD and PPi), as well as nucleotides other than ATP, act as inhibitors of the FMNAT activity (Bowers-Komro *et al.*, 1989; Torchetti *et al.*, 2011). Additionally, FAD release may represent the rate-limiting step of the whole catalytic cycle and is consistent with the proposed role of eukaryotic FMNATs as *FAD chaperones*: these enzymes do not only synthesize FAD but also deliver it to the recipient apo-flavoproteins through protein-protein interactions (Giancaspero *et al.*, 2015b; Torchetti *et al.*, 2011).

Structural information of eukaryotic FMNATs is limited to ScFMNAT in complex with FAD (PDB entry 2WSI) (Leulliot *et al.*, 2010), and CgFMNAT (PDB entries 3FWK, 3G6K, 3G59 and 3G5A), free and in complex with the substrates or products of the FMNAT reaction (Huerta *et al.*, 2013). In both FMNATs, the

PAPS reductase-like domain has an  $\alpha/\beta$  fold with a twisted six-stranded  $\beta$ -sheet sandwiched by  $\alpha$ -helices, organized into a non-canonical Rossmann-fold (Dym and Eisenberg, 2001; Rossmann *et al.*, 1974). The ATP nucleotide binds in a crevice formed at the  $\beta$ -sheet, with its  $\beta\gamma$ -phosphate tail positioned in an anion-binding pocket near the N-terminus of  $\alpha 3$  (Huerta *et al.*, 2009). The flavin binding site is located on the same side of the central  $\beta$ -sheet than the ATP, in a groove created by the loop connecting  $\beta 5$  to  $\beta 6$ , helix  $\alpha 5$  and the  $\beta$ -sheet. Within this site, the adenylyl (of ATP or FAD) and isoalloxazine moieties (of FMN or FAD) are packed against each other and face inwards, and the phosphoribityl moiety faces to the solvent (Huerta *et al.*, 2009; Leulliot *et al.*, 2010). Therefore, FAD adopts a bent conformation, different from those observed in other FMN- or FAD-flavoproteins (Dym and Eisenberg, 2001), emphasizing this flavin-binding mode as a characteristic of eukaryotic FMNATs. Furthermore, the  $Mg^{2+}$  cation in the ternary complexes stabilize the phosphate groups of the substrates and products, positioning them in an optimal configuration for the adenylyl transfer reaction.

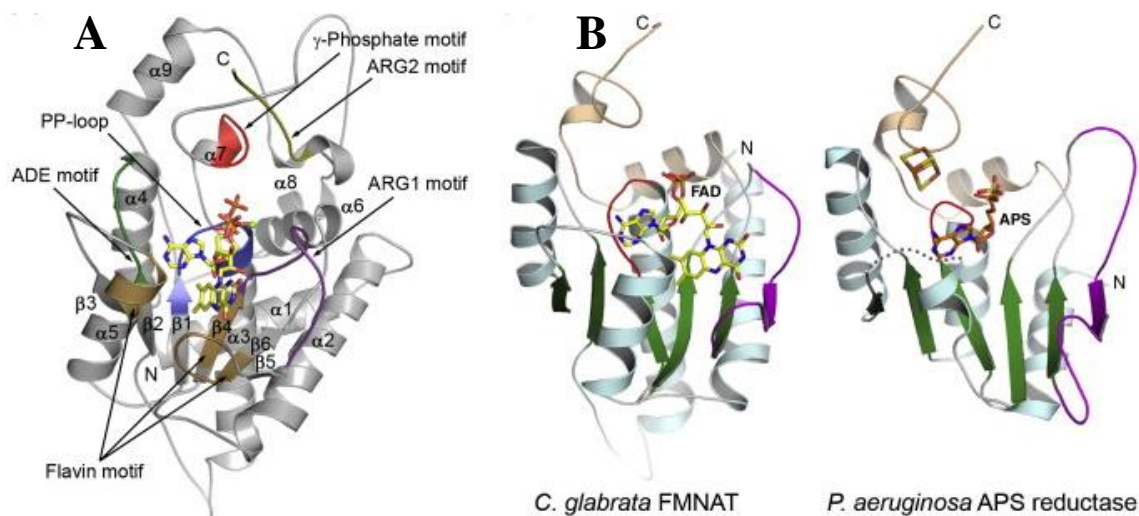


**Figure I.9.** (A) Crystallographic structure of CgFMNAT in complex with the products FAD, PPi and  $Mg^{2+}$  (PDB ID 3G6K). Secondary structure elements are labeled, together with structural motifs involved in substrate binding and catalysis. (B) Comparison of CgFMNAT with the closely related APS reductase of *P. aeruginosa*. Equivalent structural motifs are colored similarly. The characteristic PP-loop motifs are shown in red. Regions that deviate from the typical Rossmann-fold topology are shown in magenta. FAD and APS are shown as CPK colored sticks colored with carbons in orange and yellow, respectively. Figure from (Huerta *et al.*, 2009)



Altogether, the crystallographic structures are consistent with the proposed catalytic mechanism for eukaryotic FMNATs (Giancaspero *et al.*, 2015b; Huerta *et al.*, 2009; Leulliot *et al.*, 2010). ATP binds preferentially to the apo-enzyme, as its binding site would be partially blocked by FMN otherwise. Additionally, the presence of ATP may induce the binding and proper allocation of FMN through the interaction of its isoalloxazine ring with the adenosine moiety of ATP. Although the phosphoribityl tails of FMN is highly flexible and can adopt multiple conformations (as observed in the crystallographic structure of the substrate tertiary complex), this part of the FMN substrate would move close the  $\alpha$ -phosphate of ATP during the adenylation reaction. The cleavage of the  $\alpha\beta$ -phosphodiester bond is facilitated by the coordination of the  $Mg^{2+}$  ion. After the catalysis, subtle structural rearrangements are observed: the PPi group is in the same position as the  $\beta\gamma$ -phosphates of the ATP interacting with the same set of protein residues and the  $Mg^{2+}$  cation. Dissociation of PPi induces a conformational change in the  $\beta 4$ - $\beta 5$  loop, allowing release of the FAD reaction product.

#### *Human FAD synthase*

In *Homo Sapiens*, *hFADS* is encoded by the gene *FLAD1*, located on chromosome 1 at 1q21.3. Up to six isoforms have been identified as a result of alternative splicing of the same gene (**FIG I.10**) (UniProtKB database, <https://www.uniprot.org> - Q8NFF5). The three longest isoforms (*hFADS1*, 2 and 3) contain both FMNAT and FADase domains (Brizio *et al.*, 2006; Galluccio *et al.*, 2007; Torchetti *et al.*, 2011). However, two isoforms (*hFADS3* and 4) lack the *PAPS reductase* module, meanwhile the last isoform discovered (*hFADS6*) lacks the FADase module (Leone *et al.*, 2018; Olsen *et al.*, 2016). These isoforms also differ in subcellular location as well as in catalytic efficiencies and ion requirements. For example, *hFADS1* has an additional N-terminal putative mitochondrial targeting peptide, and therefore localizes in the mitochondria (Torchetti *et al.*, 2010); whereas *hFADS2* is a cytosolic isoform. In addition, FMNAT activity has also been detected in the cellular nucleus (Giancaspero *et al.*, 2013), but the nuclear isoform has not been characterized to date. Altogether, subcellular distribution of *hFADS* isoforms, together with flavin transporters, might contribute to create different flavin cofactor pools, constituting a *flavin network* presumably involved in the regulation of metabolism and homeostasis (Barile *et al.*, 2016; Giancaspero *et al.*, 2015b).

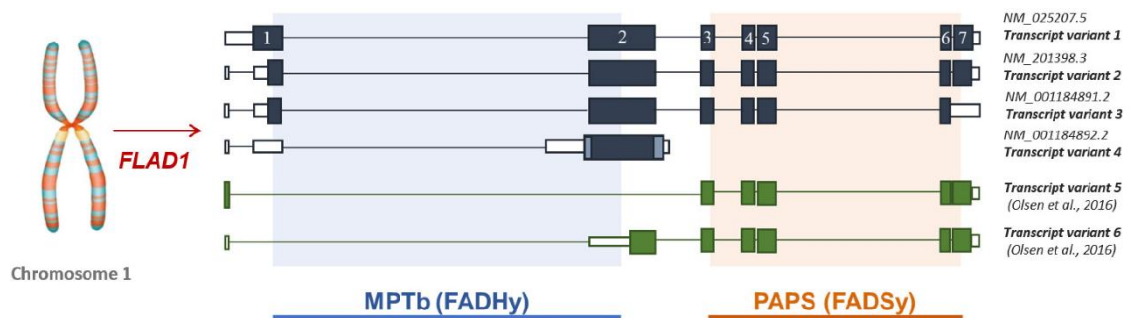


**Figure I.10.** Schematic representation of *FLAD1* transcript variants reported in RefSeq (colored in dark blue) and in (Olsen *et al.*, 2016) (in green). Colored boxes represent coding regions, while lines represent introns. The two functional domains of the longest isoforms are colored in the background. Figure from (Tolomeo *et al.*, 2020).

To date, there is no crystallographic information available for any of the *hFADS* isoforms, but some structural models have been built based on the published yeast FMNATs for the C-terminal domain and CinA of *Thermoplasma acidophilum* for the N-terminal domain (Leone *et al.*, 2018; Miccolis *et al.*, 2012, 2014; Taleb *et al.*, unpublished results).

*hFADS* has been associated with cancer development and progression (breast, gastric, liver and renal cancers), and with several diseases, some of which are responsive to the treatment with RF (Hu *et al.*, 2020; Tolomeo *et al.*, 2020). For example, mutations in *FLAD1* have been linked to LSMFLAD (lipid storage myopathy due to *FLAD1* deficiency – OMIM #255100), an autosomal recessive inborn defect in metabolism resulting in a RF responsive and not responsive mitochondrial myopathy (Muru *et al.*, 2019; Olsen *et al.*, 2016; Ryder *et al.*, 2019). The biochemical abnormalities of this disease (cyclooxygenase defect, decreased activities of mitochondrial complexes I and IV, elevation of multiple acylcarnitines...) resemble those observed in MADD (multiple acyl-CoA dehydrogenase deficiency – OMIM #231680), hence both diseases are usually confused. In addition, deregulation of flavin homeostasis, as a consequence of *FLAD1* deficiency, has also been associated with amyotrophic lateral sclerosis (ALS – OMIM #105400), a degenerative disease affecting motor neurons that control voluntary muscles (Tolomeo *et al.*, 2020).

### *Prokaryotic FAD synthases*

To date, multiple prokaryotic bifunctional FAD synthases (FADs) with RFK and FMNAT activities have been cloned, purified and characterized (Grill *et al.*, 2008; Kearney *et al.*, 1979; Manstein and Pai, 1986; Matern *et al.*, 2016; Sebastián *et al.*, 2017a, 2019; Wang *et al.*, 2004). These FADs are typically 310-340 residues in length (~36 kDa) and are folded in two nearly independent modules, each one mainly involved in one of the activities (Herguedas *et al.*, 2010; Wang *et al.*, 2003). The C-terminal module catalyzes the RFK activity, while the N-terminal module carries out the FMNAT reaction; therefore, they are usually referred as the RFK and FMNAT modules, respectively.

The RFK-module (~ 180 aa) shows an overall topology similar to that found in the eukaryotic RFKs, with differences only observed in the loops connecting secondary structure elements (Bauer *et al.*, 2003b; Karthikeyan *et al.*, 2003a). This module exhibits several consensus sequences GxVxxGxxG, G(F/Y)PT(A/L/I/V)N (including the substrate binding PTAN motif), PxxG(V/I)(Y/F), PT(F/V/I), and (L/V/I)Ex(H/F/Y/N)x(F/L)(D/N)(F/W/Y)xx(D/N/E)(L/I/A/V)Y(G/D/N], as well as the glutamic residue that acts as catalytic base (**FIG I.11**) (Cheek *et al.*, 2005; Frago *et al.*, 2008; Herguedas *et al.*, 2015).

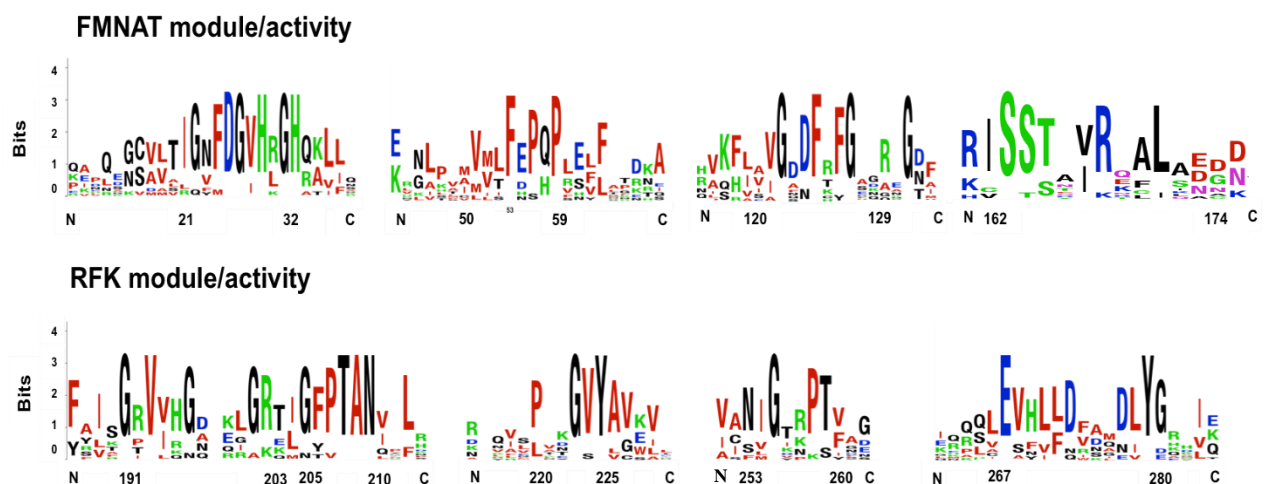


**Figure I.11.** Sequence logos of the consensus motifs of bifunctional Type I FADs. The numeration of *CaFADs* is used as reference. The sequence logo was produced using the WebLogo server (<http://weblogo.berkeley.edu>) (Crooks *et al.*, 2004).

The FMNAT module of FADSs consists of an  $\alpha/\beta$ -dinucleotide binding domain with a typical Rossmann fold topology (~ 150 aa). It presents several consensus sequences, GxFDGxHxGH and SS(T/S)x(I/V)R, which are also conserved in nucleotidyl-transferases, as well as other exclusive motifs such as FxP(H/Q)P and G(D/N)(F/Y/H)x(F/Y)G (**FIG I.11**) (Frago *et al.*, 2008). Moreover, prokaryotic FMNAT modules differ from eukaryotic FMNATs (or FADSs) both in sequence and structure, and hence they have been proposed as potential antimicrobial targets (Serrano *et al.*, 2013b)

The first tridimensional structure reported for a FADS was that from *Thermotoga maritima* (*Tm*FADS) both free and in complex with different ligands (PDB entry 1MRZ and 1T6Y) (Wang *et al.*, 2003, 2005). Nowadays, the structures of two additional bacterial FADSs are available: the FADSs from *Streptococcus pneumoniae* (*Spn*FADS, PDB entry 3OP1) (unpublished results) and *Corynebacterium ammoniagenes* (*Ca*FADS, PDB entry 2X0K) (Herguedas *et al.*, 2009, 2010). Additionally, the crystallographic structure of the *Ca*FADS RFK-module in complex with its ligands (PDB entries 5A8A, 5A88 and 5A89) has been also reported (Herguedas *et al.*, 2015).

The FADS from *C. ammoniagenes* is hitherto the best characterized member of this family from both functional and structural points of view (Arilla-Luna *et al.*, 2019; Efimov *et al.*, 1998; Frago *et al.*, 2008, 2009; Herguedas *et al.*, 2009, 2010, 2015; Marcuello *et al.*, 2013; Sebastián *et al.*, 2017b; Serrano *et al.*, 2013a, 2015, 2017, 2012). Nonetheless, other family members, such as the FADSs from *Bacillus subtilis* (*Bs*FADS) (Kearney *et al.*, 1979), *Streptomyces davawensis* (*Sd*FADS) (Grill *et al.*, 2008), *Streptococcus pneumoniae* (*Sp*FADS) (Sebastián *et al.*, 2017a, 2018a) and *Listeria monocytogenes* (*Lm1*FADS and *Lm2*FADS) (Matern *et al.*, 2016; Sebastián *et al.*, 2019) have been recently characterized. The reported differences among prokaryotic FADS include (i) the stabilization or not of transient oligomeric assemblies during catalysis, (ii) the differential modulation of RFK activity by substrates and products, (iii) the influence of the redox state of the substrates in the efficiency of RFK and/or FMNAT activities, and (iv) the cooperation in the binding of substrates and products (Grill *et al.*, 2008; Herguedas *et al.*, 2010; Kearney *et al.*, 1979; Sebastián *et al.*, 2017b, 2017a, 2018a, 2019). These differential characteristics point to species-specific strategies to regulate the biosynthesis of FMN and FAD.

***The FADS from *Corynebacterium ammoniagenes* is the best characterized member of the family***

The FADS from *C. ammoniagenes* (CaFADS) was firstly reported in 1976 as an enzyme for 5-deazaFAD synthesis from 5-deazariboflavin (Fisher *et al.*, 1976). However, it was not purified to homogeneity and further characterized until 1986 (Manstein and Pai, 1986). In 2010, the crystallographic structure of CaFADS was determined at 1.95 Å resolution (PDB entry 2X0K) (Herguedas *et al.*, 2009, 2010).

*CaFADS enzymatic activity and substrate binding*

The CaFADS is constituted by a single polypeptide of 338 residues (approximately 38 kDa of molecular weight) and an isoelectric point of 4.6. As other FADSs, it catalyzes the RF phosphorylation into FMN and the subsequent adenylation of FMN into FAD. The RFK reaction is irreversible while the FMNAT activity can be reverted to transform FAD into FMN and ATP in the presence of PPi (FADpp activity) (Efimov *et al.*, 1998).

Both enzymatic activities have different optimum conditions (Hagihara *et al.*, 1995; Manstein and Pai, 1986; Nakagawa *et al.*, 1995). The FMNAT reaction was described as dependent of the presence of the divalent cation Mg<sup>2+</sup>, whereas the RFK activity was reported to occur even in its absence (but considerably less efficiently) (Manstein and Pai, 1986). Nevertheless, the optimum Mg<sup>2+</sup> concentration for each reaction differs, being 0.8 mM for the RFK activity and 10 mM for the FMNAT one. The optimum pH and temperature were 7.8-8 and 35-37 °C for the RFK reaction and 7.0-7.4, 37-40 °C for the FMNAT one (Hagihara *et al.*, 1995; Manstein and Pai, 1986).

A key feature of CaFADS is the strong inhibition that is observed in its RFK activity when the RF substrate concentration is increased beyond ~7.5 μM (Herguedas *et al.*, 2015; Serrano *et al.*, 2013a). It has been suggested that the RF inhibitory effect might be related to the formation of non-productive enzyme-substrate (or enzyme-products) complexes (Sebastián *et al.*, 2017b; Serrano *et al.*, 2013a). In the case of the FMNAT activity, no inhibition is observed for any of the substrates, FMN and ATP (Arilla-Luna *et al.*, 2019; Serrano *et al.*, 2012).

The enzymatic activity of CaFADS is not only restricted to RF, since this enzyme exhibits a wide specificity or promiscuity to other RF-analogs (Frago *et al.*, 2010; Iamurri *et al.*, 2013; Mack and Grill, 2006; Miller and Edmondson, 1999;

Spencer *et al.*, 1976). The substrate specificity determinants comprise the position 3 of the isoalloxazine ring, the existence of a hydroxyl group at 5' and a substitution at position 7 (Walsh *et al.*, 1978). However, the protein is absolutely specific for ATP (Manstein and Pai, 1986), without detectable enzymatic activity with other nucleotides.

Both catalytic cycles follow a sequential ordered bi-substrate mechanism with the formation of an intermediate ternary complex. In the RFK cycle, ATP binds the enzyme before RF, and after the phosphorylation the FMN and ADP are released sequentially (Efimov *et al.*, 1998; Sebastián *et al.*, 2017b). In the FMNAT cycle, FMN binds to CaFADS after ATP, and PPi is released before FAD (Efimov *et al.*, 1998).

Early studies proposed two independent binding sites for adenine nucleotides, associated to RFK and FMNAT activities, and a single site for flavin binding, shared by both enzymatic activities (Efimov *et al.*, 1998). Nonetheless, subsequent studies on substrates binding through ITC demonstrate the existence of two independent flavin binding sites, one in each protein module (Frago *et al.*, 2009). Additionally, it has been demonstrated that substrate binding modulates the affinity for the other ligands, through ligand-induced structural rearrangements in the catalytic site (Frago *et al.*, 2009; Herguedas *et al.*, 2015; Sebastián *et al.*, 2017b). Therefore, CaFADS suffers a series of conformational reorganizations during substrate binding in order to accommodate the substrates in the active site and to stabilize the transition state, but also for the further release of the products of the reaction. This interaction model was further validated by the crystallographic structures of CaFADS and its truncated RFK-module (Herguedas *et al.*, 2010, 2015).

#### *CaFADS folds in two modules related to its RFK and FMNAT activities*

The analysis of the CaFADS primary structure reveals that this protein shows all the consensus sequences of RFKs and prokaryotic FMNATs (**FIG I.11**) (Frago *et al.*, 2008; Yruela *et al.*, 2010). The crystallographic structure of CaFADS has been obtained at 1.95 Å resolution (PDB entry 2X0K) (Herguedas *et al.*, 2010). The asymmetric unit contains two chains of 338 residues with similar overall folding but subtle differences in loop conformation.

The *CaFADS* monomer is a  $\sim 70$ -Å prokaryotic type-I FADS folded in two structural domains, similarly to other crystallized FADS (Sebastián *et al.*, 2017a; Wang *et al.*, 2003). The N-terminus FMNAT module (residues 1-186) shows an  $\alpha/\beta$  dinucleotide binding domain with a Rossmann fold topology (Rossmann *et al.*, 1974). This module owns a parallel  $\beta$ -sheet compound by six strands ( $\beta 1n$ – $\beta 6n$ ) and five  $\alpha$ -helixes ( $\alpha 1n$ – $\alpha 5n$ ) distributed at both sides of the  $\beta$ -sheet. At the end of the module a small subdomain built by a  $\beta$ -hairpin ( $\beta 7n$  and  $\beta 8n$ ) and two short  $\alpha$ -helixes ( $\alpha 6n$  and  $\alpha 7n$ ) can be found (FIG I.12). The main differences between the FMNAT modules of *CaFADS* and other family members are found at the strand  $\beta 1n$  (absent in *TmFADS* and other members of the *nucleotidyl-transferase* superfamily), the loops connecting secondary structure elements (L1n, L4n, L6n and L8n) and the subdomain at the end of the N-terminus module (Arilla-Luna *et al.*, 2019; Serrano *et al.*, 2017).

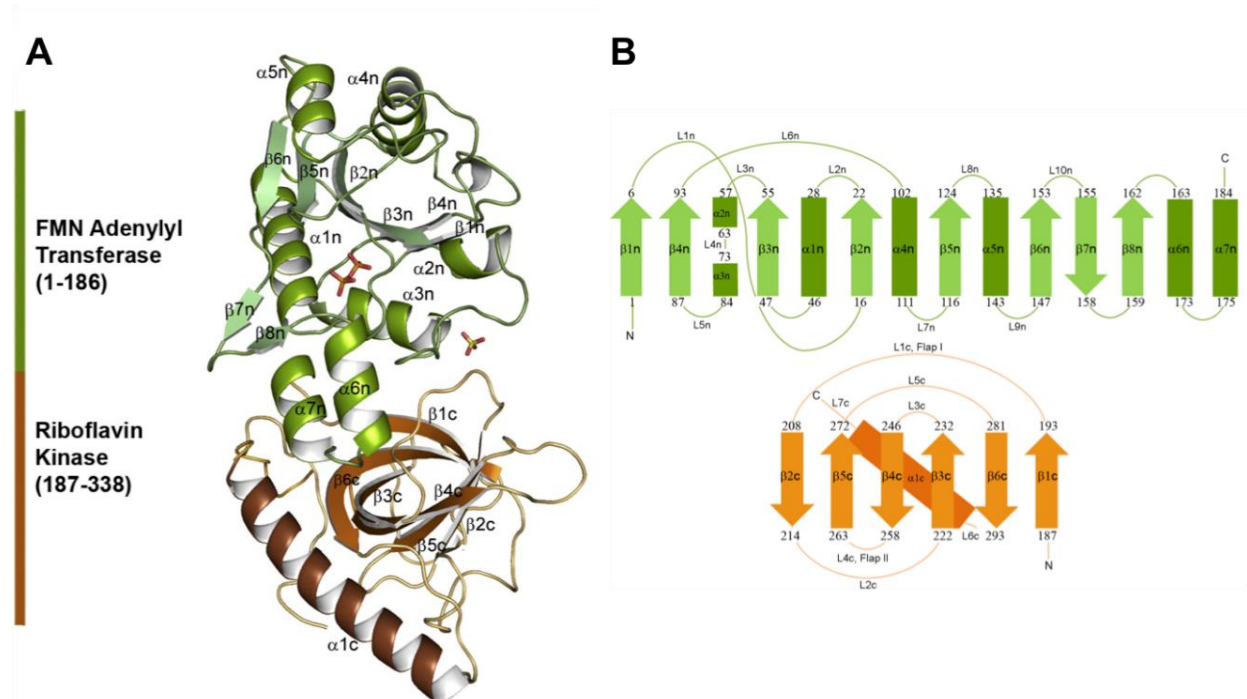


**Figure I.12.** (A) Overall structure of *CaFADS* showing the different secondary structure elements (PDB ID 2X0K). Sulfate and PPi are displayed as sticks. (B) Scheme of the *CaFADS* topology, with the names assigned to every element of secondary structure. The C-terminal or RFK domain is displayed in orange, while the N-terminal or FMNAT one is shown in green. Figure from (Herguedas *et al.*, 2010).

The *CaFADS* C-terminal module (residues 187-338) folds in a globular domain formed by a  $\beta$ -barrel with six antiparallel  $\beta$ -strands ( $\beta$ 1c-  $\beta$ 6c), a long  $\alpha$ -helix ( $\alpha$ 1c) and seven loops connecting them (**FIG I.12**) (Herguedas *et al.*, 2010). This domain displays sequence and structural homology to monofunctional RFKs and other FADS RFK-modules (Sebastián *et al.*, 2017a; Wang *et al.*, 2003), but *CaFADS* owns a 12 residues insertion in L3c (Leu232-Val246) that is only observed in corynebacteria and mycobacteria (Frago *et al.*, 2008; Herguedas *et al.*, 2010). Other differences include **(1)** the conformation of the loops L1c or FlapI (V193-T208) and L4c or FlapII (P258-E263), both involved in the stabilization of nucleotides and flavins (Herguedas *et al.*, 2015; Karthikeyan *et al.*, 2003b); **(2)** the position of the P207 and T208 residues at the 207-PTAN-210 motif (Frago *et al.*, 2008), and **(3)** the presence of a 15 residues loop (L7c, A324-S338) in two different conformations (**FIG I.13**), that is absent in eukaryotic RFKs, as *HsRFK* or *SpRFK*.

Both RFK and FMNAT modules interact with each other through H-bonds and the formation of a hydrophobic core that provides rigidity to their interface. Loop L2c, which is implicated in these inter-domain interactions, is an  $\alpha$ -helix in eukaryotic RFKs (Herguedas *et al.*, 2010).

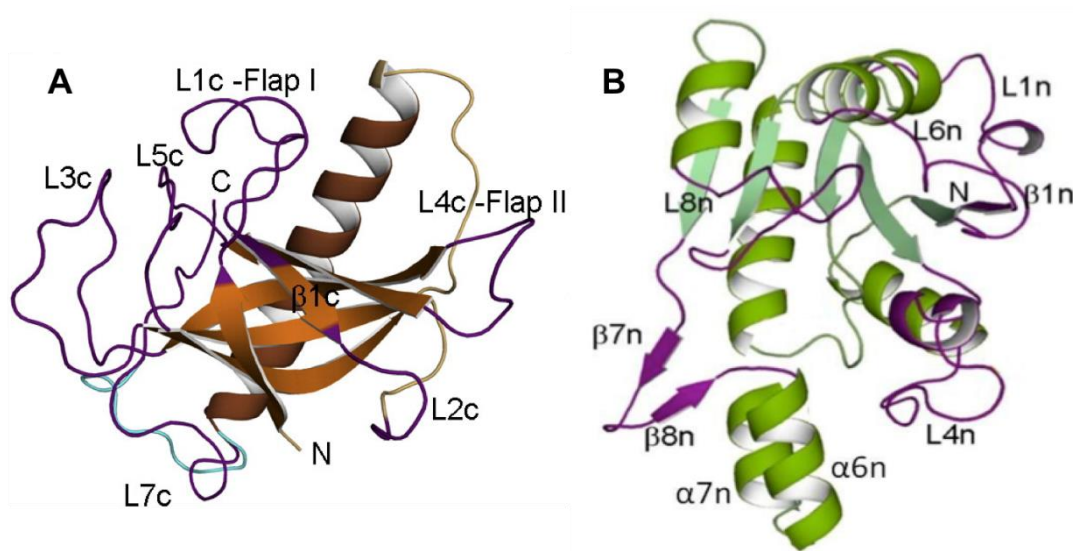


**Figure I.13.** Detailed cartoon representation of the RFK (**A**) and FMNAT (**B**) modules of *CaFADS* (PDB ID 2X0K). RFK and FMNAT modules are represented in orange and green, respectively, with their loops in purple. Secondary structure elements are labeled. In (**A**), the alternative conformation of loop L7c is shown in light blue. Figure adapted from (Herguedas *et al.*, 2010).



### *Conformational rearrangements upon CaFADS RFK catalytic cycle*

CaFADS crystallographic structures are available for the full-length protein free of ligands (apo form, PDB ID ), as well as for the RFK module in complex with adenine and flavin nucleotide ligands (holo forms) (**FIG I.14A**) (Herguedas *et al.*, 2015): binary RFK:ADP-Mg<sup>2+</sup> complex and ternary RFK:FMN:ADP-Mg<sup>2+</sup> complex (PDB entries 5A88 and 5A89, respectively). This structural information, together with computational analysis and kinetic and binding data, suggest that CaFADS suffers conformational changes during ligand binding and catalysis.

The structure of the RFK module in the apo form of the CaFADS significantly differs from those found for the binary RFK:ADP-Mg<sup>2+</sup> and the ternary RFK:FMN:ADP-Mg<sup>2+</sup> complexes (Herguedas *et al.*, 2015). Both complexes exhibit important structural rearrangements that affect the conformation of the PTAN motif, as well as most of the protein loops with the only exception of L2c.

In the apo-protein structure, the adenine nucleotide binding site of the RFK module is closed by the interaction of L1c-FlapI, L3c and L5c loops. However, in the protein-ligand, the adenine nucleotide cavity is opened by the displacement of L1c to  $\alpha$ 1c, while L3c and L5c move to the opposite direction (**FIG I.14C**). Molecular dynamics (MD) simulations of the free RFK module show that these loops establish an open-closed equilibrium for the adenine nucleotide binding site, in which the opening is favored by the presence of either flavin or adenine nucleotides (Herguedas *et al.*, 2015). Regarding the flavin binding site of the RFK module, L4c-FlapII is disarranged in the binary complex and as a consequence the flavin binding cavity is open and wide (**FIG I.14B**). However, FMN binding induces a change in the size, shape and solvent accessibility of the cavity (Herguedas *et al.*, 2015).

The consensus PTAN motif, implicated in the stabilization of ATP phosphates and Mg<sup>2+</sup> cofactor, also experiences different conformational changes upon ligand binding. In the free structure, the side chain of T208 is occupying the position where the adenine ring is in the binary and ternary complexes (**FIG I.14E**). Therefore, the binding of the adenine nucleotides should necessarily induce a conformational change that results in the opening of their binding site. MD simulations show that the presence of either the flavin or the adenine nucleotides is not sufficient to induce the Thr208 conformational change. Moreover, these simulations suggest that the coordination of its side chain with ADP/ATP through the Mg<sup>2+</sup> ion is the most probable determinant for the achievement of the catalytically competent geometry of the PTAN motif.

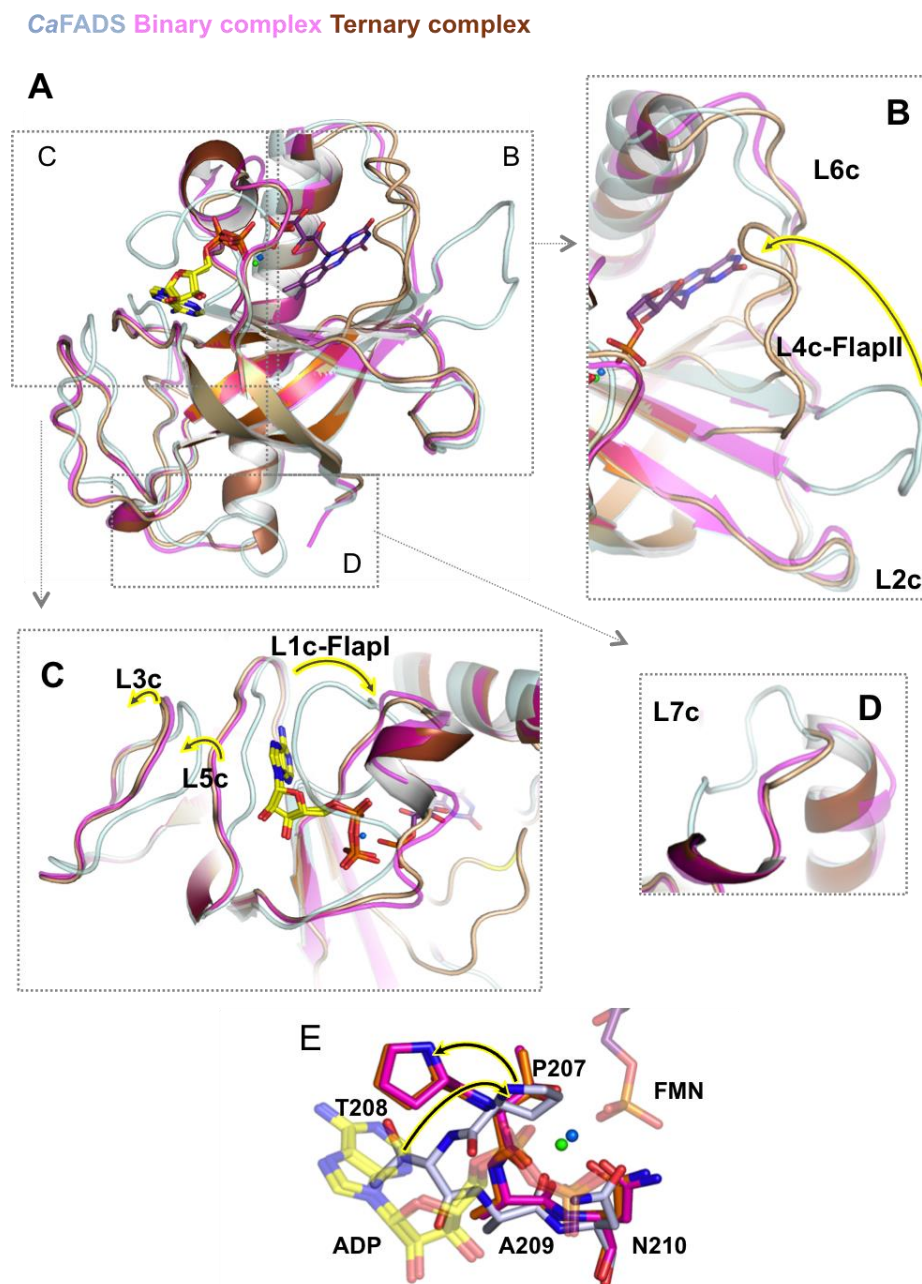


**Figure I.14.** Superposition of free *CaFADS* RFK domain (apo form, in light blue), the binary complex with ADP (in light pink) and the tertiary complex with ADP and FMN (in brown) (PDB entries 2X0K, 5A88 and 5A89, respectively). **(A)** Overall view of the structural alignment, with the main differences highlighted with squares. **(B)** Zoom in the flavin binding site, showing the displacement of loops L4c-FlapII and L6c. **(C)** Detail of the adenine nucleotide binding site, showing the conformational changes of loops L1c, L3c and L5c. **(D)** Zoom into C-terminus of the RFK module showing the displacement of L7c. **(E)** Conformation of the PTAN motif in the three models. The conformational change of Pro207 and Thr208 can be appreciated. Conformational changes are indicated with yellow arrows. Figure from (Herguedas *et al.*, 2015).

*CaFADS can stabilize quaternary assemblies in the form of a dimer of trimers*

The structural analysis of the crystal structure of *CaFADS* predicted an  $A_3B_3$  hexameric oligomer (being A and B the two chains of the asymmetric unit of the *CaFADS* crystal) (FIG I.15), constituted by a dimer of trimers ( $A_1-A_2-A_3$  and  $B_1-B_2-B_3$ , one on top of the other) (Herguedas *et al.*, 2010; Serrano *et al.*, 2015). Formation of these *in silico* predicted assemblies was imaged at the single-molecule level through atomic force microscopy techniques (AFM) and detected *in vivo* in *C. ammoniagenes* protein extracts (Marcuello *et al.*, 2013).

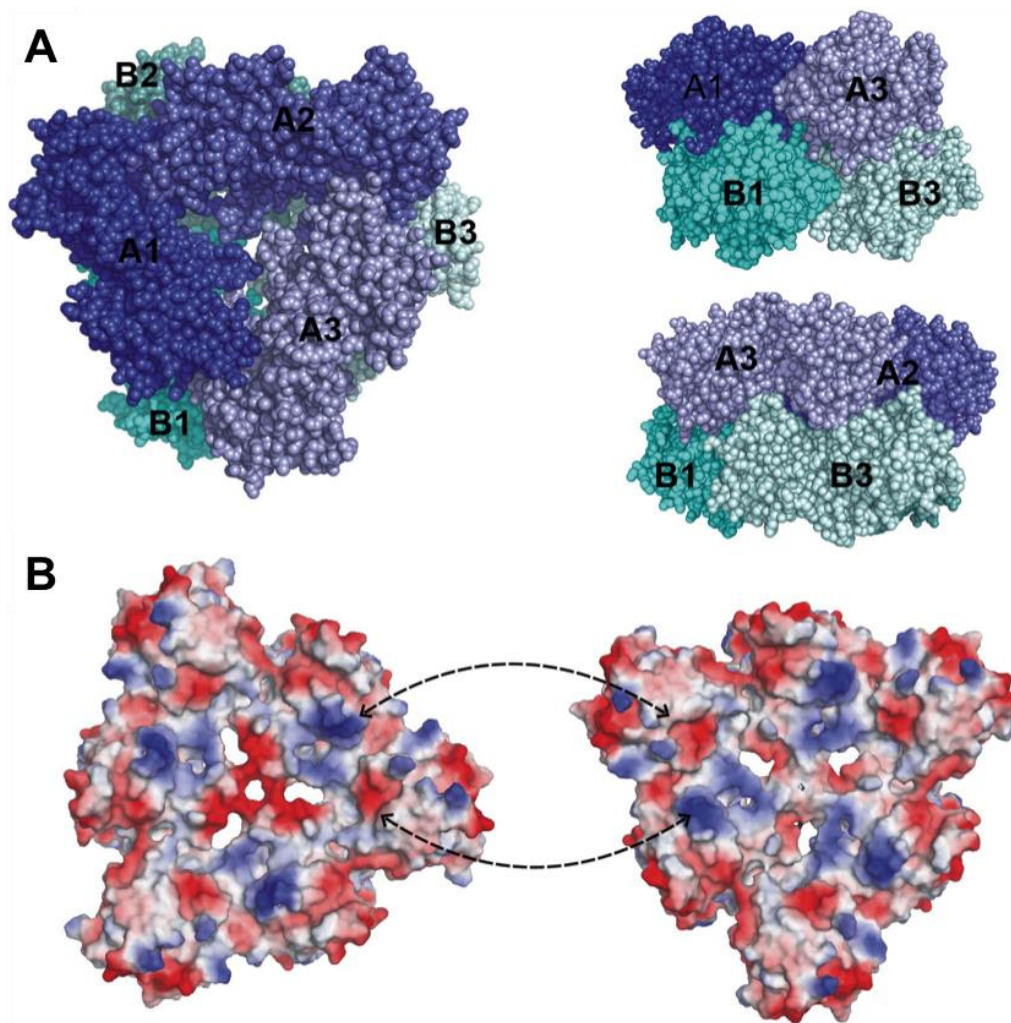


**Figure I.15.** Oligomeric state of *CaFADS*. (A) Space-filling representation of the dimer of trimers. Left, view through the 3-fold crystallographic axis. Right, lateral view of the hexamer. (B) Surface electrostatic potential of the *CaFADS* hexamer along the interaction surfaces of the two trimers (negative, positive and uncharged residues are shown in red, blue and white respectively). Arrows indicate the positions with electrostatic contacts between trimers for the formation of the hexamer. Figure from (Herguedas *et al.*, 2010).

Trimers are stabilized through contacts of different nature between 20 side chains (18 H-bonds, 18 hydrophobic contacts and 3 salt bridges) (**FIGS I.16A**) (Herguedas *et al.*, 2010; Serrano *et al.*, 2015). The interface between trimers shows electrostatic complementarity (**FIG I.15B**). Moreover, 14 H-bonds, 4 salt bridges and 12 hydrophobic contacts strengthen the hexamer (Serrano *et al.*, 2017). Additionally, sulphate ions play an crucial role the by stablishing additional H-bonds and salt bridges (Herguedas *et al.*, 2010).

Within each trimer, the protomers are organized in a head-to-tail configuration (**FIGS I.15A and I.16B**); thereby approaching the FMNAT module of one protomer to the RFK module of the neighboring protomer. In this disposition, both actives sites come in close contact which modifies both the active site environment and its solvent and ligand accessibility. The RFK cavity appears partially closed by  $\alpha 2n$  and L4n of the neighboring protomer (FMNAT module) (**FIG I.16D**), whereas the FMNAT is also partially closed by residues at  $\alpha 1c$  and L6c (RFK module) (**FIG I.16C**).

*CaFADS* oligomerization is a dynamic process occurring upon ligand binding and catalysis (Herguedas *et al.*, 2010; Marcuello *et al.*, 2013; Serrano *et al.*, 2017). Some of the substrates and products of the RFK (RF, ATP:Mg<sup>2+</sup> and FMN:ADP:Mg<sup>2+</sup>) and FMNAT activities (FAD) induce the oligomerization of *CaFADS*, yielding different quaternary assemblies (Marcuello *et al.*, 2013). Hence, the assembly of the organized dimer of trimers might occur/take place through a series of oligomerization intermediates, such as dimers, trimers and amorphous hexamers.

The oligomerization process is tightly regulated by the substrates and products of *CaFADS*, what points to be a mechanism to regulate the biosynthesis of flavin cofactors and thus maintain the flavin and flavoproteome homeostasis. Initially, it was proposed that the dimer of trimers was implicated in the channeling of the FMN product from the RFK active site to the FMNAT one, to be subsequently transformed into FAD (Herguedas *et al.*, 2010; Marcuello *et al.*, 2013). However, MD simulations suggest that the RFK module prevents catalysis at the transferase site by modulating negatively the FMN binding to the FMNAT module (Lans *et al.*, 2018). Nevertheless, it remains for future investigations to describe whether this might be a general behavior for prokaryotic FADSs or, on the contrary, a particular feature for the FADSs from *Corynebacterium* and, also probably, *Mycobacterium* species.

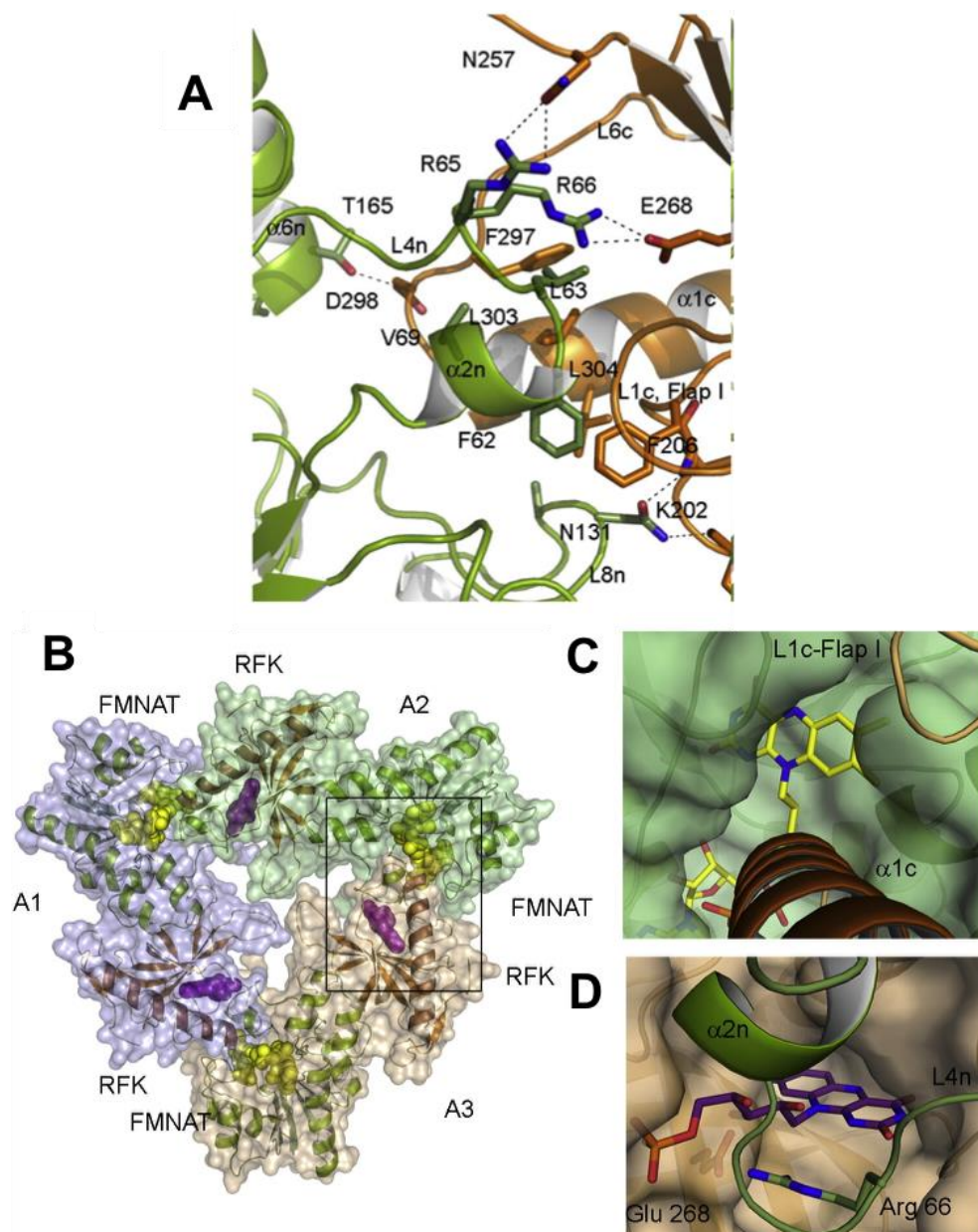


**Figure I.16.** (A) Detail of the contacts between the RFK and FMNAT modules of different protomers within a trimer, including the hydrophobic residues, H-bonds, and salt bridges involved in trimer stabilization. (B) Cartoon representation of one of the trimers conforming the hexamer. RFK and FMNAT modules are shown in orange and green, respectively, and the molecular surface of each monomer is displayed in different colors. Flavin ligands are represented as yellow spheres. (C) Detail of the active-site surface at the FMNAT module showing how  $\alpha 1c$  and L1c of the RFK module of the neighboring protomer close the binding site. (D) Detail of the active site of the RFK module.  $\alpha 2n$  and L4n of the FMNAT module of the neighboring protomer close the binding site. FMN and FAD are represented as violet and yellow sticks respectively. Figure from (Herguedas *et al.*, 2010)

*Prokaryotic FADS as potential antimicrobial targets*

The rise of antimicrobial resistance (AMR) threatens the effective prevention and treatment of an ever-increasing range of infections caused by microorganisms. Hence, the World Health Organization pointed AMR as a public health problem of growing concern (World Health Organization, 2014). Examples of microorganisms included in the list of antibiotic-resistant pathogens for which is urgent to develop new antimicrobial drugs include methicillin-resistant *Staphylococcus aureus*, *Streptococcus pneumoniae* resistant to both penicillin and macrolides, vancomycin-resistant *Enterococcus faecalis*, and multidrug and extensively drug-resistant strains of *Mycobacterium tuberculosis* (World Health Organization, 2014, 2017).

The only long-term solution to overcome this global problem is the continuous research and development of new antimicrobials, focusing on the discovery of new druggable targets. Although there are approximately 450 essential proteins conserved along prokaryotes (Christen *et al.*, 2011; Hutchison *et al.*, 2016), most of the commercially available antibiotics are directed to a limited set of antimicrobial targets: the cell wall biogenesis, the prokaryotic ribosome or the DNA replication and transcription (Lewis, 2013). Hence, the rest of essential cellular processes remain nearly unexplored as antimicrobial targets.

Until relatively recently, flavin metabolism had not been considered a potential target of antimicrobials. First compounds directed to this pathway were compounds inhibiting lumazine synthase and/or riboflavin synthase (Cushman *et al.*, 1999; Morgunova *et al.*, 2005; Ritsert *et al.*, 1995). Additionally, in 2009 and 2015, roseoflavin and ribocyl C were described as the first compounds acting indirectly on riboflavin biosynthesis through the binding to the FMN riboswitch and repression of the expression of the *rib* operon (Howe *et al.*, 2015; Lee *et al.*, 2009). Furthermore, the prokaryotic FADS was also proposed as an antimicrobial target (Serrano *et al.*, 2013b) and afterwards inhibitory compounds endowed with antimicrobial activity and targeting FADS were further discovered (Sebastián *et al.*, 2018b).

Prokaryotic bifunctional FADSs are key proteins in flavin homeostasis and in the maintenance of flavoprotein and flavoenzyme function (Frago *et al.*, 2008). Hence, the inhibition of their enzymatic activities leads into FMN and FAD deficiency, and consequently into the accumulation of the apo forms of numerous flavoproteins, which are unable to carry out their expected functions in the cellular metabolism and other essential processes (Serrano *et al.*, 2013b). Indeed,

FADS are highly conserved among prokaryotes and have been described as essential for numerous microorganisms including *Bacillus subtilis* (Kobayashi *et al.*, 2003), *Escherichia coli* (Goodall *et al.*, 2018), *M. tuberculosis* (Griffin *et al.*, 2011; Minato *et al.*, 2019; Sasseti *et al.*, 2003), *S. pneumoniae* (Liu *et al.*, 2017), *etc.*

This crucial role in cellular metabolism, together with the significant biochemical and structural differences with their eukaryotic counterparts (monofunctional RFKs and FMNATs) (Karthikeyan *et al.*, 2003a; Miccolis *et al.*, 2014), converts the FADS in an attractive potential drug target for the development of antimicrobials (Serrano *et al.*, 2013b). Thus, halting the production of FMN and FAD by inhibiting the FADSs would prevent, from the very beginning, all pathways that involve flavoproteins and flavoenzymes.

In principle, riboflavin biosynthesis inhibitors (targeting both RF synthase or lumazine synthase) would be expected to trigger similar effects than FADS inhibitors. However, RF biosynthesis is conditionally essential since some microorganisms (depending also on growth conditions) have other mechanisms, in addition to the *de novo* synthesis, to obtain RF (García-Angulo, 2017; Gutiérrez-Preciado *et al.*, 2015; Matern *et al.*, 2016). By contrast, in most bacteria (except for prokaryotes harboring monofunctional RFKs and/or FMNATs), the only pathway for FMN and FAD biosynthesis occurs through bifunctional FADS.

Druggability of prokaryotic FADSs is also supported by their strict function-structure relationship. Mutations affecting the active site (most common binding site of inhibitory compounds) would probably alter the enzymatic activity. Therefore, FADS inhibitors might be less prone to generate resistances, since mutations conferring resistance also might compromise the protein function and thus the cellular viability. Additionally, the availability of structures of several bacterial FADSs facilitates the design of both inhibitory drugs and activity assays (Herguedas *et al.*, 2010; Sebastián *et al.*, 2018b; Wang *et al.*, 2003).

In addition, the biochemical characterization of several prokaryotic FADS (including *TmFADS*, *CaFADS*, *SpFADS*, *Lm1FADS* and *Lm2FADS*) envisages significant species-specific traits in their enzymatic activity and regulatory strategies (Herguedas *et al.*, 2015; Sebastián *et al.*, 2017c, 2017a, 2019; Wang *et al.*, 2004). Such differences might provide with a framework to design species-specific antimicrobial compounds.

#### IV. FLAVOPROTEINS

Flavin cofactors show unique spectroscopic and redox properties, and thus **flavoproteins**, proteins harboring flavin as cofactors, have marveled generations of enzymologist along the time.

Among the redox cofactors, flavins can participate in both one-electron and two-electron transfer processes. Other cofactors usually catalyze exclusively one- (iron-sulfur clusters, heme groups, quinones...) or two-electron transfer processes (almost exclusively nicotinamide nucleotides). Therefore, flavoenzymes are indispensable mediators between these processes, as in the case of the well-known mitochondrial and chloroplast electron-transport chains, or beta-oxidation of fatty acids. Additionally, flavins are capable of reacting with oxygen (dioxygen activation processes). This catalytic versatility encompasses many established reaction classes, including dehydrogenation, oxidation, monooxygenation, epoxidation, Baeyer-Villiger oxidation, decarboxylation, halogenation and reduction (Leys and Scrutton, 2016; Massey, 2000; Walsh and Wencewicz, 2013). Furthermore, the complexity of flavin-catalyzed reactions is further increased when they join forces with other redox-active cofactors, such as iron-sulfur clusters ([2Fe-2S], [3Fe-4S] and/or [4Fe-4S]), heme, molybdopterin, or thiaminediphosphate.

However, the role of flavins in flavoproteins is not only limited to redox processes, as ~ 10% of flavin-dependent enzymes catalyze non-redox reactions (Macheroux *et al.*, 2011). Hence, the flavin cofactor is also widely used as signaling and sensing molecule in biological processes (**FIG I.17**). Examples would include signal transduction upon apoptosis (Natarajan and Becker, 2012; Susin *et al.*, 1999), embryonic development (Murty and Adiga, 1982), chromatin remodeling (Forneris *et al.*, 2005), nucleotide synthesis (Myllykallio *et al.*, 2002), tRNA methylation (Nishimasu *et al.*, 2009), protein folding (Gross *et al.*, 2004), defense against oxidative stress (Natarajan and Becker, 2012), among others. Flavoproteins are also implicated in detoxification of aromatic compounds (xenobiotic metabolism) (Dagley, 1987) and in light-dependent processes as luciferase light-emission (Meighen, 1991), plant phototropism (Briggs *et al.*, 2001) or DNA repair (Jorns *et al.*, 1987), in which flavin is capable of receive photons.



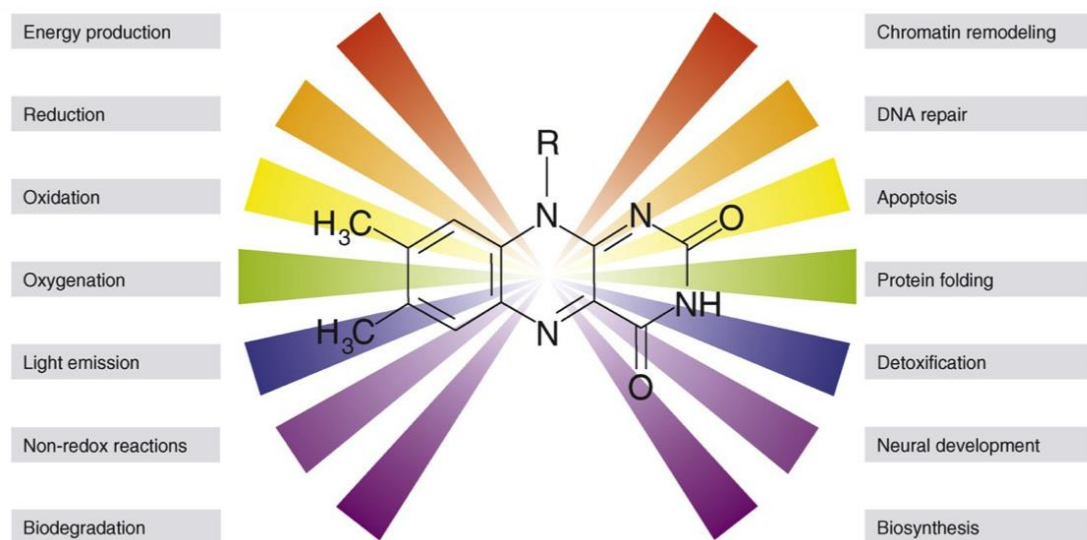


**Figure I.17.** Structure of the isoalloxazine ring of flavin cofactors and some of the biological processes they are involved in. Figure from (Joosten and van Berkel, 2007)

In a recent study, Macheroux *et al.* (2011) analyzed FMN and FAD-dependent proteins in 22 genomes, including archaea, eubacteria, protozoa and eukaryotic organisms. They reported 374 classes of flavin-dependent proteins (276 fully classified and 98 with no or partial classification and without enzymatic activity), entailing approximately the 2% of all the proteins. As expected for a redox-active cofactor, most of the 276 flavoenzymes are oxidoreductases (91%), whereas other enzymatic functions are underrepresented, such as transferases (4.3%), lyases (2.9%), isomerases (1.4%) or ligases (0.4%) (Macheroux *et al.*, 2011), although the exact percentages varies among organisms.

The majority of flavoenzymes bind FAD (75%) rather than FMN (25%). Moreover, some eukaryotic flavoproteomes are biased towards FAD-dependent enzymes, as in the case of human proteome (84% of FAD-dependent proteins) (Lienhart *et al.*, 2013; Wegrzyn *et al.*, 2019).

Additionally, in most of the cases the cofactor is noncovalently bound, although covalent attachment is also observed (approximately 10% of flavoproteins), especially for FAD-flavoproteins. FMN is preferentially bound by both the 6- and/or 8 $\alpha$ -position of the isoalloxazine ring with a nucleophilic side chain of the protein (Singer and McIntire, 1984). Covalent binding might increase protein stability, ensure cofactor retention and/or induce a more positive redox

potential of the cofactor (Heuts *et al.*, 2009). In the case of noncovalent interaction, dissociation constants ( $K_D$ ) in the low nanomolar scale are usually observed, although lower affinities have also been reported (Mayhew, 1971).

The absorption spectra of flavoproteins and free flavins are highly similar. Nevertheless, the protein environment usually induces small displacements in the position of the maxima and in their intensities, as well as the appearance of spectral shoulders. Additionally, fluorescence of the flavin when forming part of a flavoprotein can be moderately altered, completely disappear (Keilin and Hartree, 1946) or stay unaltered (Straub, 1939), depending on the manner in which the isoalloxazine ring gets embedded within the protein (Weber, 1950). This makes the spectra of each flavoprotein unique.

Although flavoproteins share the same cofactor (FMN or FAD), all of them catalyze diverse enzymatic reactions with a wide variety of substrates (Massey, 2000; Walsh and Wencewicz, 2014). This catalytic versatility comes from the modulation of the reactivity of the isoalloxazine ring by the protein environment (Miura, 2001). Flavin cofactors interact with flavoproteins through hydrogen bonds, hydrophobic and electrostatic effects (magnified by the high hydrophobicity and low dielectric constant of flavin binding sites), charge-transfer interactions (fractional electron transference from the HOMO orbital of an electron donor to the LUMO orbital of an electron acceptor), and  $\pi$ - $\pi$  stacking interactions between the isoalloxazine ring and an aromatic residue.

The protein environment at the flavin binding site not only modulates the affinity by the flavin cofactor but also alters the charge distribution along the isoalloxazine ring. Therefore, each flavoprotein interacts differentially with each oxidation and protonation state of the flavin cofactor, stabilizing preferentially some of them. Consequently, the midpoint reduction potential of the flavin (~ -200 mV when free in solution) (Clark and Lowe, 1956; Mayhew, 1999b) is modulated from -400 to +80 mV when in a flavoprotein (Ghisla and Massey, 1986, 1989). Furthermore, depending on the relative modulation of  $E_{ox/sq}$  and  $E_{sq/red}$  values, some flavoproteins reach a stabilization of near to 100% of the semiquinone state (in comparison with the 1% observed for protein-free flavins at physiological conditions) (Mayhew, 1999a). This characteristic allows flavoproteins to mediate in one- and/or two-electron transfer processes. Under physiological conditions and depending on the pH, the semiquinone state in flavoproteins can be found either in the red anionic form or in the neutral blue one. Also, under these conditions, the hydroquinone (reduced state) of

flavoproteins can only be found in the anionic and neutral forms (Clark and Lowe, 1956). Besides all these forms, electronic states where partial charge is transferred from or to one of the states previously described to a neighboring molecule, commonly termed as charge-transfer states, can be found.

#### *Flavoproteins as therapeutic targets*

In most organisms, flavoproteins have a relevant role in a wide variety of essential biochemical reactions and other cellular processes. Hence, flavin-dependent proteins are plausible targets for pharmacological treatment, from infectious diseases to neurological disorders or cancer therapies.

Concerning the treatment of infectious diseases, some prokaryotic and protozoan flavoproteins have been considered potential targets of antimicrobial compounds, such as electron transfer flavoprotein (*Burkholderia cenocepacia*), lipoamide dehydrogenase (*M. tuberculosis*, *Trypanosoma*, *Leishmania*), glutathione reductase (*Plasmodium falciparum*), thioredoxin reductase (*P. falciparum*), thymidylate synthase and decaprenylphosphoryl- $\beta$ -D-ribose 2'-oxidase (*M. tuberculosis*), and trypanothione reductase (*Trypanosoma*, *Leishmania*) (Becker *et al.*, 1990; Chernyshev *et al.*, 2007; Myllykallio *et al.*, 2002, 2003, 2018; Olin-Sandoval *et al.*, 2012; Reyes *et al.*, 1982; Subbayya *et al.*, 1997; Venugopal *et al.*, 2011). Additionally, some flavin-analogs (e.g. roseoflavin or 8-demethyl-8-amino-riboflavin) show antimicrobial activity through the *in vivo* inhibition of flavoproteins by the incorporation of a non-active cofactor instead of FMN or FAD (Langer *et al.*, 2013; Lee *et al.*, 2009; Mack and Grill, 2006). However, these antimetabolites have low to no selectivity for prokaryotic flavoproteins with respect to human or eukaryotic ones, limiting their applicability as antimicrobials.

Human flavoproteins are also associated to several disorders caused by mutations in their corresponding genes, and hence they are potential pharmacological targets. Some of them have been associated to cancer development and progression, such as apoptosis-inducing factor 1 (redox sensing and apoptosis) (Novo *et al.*, 2020; Villanueva *et al.*, 2019), lysine-specific demethylase 1 (histone methylation and chromatin remodeling) (Chen *et al.*, 2012), thioredoxine reductase (redox homeostasis maintenance) (Gromer *et al.*, 2004) or NAD(P)H:quinone oxidoreductase 1 (defense against oxidative stress) (Beaver *et al.*, 2019). Other human diseases related to flavin-dependent proteins

are depression, *Parkinson's* and *Alzheimer's* diseases (monoamine oxidase), schizophrenia (D-amino acid oxidase), xanthinuria type I (xanthine dehydrogenase), glutaric acidemias (glutaryl-CoA dehydrogenase, electron-transferring flavoprotein or electron-transferring flavoprotein-ubiquinone oxidoreductase), deficiencies in  $\beta$ -oxidation and deficiencies in mitochondrial complexes (Lienhart *et al.*, 2013).

### **NAD(P)H:quinone oxidoreductase**

NAD(P)H:quinone oxidoreductase 1 (NQO1, DT-diaphorase; EC 1.6.99.2) is a ubiquitous FAD-dependent flavoprotein that catalyzes the two-electron reduction of quinones to their hydroquinone forms (Ernster *et al.*, 1962). This enzyme utilizes the NADH and NADPH reduced pyridine nucleotide cofactors with almost equal efficiency, and strictly requires of the tightly bound flavin cofactor FAD for its catalytic activity (Lind *et al.*, 1990). In addition to quinones, NQO1 can reduce a wide variety of substrates as nitroaromatic compounds, imidazoles and iron (III) ions (Misevičiene *et al.*, 2006; Nemeikaitė-Čėnienė *et al.*, 2019; Newsome *et al.*, 2007; Sarlauskas *et al.*, 2004).

In human tissues NQO1 is physiologically expressed at high levels in epithelial cells, vascular endothelium and adipocytes. NQO1 is a cytosolic protein, but lower levels have also been detected in the mitochondria, endoplasmic reticulum and nucleus (Danson *et al.*, 2004; Shaw *et al.*, 1991; Siegel *et al.*, 2012). Noticeably, NQO1 is over-expressed in most human solid tumors including lung, colon, liver, pancreas and breast (Siegel and Ross, 2000), being associated to poor prognosis (Li *et al.*, 2015; Ma *et al.*, 2014).

NQO homologues are widely found across living organisms ranging from bacteria to mammals. In humans there is a second NQO enzyme, ribosyldihydronicotinamide quinone oxidoreductase 2 (NQO2; EC 1.10.5.1), which shows substantial sequence and structural similarity to NQO1 (Jaiswal *et al.*, 1990). However, this enzyme uses ribosyldihydronicotinamide (reduced nicotinamide ribonucleotide; NRH) as source of reducing equivalents instead of NAD(P)H (Wu *et al.*, 1997). Also, prokaryotic organisms have several enzymes with quinone oxidoreductase activity, but they are usually classified as nitroreductases or modulator of drug activity (Mda) proteins (Ryan *et al.*, 2014; Wang and Maier, 2004).

### *Crystallographic structure of NQO1*

Until now, the crystallographic structures of three mammalian NQO1s have been determined: rat (rNQO1) (Li *et al.*, 1995), mouse (mNQO1, PDB entry 1DXQ) (Faig *et al.*, 2000), and human (hNQO1, PDB entry 1D4A) (Faig *et al.*, 2000; Skelly *et al.*, 1999); as well as the human NQO2 (hNQO2, PDB entry 1QR2) (Foster *et al.*, 1999). In addition, several structures of complexes of NQO1 with substrates, chemotherapeutic drugs and inhibitors have also been reported (Faig *et al.*, 2001; Pidugu *et al.*, 2016; Strandback *et al.*, 2019; Winski *et al.*, 2001).

Structurally, NQO1 is a physiological homodimer with two interlocked monomers (**FIG I.18A**) (Faig *et al.*, 2000; Skelly *et al.*, 1999). Each monomer is constituted by two separate domains (**FIG I.18C**): a major N-terminal domain (residues 1-220), which includes the FAD-binding site and the active site; and a shorter C-terminal domain (residues 221-270), which is involved in dimerization and binding of the adenosine moiety of the pyridine nucleotide. The catalytic domain has a distinct fold within FAD-containing flavoproteins (Dym and Eisenberg, 2001) and shows structural similarity with the *Clostridium beijerinckii* flavodoxin, a FMN-dependent flavoprotein (Ludwig *et al.*, 1997; Smith *et al.*, 1977). This module comprises a twisted five-strand parallel  $\beta$ -sheet surrounded by five  $\alpha$ -helices that interconnect consecutive strands in an alternating  $\alpha/\beta$  topology. Besides, the C-terminal domain is composed by an anti-parallel hairpin motif followed by a short helix and several disordered loops, and folds against the other monomer catalytic domain.

The hNQO1 dimer is highly stabilized through extensive contacts between monomers, which result in the burial of  $\sim 5400 \text{ \AA}^2$  of solvent-accessible area. Most contacts occur between residues belonging to four main regions: residues 153-164 are in contact with residues 235-262 of the adjacent monomer (and *viceversa*), and residues 42-52 and 103-104 contact their equivalent in the other monomer.

Within the homodimer, the catalytic sites are located at the interface between monomers and, thus, both active sites are composed by residues from both dimer subunits (**FIG I.18A**). The NQO1 active sites are essentially large hydrophobic pockets with three defined binding spaces for the adenine and ribose parts of NAD(P)H, the FAD cofactor, and the nicotinamide moiety of NAD(P)H or the electron acceptor molecule (Pey *et al.*, 2016). The FAD cofactors are tightly but non-covalently bound to each monomer (dissociation constants are in the nanomolar range,  $K_D$  64 nM in hNQO1), and do not come off the enzyme under native conditions (Lienhart *et al.*, 2014).

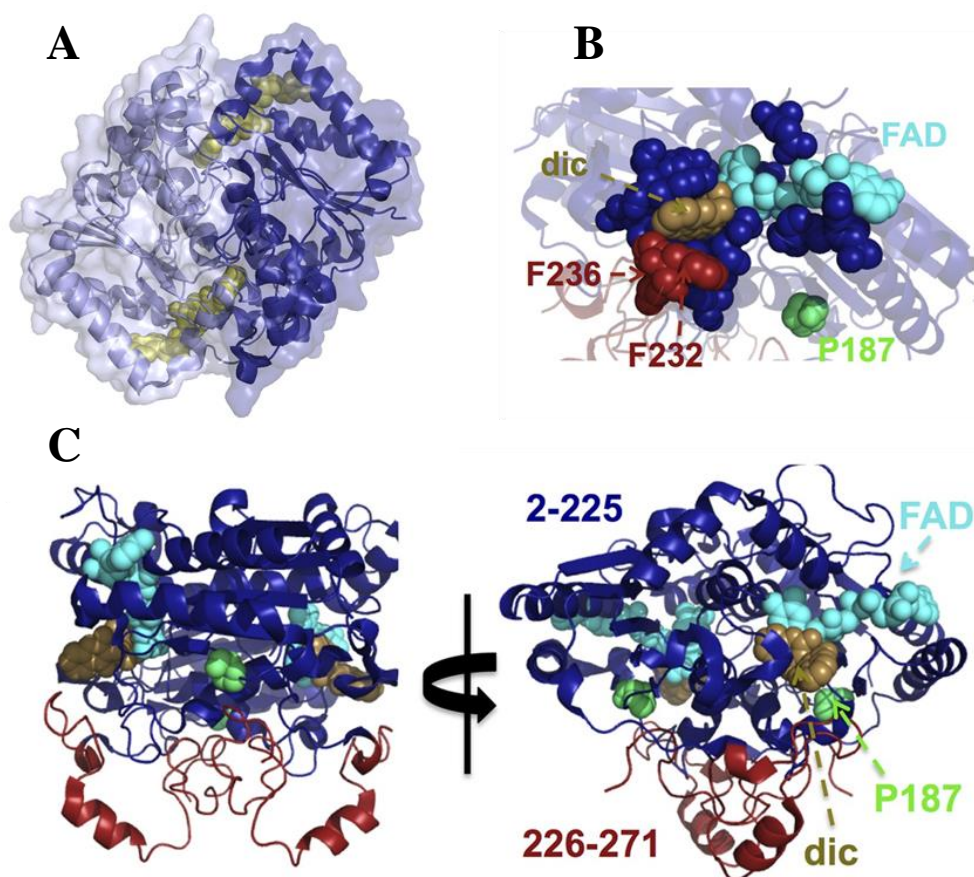


**Figure I.18** (A) Cartoon representation of the hNQO1 with the molecular surface of each monomer displayed in different colors (PDB ID 1D4A). FAD cofactor is represented as yellow spheres. (B) Close-up view of the FAD-binding site and active site of hNQO1 (PDB ID 2F1O), with the residues belonging to the N- and C-terminal domains highlighted in blue and red, respectively. FAD, dicoumarol and residue P187 are shown in cyan, light brown and green, respectively. (C) Two views of the NQO1 dimer displaying secondary structures of the N- and C-terminal domains in color blue and red, respectively. Ligands and residue P187 are depicted as in (B). Figure adapted from (Medina-Carmona *et al.*, 2017).

#### *The NQO1 catalytic cycle*

The obligatory two-electron reduction occurs through a ping-pong bi-bi catalytic mechanism (FIG I.19). First, in the reductive half-reaction, an NAD(P)H molecule binds to the enzyme in such a way that the nicotinamide ring lies parallel to the FAD. In this complex, the pro-4S hydrogen (B-side) of the NAD(P)H is at  $\sim 3.4$  Å from the N5 of the isoalloxazine ring of FAD (re-face), as predicted from the crystallographic structure of rat NQO1 (PDB entry not published) (Li *et al.*, 1995). This arrangement is ideal for the hydride transfer for

reducing the FAD to FADH<sub>2</sub> (with a second-order rate constant of  $\sim 10^6 \text{ M}^{-1} \text{ s}^{-1}$ ). Nevertheless, Lee and collaborators reported that the hydride transfer from NAD(P)H by rat liver NQO1 occurs with pro-4R (A-side) stereospecificity (Lee *et al.*, 1965). Subsequently to flavin reduction, the enzyme undergoes a conformational change that results in the release of the oxidized nicotinamide dinucleotide, NAD(P)<sup>+</sup>.

Binding of the substrate (electron acceptor) cannot occur until NAD(P)<sup>+</sup> is released because both, substrate and pyridine nucleotide, share the same site in the catalytic pocket. Finally, the electron acceptor (such as different quinones) binds to the vacated site in an orientation propitious for a second hydride transfer from FADH<sub>2</sub>, in a very fast oxidative half-reaction (with a second-order rate constant  $> 10^9 \text{ M}^{-1} \text{ s}^{-1}$ ) (Lienhart *et al.*, 2014). Consequently, the substrate is reduced (as quinones in their corresponding hydroquinone forms), regenerating the flavin in oxidized form and releasing the product.

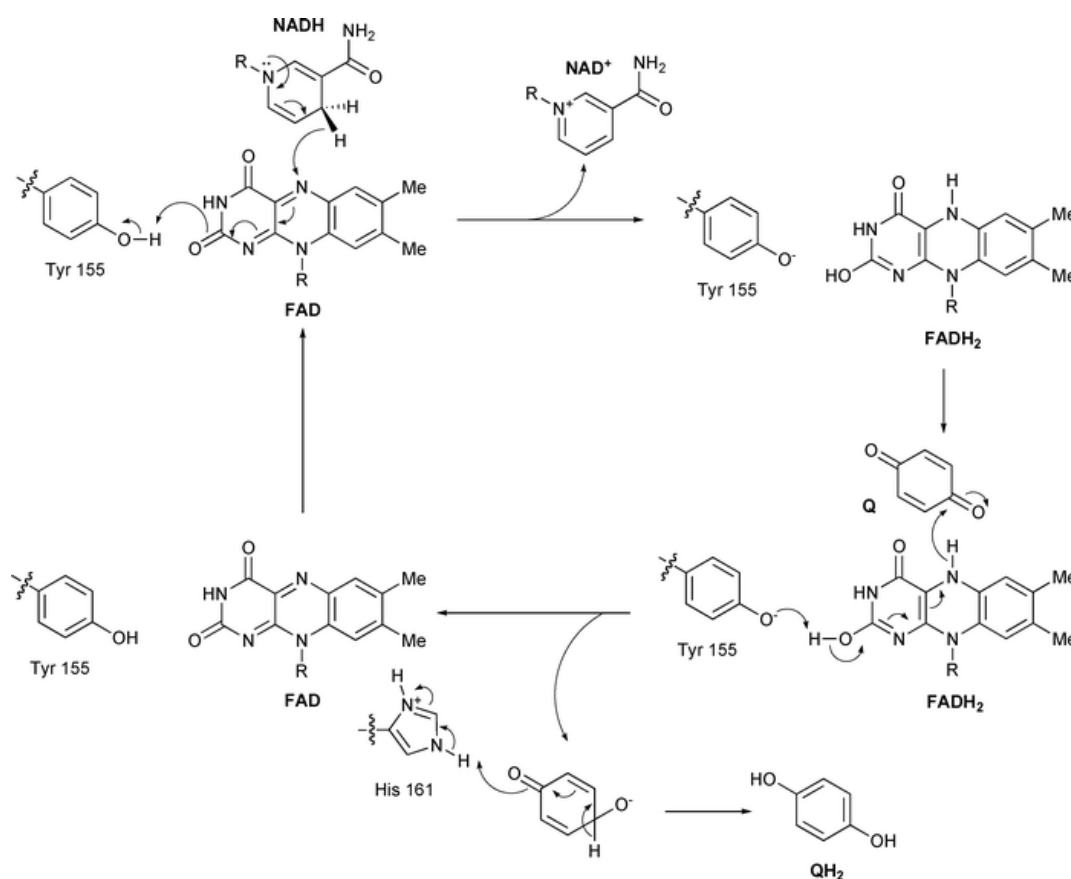


**Figure I.19.** Plausible mechanism for the two-electron reduction of quinones substrates (benzoquinone in this case) by NQO1, according to (Colucci *et al.*, 2008).

This catalytic cycle is inhibited by dicoumarol (and other coumarin-based molecules), a hydroxycoumarin with strong anticoagulant activity that acts as potent competitive inhibitor by blocking the NAD(P)H access to the active site and partially occupying its binding site (**FIG I.18B and I.18C**) (Nolan *et al.*, 2007). However, inhibitor binding causes only subtle structural rearrangements in the conformation of NQO1 (primarily located at the surface of the catalytic site) (Asher *et al.*, 2006). In addition, other selective inhibitors of NQO1 have been further identified as anti-cancer drugs due to the association of its overexpression with cancer progression and development (Nolan *et al.*, 2007, 2009, 2010; Scott *et al.*, 2011).

### *Functions of NQO1*

NQO1 catalyzes different reactions with antioxidant, detoxification and metabolic roles, such as the two-electron reduction of quinones to their hydroquinone form, thus avoiding the formation of highly reactive and cytotoxic semiquinones (Anusevičius *et al.*, 2002; Hosoda *et al.*, 1974; Lind *et al.*, 1982), reduction of coenzyme Q10 and vitamin E to their reduced state (antioxidant form) (Beyer *et al.*, 1996; Siegel *et al.*, 1997), scavenging of superoxide anions (Siegel *et al.*, 2004), reduction of catecholamines and vitamin K (Ingram *et al.*, 2013) and modulation of the NADH/NAD<sup>+</sup> redox balance (Ross and Siegel, 2018; Siegel *et al.*, 2018). Moreover, this chemoprotective role is further supported by its activity towards a wide variety of reactive species (quinones, naphthoquinones, quinone-imines, azo and nitro compounds, hexavalent chromium compounds ...) (Misevičiene *et al.*, 2006; Newsome *et al.*, 2007; Šarlauskas *et al.*, 1997; Talalay and Dinkova-Kostova, 2004) and its induction under a variety of cellular stress responses including oxidative stress (Prochaska *et al.*, 1992; Ross and Siegel, 2018). Additionally, NQO1 is also implicated in the bioreductive activation of several compounds, such as the antitumoral drugs mitomycin C and  $\beta$ -lapachone (Pink *et al.*, 2000; Siegel *et al.*, 1992).

Although NQO1 has been traditionally considered as a cellular reductase, new non-enzymatic roles have emerged recently where this enzyme binds to and regulates the stability of many biologically relevant molecules. For example, NQO1 physically interacts to 20S proteasome (Moscovitz *et al.*, 2012) and protects some intrinsically-disordered proteins from degradation such as p33, p53, p63, p73, c-Fos, C/EBP, PGC-1, Hif-1 $\alpha$  or ornithine decarboxylase (Adamovich *et al.*, 2013; Asher *et al.*, 2001). However, it is still uncertain if this protection from



degradosome degradation is through the association with the proteins undergoing degradation and/or the direct interaction with the 20S proteasome. Additionally, it has been recently found that NQO1 can bind to several mRNAs including SERPINA1 mRNA (encodes the serine protease inhibitor  $\alpha$ -1-antitrypsin) increasing its translation (Di Francesco *et al.*, 2016). These interactions seem to be modulated by NAD(P)H/NAD(P)<sup>+</sup> ratio, although the enzymatic activity of NQO1 may not be required (Asher *et al.*, 2005; Medina-Carmona *et al.*, 2017). Altogether, this suggest that the intracellular pyridine nucleotide balance regulates these interactions with its protein and RNA partners, pointing to the role of NQO1 as a redox molecular switch to modulate the downstream cellular functions (Siegel *et al.*, 2018).

### *Polymorphism in NQO1*

To date, more than 250 single-nucleotide polymorphisms (SNPs) in the NQO1 gene have been described (according to the dbSNP database, <http://www.ncbi.nlm.nih.gov/SNP>), including the two most prevalent variants in the human population, NQO1\*2 and NQO1\*3.

The NQO1\*2 polymorphism (rs1800566) is a missense SNP which replaces the cytosine 609 of the cDNA for a thymine (c.C609T), resulting in a proline-to-serine substitution at residue 187 (p.P187S). Its allelic frequency is higher in Asian populations (approximately 50%) compared with Caucasians (approximately 25%) (Gaedigk *et al.*, 1998). Additionally, this polymorphism is associated with higher cancer risk (particularly, gastrointestinal, liver, colorectal, lung, breast and thyroid cancers) (Fagerholm *et al.*, 2008; Lee *et al.*, 2013; Long *et al.*, 2002; Peng *et al.*, 2014; Stoehr *et al.*, 2012; Xu *et al.*, 2001), increased susceptibility to poisoning by benzene and other carcinogenic agents (Bauer *et al.*, 2003a; Nebert *et al.*, 2002; Rothman *et al.*, 1997), and reduced NQO1-dependent activation of antitumoral prodrugs (Traver *et al.*, 1992).

The NQO1 P187 residue is located in a loop close to the surface of the protein at the N-terminal domain (**FIG I.18C**), far away from the FAD- and NAD(P)H-binding sites. However, the p.P187S substitution produces a dramatic reduction on both NQO1 enzymatic activity and FAD binding affinity (Lienhart *et al.*, 2014; Medina-Carmona *et al.*, 2017). In addition, this polymorphism has reduced intracellular stability of the protein and is promptly ubiquitinated and degraded by the 20S/60S proteasome (Moscovitz *et al.*, 2012; Siegel *et al.*, 2001). Although

the overall crystallographic structure of p.P187S is identical to the wild-type NQO1 structure, this polymorphism causes the presence of unfolded states in solution and a significant increase in local dynamics of two functionally and structurally distant sites: the N-terminal domain associated with enzyme inactivation, and the C-terminal domain linked with its enhanced proteasomal degradation (Lienhart *et al.*, 2014; Medina-Carmona *et al.*, 2017).

The NQO1\*3 polymorphism (rs1131341) represents a cytosine for thymine change at position 465 of the NQO1 cDNA (c.C465T), and results in an arginine-to-tryptophan substitution at residue 139 (p.R139W). It has an estimated global allele frequency of 2%, reaching up to 7% in Spanish Iberian population (Gaedigk *et al.*, 1998). This polymorphism has also been associated with cancer development (specifically childhood acute lymphoblastic leukaemia and urinary bladder neoplasm) (Sanyal *et al.*, 2007; Stanulla *et al.*, 2007) and reduced responsiveness to several antitumoral drugs (Hu *et al.*, 1996; Pan *et al.*, 1995), although this NQO1 variant is less well studied than p.P187S. These deleterious effects might be result of an enhanced alternative splicing of the NQO1 pre-mRNA causing skipping of exon 4, and therefore a decrease of the expression of the active full-length enzyme (Gasdaska *et al.*, 1995; Pan *et al.*, 2002, 1995).

NQO1 R139 residue forms part of a solvent-exposed loop located in the N-terminal domain of the enzyme, without interacting with the active site residues. The p.R139W variant adopts the same tertiary structure than the wild-type as observed by X-ray crystallography and nuclear magnetic resonance spectroscopy (Lienhart *et al.*, 2017). However, this substitution causes subtle differences in enzyme kinetic properties (higher  $K_m$  values and/or lower  $k_{cat}$  values for quinone substrates), reduced *in vitro* and *in vivo* stability of the protein, and minor stabilization of protein partners such as p53 (Lienhart *et al.*, 2017; Medina Carmona *et al.*, 2016; Megarity and Timson, 2019; Pey *et al.*, 2014)

# Objectives



This thesis is focused on two interrelated topics, both associated with flavin cofactors and their crucial biological role in different organisms. The first aims to further delve into the molecular mechanisms of eukaryotic flavoenzymes of biological interest (*HsRFK*, *hFADS* and *hNQO1*), associated with flavin and redox intracellular homeostasis. The second objective deals with the identification and evaluation of potential inhibitors of the FMNAT activity of prokaryotic FADs, backing our proposal of these enzymes as potential antimicrobial targets.

With these general aims, in this study we tackle the following specific goals:

- To explore specific features of the mechanisms underlying the regulation of human RFK activity, in comparison with previous structure-function studies of RFK modules of prokaryotic FADs.
- To propose a plausible catalytic cycle for *HsRFK*, based on the kinetic and thermodynamic data and in the context of the available crystallographic structures.
- To elucidate the mechanism underlying the higher enzymatic activity of the D238E *hFADS* “supermutant” in comparison with the WT protein.
- To confirm the catalytic mechanism proposed for human FAD synthase through its kinetic and thermodynamic characterization.
- To provide an integrated perspective on the *hNQO1* catalytic mechanism by studying both the reductive and oxidative half-reactions in the pre-steady state.
- To evaluate the contribution of quantum tunneling, conformational dynamics and reorganizations in the hydride transfer process from the NADPH coenzyme to *hNQO1*.
- To characterize the effect of hit molecules envisaged to interact with *CaFADS* by either high-throughput-screening (HTS) or *in silico* screening on the RFK and FMNAT activities of *CaFADS*, and to determine the binding affinities of the best hits inhibiting its FMNAT activity.
- To evaluate the antimicrobial effect of HTS hits against several bacterial species, as well as the cytotoxic effect in eukaryotic cell lines.



# Publication I

**Human riboflavin kinase:  
species-specific traits in the  
biosynthesis of the FMN cofactor**

**Ernesto Anoz Carbonell contributions:** Experimental work: protein purification, spectroscopic characterization, steady-state enzymatic activity measurements, pre-steady-state kinetics through stopped-flow spectroscopy, and isothermal titration calorimetry experiments. Data analysis. Manuscript writing, review and editing



RESEARCH ARTICLE

# Human riboflavin kinase: Species-specific traits in the biosynthesis of the FMN cofactor

Ernesto Anoz-Carbonell<sup>1,2</sup> | Maribel Rivero<sup>1</sup> | Victor Polo<sup>2,3</sup> |  
Adrián Velázquez-Campoy<sup>1,2,4,5,6</sup> | Milagros Medina<sup>1,2</sup>

<sup>1</sup>Departamento de Bioquímica y Biología Molecular y Celular, Facultad de Ciencias, Universidad de Zaragoza, Zaragoza, Spain

<sup>2</sup>Instituto de Biocomputación y Física de Sistemas Complejos (GBsC-CSIC and BIFI-IQFR Joint Units), Universidad de Zaragoza, Zaragoza, Spain

<sup>3</sup>Departamento de Química Física, Universidad de Zaragoza, Zaragoza, Spain

<sup>4</sup>Fundación ARAID, Diputación General de Aragón, Zaragoza, Spain

<sup>5</sup>Aragon Institute for Health Research (IIS Aragon), Zaragoza, Spain

<sup>6</sup>Biomedical Research Networking Centre for Liver and Digestive Diseases (CIBERehd), Madrid, Spain

## Correspondence

Milagros Medina, Departamento de Bioquímica y Biología Molecular y Celular, Facultad de Ciencias, Pedro Cerbuna 12, Universidad de Zaragoza, 50009-Zaragoza, Spain.  
Email: mmedina@unizar.es

## Funding information

Spanish Ministry of Economy, Industry and Competitiveness, Grant/Award Number: BIO2016-75183-P AEI/FEDER; Spanish Ministry of Science and Innovation, Grant/Award Number: PID2019-103901GB-I00 AEI/FEDER; Government of Aragon-FEDER, Grant/Award Number: E35\_20R

## Abstract

Human riboflavin kinase (*HsRfK*) catalyzes vitamin B<sub>2</sub> (riboflavin) phosphorylation to flavin mononucleotide (FMN), obligatory step in flavin cofactor synthesis. *HsRfK* expression is related to protection from oxidative stress, amyloid- $\beta$  toxicity, and some malignant cancers progression. Its downregulation alters expression profiles of clock-controlled metabolic-genes and destroys flavins protection on stroke treatments, while its activity reduction links to protein-energy malnutrition and thyroid hormones decrease. We explored specific features of the mechanisms underlying the regulation of *HsRfK* activity, showing that both reaction products regulate it through competitive inhibition. Fast-kinetic studies show that despite *HsRfK* binds faster and preferably the reaction substrates, the complex holding both products is kinetically most stable. An intricate ligand binding landscape with all combinations of substrates/products competing with the catalytic complex and exhibiting moderate cooperativity is also presented. These data might contribute to better understanding the molecular bases of pathologies coursing with aberrant *HsRfK* availability, and envisage that interaction with its client-apoproteins might favor FMN release. Finally, *HsRfK* parameters differ from those of the so far evaluated bacterial counterparts, reinforcing the idea of species-specific mechanisms in RFK catalysis. These observations support *HsRfK* as potential therapeutic target because of its key functions, while also envisage bacterial RFK modules as potential antimicrobial targets.

## KEYWORDS

calorimetry, kinetics limiting step, ligand binding and cooperativity, pre-steady-state kinetics, product inhibition, riboflavin kinase, therapeutic target

**Abbreviations:** ANP, adenine nucleotide (ATP or ADP); *Ca*, *Corynebacterium ammoniagenes*; CD, circular dichroism; FADS, FAD synthase; FLV, flavinic nucleotide (FMN or FAD); FMNAT, ATP:FMN adenylyltransferase; GST, glutathione S-transferase; HPLC, high-performance liquid chromatography; *Hs*, *Homo sapiens*; ITC, isothermal titration calorimetry;  $K_a$ , association constant;  $k_{cat}$ , catalytic constant;  $K_d$ , dissociation constant;  $K_i$ , inhibition constant;  $K_M$ , Michaelis constant;  $k_{obs}$ , observed rate constant;  $k_{off}$ , dissociation rate constant;  $k_{on}$ , association rate constant; PIPES, 1,4-piperazine diethane sulfonic acid; rpm, revolutions per minute; RF, riboflavin, Vitamin B<sub>2</sub>; RFK, ATP:riboflavin kinase; SDS-PAGE, sodium dodecyl sulfate-polyacrylamide gel electrophoresis; *Sp*, *Schizosaccharomyces pombe*; *Spn*, *Streptococcus pneumoniae*;  $\alpha$ , heterotropic interaction constant;  $\epsilon$ , extinction coefficient.

## 1 | INTRODUCTION

Human riboflavin kinase (*HsRfK*; ECnonbreakingspace2.7.1.26) is an essential enzyme that catalyzes the biosynthesis of the flavin mononucleotide (FMN) cofactor using as substrates riboflavin (RF, vitamin B<sub>2</sub>) and ATP, therefore, exhibiting an ATP:riboflavin kinase activity (ECnonbreakingspace2.7.1.26).<sup>1,2</sup> Besides its key role in the synthesis of flavin cofactors, *HsRfK* is predicted as involved in a protein-protein association network that at the system level affects to different cellular processes (Figure SP1). In this context, the orthologous protein in mice has been shown essential for embryonic development, while, in both human and mouse cells, its binding to the Tumor Necrosis Factor Receptor 1 enhances assembly of the flavin adenine dinucleotide (FAD) cofactor to NADPH oxidases activating the production of reactive oxygen species as defence and signaling molecules.<sup>3</sup> *HsRfK* expression is also related to cellular protection from progression of some malignant prostate cancers.<sup>4</sup> Recently, *RfK*, as well as its FMN metabolic product, have also been reported as critical modulators of amyloid- $\beta$  toxicity.<sup>5</sup> On the contrary, its downregulation alters the expression profiles of cryptochromes and other clock-controlled metabolic genes, being also a potential risk factor for stroke by destroying the protective effect of flavin treatments.<sup>6,7</sup> Finally, insufficient conversion of RF into flavin cofactors by reduction of the *RfK* activity is reported in protein-energy malnutrition situations coursing with reduced thyroid hormone concentrations.<sup>8-10</sup> Altogether such observations point to *HsRfK* as a potential therapeutic target.

Part of the FMN produced by *HsRfK* is directly used as cofactor of FMN-dependent flavoproteins, but most of it is subsequently adenylylated by a FAD synthase (*HsFADS*), that exhibits ATP:FMN adenylyltransferase activity (FMNAT, ECnonbreakingspace2.7.7.2) and provides the flavin adenine dinucleotide (FAD) cofactor.<sup>11,12</sup> RF to FMN conversion seems to be the major rate limiting step in FAD synthesis, being therefore *HsRfK* a key element for the production of the FAD cofactor required by more than 60 human flavoenzymes.<sup>13,14</sup> *RfK* and FMNAT activities located in two independent enzymes is a trait of non-photosynthetic eukaryotes, but in most prokaryotes a single bifunctional enzyme known as type I FAD synthase (FADS) carries out both activities.<sup>15</sup> Noticeably, prokaryotic FADSs fold in two modules, being the N-terminal module associated to the FMNAT activity and the C-terminal to the *RfK* one.<sup>15,16</sup> The eukaryotic monofunctional *RfK*s and the C-terminal modules of prokaryotic FADSs are structurally homologs (both folding into a six-stranded  $\beta$  barrel core with Greek key topology), but species-specific differences in secondary structure elements are observed.<sup>1,2,16-18</sup> These variations, although apparently minor, utterly modulate conformational reorganizations occurring during substrate binding and catalysis, as

demonstrated for the *RfK* cycles of the prokaryotic FADSs of *Corynebacterium ammoniagenes* and *Streptococcus pneumoniae* (*CaFADS* and *SpnFADS*, respectively).<sup>19,20</sup> Furthermore, the substrate binding and catalytic motifs—PTAN and GxY—despite conserved, exhibit species-specific arrangements and traits (Figure 1 and SP2).<sup>2,18</sup>

As FMN and FAD are essential cofactors, not only in cell energetics metabolism, but also for the action of a plethora of flavoenzymes with very different cellular functions, their biosynthesis must be thoroughly regulated to maintain cellular and flavoproteome homeostasis.<sup>13,21</sup> In prokaryotes, we recently learned that FMN biosynthesis is regulated through mechanisms that, depending on the species, can include the inhibition of the *RfK* activity by the RF substrate and/or products, the redox state of the RF substrate, the formation of transient assemblies coupled to catalysis or the subsequent FMNAT activity occurring at the protein N-terminal module.<sup>19,20,22-27</sup> Eukaryotic cells provide additional levels of regulation by making use of different isoforms or intracellular compartmentalization. The mechanisms underlying FMN homeostasis in eukaryotes remain still poorly understood,<sup>28,29</sup> but those found in prokaryotic FADSs might also apply. In this context, the available crystallographic structures of *HsRfK* and of *RfK* from the yeast *Schizosaccharomyces pombe* (*SpRfK*) also envisage large conformational changes upon ligand binding and catalysis, particularly in the surface loops termed FlapI and FlapII (Figure 1 and SP2).<sup>1,2,17</sup>

In the present study, we focus on the intrinsic mechanisms underlying the regulation of *HsRfK* enzymatic activity. We have used the apo-*HsRfK* form, to avoid substrates and products of the reaction interfering our experimental approach. Our steady-state data indicate that *HsRfK* is inhibited by the reaction products, but not by substrates. Stopped-flow spectrophotometry allows ascertaining sequential conformational changes upon ligand binding and catalysis. Finally, ligand binding studies using isothermal titration calorimetry (ITC) display an intricate thermodynamic landscape. Our results are discussed in the context of the here modeled structure for apo-*HsRfK*, the available crystallographic structures of monofunctional *RfK*s and previous structure-function studies concerning *RfK* modules of prokaryotic FADSs.

## 2 | MATERIALS AND METHODS

### 2.1 | Cloning, expression, and purification of recombinant *HsRfK*

The coding sequence of *HsRfK* (accession number Q969G6) was codon optimized for its heterologous expression in *Escherichia coli* and synthesized by *GenScript*. This DNA sequence was cloned between the *NcoI* and *BamHI* restriction sites of a pET28a(+)-derived vector, in which the

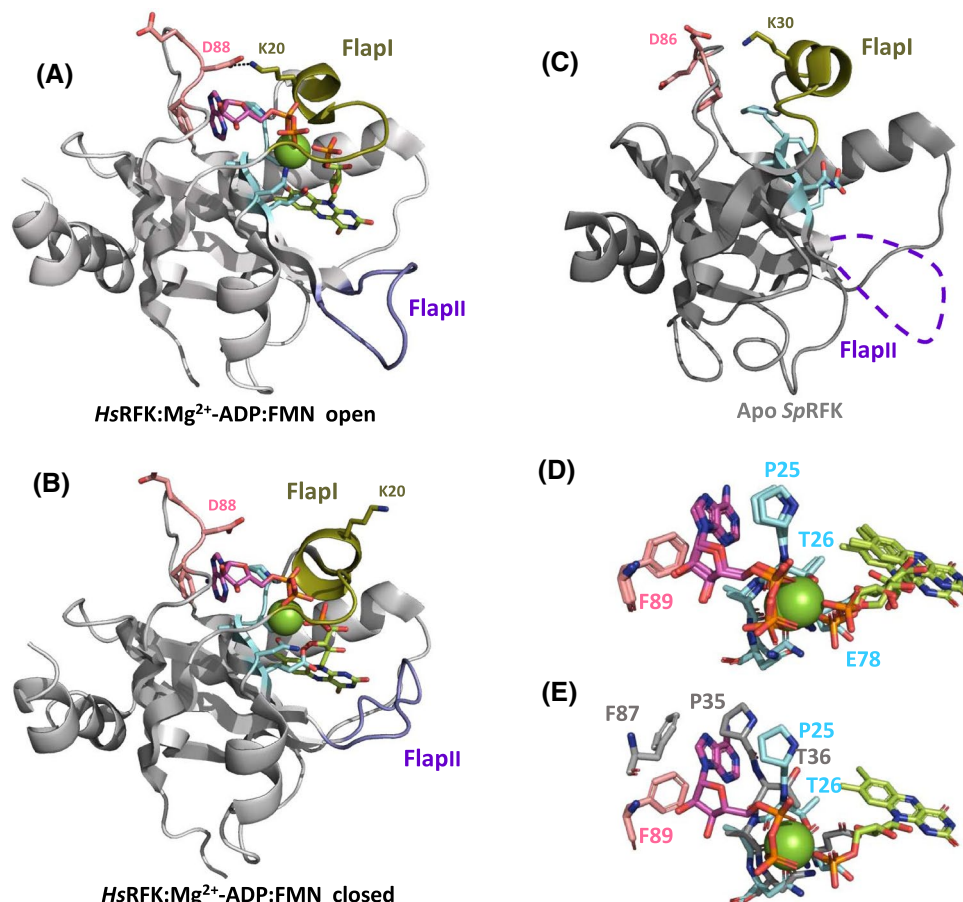


**FIGURE 1** Structural properties of RFKs. Cartoon representation of the crystallographic structure of *HsRFK* in complex with FMN and ADP in either the (A) open (PDB ID 1P4M) or the (B) closed conformation (PDB ID 1Q9S) of the flavin binding site. (C), Cartoon representation of *SpRFK* as crystallized in the apo form (PDB ID 1N05). FlapII is disordered and depicted as a dashed loop. Comparison of the organization of the active site in the closed *HsRFK*:FMN:ADP complex relative to the structures of the (D) open *HsRFK*:FMN:ADP complex and of the (E) apo-*SpRFK* (shown in grey). In all panels FMN and ADP ligands are shown as CPK colored sticks with carbons in green and magenta, respectively, and  $Mg^{2+}$  is shown as a green sphere. Unless otherwise stated, FlapI, FlapII, and L6c are highlighted in green, violet and pink, respectively, the consensus PTAN motif at the active site is in blue for *HsRFK* and grey for *SpRFK*. Relevant side-chains are in sticks

thrombin cleavage site was substituted by the PreScission Protease cleavage signal. The sequence-verified plasmid was transformed into *E coli* BL21(DE3) strain, and transformed cells were grown at 37°C in LB medium (1% (w/v) of tryptone, 0.5% (w/v) of yeast extract, and 1% (w/v) of NaCl) supplemented with 50 mg/mL of kanamycin. At an  $OD_{600\text{ nm}}$  of 0.7, cultures were induced with 0.2 mM of isopropyl  $\beta$ -D-1-thiogalactopyranoside, incubated under the same conditions and, after 24 hours, harvested. Cells were resuspended in 20 mM sodium phosphate, pH 7.4, 500 mM NaCl, and 10 mM imidazole, containing lysozyme (1 mg/mL), DNase (0.1 mg/mL), and protease inhibitors (0.2 mM of Phenylmethanesulfonyl fluoride and 10 mM of benzamide), and subsequently sonicated at 4°C. After centrifugation to remove cell debris, the supernatant containing the soluble protein was loaded into a HisTrap HP affinity column (*GE Healthcare*) and the protein was eluted applying a gradient from 10 to 500 mM of imidazole in 20 mM of

sodium phosphate, pH 7.4, 500 mM NaCl. Buffer was exchanged to 50 mM Tris/HCl, pH 7.4, 150 mM NaCl, using a HiPrep Desalting Column (*GE Healthcare*). The His<sub>6</sub>-Tag was removed by 24 hours incubation with the PreScission protease (*GE Healthcare*) at 4°C, in ratio 1:10 (w/w), and the protein was then loaded into the HisTrap HP column in tandem coupled to a GStrap 4B column (*GE Healthcare*) to eliminate both the remained His<sub>6</sub>-Tagged *HsRFK* and the PreScission protease (a GST fused product). The resulting yellowish unbound fraction was fractionated with 20% of ammonium sulfate and centrifuged for 30 minutes at 4000 g. The supernatant was loaded onto a Phenyl-Sepharose High performance (*GE Healthcare*) column equilibrated with 50 mM of Tris/HCl, pH 8.0, 20% of ammonium sulfate. The column was washed with the same buffer until most of the yellow color washed out. Finally, the protein was eluted using a 20→0% reversed-gradient of ammonium sulfate in the same buffer. Protein purity was

assessed by 17% of SDS-PAGE and buffer was finally exchanged by dialysis in 20 mM PIPES, pH 7.0. Pure protein solution was stored at  $-80^{\circ}\text{C}$  until used.

## 2.2 | Spectroscopic analysis

UV-visible spectra were recorded in a Cary 100 spectrophotometer (*Agilent Technologies*) and ligand-free HsRFK was quantified using the theoretical extinction coefficient  $\epsilon_{279\text{ nm}} = 21\,430\text{ M}^{-1}\text{cm}^{-1}$  and a molecular weight of 17.76 kDa (ProtParam). Fluorescence emission spectra were recorded in a Cary 100 spectrophotometer (*Agilent Technologies*) in 20 mM of PIPES, pH 7.0, 0.3 mM of  $\text{MgCl}_2$  at  $25^{\circ}\text{C}$ , exciting the protein aromatic residues at 280 nm. Fluorescence excitation scans were recorded at the maximum emission wavelength (323 nm) and in the same experimental conditions. Circular dichroism (CD) spectra were recorded at  $25^{\circ}\text{C}$  using a Chirascan spectropolarimeter (*Applied Photosystem Ltd.*). Samples containing  $\sim 5$  and  $\sim 20\text{ }\mu\text{M}$  of HsRFK in 20 mM of PIPES, pH 7.0, 0.3 mM of  $\text{MgCl}_2$  were used in the far-UV (cuvette path length, 0.1 cm) and near-UV CD (cuvette path length, 0.4 cm), respectively.

## 2.3 | Steady-state RFK activity

The RFK activity of HsRFK was measured at  $25^{\circ}\text{C}$  in 500  $\mu\text{L}$  of 20 mM of PIPES, pH 7.0 and 0.3 mM of  $\text{MgCl}_2$ , containing variable concentrations of RF (0.2–15  $\mu\text{M}$ ) and ATP (2–600  $\mu\text{M}$ ), as previously described.<sup>30,31</sup> The inhibitory effect of the substrates and products of the reaction was also analyzed by measuring the RFK activity in reaction mixtures at increasing concentrations of FMN (0–5  $\mu\text{M}$ ), varying the ATP concentration and keeping the RF constant for the determination of the FMN inhibitory effect; and at increasing concentrations of ADP (0–120  $\mu\text{M}$ ), varying the RF concentration and keeping ATP fixed. In all cases, reactions were initiated by addition of 40 nM HsRFK to reaction mixtures preincubated at  $25^{\circ}\text{C}$ . After 1 minute of incubation at  $25^{\circ}\text{C}$  reactions were stopped by boiling the samples at  $100^{\circ}\text{C}$  for 5 minutes. The flavin composition of the supernatant was analyzed using an Alliance HPLC system (*Waters*) equipped with a 2707 autosampler and an HSST3 column (4.6  $\times$  50 mm, 3.5 mm; *Waters*) preceded by a pre-column (4.6  $\times$  20 mm, 3.5 mm; *Waters*) as previously described.<sup>31</sup> Flavin concentrations were quantified using RF or FMN standard curves acquired under the same conditions, and the observed steady-state rates for FMN production ( $v_0$ ) were determined in units of nmoles of flavin transformed *per min per nmol* of enzyme ( $v_0/[e]$ ). The kinetic data obtained for one substrate at saturating concentrations of the second substrate were fitted to

the Michaelis-Menten kinetic model, obtaining  $k_{\text{cat}}$  and  $K_m$  values. The inhibition mechanism of the products of the RFK reaction -FMN and ADP- was determined by evaluating their effect on  $K_m$  and  $k_{\text{cat}}$  by individual fitting of data sets to the Michaelis-Menten model. Additionally, data sets acquired at variable concentrations of the product acting as inhibitor were globally fitted to the Lineweaver-Burk equation for competitive inhibition

$$\frac{[e]}{v_0} = \left(1 + \frac{[I]}{K_i}\right) \frac{K_m}{k_{\text{cat}}} \frac{1}{[S]} + \frac{1}{k_{\text{cat}}} \quad (1)$$

where  $[S]$  is the concentration of the varying substrate (RF or ATP) and  $[I]$  that of the inhibitor (FMN or ADP), and  $K_i$  is the corresponding inhibition constant. All experiments were performed in triplicate. Estimated errors in  $k_{\text{cat}}$ ,  $K_M$  and  $K_i$  values were, in general, within 10% of their values, assumed to be larger than the standard deviation between replicates and the numerical error after fitting analysis.

## 2.4 | Pre-steady-state kinetics

Kinetic experiments in the pre-steady state were registered using stopped-flow spectroscopy on an Applied Photophysics SX17.MV spectrophotometer, using the ProData SX software (*Applied Photophysics Ltd.*) for fluorescence data acquisition and kinetic data analysis. Fast kinetic measurements were carried out at  $25^{\circ}\text{C}$  in PIPES 20 mM, pH 7.0, 0.3 mM of  $\text{MgCl}_2$  as previously described.<sup>19,20</sup> In short, 0.2  $\mu\text{M}$  of HsRFK was mixed with reaction samples containing increasing concentrations of the FLV ligands in the absence or presence of saturating concentrations of ANP ligands. Evolution of flavin fluorescence after mixing was measured with an excitation wavelength of 445 nm, while fluorescence emission was recovered using a  $>530\text{ nm}$  cut-off filter. Control experiments, recorded in the same buffer but in absence of  $\text{MgCl}_2$ , produced similar profiles with significantly smaller amplitudes in the fluorescence change. All the concentrations indicated for these experiments are the final ones in the stopped-flow observation cell. Three to five reproducible traces were acquired at each time and concentration condition assayed. These kinetic traces were then fitted to exponential functions,

$$y = \sum A_i \cdot \exp(-k_{\text{obs}i} \cdot t) \quad (2)$$

where  $A_i$  and  $k_{\text{obs}i}$  are the amplitude of the fluorescence change and the observed kinetic constant for a particular spectroscopic process  $i$  that contributes to the overall time-dependent fluorescence change. The previous equation was corrected by the addition of a linear term when a process was not finished in the timeframe of the measurement.

$$y = \sum A_i \cdot \exp(-k_{\text{obs}i} \cdot t) + b \cdot t \quad (3)$$

It should be noticed that when more than one process is detected, accuracy in determination  $A_i$  and  $k_{\text{obs}i}$  for processes after the initial one decreases with the FLV concentration assayed.

$k_{\text{obs}}$  values showing a linear dependence on the FLV concentration were fitted to a one-step model associated to the binding equilibrium of the flavin ligand to *HsRfK* ( $HsRfK + FLV \rightleftharpoons HsRfK:FLV$ ), whose kinetics can be represented by the following equation

$$k_{\text{obs}} = k_{\text{on}} \cdot [FLV] + k_{\text{off}} \quad (4)$$

where  $k_{\text{on}}$  and  $k_{\text{off}}$  are the kinetic rate constants for complex formation and dissociation, respectively.

When  $k_{\text{obs}}$  values show hyperbolic dependence on the FLV concentration, data can be fitted to an induced fit model ( $HsRfK + FLV \rightleftharpoons HsRfK:FLV^* \rightarrow HsRfK:FLV$ )<sup>32</sup> that parametrizes both the ligand binding ( $K_d$ ,  $k_{\text{off}}/k_{\text{on}}$ ) and the subsequent conformational change ( $k_r$ , as the kinetic rate constant for the structural rearrangement).

$$k_{\text{obs}} = k_r \cdot \frac{[FLV]}{K_d + [FLV]} \quad (5)$$

When detected, flavin photobleaching within the stop-flow observation chamber was evaluated as previously described.<sup>20</sup>

## 2.5 | Isothermal titration calorimetry

ITC measurements were performed using a high precision Auto-iTC200 MicroCal calorimeter (*Malvern Panalytical*) thermostated at 25°C. Up to 19 injections of 2  $\mu\text{L}$  of the titrating solution were added to the calorimetric sample cell and mixed using a stirring speed of 750 rpm. Ligands and protein were both dissolved in 20mM of PIPES, pH 7.0, in absence and presence of 0.3mM of  $\text{MgCl}_2$  (cation concentration for optimal enzymatic activity). Typically, 50 $\mu\text{M}$  of RF, 70 $\mu\text{M}$  of FMN, and 80 $\mu\text{M}$  of ANP (ATP or ADP) in PIPES 20mM, pH 7.0 were used to titrate *HsRfK* (10  $\mu\text{M}$ ) in a 200 $\mu\text{L}$  sample cell. Additionally, preformed complexes of the enzyme with the FLV or ANP ligands at saturating concentrations were titrated with ANP or FLV ligands, respectively. The association constant ( $K_a$ ), the enthalpy change ( $\Delta H$ ), and the binding stoichiometry ( $N$ ) were obtained through nonlinear least squares regression of the data using a homemade model for one binding site, which was implemented in Origin 7.0 (OriginLab) as previously described.<sup>33</sup> The  $K_d$ , the free energy change ( $\Delta G$ ), and the entropy change ( $\Delta S$ ) were obtained from essential thermodynamic relationships.

Cooperative ligand binding was assessed by ITC employing an exact analysis of the heterotropic interactions considering a ternary equilibrium between the protein and two ligands approximate analysis as previously described.<sup>34-36</sup> A quasi-binary equilibrium between the protein and one ligand, with the influence of the other ligand being implicit within the apparent ligand binding parameters, was also used to confirm parameters.<sup>20</sup> Briefly, ANP ligands were used to titrate mixtures of *HsRfK* (10  $\mu\text{M}$ ) with different FLV concentrations (0-100  $\mu\text{M}$ ) in the calorimetric cell, and the cooperativity constant for the heterotropic interaction ( $\alpha$ ) between ANP and FLV ligands was determined from any single titration employing the exact methodology.<sup>34-36</sup> Additionally, titrations of *HsRfK:FLV* mixtures (at different FLV concentrations) with ANP ligands were analyzed as binary titrations, from which apparent association constants for ANP ligands at certain FLV concentrations were determined. These data were fitted to a cooperativity model that considers explicitly the influence of the FLV ligand in the protein binding affinity for the ANP ligand:<sup>19,20,34-36</sup>

$$K_a^{\text{app,ANP}} = K_a^{\text{ANP}} \frac{1 + \alpha K_a^{\text{FLV}} [FLV]}{1 + K_a^{\text{FLV}} [FLV]} \quad (6)$$

where  $K_a^{\text{app,ANP}}$  is the apparent association constant for the ANP ligand as a function of the FLV concentration,  $K_a^{\text{ANP}}$  is the intrinsic association constant for ANP (that is, in the absence of FLV ligand),  $K_a^{\text{FLV}}$  is the association constant for FLV, and  $[FLV]$  is the concentration of flavin in the calorimetric cell, from which  $\alpha$  between ANP and FLV ligands can also be determined.

ITC experiments were performed in duplicate or triplicate. The errors considered in the measured parameters (in general  $\pm 15\%$  in  $K_d$  and  $K_a$  values,  $\pm 0.3 \text{ kcal mol}^{-1}$  in  $\Delta H$ ,  $\Delta G$  and  $-\text{T}\Delta S$ , and  $\pm 20\%$  in  $\alpha$ ) were assumed to be larger than the standard deviation between replicates and the numerical error after fitting analysis.

## 2.6 | Molecular dynamics simulations

The initial model of apo-*HsRfK*, excluding any ligand, was built by removing ADP and  $\text{Mg}^{2+}$  from the crystallographic structure with PDB ID 1NB0. PROPKA software was used to assign  $\text{p}K_a$  values to structures, which were protonated to pH 7.0.<sup>37</sup> PyMOL was used for structural manipulations and figures production.<sup>38</sup> All-atom molecular dynamics (MD) simulations were performed using GROMACS 5.1.5<sup>39</sup> and AMBER ff03 parameters.<sup>40</sup> The system was placed in the center of a rhombic dodecahedron box, solvated with a TIP3P water model and neutralized by adding sodium ions. Final system consisted in 22345 total atoms. A steepest descent minimization was performed to avoid close contacts

or clashes. Desired conditions were achieved after a 100 ps simulation with NVT ensemble and the generation of random initial velocities, and a 100 ps simulation with NPT ensemble, restraining the movement of atoms of protein with a  $1000 \text{ kJ}\cdot\text{mol}^{-1}\cdot\text{nm}^{-1}$  harmonic potential. Longer NPT (300 K) simulations with positions unrestrained were then performed, collecting the data every 10 ps. Time step of 2 fs and leap-frog integrator, periodic boundary conditions, Particle Mesh Ewald method for long range electrostatic interaction, Parrinello-Rahman method for pressure control, modified Berendsen method for temperature equilibration and LINCS to restrain bonds including hydrogen atoms were used. Five replicates were made for each trajectory, which were analyzed using VMD<sup>41</sup> and GROMACS package tools.<sup>39</sup>

### 3 | RESULTS

#### 3.1 | *Hs*RFK is purified free of flavin and adenine ligands

*E. coli* BL21 (DE3) cells transformed with the recombinant pET28a-*Hs*RFK vector produced a high level of expression of active *Hs*RFK enzyme, with a typical yield after purification of 3.2 mg of protein *per* liter of culture. *Hs*RFK fractions were yellow colored, suggesting the protein was expressed in complex with a tightly bound flavinic ligand that kept bound throughout the purification process. Hence, initial purified fractions of the recombinant protein showed the typical flavoprotein bands-I and -II in the Vis absorbance spectrum (Figure SP3A). HPLC analysis of the supernatant obtained upon thermal denaturation of the enzyme demonstrated that the bound cofactor was FMN. Additionally, the other product of the RFK activity, ADP, was also detected as trapped into the purified enzyme. This was evidenced by the displacement of the aromatic absorption peak of protein toward 260 nm (characteristic of nucleotides) in some flavin-free enzyme samples and by the absorption properties of its supernatant after thermal denaturation. High affinity of the adenine nucleotide was previously reported, probably being the reason why all *Hs*RFK structures so far reported in the PDB contain it.<sup>1,2</sup> Therefore, despite the protein was pure, a phenyl-sepharose hydrophobic chromatographic step was required to remove the FMN and ADP products from *Hs*RFK. To the best of our knowledge, this will be the first purification of *Hs*RFK in its apo-form to homogeneity (spectrum shown in Figure SP3A).

Excitation of *Hs*RFK at 280nm produced a fluorescence emission band centered at 332nm (Figure SP3B), in agreement with Trp residues embedded within the protein environment. The negative couplet (195-210 nm) in the far-UV CD spectrum of *Hs*RFK (Figure SP3C) indicated secondary  $\alpha$ -helix structure, and the shoulder at 218nm also pointed to an important content of  $\beta$ -sheet. Such spectral properties are consistent with the secondary structure content derived from crystallographic

data: around 27% of  $\alpha$ -helix, 30% of  $\beta$ -sheet and a large content of loops. The near-UV CD spectrum (Figure SP3D) of *Hs*RFK showed a broad 265-295nm negative band with minima at 285 and 292nm related to the protein tertiary structure organization. Collectively, these data indicate that the purified *Hs*RFK is correctly folded and in the apo-form.

#### 3.2 | The *Hs*RFK activity is modulated by the products of the reaction

In advance to determining the *Hs*RFK kinetic parameters, we quantitatively evaluated the influence of the reducing environment (by using sodium dithionite) as well as of the presence of  $\text{Mg}^{2+}$ . Under saturating concentrations of both substrates (RF and ATP), the RFK activity resulted tightly regulated by the cation concentration, with maximal rates at a concentration of 0.3mM (Figure SP4A). Herein, a  $\text{MgCl}_2$  concentration of 0.3mM was used. On the contrary, the rate for RF transformation was independent on the concentration of the reducing agent (Figure SP4B). This later behavior resulted similar to that described for *Ca*FADS and *Spn*FADS, but differed for other species, as *Listeria monocytogenes*, whose turnover and efficiency highly depended on the redox status of the media.<sup>19,22,23,26,27</sup>

Steady-state rates for the *Hs*RFK activity showed saturation profiles for both substrates (Figure 2A). These profiles fitted to the Michaelis-Menten model allowing determination of  $k_{\text{cat}}$ ,  $K_M^{\text{RF}}$ , and  $K_M^{\text{ATP}}$ , in  $102 \text{ min}^{-1}$ ,  $2.5 \mu\text{M}$  and  $30 \mu\text{M}$  (Table 1), respectively. Furthermore, no inhibition by excess of RF substrate was detected, contrary to that reported for the RFK activity of *Ca*FADS<sup>31</sup> but in line with previous data for *Hs*RFK,<sup>42</sup> *Spn*FADS,<sup>19</sup> and *Lm*FADS-1.<sup>27</sup> Nonetheless, our *Hs*RFK data showed high efficiency for the synthesis of FMN when compared not only to bifunctional FADSs,<sup>19,20,27</sup> but also to data previously reported for *Hs*RFK<sup>43</sup> (Table 1). In the case of *Hs*RFK, such differences can be associated to different protein isolation procedures, in agreement with early reports showing different RFK pools with distinct enzymatic activity co-existing in rat liver cells. Such differences are probably due to dissimilarities in the content of ligands bound to the enzyme.

Since inhibition of the RFK activity by the reaction products contributes to maintain the flavin and flavoproteome homeostasis in prokaryotes, it is worthy to evaluate the occurrence of such effects in the *Hs*RFK activity. The Michaelis-Menten and Lineweaver-Burk plots at increasing concentrations of either ADP or FMN products showed that while  $k_{\text{cat}}$  remained constant, both  $K_M^{\text{ATP}}$  and  $K_M^{\text{RF}}$  increased (Figure 2). This pointed out to a competitive mechanism of inhibition for both reaction products, allowing determination of the apparent inhibition constants,  $K_I^{\text{ADP}}$  and  $K_I^{\text{FMN}}$  (Table 1). The similar values of  $K_I^{\text{ADP}}$  and  $K_M^{\text{ATP}}$  as well as of  $K_I^{\text{FMN}}$  and  $K_M^{\text{RF}}$  indicated that ADP and FMN bind to the free

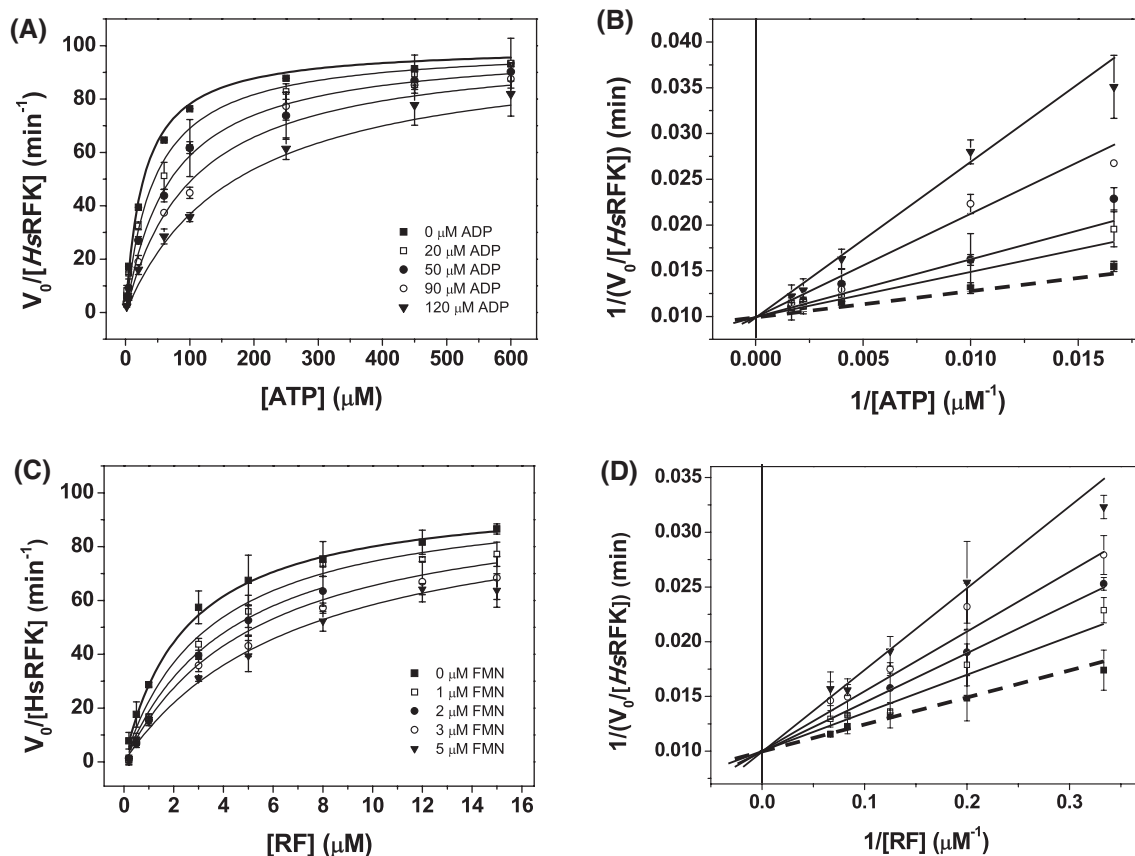


**FIGURE 2** Inhibition of *HsRFK* activity by FMN and ADP products. (A) and (C) Michaelis-Menten plots and, (B) and (D) their corresponding Lineweaver-Burk representations, as a function of different concentrations of the (A and B) ATP and (C and D) RF substrates in the presence of different concentrations of the products (A and B) ADP and (C and D) FMN. Lines correspond to global fits to the equation for competitive inhibition (Equation 1)

**TABLE 1** Steady-state kinetic parameters for the *HsRFK* activity

| RFK enzyme                            | $k_{cat}$ ( $\text{min}^{-1}$ ) | $K_M^{ATP}$ ( $\mu\text{M}$ ) | $k_{cat}/K_M^{ATP}$ ( $\text{min}^{-1} \mu\text{M}^{-1}$ ) | $K_I^{ADP}$ ( $\mu\text{M}$ ) | $K_M^{RF}$ ( $\mu\text{M}$ ) | $k_{cat}/K_M^{RF}$ ( $\text{min}^{-1} \mu\text{M}^{-1}$ ) | $K_I^{FMN}$ ( $\mu\text{M}$ ) |
|---------------------------------------|---------------------------------|-------------------------------|--|-------------------------------|------------------------------|---|-------------------------------|
| <i>HsRFK</i> <sup>a</sup>             | $102 \pm 7$                     | $30 \pm 8$                    | $3.4 \pm 1.1$  | $33 \pm 6$                    | $2.5 \pm 0.4$                | $41 \pm 9$  | $2.5 \pm 0.8$                 |
| <i>HsRFK</i> (-) <sup>b</sup>         | 18                              |                               |  |                               | 117                          | 0.16  |                               |
| <i>HsRFK</i> (+) <sup>b</sup>         | 30                              |                               |  |                               | 36                           | 0.08  |                               |
| <i>CaFADS</i> <sup>c</sup> RFK module | $130 \pm 30$                    | $40 \pm 12$                   | $3.2 \pm 1.7$  | $17 \pm 3$                    | $6.9 \pm 0.4$                | $19 \pm 5$  | $1.4 \pm 0.2$                 |
| <i>SpnFADS</i> <sup>d</sup>           | $55 \pm 2$                      | $75 \pm 7$                    | $0.7 \pm 0.1$  | $130 \pm 16$                  | $1.2 \pm 0.3$                | $46 \pm 13$   | $1.3 \pm 0.4$                 |
| <i>LmFADS-1</i> (-) <sup>e</sup>      | $33 \pm 2$                      | $41 \pm 2$                    | $0.8 \pm 0.1$  | $844 \pm 95$                  | $0.5 \pm 0.1$                | $66 \pm 4$  | $7.1 \pm 1.3$                 |
| <i>LmFADS-1</i> (+) <sup>e</sup>      | $95 \pm 7$                      | $12 \pm 1$                    | $7.9 \pm 0.9$  |                               | $10 \pm 1$                   | $95 \pm 1$  |                               |

<sup>a</sup>Experiments performed at 25°C in 20mM of PIPES, pH 7.0, 0.3 mM of  $\text{MgCl}_2$  ( $n = 3$ , mean  $\pm$  SD). Presented data calculated by global fitting.

<sup>b</sup>Data from (43). Experiments performed at 37°C in 50 mM of potassium phosphate buffer, pH 7.5, 12mM of  $\text{MgCl}_2$ , both in absence (-) and presence (+) of 24 mM of sodium dithionite.

<sup>c</sup>Data from (20). Experiments performed at 25°C in 20mM of PIPES, pH 7.0, 0.8 mM of  $\text{MgCl}_2$ .

<sup>d</sup>Data from (19). Since both ADP and FMN act as mixed inhibitors two different  $K_I$  values are shown for each. Experiments performed at 25°C in 20 mM of PIPES, pH 7.0, 0.8 mM of  $\text{MgCl}_2$ .

<sup>e</sup>Data from (27), experiments performed in 20mM of PIPES and 0.8 mM of  $\text{MgCl}_2$ , pH 7.0, at 25°C, both in absence (-) and presence (+) of 24 mM of sodium dithionite.

*HsRFK* enzyme with alike affinity to the substrates of the reaction. Also, the significantly smaller inhibition constant for FMN in comparison with ADP ( $K_I^{ADP}/K_I^{FMN} = 13.2$ ) envisages FMN as a more potent inhibitor.

*CaFADS* and *SpnFADS* also showed product inhibition of the RFK activity, but their inhibition mechanisms differed from that of *HsRFK* as well as among them: mixed for both products in *SpnFADS* versus competitive for FMN and

uncompetitive for ADP in *CaFADS*. FMN is a more potent inhibitor in *CaFADS* ( $K_M^{RF}/K_I^{FMN} = 7.1$ ) than in *SprFADS* or *HsRFK* (0.8 and 1, respectively); and also, RF is a very strong inhibitor of the RFK activity in *CaFADS* but not in the other enzymes.<sup>19,20,27</sup> Therefore, FMN biosynthesis in *Homo sapiens* will be regulated by the products of the RFK reaction. In addition, and considering that transport across membranes appears favored for the RF substrate over FMN and FAD, intracellular compartmentalization with different substrate/product concentrations and/or the presence of different isoforms might also apply in the *in vivo* *HsRFK* regulation.<sup>11,28,44</sup>

### 3.3 | Binding of *HsRFK* substrates is the kinetically preferred process

We used stopped-flow spectrophotometry to kinetically differentiate individual processes during the *HsRFK* reaction. This technique allowed us to detect small changes in the dielectric environment of the flavin isoalloxazine upon

its binding and/or dissociation to the protein, and/or as consequence of conformational changes in its environment,<sup>19,20</sup> while RF transformation into FMN is not observed due to the same fluorescence spectra and quantum yields of both flavins. When we mixed *HsRFK* with either RF or FMN, we only detected very slow and linear fluorescence decays consistent with previously reported flavin photobleaching.<sup>19,20</sup> These observations suggested that the apo-form of *HsRFK* is not able to bind RF or FMN (herein both referred as FLV) ligand, or at least to internalize its isoalloxazine ring in the expected catalytically competent enclosed conformation.

A fast and intense exponential decay in fluorescence in the 2 seconds time frame was, however, detected when mixing *HsRFK* with all combinations of ATP or ADP (denoted herein as ANP) and FLV ligands (Figure 3A). We related the fluorescence decay to FLV binding and/or internalization in the protein matrix by FlapII displacement (Figure 3A), concluding that the ANP presence/binding prones *HsRFK* to bind and internalize the FLV ligand. Noticeably, no subsequent recover of fluorescence was observed for the assayed

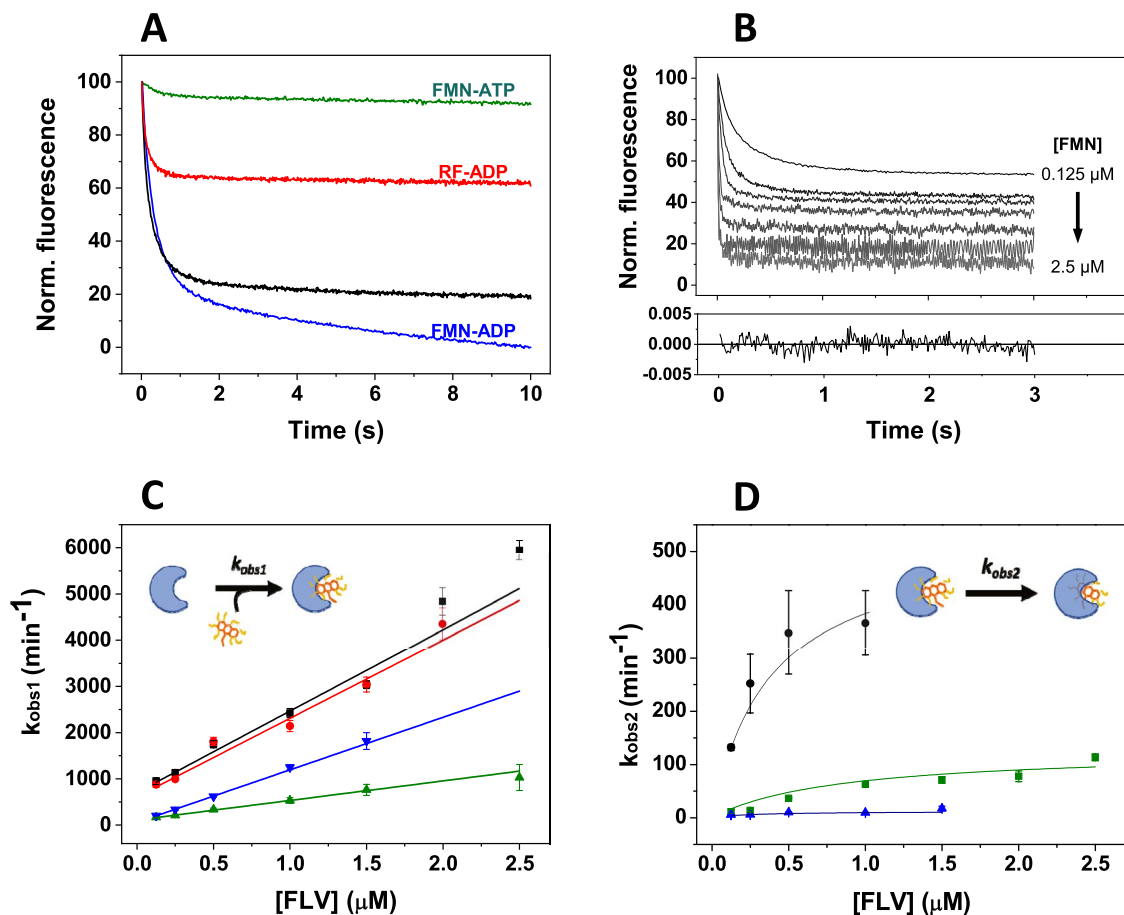


**FIGURE 3** Pre-steady-state stopped-flow kinetics of the binding of RF and FMN to *HsRFK* in the presence of adenine nucleotides. (A) Normalized evolution of kinetic changes in fluorescence upon mixing *HsRFK* (0.2 μM) with all possible FLV-ANP ligand combinations (0.125 and 250 μM, respectively). (B) Example of the fittings of kinetic traces (in this case, corresponding to mixtures of *HsRFK* with RF-ATP), and residuals of the fitting of the 1 μM RF-250 μM ATP data to a biexponential function. Evolution of (C)  $k_{obs1}$  and (D)  $k_{obs2}$  as a function of the FLV concentrations. Insets show schemes representing the corresponding processes



combinations of ligands, differing this behavior from the one reported when similarly evaluating the RFK modules of *CaFADS* and *SpnFADS*. For these two enzymes, the initial flavin fluorescence decay was followed by fluorescence recover related to an ATP-induced conformational change that re-opens the flavin binding site making the isoalloxazine accessible to the solvent after the reaction has taken place.<sup>19,20</sup>

Kinetic traces corresponding to mixtures of *HsRFK* with the RF-ADP ligands fitted to a single exponential decay, whereas two and up to three independent processes were identified when, respectively, evaluating the binding kinetics in the FLV-ATP and FMN-ADP combinations (Figure 3B). Noticeably, while the amplitude of the first process ( $A_1$ ) dominates the fluorescence decay for RF binding,  $A_1$  and  $A_2$  became similar when assaying the binding kinetics of the FMN product (no shown). Therefore, we identified the initial process, generally accounting for most of the amplitude decay, as FLV binding/internalization in *HsRFK* by FlapII displacement (up to ~14Å reorganization of amino acids comprising the loop), similarly to that reported for *CaFADS* and *SpnFADS*.<sup>19,20</sup> The succeeding fluorescence decays have to relate to subsequent conformational changes in *HsRFK* loops further contributing to additional changes in the isoalloxazine environment after the initial binding. Considering these extra processes are not observed when mixing the protein with RF-ADP, they appear related to the extra phosphates of ATP and FMN, over ADP and RF, respectively, influencing some conformational flexibility.

$k_{\text{obs1}}$  values showed a linear dependence on the FLV concentration (Figure 3C) that permitted to determine  $k_{\text{on}}$  and  $k_{\text{off}}$  for flavin binding and, as a consequence the process dissociation constant ( $K_d$ ) (Table 2). These data indicated that binding processes containing the RF substrate are the fastest (Table 2A). In addition, the largest amplitude in fluorescence decay is observed for RF and ATP (Figure 3A). Therefore, *HsRFK* binds preferably the substrates of the RFK reaction, RF and ATP, over other combinations of substrates/products, similarly to *SpnFADS* but contrary to *CaFADS*. Noticeably, binding of the FMN product in presence of ANP (particularly

ATP) were the least favored processes from the kinetic point of view (smaller  $k_{\text{on}}$ ), though the combination of FMN-ADP products showed an amplitude comparable to that of substrates and a considerably lower  $k_{\text{off}}$ . As consequence, the complex of *HsRFK* with the products of its activity exhibits the smaller  $K_d$  and appears, therefore, as the most stable one.

On their side, when detected,  $k_{\text{obs2}}$  showed a saturation profile on the FLV concentration (Figure 3D). When fitting these data to an induced fit model representing changes in the protein conformation induced by binding of the ligand,<sup>32</sup> we were able to determine an equilibrium reorganization constant as well as the kinetic constant to achieve the final state (Table 2B). Noticeably, this process presented very particular features when evaluating the FMN-ADP products; it was considerably slower ( $k_r$ ),  $A_2$  was comparable to  $A_1$ , and the product of its reorganization was the most stable ( $K_{\text{reorg}}$ ). Therefore, binding of the products of the RFK activity to the enzyme occurs through stabilization of a transient intermediate in the isoalloxazine internationalization by FlapII displacement, while these intermediate is hardly populated, or not at all, in the binding of other ligand combinations. Noticeably, this FMN-ADP combination is the only one for which a third considerably slower process (80-100 min<sup>-1</sup> at the FMN concentrations assayed), likely independent of the flavin concentration, is observed when binding to *HsRFK*. Interestingly,  $k_{\text{on}}$  and  $k_r$  values for the binding of RF-ATP substrates are substantially faster than the  $k_{\text{cat}}$ , while  $k_{\text{off}}$  for the FMN-ADP products is situated in its range (Tables 1 and 2). Collectively, these observations indicate that kinetics of products release limits the *HsRFK* catalytic activity.

These data point to differences in the regulation of the catalytic activity of *HsRFK* when compared to *CaFADS* and *SpnFADS*. In *HsRFK*, as in *SpnFADS*, the binding of substrates of the RFK reaction -RF and ATP- is the kinetically favored process,<sup>19</sup> whereas in *CaFADS* binding of any other combination of ligands is faster.<sup>20</sup> Moreover, while in *CaFADS* and *SpnFADS* the ATP substrate activates FLV ligand internalization as well as the subsequent cavity re-opening to make this ligand again solvent accessible, such

**TABLE 2** Pre-steady-state kinetic parameters for the binding and dissociation of flavins to *HsRFK* in the presence of adenine nucleotides. Experiments were performed at 25°C in 20 mM of PIPES, pH 7.0, 0.3 mM of MgCl<sub>2</sub> (n = 5, mean ± SEM) in and stopped-flow equipment

| Ligands combination | $k_{\text{obs1}}$ (flavin binding)                    |                                       |             |                                      | $k_{\text{obs2}}$ (conformational rearrangement) |                         |   |
|---------------------|---|---------------------------------------|-------------|--------------------------------------|--|-------------------------|---|
|                     | $k_{\text{on}}$ (min <sup>-1</sup> μM <sup>-1</sup> ) | $k_{\text{off}}$ (min <sup>-1</sup> ) | $K_d$ (μM)  | $\Delta G$ (kcal mol <sup>-1</sup> ) | $k_r$ (min <sup>-1</sup> )                       | $K_{\text{reorg}}$ (μM) | $\Delta G_{\text{reorg}}$ (kcal mol <sup>-1</sup> ) |
| RF-ATP              | 1760 ± 50   | 700 ± 40                              | 0.40 ± 0.02 | -8.6 ± 0.1                           | 530 ± 80   | 0.38 ± 0.08             | -8.8 ± 0.1  |
| RF-ADP              | 1670 ± 90   | 610 ± 10                              | 0.36 ± 0.03 | -8.7 ± 0.1                           | <sup>a</sup>                                     | <sup>a</sup>            | <sup>a</sup>  |
| FMN-ATP             | 420 ± 40  | 110 ± 10                              | 0.26 ± 0.04 | -8.9 ± 0.1                           | 127 ± 14   | 0.83 ± 0.41             | -8.3 ± 0.3  |
| FMN-ADP             | 1140 ± 30   | 59 ± 8                                | 0.05 ± 0.01 | -9.9 ± 0.1                           | 12 ± 2   | 0.16 ± 0.1              | -9.2 ± 0.4  |

<sup>a</sup>Process not observed for this combination of ligands.

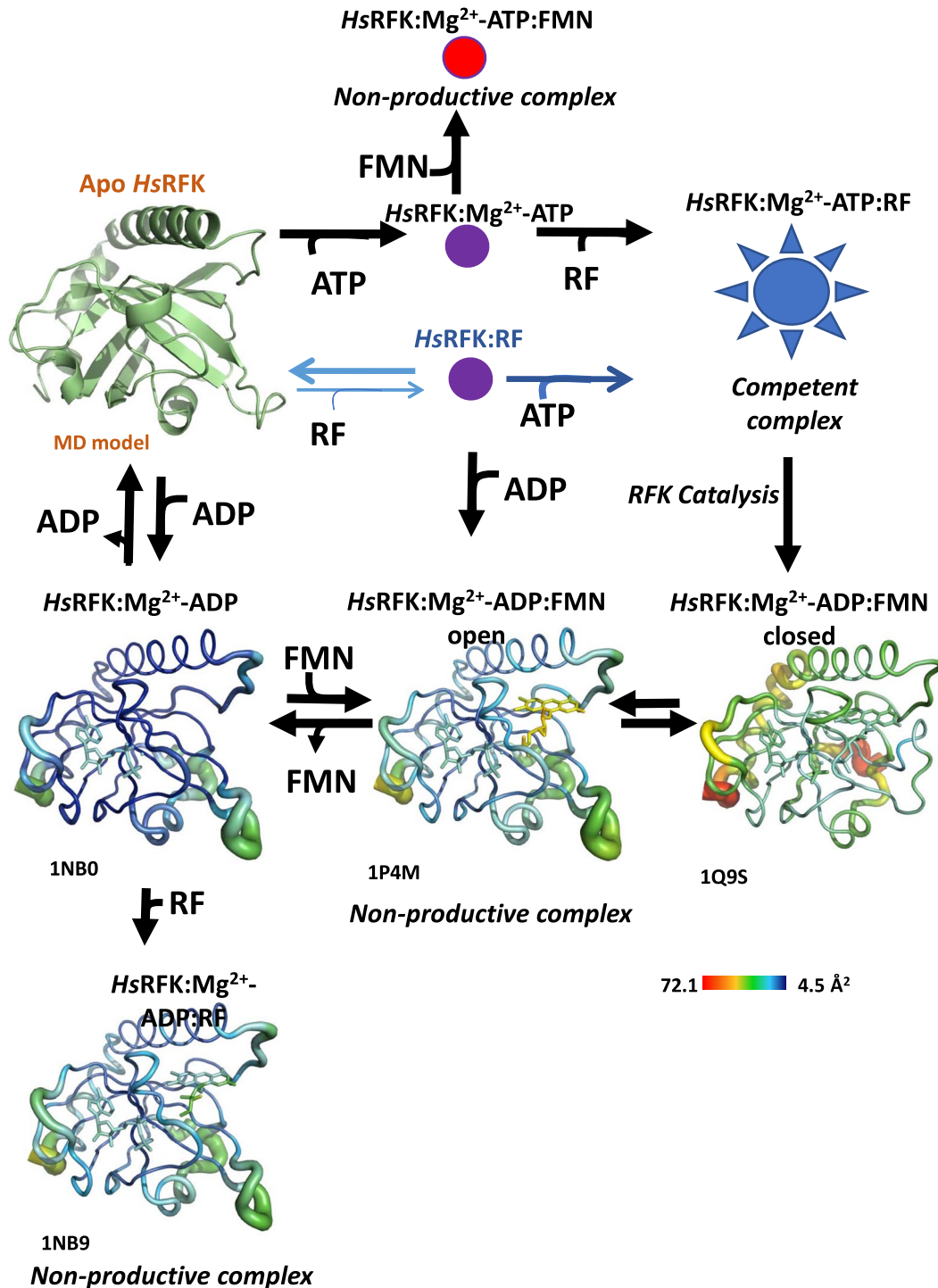


**FIGURE 4** Scheme of the conformational and ligand binding spaces along the *HsRFK* cycle. The diagram summarizes the different *HsRFK* species envisaged considering kinetic, inhibition, binding, and structural data available. All presented structures correspond to different crystal structures for *HsRFK* (PDB IDs are indicated), with the only exception of the apo-form that has been produced by MD simulations of the 1NB0 pdb after removing the ADP:Mg<sup>2+</sup> ligand. Crystal structures are represented by B-factor of backbone atoms, with higher radius of ribbons and warmer colors indicating higher fluctuations, being all snapshots normalized according the color code. Those states lacking structural data are represented by circles (nonproductive states are shown in red, alternative paths in violet and competent state in blue start). Processes leading to the formation of sub-stoichiometric complexes (*HsRFK*:RF) are highlighted with blue arrows

final exposure is not detected with *HsRFK*. In addition, this enzyme is the only from the three for which  $k_{\text{off}}$  for the FMN-ADP ligands is considerably slower than  $k_{\text{on}}$  (nearly 20-fold),

making the binding of the products stronger and envisaging different mechanisms for the FMN product release from the RFK site among these three proteins.

### 3.4 | Thermodynamics modulates the ligand binding landscape of *Hs*RFK

Subsequently, we performed ITC experiments to assess if the kinetically detected processes were significant in reaching the thermodynamic equilibrium. Binary and ternary interactions of *Hs*RFK with ANP and/or FLV ligands were analyzed at pH 7.0 and 25°C both in absence and in presence of 0.3 mM of  $Mg^{2+}$ . The corresponding determined thermodynamic parameters are summarized in Table SP1, while some examples of the experimental thermodynamic dissections are displayed in Figure SP5.

Direct titrations allowed the determination of the intrinsic binding parameters of the interaction of *Hs*RFK with substrates and products of the RFK reaction. For ANP ligands,  $K_d^{ANP}$  values were in the low micromolar range and the stoichiometry of the interaction, around 0.6, was consistent with a unique ANP-binding site, with occupancy below unity being probably associated to protein conformational heterogeneity. This agrees with low B-factors of the bound ADP- $Mg^{2+}$  in the available crystallographic structures (Figure 4). The presence of  $Mg^{2+}$  resulted in the reduction of the favorable enthalpic contribution to binding, as well as of the unfavorable entropic one (Figure SP6). Nonetheless,  $\Delta G$  remained mostly insensitive to the cation through entropy/enthalpy compensation. A similar situation was previously reported for the RFK module of *Ca*FADS.<sup>33</sup> On the contrary, FLV (RF and FMN) ligands were hardly able to directly bind *Hs*RFK. No interaction heat was detected for the protein titration with FMN, suggesting either lack of interaction, very slow binding or interaction occurring without appreciable exchange of heat. In titrations with the RF substrate, data allowed for estimation

of a  $K_d^{RF}$  value in the micromolar range, but the low interaction stoichiometry observed envisages very low occupancy (N around 0.16).  $Mg^{2+}$  further hindered RF binding due to a higher increase in the entropic contribution to the binding than in the enthalpic one (2.32- and 1.37-fold, respectively) (Table SP2, Figure SP6).

Titration of ANP:*Hs*RFK or FLV:*Hs*RFK binary mixtures with, respectively, FLV or ANP permitted to further unravel the complete thermodynamic landscape of ligand binding. Figure 5 summarizes all possible binary and tertiary interactions of the enzyme with substrates and products in absence (Figure 5A) and presence of  $Mg^{2+}$  (Figure 5B), including the fraction of binding-competent protein (N) in each case as the thickness of the arrows. Titrations involving both RF and ATP in the presence of the divalent cation (catalytic conditions) were not measured, since the heat of the catalytic reaction masked the interaction heat. As shown in the figure, pathways leading to non-competent tertiary complexes compete with formation of the *Hs*RFK:ATP:RF catalytically complex (orange pathways in Figure 5). Nevertheless, there was no thermodynamically preferred binding pathway, both in terms of final complex stability and production probability (N, interaction stoichiometry). The presence of  $Mg^{2+}$  slightly increased the fraction of protein prone to interact and, consequently, the probability of a particular path to occur, but, contrary to *Ca*FADS and *Spn*FADS,<sup>19,20</sup> hardly modulated the binding landscape (Figure 5A,B, SP5, Table SP1). The only exception to this behavior was observed for the FMN-ADP products combination, where the cation presence made enthalpic as well as entropic contributions to the *Hs*RFK binding favorable. Therefore, differences in conformation of ternary *Hs*RFK complexes as a consequence of the cation

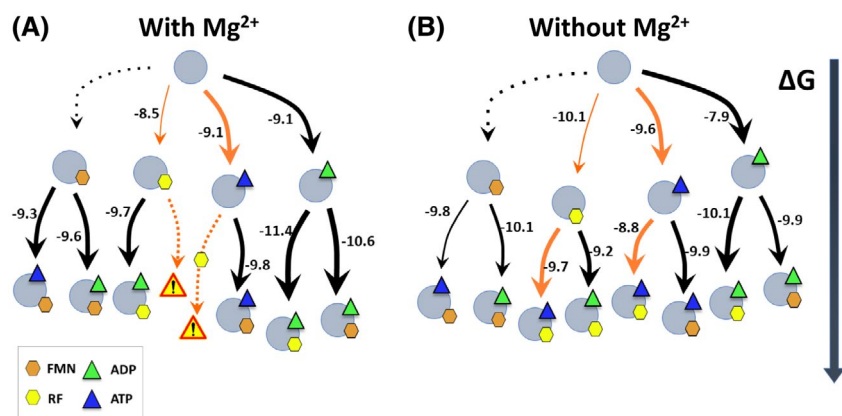


**FIGURE 5** Gibbs free energy flow for the interaction of *Hs*RFK with substrates and products. Diagrams summarize the thermodynamics of the interaction of *Hs*RFK with different combination of its ligands as obtained by ITC (Table SP1) at 25°C (A) in 20 mM of PIPES, pH 7.0, 0.3 mM of  $MgCl_2$ , and (B) in 20 mM of PIPES, pH 7.0. *Hs*RFK is represented as blue spheres, RF and FMN as orange and yellow hexagons, and ATP and ADP as green and blue triangles, respectively. The length of the arrows is proportional to the  $\Delta G$  for the interaction (value in  $kcal\ mol^{-1}$  are indicated in numbers), and its thickness is representative to the fraction of *Hs*RFK binding the titrating ligand. Processes not directly observed by ITC (interaction of *Hs*RFK with FMN) are shown as dotted arrows. Paths leading to the formation of the tertiary catalytic complex (*Hs*RFK with ATP and RF substrates) are highlighted with orange arrows. NM indicates processes that could not be measured in the presence of  $Mg^{2+}$  since the reaction heat would mask the interaction heat

**TABLE 3** Cooperativity coefficients for the binding of the different combinations of FLV and ANP ligands to *Hs*RFK in presence and absence of  $Mg^{2+}$ . Experiments were performed at 25°C in 20mM of PIPES, pH 7.0, both in absence and presence of 0.3mM of  $MgCl_2$ . (n = 5, mean  $\pm$  SEM)

| [ $MgCl_2$ ] | Ligands | $\alpha$          | N                 | $\Delta h$ kcal/mol |
|--------------|---------|-------------------|-------------------|---------------------|
| 0.3 mM       | RF-ATP  | N.M. <sup>a</sup> | N.M. <sup>a</sup> | N.M. <sup>a</sup>   |
|              | RF-ADP  | 2.2 $\pm$ 0.2     | 0.62 $\pm$ 0.01   | -1.3 $\pm$ 0.2      |
|              | FMN-ATP | 1.4 $\pm$ 0.1     | 0.49 $\pm$ 0.01   | 6.2 $\pm$ 1.0       |
|              | FMN-ADP | 2.0 $\pm$ 0.2     | 0.50 $\pm$ 0.01   | -10 $\pm$ 0.3       |
| 0 mM         | RF-ATP  | 0.87 $\pm$ 0.20   | 0.68 $\pm$ 0.01   | 5.3 $\pm$ 0.4       |
|              | RF-ADP  | 8.3 $\pm$ 1.2     | 0.46 $\pm$ 0.01   | 1.8 $\pm$ 0.6       |
|              | FMN-ATP | 0.96 $\pm$ 0.10   | 0.61 $\pm$ 0.01   | 2.7 $\pm$ 0.2       |
|              | FMN-ADP | 6.9 $\pm$ 1.2     | 0.56 $\pm$ 0.01   | -5.9 $\pm$ 0.6      |

<sup>a</sup>N.M., not measured. When mixing RF and ATP in presence of  $Mg^{2+}$ , the catalytic reaction heat conceals the interaction heat.

presence are only predicted for the formation of the ternary complex containing the FMN and ADP products, contrary to that reported for *Ca*FADS and *Spn*FADS.<sup>19,20</sup> The energy diagram in the absence of  $MgCl_2$  (Figure 5B) showed two alternative pathways leading to *Hs*RFK:ATP:RF “pseudo-reactive” complexes, which in addition are among the most probable. Therefore, the *Hs*RFK behavior is more similar to *Spn*FADS than to *Ca*FADS, enzyme that favors all the other nonproductive *Ca*FADS:ANP:FLV complexes against the *Ca*FADS:ATP:RF one.<sup>19,20</sup>

### 3.5 | ANP and FLV ligands cooperate in their binding to *Hs*RFK

Although direct FLV binding to the free protein was hardly observed by ITC or stopped-flow spectrophotometry, the presence of FLV increased *Hs*RFK affinity for ANP ligands, particularly when the cation is present (compare  $\Delta G$  values for the titrations of free *Hs*RFK and binary mixtures, Table SP1, Figure 5A and SP6). These observations suggest that, as in the bacterial RFK modules, (a) FLV ligands have a slow-binding mode to *Hs*RFK that permits to indirectly estimate their binding parameters<sup>34,45,46</sup> and (b) ANP and FLV show cooperativity in their binding.

To evaluate cooperativity, we titrated *Hs*RFK:FLV binary mixtures with ANP and fitted the resulting thermograms to a model for heterotrophic interactions applying, as explained in Materials and Methods section, two complementary methodologies.<sup>34,36,46</sup> Our data, summarized in Table 3, show that  $Mg^{2+}$  modulates ligand binding cooperativity to *Hs*RFK. In its presence, FLV and ANP ligands show positive cooperativity ( $\alpha > 1$ ). When  $Mg^{2+}$  is absent, RF-ADP and FMN-ADP binding cooperativity increases (up to 4-fold and 3-fold, respectively), while binding cooperativity becomes

slightly negative for the RF-ATP substrates combination ( $\alpha < 1$ ). In general, the magnitudes of the cooperativity constants for ligand binding to *Hs*RFK are moderated and in the range of those for *Spn*FADS, while those for *Ca*FADS are considerably larger, particularly in the presence of  $MgCl_2$ . Cooperativity in RF and ATP substrates binding to *Hs*RFK and *Spn*FADS is slightly negative and positive, respectively. Noticeably, in the case of *Ca*FADS its sign and magnitude are highly influenced by the RF substrate concentration that in this case also acts as inhibitor.<sup>19,20</sup> Thus, differences are also found in the cooperation of substrates and products binding to RFK enzymes from different organisms.

## 4 | DISCUSSION

### 4.1 | Conformational landscape in the *Hs*RFK catalytic cycle

To date, there is no an available 3D crystal structure of *Hs*RFK in the absence of any ligand, either ANP or FLV, or both. To gain insight into such conformation, we generated a model of apo-*Hs*RFK by removing  $Mg^{2+}$ :ADP from the *Hs*RFK- $Mg^{2+}$ :ADP crystal structure (PDB ID 1NB0). This model was minimized and relaxed by MD simulations (5 replicas) (Figure 6 and SP7). Trajectories for C $\alpha$  root mean square deviation (RMSD), energy, solvent accessible surface (SAS) and radius of gyration (GyR) indicate that apo-*Hs*RFK keeps overall folding along simulations (Figure SP7). The most remarkable fact was the transient breaking of the Lys20-Asp88 salt bridge, with the consequent displacement of FlapI and loop 5 (L5c), and the observation of a dynamic opening/closing of the ADP/ATP-binding cavity (Figure 6). On the contrary, the conformation of the active site, formed by the consensus PTAN motif and Glu78, retained conformations similar to those observed in the crystal binary- and ternary- *Hs*RFK complexes (Figure 6C and SP8). Such conformations resemble those in the apo-forms of *Sp*RFK and RFK module of *Spn*FADS (Figure 1 and SP7). This leaves apo-*Ca*FADS as the only RFK showing a different PTAN conformation due to its Thr exhibiting considerably different  $\Phi$  and  $\psi$  values (Figure SP8A). In conclusion, our MD data show that FlapI and L5c adopt different conformations in apo-*Hs*RFK with respect to binary *Hs*RFK:ADP complexes.<sup>2</sup> Additionally, our simulations predict an open Flavin binding site for apo-*Hs*RFK, while crystal structures indicate that closed conformations must be populated in ternary complexes due FlapII displacement toward this cavity (Figure 1 and SP2).<sup>17</sup> Therefore, it is accepted that *Hs*RFK must undergo a series of sequential conformational changes during the catalytic cycle (Figure 4).

An ordered bi-bi mechanism for mammalian RFKs was previously proposed, in which RF binding was followed by

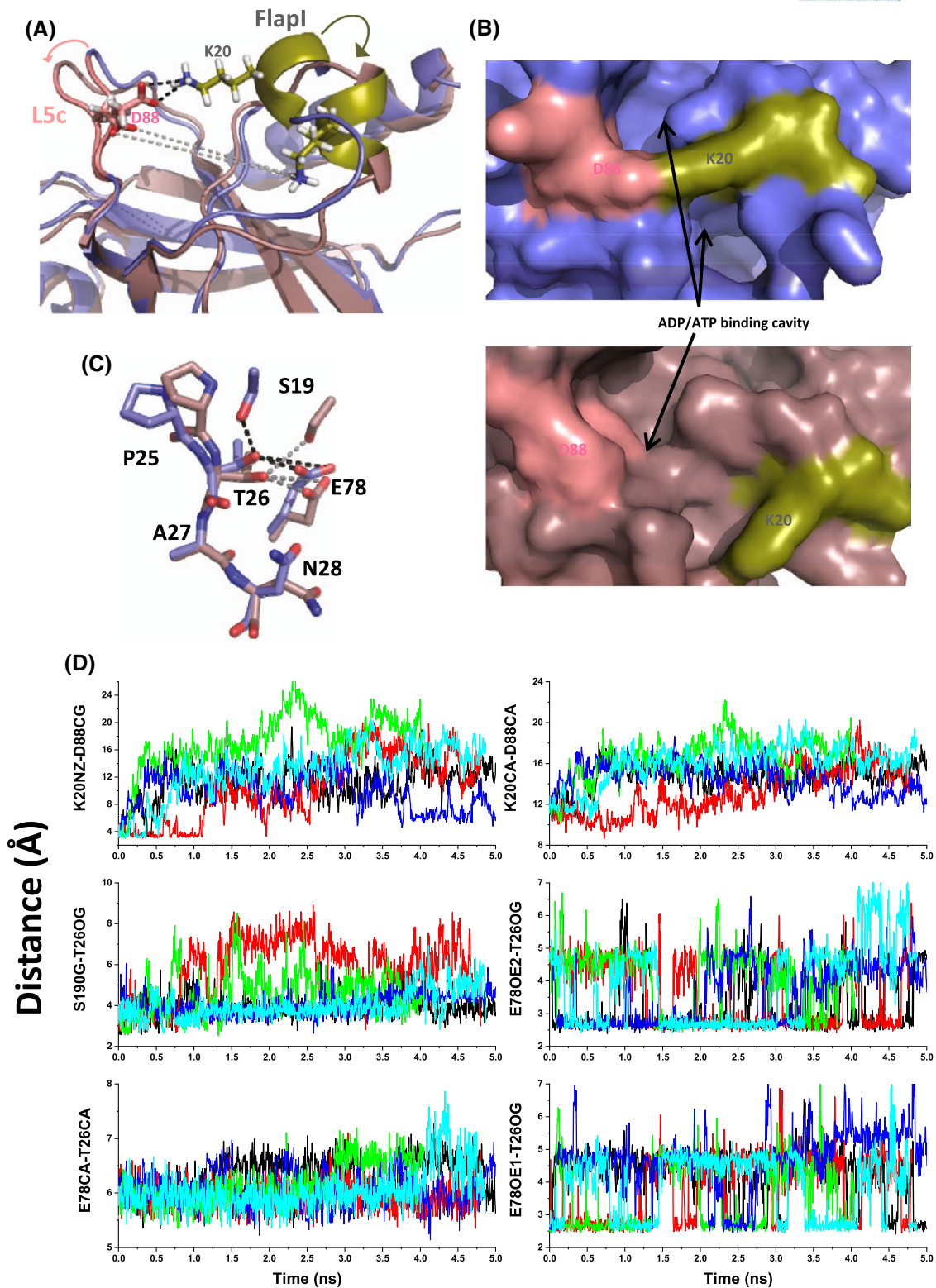


**FIGURE 6** The apo-HsRFK structural model. (A) Cartoon overlapping and (B) surfaces around the ADP/ATP binding site of apo-HsRFK structural models for the starting structure (violet) and the snapshot after 5 ns of MD (brown). L5c and FlapI are, respectively, colored in salmon and olive. Side chains for Lys20 and Asp88 are shown in sticks. (C) Stick representation of the conformation of the PTAN motif and the catalytic residue Glu78 in the starting structure (violet) and the snapshot after 5 ns of MD (brown). Panels A-C show snapshots of replica 1, and initial distances among selected atoms are shown as black dashed black lines, while corresponding distances at the end of the simulation are shown as grey dashed lines. (D) Trajectories for the evolution of the relative distances between residues Lys20 and Asp88, as well as among Thr26 at the PTAN motif and Ser19 and Glu78 along 5 ns MD simulations of apo-HsRFK. Data are shown for the 5 replicates. Simulations carried out at 300 K

ATP binding, being ADP and FMN subsequently released after catalysis.<sup>1,2,47</sup> However, our ITC and stopped-flow experiments demonstrate that FLV (RF and FMN) ligands hardly interact with *Hs*RFK in the absence of ANP ligands. The interaction of RF detected by ITC—a minority pathway in the whole interaction landscape—might be associated to the slow binding of a few molecules, probably associated to RF molecules recognizing some motives of the large flavin binding site in the open conformation expected in apo-*Hs*-RFK (Figure 4) (as observed in *Sp*RFK<sup>17</sup>). Nonetheless, RF recognition in this state appears scarce, slow and unable to trigger by itself the structural reorganization of FlapII. This is confirmed by the absence of changes indicative of internalization of the isoalloxazine ring in our stopped-flow experiments as well as in the crystallographic structures (differences in FlapI and FlapII disposition relative to *Hs*RFK:ADP:FMN complex, Figures 1, 4 and SP2). Nonetheless, the larger magnitudes for the entropic and enthalpic contributions for ATP binding to apo-*Hs*RFK when compared to the *Hs*RFK-RF mixture (Table SP1 and Figure SP6) point to structural rearrangements associated to the RF presence in its binding cavity that favors ANP binding. Nonetheless, even if RF favors the initial binding of ANP, the accommodation of the ANP in the cavity and the establishment of new FlapI-ANP interactions probably elapses the initial nonproductive RF interaction mode to a new one. Thus, conformational changes in FlapI have also an effect in FlapII conformation (see FlapI and FlapII in *Hs*RFK:ADP:FMN crystal structures, Figure 1 and SP2), further contributing to place RF in an arrangement compatible with catalysis.<sup>1,2</sup> Our transient kinetic experiments support such mechanism, since FlapII displacements can be indirectly perceived by the changes in flavin fluorescence. Thus, for mixtures of *Hs*RFK with FMN-ANP, we observed a slower reorganization process consistent with additional isoalloxazine burial into the binding pocket by FlapII reorganization. However, in the case of RF-ATP mixes,  $k_2$  is relatively faster and shows lower amplitude, probably only reflecting the protein dynamics during the catalytic turnover. Noticeably, our stopped-flow data also envisage that after catalysis the flavin binding site of *Hs*RFK remains blocked by FlapII (Figure 4), making FMN release the rate-limiting step in FMN production and envisaging that this reaction process might be controlled by factors different from the protein itself. In this context, it is worth to note that *Hs*FADS, besides its FMNAT activity, also operates as a FAD chaperone for flavin delivery to its client apoproteins.<sup>29,48</sup> Our data envisage that a similar mechanism might apply in *Hs*RFK for FMN transfer to *Hs*FADS as well as to FMN dependent client apoproteins, with direct protein-protein interaction favoring FMN release from *Hs*RFK. Such tight regulation agrees with FMN, as well as FAD, being crucial cofactors in a plethora of enzymes devoted to manage cell bioenergetics.

## 4.2 | Different organisms, different regulatory strategies

Our previous hypothesis of a species-specific inhibition and activity modulation of the RFK activity in bifunctional FADS is here reinforced, as well as extended to monofunctional proteins, by the *Hs*RFK data. Despite the overall structural similarity among eukaryotic RFK enzymes and prokaryotic RFK-modules (RMSD of core C $\alpha$  positions are only 1.2, 1.6, and 1 Å when comparing *Hs*RFK with *Sp*RFK, *Ca*FADS, and *Spn*FADS, respectively), differences among species occur in the conformation of several structural elements, including the FlapI and FlapII loops, and, particularly, the catalytic PTAN motif (Figure SP8A).<sup>18</sup> In this structural context, activity and binding studies reflect some common regulatory mechanisms, as well as highly relevant differences among *Hs*RFK and the RFK-modules of *Ca*FADS and *Spn*FADS. These variations modulate ligand binding and, consequently, catalytic cycles, resulting in a variety of species-specific mechanisms regulating the biosynthesis of flavin cofactors.

Thus, the inhibition of the RFK activity by the products of the reaction seems to be common for all of them, although inhibition potency and mechanism varies with the enzyme. For example, *Ca*FADS is more strongly inhibited by both reaction products as deduced from the  $K_1^{\text{FMN}}/K_M^{\text{RF}}$  and  $K_1^{\text{ADP}}/K_M^{\text{ATP}}$  ratios (0.2 vs 1 and 1, and 0.42 vs 1.16 and 11.2, for *Hs*RFK and *Spn*FADS, respectively).<sup>19,20</sup> Kinetic data for binding are consistent with these differences, since binding of the RFK reaction products is kinetically preferred in *Ca*FADS, while *Hs*RFK and *Spn*FADS bind the substrates faster. Thermodynamics also shows that pathways leading to the catalytic RFK complex are un-favored respect to those leading to “pseudo-reactive” complexes in *Ca*FADS,<sup>20</sup> whereas these differences either do not exist or favor formation of the catalytic complex in *Hs*RFK and *Spn*FADS, respectively (Table SP1).<sup>19</sup> Differences are also observed in heterotropic ligand binding cooperativity. Cooperativity seems to be determinant in regulating RFK activity in *Ca*FADS, while in general the *Hs*RFK behavior is more modest and resembles that of *Spn*FADS. Thus, our data indicate that *Hs*RFK, *Ca*FADS, and *Spn*FADS achieve the catalytic RFK:RF:ATP complex through mechanisms exhibiting relevant differences. *Hs*RFK and *Spn*FADS follow a random sequential binding of the RFK substrates, while substrates binding to *Ca*FADS is concerted. Differences in the substrates cooperative behavior and magnitude might relate also to the different conformations of the PTAN motif among species (Figure SP8A), which points to specific conformational changes during the RFK activity. In *Ca*FADS, the occupation of the ANP binding site by RF—when it is in excess—might prevent the ligand-induced conformational change of this motif, which is necessary for ATP binding.<sup>18</sup> This structural rearrangement is not expected to be necessary neither for *Hs*RFK (Figure 1D,E) nor for *Spn*FADS.<sup>19</sup> Therefore, the absence of

inhibition by RF in *HsRFK* and *SpnFADS* might be associated to the minimal rearrangement of PTAN motif during the catalytic cycle of these enzymes.

For all three proteins release of FMN and ADP products appears to be the reaction limiting step, but clear differences are also envisaged in the conformation of such ternary complex in solution. Thus, our stopped-flow analyses suggest that FMN is not accessible to the solvent when the *HsRFK:FMN:ADP* complex is in solution, while it is accessible when similarly evaluating the RFK modules of *CaFADS* and *SpnFADS*. This might implicate different modes for the transfer of the newly synthesized FMN to the client proteins. In this context, we must also consider that while eukaryotic RFKs are relatively small, monofunctional and monomeric proteins, their bacterial counterparts have an additional FMNAT module that duplicates its size.<sup>16</sup> Moreover, these bifunctional enzymes can stabilize quaternary assemblies with direct interaction of RFK and FMNAT ligand binding cavities, which potentially will contribute to FMN release from the RFK module by direct transfer to the FMNAT module as well as to regulate FlapII conformation and flavin accessibility to the solvent.<sup>16,25</sup>

In conclusion, we present here an integrated thermodynamic and kinetic description of the catalytic mechanism of *HsRFK* that might contribute to the better understanding of the molecular bases of certain pathologies coursing with changes in the expression or catalytic efficiency of this protein. We also report key thermodynamic, kinetic and structural differences of the regulation of the *HsRFK* catalytic cycles relative to bacterial modules performing the same activity. To date, antimicrobials only targeting the FMNAT activity of prokaryotic FADSs have been investigated,<sup>49</sup> probably because of the overall sequence and structural similarity of their RFK module to their eukaryotic counterparts envisaged specificity compromise and as a consequence deleterious effects to the host.<sup>50</sup> However, the here presented data also foresee that the bacterial RFK activity might be consider a potential antimicrobial target for some bacterial pathogens.

## ACKNOWLEDGMENTS

Authors would like to acknowledge the use of Servicios Generales de Apoyo a la Investigación-SAI, Universidad de Zaragoza.

## CONFLICT OF INTEREST

The authors declare no conflict of interest. The funders had no role in the design of the study; in the collection, analyses, or interpretation of data; in the writing of the manuscript, or in the decision to publish the results.

## AUTHOR CONTRIBUTIONS

Conceptualization, M. Medina; methodology, E. Anoz-Carbonell, M. Rivero, V. Polo, A. Velazquez-Camoy and M.

Medina; formal analysis, E. Anoz-Carbonell, M. Rivero, V. Polo and M. Medina; investigation, E. Anoz-Carbonell and M. Rivero; data curation, E. Anoz-Carbonell and M. Medina; writing—original draft preparation, E. Anoz-Carbonell and M. Medina; writing—review and editing, E. Anoz-Carbonell and M. Medina; project administration, M. Medina; funding acquisition, M. Medina.

## REFERENCES

- Karthikeyan S, Zhou Q, Mseeh F, Grishin NV, Osterman AL, Zhang H. Crystal structure of human riboflavin kinase reveals a beta barrel fold and a novel active site arch. *Structure*. 2003;11:265-273.
- Karthikeyan S, Zhou Q, Osterman AL, Zhang H. Ligand binding-induced conformational changes in riboflavin kinase: structural basis for the ordered mechanism. *Biochemistry*. 2003;42:12532-12538.
- Yazdanpanah B, Wiegmann K, Tchikov V, et al. Riboflavin kinase couples TNF receptor 1 to NADPH oxidase. *Nature*. 2009;460:1159-1163.
- Hirano G, Izumi H, Yasuniwa Y, et al. Involvement of riboflavin kinase expression in cellular sensitivity against cisplatin. *Int J Oncol*. 2011;38:893-902.
- Chen X, Ji B, Hao X, et al. FMN reduces Amyloid- $\beta$  toxicity in yeast by regulating redox status and cellular metabolism. *Nat Commun*. 2020;11:867.
- Zou YX, Zhang XH, Su FY, Liu X. Importance of riboflavin kinase in the pathogenesis of stroke. *CNS Neurosci Ther*. 2012;18:834-840.
- Hirano A, Braas D, Fu YH, Ptáček LJ. FAD regulates CRYPTOCHROME protein stability and circadian clock in mice. *Cell Rep*. 2017;19:255-266.
- Capo-chichi CD, Guéant JL, Lefebvre E, et al. Riboflavin and riboflavin-derived cofactors in adolescent girls with anorexia nervosa. *Am J Clin Nutr*. 1999;69:672-678.
- Capo-Chichi CD, Feillet F, Guéant JL, et al. Concentrations of riboflavin and related organic acids in children with protein-energy malnutrition. *Am J Clin Nutr*. 2000;71:978-986.
- Lee SS, McCormick DB. Thyroid hormone regulation of flavocoenzyme biosynthesis. *Arch Biochem Biophys*. 1985;237:197-201.
- Barile M, Giancaspero TA, Brizio C, et al. Biosynthesis of flavin cofactors in man: implications in health and disease. *Curr Pharm Des*. 2013;19:2649-2675.
- Barile M, Brizio C, Valenti D, De Virgilio C, Passarella S. The riboflavin/FAD cycle in rat liver mitochondria. *Eur J Biochem*. 2000;267:4888-4900.
- Lienhart WD, Gudipati V, Macheroux P. The human flavoproteome. *Arch Biochem Biophys*. 2013;535:150-162.
- Patel MV, Chandra TS. Metabolic engineering of *Ashbya gossypii* for enhanced FAD production through promoter replacement of FMN1 gene. *Enzyme Microb Technol*. 2020;133:109455.
- Yruela I, Arilla-Luna S, Medina M, Contreras-Moreira B. Evolutionary divergence of chloroplasts FAD synthetase proteins. *BMC Evol Biol*. 2010;10:311.
- Herguedas B, Martinez-Julvez M, Frago S, Medina M, Hermoso JA. Oligomeric state in the crystal structure of modular FAD synthetase provides insights into its sequential catalysis in prokaryotes. *J Mol Biol*. 2010;400:218-230.
- Bauer S, Kemter K, Bacher A, Huber R, Fischer M, Steinbacher S. Crystal structure of *Schizosaccharomyces pombe* riboflavin kinase reveals a novel ATP and riboflavin-binding fold. *J Mol Biol*. 2003;326:1463-1473.

18. Herguedas B, Lans I, Sebastián M, Hermoso JA, Martínez-Júlvez M, Medina M. Structural insights into the synthesis of FMN in prokaryotic organisms. *Acta Crystallogr D Biol Crystallogr*. 2015;71:2526-2542.
19. Sebastián M, Velázquez-Campoy A, Medina M. The RFK catalytic cycle of the pathogen *Streptococcus pneumoniae* shows species-specific features in prokaryotic FMN synthesis. *J Enzyme Inhib Med Chem*. 2018;33:842-849.
20. Sebastián M, Serrano A, Velázquez-Campoy A, Medina M. Kinetics and thermodynamics of the protein-ligand interactions in the riboflavin kinase activity of the FAD synthetase from *Corynebacterium ammoniagenes*. *Sci Rep*. 2017;7:7281.
21. Walsh CT, Wencewicz TA. Flavoenzymes: versatile catalysts in biosynthetic pathways. *Nat Prod Rep*. 2013;30:175-200.
22. Sebastián M, Lira-Navarrete E, Serrano A, et al. The FAD synthetase from the human pathogen *Streptococcus pneumoniae*: a bifunctional enzyme exhibiting activity-dependent redox requirements. *Sci Rep*. 2017;7:7609.
23. Matern A, Pedrolli D, Großhennig S, Johansson J, Mack M. Uptake and metabolism of antibiotics roseoflavin and 8-demethyl-8-aminoriboflavin in riboflavin-auxotrophic *Listeria monocytogenes*. *J Bacteriol*. 2016;198:3233-3243.
24. Marcuello C, Arilla-Luna S, Medina M, Lostao A. Detection of a quaternary organization into dimer of trimers of *Corynebacterium ammoniagenes* FAD synthetase at the single-molecule level and at the in cell level. *Biochim Biophys Acta*. 2013;1834:665-676.
25. Lans I, Seco J, Serrano A, et al. The dimer-of-trimers assembly prevents catalysis at the transferase site of prokaryotic FAD synthase. *Biophys J*. 2018;115:988-995.
26. Solovieva IM, Tarasov KV, Perumov DA. Main physicochemical features of monofunctional flavokinase from *Bacillus subtilis*. *Biochemistry (Mosc)*. 2003;68:177-181.
27. Sebastián M, Arilla-Luna S, Bellalou J, Yruela I, Medina M. The biosynthesis of flavin cofactors in *Listeria monocytogenes*. *J Mol Biol*. 2019;431:2762-2776.
28. Barile M, Giancaspero TA, Leone P, Galluccio M, Indiveri C. Riboflavin transport and metabolism in humans. *J Inherit Metab Dis*. 2016;39:545-557.
29. Giancaspero TA, Colella M, Brizio C, et al. Remaining challenges in cellular flavin cofactor homeostasis and flavoprotein biogenesis. *Front Chem*. 2015;3:30.
30. Serrano A, Sebastián M, Arilla-Luna S, et al. The trimer interface in the quaternary structure of the bifunctional prokaryotic FAD synthetase from *Corynebacterium ammoniagenes*. *Sci Rep*. 2017;7:404.
31. Serrano A, Frago S, Herguedas B, Martínez-Júlvez M, Velázquez-Campoy A, Medina M. Key residues at the riboflavin kinase catalytic site of the bifunctional riboflavin kinase/FMN adenylyl-transferase from *Corynebacterium ammoniagenes*. *Cell Biochem Biophys*. 2013;65:57-68.
32. Vogt AD, Di Cera E. Conformational selection or induced fit? A critical appraisal of the kinetic mechanism. *Biochemistry*. 2012;51:5894-5902.
33. Frago S, Velázquez-Campoy A, Medina M. The puzzle of ligand binding to *Corynebacterium ammoniagenes* FAD synthetase. *J Biol Chem*. 2009;284:6610-6619.
34. Martínez-Júlvez M, Abian O, Vega S, Medina M, Velázquez-Campoy A. Studying the allosteric energy cycle by isothermal titration calorimetry. *Methods Mol Biol*. 2012;796:53-70.
35. Velázquez-Campoy A, Goñi G, Peregrina JR, Medina M. Exact analysis of heterotropic interactions in proteins: Characterization of cooperative ligand binding by isothermal titration calorimetry. *Biophys J*. 2006;91:1887-1904.
36. Vega S, Abian O, Velázquez-Campoy A. A unified framework based on the binding polynomial for characterizing biological systems by isothermal titration calorimetry. *Methods*. 2015;76:99-115.
37. Olsson MHM, Søndergaard CR, Rostkowski M, Jensen JH. PROPKA3: consistent treatment of internal and surface residues in empirical pKa predictions. *J Chem Theory Comput*. 2011;7:525-537.
38. Delano WL. PyMOL: an open-source molecular graphics tool. *CCP4 Newsletter Pro Cryst*. 2002;40:82-92.
39. Abraham MJ, Murtola T, Schulz R, et al. GROMACS: High performance molecular simulations through multi-level parallelism from laptops to supercomputers. *SoftwareX*. 2015;1-2:19-25.
40. Duan Y, Wu C, Chowdhury S, et al. A point-charge force field for molecular mechanics simulations of proteins based on condensed-phase quantum mechanical calculations. *J Comput Chem*. 2003;24:1999-2012.
41. Humphrey W, Dalke A, Schulten K. VMD: visual molecular dynamics. *J Mol Graph*. 1996;14:33-38, 27-38.
42. Lee SS, McCormick DB. Effect of riboflavin status on hepatic activities of flavin-metabolizing enzymes in rats. *J Nutr*. 1983;113:2274-2279.
43. Pedrolli DB, Nakanishi S, Barile M, et al. The antibiotics roseoflavin and 8-demethyl-8-amino-riboflavin from *Streptomyces davawensis* are metabolized by human flavokinase and human FAD synthetase. *Biochem Pharmacol*. 2011;82:1853-1859.
44. Jin C, Yao Y, Yonezawa A, et al. Riboflavin transporters RFVT/SLC52A mediate translocation of riboflavin, rather than FMN or FAD, across plasma membrane. *Biol Pharm Bull*. 2017;40:1990-1995.
45. Bollen YJ, Westphal AH, Lindhoud S, van Berkel WJ, van Mierlo CP. Distant residues mediate picomolar binding affinity of a protein cofactor. *Nat Commun*. 2012;3:1010.
46. Martínez-Júlvez M, Medina M, Velázquez-Campoy A. Binding thermodynamics of ferredoxin:NADP<sup>+</sup> reductase: two different protein substrates and one energetics. *Biophys J*. 2009;96:4966-4975.
47. Yamada Y, Merrill AH Jr, McCormick DB. Probable reaction mechanisms of flavokinase and FAD synthetase from rat liver. *Arch Biochem Biophys*. 1990;278:125-130.
48. Torchetti EM, Bonomi F, Galluccio M, et al. Human FAD synthase (isoform 2): a component of the machinery that delivers FAD to apo-flavoproteins. *FEBS J*. 2011;278:4434-4449.
49. Sebastián M, Anoz-Carbonell E, Gracia B, et al. Discovery of antimicrobial compounds targeting bacterial type FAD synthetases. *J Enzyme Inhib Med Chem*. 2018;33:241-254.
50. Serrano A, Ferreira P, Martínez-Júlvez M, Medina M. The prokaryotic FAD synthetase family: a potential drug target. *Curr Pharm Des*. 2013;19:2637-2648.

## SUPPORTING INFORMATION

Additional Supporting Information may be found online in the Supporting Information section.

**How to cite this article:** Anoz-Carbonell E, Rivero M, Polo V, Velázquez-Campoy A, Medina M. Human riboflavin kinase: Species-specific traits in the biosynthesis of the FMN cofactor. *The FASEB Journal*. 2020;34:10871–10886. <https://doi.org/10.1096/fj.202000566R>



## Supplementary Material

### Human Riboflavin Kinase: species-specific traits in the biosynthesis of the essential FMN cofactor

**Ernesto Anoz-Carbonell<sup>a,b</sup>, Maribel Rivero<sup>a</sup>, Victor Polo<sup>b,c</sup>,  
Adrián Velázquez-Campoy<sup>a,b,d,e,f</sup> and Milagros Medina<sup>a,b\*</sup>**

<sup>a</sup> Departamento de Bioquímica y Biología Molecular y Celular, Facultad de Ciencias, Universidad de Zaragoza, Spain.

<sup>b</sup> Instituto de Biocomputación y Física de Sistemas Complejos (GBsC-CSIC and BIFI-IQFR Joint Units), Universidad de Zaragoza, Spain.

<sup>c</sup> Departamento de Química Física, Universidad de Zaragoza, 50009 Zaragoza, Spain.

<sup>d</sup> Fundación ARAID, Diputación General de Aragón, Spain.

<sup>e</sup> Aragon Institute for Health Research (IIS Aragon), Zaragoza, Spain.

<sup>f</sup> Biomedical Research Networking Centre for Liver and Digestive Diseases (CIBERehd), Madrid, Spain.

Abbreviated title for the running head: The biosynthesis of FMN in human cells

## SUPPLEMENTARY FIGURES

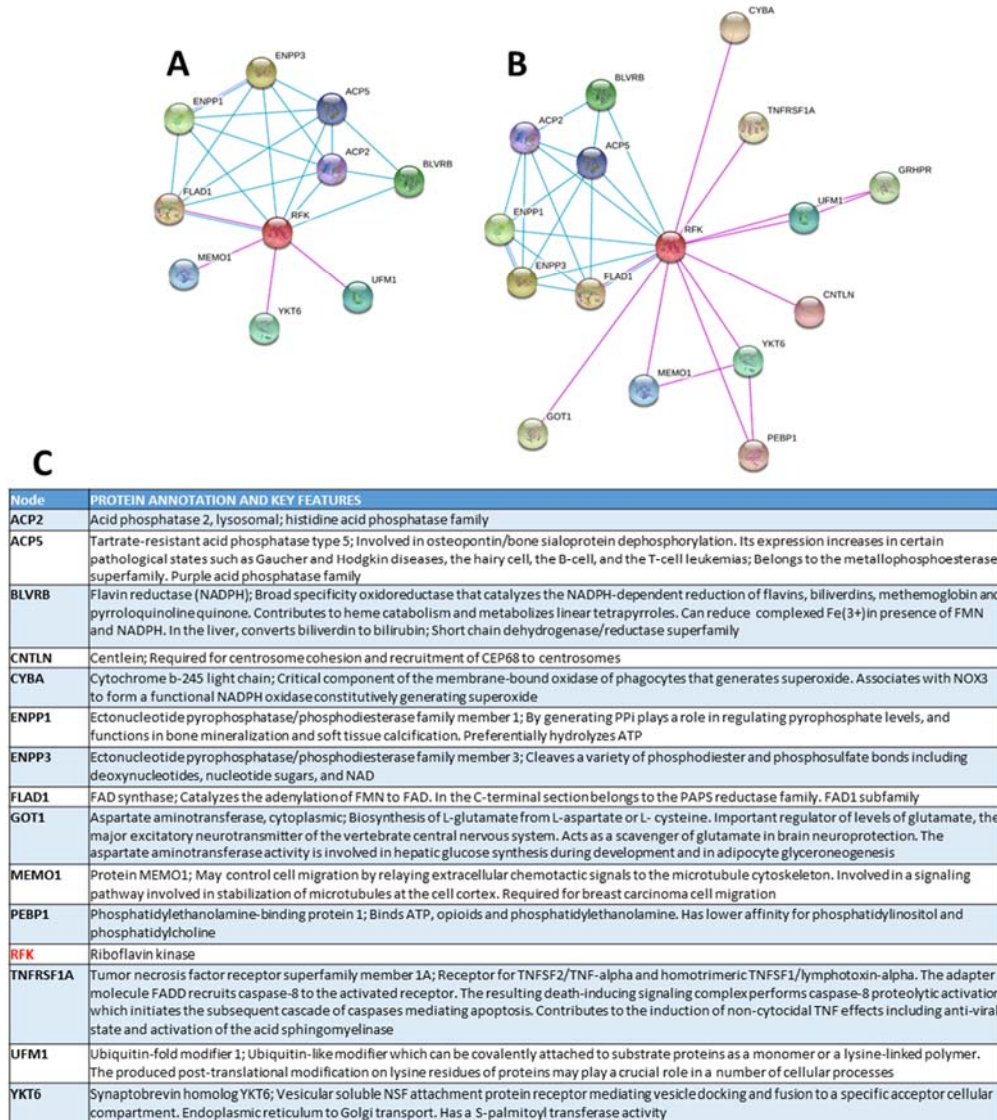


**Figure SP1. Protein-protein network predicted for *HsRFK*.** Association networks produced by STRING v11 (1) allowing up to 20 proteins. Networks are presented at (A) 'high' (0.700) and (B) 'medium' (0.400) confidence cutoffs. Evidence types contributing to this particular network include data from experiments (pink lines) and databases (blue lines). (C) Summary of main features of the proteins found in the networks.

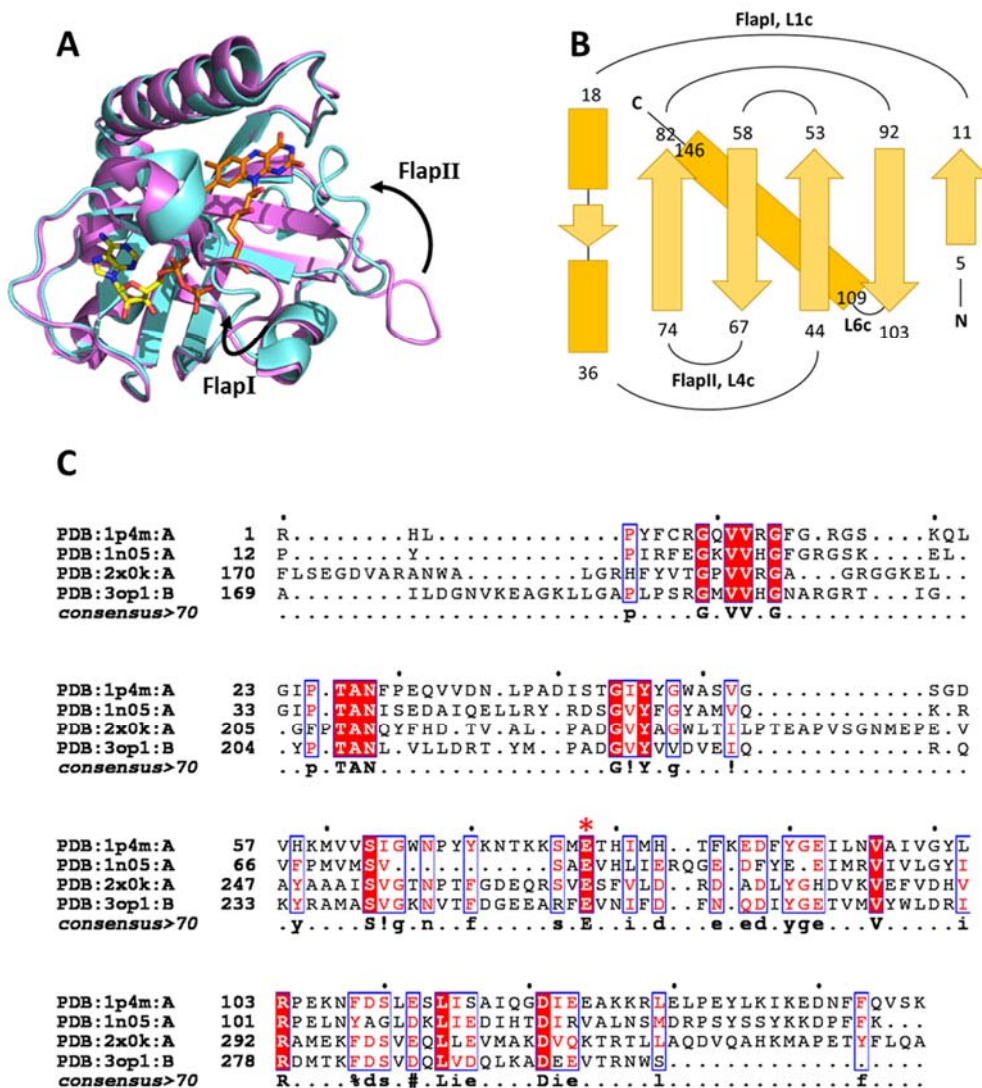


**Figure SP2. Structural properties of RFK domains.** (A) Cartoon representation of the two crystallographic structures available of *HsRFK* in complex with FMN and ADP showing the FlapII loop in either open (PDB ID 1P4M, in purple) or closed conformation (PDB ID 1Q9S, in blue). FMN and ADP are shown as CPK colored sticks colored with carbons in orange and yellow, respectively. (B) Topology of *HsRFK* with  $\alpha$  helices as dark rectangles and  $\beta$  strands as light arrows. Numbers indicate residue positions. (C) Sequence alignment including eukaryotic *HsRFK* (1P4M) and *SpRFK* (1N05) and the RFK modules of *CaFADS* (2X0K) and *SpnFADS* (3OP1). Structural alignments were generated using the PDBeFOLD server (<http://www.ebi.ac.uk/msd-srv/ssm/>) and graphically visualized using ESPript 3.0 (<http://esprict.ibcp.fr/ESPript/ESPript/>) (2). Highly conserved residues in sequence and structure are highlighted in red, including conserved RFK motifs such as PTAN, GxY and the highly conserved Glu at the active site (red asterisk). Note, the Pro of the consensus PTAN motif is not conserved in position in *CaFADS* alignment because structurally it differs in conformation regarding the corresponding residue in the other structures.

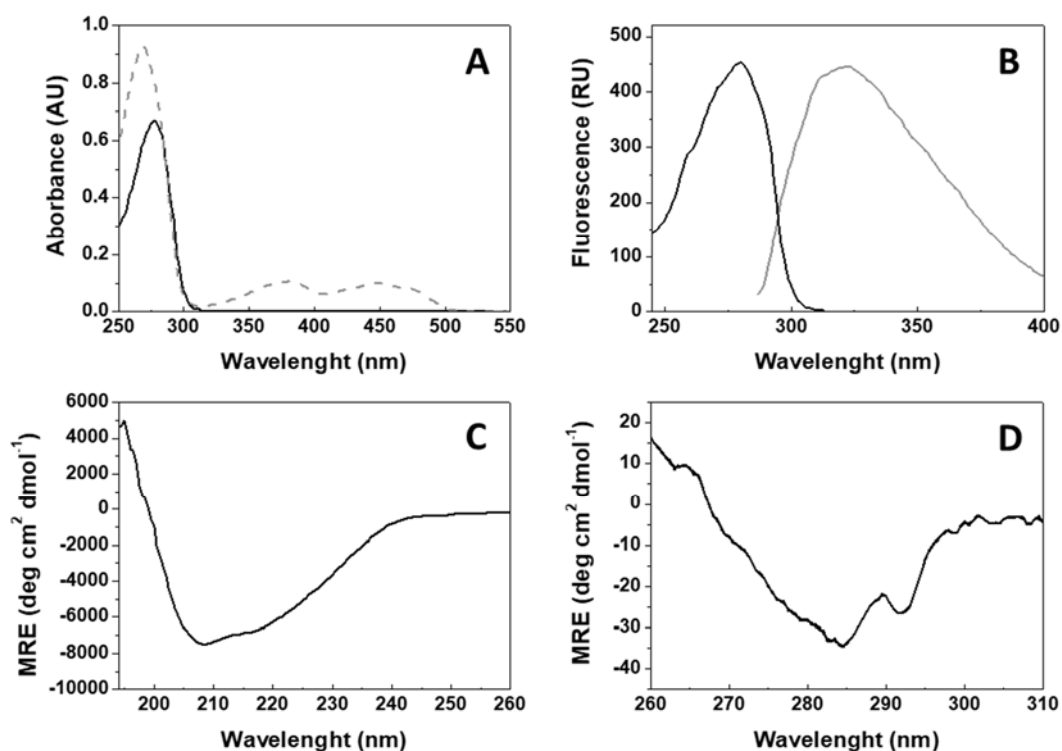


**Figure SP3. *HsRFK* spectroscopic properties.** (A) UV-visible absorption spectra of purified *HsRFK*:ADP:FMN (dashed line, before the hydrophobic chromatography) and of ligand-free *HsRFK* (solid line, after hydrophobic chromatography). (B) Fluorescence excitation (black line) and emission (gray line) spectra of ligand-free *HsRFK*. (C) Far-UV and (D) near-UV CD spectra of ligand-free *HsRFK*. Spectroscopic measurements performed in 20 mM PIPES, pH 7.0 at 25°C.

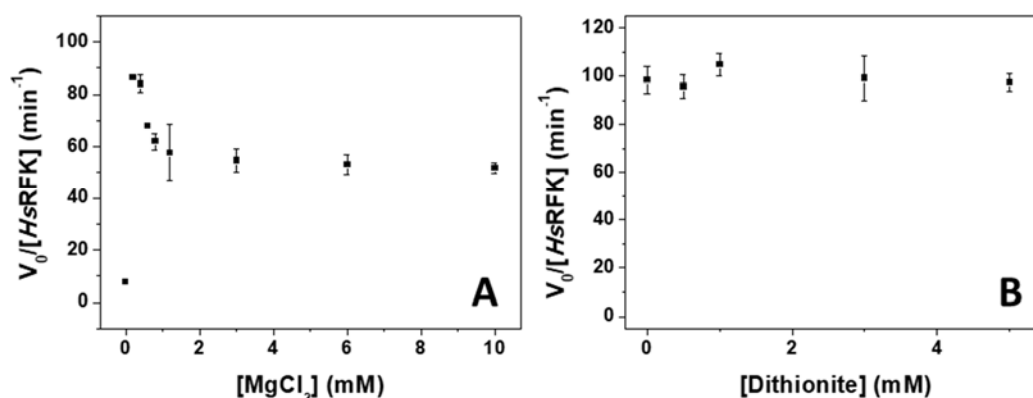


**Figure SP4. Influence of  $\text{MgCl}_2$  and reducing conditions in catalytic activity of *HsRFK*.** Activity as a function of (A)  $\text{MgCl}_2$  and (B) sodium dithionite concentrations. Reaction mixtures contained 15  $\mu\text{M}$  RF, 250  $\mu\text{M}$  ATP, and 40 nM *HsRFK*.  $\text{MgCl}_2$  was used at 0.3 mM when varying dithionite concentrations and no sodium dithionite was added when varying  $\text{MgCl}_2$ .

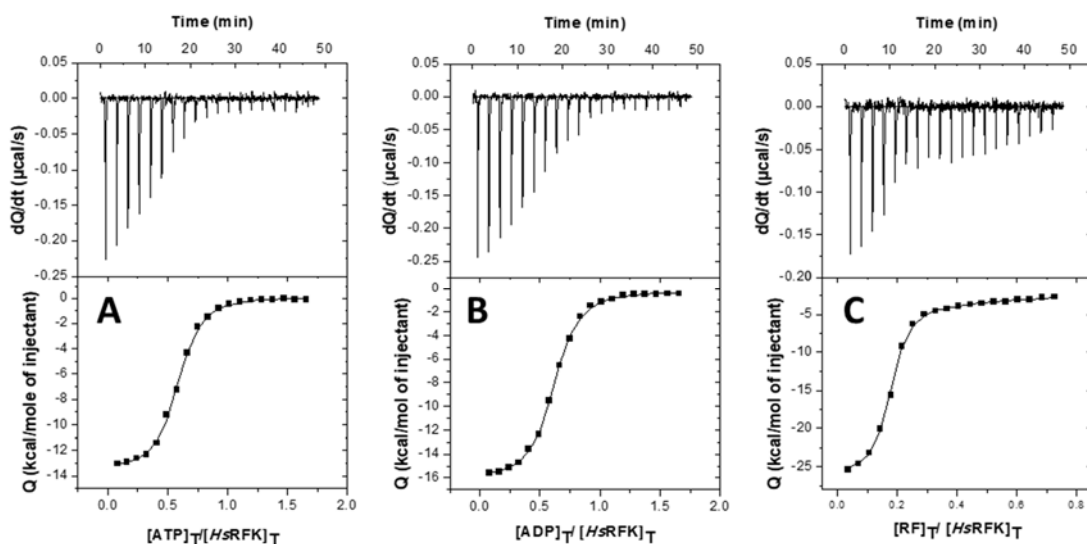


**Figure SP5. Isothermal calorimetric titrations.** Calorimetric titrations of 10  $\mu\text{M}$  *HsRFK* with (A) 80  $\mu\text{M}$  ATP, (B) 80  $\mu\text{M}$  ADP and (C) 50  $\mu\text{M}$  RF. Experiments were performed in 20 mM PIPES, pH 7.0, 0.3 mM  $\text{MgCl}_2$  at 25°C. The upper panels show the thermograms for the interactions and the lower panels show the corresponding binding isotherms with integrated heats. Data were fitted to a home-derived model for a single binding site.

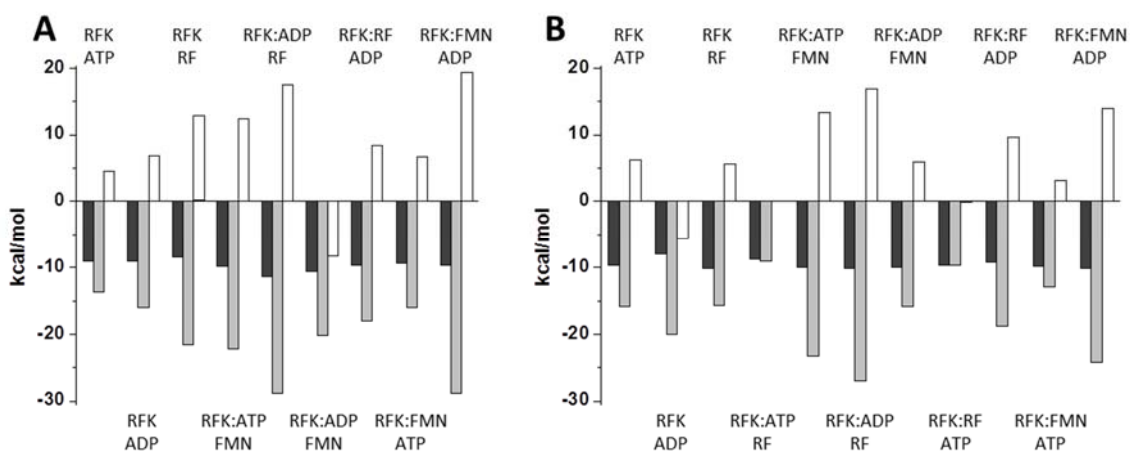


**Figure SP6. Thermodynamic dissection of the interaction of ligands with free *HsRFK* and pre-formed *HsRFK*:X (X being either FLV or ANP) binary mixtures.** Experiments carried out at 25°C in 20 mM PIPES, pH 7.0 in (A) presence of 0.3 mM  $\text{MgCl}_2$  and (B) in its absence. Gibbs energy ( $\Delta\text{G}$ ), enthalpy ( $\Delta\text{H}$ ), and entropy ( $-\text{T}\Delta\text{S}$ ) contributions to the binding are represented in black, gray and white bars, respectively. Data were obtained by fitting ITC thermograms to a home-derived model for a single binding site.

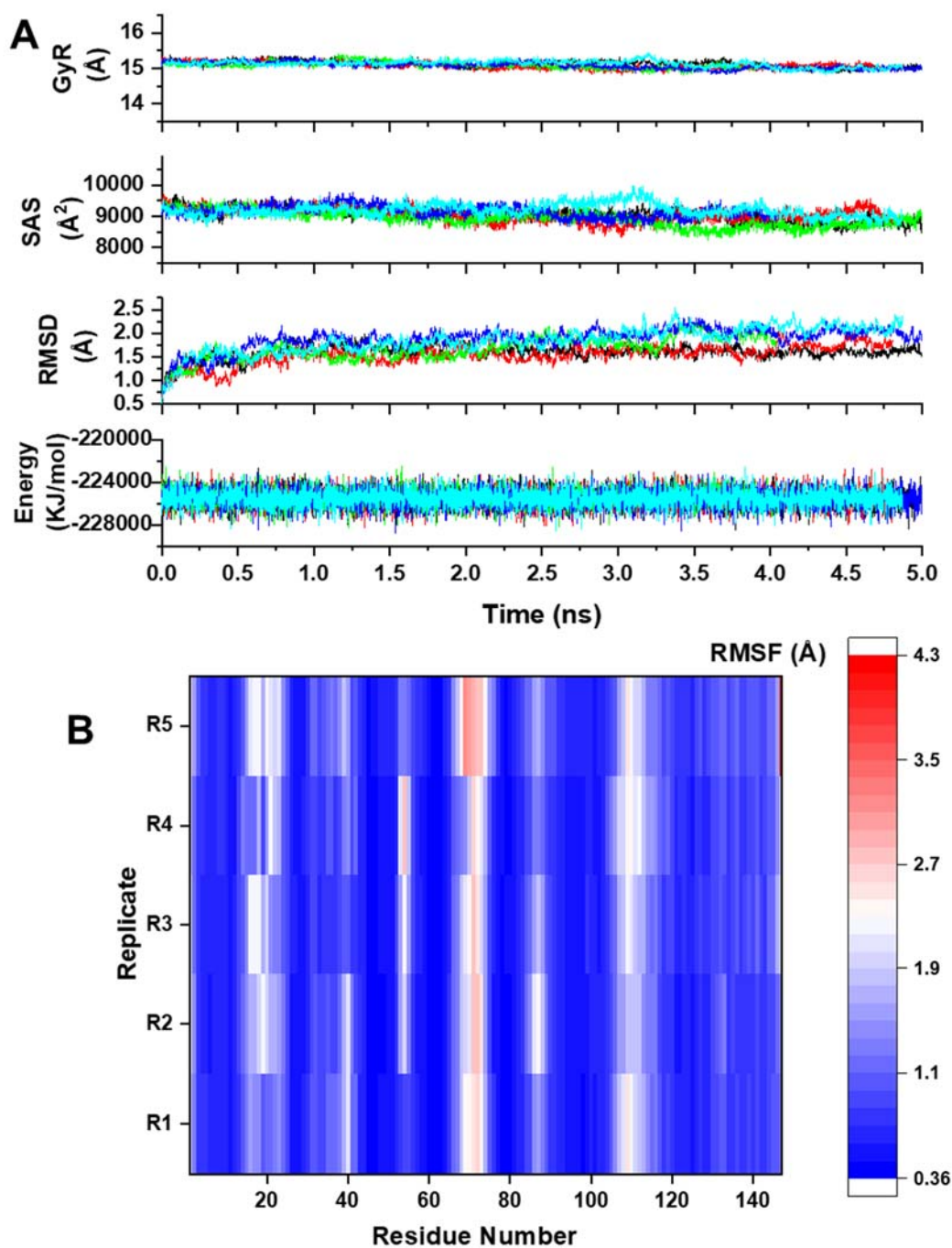


**Figure SP7. Molecular Dynamics simulations of *HsRFK*.** **(A)** Trajectories for radius of gyration (GyR), solvent accessibility surface (SAS), root mean square deviation (RMSD) against the starting structure and global energy. Trajectories are shown for the MD simulations of five replicas, with parameters corresponding to the same replicate shown in the same colour. **(B)** Heat map representation of the  $C\alpha$  root mean square fluctuation (RMSF) in the five replicates of the MD simulations.

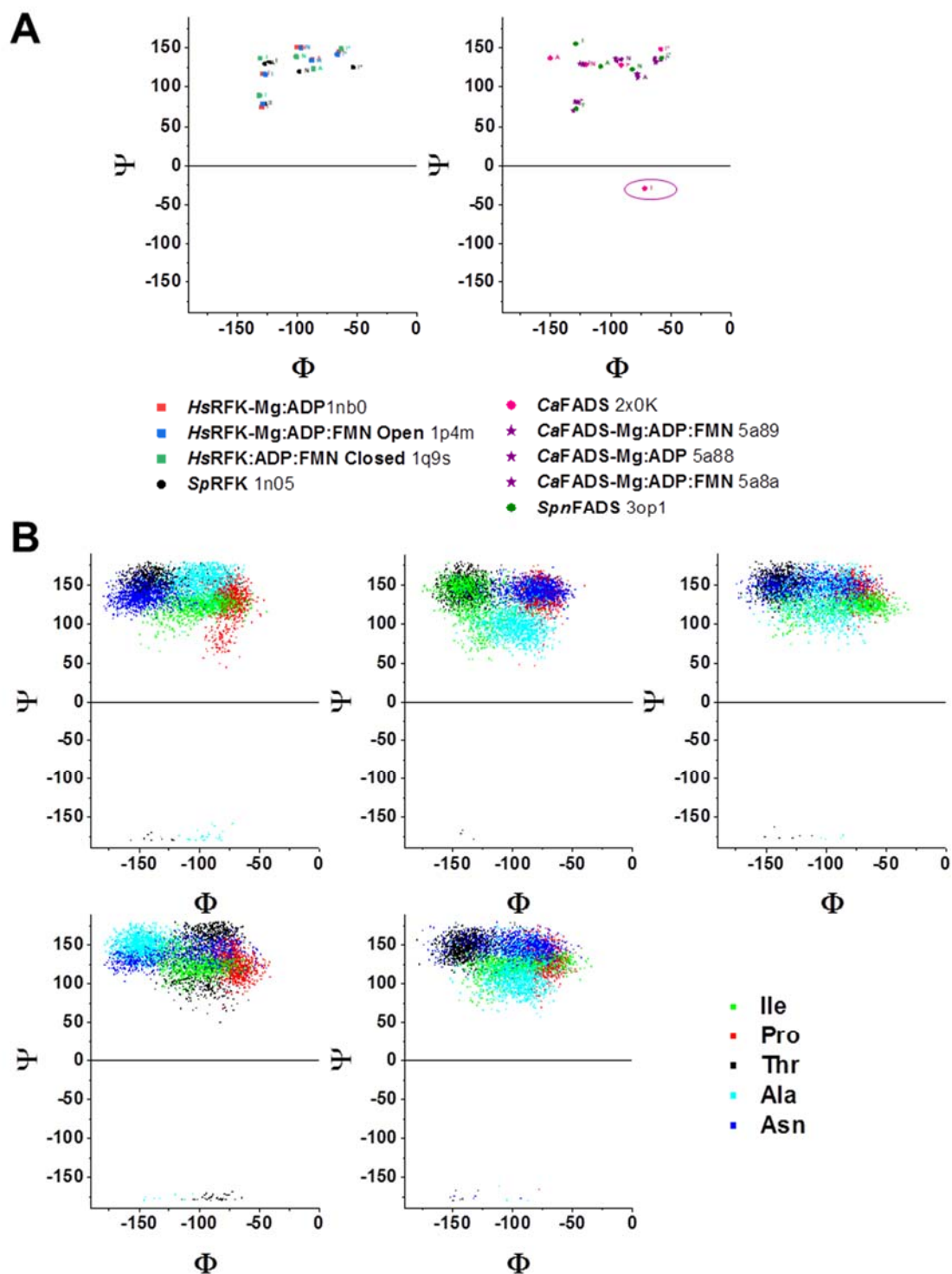


**Figure SP8. The conformation of the XPTAN motif in different species and structures.** Ramachandran representations of the main chain  $\Phi/\psi$  conformational angles of the XPTAN motif for **(A)** the available crystal structures of monofunctional eukaryotic RfKs (left panel) and prokaryotic bifunctional enzymes (right panel), and for **(B)** their distribution along the five replicas of apo *HsRfK* MD simulations. Apo *HsRfK* models do not stabilize at any point of the simulations the Thr conformation observed for apo *CaFADS* (highlighted in a pink ellipse in panel A right).

## SUPPLEMENTARY TABLES

**Table SP1.** Thermodynamic parameters for ligand (ANP or FLV) binding to free *HsRFK* and pre-formed binary *HsRFK*-FLV and *HsRFK*-ANP mixtures. Experiments carried out at 25°C in 20 mM PIPES, pH 7.0, 0.3 mM MgCl<sub>2</sub> (upper table) and 20 mM PIPES, pH 7.0 (lower table). Errors in  $\Delta G$ ,  $\Delta H$  and  $-T\Delta S$  were estimated in  $\pm 0.3$  kcal/mol and those in  $K_d$  in  $\pm 15\%$ , taken in general larger than the standard deviation between replicates (n=3) and the numerical error after fitting analysis.

| 0.3 mM MgCl <sub>2</sub> |                  |                   |                                      |                                      |  |
|--------------------------|------------------|-------------------|--------------------------------------|--------------------------------------|--|
| Pre-bound ligand         | Titrating ligand | $K_d$ ( $\mu$ M)  | $\Delta G$ (kcal mol <sup>-1</sup> ) | $\Delta H$ (kcal mol <sup>-1</sup> ) | $-T\Delta S$ (kcal mol <sup>-1</sup> ) |
| -                        | ATP              | 0.16              | -9.1                                 | -13.7                                | 4.6                                    |
| -                        | ADP              | 0.18              | -9.1                                 | -16.0                                | 6.9                                    |
| -                        | RF               | 0.52              | -8.5                                 | -21.5                                | 13                                     |
| -                        | FMN              | N.D. <sup>a</sup> | N.D. <sup>a</sup>                    | N.D. <sup>a</sup>                    | N.D. <sup>a</sup>                      |
| ATP                      | RF               | N.M. <sup>b</sup> | N.M. <sup>b</sup>                    | N.M. <sup>b</sup>                    | N.M. <sup>b</sup>                      |
| ATP                      | FMN              | 0.05              | -9.8                                 | -22.2                                | 12.4                                   |
| ADP                      | RF               | 0.003             | -11.4                                | -28.9                                | 17.5                                   |
| ADP                      | FMN              | 0.01              | -10.6                                | -20.2                                | -8.3                                   |
| RF                       | ATP              | N.M. <sup>b</sup> | N.M. <sup>b</sup>                    | N.M. <sup>b</sup>                    | N.M. <sup>b</sup>                      |
| RF                       | ADP              | 0.07              | -9.7                                 | -18.1                                | 8.4                                    |
| FMN                      | ATP              | 0.15              | -9.3                                 | -16.0                                | 6.7                                    |
| FMN                      | ADP              | 0.10              | -9.6                                 | -28.9                                | 19.3                                   |
| 0.0 mM MgCl <sub>2</sub> |                  |                   |                                      |                                      |  |
| Pre-bound ligand         | Titrating ligand | $K_d$ ( $\mu$ M)  | $\Delta G$ (kcal mol <sup>-1</sup> ) | $\Delta H$ (kcal mol <sup>-1</sup> ) | $-T\Delta S$ (kcal mol <sup>-1</sup> ) |
| -                        | ATP              | 0.07              | -9.6                                 | -15.8                                | 6.2                                    |
| -                        | ADP              | 1.37              | -7.9                                 | -20.1                                | -5.7                                   |
| -                        | RF               | 0.03              | -10.1                                | -15.7                                | 5.6                                    |
| -                        | FMN              | N.D. <sup>a</sup> | N.D. <sup>a</sup>                    | N.D. <sup>a</sup>                    | N.D. <sup>a</sup>                      |
| ATP                      | RF               | 0.29              | -8.8                                 | -9.0                                 | 0.1                                    |
| ATP                      | FMN              | 0.16              | -9.9                                 | -23.3                                | 13.4                                   |
| ADP                      | RF               | 0.04              | -10.1                                | -27.0                                | 16.9                                   |
| ADP                      | FMN              | 0.16              | -9.9                                 | -15.8                                | 5.9                                    |
| RF                       | ATP              | 0.07              | -9.7                                 | -9.6                                 | -0.1                                   |
| RF                       | ADP              | 0.18              | -9.2                                 | -18.8                                | 9.6                                    |
| FMN                      | ATP              | 0.07              | -9.8                                 | -12.9                                | 3.1                                    |
| FMN                      | ADP              | 0.04              | -10.1                                | -24.1                                | 14                                     |

<sup>a</sup> N.D. Not detected. No heat of interaction detected for this titration. <sup>b</sup> N.M. Not measured. Combinations including RF and ATP substrates in presence of Mg<sup>2+</sup> lead to the catalytic reaction, which mask the interaction heats.

### SUPPLEMENTARY REFERENCES

1. Szklarczyk, D., Gable, A. L., Lyon, D., Junge, A., Wyder, S., Huerta-Cepas, J., Simonovic, M., Doncheva, N. T., Morris, J. H., Bork, P., Jensen, L. J., and Mering, C. V. (2019) STRING v11: protein-protein association networks with increased coverage, supporting functional discovery in genome-wide experimental datasets. *Nucleic Acids Res* **47**, D607-D613
2. Robert, X., and Gouet, P. (2014) Deciphering key features in protein structures with the new ENDscript server. *Nucleic Acids Res* **42**, W320-324



## Publication II

**Mutation of aspartate 238 in FAD synthase isoform 6 increases the specific activity by weakening the FAD binding**

**Ernesto Anoz Carbonell contributions:** Experimental work: pre-steady-state kinetics through stopped-flow spectroscopy, and isothermal titration calorimetry experiments. Data analysis. Manuscript writing, review and editing



Article

# Mutation of Aspartate 238 in FAD Synthase Isoform 6 Increases the Specific Activity by Weakening the FAD Binding

Piero Leone<sup>1,2</sup>, Michele Galluccio<sup>2</sup> , Stefano Quarta<sup>1</sup>, Ernesto Anoz-Carbonell<sup>3</sup>,  
Milagros Medina<sup>3</sup> , Cesare Indiveri<sup>2</sup> and Maria Barile<sup>1,\*</sup>

<sup>1</sup> Department of Biosciences, Biotechnology and Biopharmaceutics, University of Bari, via Orabona 4–, 70126 Bari, Italy; pieroleone87@gmail.com (P.L.); quartastefano93@gmail.com (S.Q.)

<sup>2</sup> Department of Biology, Ecology and Earth Sciences (DiBEST), Unit of Biochemistry and Molecular Biotechnology, University of Calabria, via P. Bucci 4c, 87036 Arcavacata di Rende, Italy; michele.galluccio@unical.it (M.G.); cesare.indiveri@unical.it (C.I.)

<sup>3</sup> Departamento de Bioquímica y Biología Molecular y Celular, Facultad de Ciencias, Instituto de Biocomputación y Física de Sistemas Complejos (GBsC-CSIC and BIFI-IQFR Joint Units), Universidad de Zaragoza, 50009 Zaragoza, Spain; eanoz@unizar.es (E.A.-C.); mmedina@unizar.es (M.M.)

\* Correspondence: maria.barile@uniba.it

Received: 5 November 2019; Accepted: 6 December 2019; Published: 9 December 2019



**Abstract:** FAD synthase (FADS, or FMN:ATP adenylyl transferase) coded by the FLAD1 gene is the last enzyme in the pathway of FAD synthesis. The mitochondrial isoform 1 and the cytosolic isoform 2 are characterized by the following two domains: the C-terminal PAPS domain (FADSy) performing FAD synthesis and pyrophosphorolysis; the N-terminal molybdopterin-binding domain (FADHy) performing a  $\text{Co}^{++}/\text{K}^{+}$ -dependent FAD hydrolysis. Mutations in FLAD1 gene are responsible for riboflavin responsive and non-responsive multiple acyl-CoA dehydrogenases and combined respiratory chain deficiency. In patients harboring frameshift mutations, a shorter isoform (hFADS6) containing the sole FADSy domain is produced representing an emergency protein. With the aim to ameliorate its function we planned to obtain an engineered more efficient hFADS6. Thus, the D238A mutant, resembling the D181A FMNAT “supermutant” of *C. glabrata*, was overproduced and purified. Kinetic analysis of this enzyme highlighted a general increase of  $K_m$ , while the  $k_{\text{cat}}$  was two-fold higher than that of WT. The data suggest that the FAD synthesis rate can be increased. Additional modifications could be performed to further improve the synthesis of FAD. These results correlate with previous data produced in our laboratory, and point towards the following proposals (i) FAD release is the rate limiting step of the catalytic cycle and (ii) ATP and FMN binding sites are synergistically connected.

**Keywords:** FAD synthase; FMN adenylyl transferase; FADS isoform 6; supermutant

## 1. Introduction

The riboflavin (Rf) derived FMN and FAD cofactors play a pivotal role in cell economy ensuring the functionality of the flavoproteome, mainly localized in mitochondria [1,2]. Consistent with the crucial role of flavins and flavoenzymes in cell life, several diseases, including neuromuscular and neurological disorders are linked to flavin-dependent enzyme deficiency or impairment in Rf homeostasis in humans and experimental animals. These disorders, in some cases, can be cured with high doses of Rf, as the two Rf-responsive (RR) disorders Brown–Vialletto van Laere syndrome (BVVLS) [3,4] and RR-multiple acyl-CoA dehydrogenase deficiency (RR-MADD) [5–7]. In mammalian cells, Rf is taken up via translocators (SLC52A1-3, also named RFVT1-3) [8,9] and converted into FMN

and FAD via the sequential action of Rf kinase (RFK, EC 2.7.1.26) and FAD synthase or FMN-ATP adenylyl transferase (FADS, EC 2.7.7.2).

The only gene identified for coding functional FAD synthases in humans is FLAD1 gene (GenBank, A. N. DQ458779, [10]) localized on chromosome 1, which is orthologue of *flad-1* in *C. elegans*, [11], *Fad1* in *S. cerevisiae* [12] and *FMNAT* in *C. glabrata* [13]. The structures of FADSs from yeast, but not that of the human orthologue, have been solved [13,14].

The FLAD1 gene in humans generates different alternative transcript variants, with unknown differential expression profile, producing protein isoforms, only in part characterized, which have different subcellular localization [15] and domain organizations.

The most abundant variant in all the tissues and cells tested so far, is isoform 2 (NM\_201398.3 in NCBI GenBank), which corresponds to a cytosolic enzyme of 490 amino acids [15]. The FADS or FMN-AT module of this protein is localized in the C-terminus of the protein; it contains a phosphoadenosine 5-phosphosulfate (PAPS) reductase domain and it is fused with a molybdopterin binding resembling (MPTb) domain located in the N-terminus [16,17].

FAD synthesis catalyzed by hFADS2 follows a bi-bi ordered kinetics with ATP entering prior to FMN and pyrophosphate released before FAD [17]. This enzyme contains 10 cysteines, some of which are relevant for catalysis; two of them are stably reduced (C139 and C241, one for each protein domain), four are implicated in stable disulfide bridges (C399 to C402, C303 to C312, both in the PAPS domain), and the other four are forming redox sensitive disulfides (C39 to C50; C440 to C464) [18].

Following the discovery that hFADS2 is a bifunctional enzyme, with the N-terminal domain working as a  $\text{Co}^{2+}$ -dependent FAD hydrolase, the two domains of the protein were renamed as FADHY and FADSY, functionally corresponding to E.C. 3.6.1.18 and E.C. 2.7.7.2, respectively [19,20]. FADHY is also present in the other three isoforms of the protein reported in the NCBI GenBank (FLAD1 isoform 1, NM\_025207.5; FLAD1 isoform 3, NM\_001184891.2; and FLAD1 isoform 4, NM\_001184892.2). Nonetheless, it is indeed absent in the FAD1p yeast counterparts and, more interestingly, in another human isoform not yet annotated as FADS, but reported as CRA\_d in NCBI and known as hFADS6.

The isoform hFADS6 is a 320-residue long protein, containing the sole FADSY domain, whose corresponding transcript was recently described in the frame of studying FLAD1 mutations leading to RR-MADD [7]. The relevance of this novel isoform lies in its ability to ensure FAD supply to patients carrying frameshift mutations in exon 2 of the FLAD1 gene and, for this reason, it has been named an “emergency protein” for MADD patients. When produced in *E. coli* and purified at homogeneity, hFADS6 behaves as a yellow monomer, able to tightly, but not covalently, bind FAD. Recombinant hFADS6 is more stable than hFADS2 and is able to perform FAD synthesis starting from FMN and ATP. As expected, it is not able to perform FAD hydrolysis [21]. The molecular features of this novel natural form well correlate with those of a previously produced artificial construct, lacking the first 231 residues of hFADS2, which per se can fold and catalyze the FAD synthesis reaction [22]. Therefore, this novel isoform of FAD forming enzymes is, in our opinion, a good model to address remaining challenges in the catalytic behavior of the FAD synthesis reaction in humans, as compared with the our deeper understanding of the yeast orthologues [13,14], from which structure the human protein was modeled [21]. The more striking point concerning the catalytic cycle of FAD forming enzyme concerns the observation that the turn-over number of the reaction, as catalyzed by hFADS2, is quite low ( $0.069 \pm 0.011 \text{ s}^{-1}$ ), with FAD release being the limiting step of the over-all reaction [23]. This apparently sounds strange for a protein which is expected to be devoted to FAD delivery. We postulate that redox events or protein–protein interaction in a sort of chaperoning process may promote cofactor delivery to cognate apo-flavoprotein [17,23].

The aim of this work was to confirm the proposed mechanism by proving that lowering the FAD affinity toward the catalytic site (i.e., facilitating FAD release) results in increasing the turn-over number of the FAD forming reaction. To obtain these results we took into account studies on *Candida glabrata* FMN-AT (CgFMN-AT) [24] that identified a cryptic residue, precisely D181, whose mutation to Ala resulted in an increase of the  $V_{\text{max}}$ , and therefore it was named “super-mutant”. The orthologous

residue in the human enzyme is D238. We investigate, here, the effects of the D238A mutation on hFADS6 steady-state activity and binding capability to confirm our hypothesis that a weak FAD binding to the active site could led to an increased rate of synthesis. The possible final goal of this study is to open a perspective towards increasing the emergency enzyme activity in patients suffering for *FLAD1* mutations.

## 2. Results

### 2.1. Homology Model of D238A-hFADS6

The amino acid sequences of WT and D238A mutant hFADS6 were aligned by Clustal Omega software with the FMN-AT protein Q6FNA9 of *C. glabrata*. The alignment presented in Figure 1 highlights not only a high percentage identity (about 32%) between the human and the yeast proteins, but also confirms that D238 of hFADS6 corresponds to D181 of the yeast orthologue and that it is part of the flavin binding motif.

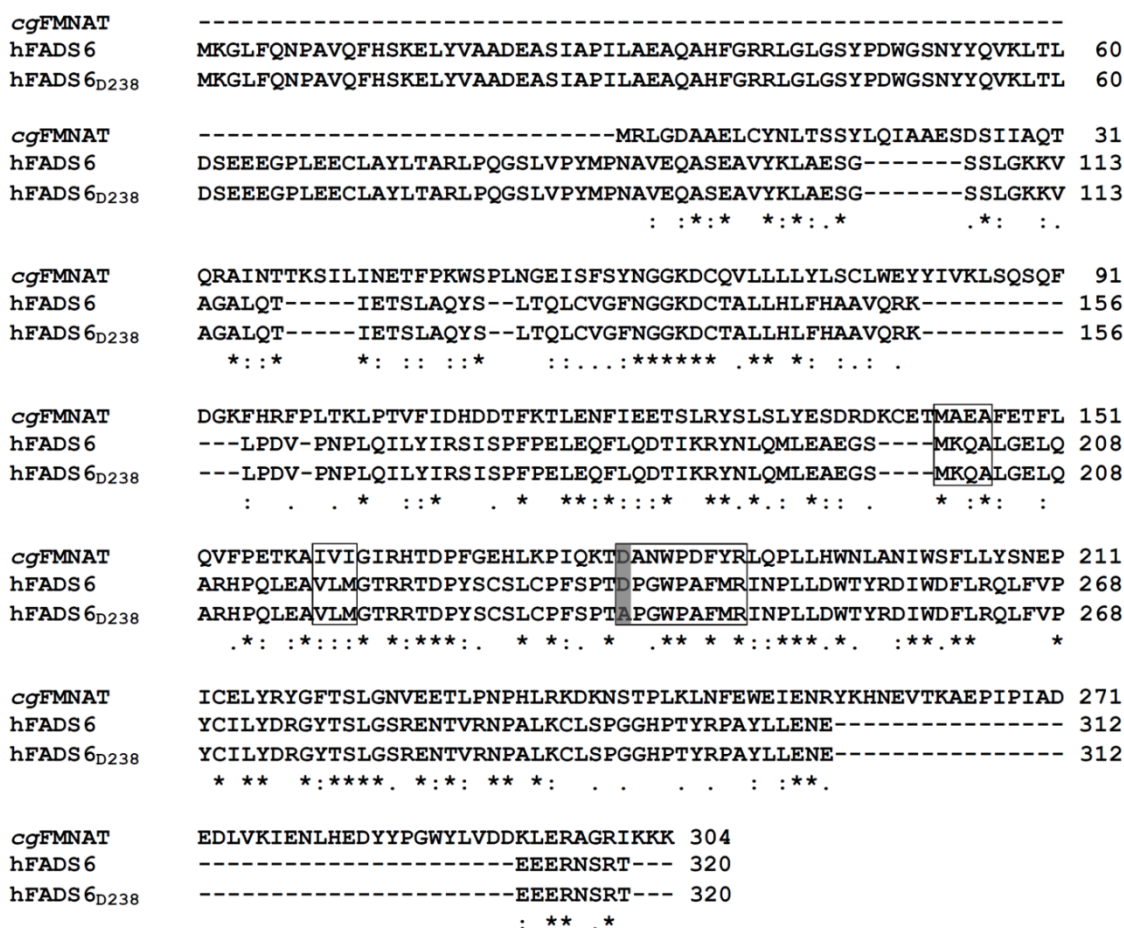


**Figure 1.** Sequence alignment of CgFMN-AT (Q6FNA9), hFADS6, and hFADS6<sub>D238A</sub>. The protein sequences were aligned by Clustal Omega software. D181 of the yeast protein, D238 of the hFADS6, and A238 in the mutant are shadowed in grey. Amino acids forming the flavin binding motif are highlighted by boxes.

Due to the lack of suitable templates for modeling the N-terminus (amino acids 1 to 108) of hFADS6, an ab initio strategy was previously adopted to obtain its three-dimensional (3D) structural model [21]. FAD was then inserted in the active site according to the structure of CgFMN-AT (3G6K) as described in Materials and Methods. Figure 2 clearly shows a reduced steric hindrance upon substitution of D238 with A. However, the major reason for varied FAD binding and release kinetics

should be the loss of the dipole interaction between the Asp-carboxylate group and the N(3)H-FAD, which most affects FAD binding.

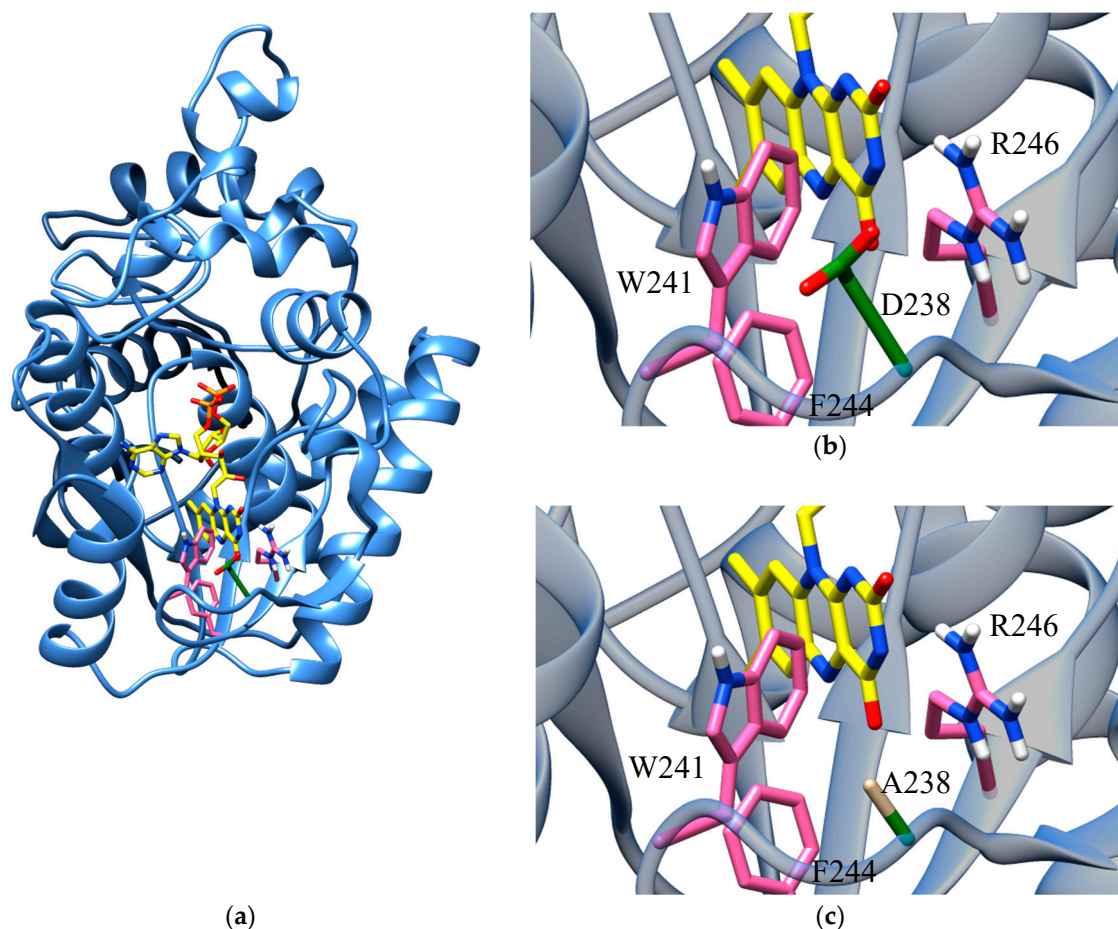


**Figure 2.** Modeling and FAD docking of hFADS6: (a) Ribbon representation of hFADS6 modeled as described in [21]. FAD transferred in the active site from PDB ID: 3G6K and represented as yellow licorice colored by heteroatom type. (b,c) Zoom into the binding site of the isoalloxazine moiety of FAD. Amino acids involved in isoalloxazine binding are colored in pink. D238 in the WT (b) and A238 in the mutant (c) are rendered as green licorice colored by heteroatom type.

## 2.2. Cloning, Expression, and Purification of the D238A-hFADS6 Isoform

The D238A mutant of the hFADS6 was constructed as described in Materials and Methods. The protein overexpressed in *E. coli* showed similar electrophoretic mobility to that of the WT [21] when purified by Ni-chelating chromatography, i.e., an apparent molecular mass of about 35 kDa. This value was compatible with the theoretical mass derived from the tagged sequence of the expressed polypeptide (38.222 kDa, Figure 3).

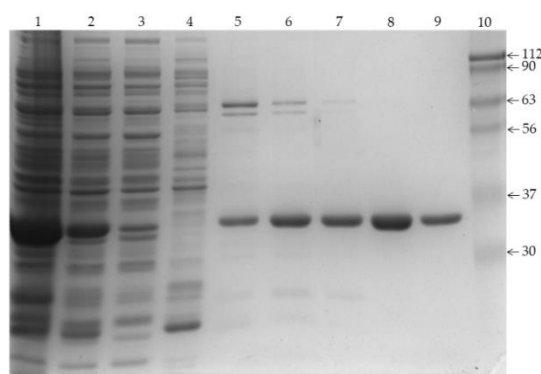


**Figure 3.** Protein fractions obtained by Ni<sup>2+</sup>-chelating chromatography were separated by SDS-PAGE on 12% polyacrylamide gel and stained with Coomassie blue. Lane 1, insoluble fraction of IPTG-induced cell lysate (6 µg); lane 2, soluble fraction of IPTG-induced cell lysate (28 µg); lane 3, first flow-through fraction (19 µg), lane 4, proteins eluted with 50 mM imidazole (13 µg), lane 5, first fraction of proteins eluted with 100 mM imidazole (2 µg), lane 6, second fraction of proteins eluted with 100 mM imidazole (3 µg), lane 7, third fraction of proteins eluted with 100 mM imidazole (2 µg); lane 8, first fraction of proteins eluted with 250 mM imidazole (5 µg); lane 9, second fraction of proteins eluted with 250 mM imidazole (1 µg); and lane 10, molecular mass markers.

The overexpressed protein was recovered in the soluble fraction of the cell lysate and was used for spectrophotometric analysis and compared with the WT protein. The spectrum of the most abundant purified mutant protein fraction (fraction 8), whose purity is higher than 98%, is shown in Figure 4. An absorbance peak at 274 nm was observed, but surprisingly, no other peaks were present at higher absorption values. As the control, the WT hFADS6 spectrum was shown, presenting two additional minor peaks, at 350 and 450 nm, typical of oxidized FAD (Figure 4). From the absorbance value at 280 and 450 nm a ratio FAD/hFADS6 of 0.43 was calculated, as reported in [21], and thus indicating the presence of some apoprotein. The spectra of fractions 5, 6, 7, and 9 showed the same features as fraction 8. The spectral features of the D238A mutant hFADS6 indicated that this protein does not stabilize the strong binding of flavins.

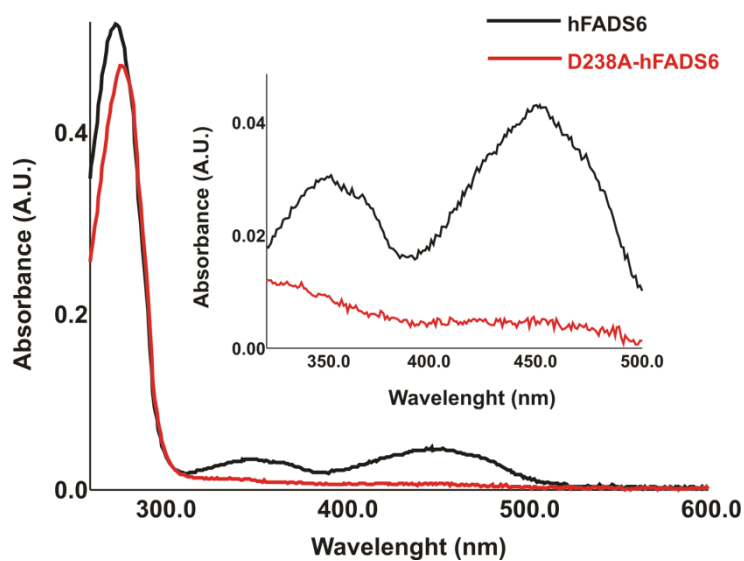


**Figure 4.** Absorption spectra of hFADS6 and D238A-hFADS6 purified to homogeneity. The spectra of WT hFADS6 (8.6 µM, grey dotted line) and of D238A-hFADS6 (9.7 µM, black line) were recorded in 40 mM HEPES/Na, 5 mM β-mercaptoethanol, pH 7.4. The protein concentration was measured as indicated in [21].

### 2.3. Kinetics of the D238A hFADS6

The mutant protein was characterized in terms of kinetics to uncover possible variations of interactions with the substrates or the effectors and inhibitors. Figure 5 shows the response of the mutant to  $Mg^{2+}$ , which is a known effector of hFADSs, including the hFADS6 isoform [21,23]. The presence of  $Mg^{2+}$  is also essential for activity in the mutant. However, a different behavior was observed. The  $AC_{50}$  (half maximum activation constant) of  $Mg^{2+}$  is quite higher in the mutant than in the WT. Its value  $3.5 \pm 0.9$  mM is twenty-fold that of the WT. Moreover, a higher value of  $V_{max}$  is measured in the case of the mutant. Another distinctive feature is the inhibition observed at higher  $Mg^{2+}$  concentrations, which was not present in the WT. The effect of  $Hg^{2+}$  was also studied because this heavy metal typically inhibits the WT protein due to interaction with the Cys residues [18,21,23]. Differently from the case of  $Mg^{2+}$ , the effect of  $Hg^{2+}$  on the mutant was very similar to that on the WT enzyme.

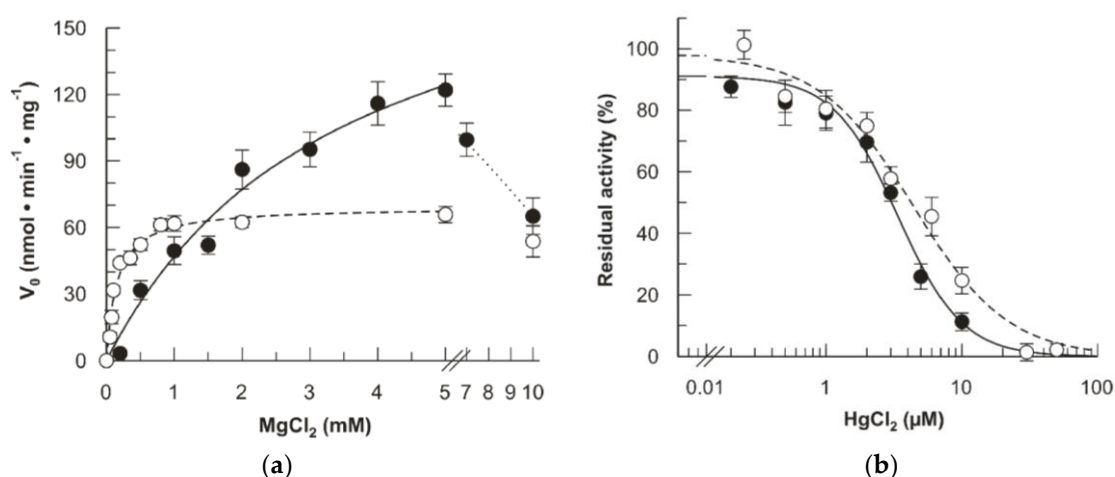


**Figure 5.** Fluorimetric evidence of FAD synthesis. The FAD synthesis reaction was started by the addition of purified recombinant proteins (hFADS6 open circle or D238A-hFADS6 closed circle) and measured by the initial rate of fluorescence decrease ( $\lambda$  excitation = 450 nm,  $\lambda$  emission = 520 nm). (a) Dependence on the  $MgCl_2$  concentration. FAD synthesis rate, catalyzed by purified hFADS6 (open circle, 10  $\mu$ g, 0.26 nmol) or D238A-hFADS6 (closed circle, 2.3  $\mu$ g, 0.06 nmol), was fluorimetrically measured at 37 °C in 2 mL of 50 mM Tris/HCl pH 7.5, in the presence of 100  $\mu$ M ATP, 2  $\mu$ M or 4  $\mu$ M FMN, respectively, and of the given  $MgCl_2$  concentrations. (b) Inactivation by the mercurial reagent  $HgCl_2$ . FAD synthesis rate, catalyzed by purified hFADS6 (open circle, 10  $\mu$ g, 0.26 nmol) or D238A-hFADS6 (closed circle, 3.2  $\mu$ g, 0.08 nmol), was fluorimetrically measured at 37 °C in 2 mL of 50 mM Tris/HCl pH 7.5, in the presence of 2  $\mu$ M or 3  $\mu$ M FMN, respectively, 100  $\mu$ M ATP, 5 mM  $MgCl_2$  and of the given  $HgCl_2$  concentrations. The values of  $V_0$  are reported as  $nmol\ min^{-1}\ mg^{-1}$  (a) and as percentages of the maximum rate (b) arbitrarily set to 100%. Data points are fitted according to the Michaelis–Menten equation (a) and according to the  $IC_{50}$  equation (b) with Grafit 3.0 software.

Then, the dependence of the FAD synthesis rate on the concentrations of the main substrates FMN and ATP was studied in the presence of saturating concentration of the counter-substrate, i.e., ATP and FMN, respectively. As shown in Figure 6a, dependences on the ATP concentration for the WT and the mutant were quite different. Both the  $K_m$  and the  $V_{max}$  increased in the mutant. The  $K_m$  for ATP increased from  $6.9 \pm 0.5$   $\mu$ M (WT) to  $44 \pm 4$   $\mu$ M (mutant). The  $V_{max}$  increased from  $79 \pm 1$  (WT) to  $145 \pm 5$   $nmol\ min^{-1}\ mg^{-1}$  protein. The derived  $k_{cat}$  of the mutant was  $0.093 \pm 0.003\ s^{-1}$  ( $5.6 \pm 0.2\ min^{-1}$ ) which is about double than that of the WT  $0.050 \pm 0.001\ s^{-1}$  ( $3.0 \pm 0.1\ min^{-1}$ ) [21]. To graphically highlight the difference in  $K_m$ , the same data were expressed as percentage of the  $V_{max}$  (Figure 6a'). A similar behavior was observed when measuring the dependence of the reaction rate on FMN concentrations. Again, the  $K_m$  for FMN and the  $V_{max}$  increased in the mutant (Figure 6b). The  $K_m$



for FMN increased from  $0.13 \pm 0.01 \mu\text{M}$  (WT) to  $1.3 \pm 0.3 \mu\text{M}$  (mutant). The  $V_{\text{max}}$  increased from  $74 \pm 1$  (WT) to  $162 \pm 12 \text{ nmol min}^{-1} \text{ mg}^{-1}$  protein (mutant). The derived  $k_{\text{cat}}$  of the mutant was  $0.103 \pm 0.007 \text{ s}^{-1}$  ( $6.2 \pm 0.5 \text{ min}^{-1}$ ) which is about twice that of the WT  $0.047 \pm 0.001 \text{ s}^{-1}$  ( $2.9 \pm 0.1 \text{ min}^{-1}$ ) [21], very similar to that obtained for the ATP kinetics. In this case, the same data were represented as percentage of the  $V_{\text{max}}$  (Figure 6b'). Table 1 summarizes the kinetic comparison between WT and D238A hFADS6.

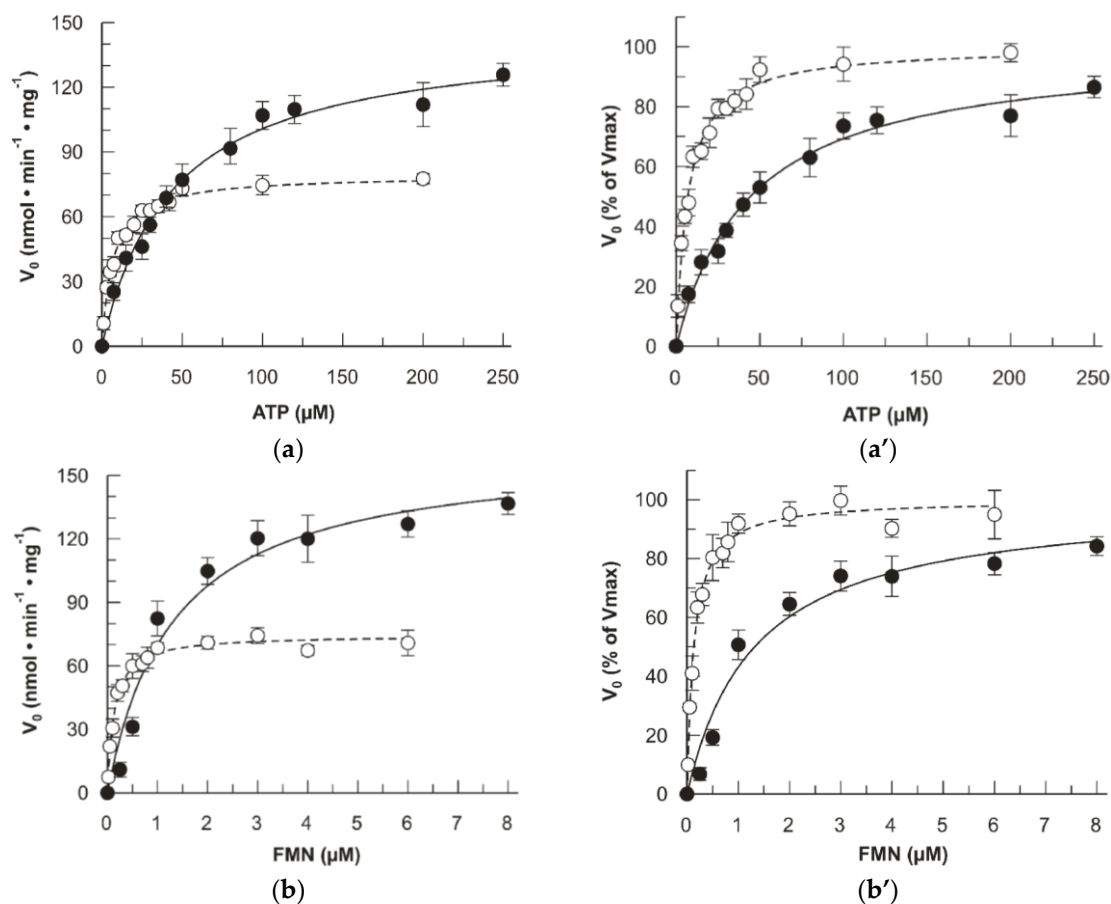


**Figure 6.** Fluorimetric evidence of FAD synthesis. The FAD synthesis reaction was started by the addition of purified recombinant proteins (hFADS6 open circle or D238A-hFADS6 closed circle) and measured by the initial rate of fluorescence decrease ( $\lambda$  excitation = 450 nm and  $\lambda$  emission = 520 nm).  $V_0$  was expressed as  $\text{nmol min}^{-1} \text{ mg}^{-1}$  (a,b) and as a percentage of the  $V_{\text{max}}$  value (a',b') set arbitrarily to 100%. Data points are fitted according to the Michaelis–Menten equation with Grafit 3.0 software. (a) ATP concentration dependence. FAD synthesis rate, catalyzed by purified hFADS6 (open circle, 10  $\mu\text{g}$ , 0.26 nmol) or D238A-hFADS6 (closed circle, 4.2  $\mu\text{g}$ , 0.11 nmol), was fluorimetrically measured at 37  $^\circ\text{C}$  in 2 mL of 50 mM Tris/HCl pH 7.5, in the presence of 5 mM  $\text{MgCl}_2$ , 2  $\mu\text{M}$  or 3  $\mu\text{M}$  FMN, respectively, and of the given ATP concentrations. (b) FMN concentration dependence. FAD synthesis rate catalyzed by purified hFADS6 (open circle, 10  $\mu\text{g}$ , 0.26 nmol) or D238A-hFADS6 (closed circle, 3.9  $\mu\text{g}$ , 0.10 nmol) was fluorimetrically measured at 37  $^\circ\text{C}$  in 2 mL of 50 mM Tris/HCl pH 7.5, in the presence of 5 mM  $\text{MgCl}_2$ , 100  $\mu\text{M}$  ATP, and of the given FMN concentrations.

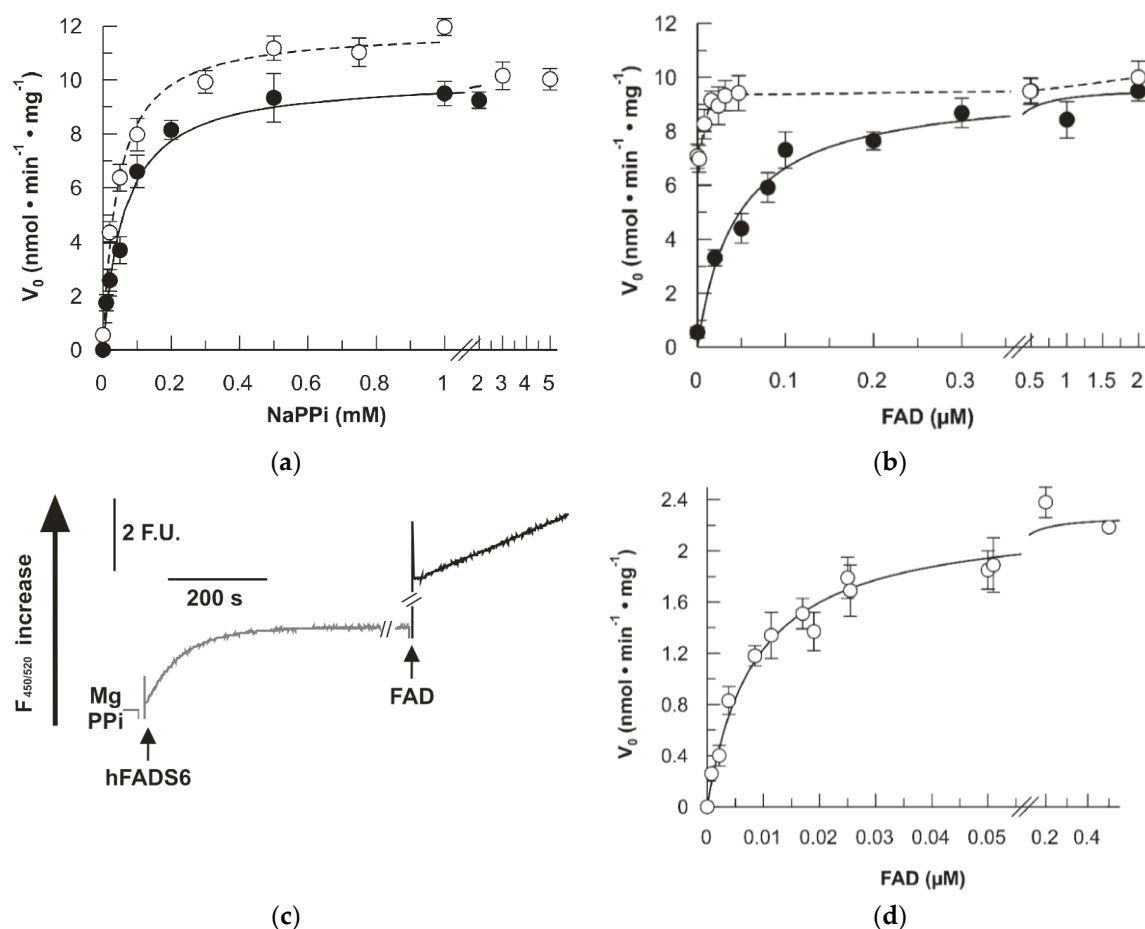


**Figure 7.** Fluorimetric evidence of FAD cleavage. The FAD cleavage (i.e., pyrophosphorolysis) reaction was started by the addition of purified recombinant proteins (hFADS6 open circle, or D238A-hFADS6 closed circle) and measured by the initial rate of fluorescence increase ( $\lambda$  excitation = 450 nm and  $\lambda$  emission = 520 nm). Data points are fitted according to the Michaelis–Menten equation with Grafit 3.0 software. **(a)** NaPPi concentration dependence. FAD cleavage (i.e., pyrophosphorolysis) rate, catalyzed by purified hFADS6 (open circle, 10  $\mu$ g, 0.26 nmol) or 6His-D238A-hFADS6 (closed circle, 10  $\mu$ g, 0.26 nmol), was measured fluorimetrically at 37  $^{\circ}$ C in 2 mL of 50 mM Tris/HCl pH 7.5, in the presence of 5 mM  $MgCl_2$ , 0.5  $\mu$ M FAD, and of the given NaPPi concentrations. **(b)** FAD concentration dependence. FAD cleavage (i.e., pyrophosphorolysis) rate, catalyzed by purified hFADS6 (open circle, 10  $\mu$ g, 0.26 nmol) or D238A-hFADS6 (closed circle, 10  $\mu$ g, 0.26 nmol), was measured fluorimetrically at 37  $^{\circ}$ C in 2 mL of 50 mM Tris/HCl pH 7.5, in the presence of 5 mM  $MgCl_2$ , 1 mM NaPPi, and the given FAD concentrations. **(c)** Exogenous FAD cleavage following endogenous FAD removal from hFADS6. The reaction catalyzed by purified hFADS6 (5  $\mu$ g, 0.13 nmol) was followed at 37  $^{\circ}$ C in 2 mL of 50 mM Tris/HCl pH 7.5, in the presence of 5 mM  $MgCl_2$  and 1 mM NaPPi until the fluorescence reached a constant value corresponding to complete endogenous FAD conversion to FMN (grey line). When indicated exogenous FAD (0.5  $\mu$ M) was added to calculate the rate of pyrophosphorolysis (black line). **(d)** FAD concentration dependence of hFADS6 apo-form. FAD cleavage rate, catalyzed by apo-form of hFADS6 (5  $\mu$ g, 0.13 nmol), was measured fluorimetrically at 37  $^{\circ}$ C in 2 mL of 50 mM Tris/HCl pH 7.5, in the presence of 5 mM  $MgCl_2$ , 1 mM NaPPi, and the given added FAD concentrations as described in Material and Methods (paragraph 4.6.) and graphically explained in (c).

**Table 1.** Comparison between  $K_m$ s for substrates of hFADS6 and D238A-hFADS6. \* The value was obtained using the autocatalytically formation of apo-enzyme as described in Materials and Methods and graphically explained in Figure 7c.  $K_m$  values of the mutant are in bold

|                          | 6His-hFADS6           | 6His-D238A-hFADS6                   |
|--------------------------|-----------------------|-------------------------------------|
| <b>Forward reaction</b>  |                       |                                     |
| $K_m$ FMN ( $\mu$ M)     | 0.13 $\pm$ 0.01       | <b>1.3 <math>\pm</math> 0.3</b>     |
| $K_m$ ATP ( $\mu$ M)     | 6.9 $\pm$ 0.5         | <b>44 <math>\pm</math> 4</b>        |
| $Ac_{50}$ $Mg^{2+}$ (mM) | 0.15 $\pm$ 0.02       | <b>3.5 <math>\pm</math> 0.9</b>     |
| <b>Reverse reaction</b>  |                       |                                     |
| $K_m$ PPi (mM)           | 0.042 $\pm$ 0.006     | <b>0.060 <math>\pm</math> 0.008</b> |
| $K_m$ FAD ( $\mu$ M)     | 0.0079 $\pm$ 0.0017 * | <b>0.045 <math>\pm</math> 0.008</b> |

The reverse reaction, i.e., pyrophosphorolysis was also revealed by using recombinant FADS enzymes [21,23]. The kinetics of this reverse reaction was measured for the mutant in comparison with the WT. In the reverse reaction, the  $K_m$  for NaPPi (Figure 7a) and for FAD (Figure 7b) increased in the mutant, while the  $V_{max}$  remained very similar. Even though an increase of  $K_m$  for FAD (0.045  $\pm$  0.008  $\mu$ M) is clearly evident in the mutant, the  $K_m$  value for the WT could not be accurately measured due to both instrumental limitations and to the presence of tightly bound FAD in the active site of the WT protein [21,23]. Therefore, to measure a reliable  $K_m$  of FAD for the WT, the apo-enzyme was prepared autocatalytically, i.e., by incubating the purified protein at 37 °C for 10 min in the presence of  $MgCl_2$  and NaPPi and in the absence of externally added FAD, allowing the reverse reaction to occur using the endogenous bound FAD. At this stage, after endogenous FAD conversion to FMN, external FAD was added, and the reverse reaction started (Figure 7c). Under this condition, in which the reaction rate could be measured, being much lower than in the case of the holo-enzyme and, hence, an accurate value of  $K_m$  could be calculated. As shown in Figure 7d, the  $K_m$  for FAD of the WT was derived from the curve of Figure 7d. Its value was 0.0079  $\pm$  0.0017  $\mu$ M. This data correlates well with the data of Figure 7b, confirming that, indeed, the  $K_m$  of the mutant is much higher.

Since some nucleotides have been proposed to affect the enzyme activity of FADS [20], we have also tested the effect of GTP and  $NAD^+$  on the mutant activities. The D238A-hFADS6 was inhibited by GTP and by NADH in analogy with the typical behavior of a FADS enzyme (Supplementary Figure S1a,b).

#### 2.4. Impact of the D238A Mutation in the Binding Kinetics of Flavinic Substrates

In the attempt to kinetically dissect the binding of substrates from the overall catalytic reaction process we used stopped-flow spectrophotometry to evaluate the forward (ATP + FMN) and reverse (PPi + FAD) reactions in both WT and D238A hFADS6. Binding and catalysis processes might induce changes in the fluorescence of the flavin isoalloxazine; the first due to changes in its electronic environment [25,26], and the second because of the lower FAD fluorescent yield. No relevant changes in flavin fluorescence are detected when mixing WT or D238A hFADS6 with FMN, FAD, or a mixture containing FMN and ADP. These results agree with isothermal titration calorimetry (ITC) lacking to detect direct FMN binding and just envisaging slow direct binding of FAD (Supplementary Figure S2). On the contrary, when introducing the stopped-flow mixtures, in addition to the flavin substrate, the second substrate of the FMN-AT or FADpp activities, ATP or PPi, respectively, noticeably changes in the fluorescence of the flavins are detected (Figure 8).

In mixtures containing substrates of the forward reaction, ATP and FMN, the relevant decrease in the flavin fluorescence is indicative of internalization of the isoalloxazine or FMN transformation into FAD. These observations also agree with ATP binding to the protein prior to FMN in the bi-bi ordered kinetic mechanism reported for hFADSs [17]. Nonetheless, features for this fluorescence decay also differ between WT and D238A hFADSs (Figure 8a). WT hFADS6 shows an initial biexponential

fluorescence decay followed by a linear one. The first exponential decay has observed rate constants ( $k_{obs1}$ ) in the low seconds range which depend linearly on the FMN concentration, while its amplitude is concentration independent (Supplementary Figure S3a,b).  $k_{obs2}$  for the second exponential decay indicate a slower process nearly FMN concentration independent, with amplitude increasing with FMN concentration (Supplementary Figure S3a,b). Linear dependence of  $k_{obs1}$  on substrate concentration indicates this process relates to FMN binding to the protein, and determines the kinetic constants for FMN binding ( $k_{on} = 3.4 \pm 0.1 \mu\text{M}^{-1} \text{s}^{-1}$ ) and dissociation ( $k_{off} = 0.32 \pm 0.001 \text{s}^{-1}$ ) for the WT hFADS6:ATP complex, as well as a dissociation constant ( $K_d^{\text{FMN}} = k_{off}/k_{on}$ ) for the ternary hFADS6::ATP:FMN complex (Table S1). The derived  $K_d^{\text{FMN}}$ ,  $0.094 \pm 0.004 \mu\text{M}$ , agrees well with the above derived  $K_m^{\text{FMN}}$  for WT hFADS6. Features of the second exponential process suggest it might represent reorganization of the initial complex to achieve the catalytic organization. Finally, the continuous and linear flavin fluorescence decay established after the exponential processes fits well with the settlement of the catalytic steady-state transformation of FMN into FAD, showing, in addition, rates in the ranges of  $V_{max}$  and  $k_{cat}$ . When similarly evaluating D238A hFADS6, the exponential flavin fluorescence decays related to FMN binding collapse in a single process that becomes hardly detectable, suggesting a deleterious effect of the mutation in the isoalloxazine internalization within the protein. Nonetheless, fluorescence decay related to FMN transformation into FAD follows similar traits to the WT ones (Figure 8a). Kinetic parameters for FMN binding to D238A hFADS6:ATP are as a consequence difficult to unambiguously quantify (Table S1), but data make clear that binding of FMN to the mutant is considerably slower and less efficiently than to WT (Figure S3a). Collectively, these observations further confirm that the D238A mutation has a deleterious effect in the FMN binding process.

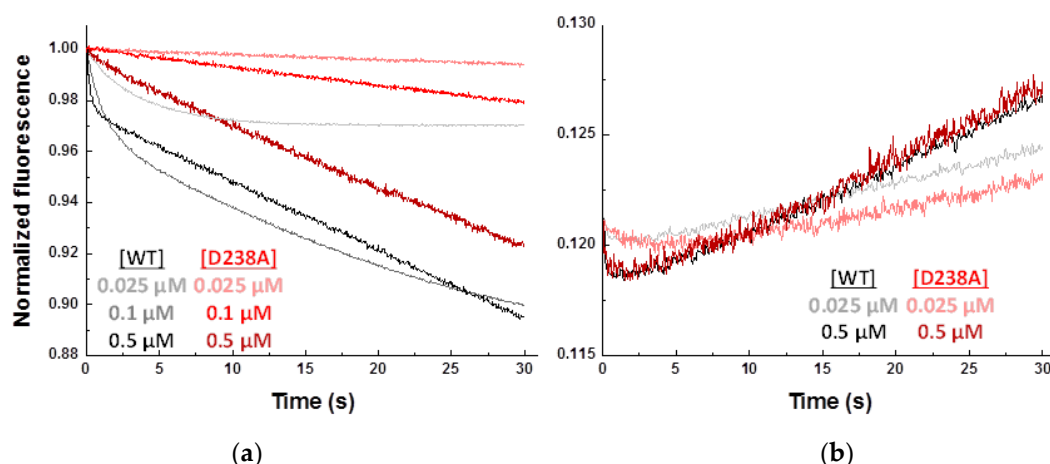


**Figure 8.** Dissection of the kinetics of the substrates binding process from the catalytic reaction by stopped-flow spectrophotometry. Normalized kinetic traces for the flavin fluorescence evolution upon mixing the protein with substrates for the (a) forward (ATP + FMN) and (b) reverse (PPi + FAD) reactions. Traces for WT and D238A hFADS are shown in colored grey and red scales as a function of the flavin given concentrations. Normalized signals regarding the fluorescence of the forward reaction at maximum FMN concentration are shown. Kinetic traces were obtained at 25 °C in mixtures containing 100 nM of protein and 250 μM of either ATP (a) or PPi (b) in 50 mM HEPES/NaOH, 10 mM MgCl<sub>2</sub>, pH 7.0, 5 mM β-mercaptoethanol. All concentrations are final after mixing.

When similarly evaluating the reverse reaction, kinetic traces for both WT and the D238A mutant show an initial fluorescence exponential decay of small amplitude that is followed by a linear increase of the signal (Figure 8b). We again deduce the kinetics for binding of FAD from the exponential decay, while rates for the subsequent linear fluorescence increase relate well to steady-state kinetic parameters for the transformation of FAD into FMN. Although the small amplitudes for FAD binding make it difficult to accurately determine  $k_{obs}$  values, both parameters show a dependence on the substrate concentration (Supplementary Figure S3a,b). Errors in estimated kinetic parameters when using these

data are high, but obtained values are again indicative of the mutant binding FAD slower and weaker than the WT (Supplementary Table S1 and Figure S3c,d).

### 3. Discussion

The substitution of the D238 residue with A in hFADS6, reproduces the previously described mutation of the homologous residue of the Cg FMN-AT that generated an enzyme exhibiting a higher rate of FAD production. The hFADS6 mutant shows similar kinetic changes. The data correlate well with the high conservation of the FAD binding site of eukaryotic FAD synthesizing enzymes along the different species as previously highlighted [16]. This work provides the first evidence that the human FAD synthesizing domain, which corresponds to the hFADS6 enzyme isoform, can be engineered improving its  $k_{\text{cat}}$  as in the case of the lower eukaryotic organism. Although the  $k_{\text{cat}}$  value increases, currently, only two-fold, this result can be a promising starting point for further studies based on computational analysis (molecular dynamics) together with additional site-directed mutagenesis to obtain an engineered enzyme with optimized kinetics.

On the basis of changes in both ATP and FMN  $K_{\text{m}}$ s measured here in the forward reaction and of previous observations [17], the binding of the two substrates appears to be synergistic.

Indeed, the extremely low  $K_{\text{m}}$  for FAD, measured in the course of the reverse reaction, indicates the presence of a very stable bond between FAD. This is in agreement with the finding that size exclusion chromatography is not able to remove FAD from the protein [21,22]. However, the presence of a covalent linkage was previously excluded on the basis of the acidic treatment [23]. Similar strong but non-covalent interactions have been well described for the mitochondrial ADP/ATP binding to carboxyatractilose [27]. Indeed, a reliable  $K_{\text{m}}$  value has only been measured in the present work after using a strategy for removing the bound cofactor (see Figure 7d).

The residue 238 has a major role in this strong interaction. The molecular bases of the improved synthesis rate rely in the correlation between the  $K_{\text{m}}$  for the FAD and the increase in  $k_{\text{cat}}$ . Indeed, the increased  $K_{\text{m}}$  derives by a weaker binding of the FMN or FAD to the enzyme active site. This correlates well with the binding data. These experimental evidences confirm the hypothesis that a labile binding allows a faster release of the newly formed cofactor, and hence an increase of the rate of synthesis. The mechanism was firstly hypothesized in the case of the *C. glabrata* enzyme [24]. In this work, in addition to confirming the kinetic data at the basis of the hypothesis, we provide further evidences based on the variations of the binding after FAD conversion into FMN. Moreover, using the stopped-flow procedure that allows dissecting the binding from the overall catalytic process we provide evidences that the increase of  $K_{\text{m}}$  observed in the mutant can be attributed mostly to a lower binding affinity in the mutant. This could be the basis of a faster release of FAD.

On a structural point of view, the substitution of a hydrophilic residue (Asp) with a hydrophobic one (Ala) weakens the bonds among the FAD molecule and the amino acid residues of the protein active site. The weakening is explained at the molecular level by some structural changes. First, putative hydrogen bonds that fixed FAD to the site are abolished upon substitution of Asp (which can form hydrogen bonds) by Ala (whose side chain is hydrophobic). In addition, the decrease of the side chain size of the 238 residues, resulting from substituting Asp by Ala, favors the release of the cofactor to the external solvent (see Figure 2). This is in agreement with the proposal, which is depicted in the sketch of Figure 9, that the limiting step of the overall catalytic process is the FAD releasing step. This hypothesis has been previously put forward on the bases of steady-state kinetics and cofactor release dynamics in the case of isoform 2 [17,23].

The described changes at the molecular level only affect the active site and its relationships with the cofactor. Indeed, other typical features of the enzyme, such as the inhibition by GTP is similar to the FADS WT enzymes [22,23]. Interestingly, NADH, but not NAD, inhibits the rate of FAD synthesis, thus suggesting an interconnection between the two cofactors and the ability to discriminate between the redox state of nicotinamide pool. The discrimination may be related to the positive charge of

the nicotinamide ring. The same features were demonstrated with isoform 2; when measuring FAD hydrolase activity NADH is also substrate of FADHy domain [20].

Again, the response to the SH binding reagent  $\text{HgCl}_2$ , is not affected by the mutation, correlating with the previous finding that the SH sensitive residue(s) are not in close proximity to the active site [18]. This phenomenon of  $k_{\text{cat}}$  increases also introduces important perspectives in human health. The hFADS6 has been previously described as an “emergency protein” on the basis of its expression in patients with FADS gene defects [7] and of its functional and biochemical characterization [21]. In these patients, a decrease of FAD synthesis is the cause of the pathological alterations. Thus, the knowledge of a strategy to increase the reaction rate, i.e., the capacity of synthesizing FAD, of the emergency protein hFADS6, could open the possibility to ameliorate therapeutic interventions. As an example, targeting the D238 residue by specific chemical reagents (drugs) that reduce the hydrophilic property of this residue could partly mimic the effect of the mutation. Chemical screening and further mutations are under investigation to find conditions for further increasing the FAD synthesis rate of hFADS6.

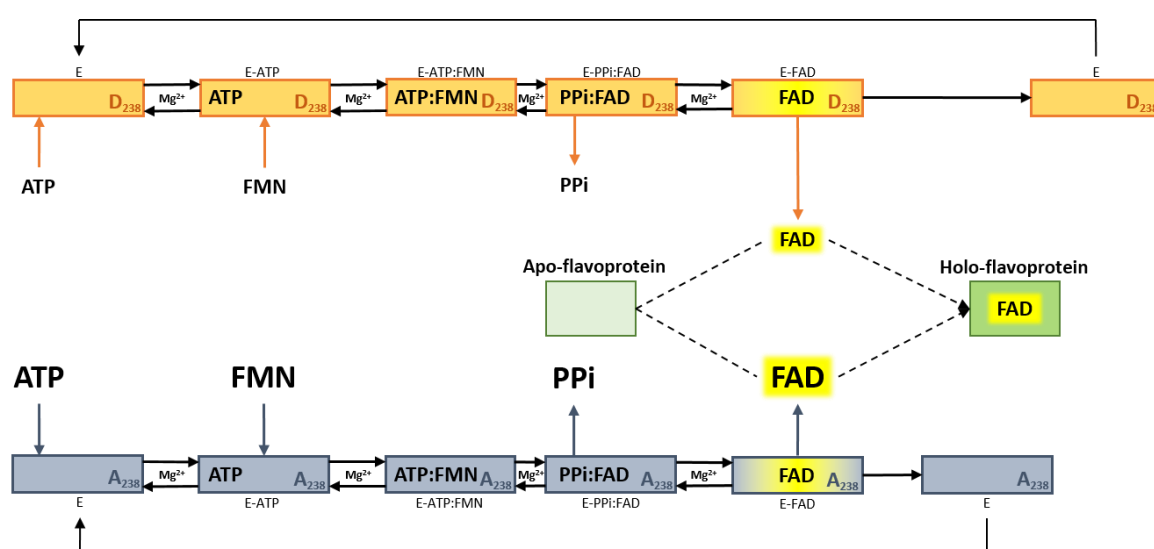


**Figure 9.** Sketch of the catalytic cycle of FAD synthases. In the figure the schematic representation of FAD synthesis performed by hFADS6 (orange boxes) or hFADS6-D238A (blue boxes), and next cofactor delivery to client apo-flavoprotein (green boxes). Both recombinant proteins show the same catalytic cycle, in addition, several differences are highlighted in the picture: in the mutant, the increased  $K_m$ s for substrates ATP and FMN (in the forward reaction) and  $\text{PPi}$  and FAD (in the reverse reaction) are highlighted by increasing font size; the increased  $k_{\text{cat}}$  in the mutant is highlighted by decreasing arrow length in the last step from the enzyme-FAD (E-FAD) complex to free enzyme (E); the increased ability, in the mutant, to deliver the cofactor to client apo-flavoprotein is highlighted by decreasing arrow length from the enzyme-FAD (E-FAD) complex to product FAD. This picture is based on results obtained with the isoform 2 in [17] and with D238A-hFADS6 in this work.

## 4. Materials and Methods

### 4.1. Materials

All chemicals were from Sigma-Aldrich (St. Louis, MO, USA), unless otherwise specified. The *Escherichia coli* Rosetta(DE3) strain was purchased from Novagen (Madison, WI, USA). Restriction endonucleases and other cloning reagents were purchased from Fermentas (Glen Burnie, MD, USA). Chelating Sepharose Fast Flow was from Amersham Biosciences (Arlington Heights, IL, USA), and the Isolate II PCR and Gel Kit (Bioline, London, UK). The dye reagent for protein assay was from Bio-Rad (Hemel Hempstead, Herts, UK).

#### 4.2. Site-Directed Mutagenesis of the hFADS6

The hFADS6-D238A mutant was obtained by PCR overlap extension method [18] using as forward and reverse mutagenic primers 5'-TTCAGCCCCACTGCTCCAGGCTGGCCCCGCATTCAT-3' and 5'-ATGAATGCGGGCCAGCCTGGAGCAGTGGGGCTGAA-3', respectively. The external forward and reverse wild type primers allowed the directional cloning of the desired hFADS6-D238A cDNA between *EcoRI* (at 5' end) and *XhoI* (at 3' end) restriction sites of the pH6EX3 expression vector. The resulting recombinant protein carried the extra N-terminal sequence MSPIHHHHHHLVPRGSEASNS.

#### 4.3. Expression of the WT hFADS6 and hFADS6-D238A Proteins in *E. coli*

Rosetta(DE3) strain was transformed with either pH6EX3-hFADS6 or pH6EX3-hFADS6-D238A plasmids by calcium chloride treatment. Selection of transformed colonies was performed on LB-agar plates containing 100 µg/mL ampicillin and 34 µg/mL chloramphenicol. *E. coli* Rosetta(DE3) cells carrying the recombinant plasmids were inoculated in 10 mL of LB medium (1% tryptone, 0.5% yeast extract, 0.5% NaCl, pH 7.0) supplemented with 100 µg/mL ampicillin and 34 µg/mL chloramphenicol, and cultured overnight at 37 °C with rotary shaking (~180 rpm). The day after, a 5 mL aliquot of the cell culture was transferred to 0.5 L of fresh LB medium supplemented with antibiotics and grown at 37 °C to A600 equal to 0.8 to 1. Then, 0.5 mM IPTG was added to induce the expression of the recombinant WT and mutant proteins. Growth was continued overnight at 20 °C, bacteria were harvested by centrifugation at 3000× *g* for 10 min at 4 °C and the pellets stored at −20 °C. The bacterial pellet (about 4 g wet weight) was thawed on ice and resuspended in 30 mL start buffer (500 mM NaCl, 40 mM HEPES/Na, pH 7.4) supplemented with protease inhibitor cocktail (P8849, Sigma-Aldrich, Merck, Milan, Italy 1 mL/20 g of cells wet weight) and 0.5 mM phenylmethyl sulfonyl fluoride (PMSF, P7626, Sigma-Aldrich, Merck, Milan, Italy). Cells were disrupted by mild sonication (one cycle of 10 min and one cycle of 5 min with 1 s Pulse ON and 1 s Pulse OFF, at 40 W) on ice bath using a VCX-130 Sonifier (Sonic). The soluble and the insoluble cell fractions were separated by centrifugation of the cell lysate at 20,000× *g* for 30 min at 4 °C. The supernatant, containing the soluble overexpressed 6His-hFADS6 or 6His-D238A-hFADS6 proteins, was used for SDS-PAGE analysis, FADS activity assay and further protein purification (see below).

#### 4.4. Purification of Recombinant hFADS6-D238A

A 40 mL aliquot of the soluble cell fraction, obtained from *E. coli* Rosetta(DE3) strain transformed with the pH6EX3-hFADS6-D238A plasmid, was applied onto a Chelating Sepharose Fast Flow column (3.5 mL packed resin), previously charged with 200 mM NiSO<sub>4</sub> according to the producer's protocol, and equilibrated with the start buffer. The column was first washed with 35 mL start buffer, then, developed with a step gradient of 50 mM, 100 mM, 250 mM, and 500 mM imidazole in the same buffer. At each step of the purification procedure, the FADS activity was measured (see below) and the purity of the proteins was checked by SDS-PAGE. Prior to storing or further processing, fractions containing the purified recombinant protein were desalted by gel filtration on a PD10 column in 40 mM HEPES/Na, 5 mM β-mercaptoethanol, pH 7.4. These protein samples were stable for at least 30 days at 4 °C.

Protein concentration and FAD/protein monomer ratio measurements were carried out as previously described [21].

#### 4.5. 3D Modeling and Docking of the WT hFADS6 and hFADS6-D238A Proteins

The 3D model of the hFADS6 protein was obtained by ab initio using the server Robetta (available at <http://robetta.bakerlab.org/>) as previously described [21]. FAD was docked in the same position as in the 3G6K structure by aligning the two structures with the MatchMaker tool of the Chimera software using Needleman-Wunsch algorithm and BLOSUM-62 matrix [28]. D238A mutation in hFADS6 structure was introduced using a rotamer library according to Shapovalov and Dunbrack [29].

#### 4.6. Measurements of Enzyme Catalyzed Rates for FAD Synthesis and FAD Pyrophosphorolysis

The rate of FAD synthesis and FAD cleavage were measured in continuo as in [23], by exploiting the different fluorescence properties of FAD with respect to FMN. Fluorescence time courses ( $\lambda$  excitation at 450 nm and  $\lambda$  emission at 520 nm) were followed at 37 °C in a FP-8300 Jasco spectrofluorometer. In each experiment, FMN and FAD fluorescence were calibrated by using standard solutions whose concentrations (used in  $\mu\text{M}$  range) were calculated by using  $\epsilon_{450}$  of  $12.2 \text{ mM}^{-1} \text{ cm}^{-1}$  for FMN and  $11.3 \text{ mM}^{-1} \text{ cm}^{-1}$  for FAD. Under the experimental condition used here, the specific relative FAD fluorescence coefficient ( $\phi_{\text{FAD}}$ ) proved to be about ten times lower than those of FMN ( $\phi_{\text{FMN}}$ ) [30,31].

For FAD synthesis rate measurements, purified protein fractions (2 to 10  $\mu\text{g}$ , 0.06 to 0.26 nmol protein as monomer, unless otherwise indicated) were incubated in 50 mM Tris/HCl, pH 7.5, containing 5 mM  $\text{MgCl}_2$ , 3  $\mu\text{M}$  FMN, 100  $\mu\text{M}$  ATP, and additional reagents as appropriate. The rate of FAD synthesis, expressed as  $\text{nmol FAD min}^{-1} \text{ mg protein}^{-1}$ , was calculated from the rate of fluorescence decrease, measured as the tangent to the initial part of the experimental curve by applying the following equation:

$$V_0 = [(\Delta F_{450/520} / \Delta \phi_{450/520}) \times V_f] / (t \times m) \quad (1)$$

where  $\Delta F$  is expressed in fluorescence arbitrary units,  $\Delta \phi = \phi_{\text{FMN}} - \phi_{\text{FAD}}$  is expressed as  $\mu\text{M}^{-1}$ ,  $V_f$  is expressed in mL,  $t$  is time expressed in min, and  $m$  is the mass of protein in mg.

The rate of FAD pyrophosphorolysis catalyzed by 6His-D238A-hFADS6 (5 to 10  $\mu\text{g}$ , 0.13 to 0.26 nmol protein as monomer) was measured in 50 mM Tris/HCl, pH 7.5, containing 5 mM  $\text{MgCl}_2$  in the presence of 5 mM  $\text{MgCl}_2$ , 1 mM NaPPi (sodium pyrophosphate), and 0.5  $\mu\text{M}$  FAD, unless otherwise indicated. The rate of FAD cleavage was expressed as  $\text{nmol FAD min}^{-1} \text{ mg protein}^{-1}$ , and was calculated from the rate of fluorescence increase, measured as the tangent to the initial part of the experimental curve, as previously described.

In the case of using WT hFADS6, which is a FAD binding protein, the measurement of  $K_m$  for FAD might not be accurate. To overcome this limitation, the apo-form of the protein was obtained by a rapid procedure in the cuvette simply by allowing autocatalytic endogenous bound FAD conversion to FMN by adding only 1 mM NaPPi. The reaction was followed for about 10 min until endogenous bound FAD is completely converted to FMN, i.e., the fluorescence does not change. At this stage, external FAD was added at different concentrations and the dependence of the reaction rate was studied.

#### 4.7. Kinetics for the Binding of Flavinic Ligands to WT hFADS6 and hFADS6-D238A Proteins

Pre-steady-state kinetic experiments were performed using stopped-flow spectroscopy on an Applied Photophysics SX17.MV spectrophotometer using the Pro-Data SX software (Applied Photophysics Ltd. Leatherhead, Surrey, UK). The fluorescence of flavins was measured in a continuous assay with an excitation wavelength of 445 nm, while the emission was recovered using a  $>530 \text{ nm}$  cut-off filter and the voltage was set to 350 V. Then, 100 nM hFADS6 samples were mixed with samples that contained increasing concentrations of FMN or FAD (which varied in the range 0.025–1  $\mu\text{M}$ ), in the absence and in the presence of saturating concentrations of their respective co-substrates ATP or PPi (250  $\mu\text{M}$ ). All the indicated concentrations are final ones in the stopped-flow observation cell. Measurements were carried out at 25 °C in 50 mM HEPES/NaOH, 10 mM  $\text{MgCl}_2$ , pH 7.0, 5 mM  $\beta$ -mercaptoethanol. At least three reproducible kinetic traces of changes in fluorescence were recorded for each condition and fitted to exponential equations (usually one or two exponentials were used)

$$y = \sum A_i e^{-k_{\text{obs},i} t} \quad (2)$$

where  $A_i$  and  $k_{\text{obs},i}$  represent the amplitude and the observed rate constant, respectively, for each of the processes (i) that contribute to the overall time-dependent fluorescence change for each experimental condition. Processes whose  $k_{\text{obs}}$  showed a linear dependence on flavin concentration were fit to a



one-step model that accounts for the kinetic equilibrium of the formation and dissociation of the protein-flavin complex, whose kinetics can be represented by

$$k_{\text{obs}} = k_{\text{on}}[\text{FLV}] + k_{\text{off}} \quad (3)$$

where  $k_{\text{on}}$  and  $k_{\text{off}}$  are the kinetic constants for complex formation and dissociation, respectively.

#### 4.8. Isothermal Titration Calorimetry (ITC)

Measurements were carried out using an Auto-ITC200 microcalorimeter (MicroCal LLC, Northampton, MA, USA) thermostated at 25 °C. Ligand (100  $\mu\text{M}$  FMN or FAD) and proteins (~15  $\mu\text{M}$ ) were dissolved in 50 mM HEPES/NaOH, 10 mM  $\text{MgCl}_2$ , pH 7.0, 2 mM  $\beta$ -mercaptoethanol, and degassed prior to titration. Up to 19 injections of 2  $\mu\text{L}$  of ligand were added to the sample cell (~0.2 mL) containing the enzyme and then mixed via the rotating (1000 rpm) stirrer syringe. Since either no binding or slow binding was detected, data fitting to obtain thermodynamic binding parameters was not reliable.

#### 4.9. Electrophoretic Analysis

Proteins were separated by SDS-PAGE on 12% total polyacrylamide gels, according to Laemmli [32]. Quantitative evaluation of Coomassie blue-stained protein bands was carried out using the Chemidoc imaging system and the Quantity One software (Bio-Rad), as described previously [33].

**Supplementary Materials:** Supplementary materials can be found at <http://www.mdpi.com/1422-0067/20/24/6203/s1>.

**Author Contributions:** M.G. and C.I. were involved in hFADS6 D238A cloning, expression, and modeling; P.L., S.Q., and M.B. were involved in protein purification and characterization; M.M. was involved in conceptualization and supervision of data on stopped-flow analysis; E.A.-C. was involved in data curation, formal analysis, and methodology investigation. All authors discussed the results and contributed to writing the manuscript. M.B. coordinated and supervised the work and the manuscript writing.

**Funding:** This work was supported by “Fondi di Ateneo” the Università degli Studi di Bari (to M.B.); “Effetto di mutazioni di FLAD1 e di alterazioni dell’omeostasi delle flavine sullo stato redox e sulla biogenesi mitocondriale: uno studio integrato su fibroblasti umani” the Università degli Studi di Bari (to M.B.); “Fondi di Ateneo” the Università della Calabria (to C.I. and M.G.); the Spanish Agencia Estatal de Investigación and Fondo Europeo de Desarrollo Regional BIO2016-75183-P AEI/FEDER, UE (to M.M.), and the Government of Aragón-FEDER Grupo de Referencia Biología Estructural E35\_17R (to M.M.).

**Acknowledgments:** The helpful collaboration of Maria Tolomeo (University of Bari) who participated in preparation of cellular cultures, and the technical assistance of Vito Giannoccaro (University of Bari) are gratefully acknowledged. Authors would like to acknowledge the use of Servicio General de Apoyo a la Investigación-SAI, Universidad de Zaragoza.

**Conflicts of Interest:** The authors declare no conflict of interest.

#### Abbreviations

|         |  |
|---------|--|
| FADS    | FAD synthase   |
| FMNAT   | FMN adenylyl transferase   |
| hFADS6  | human FAD synthase isoform 6                                     |
| Rf      | riboflavin   |
| FMN     | flavin mono nucleotide   |
| FAD     | flavin adenine dinucleotide                                      |
| PAPS    | phosphoadenosine 5-phosphosulfate                                |
| FADSy   | FAD synthase domain  |
| MPTb    | molybdopterin binding  |
| FADHy   | FAD hydrolase domain   |
| BVVLS   | Brown–Vialeto-van Laere syndrome                                 |
| RR-MADD | riboflavin responsive multiple acyl-CoA dehydrogenase deficiency |
| PMSF    | phenylmethyl sulfonyl fluoride                                   |

## References

1. Barile, M.; Giancaspero, T.A.; Leone, P.; Galluccio, M.; Indiveri, C. Riboflavin transport and metabolism in humans. *J. Inherit. Metab. Dis.* **2016**, *39*, 545–557. [[CrossRef](#)] [[PubMed](#)]
2. Lienhart, W.D.; Gudipati, V.; Macheroux, P. The human flavoproteome. *Arch. Biochem. Biophys.* **2013**, *535*, 150–162. [[CrossRef](#)] [[PubMed](#)]
3. Green, P.; Wiseman, M.; Crow, Y.J.; Houlden, H.; Riphagen, S.; Lin, J.P.; Raymond, F.L.; Childs, A.M.; Sheridan, E.; Edwards, S.; et al. Brown-Vialetto-Van Laere syndrome, a ponto-bulbar palsy with deafness, is caused by mutations in c20orf54. *Am. J. Hum. Genet.* **2010**, *86*, 485–489. [[CrossRef](#)] [[PubMed](#)]
4. Jaeger, B.; Bosch, A.M. Clinical presentation and outcome of riboflavin transporter deficiency: mini review after five years of experience. *J. Inherit. Metab. Dis.* **2016**, *39*, 559–564. [[CrossRef](#)] [[PubMed](#)]
5. Ryder, B.; Tolomeo, M.; Nochi, Z.; Colella, M.; Barile, M.; Olsen, R.K.; Inbar-Feigenberg, M. A Novel Truncating FLAD1 Variant, Causing Multiple Acyl-CoA Dehydrogenase Deficiency (MADD) in an 8-Year-Old Boy. *JIMD Rep.* **2019**, *45*, 37–44. [[PubMed](#)]
6. Balasubramaniam, S.; Christodoulou, J.; Rahman, S. Disorders of riboflavin metabolism. *J. Inherit. Metab. Dis.* **2019**, *42*, 608–619. [[CrossRef](#)]
7. Olsen, R.K.J.; Konarikova, E.; Giancaspero, T.A.; Mosegaard, S.; Boczonadi, V.; Matakovic, L.; Veauville-Merllie, A.; Terrile, C.; Schwarzmayr, T.; Haack, T.B.; et al. Riboflavin-Responsive and -Non-responsive Mutations in FAD Synthase Cause Multiple Acyl-CoA Dehydrogenase and Combined Respiratory-Chain Deficiency. *Am. J. Hum. Genet.* **2016**, *98*, 1130–1145. [[CrossRef](#)]
8. Yonezawa, A.; Inui, K. Novel riboflavin transporter family RFVT/SLC52: identification, nomenclature, functional characterization and genetic diseases of RFVT/SLC52. *Mol. Asp. Med.* **2013**, *34*, 693–701. [[CrossRef](#)]
9. Console, L.; Tolomeo, M.; Colella, M.; Barile, M.; Indiveri, C. Reconstitution in Proteoliposomes of the Recombinant Human Riboflavin Transporter 2 (SLC52A2) Overexpressed in *E. coli*. *Int. J. Mol. Sci.* **2019**, *20*, 4416. [[CrossRef](#)]
10. Brizio, C.; Galluccio, M.; Wait, R.; Torchetti, E.M.; Bafunno, V.; Accardi, R.; Gianazza, E.; Indiveri, C.; Barile, M. Over-expression in *Escherichia coli* and characterization of two recombinant isoforms of human FAD synthetase. *Biochem. Biophys. Res. Commun.* **2006**, *344*, 1008–1016. [[CrossRef](#)]
11. Liuzzi, V.C.; Giancaspero, T.A.; Gianazza, E.; Banfi, C.; Barile, M.; De Giorgi, C. Silencing of FAD synthase gene in *Caenorhabditis elegans* upsets protein homeostasis and impacts on complex behavioral patterns. *Biochim. Biophys. Acta* **2012**, *1820*, 521–531. [[CrossRef](#)] [[PubMed](#)]
12. Wu, M.; Repetto, B.; Glerum, D.M.; Tzagoloff, A. Cloning and characterization of FAD1, the structural gene for flavin adenine dinucleotide synthetase of *Saccharomyces cerevisiae*. *Mol. Cell Biol.* **1995**, *15*, 264–271. [[CrossRef](#)] [[PubMed](#)]
13. Huerta, C.; Borek, D.; Machius, M.; Grishin, N.V.; Zhang, H. Structure and mechanism of a eukaryotic FMN adenylyltransferase. *J. Mol. Biol.* **2009**, *389*, 388–400. [[CrossRef](#)] [[PubMed](#)]
14. Leulliot, N.; Blondeau, K.; Keller, J.; Ulryck, N.; Quevillon-Cheruel, S.; van Tilbeurgh, H. Crystal structure of yeast FAD synthetase (Fad1) in complex with FAD. *J. Mol. Biol.* **2010**, *398*, 641–646. [[CrossRef](#)] [[PubMed](#)]
15. Torchetti, E.M.; Brizio, C.; Colella, M.; Galluccio, M.; Giancaspero, T.A.; Indiveri, C.; Roberti, M.; Barile, M. Mitochondrial localization of human FAD synthetase isoform 1. *Mitochondrion* **2010**, *10*, 263–273. [[CrossRef](#)] [[PubMed](#)]
16. Barile, M.; Giancaspero, T.A.; Brizio, C.; Panebianco, C.; Indiveri, C.; Galluccio, M.; Vergani, L.; Eberini, I.; Gianazza, E. Biosynthesis of flavin cofactors in man: implications in health and disease. *Curr. Pharm. Des.* **2013**, *19*, 2649–2675. [[CrossRef](#)] [[PubMed](#)]
17. Giancaspero, T.A.; Colella, M.; Brizio, C.; Difonzo, G.; Fiorino, G.M.; Leone, P.; Brandsch, R.; Bonomi, F.; Iametti, S.; Barile, M. Remaining challenges in cellular flavin cofactor homeostasis and flavoprotein biogenesis. *Front. Chem.* **2015**, *3*, 30. [[CrossRef](#)]
18. Miccolis, A.; Galluccio, M.; Nitride, C.; Giancaspero, T.A.; Ferranti, P.; Iametti, S.; Indiveri, C.; Bonomi, F.; Barile, M. Significance of redox-active cysteines in human FAD synthase isoform 2. *Biochim. Biophys. Acta* **2014**, *1844*, 2086–2095. [[CrossRef](#)]

19. Giancaspero, T.A.; Galluccio, M.; Miccolis, A.; Leone, P.; Eberini, I.; Iametti, S.; Indiveri, C.; Barile, M. Human FAD synthase is a bi-functional enzyme with a FAD hydrolase activity in the molybdopterin binding domain. *Biochem. Biophys. Res. Commun.* **2015**, *465*, 443–449. [[CrossRef](#)]
20. Leone, P.; Galluccio, M.; Brizio, C.; Barbiroli, A.; Iametti, S.; Indiveri, C.; Barile, M. The hidden side of the human FAD synthase 2. *Int. J. Biol. Macromol.* **2019**, *138*, 986–995. [[CrossRef](#)]
21. Leone, P.; Galluccio, M.; Barbiroli, A.; Eberini, I.; Tolomeo, M.; Vrenna, F.; Gianazza, E.; Iametti, S.; Bonomi, F.; Indiveri, C.; et al. Bacterial Production, Characterization and Protein Modeling of a Novel Monofunctional Isoform of FAD Synthase in Humans: An Emergency Protein? *Molecules* **2018**, *23*, 116. [[CrossRef](#)]
22. Miccolis, A.; Galluccio, M.; Giancaspero, T.A.; Indiveri, C.; Barile, M. Bacterial over-expression and purification of the 3'phosphoadenosine 5'phosphosulfate (PAPS) reductase domain of human FAD synthase: functional characterization and homology modeling. *Int. J. Mol. Sci.* **2012**, *13*, 16880–16898. [[CrossRef](#)]
23. Torchetti, E.M.; Bonomi, F.; Galluccio, M.; Gianazza, E.; Giancaspero, T.A.; Iametti, S.; Indiveri, C.; Barile, M. Human FAD synthase (isoform 2): A component of the machinery that delivers FAD to apo-flavoproteins. *FEBS J.* **2011**, *278*, 4434–4449. [[CrossRef](#)]
24. Huerta, C.; Grishin, N.V.; Zhang, H. The “super mutant” of yeast FMN adenylyltransferase enhances the enzyme turnover rate by attenuating product inhibition. *Biochemistry* **2013**, *52*, 3615–3617. [[CrossRef](#)]
25. Weber, G. Fluorescence of riboflavin and flavin-adenine dinucleotide. *Biochem. J.* **1950**, *47*, 114–121. [[CrossRef](#)]
26. Sebastián, M.; Velázquez-Campoy, A.; Medina, M. The RFK catalytic cycle of the pathogen *Streptococcus pneumoniae* shows species-specific features in prokaryotic FMN synthesis. *J. Enzyme Inhib. Med. Chem.* **2018**, *33*, 842–849. [[CrossRef](#)]
27. Pebay-Peyroula, E.; Dahout-Gonzalez, C.; Kahn, R.; Trezeguet, V.; Lauquin, G.J.; Brandolin, G. Structure of mitochondrial ADP/ATP carrier in complex with carboxyatractyloside. *Nature* **2003**, *426*, 39–44. [[CrossRef](#)]
28. Pettersen, E.F.; Goddard, T.D.; Huang, C.C.; Couch, G.S.; Greenblatt, D.M.; Meng, E.C.; Ferrin, T.E. UCSF Chimera—A visualization system for exploratory research and analysis. *J. Comput. Chem.* **2004**, *25*, 1605–1612. [[CrossRef](#)]
29. Shapovalov, M.V.; Dunbrack, R.L., Jr. A smoothed backbone-dependent rotamer library for proteins derived from adaptive kernel density estimates and regressions. *Structure* **2011**, *19*, 844–858. [[CrossRef](#)]
30. Barile, M.; Passarella, S.; Bertoldi, A.; Quagliariello, E. Flavin adenine dinucleotide synthesis in isolated rat liver mitochondria caused by imported flavin mononucleotide. *Arch. Biochem Biophys* **1993**, *305*, 442–447. [[CrossRef](#)]
31. Barile, M.; Brizio, C.; De Virgilio, C.; Delfino, S.; Quagliariello, E.; Passarella, S. Flavin adenine dinucleotide and flavin mononucleotide metabolism in rat liver—The occurrence of FAD pyrophosphatase and FMN phosphohydrolase in isolated mitochondria. *Eur. J. Biochem.* **1997**, *249*, 777–785. [[CrossRef](#)]
32. Laemmli, U.K. Cleavage of structural proteins during the assembly of the head of bacteriophage T4. *Nature* **1970**, *227*, 680–685. [[CrossRef](#)]
33. Brizio, C.; Brandsch, R.; Bufano, D.; Pochini, L.; Indiveri, C.; Barile, M. Over-expression in *Escherichia coli*, functional characterization and refolding of rat dimethylglycine dehydrogenase. *Protein Expr. Purif.* **2004**, *37*, 434–442. [[CrossRef](#)]





Article

# Mutation of Aspartate 238 in FAD Synthase Isoform 6 Increases the Specific Activity by Weakening the FAD Binding

Piero Leone <sup>1,2</sup>, Michele Galluccio <sup>2</sup>, Stefano Quarta <sup>1</sup>, Ernesto Anoz-Carbonell <sup>3</sup>, Milagros Medina <sup>3</sup>, Cesare Indiveri <sup>2</sup> and Maria Barile <sup>1,\*</sup>

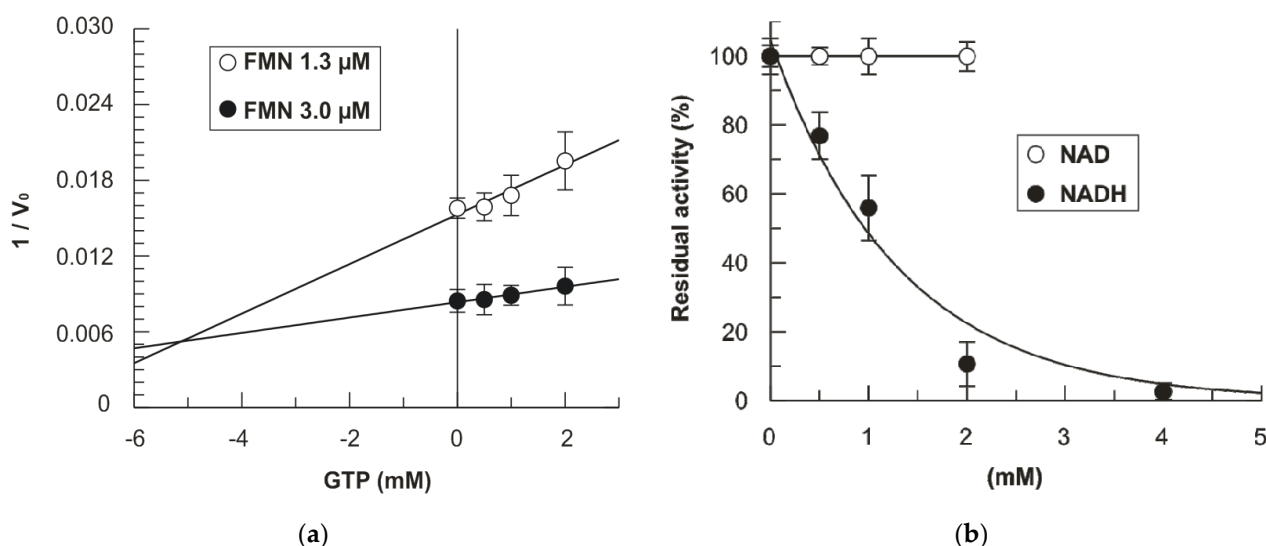
<sup>1</sup> Department of Biosciences, Biotechnology and Biopharmaceutics, University of Bari, via Orabona 4 –, 70126 Bari, Italy; pieroleone87@gmail.com (P.L.); quartastefano93@gmail.com (S.Q.)

<sup>2</sup> Department of Biology, Ecology and Earth Sciences (DiBEST), Unit of Biochemistry and Molecular Biotechnology, University of Calabria, via P. Bucci 4c, 87036 Arcavacata di Rende, Italy; michele.galluccio@unical.it (M.G.); cesare.indiveri@unical.it (C.I.)

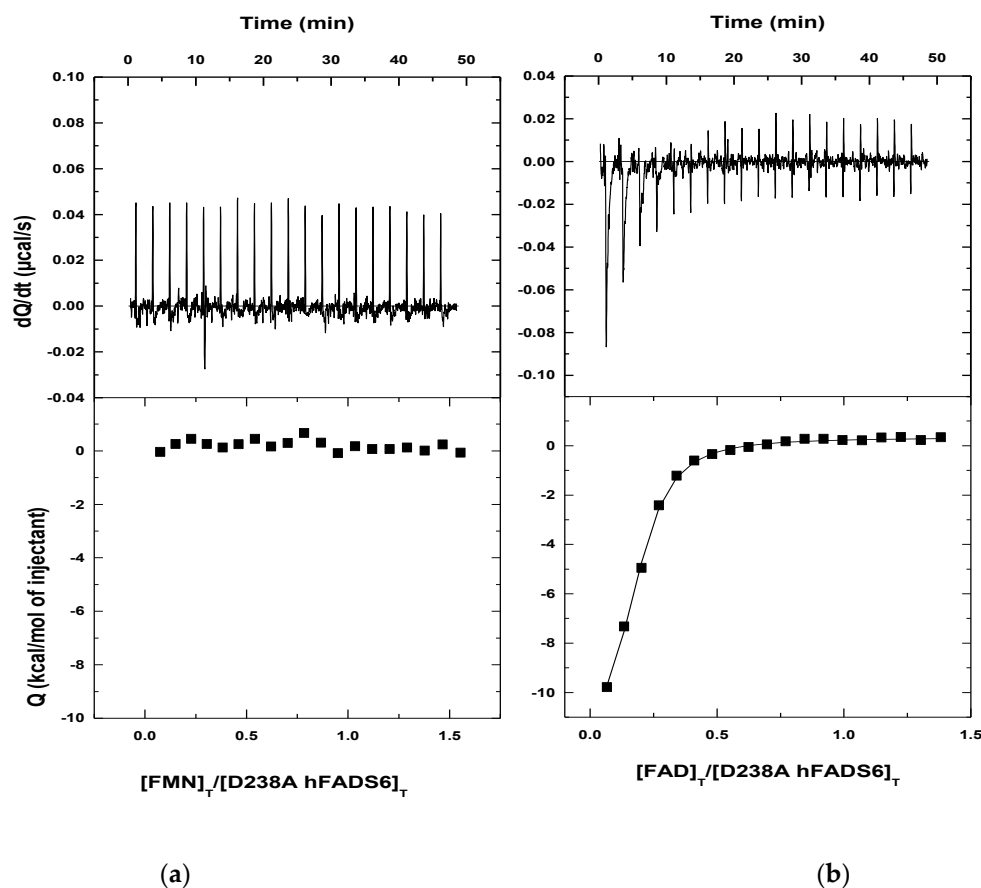
<sup>3</sup> Departamento de Bioquímica y Biología Molecular y Celular, Facultad de Ciencias, Instituto de Biocomputación y Física de Sistemas Complejos (GBsC-CSIC and BIFI-IQFR Joint Units), Universidad de Zaragoza, Zaragoza 50009, Spain; eanoz@unizar.es (E.A.-C.); mmedina@unizar.es (M.M.)

\* Correspondence: maria.barile@uniba.it

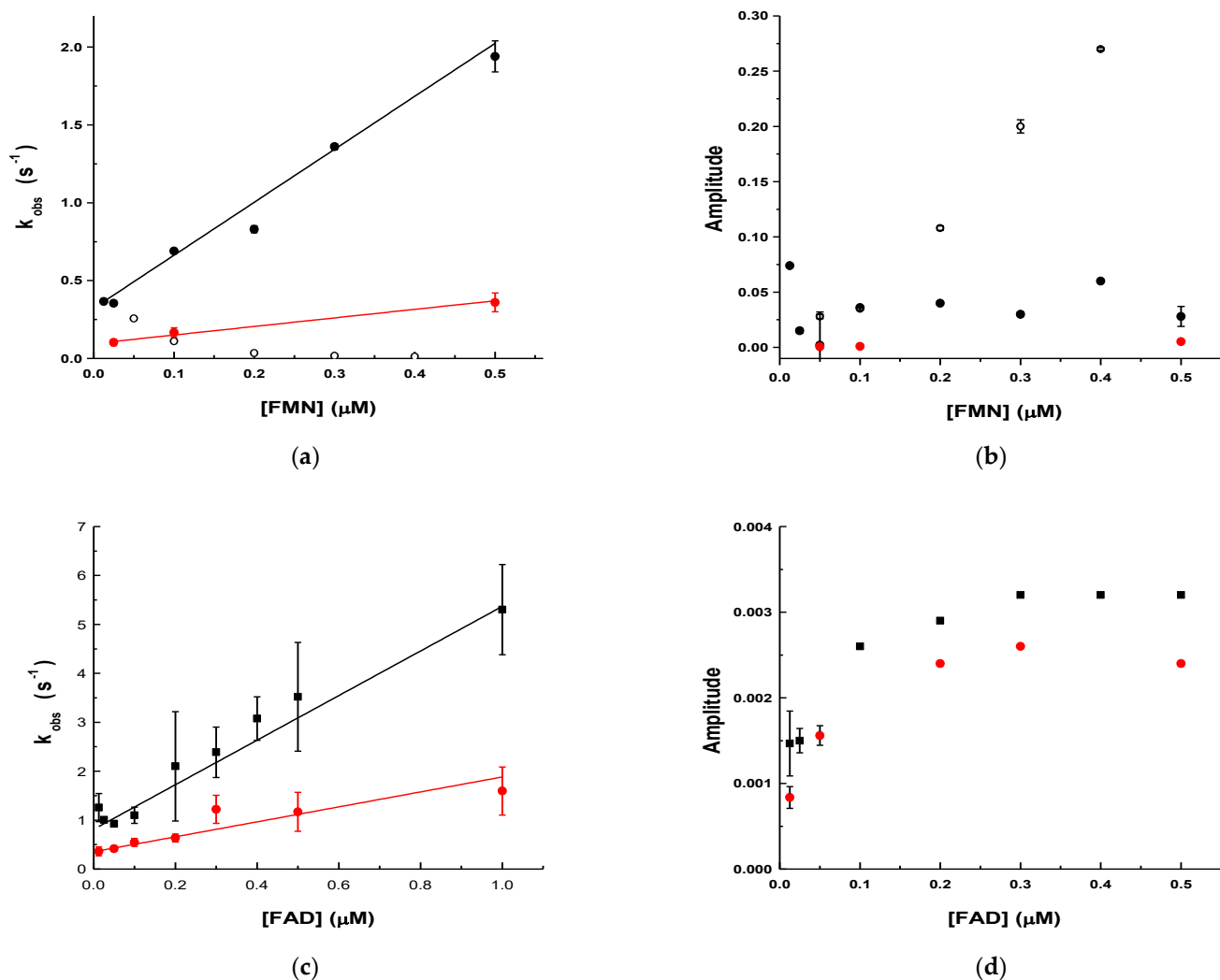
**Supplementary Materials:** Supplementary materials can be found at [www.mdpi.com/xxx/s1](http://www.mdpi.com/xxx/s1).



**Supplementary Figure 1.** (a) GTP inhibition on FAD synthesis catalyzed by D238A-hFADS6. The FAD synthesis reaction was started by the addition of purified recombinant protein D238A-hFADS6 and measured by the initial rate of fluorescence decrease ( $\lambda$  excitation = 450 nm,  $\lambda$  emission = 520 nm). FAD synthesis rate, catalyzed by purified D238A-hFADS6 (2.9  $\mu$ g, 0.08 nmol), was fluorimetrically measured at 37 °C in 2 ml of 50 mM Tris/HCl pH 7.5, in the presence of 100  $\mu$ M ATP, 5 mM MgCl<sub>2</sub>, 3  $\mu$ M (closed circle) or 1.3  $\mu$ M (open circle) FMN, and of the given GTP concentrations. Data points are fitted according to the linear equation with Grafit 3.0 software. (b) NAD<sup>+</sup> and NADH inhibition on FAD synthesis. The FAD synthesis reaction was started by the addition of purified recombinant protein 6His-D238A-hFADS6 and measured by the initial rate of fluorescence decrease ( $\lambda$  excitation = 450 nm,  $\lambda$  emission = 520 nm). FAD synthesis rate, catalyzed by purified D238A-hFADS6 (8  $\mu$ g, 0.21 nmol), was fluorimetrically measured at 37°C in 2 ml of 50 mM Tris/HCl pH 7.5, in the presence of 100  $\mu$ M ATP, 5 mM MgCl<sub>2</sub>, 1.3  $\mu$ M FMN, and of the given NAD<sup>+</sup> (open circle) and NADH (closed circle) concentrations. Data points are fitted according to the exponential or linear equations for NADH and NAD<sup>+</sup> respectively with Grafit 3.0 software.



**Supplementary Figure 2.** Isothermal titration calorimetric analysis of the binding of flavinic substrates to D238A hFADS6 in the absence of the second substrate. Thermogram (upper panels) and binding isotherms with integrated heat (lower panels) for the titration with (a) FMN and (b) FAD. No interaction heat is detected (a) for the titration of FMN, suggesting under the assayed conditions binding is not produced. Thermograms for the titration with FAD titration envisage binding to less than 20% of the protein molecules (suggesting a slow-binding process) under the assayed conditions, as well as  $K_d^{\text{FAD}}$  below 1  $\mu\text{M}$ . Titrations were performed at 25 °C in 50 mM Hepes/NaOH, 10 mM  $\text{MgCl}_2$ , pH 7.0, 5 mM  $\beta$ -mercaptoethanol. The low stability of WT hFADS6 along the ITC assay prevented the production of the corresponding thermograms.



**Supplementary Figure 3.** Dependence of flavin binding pre-steady-state kinetic parameters on the concentration of the flavin substrates. Evolution of binding parameters for the FAD biosynthesis: (a)  $k_{obs1}$  (closed circles) and  $k_{obs2}$  (open circles) and (b) their corresponding amplitudes, Amp1 (closed circles) and Amp2 (open circles), obtained when mixing WT (black) and D238A (red) hFADS6s with saturating ATP and different FMN concentrations. Evolution of binding parameters for the FAD pyrophosphorolysis: (c)  $k_{obs}$  (closed circles) and (d) Amp (closed circles) obtained when mixing WT (black) and D238A (red) hFADS6s with saturating PPi and different FAD concentrations. Data were obtained at 25 °C in mixtures containing 100 nM of protein and 250 μM of either ATP or PPi (respectively for FAD synthesis and FAD pyrophosphorolysis) in 50 mM Hepes/NaOH, 10 mM MgCl<sub>2</sub>, pH 7.0, 5 mM β-mercaptoethanol.

**Supplementary Table 1.** Kinetic parameters derived from stopped-flow data for the binding of FMN and FAD to WT and D238A hFADS6 in the presence of the second substrate (ATP or PPI, respectively).  $k_{on}$  and  $k_{off}$  the kinetic constants for complex formation and dissociation were obtained by fitting lineal data corresponding to  $k_{obs1}$  dependences on flavin concentration presented in Supplementary Figures 3a and 3c ( $n = 3$ , mean  $\pm$  SD). Dissociation constants determined as  $k_{off}/k_{on}$ . Data obtained at 25 °C at 25 °C in 50 mM Hepes/NaOH, 10 mM MgCl<sub>2</sub>, pH 7.0, 5 mM  $\beta$ -mercaptoethanol.

| <b>FMN-ATP mixtures (FMN binding)</b>              |   |                               |                                      |
|--|---|-------------------------------|--------------------------------------|
| <b>hFADS6</b>                                      | $k_{on}$ ( $\mu\text{M}^{-1}\cdot\text{s}^{-1}$ ) | $k_{off}$ ( $\text{s}^{-1}$ ) | $K_d^{\text{FMN}}$ ( $\mu\text{M}$ ) |
| <b>WT</b>  | $3.4 \pm 0.1$                                     | $0.32 \pm 0.01$               | $0.094 \pm 0.004$                    |
| <b>D238A</b>                                       | $0.55^a$  | $0.09^a$                      | $>0.18^a$                            |
| <b>FAD-NaPP<sub>i</sub> mixtures (FAD binding)</b> |   |                               |                                      |
|  | $k_{on}$ ( $\mu\text{M}^{-1}\cdot\text{s}^{-1}$ ) | $k_{off}$ ( $\text{s}^{-1}$ ) | $K_d^{\text{FAD}}$ ( $\mu\text{M}$ ) |
| <b>WT</b>  | $4.5 \pm 0.6$                                     | $0.81 \pm 0.05$               | $0.18 \pm 0.04$                      |
| <b>D238A</b>                                       | $1.5^a$   | $0.35^a$                      | $>0.3^a$                             |

<sup>a</sup> Error in the determination of parameters for the mutant is high, at least  $\pm 30\%$ , due to small amplitudes in the exponential decays and/or low data reproducibility.





## **Publication III**

**The catalytic cycle of the antioxidant and cancer-associated human NQO1 enzyme: hydride transfer, conformational dynamics and functional cooperativity**

**Ernesto Anoz Carbonell contributions:** Experimental work: steady-state enzymatic activity measurements and pre-steady-state kinetics through stopped-flow spectroscopy. Data analysis. Manuscript writing, review and editing



Article

# The Catalytic Cycle of the Antioxidant and Cancer-Associated Human NQO1 Enzyme: Hydride Transfer, Conformational Dynamics and Functional Cooperativity

Ernesto Anoz-Carbonell <sup>1</sup>, David J. Timson <sup>2</sup> , Angel L. Pey <sup>3,\*</sup> and Milagros Medina <sup>1,\*</sup>

<sup>1</sup> Departamento de Bioquímica y Biología Molecular y Celular, Facultad de Ciencias, Instituto de Biocomputación y Física de Sistemas Complejos (GBsC-CSIC and BIFI-IQFR Joint Units), Universidad de Zaragoza, 50009 Zaragoza, Spain; eanoz@unizar.es

<sup>2</sup> School of Pharmacy and Biomolecular Sciences, The University of Brighton, Brighton BN2 4GJ, UK; D.Timson@brighton.ac.uk

<sup>3</sup> Departamento de Química Física, Unidad de Excelencia de Química Aplicada a Biomedicina y Medioambiente, Facultad de Ciencias, Universidad de Granada, 18071 Granada, Spain

\* Correspondence: angelpey@ugr.es (A.L.P.); mmedina@unizar.es (M.M.)

Received: 3 July 2020; Accepted: 18 August 2020; Published: 20 August 2020



**Abstract:** Human NQO1 [NAD(H):quinone oxidoreductase 1] is a multi-functional and stress-inducible dimeric protein involved in the antioxidant defense, the activation of cancer prodrugs and the stabilization of oncosuppressors. Despite its roles in human diseases, such as cancer and neurological disorders, a detailed characterization of its enzymatic cycle is still lacking. In this work, we provide a comprehensive analysis of the NQO1 catalytic cycle using rapid mixing techniques, including multiwavelength and spectral deconvolution studies, kinetic modeling and temperature-dependent kinetic isotope effects (KIEs). Our results systematically support the existence of two pathways for hydride transfer throughout the NQO1 catalytic cycle, likely reflecting that the two active sites in the dimer catalyze two-electron reduction with different rates, consistent with the cooperative binding of inhibitors such as dicoumarol. This negative cooperativity in NQO1 redox activity represents a sort of half-of-sites activity. Analysis of KIEs and their temperature dependence also show significantly different contributions from quantum tunneling, structural dynamics and reorganizations to catalysis at the two active sites. Our work will improve our understanding of the effects of cancer-associated single amino acid variants and post-translational modifications in this protein of high relevance in cancer progression and treatment.

**Keywords:** antioxidant enzyme; antioxidant response; cancer; oxidoreductase; enzyme kinetic analysis; functional cooperativity; hydride transfer; kinetic isotope effects; quantum tunneling; conformational dynamics

## 1. Introduction

NAD(P)H quinone oxidoreductase 1 (NQO1; DT-diaphorase; EC 1.6.5.2) is a multi-functional and stress-inducible flavoprotein whose activity is associated with different pathologies, particularly with cancer [1,2]. NQO1 has a wide range of substrates and enzymatic functions associated with antioxidant defense and cancer development, including the NAD(P)H-dependent two-electron reduction of quinones to form hydroquinones, thus avoiding the formation of highly reactive and cytotoxic semiquinones [3,4], the maintenance of vitamin K<sub>3</sub> and ubiquinone in their reduced state [5–8] and scavenging of superoxide anions [9]. NQO1 activity is also required for the activation of cancer

prodrugs [10–14]. In addition, NQO1 is capable of interacting with over forty different proteins, such as p53, p73 $\alpha$  and HIF-1 $\alpha$ , and the general effect of these interactions is the protection of protein partners against proteasomal degradation [4,15,16].

NQO1 is upregulated transcriptionally in response to stress [17–20]. The activation of the antioxidant response induces the expression of NQO1, as well as that of enzymes involved in NADPH generation [21–25]. The expression of NQO1 can also be induced by some antioxidants (such as resveratrol) through the antioxidant response pathway [26,27].

Changes in the activity of NQO1 are associated to different pathologies, including cancer and cardiovascular and neurodegenerative diseases [2]. Intriguingly, the role of NQO1 in cancer development seems to be twofold. NQO1 is overexpressed in certain types of cancer and its inhibition by dicoumarol (Dic), and analogs thereof, arrests the growth of certain cancer cell lines [28,29]. Its overexpression may also contribute to tumor growth through the stabilization of HIF-1 $\alpha$ , a master regulator of angiogenesis, thus critical in cancer development [16]. Conversely, cancer cell lines that express inactivating and destabilizing NQO1 polymorphic variants (such as p.P187S and p.R139W) are resistant to certain cancer treatments and are associated with increased cancer risk and poor prognosis [2,30–32].

Structurally, NQO1 forms functional homodimers in which each monomer has a two-domain structure, with a large N-terminal domain (approximately residues 1–225) that contains most of the active site and a tightly bound FAD molecule and C-terminal domain (approximately residues 225–274) that complete the active site (i.e., the NAD(P)H and substrate binding sites) and the monomer:monomer interface [33–37]. The enzymatic cycle of NQO1 follows a ping-pong bi-bi mechanism that can be grossly divided into two half-reactions, each of them containing ligand binding/release events, as well as hydride transfer (HT) reactions [2,38,39] (Figure 1A). First, in the reductive half-reaction, NAD(P)H binds to holo-NQO1 (the bound flavin is not released during the enzymatic cycle) and reduces FAD to FADH<sub>2</sub>, thus releasing NAD(P)<sup>+</sup>. This step is fast, with a second-order rate constant in the order of 10<sup>5</sup>–10<sup>6</sup> M<sup>-1</sup>·s<sup>-1</sup>. It has been proposed that the reduction of FAD by NAD(P)H occurs by direct HT between them, likely leading to the formation of FADH<sub>2</sub> in the enolate form. This tautomer would have a negatively charged O2F that may become stabilized upon sequential proton transfer with the side chains of Y156 and H162. In the oxidative half-reaction, the substrate binds and is reduced by FADH<sub>2</sub> (this half-reaction is much faster, with a second-order rate constant of 10<sup>9</sup> M<sup>-1</sup>·s<sup>-1</sup>), thus releasing the reduced substrate and regenerating the holo-enzyme [2,34]. In this second half-reaction, the charge/proton transfer between FADH<sub>2</sub>, Y156 and H162 would likely occur in the reverse sense [40,41].

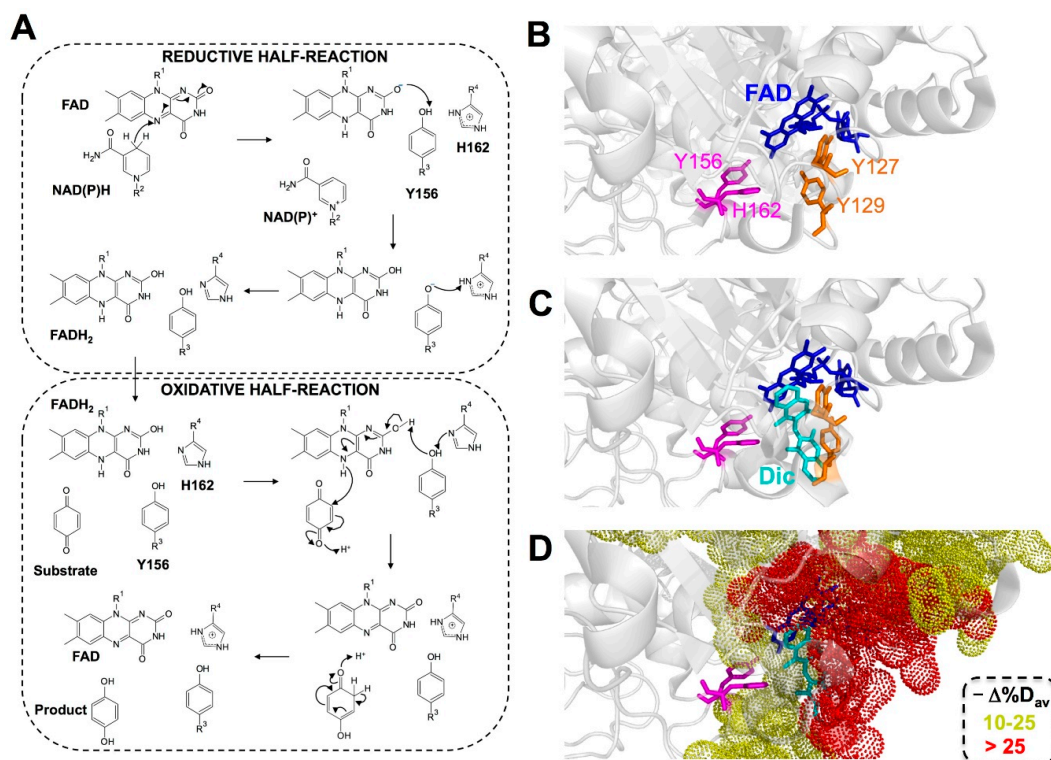


**Figure 1.** NQO1 catalytic mechanism and protein dynamics. **(A)** Plausible mechanism for the reductive and oxidative half-reactions (for details see the main text). FADH<sub>2</sub> undergoes keto/enol tautomerism. Here, we show the initial and final structures of FAD in the enol tautomer. Some reaction steps require the enol or enolate tautomer. **(B)** Changes in NQO1 structural dynamics upon Dic binding from hydrogen-deuterium exchange (HDX) analysis [42]. The upper panel shows the position of the FAD, Y156 and H162 (involved in the stabilization of FADH<sub>2</sub>) and Y127 and Y129 (critical for Dic and NAD<sup>+</sup> binding). **(C and D)** Dic binding. **(C)** leads to decreased dynamics in residues covering the whole active site, particularly regarding the inhibitor and the FAD binding sites that may contribute to optimizing HT from NAD(P)H and FADH<sub>2</sub>. **(D)**  $\Delta\%D_{av}$  is a simple stability metric that refers to the averaged maximal difference in HDX kinetics between two given ligation states according to [42], and a negative value for this parameter reflects an increase in local stability for a given protein segment upon ligand binding (i.e., either HDX is slower and/or its amplitude is reduced upon ligand binding, thus reflecting a locally stabilizing effect upon ligand binding). Note that residue numbering follows the full-length sequence of the protein.

Importantly, most of our knowledge on the NQO1 kinetic mechanism has come from analysis of either ligand binding/release events from crystallographic analyses, or from single-wavelength kinetic analyses focused on the changes in FAD spectral properties associated with chemical steps (i.e., HT) [34,38,40,43,44]. Several studies have supported that changes in molecular dynamics throughout the catalytic cycle should also be considered [42,45]. The use in these studies of Dic, a potent competitive inhibitor of NAD(P)H [6,39], has supported the proposal that NAD(P)H binding may cause minimal structural changes [46,47] but affects the stability and structural dynamics of the active site, which contributes to the enhancement of catalysis by reducing the reaction free energy barrier(s) and/or promoting quantum tunneling effects [42,45] (Figure 1B). Interestingly, Dic binding might also allow for the communication of local stability effects between active sites during the catalytic cycle [42,48,49]. The existence of functional and structural non-equivalence between the active sites may also explain the apparent negative cooperativity found for Dic binding (mainly reflected by inhibition studies with the holo-protein) [48,49]. A critical role of protein dynamics in the activity and stability of NQO1 is further supported by the study of the inactivating and destabilizing effects of the cancer-associated p.P187S polymorphism [30,31,50–53]. Importantly, long-range communication

of stability effects due to inactivating mutations and polymorphisms, as well as due to the presence of suppressor mutations and ligand binding (Figure 1B), seems to be a general phenomenon in NQO1 [30,33,41,42,50,54–57].

A deep understanding of the kinetic mechanism of this important metabolic and antioxidant enzyme would allow us to rationalize the effects of missense variants and enable the improved design of inhibitors and drugs which are activated by NQO1 as chemotherapeutics [58–63]. However, to the best of our knowledge, no study has investigated the NQO1 kinetic mechanism from an integrated perspective of the changes occurring in the NQO1 structure and dynamics that facilitate HT reactions. We provide here such an integrated perspective on the NQO1 catalytic mechanism by kinetically evaluating the different events occurring in the reductive and oxidative half-reactions by using stopped-flow spectrophotometry with photodiode detection combined with temperature-dependent kinetic isotopic effects (KIEs) [64]. Overall, our results show that HT from NAD(P)H to FAD occurs through two different pathways with widely different kinetics, likely reflecting that the two active sites in the NQO1 dimer are not equivalent. This non-equivalence may explain the binding cooperativity observed for Dic. In addition, these two pathways largely differ in the contributions from structural and vibrational dynamics along the reaction coordinate(s). Thus, this work constitutes an important advance in deciphering the dynamics at the active site of this structurally complex enzyme during catalysis. Our work will help in the rational design of more potent and specific mechanism-based NQO1 inhibitors, as well as to understand the functional consequences of naturally occurring NQO1 missense variants and post-translational modifications and the structural and energetic basis of functional cooperativity in this enzyme.

## 2. Materials and Methods

### 2.1. Materials

All the chemicals were purchased with high purity (typically > 99%) from Sigma-Aldrich and Merck, and these were used without further purification, unless otherwise indicated. The 5-deazariboflavin was a gift from the G. Tollin Lab (University of Arizona). The stereospecifically labeled nicotinamide nucleotide [4R-<sup>2</sup>H<sub>1</sub>]-NADH (with the deuterium in the A face of the nicotinamide ring, NADD) was synthesized enzymatically using [<sup>2</sup>H<sub>8</sub>]-propanol/alcohol dehydrogenase following previously described protocols [65]. Milli-Q water was obtained from a Milli-Q<sup>®</sup> Reference water purification system (Millipore, Madrid, Spain) and used for the preparation of all buffers and media.

### 2.2. Protein Expression and Purification

The wild-type (WT) NQO1 cDNA was cloned into a pET-46 Ek/LIC vector [31]. This plasmid was used to transform BL21(DE3) cells (Agilent) for protein expression. Transformed cells were grown in 240 mL of autoclaved Luria–Bertani (LB) medium containing 0.1 mg·mL<sup>-1</sup> ampicillin (Canvax Biotech) (LBA) overnight at 37 °C. These cultures were diluted into 4.8 L of LBA and grown at 37 °C for 3 h under shaking (at 150–160 rpm) to reach an optical density of about 0.6. Then, cultures were cooled down to 25 °C and induced with 0.5 mM isopropyl β-D-1-thiogalactopyranoside (IPTG, Canvax Biotech). After 4 h, cells were harvested by centrifugation (8000 g, 15 min, 4 °C) and cells were frozen and maintained at –80 °C overnight. Cells were resuspended in binding buffer (BB; 20 mM NaH<sub>2</sub>PO<sub>4</sub>, 300 mM NaCl, 50 mM imidazole; pH was adjusted to 7.4 using concentrated HCl) plus 1 mM phenylmethylsulfonyl fluoride (PMSF), sonicated in an ice bath and centrifuged at 24,000 g for 20 min at 4 °C. Supernatants (soluble extracts) were loaded into immobilized-metal affinity chromatography (IMAC) columns (His Gravitrap, Ni Sepharose 6 fast flow resin, 1 mL bed volume, GE Healthcare), washed with 25 volumes of BB and eluted with 2.5 mL of BB containing 500 mM imidazole (pH was adjusted to 7.4 by addition of concentrated HCl). These eluates were buffer exchanged using PD-10 columns (GE Healthcare) to the storage buffer (50 mM HEPES-KOH pH 7.4), frozen in liquid nitrogen and stored at –80 °C. Typically, this procedure yielded about 20 mg of purified NQO1 protein.

About 20 mg of protein from IMAC were thawed, centrifuged for 10 min at 24,000  $g$  and 4 °C, diluted in storage buffer to a final volume of 5.5 mL and 5 mL of this protein solution were injected into a HiLoad® 16/600 Superdex® 200 pg (GE Healthcare). Size-exclusion chromatography (SEC) was carried out using 20 mM HEPES-NaOH, 200 mM NaCl pH 7.4 as a mobile phase at 20 °C and using a 1.5 mL·min<sup>-1</sup> flow rate. Void ( $V_0$ ) and total ( $V_T$ ) volumes were determined using blue dextran and acetone, respectively (Figure 2A). Fractions eluting between 75 and 90 mL were pooled, concentrated using Amicon® Ultra-15 Centrifugal Filter Units-30,000 NMWL (Millipore), mixed with a final concentration of 1 mM FAD and exchanged to HEPES-KOH 50 mM pH 7.4 using PD-10 columns. The UV-visible absorption spectra of the purified protein were collected at a 20  $\mu$ M protein concentration using 1-cm pathlength quartz cuvettes on a Cary 50 or 100 spectrophotometer (Agilent). Protein concentration and FAD content were determined from the absorbance at 280 nm and 450 nm, respectively [50]. Briefly, the experimental spectrum was converted into molar extinction units ( $M^{-1}\cdot cm^{-1}$ ) using the absorbance at 280 nm considering that the extinction coefficient of NQO1 monomer with bound FAD is the sum of its intrinsic protein extinction coefficient (47,900  $M^{-1}\cdot cm^{-1}$ , based on its amino acid sequence) plus the contribution from bound FAD (22,000  $M^{-1}\cdot cm^{-1}$  ·fraction of bound FAD per monomer) [31]. The former contribution can be assessed experimentally for each spectrum from the absorbance at 450 nm ( $\epsilon_{450} = 11,300 M^{-1}\cdot cm^{-1}$ ) [66]. As we have previously indicated [50], this approach considers that the spectral properties of FAD are similar when bound to NQO1 to those of the free ligand. NQO1 samples obtained from different purifications contained 0.97–0.99 moles of FAD per mole of NQO1 monomer as assessed by this procedure (Figure 2B).

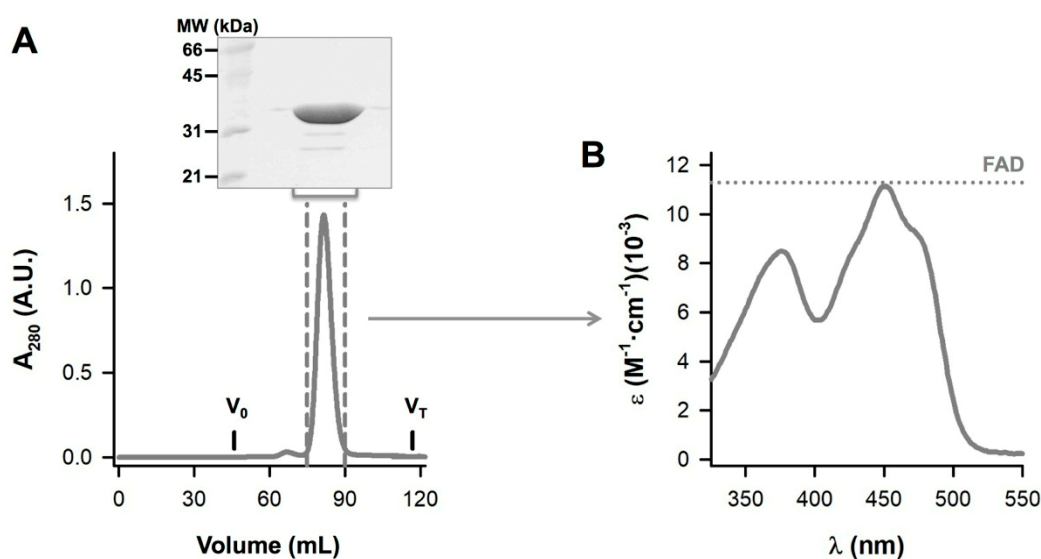


**Figure 2.** Purification of NQO1. (A) Size-exclusion chromatography (SEC) chromatogram of NQO1 protein. About 20 mg of protein from IMAC (immobilized-metal affinity chromatography) were injected into a HiLoad® 16/600 Superdex® 200 pg (GE Healthcare) running on 20 mM HEPES-NaOH, 200 mM NaCl pH 7.4 at 20 °C. Void ( $V_0$ ) and total ( $V_T$ ) volumes are indicated. Fractions eluted between 75 and 90 mL were pooled and concentrated. The purity was checked by SDS-PAGE in 12% acrylamide gels (inset). (B) Concentrated protein was exchanged to HEPES-KOH 50 mM pH 7.4 and the UV-visible absorption spectrum was collected at a 20  $\mu$ M protein concentration. The extinction coefficient of free FAD is indicated for sake of comparison.

### 2.3. NQO1 Redox Properties Evaluated by Absorption Spectroscopy

Photoreduction of NQO1 was achieved by irradiating the oxidized protein (NQO1<sub>ox</sub>) under anaerobic conditions in the presence of 2 mM EDTA and 8  $\mu$ M 5-deazariboflavin [67]. Experiments were performed in HEPES-KOH, pH 7.4 at 25 °C in home-made spectrophotometer cuvettes. Glucose (at a 310 mM final concentration) and glucose oxidase (at a 10 units·mL<sup>-1</sup> final concentration) were

added to all the solutions to remove trace amounts of oxygen. The stepwise reduction of the protein was achieved by light irradiation from a 250 W slide projector for different periods of time, for which the UV–visible spectrum was then recorded in a Cary 100 spectrophotometer (Agilent). Once fully reduced (no variation in the UV–visible spectra despite further irradiation), the protein was re-oxidized by breaking the anaerobic conditions and exposure to atmospheric air, and absorption spectra were recorded until complete re-oxidation.

The ability of  $\text{NAD}^+$  to re-oxidize the hydroquinone form of the protein ( $\text{NQO1}_{\text{hq}}$ ) was evaluated by using anaerobic solutions of photoreduced NQO1 (7.5  $\mu\text{M}$ ), produced by following the above described procedure in specially designed cuvettes.  $\text{NQO1}_{\text{hq}}$  was then mixed with an  $\text{NAD}^+$  solution placed in the same cuvette lateral arm, providing a final 1:1 protein:coenzyme ratio and the kinetics of the re-oxidation of the enzyme were followed in the full protein spectral range using an Agilent 8453 photodiodearray spectrophotometer (Agilent).

#### 2.4. Stopped-Flow Pre-Steady-State Kinetic Measurements

Fast HT reactions from  $\text{NAD(P)H/D}$  to  $\text{NQO1}_{\text{ox}}$ , as well as from  $\text{NQO1}_{\text{hq}}$  (generated by  $\text{NQO1}_{\text{ox}}$  mixed with NADH at stoichiometric ratio) to 2,6-dichlorophenol indophenol (DCPIP), were measured using a stopped-flow spectrophotometer from Applied Photophysics (SX.18MV, Applied Photophysics Ltd., Leatherhead, UK) interfaced with a photodiode array detector and under anaerobic conditions, following previously established protocols [68,69]. All samples were made anaerobic (in specially designed tonometers by successive evacuation and  $\text{O}_2$ -free argon flushing) before introduction into the stopped-flow syringes.  $\text{NQO1}_{\text{ox}}$  (7.5  $\mu\text{M}$ ) was mixed with NADH/D at concentrations ranging from 1:1 to 1:14  $\text{NQO1}_{\text{ox}}:\text{NADH/D}$  ratios, while when using NADPH, the single 1:1 ratio was used. To evaluate re-oxidation,  $\text{NQO1}_{\text{hq}}$  (7.5  $\mu\text{M}$ ) was mixed with stoichiometric amounts of DCPIP. Additionally, Dic was used as an inhibitor of both the reductive and oxidative half-reactions, adding it at 1:1 and 1:4  $\text{NQO1}:\text{Dic}$  ratios. Reactions were studied in 20 mM HEPES-KOH, pH 7.4 with glucose/glucose oxidase (310 mM/10 units· $\text{mL}^{-1}$ ), at 25 °C and/or 6 °C. Multiple wavelength absorption data in the flavin absorption region (400–900 nm) were collected and processed using the ProData-SX software (Applied Photophysics Ltd.). Time-dependent spectral deconvolution was performed by global analysis and numerical integration methods using Pro-Kineticist (Applied Photophysics Ltd.). Collected data were fitted to either single- or multi-step ( $\text{A} \rightarrow \text{B} \rightarrow \text{n} \dots \rightarrow \text{Z}$ ) models allowing for estimation of the corresponding observed conversion rate constants ( $k_{\text{obsA} \rightarrow \text{B}}$ ,  $k_{\text{obsB} \rightarrow \text{C}}$ , ...) at each  $\text{NAD(P)H/D}$  concentration, as well of the spectra of intermediate and final species [70]. A, B, n and Z are *spectral species*, reflecting a distribution of enzyme species at any time throughout the course of the enzyme: coenzyme interaction, including HT (or deuteride transfer, DT) or reorganization processes, and do not necessarily represent a single distinct enzyme intermediate. Since none of them represents individual species, their spectra cannot be included as fixed in the global fitting.

The  $k_{\text{obs}}$  values showing hyperbolic dependence profiles on the  $\text{NAD(P)H/D}$  concentration were fitted to a function (1) that describes binding at a single site followed by reorganization or HT/DT processes, allowing for the determination of the corresponding equilibrium constant ( $K_d$ ), as well as the rate constant for the subsequent process ( $k$ ) [69,70]:

$$k_{\text{obs}} = k_{\text{A} \rightarrow \text{B}} = k_{\text{B} \rightarrow \text{C}} = \frac{k \cdot [\text{NAD(P)H}]}{[\text{NAD(P)H}] + K_d} \quad (1)$$

Depending on the process,  $k$  might account for the rate constant of the rate-limiting step for complex formation,  $k_{\text{on}}$ , or for the HT/DT rate constant,  $k_{\text{HT}}$  or  $k_{\text{DT}}$ .  $K_d$  might respectively account for the complex dissociation constant,  $K_d^{\text{NADH/D}}$ , or for a *reorganization* constant related to the transition between reaction intermediate species,  $K_d^{\text{reg}}$ .



### 2.5. Kinetic Isotopic Effects (KIEs)

For the estimation of primary kinetic isotopic effects in the HT process [68], HT or DT observed rate constants ( $^{HT}k_{obs}$  or  $^{DT}k_{obs}$ ) from NADH/D to NQO1<sub>ox</sub> were evaluated at different temperatures in the 5.3–20 °C range, in samples containing equimolecular mixtures (7.5 μM of each component) using NADH and [4R-<sup>2</sup>H]-NADD, unless otherwise indicated.

Kinetic isotope effects (KIEs) on rate constants were calculated as follows:

$$\text{KIE} = \frac{k_{HT}}{k_{DT}} = \frac{^{HT}k_{obs}}{^{DT}k_{obs}} \quad (2)$$

For each isotope, the fitting of the observed rates to the Arrhenius equation was calculated:

$$k = A * e^{-\frac{E_a}{RT}} \quad (3)$$

providing the values corresponding to Arrhenius pre-exponential (frequency) factors ( $A_H$  and  $A_D$ ) and activation energies ( $E_{aH}$  and  $E_{aD}$ ). The temperature dependence of the KIE was analyzed by combining Equations (2) and (3). Additionally, the activation enthalpies ( $\Delta H^\ddagger$ ) and entropies ( $\Delta S^\ddagger$ ) were calculated using the Eyring equation:

$$\ln\left(\frac{k_{obs}}{T}\right) = \ln\left(\frac{k_B}{h}\right) + (\Delta S^\ddagger/R) - \left(\frac{\Delta H^\ddagger}{R \cdot T}\right) \quad (4)$$

where  $k_B$  is the Boltzmann constant ( $1.3806 \cdot 10^{-23}$  J·K<sup>-1</sup>) and  $h$  is the Planck constant ( $6.626 \cdot 10^{-34}$  J·s).

## 3. Results and Discussion

### 3.1. Human NQO1 Does Not Stabilize Intermediate Semiquinone States upon Photoreduction

NQO1<sub>ox</sub> exhibits the characteristic UV–visible spectra of flavoproteins, with maxima at 278, 375 and 449 nm, and shoulders at 422 and 475 nm (Figure 3). Upon photoreduction, the FAD cofactor exists in the hydroquinone state, NQO1<sub>hq</sub> (i.e., a two-electron reduction), as denoted by the decrease in absorbance at 370 and 450 nm. Full reduction was achieved after 15 min of irradiation, with equivalent spectral features to those observed upon reduction with an excess of sodium dithionite (Figure 3). The photoreduction occurs without the appearance of any red-shifted absorbance band, indicative of the stabilization of the FAD blue-neutral semiquinone, but subtle changes in absorbance at 375, 400 and 480 nm might point to traces of the red-anionic semiquinone radical [71], as observed for other oxidases, including rat liver NQO1 [44]. Such a lack of semiquinone intermediates indicates that reduction of the semiquinone to the hydroquinone state is thermodynamically more favorable and kinetically faster than the reduction of the oxidized to the semiquinone species [72]. This observation agrees with the absence of detectable semiquinone paramagnetic signals when evaluating the redox cycle of the enzyme and with mammalian quinone oxidoreductases, which are a notable exception in that they only function by a compulsory two-electron transfer [73]. Such observations denote a less negative midpoint reduction potential of the FADH/FADH<sub>2</sub> couple with respect to the FAD/FADH· one. Finally, upon mixing the photoreduced protein with atmospheric air, the initial absorbance spectrum of the oxidized protein was restored (not shown).

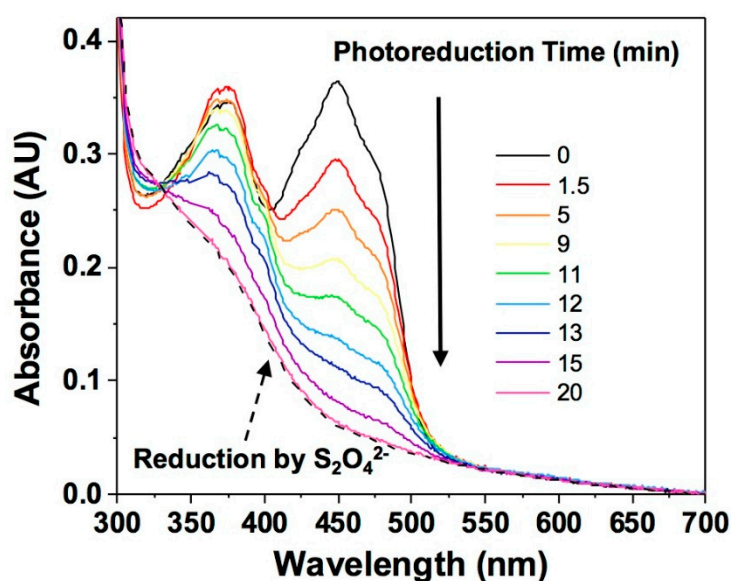


**Figure 3.** Photoreduction of NQO1. Colored spectra correspond to different illumination time points throughout the photoreduction process. The dashed black line indicates the spectra corresponding to a sample chemically reduced by dithionite ( $S_2O_4^{2-}$ ).

### 3.2. The Catalytic Cycle of NQO1

To evaluate the kinetics of the reductive and oxidative half-reactions in the catalytic cycle of NQO1 (Figure 1A), we studied the spectral changes occurring in the band-I (400–500 nm range) of the flavin by using fast kinetics stopped-flow spectrophotometry.

#### 3.2.1. Non-Equivalent Active Sites in the NQO1 Dimer throughout the Reductive Half-Reaction

We first evaluated the kinetics of the reductive half-reaction by mixing NQO1<sub>ox</sub> with NADH at 6 °C under strict anaerobic conditions. A decrease in the absorption at the FAD band-I was quickly observed without detection of semiquinone traces (Figure 4A), in agreement with FAD reduction to the hydroquinone form. The final spectrum after the overall HT compares well with the fully photoreduced NQO1 and dithionite reduced spectra, suggesting full reduction of the cofactor was achieved (Figure 3 vs. Figure 4A). This observation envisages a less negative reduction potential of the NQO1 FAD/FADH<sub>2</sub> pair regarding the NAD<sup>+</sup>/NADH redox pair ( $E'_0 = -320$  mV) [74] under our experimental conditions. This agrees with the value of  $-159$  mV previously reported for the rat enzyme [44].

To provide further insight into the mechanism of the reductive half-reaction, we submitted these kinetic data to global spectral deconvolution (Figure 4B). Several mechanisms were evaluated, but only a minimal three-step non-reversible mechanism (A→B→C→D) (Figure 4B–D) reproduced the experimental data well. The lack of major spectral changes in the instrumental dead time suggested that species A corresponds with the initial mixing of NQO1<sub>ox</sub> and NADH. The conversion of species A into B was very fast (initial ~10–40 ms of reaction) and contributed to nearly 75% of the decay of the band-I absorption (Figure 4B). Therefore, this step comprises the HT process from NADH to FAD and its reduction. The observed rate constants for this process,  $k_{\text{obsA} \rightarrow \text{B}}$ , showed hyperbolic dependence on NADH concentration (Figure 4E), allowing for the determination of a NADH dissociation constant ( $K_d^{\text{NADH}}$ ), as well as of a limiting HT rate constant ( $k_{\text{HT1}}$ ), without considering the occurrence of any reverse HT reaction. The limiting value for  $k_{\text{HT1}}$  of  $284 \pm 17$  s<sup>-1</sup> (at 6 °C) indicates a very fast HT from NADH to NQO1<sub>ox</sub>, which compares well with the steady-state catalytic constant ( $k_{\text{cat}}$ ) of 180–200 s<sup>-1</sup> (at 30–37 °C) [31,33,48]. This agreement supports that the HT process is the rate-limiting step within the reductive half-reaction. Alternative scenarios, in which substrate binding and/or product release could be rate-limiting steps are discussed in Appendix A. Kinetic analysis on the A→B process also

allows us to determine a  $K_d^{\text{NADH}}$  of  $16 \pm 3 \mu\text{M}$ , a value 10-times lower than the reported  $K_M^{\text{NADH}}$  (160–240  $\mu\text{M}$ , using DCPIP as substrate) [31,33,48]. This observation indicates a tighter interaction in the reactive  $\text{NQO1}_{\text{ox}}:\text{NADH}$  complex than in the subsequent complexes formed throughout the reaction, and justifies the lack of spectroscopic detection of charge–transfer complexes (CTCs).

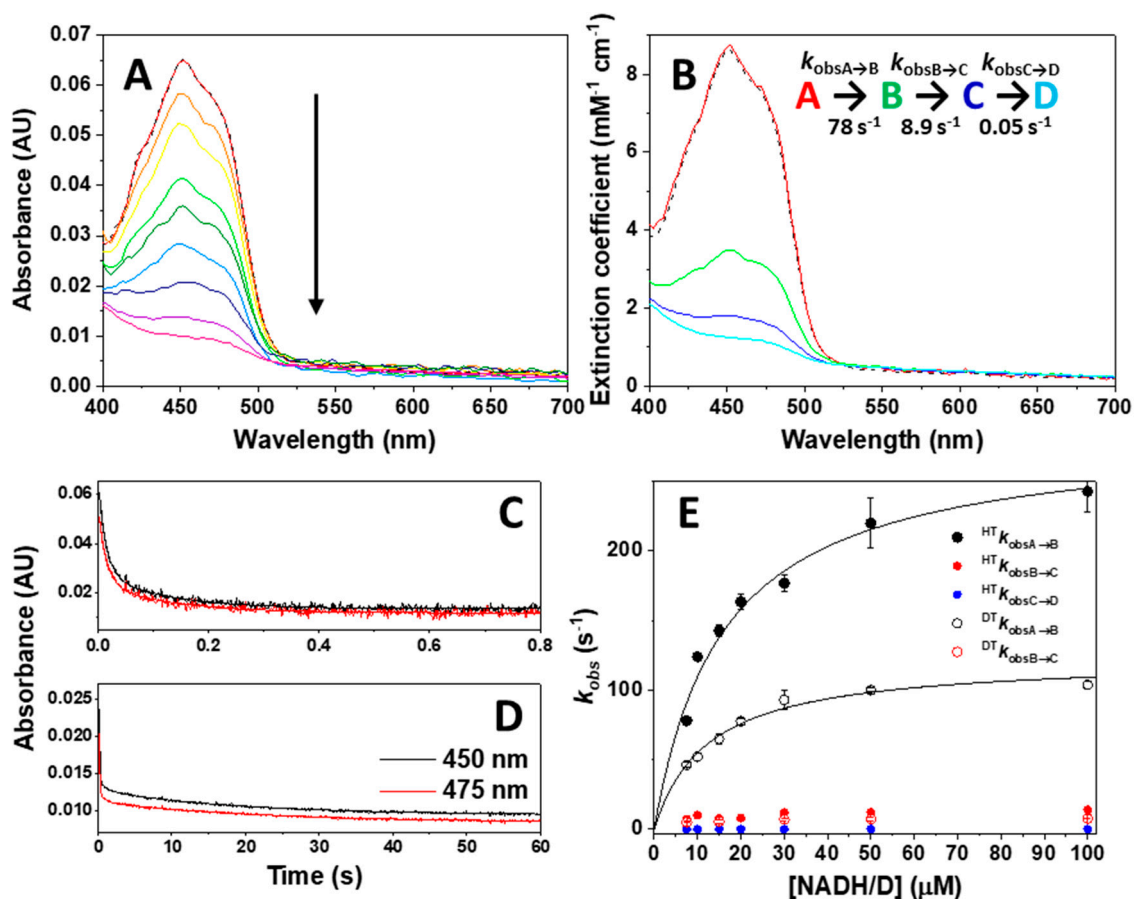


**Figure 4.** Kinetics of the NQO1 flavin reduction by NADH/D. (A) Spectral evolution on a 0–60 s timescale after mixing  $\text{NQO1}_{\text{ox}}$  (7.5  $\mu\text{M}$ ) with NADH (7.5  $\mu\text{M}$ ) in 20 mM HEPES-KOH, pH 7.4, at 6 °C. Different colored lines correspond to the spectra at different reaction times. (B) Spectral deconvolution of intermediate species observed during the reaction when fitting to a four-state model and the corresponding calculated observed rate constants. In panels A and B, the dashed line represents the spectrum of  $\text{NQO1}_{\text{ox}}$  before mixing. (C,D) Decay of kinetic traces at 450 nm and 475 nm and fittings to the model. (E) Dependence of  $k_{\text{obs}}$  values on the NADH/D concentration. The trace for the fitting to Equation (1) for  $k_{\text{obsA} \rightarrow \text{B}}$  values is shown as a black line. Error bars correspond to the SD for at least three different replicates. Spectral evolution (A) and deconvolution (B) are from a single measurement and representative from  $n > 3$ .

This initially observed HT step (A to B) was followed by another process (B to C) that led to the nearly full reduction of the flavin bound to NQO1. In fact, this process essentially accounted for the remaining 25% of the total absorption decrease at the flavin band-I, and, therefore, must also be related to an HT process. The  $k_{\text{obsB} \rightarrow \text{C}}$  values were considerably slower than those for  $k_{\text{obsA} \rightarrow \text{B}}$ , and roughly dependent on the coenzyme concentration (Figure 4E), providing a limiting rate for this second HT event,  $k_{\text{HT2}}$ , in the 10–15  $\text{s}^{-1}$  range. Our kinetic analysis showed a final step to achieve full FAD reduction (C to D), but this process accounted for a very small and slow spectroscopic change (with rate constants 5000 times slower than for the A→B process), suggesting that it might not be of catalytic relevance.

NQO1 can also use NADPH as electron donor, which is a better reductant than NADH (with six-fold higher catalytic efficiency and a four-fold enhancement in  $k_{\text{cat}}$ , [31,34,75]). Consequently, NQO1<sub>ox</sub> mixed with NADPH at a 1:1 ratio shows a faster FAD reduction than when using NADH, part of which occurs in the instrumental dead time (Figure 5A). The process was best described as a two-step process (A→B→C) (Figure 5B), with at least 80% of flavin reduction occurring in the first step. The  $k_{\text{obsA} \rightarrow \text{B}}$  and  $k_{\text{obsB} \rightarrow \text{C}}$  values at stoichiometric concentrations were  $261 \pm 13$  and  $7.8 \pm 0.3 \text{ s}^{-1}$ , respectively, with  $k_{\text{obsA} \rightarrow \text{B}}$  being 3.7 times faster than when using the same NADH ratio, while  $k_{\text{obsB} \rightarrow \text{C}}$  values resulted in the same range. Hence, the overall HT process is faster when NADPH is the hydride donor, consequently preventing studies using higher coenzyme concentrations.

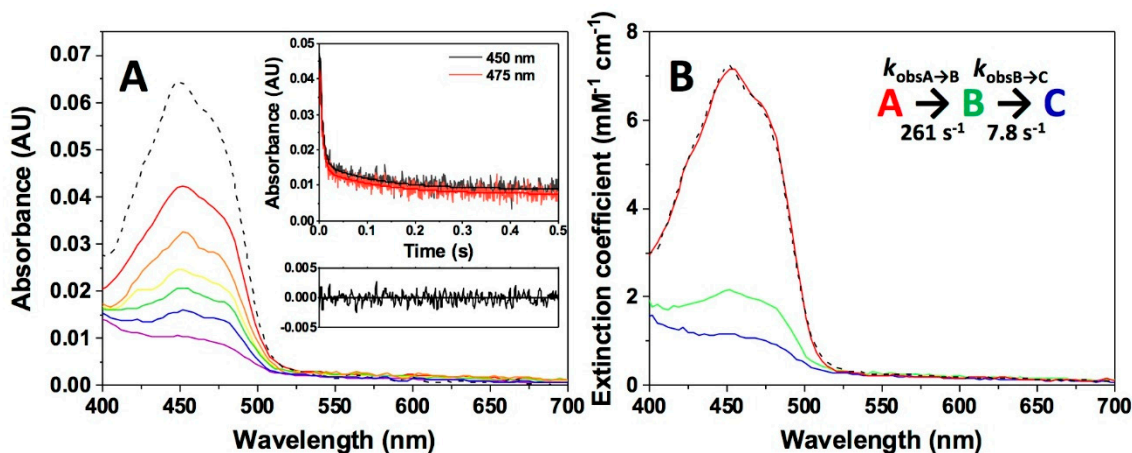


**Figure 5.** Kinetics of the NQO1 flavin reduction by NADPH. (A) Spectral evolution on a 0–0.5 s timescale after the mixing NQO1<sub>ox</sub> (7.5  $\mu\text{M}$ ) with NADH (7.5  $\mu\text{M}$ ) in 20 mM HEPES-KOH, pH 7.4, at 6  $^{\circ}\text{C}$ . Different colored lines correspond to the spectra at different reaction times. The inset shows the decay of kinetic traces at 450 nm and 475 nm, the fittings to the model, and the residuals at 450 nm to show the quality of the fitting. (B) Spectral deconvolution into the different species observed along the reaction from fittings to a two-step model and calculated rate constants. Spectral evolution (A) and deconvolution (B) are from a single measurement and representative from  $n > 3$ .

Altogether, and considering that NQO1<sub>ox</sub> is a dimer, these data allowed us to suggest that the reduction of each protomer within the dimer might occur at very different rates. We must note that, according to the change in the flavin band-I magnitudes for the A→B and B→C steps, a part of the reduction of the *slower protomer* might occur within the first A→B step. To test this hypothesis, we used Dic to slow down the reductive half-reaction of NQO1 by NADH [6,39]. Dic competes for the NAD(P)H binding site, blocking access to the nicotinamide part of the coenzyme and, as a consequence, preventing the HT from the nicotinamide to the flavin cofactor [46]. As shown in Figure 6, the presence of Dic causes a considerable slowdown of the overall HT processes by NADH. Moreover, the spectral evolution was best described by a two-step mechanism (A→B→C), with each of the two steps accounting for half of the spectral change corresponding to FAD reduction. The full observation of both individual processes was likely possible because of the considerable reduction in  $k_{\text{obsA} \rightarrow \text{B}}$  and  $k_{\text{obsB} \rightarrow \text{C}}$  caused by Dic, respectively  $0.034 \pm 0.003$  and  $0.0065 \pm 0.0005 \text{ s}^{-1}$  at stoichiometric concentrations, which implies a  $\sim 2000$ -fold decrease. Higher Dic ratios (1:1:4 protein/NADH/dicoumarol) produced further slowdowns of both steps (Table 1), while increasing NADH concentrations (50  $\mu\text{M}$ , 1:6.6:4 of protein/NADH/Dic) only slightly increased reduction rate constants, hardly preventing Dic inhibition. Such observations are easily explained by the higher affinity of three orders of magnitude of Dic vs. NADH ( $K_{\text{d}}^{\text{Dic}}$  typically in the 1–20 nM range; [33,49,55] and Section 3.2.1). Therefore, these inhibition studies with Dic strongly supported that the reduction of the FAD cofactor at the two active sites of the NQO1 dimer occurs at different rates.

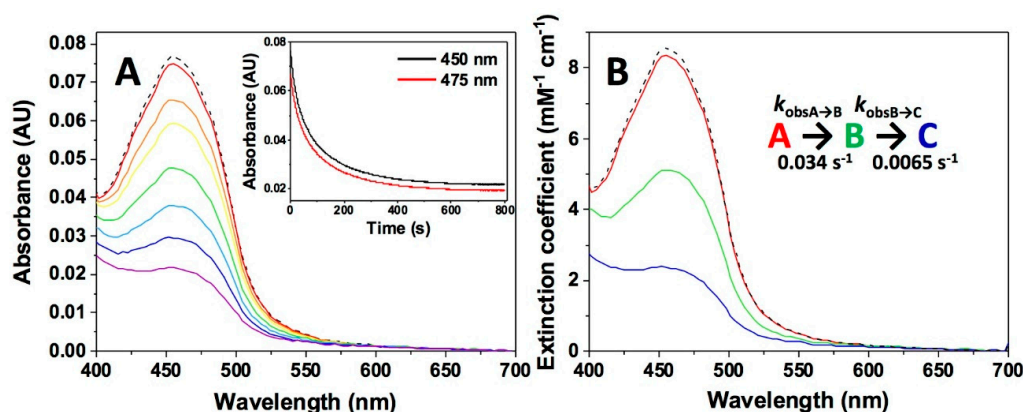


**Figure 6.** Kinetics of NQO1 flavin reduction by NADH in the presence of the Dic inhibitor. (A) Spectral evolution after the mixing in the stopped-flow equipment of NQO1<sub>ox</sub> (7.5  $\mu$ M) with NADH (7.5  $\mu$ M) in the presence of Dic (7.5  $\mu$ M) in 20 mM HEPES-KOH, pH 7.4, at 6  $^{\circ}$ C on a 0–800 s timescale. Different colored lines correspond to the spectra at different reaction times. The inset shows the decay of kinetic traces at 450 nm and 475 nm, as well as the fitting to a three-state model. (B) Spectral deconvolution of intermediate species observed during the reaction upon fitting to a two-step model and calculated observed rate constants. In panels A and B, the dashed line represents the protein spectrum before mixing. Spectral evolution (A) and deconvolution (B) are from a single measurement and representative from  $n > 3$ .

So far, our analyses for the reductive half-reaction of NQO1<sub>ox</sub> by NAD(P)H have pointed to the reverse HT reactions being practically negligible. To confirm this, we mixed photoreduced NQO1<sub>hq</sub> with stoichiometric concentrations of NAD<sup>+</sup>, in specially designed spectrophotometer cuvettes and under anaerobic conditions, and followed spectral changes over the time. Once the reaction components were mixed, the FAD cofactor became very slowly re-oxidized without the stabilization of any semiquinone or CTC intermediates (Figure 7). The overall protein re-oxidation resulted in a monophasic process with a rate constant of  $0.0025 \pm 0.0005 \text{ s}^{-1}$ . This parameter would relate to the apparent HT rate constant for the backward reaction ( ${}^{\text{app}}k_{\text{HT-1}}$ ), being around 28,000 times slower than the corresponding forward process. Therefore, the equilibrium of the reductive half-reaction is fully displaced towards the production of NQO1<sub>hq</sub>, in agreement with the main physiological role of the enzyme in the detoxification of quinones by their reduction.

**Table 1.** Summary of observed rate constants ( $k_{\text{obs}}$ ) for the reductive and oxidative half-reactions involving NQO1. Measurements were carried out in 20 mM HEPES-KOH, pH 7.4 at 6  $^{\circ}$ C and the ratios are indicated between brackets for each reactant. Evolution of the reaction was followed in the 400–1000 nm wavelength range using stopped-flow equipment with a photodiode array detector ( $n > 3$ , mean  $\pm$  SD).

| Sample in Tonometer 1 | Sample in Tonometer 2 | $k_{\text{obsA} \rightarrow \text{B}}$<br>( $\text{s}^{-1}$ ) | $k_{\text{obsB} \rightarrow \text{C}}$<br>( $\text{s}^{-1}$ ) |
|-----------------------|-----------------------|---|---|
| NQO1 (1)              | NADH (1)              | $78 \pm 1$  | $8.9 \pm 0.9$   |
| NQO1 (1)              | 4R-NADD (1)           | $44 \pm 2$  | $6.3 \pm 0.2$   |
| NQO1 (1)              | NADPH (1)             | $261 \pm 13$  | $7.8 \pm 0.3$   |
| NQO1 (1) + Dic (1)    | NADH (1)              | $0.034 \pm 0.003$   | $0.0065 \pm 0.0005$   |
| NQO1 (1) + Dic (1)    | NADH (6.6)            | $0.036 \pm 0.002$   | $0.010 \pm 0.001$   |
| NQO1 (1) + Dic (4)    | NADH (1)              | $0.018 \pm 0.003$   | $0.0015 \pm 0.0001$   |
| NQO1 (1) + Dic (1)    | NADPH (1)             | $0.036 \pm 0.006$   | $0.0070 \pm 0.0008$   |
| NQO1 (1) + Dic (4)    | NADPH (1)             | $0.017 \pm 0.001$   | $0.0020 \pm 0.0001$   |
| NQO1 (1) + NADH (1)   | DCPIP (1)             | $>500$  | $160 \pm 14$  |
| NQO1 (1) + NADH (1)   | DCPIP (1) + Dic (1)   | $38 \pm 3$  | $6.3 \pm 1.2$   |
| NQO1 (1) + NADH (1)   | DCPIP (1) + Dic (4)   | $7.7 \pm 0.2$   | $1.3 \pm 0.1$   |
| NQO1 (1) + NADH (1)   | Ferricyanide          | $219 \pm 12$  | $29 \pm 4$  |

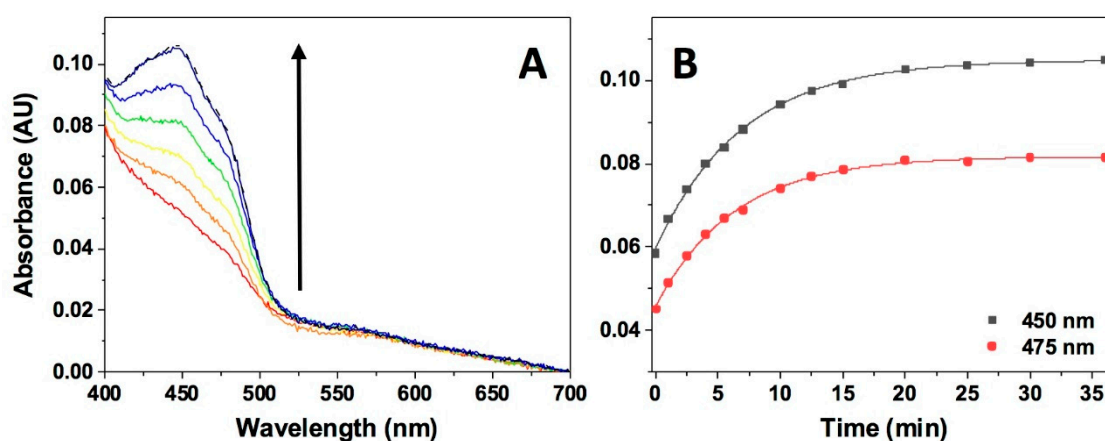


**Figure 7.** Kinetics of the reaction of NQO1<sub>hq</sub> with NAD<sup>+</sup>. (A) Spectral evolution after mixing (in an anaerobic cuvette) NQO1<sub>hq</sub> (7.5 μM) with a 1:1 ratio of NAD<sup>+</sup> in 20 mM HEPES-KOH, pH 7.0, at 6 °C on a 0–35 min timescale. Different colored lines correspond to the spectra at different reaction times. (B) Detail of kinetic traces at 450 nm and 475 nm and fitting to a single exponential function. Spectral evolution (A) is from a single measurement and representative from  $n > 3$ .

### 3.2.2. Non-Equivalent Active Sites in the NQO1 Dimer throughout the Oxidative Half-Reaction

Although NQO1 can reduce a wide variety of substrates [4], most of them are not appropriate for enzymatic studies due to their low solubility in aqueous solutions, their characteristic spectral properties or, in some cases, their fast reduction that precludes pre-steady-state kinetic characterization using stopped-flow spectroscopy [34,44]. We have here used DCPIP, a suitable and artificial electron acceptor often used in activity measurements of human NQO1 [4], to study its oxidative half-reaction. Nonetheless, mixing NQO1<sub>hq</sub> with DCPIP at equimolar concentrations also resulted in the extremely fast re-oxidation of the protein, even at low temperatures, and with nearly 50% of the spectral changes occurring in the instrumental dead time (Figure 8A–C). The observed overall process was best fitted to a two-step mechanism (A→B→C), with the initial step accounting for most of the spectroscopic changes and exhibiting observed rate constants,  $k_{\text{obsA} \rightarrow \text{B}}$ , above the instrumental measurement limit ( $>500 \text{ s}^{-1}$ , at stoichiometric reactant ratios). Conversely, the second step (B→C) shows minor, and probably *biased*, contributions both in terms of  $k_{\text{obsB} \rightarrow \text{C}}$  ( $160 \text{ s}^{-1}$ ) and amplitude. These values for the rate constants in the oxidative half-reaction further reinforce that the reductive half-reaction is rate-limiting in NQO1 catalysis, also preventing additional analyses at higher NQO1<sub>hq</sub>:DCPIP ratios.

Although Dic is usually reported as an inhibitor of the reductive half-reaction, we also evaluated its effect in the oxidative half-reaction. The re-oxidation of NQO1<sub>hq</sub> by DCPIP is also significantly slowed down in the presence of Dic (1:1 of protein/NADH mixed with 1:1 DCPIP/Dic, Figure 8D,E), which might not be surprising because Dic shares the binding site with both the electron donor and acceptor [46]. The presence of Dic has a considerable effect on both  $k_{\text{obsA} \rightarrow \text{B}}$  and  $k_{\text{obsB} \rightarrow \text{C}}$ , which decreased to  $38 \pm 3$  and  $6.3 \pm 1.2 \text{ s}^{-1}$ , respectively, at a 1:1 ratio and even more at higher Dic concentrations (Table 1), while the amplitudes of the changes became similar for both processes (Figure 8D–F). These data indicate that the two active sites of NQO1 are also non-equivalent regarding the kinetics of the oxidative half-reaction.

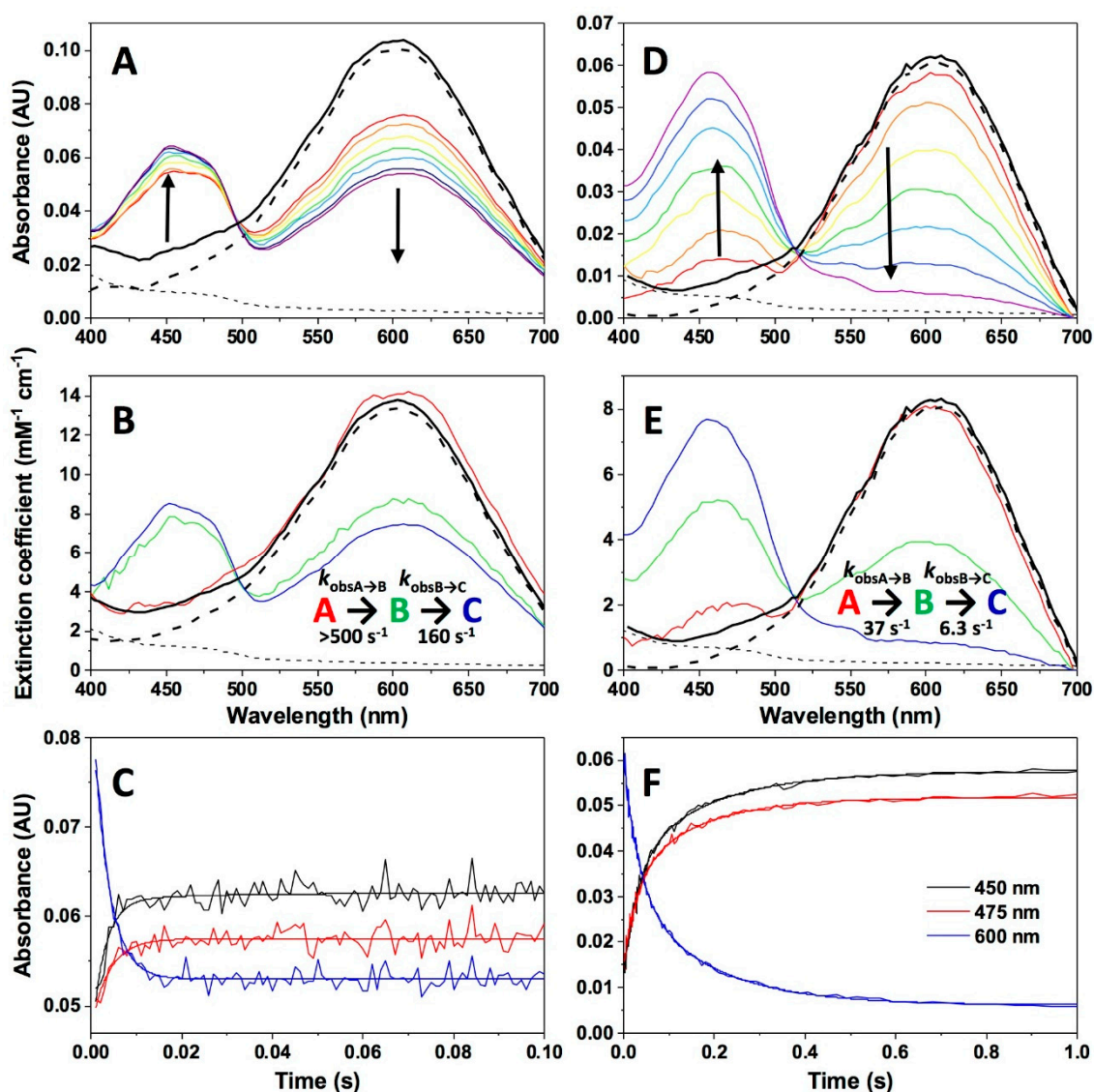


**Figure 8.** Kinetics of NQO1<sub>hq</sub> re-oxidation by DCPIP (2,6-dichlorophenol indophenol). (A) Spectral evolution after mixing NQO1<sub>hq</sub> (7.5 μM) with DCPIP (7.5 μM) in 20 mM HEPES-KOH, pH 7.4, at 6 °C on a 0–0.1 s timescale. (B) Spectral deconvolution of intermediate species observed during the reaction when using a three-state model. (C) Kinetic traces at 450 nm, 475 nm and 600 nm. Experimental data as well as the fitting to the three-state mechanism are shown. (D) Spectral evolution after mixing NQO1<sub>hq</sub> (7.5 μM) with DCPIP (7.5 μM) in the presence of Dic (7.5 μM) in 20 mM HEPES-KOH, pH 7.4, at 6 °C on a 0–1 s timescale. (E) Spectral deconvolution of intermediate species obtained from analysis using a three-state model. (F) Kinetic traces at 450 nm, 475 nm and 600 nm. Experimental data as well as the fitting to the three-state mechanisms are shown. Dashed lines (panels A,B and D,E) correspond to the initial spectra of NQO1<sub>hq</sub> and DCPIP (bold), the bold black line is the addition of these two spectra (species at t = 0) and the different colored lines correspond to the spectra at different reaction times. Spectral evolution (A,D) and deconvolution (B,E) are from a single measurement and representative from n > 3.

Although the main enzymatic role of NQO1 is associated with the mandatory two-electron reduction of substrates, reactivity with artificial one-electron oxidants, such as ferricyanide, has been widely reported for the characterization of *Saccharomyces cerevisiae* Lot6p and rat and human NQO1 [76,77]. The rapid mixing of reduced NQO1<sub>hq</sub> with ferricyanide (1:1 reduction equivalent ratio) coursed with the re-oxidation of the FAD cofactor (in ~ 0.4 s) without any trace of semiquinone

stabilization and with  $k_{\text{obsA} \rightarrow \text{B}}$  of  $219 \pm 12 \text{ s}^{-1}$  and  $k_{\text{obsB} \rightarrow \text{C}}$  of  $29 \pm 4 \text{ s}^{-1}$ , values considerably lower when compared to two-electron substrates.

### 3.3. Dynamics at the NQO1 Active Sites Differentially Contribute to the Two HT Events Representing the Reductive Half-Reaction

We then used fast kinetics measurements to investigate primary KIEs (using [4R-<sup>2</sup>H]-NADD), as well as the temperature dependence of the rate constants and KIEs, in the context of the Arrhenius equation. The resulting parameters may provide information on the structural organization and dynamics at the active site of enzymes during HT catalysis [68]. Due to  $^{\text{HT}}k_{\text{obsA} \rightarrow \text{B}}$  values being close to the instrumental limit upon increasing the coenzyme concentration (see black closed circles in Figure 4E), equimolecular concentrations of enzyme and coenzyme were the most suitable choice to overcome the technical limitations for the temperature-dependent studies. Nonetheless, since  $K_{\text{d}}^{\text{NADD}}$  may differ from  $K_{\text{d}}^{\text{NADH}}$ , the KIEs obtained in this way might be apparent. However, this does not seem to be the case, since the  $K_{\text{d}}^{\text{NADD}}$  at 6 °C is quite similar to that of  $K_{\text{d}}^{\text{NADH}}$  ( $12 \pm 2 \mu\text{M}$  vs.  $16 \pm 3 \mu\text{M}$ , Figure 4E), indicating that, at this temperature, the deuterated substrate hardly influences this parameter. Moreover, the comparison of the limiting  $k_{\text{DT1}}$  of  $122 \pm 5 \text{ s}^{-1}$  with  $k_{\text{HT1}}$  ( $284 \pm 17 \text{ s}^{-1}$ ) resulted in a moderate value of  $2.3 \pm 0.5$  for the  $\text{KIE}_{\text{A} \rightarrow \text{B}}$  at 6 °C. On their side,  $^{\text{DT}}k_{\text{obsB} \rightarrow \text{C}}$  values were considerably lower (Figure 4E, red open circles) with a limiting  $k_{\text{DT2}} \sim 7 \text{ s}^{-1}$  and therefore a  $\text{KIE}_{\text{B} \rightarrow \text{C}}$  may also be close to a value of 2. KIEs usually exhibit maximal values at lower temperatures, suggesting this might be a nearly limiting value. The magnitude of primary H/D KIEs theoretically can reach a maximum value of 8, although there are considerably larger values reported for some enzymes [78]. Nonetheless, primary KIEs can also decrease towards 1 when the C-H bond is either broken *less* (i.e., earlier transition state) or *more* (i.e., later transition state) in the transition state structure (asymmetrical), or if the transition state is nonlinear [79,80]. This suggests that, in the NQO1 reductive half-reaction, the transition state, at least for the first HT, is either moving away from symmetrical or it is non-linear.

The magnitude of the KIE is itself informative, but the size of its temperature dependence also serves as a key descriptor of the reaction coordinate [64]. In particular, we applied the environmentally coupled tunneling model by determining HT and DT observed rate constants, namely  $^{\text{HT}}k_{\text{obsA} \rightarrow \text{B}}$ ,  $^{\text{HT}}k_{\text{obsB} \rightarrow \text{C}}$ ,  $^{\text{DT}}k_{\text{obsA} \rightarrow \text{B}}$  and  $^{\text{DT}}k_{\text{obsB} \rightarrow \text{C}}$ , at different temperatures (Figure 9A). As indicated above, we used equimolecular concentrations of the enzyme and the coenzyme substrate (instead of saturating) to avoid entering the detection limit of the instrument upon increasing the temperature. The determined  $k_{\text{obs}}$  values provided apparent  $\text{KIE}_{\text{A} \rightarrow \text{B}}$  and  $\text{KIE}_{\text{B} \rightarrow \text{C}}$  values of  $\sim 1.8$  (Table 2), which were temperature independent (Figure 9B). Despite these values being apparent, they match with the limiting one obtained under saturating conditions and low temperature.  $^{\text{HT}}k_{\text{obsA} \rightarrow \text{B}}$  and  $^{\text{DT}}k_{\text{obsA} \rightarrow \text{B}}$  showed a weaker temperature dependence than  $^{\text{HT}}k_{\text{obsB} \rightarrow \text{C}}$  and  $^{\text{DT}}k_{\text{obsB} \rightarrow \text{C}}$ , and in both cases the Arrhenius plots for HT and DT hardly deviated from parallel lines, indicating very similar  $E_{\text{a}}$  values (Figure 9A).  $E_{\text{a}}$  values are moderate for the fast HT/DT event and 1.5 times larger for the second process, while  $\Delta E_{\text{a}}$  ( $E_{\text{aDT}} - E_{\text{aHT}}$ ) is nearly 0 for both processes. In addition, the calculated isotope effect on the Arrhenius frequency factor ( $A_{\text{H}}/A_{\text{D}}$ ) strongly differed between both HT/DT events, with a value close to the unity for the faster one and about 10 for the slower one. As a consequence of the marginal differences between  $E_{\text{aDT}}$  and  $E_{\text{aHT}}$  and the small values for the apparent KIEs, the activation enthalpies and entropies for HT and DT are also small when these results are analyzed in the context of the Eyring equation (Equation (4), see Figure 9C and Table 3).



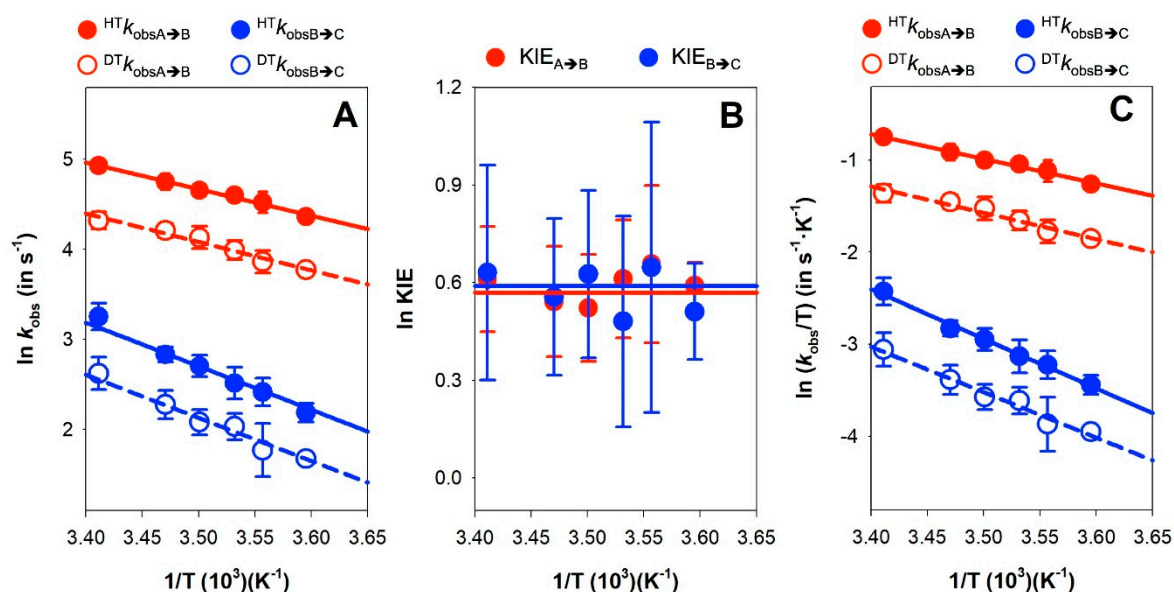


**Figure 9.** Temperature dependence of kinetic parameters for the two hydride/deuteride transfer (HT/DT) processes from NADH to NQO1. (A) Arrhenius plots of kinetic constants. (B) Temperature dependence of the kinetic isotope effects (KIEs). (C) Eyring plots of kinetic constants.

**Table 2.** KIEs for the HT in the reduction of NQO1 by NADH. All values correspond to data obtained with equimolar concentrations of the reactants in the stopped-flow equipment. ( $n > 3$ , mean  $\pm$  SD). Analysis was performed using Equations (2) and (3) (see Figure 9A,B).

|     | HT                             |  |                            | DT                             |  |                            | KIE           | $\Delta E_a$<br>$E_{aDT} - E_{aHT}$<br>( $kcal \cdot mol^{-1}$ ) | $A_H/A_D$     |
|-----|--------------------------------|--|----------------------------|--------------------------------|--|----------------------------|---------------|--|---------------|
|     | $HT k_{obs}^a$<br>( $s^{-1}$ ) | $E_{aHT}$<br>( $kcal \cdot mol^{-1}$ ) | $A_H$<br>( $s^{-1}$ )      | $DT k_{obs}^a$<br>( $s^{-1}$ ) | $E_{aDT}$<br>( $kcal \cdot mol^{-1}$ ) | $A_D$<br>( $s^{-1}$ )      |               |  |               |
| A→B | $78 \pm 1$                     | $6.1 \pm 0.2$                          | $(5.3 \pm 1.2) \cdot 10^6$ | $44 \pm 2$                     | $6.3 \pm 0.4$                          | $(4.1 \pm 1.1) \cdot 10^6$ | $1.8 \pm 0.1$ | $0.2 \pm 0.4$  | $1.3 \pm 0.6$ |
| B→C | $8.9 \pm 0.9$                  | $10.9 \pm 0.5$                         | $(3.4 \pm 0.9) \cdot 10^9$ | $5.3 \pm 0.2$                  | $9.8 \pm 0.5$                          | $(2.6 \pm 0.6) \cdot 10^8$ | $1.8 \pm 0.3$ | $-1.1 \pm 0.7$   | $13 \pm 6$    |

<sup>a</sup> Values at 6 °C.

The temperature independence of the KIE is generally interpreted in the context of full tunneling models, where the reaction barrier is attributed to the heavy atom motions that affect the probability of wave function overlap and little, or no, sampling of the distance of the reacting atoms [81]. Thus, our data show that both HT events in NQO1 are consistent with transitions under the barrier (i.e., quantum tunneling) and with asymmetrical or non-linear transition states. Moreover, the lower  $E_a$  and close to zero  $\Delta E_a$  values and, particularly, the close to unity  $A_H/A_D$  ratio for the fast HT process support for this event some contribution of dynamics, and/or donor–acceptor distance (DAD) fluctuations of the active site heavy atoms, to the tunneling. Thus, the fast HT process resembles the behavior most commonly found in native enzyme-mediated HT processes, in which catalytic enhancement is achieved by promoting and optimizing vibrations in active sites that minimize DAD fluctuations [81,82]. Conversely, the second HT event also shows almost temperature-independent KIEs and still similar  $E_{aD}$  and  $E_{aH}$  values, but higher  $E_a$  and  $A_H/A_D$  considerably greater than the unity (Figure 9, Table 2). The higher  $E_{aH}$  values suggest larger reorganization energies as the main source of the  $E_a$ , whereas the rest of the parameters, particularly the  $A_H/A_D$  ratio, support a larger contribution to the active site environment to promote a close approach between the hydride donor and the acceptor atom with little DAD sampling. Altogether, these data indicate that for the slower HT process the initial pre-organization complex situates the reacting atoms, N5 of FAD and the C4-H of the nicotinamide of NADH, at optimal tunneling distance, creating a stiffer active site for the competent HT when compared to the active site of the fast HT process.

**Table 3.** Activation enthalpies ( $\Delta H^\ddagger$ ) and entropies ( $\Delta S^\ddagger$ ) obtained using the Eyring equation (Equation (4)) and temperature-dependent  $k_{\text{obs}}$  values (see Figure 9C).

| Activation Parameters   | HT        |         | DT        |           |
|---|-----------|---------|-----------|-----------|
|   | A→B       | B→C     | A→B       | B→C       |
| $\Delta H^\ddagger$ (kcal·mol <sup>-1</sup> )                 | 5.3 ± 0.3 | 11 ± 1  | 5.7 ± 0.6 | 9.8 ± 0.8 |
| $\Delta S^\ddagger$ (cal·mol <sup>-1</sup> ·K <sup>-1</sup> ) | -31 ± 1   | -16 ± 2 | -30 ± 2   | -20 ± 3   |

#### 4. Conclusions

Our understanding of the roles of the multifunctional NQO1 protein in many physiological and pathological states, particularly in those associated with oxidative insults such as cancer and neurological disorders, is growing steadily [1,2,4,16]. In addition, NQO1 is an excellent example of an oligomeric human protein in which functional ligands exert remarkable cooperative effects with important implications for the understanding of how human genetic variability, divergent evolution and post-translational modifications shape the complex functional chemistry of multifunctional proteins [2,28,31,34,42,50,51,54–57,83]. We provide here a kinetic analysis of the oxidoreductase cycle of NQO1 in unprecedented detail. One of the main conclusions of our study is the existence of non-equivalent active sites in the protein dimer that differ in activity by about 20-fold and, thus, this could explain previous reports on the negative binding cooperativity towards inhibitors such as Dic [48,49]. At this point, we must note that in a *thermodynamic* sense, the existence of two active sites with different efficiencies (i.e., non-identical active sites) cannot be distinguished from two active sites displaying negative cooperativity (i.e., identical and non-independent active sites) [32,84]. We also report details on chemical aspects of the NQO1 catalytic cycle, such as the contributions to HT from quantum tunneling, and asymmetric transition states, as well as conformational and vibrational dynamics along the reaction coordinate. We anticipate that this detailed kinetic analysis will be valuable for understanding the effects of naturally occurring missense variants and post-translational modifications in NQO1, as well as in the rational design of novel inhibitors targeting NQO1 activity and biomacromolecular interactions [2,4].

Considering previous equilibrium binding and kinetic studies [31,48,49,54], the strong evidence provided in this work for the existence of non-equivalent active sites in the human NQO1 is not striking. Thus, our work helps to reconcile previous binding and steady-kinetic analyses focused on NAD(P)H and Dic. By looking at the NAD(P)H coenzyme, we have found strong evidence for HT occurring with a 20-fold difference in rate constants between active sites, although the fast process accounts for 75–80% of the overall HT process. This could imply that the fast pathway for HT using this coenzyme dominates the observed steady-state kinetics, thus contributing to an explanation for the lack of negative cooperativity observed in coenzyme dependence studies by steady-state kinetics [31]. However, we observed that about half of the HT process occurred through *fast* and *slow* pathways in the presence of Dic (that slowed down both pathways by three orders of magnitude). These results indicate that Dic binding causes a larger kinetic uncoupling between the two active sites, thus contributing to an explanation for the negative, but *not extreme*, cooperativity observed in inhibition studies (with Hill coefficients of about 0.5, corresponding to a cooperative binding Gibbs energy of about 1.5 kcal·mol<sup>-1</sup>; [48,49]). Interestingly, negative cooperativity between FAD binding sites of a similar magnitude is also observed in the apo-enzyme [54]. A detailed structural explanation for these observations, and the derived mechanistic implications, is difficult to provide for several reasons. If we consider that the two active sites *intrinsically differ* (i.e., non-identical and independent active sites), high-resolution structural information of the holo-enzyme with and without bound Dic would have revealed such structural differences between the monomers in the dimer. However, this has not been the case to the best of our knowledge (of course, we can always suggest that the reported technical aspects of the X-ray crystallography experiments, such as low temperature data acquisition, the refinement approaches used and the fact that the protein is not in solution, might

have contributed to *hiding* such structural heterogeneity) [36,46]. If negative cooperativity exists (i.e., identical and dependent active sites), the clue would reside in the properties of the half-ligated species (i.e., the holo-enzyme dimer with one NAD(P)H/Dic binding site occupied) [42]. However, again, we have no structural information on these half-ligated states. However, recent molecular dynamics (MD) simulations and hydrogen-deuterium exchange (HDX) analyses have provided some clues to the structural basis of these cooperative effects [42,48]. MD simulations combined with a Gaussian network model have supported that, in the half-ligated species, the binding of Dic to one site might trigger changes in dynamics that propagate to the (empty) binding site of the adjacent monomer [48]. In addition, the holo-protein in solution shows a remarkably complex behavior in terms of local stability, supporting that, in the absence and the presence of bound Dic, different conformational substates with widely different local stability (and plausibly, intrinsic binding affinities for this inhibitor) may also be populated [42].

The kinetic heterogeneity described in this work for the two active sites in NQO1 has been further characterized by analysis of the KIEs for this enzymatic reaction. Although we must be cautious in the interpretation of these potentially apparent KIEs, according to current models of HT [64,81], these analyses supported different contributions from quantum tunneling, conformational dynamics and molecular vibrations for the fast and the slow HT processes catalyzed by NQO1. For instance, the activation enthalpies and entropies for the fast and slow pathways clearly differed, showing that the fast pathway must overcome a larger activation entropic component (Table 3). Importantly, as indicated by one of the reviewers, more robust conclusions will be drawn when several technical issues are overcome to yield the values of intrinsic KIEs in NQO1. However, at this point, it is important to keep in mind that the overall enzyme dynamics are substantially altered (not only at the active site) when Dic, the competitive inhibitor of NADH, binds to the enzyme [42] (Figure 1B). In addition, the conformational dynamics of the holo-enzyme (and to a lower extent when Dic is bound) is significantly altered by disease-associated and artificial mutants of NQO1 [30,33,50,55], as well as by phosphorylation at S82 [57], and these effects are long range (i.e., dynamic alterations are observed at regions far from the perturbed site). Therefore, the methodology presented here will pave the way to dissect at the molecular level how the dynamic alterations caused by these single-site perturbations may differently affect the fast and slow HT processes catalyzed by NQO1.

**Author Contributions:** Conceptualization, E.A.-C., A.L.P. and M.M.; methodology, E.A.-C. and M.M.; software, E.A.-C. and M.M.; validation, E.A.-C., A.L.P. and M.M.; formal analysis, E.A.-C. and M.M.; investigation, E.A.-C., A.L.P. and M.M.; resources, A.L.P., D.J.T. and M.M.; data curation, E.A.-C., A.L.P. and M.M.; writing-original draft preparation, E.A.-C., D.J.T., A.L.P. and M.M.; writing-review and editing, E.A.-C., D.J.T., A.L.P. and M.M.; visualization, E.A.-C., A.L.P. and M.M.; supervision, A.L.P. and M.M.; project administration, A.L.P. and M.M.; funding acquisition, A.L.P. and M.M. All authors have read and agreed to the published version of the manuscript.

**Funding:** This research was funded by the ERDF/Spanish Ministry of Science, Innovation and Universities—State Research Agency (Grant RTI2018-096246-B-I00, to A.L.P.), Spanish Ministry of Science and Innovation—State Research Agency (Grant PID2019-103901GB-I00, to M.M.), Consejería de Economía, Conocimiento, Empresas y Universidad, Junta de Andalucía (Grants P11-CTS-07187 and P18-RT-2413, to A.L.P.) and Gobierno de Aragón-FEDER (Grant E35\_20R).

**Acknowledgments:** The authors would like to acknowledge the use of Servicios Generales de Apoyo a la Investigación-SAI, Universidad de Zaragoza.

**Conflicts of Interest:** The authors declare no conflict of interest. The funders had no role in the design of the study; in the collection, analyses, or interpretation of data; in the writing of the manuscript, or in the decision to publish the results.

## Appendix A. Kinetic Solvent Viscosity Effects (KSVEs)

As pointed out by one of the reviewers, the role of additional steps, such as substrate binding/product release as a rate-limiting step, should be considered. To this end, we analyzed the so-called *kinetic solvent viscosity effects* (KSVEs) on the steady-state parameters of NQO1. [85]. The diaphorase activity of NQO1 was evaluated using DCPIP as the electron acceptor at different concentrations of glycerol as a viscogen. Reaction mixtures contained 20  $\mu$ M DCPIP, 1 nM recombinant

NQO1 and NADH at varying concentrations at 25 °C. The reaction was triggered by the addition of the enzyme and followed by absorption changes at 600 nm for 1 min in 1-cm path length quartz cuvettes in a thermostated Cary 100 spectrophotometer (Agilent). The specific activity was calculated using  $\epsilon_{620\text{nm}} = 21,000 \text{ M}^{-1}\cdot\text{cm}^{-1}$  for DCPIP. Kinetic parameters were determined by varying the NADH concentration [34]. The  $k_{\text{cat}}$  and  $K_{\text{M}}$  values were determined using the Michaelis–Menten equation.

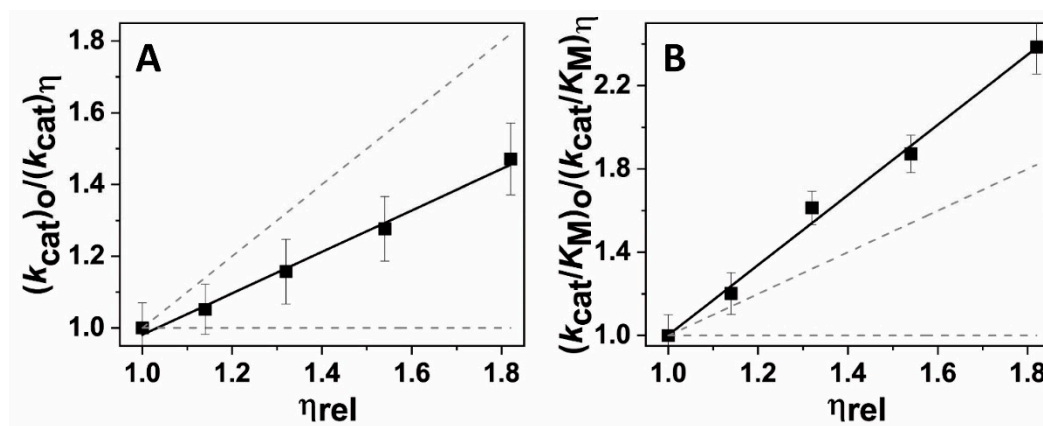


**Figure A1.** Viscosity dependence of NQO1 steady-state parameters. (A) Plot of  $(k_{\text{cat}}/K_{\text{M}})_o / (k_{\text{cat}}/K_{\text{M}})_\eta$  vs.  $\eta_{\text{rel}}$ . (B)  $(k_{\text{cat}})_o / (k_{\text{cat}})_\eta$  vs.  $\eta_{\text{rel}}$ . Dashed lines guide the eye along slopes with values of 1 and 0, respectively.

A plot of  $(k_{\text{cat}})_o / (k_{\text{cat}})_\eta$  vs. relative viscosity ( $\eta_{\text{rel}}$ ) yields a slope below unity ( $0.55 \pm 0.05$ ) (Figure A1), indicating that product(s) release could be partially limiting the enzyme turnover rate. A plot of  $(k_{\text{cat}}/K_{\text{M}})_o / (k_{\text{cat}}/K_{\text{M}})_\eta$  vs.  $\eta_{\text{rel}}$  yields a slope over 1 ( $1.6 \pm 0.1$ ) (Figure A1), thus supporting that the diffusion of substrates is not relevant and that the viscogen could manifest inhibitory behavior due to effects on structural dynamics (e.g., in protein loops).

## References

- Ross, D.; Siegel, D. NQO1 in protection against oxidative stress. *Curr. Opin. Toxicol.* **2018**, *7*, 67–72. [CrossRef]
- Beaver, S.K.; Mesa-Torres, N.; Pey, A.L.; Timson, D.J. NQO1: A target for the treatment of cancer and neurological diseases, and a model to understand loss of function disease mechanisms. *Biochim. Biophys. Acta Proteins Proteom.* **2019**, *1867*, 663–676. [CrossRef] [PubMed]
- Anusevicius, Z.; Sarlauskas, J.; Cenas, N. Two-electron reduction of quinones by rat liver NAD(P)H: Quinone oxidoreductase: Quantitative structure-activity relationships. *Arch. Biochem. Biophys.* **2002**, *404*, 254–262. [CrossRef]
- Salido, E.; Timson, D.J.; Betancor-Fernández, I.; Palomino-Morales, R.; Pey, A.L. Targeting HIF-1alpha Function in Cancer through the Chaperone Action of NQO1. *Preprints* **2020**, *2020*, 030285.
- Ingram, B.O.; Turbyfill, J.L.; Bledsoe, P.J.; Jaiswal, A.K.; Stafford, D.W. Assessment of the contribution of NAD(P)H-dependent quinone oxidoreductase 1 (NQO1) to the reduction of vitamin K in wild-type and NQO1-deficient mice. *Biochem. J.* **2013**, *456*, 47–54. [CrossRef]
- Ernster, L.; Danielson, L.; Ljunggren, M. DT diaphorase. I. Purification from the soluble fraction of rat-liver cytoplasm, and properties. *Biochim. Biophys. Acta* **1962**, *58*, 171–188. [CrossRef]
- Ross, D.; Siegel, D. Functions of NQO1 in Cellular Protection and CoQ10 Metabolism and its Potential Role as a Redox Sensitive Molecular Switch. *Front. Physiol.* **2017**, *8*, 595. [CrossRef]
- Beyer, R.E.; Segura-Aguilar, J.; Bernardo, S.D.; Cavazzoni, M.; Fato, R.; Fiorentini, D.; Galli, M.C.; Setti, M.; Landi, L.; Lenaz, G. The role of DT-diaphorase in the maintenance of the reduced antioxidant form of coenzyme Q in membrane systems. *Proc. Natl. Acad. Sci. USA* **1996**, *93*, 2528–2532. [CrossRef]
- Siegel, D.; Gustafson, D.L.; Dehn, D.L.; Han, J.Y.; Boonchoong, P.; Berliner, L.J.; Ross, D. NAD(P)H: Quinone oxidoreductase 1: Role as a superoxide scavenger. *Mol. Pharm.* **2004**, *65*, 1238–1247. [CrossRef]

10. Walton, M.I.; Smith, P.J.; Workman, P. The role of NAD(P)H: Quinone reductase (EC 1.6.99.2, DT-diaphorase) in the reductive bioactivation of the novel indoloquinone antitumor agent EO9. *Cancer Commun.* **1991**, *3*, 199–206. [[CrossRef](#)]
11. Brunmark, A.; Cadenas, E.; Lind, C.; Segura-Aguilar, J.; Ernster, L. DT-diaphorase-catalyzed two-electron reduction of quinone epoxides. *Free Radic. Biol. Med.* **1987**, *3*, 181–188. [[CrossRef](#)]
12. Siegel, D.; Gibson, N.W.; Preusch, P.C.; Ross, D. Metabolism of mitomycin C by DT-diaphorase: Role in mitomycin C-induced DNA damage and cytotoxicity in human colon carcinoma cells. *Cancer Res.* **1990**, *50*, 7483–7489. [[PubMed](#)]
13. Siegel, D.; Beall, H.; Senekowitsch, C.; Kasai, M.; Arai, H.; Gibson, N.W.; Ross, D. Bioreductive activation of mitomycin C by DT-diaphorase. *Biochemistry* **1992**, *31*, 7879–7885. [[CrossRef](#)] [[PubMed](#)]
14. Siegel, D.; Yan, C.; Ross, D. NAD(P)H: Quinone oxidoreductase 1 (NQO1) in the sensitivity and resistance to antitumor quinones. *Biochem. Pharm.* **2012**, *83*, 1033–1040. [[CrossRef](#)] [[PubMed](#)]
15. Asher, G.; Tsvetkov, P.; Kahana, C.; Shaul, Y. A mechanism of ubiquitin-independent proteasomal degradation of the tumor suppressors p53 and p73. *Genes Dev.* **2005**, *19*, 316–321. [[CrossRef](#)] [[PubMed](#)]
16. Oh, E.T.; Kim, J.W.; Kim, S.J.; Lee, J.S.; Hong, S.S.; Goodwin, J.; Ruthenborg, R.J.; Jung, M.G.; Lee, H.J.; Lee, C.H.; et al. NQO1 inhibits proteasome-mediated degradation of HIF-1 $\alpha$ . *Nat. Commun.* **2016**, *7*, 13593. [[CrossRef](#)]
17. Ross, D.; Kepa, J.K.; Winski, S.L.; Beall, H.D.; Anwar, A.; Siegel, D. NAD(P)H:quinone oxidoreductase 1 (NQO1): Chemoprotection, bioactivation, gene regulation and genetic polymorphisms. *Chem. Biol. Interact.* **2000**, *129*, 77–97. [[CrossRef](#)]
18. Rushmore, T.H.; Morton, M.R.; Pickett, C.B. The antioxidant responsive element. Activation by oxidative stress and identification of the DNA consensus sequence required for functional activity. *J. Biol. Chem.* **1991**, *266*, 11632–11639.
19. Nioi, P.; Hayes, J.D. Contribution of NAD(P)H: Quinone oxidoreductase 1 to protection against carcinogenesis, and regulation of its gene by the Nrf2 basic-region leucine zipper and the arylhydrocarbon receptor basic helix-loop-helix transcription factors. *Mutat. Res.* **2004**, *555*, 149–171. [[CrossRef](#)]
20. Brauze, D.; Widerak, M.; Cwykiel, J.; Szyfter, K.; Baer-Dubowska, W. The effect of aryl hydrocarbon receptor ligands on the expression of AhR, AhRR, ARNT, Hif1 $\alpha$ , CYP1A1 and NQO1 genes in rat liver. *Toxicol. Lett.* **2006**, *167*, 212–220. [[CrossRef](#)]
21. Tonelli, C.; Chio, I.I.C.; Tuveson, D.A. Transcriptional Regulation by Nrf2. *Antioxid. Redox Signal.* **2018**, *29*, 1727–1745. [[CrossRef](#)] [[PubMed](#)]
22. Sun, Z.; Chin, Y.E.; Zhang, D.D. Acetylation of Nrf2 by p300/CBP augments promoter-specific DNA binding of Nrf2 during the antioxidant response. *Mol. Cell. Biol.* **2009**, *29*, 2658–2672. [[CrossRef](#)] [[PubMed](#)]
23. Sekine, H.; Okazaki, K.; Ota, N.; Shima, H.; Katoh, Y.; Suzuki, N.; Igarashi, K.; Ito, M.; Motohashi, H.; Yamamoto, M. The Mediator Subunit MED16 Transduces NRF2-Activating Signals into Antioxidant Gene Expression. *Mol. Cell. Biol.* **2016**, *36*, 407–420. [[CrossRef](#)] [[PubMed](#)]
24. Hayes, J.D.; Dinkova-Kostova, A.T. The Nrf2 regulatory network provides an interface between redox and intermediary metabolism. *Trends Biochem. Sci.* **2014**, *39*, 199–218. [[CrossRef](#)] [[PubMed](#)]
25. Wu, K.C.; Cui, J.Y.; Klaassen, C.D. Beneficial role of Nrf2 in regulating NADPH generation and consumption. *Toxicol. Sci.* **2011**, *123*, 590–600. [[CrossRef](#)] [[PubMed](#)]
26. Valerio, L.G., Jr.; Kepa, J.K.; Pickwell, G.V.; Quattrochi, L.C. Induction of human NAD(P)H:quinone oxidoreductase (NQO1) gene expression by the flavonol quercetin. *Toxicol. Lett.* **2001**, *119*, 49–57. [[CrossRef](#)]
27. Hsieh, T.C.; Lu, X.; Wang, Z.; Wu, J.M. Induction of quinone reductase NQO1 by resveratrol in human K562 cells involves the antioxidant response element ARE and is accompanied by nuclear translocation of transcription factor Nrf2. *Med. Chem.* **2006**, *2*, 275–285.
28. Nolan, K.A.; Scott, K.A.; Barnes, J.; Doncaster, J.; Whitehead, R.C.; Stratford, I.J. Pharmacological inhibitors of NAD(P)H quinone oxidoreductase, NQO1: Structure/activity relationships and functional activity in tumour cells. *Biochem. Pharm.* **2010**, *80*, 977–981. [[CrossRef](#)]
29. Nolan, K.A.; Zhao, H.; Faulder, P.F.; Frenkel, A.D.; Timson, D.J.; Siegel, D.; Ross, D.; Burke, T.R., Jr.; Stratford, I.J.; Bryce, R.A. Coumarin-based inhibitors of human NAD(P)H: Quinone oxidoreductase-1. Identification, structure-activity, off-target effects and in vitro human pancreatic cancer toxicity. *J. Med. Chem.* **2007**, *50*, 6316–6325. [[CrossRef](#)]

30. Medina-Carmona, E.; Palomino-Morales, R.J.; Fuchs, J.E.; Padín-Gonzalez, E.; Mesa-Torres, N.; Salido, E.; Timson, D.J.; Pey, A.L. Conformational dynamics is key to understanding loss-of-function of NQO1 cancer-associated polymorphisms and its correction by pharmacological ligands. *Sci. Rep.* **2016**, *6*, 20331. [[CrossRef](#)]
31. Pey, A.L.; Megarity, C.F.; Timson, D.J. FAD binding overcomes defects in activity and stability displayed by cancer-associated variants of human NQO1. *Biochim. Biophys. Acta* **2014**, *1842*, 2163–2173. [[CrossRef](#)] [[PubMed](#)]
32. Pan, S.S.; Forrest, G.L.; Akman, S.A.; Hu, L.T. NAD(P)H: Quinone oxidoreductase expression and mitomycin C resistance developed by human colon cancer HCT 116 cells. *Cancer Res.* **1995**, *55*, 330–335. [[PubMed](#)]
33. Medina-Carmona, E.; Neira, J.L.; Salido, E.; Fuchs, J.E.; Palomino-Morales, R.; Timson, D.J.; Pey, A.L. Site-to-site interdomain communication may mediate different loss-of-function mechanisms in a cancer-associated NQO1 polymorphism. *Sci. Rep.* **2017**, *7*, 44352. [[CrossRef](#)] [[PubMed](#)]
34. Lienhart, W.D.; Gudipati, V.; Uhl, M.K.; Binter, A.; Pulido, S.A.; Saf, R.; Zangger, K.; Gruber, K.; Macheroux, P. Collapse of the native structure caused by a single amino acid exchange in human NAD(P)H: Quinone oxidoreductase (1). *FEBS J.* **2014**, *281*, 4691–4704. [[CrossRef](#)] [[PubMed](#)]
35. Chen, S.; Deng, P.S.; Bailey, J.M.; Swiderek, K.M. A two-domain structure for the two subunits of NAD(P)H: Quinone acceptor oxidoreductase. *Protein Sci.* **1994**, *3*, 51–57. [[CrossRef](#)] [[PubMed](#)]
36. Faig, M.; Bianchet, M.A.; Talalay, P.; Chen, S.; Winski, S.; Ross, D.; Amzel, L.M. Structures of recombinant human and mouse NAD(P)H: Quinone oxidoreductases: Species comparison and structural changes with substrate binding and release. *Proc. Natl. Acad. Sci. USA* **2000**, *97*, 3177–3182. [[CrossRef](#)] [[PubMed](#)]
37. Li, R.; Bianchet, M.A.; Talalay, P.; Amzel, L.M. The three-dimensional structure of NAD(P)H: Quinone reductase, a flavoprotein involved in cancer chemoprotection and chemotherapy: Mechanism of the two-electron reduction. *Proc. Natl. Acad. Sci. USA* **1995**, *92*, 8846–8850. [[CrossRef](#)]
38. Bianchet, M.A.; Faig, M.; Amzel, L.M. Structure and mechanism of NAD[P]H:quinone acceptor oxidoreductases (NQO). *Methods Enzymol.* **2004**, *382*, 144–174.
39. Hosoda, S.; Nakamura, W.; Hayashi, K. Properties and reaction mechanism of DT diaphorase from rat liver. *J. Biol. Chem.* **1974**, *249*, 6416–6423.
40. Bianchet, M.A.; Erdemli, S.B.; Amzel, L.M. Structure, function, and mechanism of cytosolic quinone reductases. *Vitam. Horm.* **2008**, *78*, 63–84.
41. Pey, A.L.; Megarity, C.F.; Timson, D.J. NAD(P)H quinone oxidoreductase (NQO1): An enzyme which needs just enough mobility, in just the right places. *Biosci. Rep.* **2019**, *39*, BSR20180459. [[CrossRef](#)] [[PubMed](#)]
42. Vankova, P.; Salido, E.; Timson, D.J.; Man, P.; Pey, A.L. A dynamic core in human NQO1 controls the functional and stability effects of ligand binding and their communication across the enzyme dimer. *Biomolecules* **2019**, *9*, 728. [[CrossRef](#)] [[PubMed](#)]
43. Tedeschi, G.; Chen, S.; Massey, V. Active site studies of DT-diaphorase employing artificial flavins. *J. Biol. Chem.* **1995**, *270*, 2512–2516. [[CrossRef](#)] [[PubMed](#)]
44. Tedeschi, G.; Chen, S.; Massey, V. DT-diaphorase. Redox potential, steady-state, and rapid reaction studies. *J. Biol. Chem.* **1995**, *270*, 1198–1204. [[CrossRef](#)] [[PubMed](#)]
45. Cavelier, G.; Amzel, L.M. Role of Fluctuations in Quinone Reductase Hydride Transfer: A Combined Quantum Mechanics and Molecular Dynamics Study. In Proceedings of the AIP Conference, Zaragoza, Spain, 8–11 February 2006; Volume 851. Meeting: FROM PHYSICS TO BIOLOGY: The Interface between Experiment and Computation - BIFI 2006 II International.
46. Asher, G.; Dym, O.; Tsvetkov, P.; Adler, J.; Shaul, Y. The crystal structure of NAD(P)H quinone oxidoreductase 1 in complex with its potent inhibitor dicoumarol. *Biochemistry* **2006**, *45*, 6372–6378. [[CrossRef](#)] [[PubMed](#)]
47. Timson, D.J. Dicoumarol: A Drug which Hits at Least Two Very Different Targets in Vitamin K Metabolism. *Curr. Drug Targets* **2017**, *18*, 500–510. [[CrossRef](#)]
48. Megarity, C.F.; Abdel-Bettley, H.; Caraher, M.C.; Scott, K.A.; Whitehead, R.C.; Jowitt, T.A.; Gutierrez, A.; Bryce, R.A.; Nolan, K.A.; Stratford, I.J.; et al. Negative cooperativity in NADP(H) quinone oxidoreductase 1 (NQO1). *ChemBioChem* **2019**, *20*, 2841–2849. [[CrossRef](#)]
49. Megarity, C.F.; Timson, D.J. Cancer-associated variants of human NQO1: Impacts on inhibitor binding and cooperativity. *Biosci. Rep.* **2019**, *39*. [[CrossRef](#)]

50. Medina-Carmona, E.; Fuchs, J.E.; Gavira, J.A.; Mesa-Torres, N.; Neira, J.L.; Salido, E.; Palomino-Morales, R.; Burgos, M.; Timson, D.J.; Pey, A.L. Enhanced vulnerability of human proteins towards disease-associated inactivation through divergent evolution. *Hum. Mol. Genet.* **2017**, *26*, 3531–3544. [[CrossRef](#)]
51. Munoz, I.G.; Morel, B.; Medina-Carmona, E.; Pey, A.L. A mechanism for cancer-associated inactivation of NQO1 due to P187S and its reactivation by the consensus mutation H80R. *FEBS Lett.* **2017**, *591*, 2826–2835. [[CrossRef](#)]
52. Martinez-Limon, A.; Alriquet, M.; Lang, W.H.; Calloni, G.; Wittig, I.; Vabulas, R.M. Recognition of enzymes lacking bound cofactor by protein quality control. *Proc. Natl. Acad. Sci. USA* **2016**, *113*, 12156–12161. [[CrossRef](#)] [[PubMed](#)]
53. Siegel, D.; Anwar, A.; Winski, S.L.; Kepa, J.K.; Zolman, K.L.; Ross, D. Rapid polyubiquitination and proteasomal degradation of a mutant form of NAD(P)H: Quinone oxidoreductase 1. *Mol. Pharm.* **2001**, *59*, 263–268. [[CrossRef](#)] [[PubMed](#)]
54. Claveria-Gimeno, R.; Velazquez-Campoy, A.; Pey, A.L. Thermodynamics of cooperative binding of FAD to human NQO1: Implications to understanding cofactor-dependent function and stability of the flavoproteome. *Arch. Biochem. Biophys.* **2017**, *636*, 17–27. [[CrossRef](#)] [[PubMed](#)]
55. Pey, A.L. Biophysical and functional perturbation analyses at cancer-associated P187 and K240 sites of the multifunctional NAD(P)H: Quinone oxidoreductase 1. *Int. J. Biol. Macromol.* **2018**, *118*, 1912–1923. [[CrossRef](#)]
56. Medina-Carmona, E.; Betancor-Fernández, I.; Santos, J.; Mesa-Torres, N.; Grottelli, S.; Batlle, C.; Naganathan, A.N.; Oppici, O.; Cellini, B.; Ventura, S.; et al. Insight into the specificity and severity of pathogenic mechanisms associated with missense mutations through experimental and structural perturbation analyses. *Hum. Mol. Genet.* **2019**, *28*, 1–15. [[CrossRef](#)]
57. Medina-Carmona, E.; Rizzuti, B.; Martin-Escolano, R.; Pacheco-Garcia, J.L.; Mesa-Torres, N.; Neira, J.L.; Guzzi, R.; Pey, A.L. Phosphorylation compromises FAD binding and intracellular stability of wild-type and cancer-associated NQO1: Insights into flavo-proteome stability. *Int. J. Biol. Macromol.* **2019**, *125*, 1275–1288. [[CrossRef](#)]
58. Reigan, P.; Colucci, M.A.; Siegel, D.; Chilloux, A.; Moody, C.J.; Ross, D. Development of indolequinone mechanism-based inhibitors of NAD(P)H: Quinone oxidoreductase 1 (NQO1): NQO1 inhibition and growth inhibitory activity in human pancreatic MIA PaCa-2 cancer cells. *Biochemistry* **2007**, *46*, 5941–5950. [[CrossRef](#)]
59. Colucci, M.A.; Reigan, P.; Siegel, D.; Chilloux, A.; Ross, D.; Moody, C.J. Synthesis and evaluation of 3-aryloxymethyl-1,2-dimethylindole-4,7-diones as mechanism-based inhibitors of NAD(P)H: Quinone oxidoreductase 1 (NQO1) activity. *J. Med. Chem.* **2007**, *50*, 5780–5789. [[CrossRef](#)]
60. Dehn, D.L.; Siegel, D.; Swann, E.; Moody, C.J.; Ross, D. Biochemical, cytotoxic, and genotoxic effects of ES936, a mechanism-based inhibitor of NAD(P)H:quinone oxidoreductase 1, in cellular systems. *Mol. Pharm.* **2003**, *64*, 714–720. [[CrossRef](#)]
61. Dehn, D.L.; Siegel, D.; Zafar, K.S.; Reigan, P.; Swann, E.; Moody, C.J.; Ross, D. 5-Methoxy-1,2-dimethyl-3-[(4-nitrophenoxy)methyl] indole-4,7-dione, a mechanism-based inhibitor of NAD(P)H: Quinone oxidoreductase 1, exhibits activity against human pancreatic cancer in vitro and in vivo. *Mol. Cancer* **2006**, *5*, 1702–1709. [[CrossRef](#)]
62. Xu, S.; Yao, H.; Pei, L.; Hu, M.; Li, D.; Qiu, Y.; Wang, G.; Wu, L.; Yao, H.; Zhu, Z.; et al. Design, synthesis, and biological evaluation of NAD(P)H: Quinone oxidoreductase (NQO1)-targeted oridonin prodrugs possessing indolequinone moiety for hypoxia-selective activation. *Eur. J. Med. Chem.* **2017**, *132*, 310–321. [[CrossRef](#)] [[PubMed](#)]
63. Zhang, X.; Bian, J.; Li, X.; Wu, X.; Dong, Y.; You, Q. 2-Substituted 3,7,8-trimethylnaphtho [1-b]furan-4,5-diones as specific L-shaped NQO1-mediated redox modulators for the treatment of non-small cell lung cancer. *Eur. J. Med. Chem.* **2017**, *138*, 616–629. [[CrossRef](#)] [[PubMed](#)]
64. Klinman, J.P.; Offenbacher, A.R. Understanding Biological Hydrogen Transfer Through the Lens of Temperature Dependent Kinetic Isotope Effects. *Acc. Chem. Res.* **2018**, *51*, 1966–1974. [[CrossRef](#)] [[PubMed](#)]
65. Pollock, V.V.; Barber, M.J. Kinetic and mechanistic properties of biotin sulfoxide reductase. *Biochemistry* **2001**, *40*, 1430–1440. [[CrossRef](#)] [[PubMed](#)]
66. Whitby, L.G. A new method for preparing flavin-adenine dinucleotide. *Biochem. J.* **1953**, *54*, 437–442. [[CrossRef](#)]

67. Frago, S.; Goni, G.; Herguedas, B.; Peregrina, J.R.; Serrano, A.; Perez-Dorado, I.; Molina, R.; Gomez-Moreno, C.; Hermoso, J.A.; Martinez-Julvez, M.; et al. Tuning of the FMN binding and oxido-reduction properties by neighboring side chains in Anabaena flavodoxin. *Arch. Biochem. Biophys.* **2007**, *467*, 206–217. [[CrossRef](#)]
68. Sanchez-Azqueta, A.; Catalano-Dupuy, D.L.; Lopez-Rivero, A.; Tondo, M.L.; Orellano, E.G.; Ceccarelli, E.A.; Medina, M. Dynamics of the active site architecture in plant-type ferredoxin-NADP(+) reductases catalytic complexes. *Biochim. Biophys. Acta* **2014**, *1837*, 1730–1738. [[CrossRef](#)]
69. Perez-Amigot, D.; Taleb, V.; Boneta, S.; Anoz-Carbonell, E.; Sebastian, M.; Velazquez-Campoy, A.; Polo, V.; Martinez-Julvez, M.; Medina, M. Towards the competent conformation for catalysis in the ferredoxin-NADP(+) reductase from the *Brucella ovis* pathogen. *Biochim. Biophys. Acta Bioenerg.* **2019**, *1860*, 148058. [[CrossRef](#)]
70. Tejero, J.; Peregrina, J.R.; Martinez-Julvez, M.; Gutierrez, A.; Gomez-Moreno, C.; Scrutton, N.S.; Medina, M. Catalytic mechanism of hydride transfer between NADP+/H and ferredoxin-NADP+ reductase from *Anabaena* PCC 7119. *Arch. Biochem. Biophys.* **2007**, *459*, 79–90. [[CrossRef](#)]
71. Massey, V.; Muller, F.; Feldberg, R.; Schuman, M.; Sullivan, P.A.; Howell, L.G.; Mayhew, S.G.; Matthews, R.G.; Foust, G.P. The reactivity of flavoproteins with sulfite. Possible relevance to the problem of oxygen reactivity. *J. Biol. Chem.* **1969**, *244*, 3999–4006.
72. Clark, W.M. *Oxidation-Reduction Potentials of Organic Systems*; The Williams & Wilkins Company: Baltimore, MD, USA, 1960.
73. Dinkova-Kostova, A.T.; Talalay, P. NAD(P)H: Quinone acceptor oxidoreductase 1 (NQO1), a multifunctional antioxidant enzyme and exceptionally versatile cytoprotector. *Arch. Biochem. Biophys.* **2010**, *501*, 116–123. [[CrossRef](#)] [[PubMed](#)]
74. Burton, K. The enthalpy change for the reduction of nicotinamide—Adenine dinucleotide. *Biochem. J.* **1974**, *143*, 365–368. [[CrossRef](#)] [[PubMed](#)]
75. Lind, C.; Cadenas, E.; Hochstein, P.; Ernster, L. DT-diaphorase: Purification, properties, and function. *Methods Enzymol.* **1990**, *186*, 287–301. [[PubMed](#)]
76. Merker, M.P.; Audi, S.H.; Bongard, R.D.; Lindemer, B.J.; Krenz, G.S. Influence of pulmonary arterial endothelial cells on quinone redox status: Effect of hyperoxia-induced NAD(P)H: Quinone oxidoreductase 1. *Am. J. Physiol. Lung Cell. Mol. Physiol.* **2006**, *290*, L607–L619. [[CrossRef](#)] [[PubMed](#)]
77. Bongard, R.D.; Krenz, G.S.; Gastonguay, A.J.; Williams, C.L.; Lindemer, B.J.; Merker, M.P. Characterization of the threshold for NAD(P)H: Quinone oxidoreductase activity in intact sulforaphane-treated pulmonary arterial endothelial cells. *Free Radic. Biol. Med.* **2011**, *50*, 953–962. [[CrossRef](#)]
78. Klinman, J.P. Moving Through Barriers in Science and Life. *Annu. Rev. Biochem.* **2019**, *88*, 1–24. [[CrossRef](#)]
79. Nelson, S.D.; Trager, W.F. The use of deuterium isotope effects to probe the active site properties, mechanism of cytochrome P450-catalyzed reactions, and mechanisms of metabolically dependent toxicity. *Drug Metab. Dispos.* **2003**, *31*, 1481–1498. [[CrossRef](#)]
80. Yoshimoto, F.K.; Zhou, Y.; Peng, H.M.; Stidd, D.; Yoshimoto, J.A.; Sharma, K.K.; Matthew, S.; Auchus, R.J. Minor activities and transition state properties of the human steroid hydroxylases cytochromes P450c17 and P450c21, from reactions observed with deuterium-labeled substrates. *Biochemistry* **2012**, *51*, 7064–7077. [[CrossRef](#)]
81. Nagel, Z.D.; Klinman, J.P. Update 1 of: Tunneling and dynamics in enzymatic hydride transfer. *Chem. Rev.* **2010**, *110*, PR41–PR67. [[CrossRef](#)]
82. Nagel, Z.D.; Klinman, J.P. A 21st century revisionist's view at a turning point in enzymology. *Nat. Chem. Biol.* **2009**, *5*, 543–550. [[CrossRef](#)]
83. Mesa-Torres, N.; Betancor-Fernández, I.; Oppici, E.; Cellini, B.; Salido, E.; Pey, A.L. Evolutionary Divergent Suppressor Mutations in Conformational Diseases. *Genes* **2018**, *9*, 352. [[CrossRef](#)] [[PubMed](#)]
84. Wyman, J.; Gill, S.J. *Binding and Linkage. Functional Chemistry of Biological Macromolecules*; University Science Books: Mill Valley, CA, USA, 1990.
85. Gadda, G.; Sobrado, P. Kinetic Solvent Viscosity Effects as Probes for Studying the Mechanisms of Enzyme Action. *Biochemistry* **2018**, *57*, 3445–3453. [[PubMed](#)]





# Publication IV




**Discovery of antimicrobial compounds  
targeting bacterial type FAD synthases**

**Ernesto Anoz Carbonell contributions:** Experimental work: protein purification, steady-state enzymatic activity measurements and antimicrobial activity assays. Data analysis. Manuscript writing, review and editing

RESEARCH PAPER



## Discovery of antimicrobial compounds targeting bacterial type FAD synthetases

María Sebastián<sup>a,b</sup> , Ernesto Anoz-Carbonell<sup>a,b,c</sup>, Begoña Gracia<sup>c,d</sup>, Pilar Cossio<sup>e,f</sup>, José Antonio Aínsa<sup>b,c,d</sup> ,  
Isaías Lans<sup>f</sup> and Milagros Medina<sup>a,b</sup> 

<sup>a</sup>Departamento de Bioquímica y Biología Molecular y Celular, Facultad de Ciencias, Universidad de Zaragoza, Zaragoza, Spain; <sup>b</sup>Institute of Biocomputation and Physics of Complex Systems (BIFI-IQFR and CBsC-CSIC Joint Units), Universidad de Zaragoza, Zaragoza, Spain; <sup>c</sup>Grupo de Genética de Micobacterias, Departamento de Microbiología, Medicina Preventiva y Salud Pública. Facultad de Medicina, Universidad de Zaragoza, Zaragoza, Spain; <sup>d</sup>CIBER Enfermedades Respiratorias (CIBERES), Instituto de Salud Carlos III, Madrid, Spain; <sup>e</sup>Department of Theoretical Biophysics, Max Planck Institute of Biophysics, Frankfurt, Germany; <sup>f</sup>Biophysics of Tropical Diseases, Max Planck Tandem Group, University of Antioquia, Medellín, Colombia

### ABSTRACT

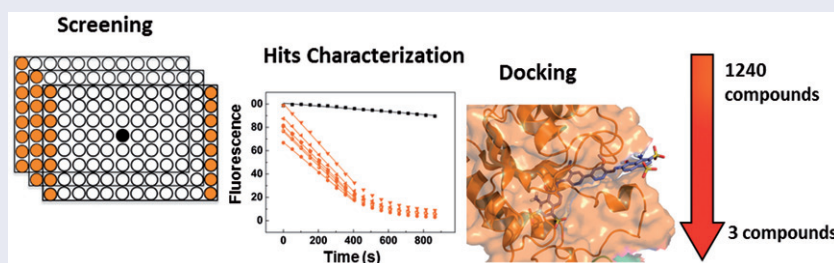
The increase of bacterial strains resistant to most of the available antibiotics shows a need to explore novel antibacterial targets to discover antimicrobial drugs. Bifunctional bacterial FAD synthetases (FADs) synthesise the flavin mononucleotide (FMN) and flavin adenine dinucleotide (FAD). These cofactors act in vital processes as part of flavoproteins, making FADs an essential enzyme. Bacterial FADs are potential antibacterial targets because of differences to mammalian enzymes, particularly at the FAD producing site. We have optimised an activity-based high throughput screening assay targeting *Corynebacterium ammoniagenes* FADs (CaFADs) that identifies inhibitors of its different activities. We selected the three best high-performing inhibitors of the FMN:adenylyltransferase activity (FMNAT) and studied their inhibition mechanisms and binding properties. The specificity of the CaFADs hits was evaluated by studying also their effect on the *Streptococcus pneumoniae* FADs activities, envisaging differences that can be used to discover species-specific antibacterial drugs. The antimicrobial effect of these compounds was also evaluated on *C. ammoniagenes*, *S. pneumoniae*, and *Mycobacterium tuberculosis* cultures, finding hits with favourable antimicrobial properties.

### ARTICLE HISTORY

Received 17 October 2017  
Revised 28 November 2017  
Accepted 28 November 2017

### KEYWORDS



Bacterial FAD Synthetase;  
high-throughput screening;  
*Streptococcus pneumoniae*;  
drug discovery




### Introduction

An important innovation gap in the discovering of antibiotics has occurred during the last two decades<sup>1</sup>, with only five new classes available and 51 new antimicrobials in clinical development<sup>2–4</sup>. In addition, the selection of multi-drug resistant microorganisms<sup>5</sup> encourages to search for new antimicrobial drugs capable of inhibiting novel protein targets, such as those controlling the biosynthesis of essential biomolecules. Flavin mononucleotide (FMN) and flavin adenine dinucleotide (FAD) are the cofactors of flavo-proteins. All living organisms contain a great number of such proteins and many of them are involved in essential functions<sup>6–8</sup>, including protein folding<sup>9</sup>, electron transport in the respiratory and photosynthetic chains<sup>10</sup>,  $\beta$ -oxidation of fatty acids<sup>11</sup>, nucleotide synthesis or signal transduction<sup>12</sup>, among others. Lack, or low

levels, of FMN and FAD lead to the accumulation of apoflavoproteins, unable to perform the flavin-dependent functions, resulting in the concomitant death of the cell or the organism<sup>13,14</sup>. Prokaryotic bifunctional FAD synthetases (FADs) synthesise both FMN and FAD, being therefore potential new antimicrobial targets<sup>15</sup>. Such hypothesis is sustained by several facts; (i) halting the production of FMN and FAD prevents, from the very beginning, all pathways that involve flavoproteins and flavoenzymes, (ii) in most bacteria the only pathway for FMN and FAD biosynthesis occurs with bifunctional FADs<sup>13,14</sup>, (iii) prokaryotic FADs differ structurally and biochemically from the mammalian proteins that transform FMN into FAD<sup>16–19</sup>, so drugs that target these proteins are likely to be selective for bacteria and (iv) the availability of structures of several bacterial FADs facilitates the design of both inhibitory drugs and activity assays<sup>20–22</sup>.

**CONTACT** Milagros Medina  [mmedina@unizar.es](mailto:mmedina@unizar.es)  Departamento de Bioquímica y Biología Molecular y Celular, Facultad de Ciencias, Universidad de Zaragoza, Pedro Cerbuna, 12. 50009 Zaragoza, Spain

 Supplemental data for this article can be accessed [here](#).

© 2017 The Author(s). Published by Informa UK Limited, trading as Taylor & Francis Group.

This is an Open Access article distributed under the terms of the Creative Commons Attribution License (<http://creativecommons.org/licenses/by/4.0/>), which permits unrestricted use, distribution, and reproduction in any medium, provided the original work is properly cited.

Bacterial FADSs have both ATP:riboflavin kinase (RFK, EC 2.7.1.26) and ATP:FMN:adenylyltransferase (FMNAT, EC 2.7.7.2) activities, being the latter reversible (FAD pyrophosphorylase) in some species<sup>17,23</sup>. FADSs synthesise FMN and FAD from riboflavin (RF, vitamin B2) through two sequential reactions: RF is first phosphorylated to FMN by the RFK activity, and then the FMNAT activity transfers an adenylyl group from ATP to FMN producing FAD. These catalytic activities are performed by two almost independent modules (Supplementary Figure SD1). The C-terminus module produces FMN from RF (named RFK module), while the N-terminal module transforms FMN into FAD (FMNAT module). The RFK module shows sequence and structural homology with the monofunctional eukaryotic RFKs, while the FMNAT module does not present neither sequence nor structural similarity with the proteins that synthesise FAD in mammals<sup>16,21,24,25</sup>. Because the enzymes leading to FAD production in prokaryotes and eukaryotes use different chemistry, and belong to different structural families, potential inhibitors that specifically target the FMNAT module of bacterial FADSs are an interesting option for the novel drug development<sup>15</sup>.

In this work, we have used as a model the FADS from the non-pathogenic organism *Corynebacterium ammoniagenes* (CaFADS), which is the best known model to characterise members of the prokaryotic FADSs family<sup>17,24,26–30</sup>, in an activity-based high-throughput screening (HTS) assay to find potential inhibitors. The HTS hits were assayed to determine their specificity and potency for the RFK and FMNAT activities. We also studied the kinetic inhibition mechanism of the three most potent and selective inhibitors of the FMNAT activity (FMNAT hits), as well as their binding properties. Furthermore, considering the structural similarity among CaFADS and the FADSs from the human pathogens *Streptococcus pneumoniae* (included in the World Health Organisation [WHO] priority list of antibiotic resistant pathogens; SpnFADS) and *Mycobacterium tuberculosis* (the World's leading infectious killer; MtFADS), we explored the potential antimicrobial effect of the FADS HTS hits in these microorganisms by determining their minimal inhibitory concentration (MIC). Some of the HTS hits demonstrated high FADS inhibitory activity *in vitro*, but their antimicrobial activity revealed that uptake of these compounds by bacterial cells could be suboptimal. Collectively, our results validate our approach for discovering antimicrobials targeting bacterial FADSs, and for identifying inhibitors that constitute a great starting point for future developments of novel antimicrobials.

## Methods

### Protein purification and quantification

Recombinant CaFADS was overexpressed in BL21 (DE3) *E. coli* cells and purified as previously described<sup>30</sup>. Recombinant SpnFADS was overexpressed in *E. coli* strain BI21 Star<sup>TM</sup> (DE3) and purified as previously described<sup>23</sup>. Pure samples were dialysed against 20 mM PIPES, pH 7.0 and quantified using the theoretical extinction coefficients  $\epsilon_{279}=27.8\text{ mM}^{-1}\text{ cm}^{-1}$  and  $28.8\text{ mM}^{-1}\text{ cm}^{-1}$  for CaFADS and SpnFADS, respectively. The purity of each protein was tested by 15% SDS-PAGE.

### Chemicals

The Prestwick Chemical Library<sup>®</sup>, containing 1240 molecules approved by the Food and Drugs Administration (FDA) and European Medicines Agency (EMA), was selected for the HTS. Compounds were dissolved in 100% DMSO at 10 mM. All the HTS hits were subsequently acquired from Sigma Aldrich, Prestwick or Carboxynth and dissolved in 100% DMSO to prepare stock

solutions at 50 and 10 mM. The purity of all compounds was >95%, as determined by High performance liquid chromatography (HPLC), thin layer chromatography (TLC), NMR, IR or basic titration.

### Activity-based high-throughput screening for CaFADS

An activity-based HTS was performed on the 1240 compounds of the Prestwick Chemical Library<sup>®</sup>. The assays consisted in recording the time dependent decrease in the fluorescence of the isoalloxazine ring, produced upon transformation of RF and FMN into FAD, as a consequence of the fluorescence quenching in this later flavin<sup>27</sup>. When either the RFK or the FMNAT activities were inhibited, less FAD was produced and, consequently, the fluorescence decrease registered in a specific time interval was less pronounced. Measurements were carried out using a multi-mode microplate reader, Synergy<sup>TM</sup> HT Biotek, with BRAND 96-well plates pure Grade<sup>TM</sup>. To optimise the assay conditions, a previous study was performed using constant concentrations of RF, ATP and CaFADS ( $\sim 5$ ,  $\sim 50$  and  $\sim 0.4\ \mu\text{M}$ , respectively) and variable concentrations of  $\text{MgCl}_2$  (0.2–10 mM) and DMSO (0–12.5% v/v). Optimum conditions were 2.5% DMSO, 10 mM  $\text{MgCl}_2$  and sensitivity 70.

HTS reaction mixtures contained  $5\ \mu\text{M}$  RF,  $0.4\ \mu\text{M}$  CaFADS, 10 mM  $\text{MgCl}_2$ , in PIPES 20 mM, pH 7.0, 2.5% DMSO, and the corresponding compound of the chemical library at a final concentration of  $250\ \mu\text{M}$ . Reactions were initiated through addition of  $50\ \mu\text{M}$  ATP, being the final reaction volume  $100\ \mu\text{l}$ . Controls, which contained the reaction mixture but not any chemical from the library, were added both to the first and last columns of the plate. Flavin fluorescence in each well was registered at  $25\ ^\circ\text{C}$ , every 50 s during 15 min. Excitation and emission wavelengths were 440 and 530 nm, respectively. The slope of the resulting line, recorded between 0 and 6 min, was calculated for every compound, and also for the controls, as well as the fluorescence change per time unit ( $\Delta F/\Delta t$ ). The compounds that decreased the reaction rate below the average reaction rate of the controls minus the standard deviation could be preselected as potential inhibitors, but we reduced further the cut-off by selecting only those compounds inhibiting more than 50% of the controls activity as HTS hits.

### Identification of the activity inhibited by each of the HTS hits

The decreasing of the reaction rate by the presence of the HTS hits might be consequence of the compounds inhibiting the RFK activity, the FMNAT one, or both of them; also, it could be a false positive due to the properties of pan assay interference compounds (PAINS). To clarify this point, we first checked that there were no PAINS among the HTS hits using the FAF-Drug4 web server<sup>31</sup>. Then, the RFK and FMNAT reactions were individually assayed in the presence of the HTS hits at  $25\ ^\circ\text{C}$ . Reaction mixtures contained  $50\ \mu\text{M}$  ATP,  $5\ \mu\text{M}$  RF,  $0.4\ \mu\text{M}$  CaFADS in 20 mM PIPES, pH 7.0,  $0.8\ \text{mM}$   $\text{MgCl}_2$ , when assaying the RFK activity, and  $50\ \mu\text{M}$  ATP,  $10\ \mu\text{M}$  FMN,  $0.4\ \mu\text{M}$  CaFADS in 20 mM PIPES, pH 7.0,  $10\ \text{mM}$   $\text{MgCl}_2$  when measuring the FMNAT reaction. Each HTS hit was tested again at  $250\ \mu\text{M}$  for each of the two enzymatic reactions. Finally, reactions were stopped by boiling the samples at  $100\ ^\circ\text{C}$  for 5 min, and the precipitated protein was eliminated through centrifugation. The transformation of RF into FMN or FAD was evaluated through flavins separation by HPLC, as previously described<sup>27</sup>. Those HTS hits decreasing the FMNAT activity by more than 95% of the controls, without significantly affecting the RFK activity (rates over 75% those of the controls) were selected as FMNAT hits for further assessment. When assaying the HTS hits against

the FMNAT activity of *SpnFADS*, similar conditions were used but samples contained 3 mM sodium dithionite to maintain the flavin in its reduced state<sup>23</sup>. Data were processed as previously reported<sup>27</sup>. All the experiments were performed in triplicate.

#### Determination of the potency of FMNAT hits

To determine the IC<sub>50</sub> values of the FMNAT hits, the FMNAT activity was assayed at different concentrations of each inhibitor (0–100 μM range) and 25 °C. Experiments were performed and analysed through HPLC as described above. Positive controls (without any hit compound) were included in every reaction set. DMSO concentration was kept at 2.5% in all samples. All the experiments were performed in triplicate.

#### Determination of the inhibition mechanism of CaFADS by FMNAT hits 24, 27 and 31

The inhibition mechanism was further studied for the three FMNAT hits that showed the lowest IC<sub>50</sub> and minimal residual FMNAT activities, namely, 24, 27 and 31. Reaction mixtures containing 0–100 μM of each compound, 1–20 μM FMN and 400 μM ATP were used when analysing the inhibitory effect of the compound regarding the FMN substrate, while 5–400 μM ATP and 15 μM FMN when analysing the effect of the inhibitor regarding the ATP substrate. All the experiments were carried out in 20 mM PIPES, 10 mM MgCl<sub>2</sub>, pH 7.0, 2.5% DMSO at 25 °C, being the final reaction volume 500 μL. The reactions were initiated by addition of CaFADS at a final concentration of ~40 nM, followed by 1 min incubation. The flavin composition of the supernatant was analysed as previously described<sup>27</sup>. All the experiments were performed in triplicate. The effect of the inhibitors on K<sub>m</sub> and V<sub>max</sub> was determined by fitting the data sets to the Michaelis–Menten model. Additionally, data were globally fit to Lineweaver–Burk equations for competitive, uncompetitive, non-competitive or mixed inhibition, yielding K<sub>i</sub>, as well as K<sub>i</sub>' when applying, for each compound (Equations (1–4), respectively).

$$\frac{1}{V_0} = \frac{\left(1 + \frac{[I]}{K_i}\right) \cdot K_m}{V_{\max}} \cdot \frac{1}{[S]} + \frac{1}{V_{\max}} \quad (1)$$

$$\frac{1}{V_0} = \frac{\left(1 + \frac{[I]}{K_i'}\right)}{V_{\max}} + \frac{K_m}{V_{\max}} \cdot \frac{1}{[S]} \quad (2)$$

$$\frac{1}{V_0} = \frac{\left(1 + \frac{[I]}{K_i}\right)}{V_{\max}} + \frac{\left(1 + \frac{[I]}{K_i}\right) \cdot K_m}{V_{\max}} \cdot \frac{1}{[S]} \quad (3)$$

$$\frac{1}{V_0} = \frac{\left(1 + \frac{[I]}{K_i}\right) \cdot K_m}{V_{\max}} \cdot \frac{1}{[S]} + \frac{\left(1 + \frac{[I]}{K_i'}\right)}{V_{\max}} \quad (4)$$

#### Thermodynamic characterisation of binding of hits 24, 27 and 31 through isothermal titration calorimetry (ITC)

ITC experiments were performed to characterise the protein's affinity for the selected compounds, as also the thermodynamic parameters that drive the interaction. Experiments were carried out in an AutoITC200 (*MicroCal*) thermostated at 25 °C. In these experiments, ~400 μM of each compound were used to titrate ~25 μM CaFADS contained in a 200 μL cell. However, when saturation of the protein was not reached, higher concentrations of compounds were employed. The titrations were performed by stepwise injections of the titrating compound. Up to 19 injections of 2 μL were added to the cell sample and mixed using a 1000 rpm

stirrer syringe. The compounds and the protein were dissolved in 20 mM PIPES, pH 7.0, 10 mM MgCl<sub>2</sub> and degassed prior to titration. DMSO was added to the protein and ligand samples, until reach a final concentration of 3%. The association constant (K<sub>a</sub>), the enthalpy variation (ΔH) and the binding stoichiometry (N), were obtained through non-linear regression of the data to a model for one or two independent binding sites, implemented in Origin 7.0 (*OriginLab*) as previously described<sup>27,29</sup>. The entropic contribution (–TΔS), the Gibbs free energy (ΔG) and the dissociation constant (K<sub>d</sub>) were obtained through essential thermodynamic equations.

#### Docking of hits 24, 27 and 31 to the FMNAT module of CaFADS

The AutoDock4.2 software<sup>32–34</sup> and the coordinates of a monomer from CaFADS (PDB 2X0K)<sup>24</sup> were used to obtain the interaction models with 24, 27 and 31. The space sampling was defined using a grid box of 90 points in each dimension, and placing the H57 NE atom of the FMNAT module as the grid box centre. The grid size was 0.375 Å. The search was performed using the Lamarckian genetic algorithm, with a starting population of 150 individuals, using 25,000,000 energy evaluations and 27,000 generations. The 24, 27 and 31 initial structures for the docking protocol were optimised using the functional B3LYP with the basis set 6–31 G (d,p) and the gaussian09 software<sup>35</sup>. The structural poses with the lowest docking score were selected and analysed.

#### Determination of the antibacterial activity of the HTS hits

The antimicrobial activity of the HTS hits was tested by the colorimetric method of the resazurin microplate assay<sup>36</sup> according to broth microdilution method guidelines (CLSI; Clinical and Laboratory Standards Institute). Serial 2-fold dilutions of the HTS hits were performed in BHI medium, in 96-well microtiter plates, with a final volume of 100 μL per well. Subsequently, liquid cultures of *C. ammoniagenes* ATCC 6872 in logarithmic phase were adjusted to 10<sup>6</sup> CFU/ml in BHI broth, and 100 μL of this suspension were added to each well, making a final inoculum of 5 × 10<sup>5</sup> CFU/ml. Plates were incubated 16 h at 37 °C. 30 μL of 0.1 mg/ml resazurin solution were then added to each well, and results were observed after 4 h of incubation at 37 °C. Resazurin (blue) is an indicator of bacterial growth, since metabolic activity of bacteria reduces it to resorufin (pink). The minimum inhibitory concentration (MIC) is the lowest concentration of compound that does not change the resazurin colour from blue to pink.

Similarly, the HTS hits were also assayed at 37 °C against *M. tuberculosis* ATCC 27,294 and *S. pneumoniae* ATCC 49619 cells. In these experiments the initial cell concentration was also 5 × 10<sup>5</sup> CFU/ml, and plates were incubated for 10 h (*S. pneumoniae*), and 6 days (*M. tuberculosis*) before addition of resazurin. Results were observed after incubation with resazurin 4 h and two days for *S. pneumoniae* and *M. tuberculosis*, respectively. In these experiments, culture media were; Middlebrook 7H9 (Difco) supplemented with 10% ADC (0.2% dextrose, 0.5% V fraction BSA and 0.0003% bovine catalase) (BD Difco) and with 0.5% glycerol (Scharlau) for *M. tuberculosis* growth, and BHI supplemented with 4% FBS (Gibco) for *S. pneumoniae* growth.

#### Statistics

Results are expressed as the mean ± the standard deviation (SD) or as the mean ± the standard error (SE) of the regression. When indicated, one-way analysis of variance (ANOVA) was performed to determine statistical significance.

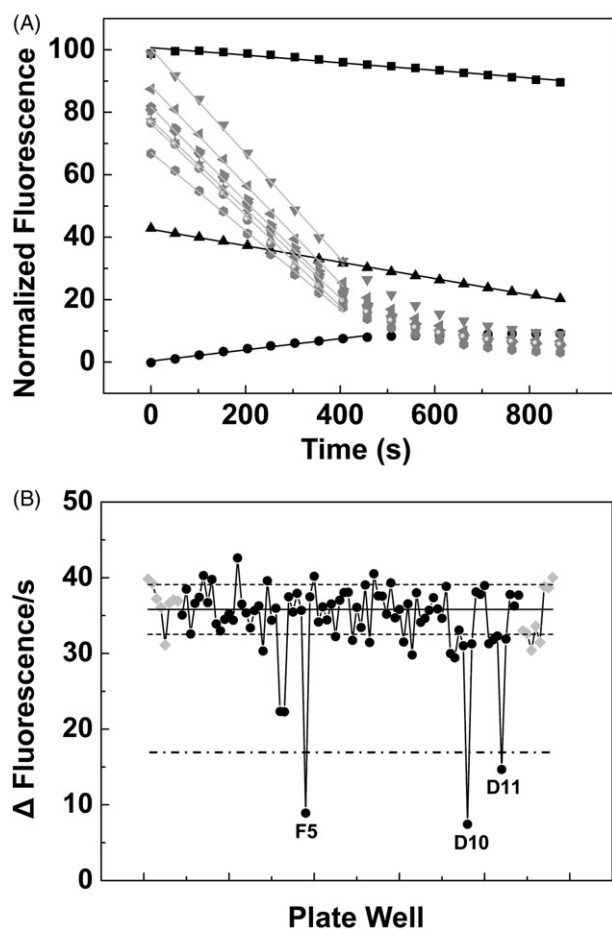


**Figure 1.** Activity-based high throughput screening (HTS) for the discovery of inhibitors of the RFK and/or the FMNAT activities of *CaFADS*. (A) Example of the flavin fluorescence evolution over time for three of the identified hits and for control assays. Reaction mixtures were incubated at 25 °C and contained 5 μM RF, 50 μM ATP, 0.4 μM *CaFADS*, 10 mM MgCl<sub>2</sub>, in PIPES 20 mM, pH 7.0, 2.5% DMSO. The black symbols and lines correspond to kinetic traces at wells containing library compounds at 250 μM, while grey ones correspond to control wells. (B) Initial velocities (Δfluorescence/s) for the reactions in each of the wells of a HTS plate. Data from wells containing chemical library compounds are in black while controls are in grey. The solid line represents the average velocity obtained for the positive controls of the reaction and the dotted lines are the average velocity plus and minus the standard deviation. The letters and numbers indicate the position of the well in the plate (row and a column respectively) for each specific selected measurement. A bold dashed line indicates 50% the rates of controls.

## Results

### Identification of potential inhibitors of the *CaFADS* activities through HTS

To identify potential inhibitors of the *CaFADS* activities we designed the activity-based HTS assay described in the methods section, which allowed to determine rates for the transformation of RF into FAD (via the FMN intermediate) in each one of the plate wells. Wells containing chemicals of the library and decreasing reaction rates relative to the controls (absence of chemicals) were preselected as containing compounds that are potential inhibitors of at least one of the *CaFADS* activities. Thus, among the 1240 compounds of the chemical library, 140 (13.5%) reduced the *CaFADS* activity levels below the mean of the positive controls minus twice its standard deviation, and of them, 37 (3.6%) reduced the positive controls average rate for FAD formation in a factor higher than 0.5 (Figure 1). Those 37 compounds were selected as the HTS hits (Supplementary Chart SD1).

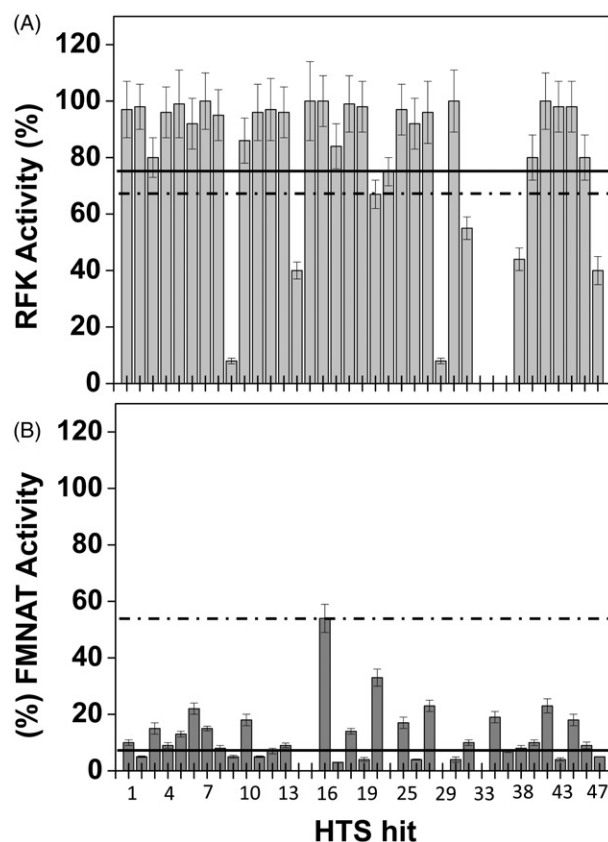


**Figure 2.** Effect of the HTS hits on the RFK and FMNAT activities of *CaFADS*. Residual (A) RFK and (B) FMNAT activities when assayed in the presence of 250 μM of the 37 HTS hits. In (A), the columns below the dashed line present statistical significant inhibition by the corresponding hit ( $p < 0.002$ , 67% remaining activity) related to the control *CaFADS* RFK activity. In (B), all hits produce statistical significant inhibition ( $p < 0.0001$ , dashed line) when compared with the controls of the *CaFADS* FMNAT activity. Solid lines indicate 75 and 5% of the control RFK and FMNAT activities, respectively. The HTS hits displaying <5% and >75% of the control FMNAT and RFK activities, respectively, were selected for further study. Experiments carried out in 20 mM PIPES, pH 7.0, 2.5% DMSO at 25 °C, with 7.5 μM RF, 350 μM ATP, 0.8 mM MgCl<sub>2</sub> (for the RFK activity) or 15 μM FMN, 350 μM ATP, 10 mM MgCl<sub>2</sub> (for the FMNAT activity) ( $n = 3$ ; mean ± SD).

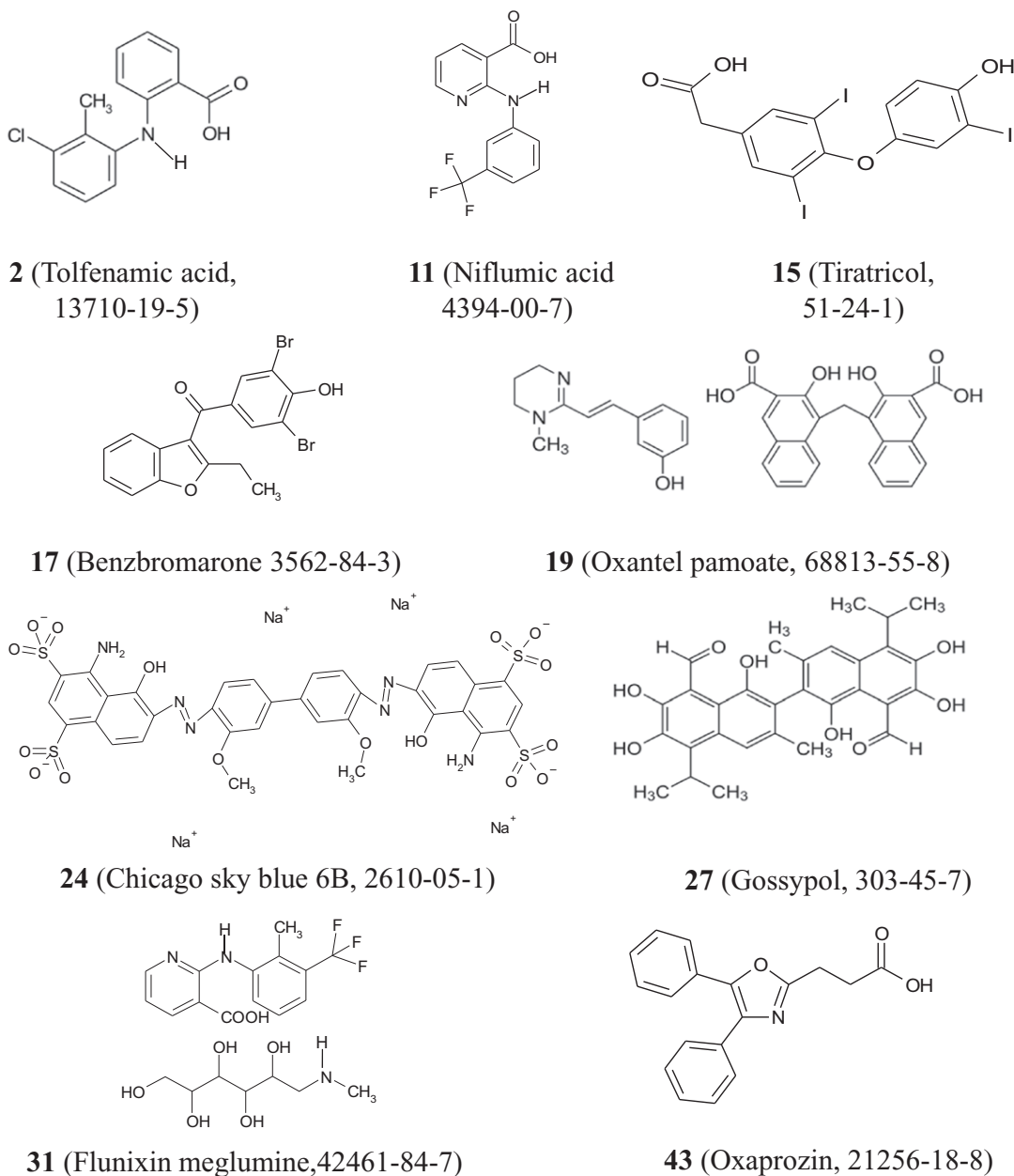
### Effect of the HTS hits on the RFK and FMNAT activities of *CaFADS*

We then move to identify which one of the activities (RFK or FMNAT), and in which extension, was affected by each one of these 37 HTS hits. With this aim, we assayed the effect of the HTS hits both on the *CaFADS* RFK and FMNAT activities. Figure 2 and Table 1 summarise the results. Comparison of Figure 2(A,B) shows that, in general and under the assay conditions, the 37 HTS hits produced a stronger deleterious effect on the FMNAT activity (all decreased the activity of the controls in more than 50%) than on the RFK one. The FMNAT module of *CaFADS* does not have sequence or structural homology with the mammalian protein but the RFK module belongs to the eukaryotic RFKs family. Therefore, we decided to continue the study with the HTS hits that inhibit the FMNAT activity, since they are more likely to be specific to the bacterial proteins. Thus, we choose the HTS hits that decreased the FMNAT activity below 5% of that of the controls, but maintained over 75% the RFK activity (Figure 2, Table 1). Thus, among (2)\(11), tiratricol (15), benzbromarone (17), oxantel pamoate (19), Chicago sky blue 6B (24), gossypol (27), flunixin meglumine (31) and oxaprozin (43) (Chart 1) were selected as FMNAT hits. It is

**Table 1.** RFK and FMN residual activities of CaFADS in the presence of the HTS hits.

|                           | % Residual RFK activity |       |       |   |
|---------------------------|-------------------------|-------|-------|---|
|                           | ≤ 5                     | 5–50  | 50–75 | ≥ 75  |
| % Residual FMNAT activity |                         |       |       |   |
| ≤ 5                       | 9, 29, 33, 37           | 14,47 |       | 2, 11, 15, 17, 19, 24, 27, 31, 43                               |
| 5–50                      | 35                      | 38    | 22,32 | 1, 3, 4, 5, 6, 7, 8, 10, 12, 13, 16, 18, 25, 28, 39, 40, 44, 46 |
| ≥ 50                      | –                       | –     | –     | –   |

Values measured at 25 °C, in 20 mM PIPES, pH 7.0, 2.5% DMSO and 0.8 or 10 mM MgCl<sub>2</sub> when assaying the RFK or the FMNAT activities, respectively. The final concentration of each HTS hit was 250 μM and saturating concentrations of all the substrates were used. The compounds highlighted in italics completely inhibited the FMNAT activity with minor effects on the RFK one, and were selected as FMNAT hits.

**Chart 1.** Chemical structures of compounds selected as FMNAT hits for CaFADS.

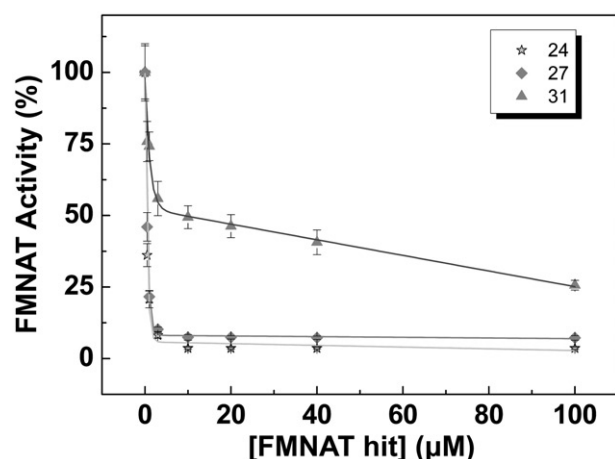


**Figure 3.** Dose–response curves for the FMNAT activity of *CaFADS* in the presence of representative hits. Values derived from these representations are included in Table 2. Experiments performed at 25 °C in 20 mM PIPES, pH 7.0, 10 mM MgCl<sub>2</sub>, 2.5% DMSO, with 15 μM FMN and 350 μM ATP ( $n = 3$ , mean  $\pm$  SD).

worth noticing that although some of these compounds are apparently structurally related with other of the HTS hits, slight differences in functional groups and geometries induce different enzymatic responses in the FMNAT or RFK activities. This is a fact of particular interest when developing specific inhibitors.

To rate the power of these 9 FMNAT hits as inhibitors of the *CaFADS* FMNAT activity, their half maximal inhibitory concentrations (IC<sub>50</sub>) and the remaining activity at 50 μM of each compound were determined (Figure 3, Table 2). The 9 compounds yielded IC<sub>50</sub> values in the micromolar range, reducing by more than half the activity of the controls. Considering both their IC<sub>50</sub> value and residual activity, the most potent inhibitors were 24 (IC<sub>50</sub> = 0.4  $\pm$  0.1 μM), 27 (IC<sub>50</sub> = 0.5  $\pm$  0.1 μM) and 31 (IC<sub>50</sub> = 6.6  $\pm$  0.6 μM). These three compounds produce residual activities below 25% of the controls. Compound 43 also showed high inhibitory potency, but due to its low solubility in the working buffer it was discarded.

#### The inhibition mechanisms of 24, 27 and 31

To determine the inhibition mechanism of the hits 24, 27 and 31, we measured the FMNAT activity of *CaFADS* in the presence of increasing concentrations of each compound. Considering that this is a bi-substrate activity, for each compound we carried out two set of experiments at; (i) saturating ATP and different FMN concentrations, and (ii) saturating FMN and increasing ATP concentrations. Then we fit our experimental data to the Michaelis–Menten model, obtaining  $K_m$  and  $k_{cat}$  values. The analysis of the evolution of these constants on the hits concentrations, together with the corresponding Lineweaver–Burk plots [representation of data as double inverses and fit to Equations (1–4)] (Figure 4, Supplementary Figures SD2 and SD3, Supplementary Table SP1) allowed identifying the inhibitory mechanisms of the 24, 27 and 31 hits, as well as the corresponding inhibition constants ( $K_i$  or  $K_j$  and  $K'_i$ ) (Table 3). The experiments carried out at saturating ATP (varying the FMN concentrations), revealed that the three compounds are strong non-competitive inhibitors of the *CaFADS* FMNAT activity regarding the FMN substrate ( $K_i$  values around 0.08 μM, Table 3). Nevertheless, when using a constant and saturating FMN concentration but varying the ATP concentration, their inhibition mechanisms differ among

**Table 2.** Effect of the FMNAT hits on the FMNAT activity of *CaFADS*.

| FMNAT hit       | Residual activity <sup>a</sup> (%) | IC <sub>50</sub> <sup>b</sup> (μM) |
|-----------------|------------------------------------|------------------------------------|
| 2               | 41.1 $\pm$ 5.2                     | 8.9 $\pm$ 1.0                      |
| 11              | 34.6 $\pm$ 4.9                     | 9.0 $\pm$ 1.3                      |
| 15              | 45.3 $\pm$ 4.2                     | 40.7 $\pm$ 3.9                     |
| 17              | 33.5 $\pm$ 10.1                    | 12.8 $\pm$ 3.4                     |
| 19              | 43.3 $\pm$ 3.9                     | 20.8 $\pm$ 2.6                     |
| 24              | 3.6 $\pm$ 0.2                      | 0.4 $\pm$ 0.1                      |
| 27              | 6.9 $\pm$ 0.8                      | 0.5 $\pm$ 0.1                      |
| 31              | 24.5 $\pm$ 1.9                     | 6.6 $\pm$ 0.6                      |
| 43 <sup>c</sup> | 20.3 $\pm$ 5.2                     | 1.0 $\pm$ 0.5                      |

Experiments carried out at 25 °C, in 20 mM PIPES, pH 7.0, 10 mM MgCl<sub>2</sub> at saturating FMN and ATP. All samples contained 2.5% DMSO ( $n = 3$ , mean  $\pm$  SD).

<sup>a</sup>Remaining activity in the presence of 50 μM of each compound. All data show statistical significance differences when compared with activity in the compound absence (\*\*\*)  $p < 0.0001$ .

<sup>b</sup>Compounds assayed in the 0–100 μM concentration range.

<sup>c</sup>This compound shows very low water solubility, so it was discarded to continue the study even though its good properties.

them. 24 is a strong ATP uncompetitive inhibitor ( $K_i = 0.08 \pm 0.03$  μM), therefore, it is able to bind the *CaFADS*-ATP complex and reduce the amount of enzyme that is available to react. 27 is a strong competitive inhibitor regarding the ATP substrate ( $K_i = 0.06 \pm 0.01$  μM), while 31 is a considerably poorer mixed inhibitor. Thus, 31 is able to bind to both the free enzyme and the *CaFADS*-ATP complex, although binding constants indicate that binding to free *CaFADS* is preferred ( $K_i = 3.5 \pm 1.0$  μM versus  $K'_i = 18.4 \pm 4.0$  μM, Table 3).

#### Binding of 24, 27 and 31 to CaFADS

The interaction of *CaFADS* with compounds 24, 27 and 31 was characterised using ITC. This is a very powerful technique because first the shape of the thermograms informs us about the number of binding sites related to the thermodynamic nature of binding. Then, fitting of experimental data to the equations describing binding models allow determining thermodynamic binding parameters, as well as binding stoichiometry at each of the different binding sites. Thus, analysis of our ITC titrations indicates that the three compounds bind the enzyme at, at least, one binding site (Figure 5(A), Table 4). Thus, we identified in *CaFADS* a unique binding site of moderate-low affinity for 31 ( $N \approx 1$ ,  $K_d = 30.9 \pm 2.8$  μM) and two binding sites of high and similar affinity for 27 ( $N \approx 2$ ,  $K_{d,av} = 0.7 \pm 0.07$  μM, this  $K_{d,av}$  value is an average value, since the similarity between the two binding sites prevents them to be distinguished). These 27 and 31 binding sites are expected to be located at the enzyme FMNAT domain, since that is the inhibited activity. The interaction between the hit 24 and the enzyme resulted more complicated, because our ITC data indicate that compound 24 binds to the protein at three sites. Two of them show similar and strong affinity ( $K_{d,av} = 1.1 \pm 0.1$  μM) and therefore, we suggest that they might be located at the FMNAT module, since that is the activity mainly inhibited by compound 24. The third site for 24 binding has lower affinity ( $K_d = 161 \pm 20$  μM). Since this compound also mildly inhibits the RFK activity, we presume this third binding site may be at the RFK module. All bindings here characterised (with the only exception of the low affinity binding site for 24) are favoured by the enthalpic contribution (Figure 5(B), Table 4). This suggests a net gain of H-bonding and ion-pair interactions and indicates specific binding interactions. Regarding the entropic contribution to the binding free energy, it is small and favourable for 24 and 27, and only slightly unfavourable for 31 (Figure 5(B), Table 4). However, it drives the binding of 24 to the



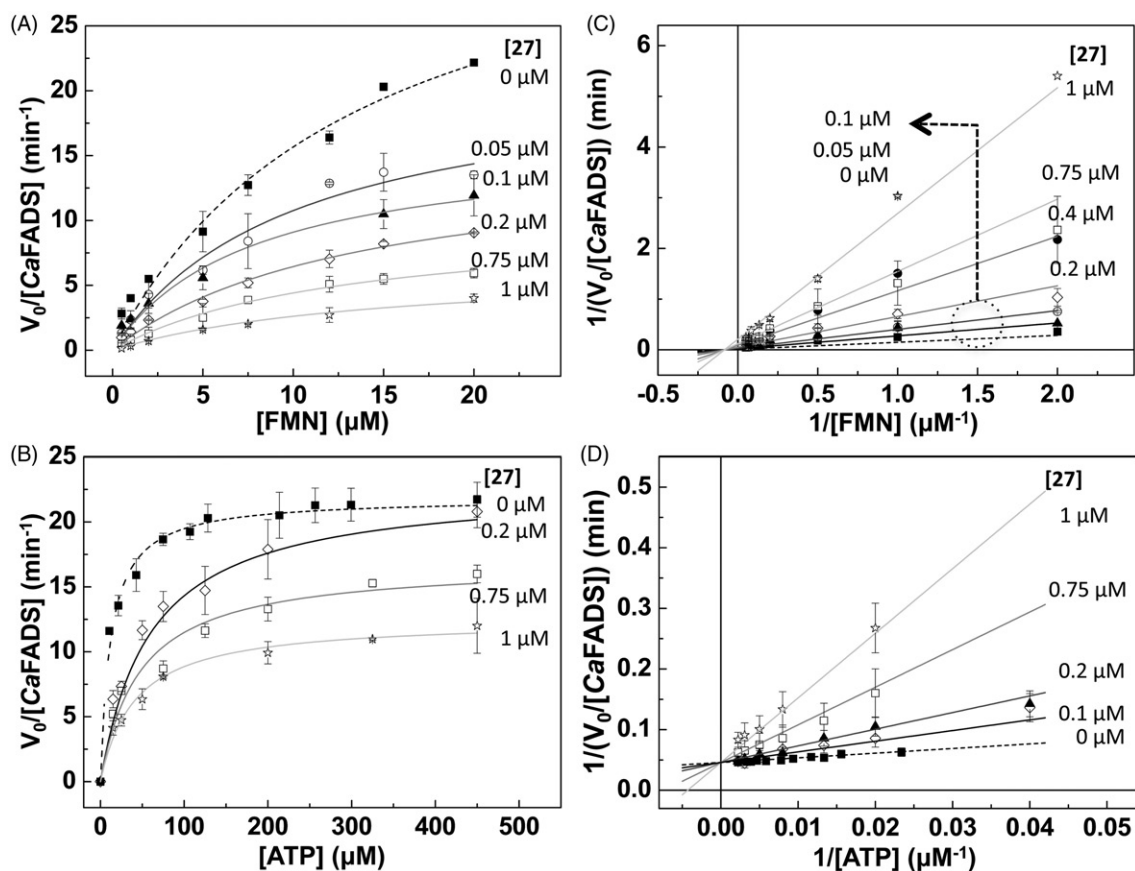


**Figure 4.** Hit 27 as an inhibitor of the FMNAT activity of CaFADS. Michaelis–Menten plots at different concentrations of 27 and saturation (A) of ATP and (B) of FMN. Lineweaver–Burk representations with global fit to (C) non-competitive inhibition at saturating ATP and (D) competitive inhibition at saturating FMN. Reaction rates obtained in 20 mM PIPES, pH 7.0, 10 mM MgCl<sub>2</sub> at 25 °C, with 15 μM FMN and 10–450 μM ATP (FMN saturating) or with 350 μM ATP and 0.5–20 μM FMN (ATP saturating). All samples contained 2.5% DMSO ( $n = 3$ , mean  $\pm$  SD).

**Table 3.** Inhibition constants and mechanisms of the best FMNAT hits relative to the FMNAT activity of CaFADS.

|    | Saturating ATP          |                      | Saturating FMN          |                          |                      |
|----|-------------------------|----------------------|-------------------------|--------------------------|----------------------|
|    | $K_i$ ( $\mu\text{M}$ ) | Inhibition mechanism | $K_i$ ( $\mu\text{M}$ ) | $K'_i$ ( $\mu\text{M}$ ) | Inhibition mechanism |
| 24 | $0.07 \pm 0.01$         | Non-competitive      | $0.08 \pm 0.03$         | –                        | Uncompetitive        |
| 27 | $0.08 \pm 0.01$         | Non-competitive      | $0.06 \pm 0.01$         | –                        | Competitive          |
| 31 | $0.09 \pm 0.03$         | Non-competitive      | $3.5 \pm 1.0$           | $18.4 \pm 4.0$           | Mixed                |

Experimental data recorded at 25 °C in 20 mM PIPES, pH 7.0, 10 mM MgCl<sub>2</sub> and 2.5% DMSO. Data obtained by globally fitting the experimental data to the corresponding Lineweaver–Burk inhibition model.

RFK module (site 3 [Figure 5\(B\)](#)), revealing that it might be non-specific and that could occur due to the compound hydrophobicity and rigidity<sup>37</sup>.

To investigate how the FMNAT module of CaFADS accommodates these compounds, we performed a computational protein–ligand docking ([Figure 6](#) and [Supplementary Figure SD4](#)). In the highest-scoring docking mode, as well as for the best five poses (purple molecule in [Figure 6\(B\)](#), [Supplementary Figure SD4](#), respectively), 24<sub>1</sub> (1 indicates the first molecule of 24 docked) is situated in the substrates binding pockets ([Figure 6A](#))<sup>24</sup>. One of the 24<sub>1</sub> moieties binds through one of its sulphates to S164 and H31. 24<sub>1</sub> is in addition H-bonded to the N125 catalytic base<sup>17</sup>, as well as to Y106, T127 and N131 at the loop that forms the upper flavin ring binding site ([Figure 6\(B\)](#)). Since our ITC data suggest two binding sites for compound 24 at the FMNAT module, we carried out an additional docking analysis to identify the second site, 24<sub>2</sub> (pink molecule in [Figure 6\(B\)](#)), using as receptor our highest-scoring FADS:24<sub>1</sub> model. Considering the binding

energies ([Table 4](#)) this site is expected to be less populated, but given that 24 is an ATP uncompetitive inhibitor, the docking binding energy could improve if we consider the ATP substrate presence instead of the 24<sub>1</sub> molecule. Additionally, it is worth noting that in the presence of substrates or products, the 24 binding conformations might differ from the ones presented here. In the most favourable docking poses, the first molecule of 27 bound to the protein (27<sub>1</sub>) is H-bonded by T127 and the N125 catalytic base at the binding site of the ATP phosphates<sup>17</sup> (purple molecule in [Figure 6\(C\)](#) and [SD4](#)), in agreement with 27 being an ATP competitive inhibitor. Because two binding sites were again predicted by ITC at the FMNAT site, we carried out a second docking using as receptor the highest-scoring FADS:27<sub>1</sub> model. 27<sub>2</sub> is stabilised by H-bonds with the N-terminal of the  $\alpha 6n$  helix, T165 and R168, at the ATP binding site entrance (pink molecule in [Figure 6\(C\)](#)). We observed direct interaction between the two 27 molecules, and 27<sub>2</sub> somehow resembling the 24<sub>1</sub> binding (purple molecule in [Figure 6\(B\)](#)). For 31, we only carried

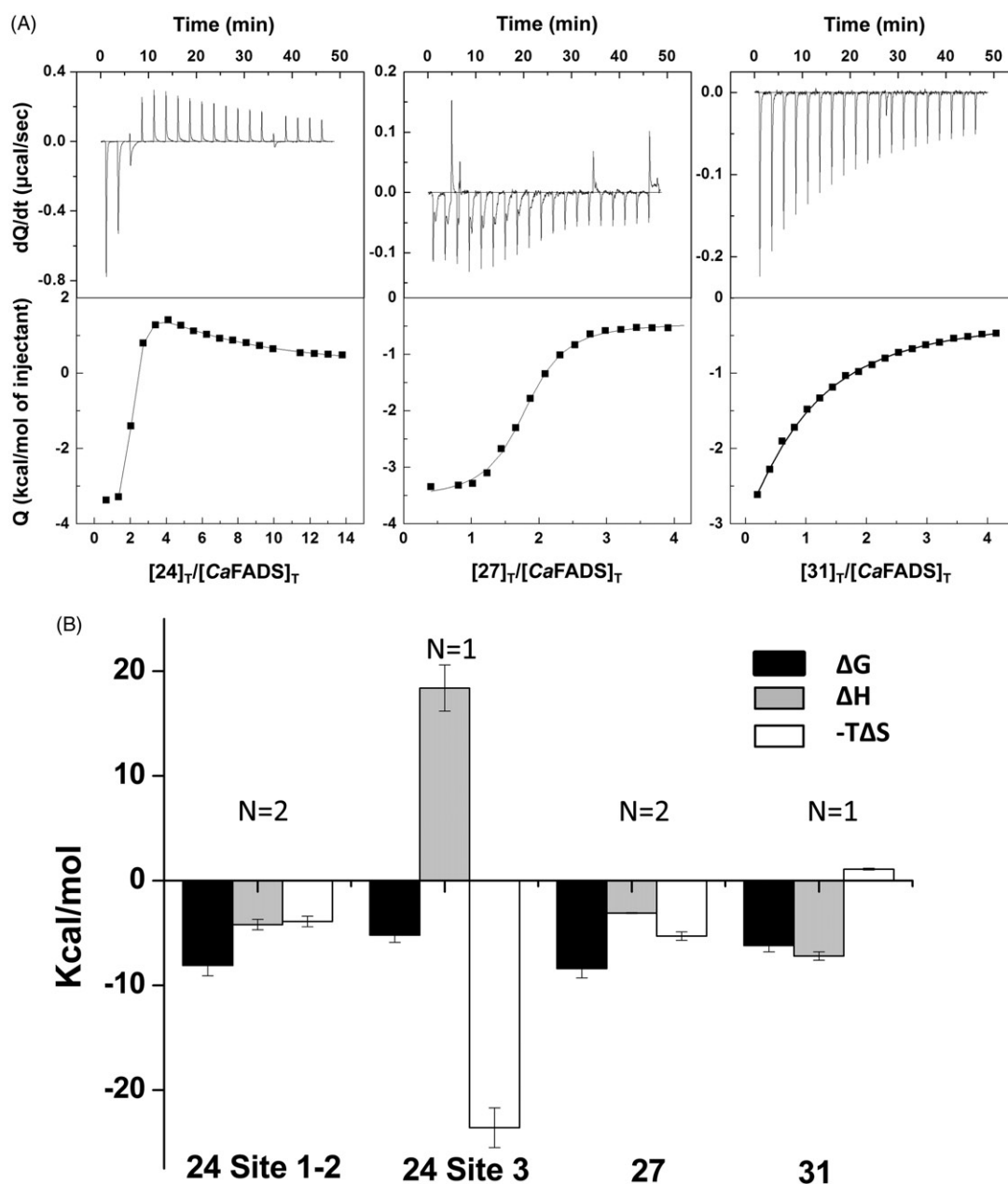


**Figure 5.** Thermodynamic analysis of the binding of the selected FMNAT hits to CaFADS. (A) Calorimetric titrations for the 24, 27 and 31 compounds. The upper panels show the thermograms for the interaction and the lower panels show the corresponding binding isotherms with integrated heats. (B) Thermodynamic dissections of the interaction of CaFADS with each of the selected compounds. The binding Gibbs energy ( $\Delta G$ ), enthalpy ( $\Delta H$ ) and entropy ( $-T\Delta S$ ) are represented in black, grey and white bars, respectively. Experiments were carried out at 25 °C, in 20 mM PIPES, pH 7.0, 10 mM MgCl<sub>2</sub> and 3% DMSO.

**Table 4.** Thermodynamic parameters for the interaction of CaFADS with the hits 24, 27 and 31.

| Hit      | N           | $K_d$ ( $\mu$ M) | $\Delta G$ (kcal/mol) | $\Delta H$ (kcal/mol) | $-T\Delta S$ (kcal/mol) | Docking $\Delta G^b$ (kcal/mol) |
|----------|-------------|------------------|-----------------------|-----------------------|-------------------------|---------------------------------|
| 24       |             |                  |                       |                       |                         |                                 |
| Site 1-2 | $\approx 2$ | $1.1 \pm 0.1^a$  | $-8.1 \pm 1.0^a$      | $-4.2 \pm 0.5^a$      | $-3.9 \pm 0.5^a$        | $-8.2 \pm 0.5/-4.2 \pm 0.4$     |
| Site 3   | $\approx 1$ | $161 \pm 20$     | $-5.2 \pm 0.7$        | $18.4 \pm 2.2$        | $-23.6 \pm 1.9$         | n.d. <sup>c</sup>               |
| 27       | $\approx 2$ | $0.7 \pm 0.07^a$ | $-8.4 \pm 0.9^a$      | $-3.1 \pm 0.1^a$      | $-5.3 \pm 0.4^a$        | $-11.9 \pm 0.1/-9.1 \pm 0.1$    |
| 31       | $\approx 1$ | $30.9 \pm 2.8$   | $-6.2 \pm 0.6$        | $-7.2 \pm 0.4$        | $1.1 \pm 0.1$           | $-6.59 \pm 0.1$                 |

ITC experiments performed at 25 °C, in PIPES 20 mM, pH 7.0, 10 mM MgCl<sub>2</sub>, 3% DMSO.

<sup>a</sup>These parameters correspond to average values for the binding of two hit molecules.

<sup>b</sup>Docking score for the best pose, with standard deviation for the best five poses.

<sup>c</sup>Not calculated.

out the flunixin docking, given that this compound is the bio-active agent of 31 and meglumine is the excipient. The best poses for 31 binding are suggested at the ATP binding site (Figure 6(D) and SD4), stabilised by a H-bond with H31. This

binding is coherent with the ATP mixed inhibition mechanism of 31. In all cases, the H-bond interactions explain the favourable enthalpic binding contributions revealed by ITC, while the favourable entropic contributions can be attributed to the expelling of

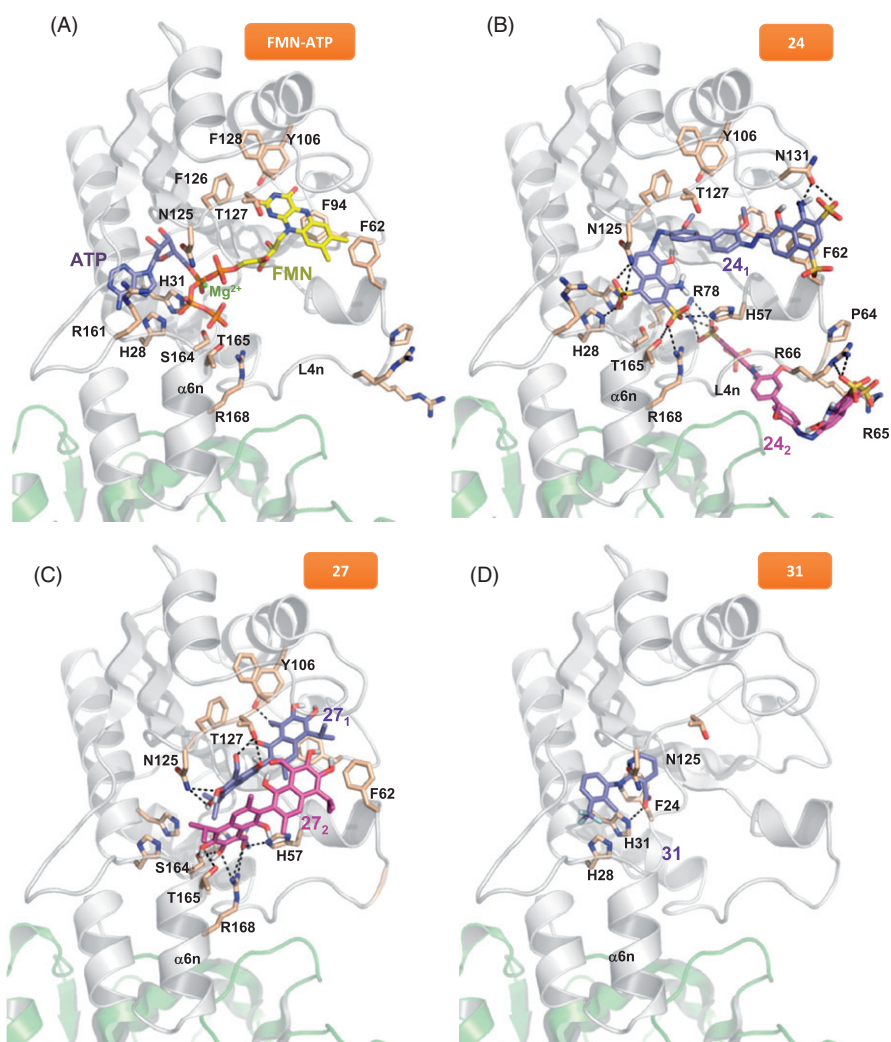


**Figure 6.** Docking models for the binding conformations of the selected FMNAT hits to the *CaFADS* FMNAT module. (A) Model of the theoretical placement of substrates. ATP in violet,  $Mg^{2+}$  as a green dot and FMN in yellow. Data from (24). Best docking pose of (B) FADS:24<sub>1</sub> and FADS:24<sub>1</sub>:24<sub>2</sub> models (24<sub>1</sub> in violet, 24<sub>2</sub> in pink), (C) FADS:27 and FADS:27<sub>1</sub>:27<sub>2</sub> models (27<sub>1</sub> in violet, 27<sub>2</sub> in pink), and (D) FADS:31 (31 in violet, docking corresponds only to the flunixin bioactive part of 31, meglumine is the excipient). Side-chains of key residues are shown as CPK sticks with carbons in wheat. H-bonds are indicated as dashed lines. The protein is shown as a cartoon, having the FMNAT and RFK modules coloured in grey and green, respectively. Docking was performed using Autodock4.2.

structural water molecules from the binding cavities, particularly at the substrates binding sites.

#### Effect of the HTS hits on the RFK and FMNAT activities of *SpnFADS*

To determine whether the 37 HTS hits were specific for *CaFADS* or might have effect on other similar bacterial FADS family members, we tested their effects on the RFK and FMNAT activities of the also bimodular and bifunctional *SpnFADS*. Eleven of the 37 HTS hits inhibited either the RFK or the FMNAT activities of *SpnFADS* (Table 5). However, most compounds exhibited  $IC_{50}$  in the high micromolar range ( $>65 \mu M$ ). Only fluvastatin sodium salt (37) for the FMNAT activity, and thonzonium bromide (9) and 27 for the RFK one showed  $IC_{50}$  lower than  $10 \mu M$ . 37 ( $IC_{50} = 7 \pm 1 \mu M$ ) and 9 ( $IC_{50} = 6 \pm 1 \mu M$ ) inhibit completely the corresponding activity, but the residual RFK activity with 27 was too high to be considered as a good inhibitor.

#### Effect of selected HTS hits on different bacterial cells

To assess the effect of the HTS hits on the growth of different bacteria, we determined their MIC (Table 6). Bacterial cells of *C.*

*ammoniagenes*, *M. tuberculosis* and *S. pneumoniae* were grown in the presence of increasing concentrations of the selected HTS hits. Among the 37 HTS hits, only twelve, six and nine compounds inhibited, respectively, the growth of *C. ammoniagenes*, *M. tuberculosis* and *S. pneumoniae*. Among these, only 9, benzenethonium chloride (14), methyl-benzethonium chloride (29), alexidine dihydrochloride (33) and verteporfin (47) showed MIC values for *C. ammoniagenes* lower than  $2 \mu M$ , while 17, 24, diethylstilbestrol (32) and dienestrol (35) show values between 2 and  $16 \mu M$  (Table 6). Interestingly, the compounds that presented better properties against the *CaFADS* FMNAT activity (24, 27 and 31) have a poor growth inhibitory effect on the bacterial cells (24 and 27 have  $MIC \approx 32$  and  $64 \mu M$ , respectively, whereas the MIC of 31 was  $>64 \mu M$ ). Nonetheless, it is worth to notice that 9, 14, 29, 33 and 47 show in common the considerable ability to inhibit both of the *CaFADS* enzymatic activities as well as to greatly affect the *C. ammoniagenes* growth (Table 1, Figure 7). Regarding *M. tuberculosis* growth, sulfasalazine (8), 9, 24 and 29 produced mild effects on cell growth, but only 14 and 33 showed MIC values below  $8 \mu M$ . Table 6 summarises the effect of some selected compounds on *S. pneumoniae*, indicating that 9, 14, 29 and 33 inhibit moderately its growth.

**Table 5.** Effect of selected HTS hits on the RFK and FMNAT activities of *SpnFADS*.

| HTS hit | RFK activity                   |                                    | FMNAT activity                 |                                    |
|---------|--------------------------------|------------------------------------|--------------------------------|------------------------------------|
|         | Res. activity <sup>a</sup> (%) | IC <sub>50</sub> <sup>b</sup> (μM) | Res. activity <sup>a</sup> (%) | IC <sub>50</sub> <sup>b</sup> (μM) |
| 1       | 100 ± 15                       | –                                  | 0 ± 0***                       | 69 ± 5                             |
| 2       | 78 ± 10                        | >100                               | 100 ± 12                       | –                                  |
| 7       | 92 ± 10                        | >100                               | 0 ± 0***                       | 73 ± 7                             |
| 9       | 0 ± 0***                       | 6 ± 1                              | 7 ± 1***                       | 78 ± 6                             |
| 10      | 100 ± 12                       | –                                  | 0 ± 0***                       | 68 ± 7                             |
| 14      | 100 ± 10                       | –                                  | 63 ± 7***                      | >100                               |
| 24      | 84 ± 9                         | >100                               | 0 ± 0***                       | 70 ± 6                             |
| 25      | 81 ± 8                         | >100                               | 0 ± 0***                       | 70 ± 6                             |
| 27      | 25 ± 4 ***                     | 6 ± 1                              | 0 ± 0 ***                      | 51 ± 6                             |
| 29      | 71 ± 8*                        | >100                               | 0 ± 0 ***                      | 64 ± 5                             |
| 33      | 26 ± 3 ***                     | 33 ± 4                             | 93 ± 11                        | >100                               |
| 37      | 96 ± 10                        | >100                               | 0 ± 0 ***                      | 7 ± 1                              |
| 38      | 40 ± 5 ***                     | 88 ± 6                             | 68 ± 7 **                      | >100                               |
| 43      | 32 ± 3 ***                     | 14 ± 2                             | 100 ± 15                       | –                                  |

All the experiments were carried out at 25 °C, in 20 mM PIPES pH 7.0, 10 mM MgCl<sub>2</sub> at saturating concentrations of FMN and ATP and in the presence of 2.5% DMSO. (*n* = 3, mean ± SD).

<sup>a</sup>Remaining activity in the presence of 100 μM of each compound. Data showing statistical significance differences when compared with activity in the absence of compound (\*\*\*)*p* < 0.0001; (\*\*)*p* > 0.0021 > *p* > 0.0001; (\*0.033 > *p* > 0.0021).

<sup>b</sup>Compounds assayed in the 0–100 μM concentration range.

**Table 6.** Minimal inhibitory concentration (MIC) of selected HTS hits against different microorganisms.

| HTS hit | <i>C. ammoniagenes</i> (μM) | <i>M. tuberculosis</i> (μM) | <i>S. pneumoniae</i> (μM) |
|---------|-----------------------------|-----------------------------|---------------------------|
| 1       | >64                         | >64                         | >64                       |
| 2       | >64                         | >64                         | >64                       |
| 9       | 2                           | 16                          | 1–2                       |
| 11      | >64                         | >64                         | >64                       |
| 14      | 0.25                        | 8                           | 2                         |
| 15      | 32                          | >64                         | 64                        |
| 17      | 8                           | >64                         | >64                       |
| 24      | 16–32                       | 16–32                       | >64                       |
| 27      | 64                          | >64                         | >64                       |
| 29      | 0.125                       | 16–32                       | 1                         |
| 31      | 32–64                       | >64                         | >64                       |
| 32      | 8                           | >64                         | 64                        |
| 33      | 0.125                       | 2–4                         | 0.5                       |
| 35      | 16–32                       | >64                         | 64                        |
| 37      | >64                         | >64                         | >64                       |
| 38      | 32                          | >64                         | 16–32                     |
| 47      | 2–4                         | 8                           | 4                         |

The FMNAT hits are shown in italics. Compounds were assayed in the 0.125–64 μM range.

## Discussion

### Validation of the HTS protocol

Here we have designed and optimised an enzymatic activity-based HTS protocol to discover specific inhibitors for *CaFADS*. In this protocol, the direct evaluation of the FMNAT enzymatic activity allows for the selection of species-specific inhibitors<sup>38,39</sup>. Our HTS protocol is simple, effective and consumes little protein (1.5 ng/compound against the ~5 μg/compound required for some differential scanning fluorescence-based HTSs). Our protocol monitors directly the activity of the enzyme that we want to inhibit (Figure 1(A)), therefore, minimises the number of false positives and PAINS. In addition, because the chemicals in the library are approved drugs, their toxicity in mammalian cells is expected to be limited. The 37 HTS hits obtained (3.6% of the chemical library) were further assayed against the RFK and FMNAT activities of *CaFADS*. Nine of the HTS hits (when assayed at 250 μM) almost completely inhibited the FMNAT activity without practically

affecting the RFK one (Table 1). Because the FMNAT activity of *CaFADS* appeared as a preferred target, due to the different active site regarding eukaryotic enzymes, we further assessed the inhibitory power of these FMNAT hits.

### Inhibitors targeting the FMNAT activity of *CaFADS*

We choose the three FMNAT hits that showed the lowest IC<sub>50</sub> and residual activity (24, 27 and 31, 8% of the HTS hits) (Table 2) to further determine their binding affinities and inhibition mechanisms. Chicago Sky Blue 6B (CSB), here 24, is an allosteric inhibitor of the Macrophage Inhibitor Factor, and shows promising *in vivo*-effects for the treatment of spinal cord injury<sup>40</sup>. Additionally, 24 can act as an anticancer drug through the specific inhibition of Rad 51, as well as a potential resource for Alzheimer disease treatment by inhibiting the binding of β-amyloid to the prion protein<sup>41,42</sup>. Furthermore, the inhibition of vesicular glutamate transporters by 24 attenuates expressions of behavioural sensitization<sup>43</sup>. In our study, CSB is the most potent inhibitor of the *CaFADS* FMNAT activity, as shown by its lowest values of residual activity and IC<sub>50</sub> (Table 2), targeting the free enzyme as well as the FMN-protein and ATP-protein complexes (Table 3, Supplementary Figure SD2). Moreover, 24 binds to both enzyme modules being the binding to the FMNAT site highly favourable and enthalpically driven (Table 4, Figure 5). This is an advantage for an inhibitor, since high binding enthalpy denotes lots of specific interactions<sup>44</sup>.

Gossypol, here 27, was used some years ago in China as a masculine contraceptive<sup>45</sup>, however, its side effects stopped its pharmacological use. More recently, 27 has demonstrated anti-cancer effects through the inhibition of antiapoptotic proteins belonging to the Bcl-2 family and of molecules implicated in tumour progression<sup>46,47</sup>. Additionally, 27 inhibits the HIV-1 replication *in vitro*<sup>48</sup>. 27 is a potent inhibitor of the *CaFADS* FMNAT activity, as shown by the low IC<sub>50</sub> and residual FMNAT activity (Table 2), while does not affect the RFK one (Table 1, Figure 2). This compound competes with ATP for its binding at the FMNAT site (Table 3, Figures 4 and 6(C)). The lower *K<sub>d</sub>* value for 27 when compared with that of FMN<sup>29</sup>, makes the inhibitor a preferred ligand for *CaFADS*.

31, or flunixin meglumine, is a non-steroidal anti-inflammatory drug, analgesic and antipyretic extensively used in horses, pigs and cattle<sup>49–51</sup>. This fact guarantees that 31 can be used securely in mammals. In this study, 31 arises as a mixed inhibitor of the *CaFADS* FMNAT activity. This is in agreement with our docking model and its small size, envisaging that binding of this compound might coexist with binding of substrates or products in non-competent conformations. Although 31 is the less potent inhibitor of the three here characterised (Table 2, Figure 3), its binding thermodynamic properties, together with its bio-security in mammals, reveals its potentiality as a drug precursor.

Our docking models supply additional details about the molecular inhibition mechanisms of 24, 27 and 31. Because 27 is a competitive inhibitor it occupies the active site substituting ATP, as demonstrated with the best docking poses (Figure 6(C)). However, the way in which 24 and 31 inhibit the FMNAT activity is not obvious. The 31 binding conformation (Figure 6(D)) could be affected by the ATP ligand, and, given the small size of 31, it could coexist with ATP in the active site, causing the previously described intricate mechanism. In presence of ATP, the 24 binding conformation should be different to the one of our FADS:24<sub>1</sub> model, because ATP has to displace 24 from the binding site, given that 24 partially occupies it<sup>24</sup>. It is probable that with ATP in

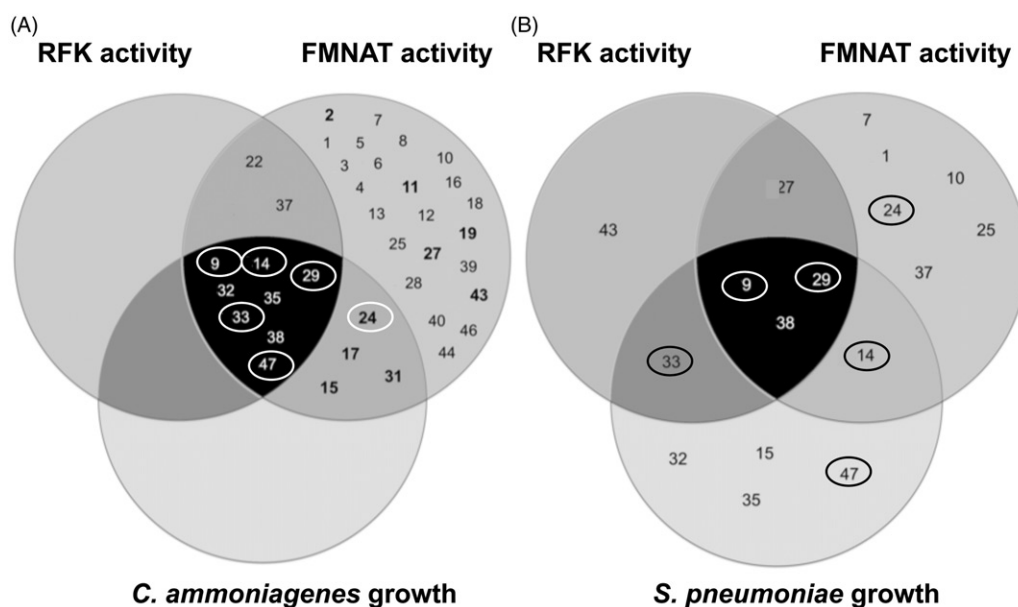


**Figure 7.** Venn diagrams for the HTS hits effects on *C. ammoniagenes* and *S. pneumoniae*. (A) HTS hits that inhibit the RFK (dark grey circle) and FMNAT (medium grey circle) activities of *CaFADS* as well as the growth of *C. ammoniagenes* cells (pale grey circle). (B) HTS hits that inhibit the RFK (dark grey circle) and FMNAT (medium grey circle) activities of *SpnFADS* and the *S. pneumoniae* cellular growth (pale grey circle). In (A), The hits whose inhibition potency was experimentally assessed in this study (inhibit the FMNAT activity without affecting the RFK one) are highlighted in bold. The hits surrounded by a circle, both in (A) and (B), also inhibit the proliferation of *M. tuberculosis*.

the active site, and taking into account the large size of this molecule, 24 only interacts with the active site via the N-terminal of the  $\alpha 6n$  helix (pink molecule in Figure 6(B)) and the flexible loop L4n that forms the external and entry part of the FMNAT substrates cavities<sup>23,24</sup>. In this way, the 24 sulphates would be able to coordinate the magnesium ion to potentially induce a change in the ATP phosphates orientation, negatively affecting their orientation for the FMNAT activity as well as the entry and exit of the reaction ligands.

#### Inhibition of other bacterial FADS by *CaFADS* FMNAT hits

*S. pneumoniae* causes more than 25% of the cases of community-acquired pneumonia<sup>52</sup>, generating more deaths than any other vaccine-preventable bacterial disease. *M. tuberculosis* causes tuberculosis, the most common cause of death among infectious diseases<sup>53</sup>. *SpnFADS* has a similar native structure to *CaFADS* (Supplementary Figure SD1), while the *MtFADS* sequence shows 45% identity with *CaFADS* and 59% of conservation<sup>30</sup>. Since the attempts to produce stable purified *MtFADS* have so far failed, we considered *CaFADS* a good model for *MtFADS*, as reported for other proteins of these two genera<sup>54</sup>. Thus, we tested the effect of the *CaFADS* HTS hits on the RFK and FMNAT activities of *SpnFADS*. We can find that only 30% of the HTS hits have inhibitory effects on *SpnFADS*, and the high values of residual activities and  $IC_{50}$  reveal that they are worse inhibitors for *SpnFADS* (Table 5). Nevertheless, among the HTS hits, 9, 27, 37 and 43 are interesting inhibitors of *SpnFADS* (Table 5). 27 and 43, which did not inhibit the *CaFADS* RFK activity (Table 1), have an important effect on the *SpnFADS* one. 9, inhibits both *SpnFADS* activities (Table 5). This compound is a monocationic detergent that has been commonly used in cortisporin-TC ear drops to help penetration of active ingredients through cellular debris. Additionally, 9 inhibits vacuolar ATPase, showing cytotoxic effects at concentrations higher than 10  $\mu$ M<sup>55</sup>. It is also an inhibitor of the RANK-L induced osteoclast

formation<sup>56</sup>. 37, inhibited both *CaFADS* activities, but only affects the FMNAT one in *SpnFADS*. 37 inhibits the HMG-CoA reductase, being used to treat hypercholesterolemia<sup>57</sup>. 37 has positive effects in myocardial fibrosis by favouring ACE2 expression, and also modestly inhibits replication of the hepatitis C virus<sup>58,59</sup>. 43 is used as analgesic (inhibits anandamide hydrolase in neurons) and as anti-inflammatory<sup>60,61</sup>, acting as a non-selective cyclooxygenase inhibitor. Additionally, it inhibits  $NF-\kappa B$  in activated monocytes, being a promising drug for the treatment of rheumatoid arthritis<sup>62</sup>. Regarding the three FMNAT hits of *CaFADS*: 24 has a poor inhibitory effect on *SpnFADS* (Table 5), which might be of interest as selective inhibitor; 27 inhibits both *CaFADS* and *SpnFADS* activities (Tables 1 and 5), appearing as a broad inhibitor of FADS; and 31 has no effect on *SpnFADS* (Table 5), indicating the specificity of this compound for *CaFADS*.

Recent studies<sup>23,28,63–65</sup> revealed important differences in catalysis among bifunctional FADS, probably related to dissimilarities in the active site conformation during catalysis. This is consistent with the differential inhibitory mechanisms of the HTS hits against *CaFADS* and *SpnFADS*, as observed in the present work. Such mechanistic variations could determine the binding or the inhibitory capability of the hits. These observations highlight the potentiality of our method to find selective drugs targeting a specific protein of a particular microorganism. The development of such species-selective drugs is of great importance for the treatment of infections by avoiding undesired side-effects on normal microbiota of the host<sup>66</sup>, and for minimising the selection of resistant bacterial strains.

#### Antimicrobial activity of the *CaFADS* FMNAT hits

Finally, we also tested the inhibitory activity of the best FMNAT hits on the growth of *C. ammoniagenes*, *S. pneumoniae* and *M. tuberculosis* cultures. 24 shows moderate effects on the *C. ammoniagenes* and *M. tuberculosis* growth (Table 6, Figure 7). However,

it does not inhibit the pneumococci growth. 27 and 31 do not inhibit the growth of *C. ammoniagenes*, *S. pneumoniae* or *M. tuberculosis* cells. This might be due to their inability to enter in the bacterial cell, or because efflux pumps eject them once in the bacterial cytoplasm. Tools to favour their bactericide effects can be obtained by deriving second generation hits, using vehiculization systems to move drugs across the membrane, or using efflux pumps inhibitors<sup>67–69</sup>. In this context, we remark that inhibition of FAD synthesis in *M. tuberculosis* could have an immediate impact in current antituberculosis drug discovery programmes. Benzothiazinones are antituberculosis compounds that block arabinan synthesis by targeting the flavoprotein decaprenylphosphoryl- $\beta$ -D-ribose 2'-epimerase DprE1<sup>70</sup>. It is expected that the antituberculosis activity of benzothiazinones, which are currently in phase I clinical trials<sup>4</sup>, could be enhanced by FADS inhibition, in a synergistic manner. Among the other FMNAT hits, only 15, 17 and 31 show mild inhibitory activity on the growth of *C. ammoniagenes*, but do not have an effect on *S. pneumoniae* and *M. tuberculosis* cultures (Figure 7).

We find five HTS hits (9, 14, 29, 33 and 47) as strong inhibitors of the *C. ammoniagenes* growth (Table 6, Figure 7). These five HTS hits also inhibit the growth of *S. pneumoniae* (Table 6, Figure 7), while only the first four mildly affect *M. tuberculosis*. Noticeably, these five HTS hits are good inhibitors of both CaFADS activities (Table 1, Figure 7). 9 and 29 also appear as potent inhibitors of the SpnFADS RFK and/or FMNAT activities. The effect of the other three compounds as SpnFADS inhibitors is milder, suggesting mechanisms that do not involve FADS in preventing cell proliferation. Overall, our results suggest that targeting both activities of bifunctional FADSs can be a strategy in the discovery of new antibacterial drugs. Thus, the non-selective antimicrobial properties of 9 and 29 seem interesting tools to be explored.

In this context, and despite all compounds in the library are approved by FAD and EMA, it remains for future studies to test the effect of the most promising compounds on the homologous human proteins and cells. In addition, future studies should also focus on the improvement of these compounds regarding potency, selectivity, pharmacokinetics and drug-likeness.

## Conclusions

The FMNAT activity of bifunctional FADS enzymes is a potential antimicrobial target for drug discovery. The transformation of FMN into FAD is performed by different catalytic mechanisms in prokaryotes and eukaryotes, and the FMN and FAD deficiency inactivates an important number of flavoproteins. In this work, we have optimised an activity-based HTS that can be used to discover new antibacterial drugs, targeting the RFK and/or FMNAT activities of bifunctional FADSs. Our method allows identifying bacterial FADS inhibitors with different levels of selectivity regarding the inhibition of bacterial growth. The method is fast, effective and requires small protein quantities. We have confirmed that bacterial FADS are promising species-selective drug targets. Among the 1240 compounds from the Prestwick Chemical Library<sup>®</sup>, 37 inhibited CaFADS, and three were potent inhibitors of its FMNAT (but not of the RFK) activity. Two of these compounds were not species-selective because they also affected SpnFADS, but the third one, 31, was selective for CaFADS versus SpnFADS. These three compounds are promising as non-selective or selective inhibitors at the enzyme level. However, they do not produce observable antimicrobial effects, suggesting that they do not reach inhibitory concentrations at the intracellular level, possibly due to a poor uptake, efficient efflux or *in vivo* fast degradation. Nevertheless,

some HTS hits show good antimicrobial properties, probably due to the inhibition of both RFK and FMNAT activities of FADS.

## Acknowledgements

The authors thank Dr J. Sancho for access to the chemical library, Dr A. Velázquez-Campoy for support on ITC experiments and both of them for helpful discussions. I.L. and P.C. were supported by Colciencias and University of Antioquia (Colombia) and the Max Planck society (Germany).

## Disclosure statement

The authors report no conflicts of interest.

## Funding

This work has been supported by the Spanish Ministry of Economy, Industry and Competitiveness (MINEICO) [BIO2016–75183-P AEI/FEDER, UE to M.M.] and the Government of Aragón – FEDER [B18]. M.S. received a PhD Contract from Government of Aragón.

## ORCID

María Sebastián  <http://orcid.org/0000-0002-5593-8624>  
 José Antonio Aínsa  <http://orcid.org/0000-0003-2076-844X>  
 Milagros Medina  <http://orcid.org/0000-0001-8743-0182>

## References

1. Spellberg B, Powers JH, Brass EP, et al. Trends in antimicrobial drug development: implications for the future. *Clin Infect Dis* 2004;38:1279–86.
2. Conly J, Johnston B. Where are all the new antibiotics? The new antibiotic paradox. *Can J Infect Dis Med Microbiol* 2005;16:159–60.
3. Walsh CT, Wencewicz TA. Prospects for new antibiotics: a molecule-centered perspective. *J Antibiot (Tokyo)* 2014;67:7–22.
4. WHO. Antibacterial agents in clinical development: an analysis of the antibacterial clinical development pipeline, including tuberculosis. WHO/EMP/IAU/2017.11 ed. World Health Organization: Geneva; 2017.
5. Brown ED, Wright GD. Antibacterial drug discovery in the resistance era. *Nature* 2016;529:336–43.
6. Lienhart WD, Gudipati V, Macheroux P. The human flavoproteome. *Arch Biochem Biophys* 2013;535:150–62.
7. Gudipati V, Koch K, Lienhart WD, Macheroux P. The flavoproteome of the yeast *Saccharomyces cerevisiae*. *Biochim Biophys Acta* 2014;1844:535–44.
8. Barile M, Giancaspero TA, Leone P, et al. Riboflavin transport and metabolism in humans. *J Inher Metab Dis* 2016;39:545–57.
9. Gross E, Kastner DB, Kaiser CA, Fass D. Structure of Ero1p, source of disulfide bonds for oxidative protein folding in the cell. *Cell* 2004;117:601–10.
10. Parsons HG, Dias VC. Intramitochondrial fatty acid metabolism: riboflavin deficiency and energy production. *Biochem Cell Biol* 1991;69:490–7.

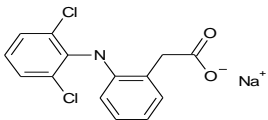
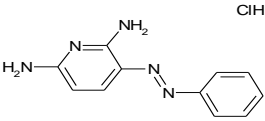
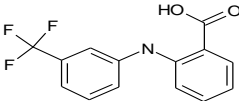
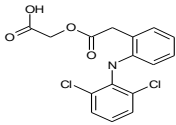
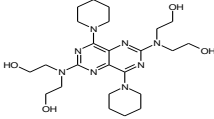
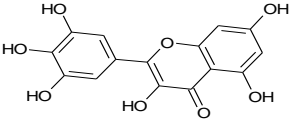
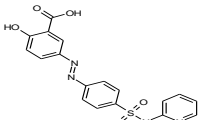
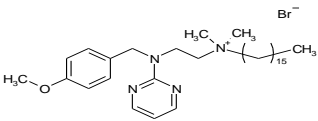
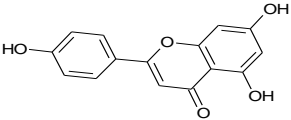
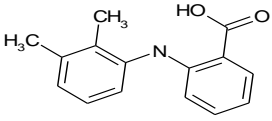
11. Myllykallio H, Lipowski G, Leduc D, et al. An alternative flavin-dependent mechanism for thymidylate synthesis. *Science* 2002;297:105–7.
12. Susin SA, Lorenzo HK, Zamzami N, et al. Molecular characterization of mitochondrial apoptosis-inducing factor. *Nature* 1999;397:441–6.
13. Sassetti CM, Boyd DH, Rubin EJ. Genes required for mycobacterial growth defined by high density mutagenesis. *Mol Microbiol* 2003;48:77–84.
14. Griffin JE, Gawronski JD, Dejesus MA, et al. High-resolution phenotypic profiling defines genes essential for mycobacterial growth and cholesterol catabolism. *PLoS Pathog* 2011;7:e1002251.
15. Serrano A, Ferreira P, Martínez-Júlvez M, Medina M. The prokaryotic FAD synthetase family: a potential drug target. *Curr Pharm Des* 2013;19:2637–48.
16. Barile M, Passarella S, Bertoldi A, Quagliariello E. Flavin adenine dinucleotide synthesis in isolated rat liver mitochondria caused by imported flavin mononucleotide. *Arch Biochem Biophys* 1993;305:442–7.
17. Serrano A, Frago S, Velázquez-Campoy A, Medina M. Role of key residues at the flavin mononucleotide (FMN):adenylyltransferase catalytic site of the bifunctional riboflavin kinase/flavin adenine dinucleotide (FAD) synthetase from *Corynebacterium ammoniagenes*. *Int J Mol Sci* 2012;13:14492–517.
18. Efimov I, Kuusk V, Zhang X, McIntire WS. Proposed steady-state kinetic mechanism for *Corynebacterium ammoniagenes* FAD synthetase produced by *Escherichia coli*. *Biochemistry* 1998;37:9716–23.
19. Mack M, van Loon AP, Hohmann HP. Regulation of riboflavin biosynthesis in *Bacillus subtilis* is affected by the activity of the flavokinase/flavin adenine dinucleotide synthetase encoded by ribC. *J Bacteriol* 1998;180:950–5.
20. Herguedas B, Martínez-Júlvez M, Frago S, et al. Crystallization and preliminary X-ray diffraction studies of FAD synthetase from *Corynebacterium ammoniagenes*. *Acta Crystallogr Sect F Struct Biol Cryst Commun* 2009;65:1285–8.
21. Wang W, Kim R, Yokota H, Kim SH. Crystal structure of flavin binding to FAD synthetase of *Thermotoga maritima*. *Proteins* 2005;58:246–8.
22. Wang W, Kim R, Jancarik J, et al. Crystal structure of a flavin-binding protein from *Thermotoga maritima*. *Proteins* 2003;52:633–5.
23. Sebastián M, Lira-Navarrete E, Serrano A, et al. The FAD synthetase from the human pathogen *Streptococcus pneumoniae*: a bifunctional enzyme exhibiting activity-dependent redox requirements. *Sci Rep* 2017;7:7609.
24. Herguedas B, Martinez-Julvez M, Frago S, et al. Oligomeric state in the crystal structure of modular FAD synthetase provides insights into its sequential catalysis in prokaryotes. *J Mol Biol* 2010;400:218–30.
25. Giancaspero TA, Galluccio M, Miccolis A, et al. Human FAD synthase is a bi-functional enzyme with a FAD hydrolase activity in the molybdopterin binding domain. *Biochem Biophys Res Commun* 2015;465:443–9.
26. Serrano A, Sebastian M, Arilla-Luna S, et al. Quaternary organization in a bifunctional prokaryotic FAD synthetase: involvement of an arginine at its adenylyltransferase module on the riboflavin kinase activity. *Biochim Biophys Acta* 2015;1854:897–906.
27. Serrano A, Frago S, Herguedas B, et al. Key residues at the riboflavin kinase catalytic site of the bifunctional riboflavin kinase/FMN adenylyltransferase from *Corynebacterium ammoniagenes*. *Cell Biochem Biophys* 2013;65:57–68.
28. Herguedas B, Lans I, Sebastián M, et al. Structural insights into the synthesis of FMN in prokaryotic organisms. *Acta Crystallogr D Biol Crystallogr* 2015;71:2526–42.
29. Frago S, Velázquez-Campoy A, Medina M. The puzzle of ligand binding to *Corynebacterium ammoniagenes* FAD synthetase. *J Biol Chem* 2009;284:6610–19.
30. Frago S, Martínez-Júlvez M, Serrano A, Medina M. Structural analysis of FAD synthetase from *Corynebacterium ammoniagenes*. *BMC Microbiol* 2008;8:160.
31. Lagorce D, Oliveira N, Miteva MA, Villoutreix BO. Pan-assay interference compounds (PAINS) that may not be too painful for chemical biology projects. *Drug Discov Today* 2017;22:1131–3.
32. Cosconati S, Forli S, Perryman AL, et al. Virtual screening with AutoDock: theory and practice. *Expert Opin Drug Discov* 2010;5:597–607.
33. Morris GM, Huey R, Lindstrom W, et al. AutoDock4 and AutoDockTools4: automated docking with selective receptor flexibility. *J Comput Chem* 2009;30:2785–91.
34. Forli S, Olson AJ. A force field with discrete displaceable waters and desolvation entropy for hydrated ligand docking. *J Med Chem* 2012;55:623–38.
35. Frisch MJ, Trucks GW, Schlegel HB, et al. Gaussian 09. Wallingford, CT: Gaussian Inc.; 2016.
36. Palomino JC, Martin A, Camacho M, et al. Resazurin microtiter assay plate: simple and inexpensive method for detection of drug resistance in *Mycobacterium tuberculosis*. *Antimicrob Agents Chemother* 2002;46:2720–2.
37. Olsson TS, Williams MA, Pitt WR, Ladbury JE. The thermodynamics of protein-ligand interaction and solvation: insights for ligand design. *J Mol Biol* 2008;384:1002–17.
38. Deu E, Yang Z, Wang F, et al. Use of activity-based probes to develop high throughput screening assays that can be performed in complex cell extracts. *PLoS One* 2010;5:e11985.
39. Zhang G. Protease assays. Available from: <http://www.ncbi.nlm.nih.gov/books/NBK92006/>
40. Saxena T, Loomis KH, Pai SB, et al. Nanocarrier-mediated inhibition of macrophage migration inhibitory factor attenuates secondary injury after spinal cord injury. *ACS Nano* 2015;9:1492–505.
41. Normand A, Rivière E, Renodon-Cornière A. Identification and characterization of human Rad51 inhibitors by screening of an existing drug library. *Biochem Pharmacol* 2014;91:293–300.
42. Risse E, Nicoll AJ, Taylor WA, et al. Identification of a compound that disrupts binding of Amyloid- $\beta$  to the prion protein using a novel fluorescence-based assay. *J Biol Chem* 2015;290:17020–8.
43. He Z, Yan L, Yong Z, et al. Chicago sky blue 6B, a vesicular glutamate transporters inhibitor, attenuates methamphetamine-induced hyperactivity and behavioral sensitization in mice. *Behav Brain Res* 2013;239:172–6.
44. Klebe G. Applying thermodynamic profiling in lead finding and optimization. *Nat Rev Drug Discov* 2015;14:95–110.
45. Soufir JC. Hormonal, chemical and thermal inhibition of spermatogenesis: contribution of French teams to international data with the aim of developing male contraception in France. *Basic Clin Androl* 2017;27:3.
46. Ferdek PE, Jakubowska MA, Nicolaou P, et al. BH3 mimetic-elicited Ca(2+) signals in pancreatic acinar cells are dependent on Bax and can be reduced by Ca(2+)-like peptides. *Cell Death Dis* 2017;8:e2640.

47. Xiong J, Li J, Yang Q, et al. Gossypol has anti-cancer effects by dual-targeting MDM2 and VEGF in human breast cancer. *Breast Cancer Res* 2017;19:27
48. Polsky B, Segal SJ, Baron PA, et al. Inactivation of human immunodeficiency virus in vitro by gossypol. *Contraception* 1989;39:579–87.
49. Newby NC, Leslie KE, Dingwell HD, et al. The effects of periparturient administration of flunixin meglumine on the health and production of dairy cattle. *J Dairy Sci* 2017;100:582–7.
50. Kleinhenz MD, Van Engen NK, Gorden PJ, et al. The pharmacokinetics of transdermal flunixin meglumine in Holstein calves. *J Vet Pharmacol Ther* 2016;39:612–15.
51. Burkett BN, Thomason JM, Hurdle HM, et al. Effects of firocoxib, flunixin meglumine, and phenylbutazone on platelet function and thromboxane synthesis in healthy horses. *Vet Surg* 2016;45:1087–94.
52. Torres A, Blasi F, Peetermans WE, et al. The aetiology and antibiotic management of community-acquired pneumonia in adults in Europe: a literature review. *Eur J Clin Microbiol Infect Dis* 2014;33:1065–79.
53. WHO. Global Tuberculosis Report. Geneva: WHO; 2016.
54. Seidel M, Alderwick LJ, Sahn H, et al. Topology and mutational analysis of the single Emb arabinofuranosyltransferase of *Corynebacterium glutamicum* as a model of Emb proteins of *Mycobacterium tuberculosis*. *Glycobiology* 2007;17:210–19.
55. Chan CY, Prudom C, Raines SM, et al. Inhibitors of V-ATPase proton transport reveal uncoupling functions of tether linking cytosolic and membrane domains of V0 subunit a (Vph1p). *J Biol Chem* 2012;287:10236–50.
56. Zhu X, Gao JJ, Landao-Bassonga E, et al. Thonzonium bromide inhibits RANKL-induced osteoclast formation and bone resorption in vitro and prevents LPS-induced bone loss in vivo. *Biochem Pharmacol* 2016;104:118–30.
57. Weng TC, Yang YH, Lin SJ, Tai SH. A systematic review and meta-analysis on the therapeutic equivalence of statins. *J Clin Pharm Ther* 2010;35:139–51.
58. Shin YH, Min JJ, Lee JH, et al. The effect of fluvastatin on cardiac fibrosis and angiotensin-converting enzyme-2 expression in glucose-controlled diabetic rat hearts. *Heart Vessels* 2017;32:618–27.
59. Bader T, Fazili J, Madhoun M, et al. Fluvastatin inhibits hepatitis C replication in humans. *Am J Gastroenterol* 2008;103:1383–9.
60. Dallegrì F, Bertolotto M, Ottonello L. A review of the emerging profile of the anti-inflammatory drug oxaprozin. *Expert Opin Pharmacother* 2005;6:777–85.
61. Kara IM, Polat S, Inci MF, et al. Analgesic and anti-inflammatory effects of oxaprozin and naproxen sodium after removal of impacted lower third molars: a randomized, double-blind, placebo-controlled crossover study. *J Oral Maxillofac Surg* 2010;68:1018–24.
62. Montecucco F, Bertolotto M, Ottonello L, et al. Oxaprozin-induced apoptosis on CD40 ligand-treated human primary monocytes is associated with the modulation of defined intracellular pathways. *J Biomed Biotechnol* 2009;2009:478785.
63. Grill S, Busenbender S, Pfeiffer M, et al. The bifunctional flavokinase/flavin adenine dinucleotide synthetase from *Streptomyces davawensis* produces inactive flavin cofactors and is not involved in resistance to the antibiotic roseoflavin. *J Bacteriol* 2008;190:1546–53.
64. Matern A, Pedrolli D, Groszhennig S, et al. Uptake and metabolism of antibiotics roseoflavin and 8-demethyl-8-aminoriboflavin in riboflavin-auxotrophic listeria monocytogenes. *J Bacteriol* 2016;198:3233–43.
65. Marcuello C, Arilla-Luna S, Medina M, Lostao A. Detection of a quaternary organization into dimer of trimers of *Corynebacterium ammoniagenes* FAD synthetase at the single-molecule level and at the in cell level. *Biochim Biophys Acta* 2013;1834:665–76.
66. Lewis K. Platforms for antibiotic discovery. *Nat Rev Drug Discov* 2013;12:371–87.
67. Stermitz FR, Lorenz P, Tawara JN, et al. Synergy in a medicinal plant: antimicrobial action of berberine potentiated by 5'-methoxyhydrnocarpin, a multidrug pump inhibitor. *Proc Natl Acad Sci USA* 2000;97:1433–7.
68. Rodrigues L, Parish T, Balganes M, Ainsa JA. Antituberculosis drugs: reducing efflux = increasing activity. *Drug Discov Today* 2017;22:592–99.
69. Ladbury JE, Klebe G, Freire E. Adding calorimetric data to decision making in lead discovery: a hot tip. *Nat Rev Drug Discov* 2010;9:23–7.
70. Makarov V, Manina G, Mikusova K, et al. Benzothiazinones kill *Mycobacterium tuberculosis* by blocking Arabinan synthesis. *Science* 2009;324:801–4.

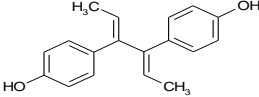
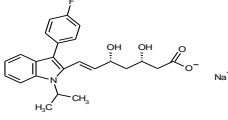
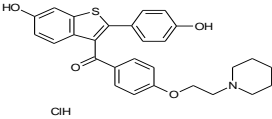
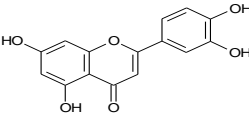
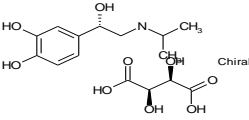
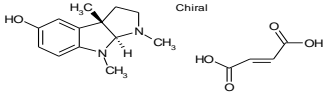
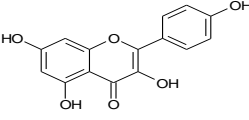
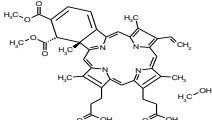


## Supplementary Charts

**Chart SD1.** Structures of the 37 compounds selected as HTS hits for *CaFADS*.

| Compound number | Name                          | CAS number | Structure   |
|-----------------|-------------------------------|------------|---|
| 1               | Diclofenac sodium             | 15307-29-6 |     |
| 3               | Phenazopyridine hydrochloride | 136-40-3   |     |
| 4               | Flufenamic acid               | 530-78-9   |     |
| 5               | Aceclofenac                   | 89796-99-6 |   |
| 6               | Dipyridamole                  | 58-32-2    |  |
| 7               | Myricetin                     | 529-44-2   |   |
| 8               | Sulfasalazine                 | 599-79-1   |  |
| 9               | Thonzonium bromide            | 553-08-2   |   |
| 10              | Apigenin                      | 520-36-5   |   |
| 12              | Mefenamic acid                | 61-68-7    |   |

| Compound number | Name                                      | CAS number | Structure |
|-----------------|---|------------|-----------|
| 13              | Diflunisal                                | 22494-42-4 |           |
| 14              | Benzethonium chloride                     | 121-54-0   |           |
| 16              | Meclofenamic acid sodium salt monohydrate | 6385-02-0  |           |
| 18              | Clomiphene citrate (Z,E)                  | 50-41-9    |           |
| 22              | Butoconazole nitrate                      | 64872-77-1 |           |
| 25              | Quercetin dihydrate                       | 6151-25-3  |           |
| 28              | Karakoline                                | 39089-30-0 |           |
| 29              | Methylbenzethonium chloride               | 25155-18-4 |           |
| 32              | Diethylstilbestrol                        | 56-53-1    |           |
| 33              | Alexidine dihydrochloride                 | 1715-30-6  |           |

| Compound number | Name                                  | CAS number  | Structure   |
|-----------------|---------------------------------------|-------------|---|
| 35              | Dienestrol                            | 84-17-3     |    |
| 37              | Fluvastatin sodium salt               | 93957-55-2  |    |
| 38              | Raloxifene hydrochloride              | 82640-04-8  |     |
| 39              | Luteolin                              | 491-70-3    |    |
| 40              | (+)-Isoproterenol (+)-bitartrate salt | 54750-10-6  |   |
| 44              | (-)-Eseroline fumarate salt           | 70310-73-5  |   |
| 46              | Kaempferol                            | 520-18-3    |  |
| 47              | Verteporfin                           | 129497-78-5 |  |

## Supplementary Figures

**Figure SD1.** Similarity within members of the bacterial bifunctional FADS family. (A) Sequence alignment of *CaFADS* (Q59263), *SpnFADS* (A0A0H2UPY5) and *MtFADS* (NP\_217302.1) obtained using CLUSTAL W (<http://www.ebi.ac.uk/clustalw/>) with default parameters. The consensus sequence is indicated on the top. Equivalent residues at each position show same color. Deep and light blue upper bars indicate regions for the FMNAT and RFK modules, respectively. (B) Structures of *CaFADS* (PDB 2X0K), with the FMNAT and RFK modules in blue and light blue respectively, and of *SpnFADS* (PDB 3OP1), with the FMNAT and RFK modules in pink and light pink respectively. The reaction catalyzed by each module is next to the corresponding module. On the right it is shown the structural alignment showing an r.m.s.d. of 1.63 Å for 247 C $\alpha$  atoms. Structural figures were produced with PyMol (Delano 2002).

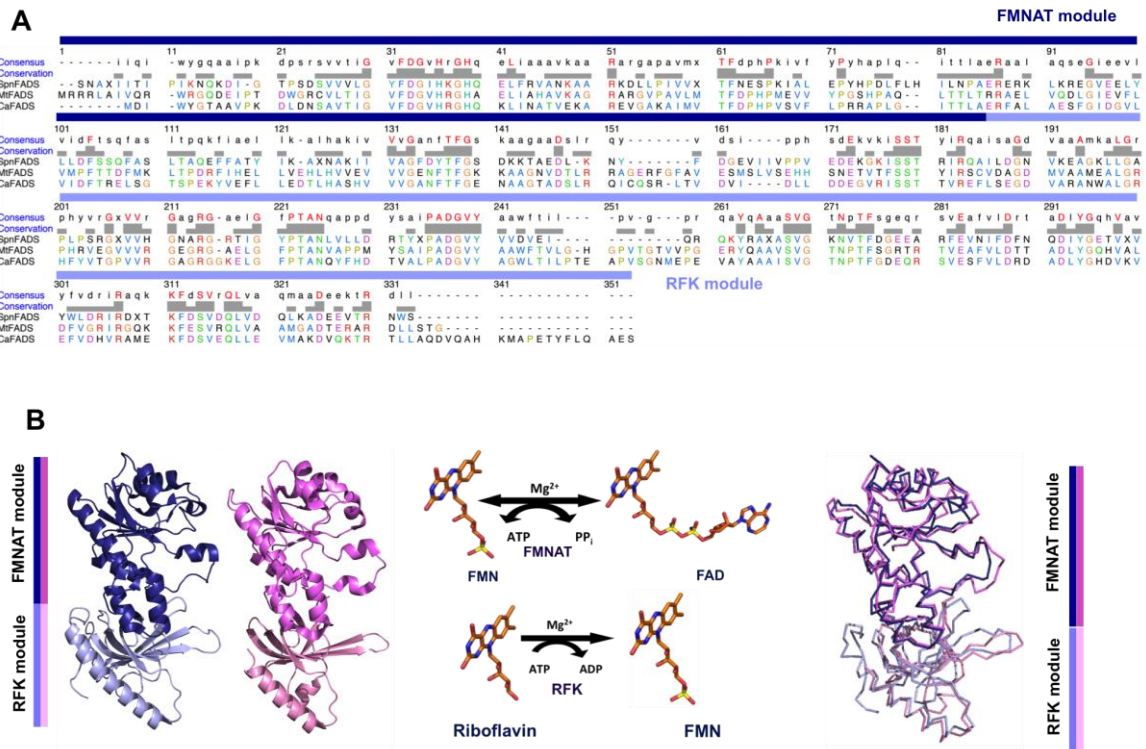


**Figure SD2.** Hit 24 as inhibitor of the FMNAT activity of *CaFADS*. Michaelis-Menten plots at different concentrations of 24 and saturation (A) of ATP and (B) of FMN. Lineaweaver-Burk representations with global fit (C) to non-competitive inhibition model when ATP saturating and (D) to competitive inhibition model when FMN saturating. Reaction rates obtained in 20 mM PIPES, pH 7.0, 10 mM MgCl<sub>2</sub>, 2.5 % DMSO, at 25 °C, with 15 μM FMN and 10-450 μM ATP (FMN saturating) or with 350 μM ATP and 0.5-20 μM FMN (ATP saturating) (n=3, mean ± SD).

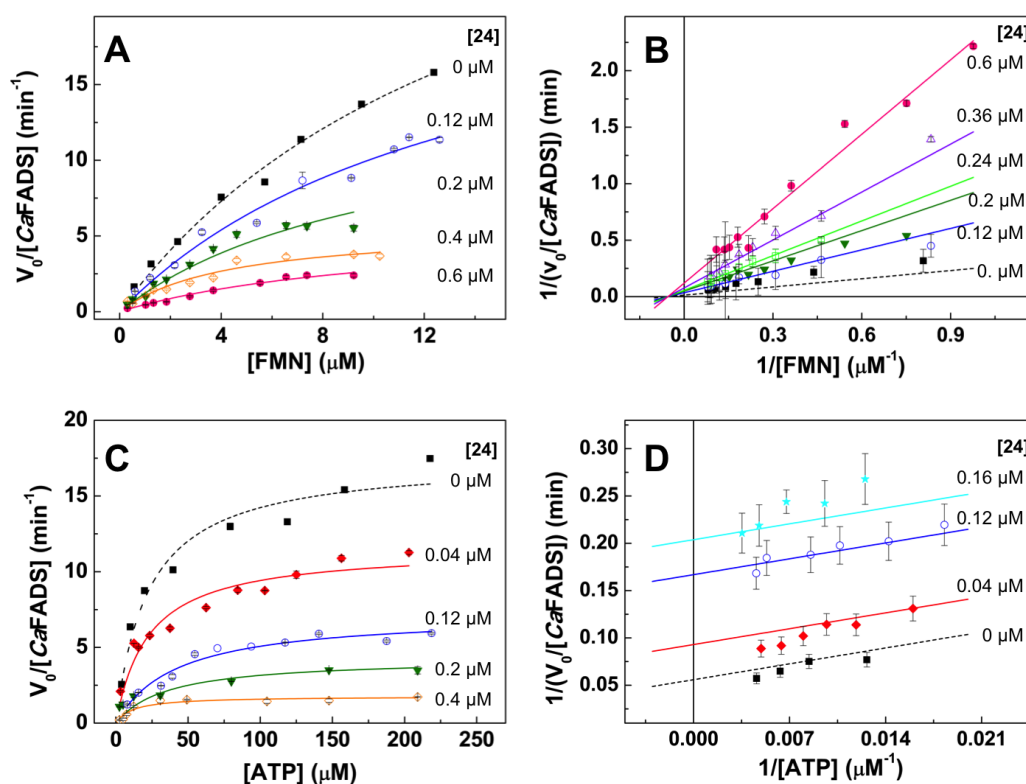


**Figure SD3.** Hit 31 as inhibitor of the FMNAT activity of *CaFADS*. Michaelis-Menten plots at different concentrations of 31 and saturation (A) of ATP and (B) of FMN. (C) Lineaweaver-Burk representations with global fit to non-competitive inhibition model when ATP saturating, and (D) to competitive inhibition model when FMN saturating. Reaction rates obtained in 20 mM PIPES, pH 7.0, 10 mM MgCl<sub>2</sub>, 2.5% DMSO, at 25 °C, with 15 μM FMN and 10-450 μM ATP (FMN saturating) or with 350 μM ATP and 0.5-20 μM FMN (ATP saturating) (n=3, mean ± SD).

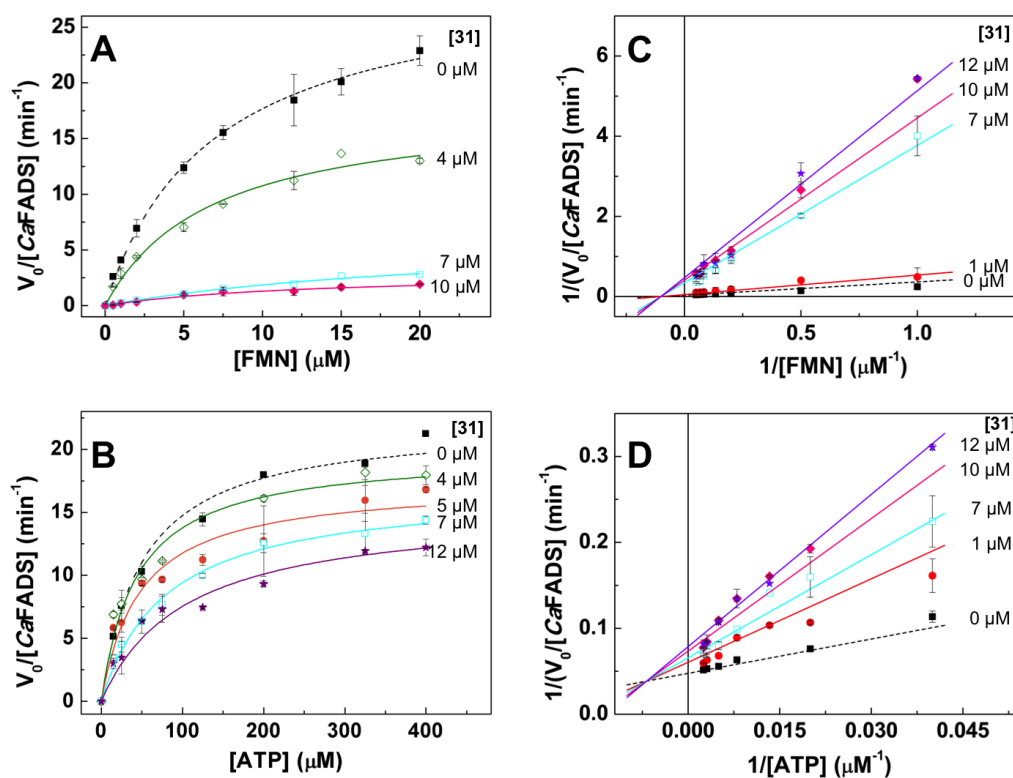
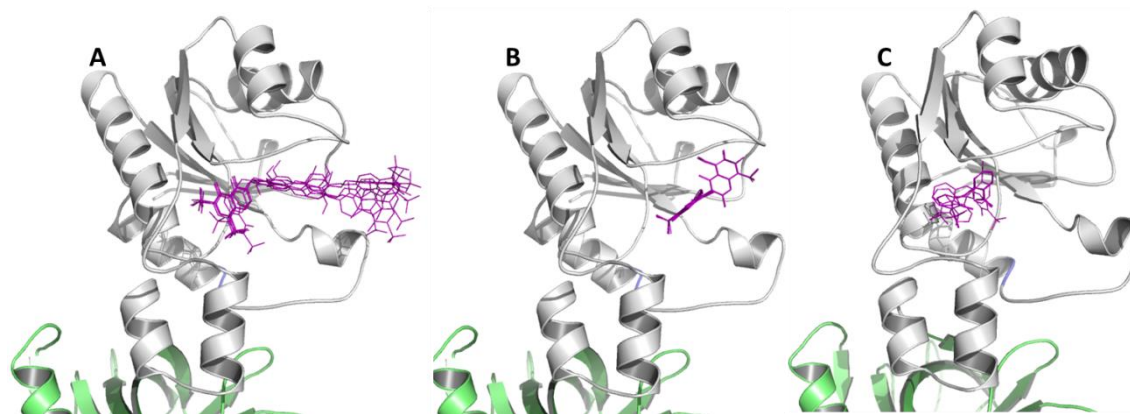


**Figure SD4.** Results from the docking analysis of the best five poses of the inhibitors (A) 24, (B) 27 (the five with almost identical orientation) and (C) 31 at the *Ca*FADS FMNAT site. Inhibitors, FMNAT module and RFK module are showed in purple, gray and green, respectively. The poses for 24 and 27 correspond to the docking performed for the first molecular binding at the FMNAT module ( $24_1$  and  $27_1$ ).



## Supporting Tables

**Table SP1.** Apparent kinetic parameters for the FMNAT activity of *CaFADS* at different concentrations of the 24, 27 and 31 inhibitors. Data obtained at 25°C in 20 mM PIPES, pH 7.0, 10 mM MgCl<sub>2</sub>, 2.5% DMSO.

| Saturating ATP            |                                    |                            | Saturating FMN            |                                    |                            |
|---------------------------|------------------------------------|----------------------------|---------------------------|------------------------------------|----------------------------|
| [24]<br>( $\mu\text{M}$ ) | $k_{cat}$<br>( $\text{min}^{-1}$ ) | $K_m$<br>( $\mu\text{M}$ ) | [24]<br>( $\mu\text{M}$ ) | $k_{cat}$<br>( $\text{min}^{-1}$ ) | $K_m$<br>( $\mu\text{M}$ ) |
| 0                         | 34 ± 3.8                           | 16.3 ± 3.2                 | 0                         | 22.4 ± 0.7                         | 29.4 ± 4.9                 |
| 0.12                      | 24.3 ± 4.1 <sup>a</sup>            | 14.0 ± 3.9                 | 0.04                      | 22.5 ± 4.8                         | 11.5 ± 0.7 <sup>a</sup>    |
| 0.2                       | 9.8 ± 1.3 <sup>a</sup>             | 10.6 ± 2.4                 | 0.12                      | 7.2 ± 0.4 <sup>a</sup>             | 42.1 ± 3.9 <sup>a</sup>    |
| 0.4                       | 5.6 ± 0.6 <sup>a</sup>             | 4.3 ± 1.0 <sup>a</sup>     | 0.2                       | 4.3 ± 0.4 <sup>a</sup>             | 35.8 ± 3.2                 |
| 0.6                       | 5.7 ± 1.3 <sup>a</sup>             | 11.1 ± 3.9                 | 0.4                       | 1.8 ± 0.1 <sup>a</sup>             | 12.0 ± 3.6 <sup>a</sup>    |

| Saturating ATP            |                                    |                            | Saturating FMN            |                                    |                            |
|---------------------------|------------------------------------|----------------------------|---------------------------|------------------------------------|----------------------------|
| [27]<br>( $\mu\text{M}$ ) | $k_{cat}$<br>( $\text{min}^{-1}$ ) | $K_m$<br>( $\mu\text{M}$ ) | [27]<br>( $\mu\text{M}$ ) | $k_{cat}$<br>( $\text{min}^{-1}$ ) | $K_m$<br>( $\mu\text{M}$ ) |
| 0                         | 34 ± 3.8 <sup>a</sup>              | 16.3 ± 3.2                 | 0                         | 22.4 ± 0.7                         | 29.4 ± 4.9                 |
| 0.05                      | 21.6 ± 2.9 <sup>a</sup>            | 10.1 ± 2.9                 | 0.1                       | 22.8 ± 1.3                         | 59.7 ± 5.7 <sup>a</sup>    |
| 0.1                       | 16.1 ± 1.7 <sup>a</sup>            | 7.7 ± 2.1                  | 0.2                       | 22.2 ± 1.4                         | 48.2 ± 5.6 <sup>a</sup>    |
| 0.2                       | 15.1 ± 1.5 <sup>a</sup>            | 13.5 ± 2.6                 | 0.4                       | 18.1 ± 1.6                         | 51.8 ± 5.5 <sup>a</sup>    |
| 0.75                      | 10.0 ± 0.8 <sup>a</sup>            | 12.8 ± 2.1                 | 0.75                      | 17.1 ± 3.3                         | 51.5 ± 4.9 <sup>a</sup>    |
| 1                         | 6.5 ± 0.2 <sup>a</sup>             | 15.0 ± 2.0                 | 1                         | 12.5 ± 0.5 <sup>a</sup>            | 40.9 ± 5.7                 |

| Saturating ATP            |                                    |                            | Saturating FMN            |                                    |                            |
|---------------------------|------------------------------------|----------------------------|---------------------------|------------------------------------|----------------------------|
| [31]<br>( $\mu\text{M}$ ) | $k_{cat}$<br>( $\text{min}^{-1}$ ) | $K_m$<br>( $\mu\text{M}$ ) | [31]<br>( $\mu\text{M}$ ) | $k_{cat}$<br>( $\text{min}^{-1}$ ) | $K_m$<br>( $\mu\text{M}$ ) |
| 0                         | 34 ± 3.8                           | 16.3 ± 3.2                 | 0                         | 22.4 ± 0.7                         | 29.4 ± 4.9                 |
| 1                         | 24.6 ± 2.9 <sup>a</sup>            | 13.3 ± 3.1                 | 4                         | 19.7 ± 1.0 <sup>a</sup>            | 43.3 ± 7.9                 |
| 4                         | 18.1 ± 1.4 <sup>a</sup>            | 6.8 ± 1.3                  | 5                         | 17.3 ± 1.1 <sup>a</sup>            | 47.5 ± 5.7 <sup>a</sup>    |
| 5                         | 6.4 ± 1.2 <sup>a</sup>             | 24.4 ± 7.0                 | 7                         | 16.9 ± 0.6 <sup>a</sup>            | 79.1 ± 8.7 <sup>a</sup>    |
| 7                         | 3.0 ± 0.4 <sup>a</sup>             | 13.3 ± 3.6                 | 10                        | 15.3 ± 1.3 <sup>a</sup>            | 102.9 ± 24.2 <sup>a</sup>  |
| 10                        | 3.0 ± 0.4 <sup>a</sup>             | 12.3 ± 3.6                 | 12                        | 13.8 ± 1.0 <sup>a</sup>            | 92.1 ± 14.9 <sup>a</sup>   |

<sup>a</sup> Values showing statistically significant differences,  $p < 0.002$ , from the values in the absence of compounds, as determined by the one-way ANOVA test (n=3, confidence interval 95%).

Delano, W. L. (2002). "They PyMOL molecular graphics system." DeLano Scientific, San Carlos, CA, USA: <http://www.pymol.org>.



## Publication V

***In silico* discovery and biological validation  
of ligands of FAD synthase, a promising  
new antimicrobial target**

**Ernesto Anoz Carbonell contributions:** Experimental work: protein purification, steady-state enzymatic activity measurements, and antimicrobial and eukaryotic cytotoxic activity assays. Data analysis. Manuscript writing, review and editing.

## RESEARCH ARTICLE

# *In silico* discovery and biological validation of ligands of FAD synthase, a promising new antimicrobial target

Isaias Lans<sup>1</sup>, Ernesto Anoz-Carbonell<sup>2,3,4</sup>, Karen Palacio-Rodríguez<sup>1</sup>, José Antonio Aínsa<sup>3,4,5</sup>, Milagros Medina<sup>2,3</sup>, Pilar Cossio<sup>1,6\*</sup>

**1** Biophysics of Tropical Diseases, Max Planck Tandem Group, University of Antioquia UdeA, Medellin, Colombia, **2** Departamento de Bioquímica y Biología Molecular y Celular, Facultad de Ciencias, Universidad de Zaragoza, Spain, **3** Instituto de Biocomputación y Física de Sistemas Complejos (Unidades Asociadas BIFI-IQFR y CBsC-CSIC), Universidad de Zaragoza, Spain, **4** Grupo de Genética de Micobacterias, Departamento de Microbiología, Pediatría, Radiología y Salud Pública. Facultad de Medicina, Universidad de Zaragoza, Zaragoza, Spain, **5** CIBER Enfermedades Respiratorias (CIBERES), Instituto de Salud Carlos III, Spain, **6** Department of Theoretical Biophysics, Max Planck Institute of Biophysics, Frankfurt, Germany

\* [picossio@biophys.mpg.de](mailto:picossio@biophys.mpg.de)**OPEN ACCESS**

**Citation:** Lans I, Anoz-Carbonell E, Palacio-Rodríguez K, Aínsa JA, Medina M, Cossio P (2020) *In silico* discovery and biological validation of ligands of FAD synthase, a promising new antimicrobial target. PLoS Comput Biol 16(8): e1007898. <https://doi.org/10.1371/journal.pcbi.1007898>

**Editor:** Alexander MacKerell, University of Maryland School of Pharmacy, UNITED STATES

**Received:** April 16, 2020

**Accepted:** July 9, 2020

**Published:** August 14, 2020

**Peer Review History:** PLOS recognizes the benefits of transparency in the peer review process; therefore, we enable the publication of all of the content of peer review and author responses alongside final, published articles. The editorial history of this article is available here: <https://doi.org/10.1371/journal.pcbi.1007898>

**Copyright:** © 2020 Lans et al. This is an open access article distributed under the terms of the [Creative Commons Attribution License](https://creativecommons.org/licenses/by/4.0/), which permits unrestricted use, distribution, and reproduction in any medium, provided the original author and source are credited.

**Data Availability Statement:** All relevant data are within the manuscript and its Supporting Information files.

## Abstract

New treatments for diseases caused by antimicrobial-resistant microorganisms can be developed by identifying unexplored therapeutic targets and by designing efficient drug screening protocols. In this study, we have screened a library of compounds to find ligands for the flavin-adenine dinucleotide synthase (FADS) -a potential target for drug design against tuberculosis and pneumonia- by implementing a new and efficient virtual screening protocol. The protocol has been developed for the *in silico* search of ligands of unexplored therapeutic targets, for which limited information about ligands or ligand-receptor structures is available. It implements an integrative funnel-like strategy with filtering layers that increase in computational accuracy. The protocol starts with a pharmacophore-based virtual screening strategy that uses ligand-free receptor conformations from molecular dynamics (MD) simulations. Then, it performs a molecular docking stage using several docking programs and an exponential consensus ranking strategy. The last filter, samples the conformations of compounds bound to the target using MD simulations. The MD conformations are scored using several traditional scoring functions in combination with a newly-proposed score that takes into account the fluctuations of the molecule with a Morse-based potential. The protocol was optimized and validated using a compound library with known ligands of the *Corynebacterium ammoniagenes* FADS. Then, it was used to find new FADS ligands from a compound library of 14,000 molecules. A small set of 17 *in silico* filtered molecules were tested experimentally. We identified five inhibitors of the activity of the flavin adenylyl transferase module of the FADS, and some of them were able to inhibit growth of three bacterial species: *C. ammoniagenes*, *Mycobacterium tuberculosis*, and *Streptococcus pneumoniae*, where the last two are human pathogens. Overall, the results show that the integrative VS protocol is a cost-effective solution for the discovery of ligands of unexplored therapeutic targets.

**Funding:** This research was founded by Colciencias, University of Antioquia, Ruta N, Colombia, and the Max Planck Society, Germany. Also by the Spanish Ministry of Economy, Industry and Competitiveness (MINECO) [BIO2016-75183-P AEI/FEDER, UE to M.M.], the Spanish Ministry of Science and Innovation (MICINN) (PID2019-103901GB-I00 AEI/FEDER, UE to M.M.) and the Government of Aragón-FEDER [Grupo de Referencia Biología Estructural (E35-20R to M.M.)]. The funders had no role in study design, data collection and analysis, decision to publish, or preparation of the manuscript.

**Competing interests:** The authors have declared that no competing interests exist.

## Author summary

Developing cures for antimicrobial-resistant microorganisms is a pressing necessity. Addressing this problem requires the discovery of novel therapeutic targets -for example, bacterial proteins with no human homologues- and the development of cost-effective drug screening protocols. In this work, we tackled the problem on both sides. We developed an efficient and successful integrative computational protocol for screening inhibitory-molecules for unexplored targets. We used it to discover five novel inhibitors of flavin-adenine dinucleotide synthase (FADS), a promising protein target of pathogens causing tuberculosis and pneumonia.

## Introduction

Given the growing incidence of infections caused by antimicrobial resistant pathogens, international institutions, such as the World Health Organization [1], have informed about the lack of potential therapeutic options for these pathogens, and have named a list of pathogens for which is critical to develop novel antimicrobial agents. The development of such treatments should involve efficient drug design protocols and the discovery of new molecular targets to fight antimicrobial resistance. A straightforward and effective way to increase the chances of success of the drug-screening pipeline is through the implementation of efficient virtual screening (VS) protocols. These methods provide powerful tools to reduce the costs of drug discovery by reducing the number of compounds to be tested in experimental trials [2–5]. Moreover, VS protocols increase the success rate (*i.e.*, active compounds found) and reduce the false negatives in high-throughput compound screening [2, 3, 6–12].

Efficient VS protocols have to be able to screen large compound libraries in short computational times. Therefore, these protocols usually implement a funnel-like strategy, which start from fast but less accurate methods (where a large number of molecules are filtered) and more accurate and time-consuming tools are used in the last steps [13–15]. Usually, pharmacophore-based tools are implemented in the first stages of VS, given their ability to quickly screen large compounds libraries [16–18]. While more sophisticated tools such as docking or molecular dynamics (MD) are implemented in the latter steps to predict ligand affinities [11, 13, 19–26].

Special attention deserve the tools used in the first steps of the VS, because these impact the ability of the protocol to explore large compound libraries and the chemical space of the compounds, such as the pharmacophore-based strategies [16–18, 27–30]. Despite the usefulness of these methods, which accelerate the first steps of the VS, these strategies have some limitations. Several pharmacophore-based methods require knowing ligands or ligand-receptor structures for their training, limiting the chemical space of the filtered molecules to that associated with the training set [16]. Recently, the flexi-pharma method, a VS strategy that uses pharmacophores from MD conformations was developed to overcome these limitations [31]. However, in general, new protein targets, which have limited structural information available, such as the bifunctional enzyme flavin-adenine dinucleotide synthase (FADS), are challenging for the funnel-like VS strategies.

FADS is a potential target for drug design against antimicrobial-resistant organisms, such as the human pathogens *Mycobacterium tuberculosis* and *Streptococcus pneumoniae*. FADS is a bi-functional and bi-modular enzyme that catalyzes the synthesis of two essential co-factors: flavin mononucleotide (FMN) and flavin-adenine dinucleotide (FAD). These are essential for a large number of proteins participating in energy transformation or metabolic processes, in

prokaryotic and eukaryotic organisms [32–34]. For FADS, the synthesis of FMN occurs at the C-terminal module (the RKF module) and that of FAD at the N-terminal module (FMNAT module) [35–38]. The RKF module has a similar structure and sequence to the equivalent enzyme in eukaryotic organisms. However, because the FMNAT module lacks both sequence and structural similarity with the equivalent enzymes in eukaryotic systems, the prokaryotic FADSs have emerged as potential antimicrobial targets [35, 39–41].

The most characterized FADS is the enzyme of *Corynebacterium ammoniagenes* (CaFADS), which is considered a good representative model for the FADS of the human pathogen *M. tuberculosis* (MtFADS) [40, 41]. However, limited structural information about this enzyme is available. Moreover, no experimental structures of the FADS-FMNAT module in complex with substrates are reported. The only ligand-CaFADS FMNAT module structures correspond to theoretical or computational models [35, 42].

The objective of this work is to discover molecules able to inhibit the FMNAT activity of FADS using a novel integrative VS protocol. This promising protocol addresses some of the limitations found with traditional VS, for example, it does not require knowledge of ligands or ligand-receptor structures, and its attributes enable a better exploration of the chemical space of large compound libraries.

This manuscript is organized as follows. First, we describe the integrative computational protocol, which includes several filtering layers: *i*) flexi-pharma screening [31], *ii*) consensus docking screening [43], *iii*) MD sampling and scoring, and *iv*) compound activities measured by experimental assays. The protocol is tested and optimized using a library of 1993 compounds from which 39 compounds are true ligands of the CaFADS [41]. Subsequently, the optimized protocol is implemented over a library of 14000 compounds. A final list of 17 filtered compounds is tested experimentally. We discover that six molecules are able to inhibit the FMNAT-FADS activity, five bind to the FMNAT-FADS and five present growth inhibitory activity against *C. amoniagenes*, *M. tuberculosis* or *S. pneumoniae*. We conclude that the VS protocol and the new inhibitory compounds can contribute to further development of novel therapeutic strategies against antimicrobial-resistant pathogens such as *M. tuberculosis* and *S. pneumoniae*.

## Materials and methods

### Computational methods

**FAD structure.** The Cartesian coordinates of the FMNAT module (M1-H186) of CaFADS were taken from the crystal structure with PDB code 2X0K [35]. These were used for the MD simulations in the flexi-pharma or molecular docking stage.

**Flexi-pharma method.** The flexi-pharma protocol [31] has three substages: run an MD simulation of the receptor target, generate a set of pharmacophores from each ligand-free receptor MD conformation, and assign a vote to each molecule every time it matches at least one pharmacophore from each MD conformation.

First, an MD simulation of receptor was performed. For CaFADS, we used the results from a simulation of this system performed in a previous work [42]. Specifically, we used 600 equidistant ligand-free CaFADS conformations from 60 ns of MD at 300.15K (for details about the MD parameters see ref. [42]). To generate the pharmacophore set from each ligand-free MD conformation, we used Autogrid4.2 [44] to calculate the affinity maps of several atom-types: hydrogen-bond donor, hydrogen-bond acceptor, hydrophobic, aromatic and charged atoms. Some atom-type affinity grids were first discarded if they show a flat distribution of the affinity values of the map (for this work, the affinity maps that have a histogram with kurtosis larger than 3). Then, we defined a grid-percentage threshold to determine the hotspots (clusters of

grid-cells) for each atom type. The threshold is a percentage of the total number of cells in the grid with negative affinity energy. We clustered the selected cells to generate a pharmacophoric feature (given by a center, a radius of gyration, an atom type and in some cases a direction). A pharmacophore was built by combining three features. The pharmacophore set consists of all possible combinations of triplets of features from different active spaces (*i.e.*, centers of the affinity grids) together with a volume exclusion term. The Pharmer [45] program was used to screen the compound library with the created pharmacophore set. An example of the pharmacophore mapping is shown in S1 Fig.

Flexi-pharma gives a score to each compound by means of a voting strategy. If a molecule, from the compounds library, matches any pharmacophore obtained from a specific MD frame, then the molecule obtains a vote. The total number of votes is used as a score of the molecule. For more details about the flexi-pharma method see ref. [31].

**Molecular docking.** The molecular docking was carried out using the programs: Autodock4.2 [44, 46, 47], Vina [48], and Smina [49]. All programs used the same molecule input format that was AutoDock pdbqt. The protonation state for each molecule was determined from the compound libraries. Also for these programs, the sampling space was defined using a grid box of  $15 \times 15 \times 15$  Å centered at the oxygen of the amide group of the catalytic residue ASN125 [50]. The number of requested poses was 50.

Autodock4.2 [44, 46, 47] was used with a grid spacing of 0.25 Å. The search was performed using the Lamarckian genetic algorithm implemented in Autodock, with a starting population of 50 individuals, using 25000000 energy evaluations and 27000 generations. The resultant poses were clustered using the RMSD of the atomic positions, with a tolerance of 2.0 Å, using the default clustering method. In addition, to the sampling space and the number of poses, Vina [48] and Smina [49] were used with the default parameters. For Smina, the Vinardo [51] scoring function was used.

**Molecular dynamics simulations.** The best pose for each compound from the docking stage, obtained with the Autodock4.2 program, was used as the initial conformation for the MD simulation. Since, the output poses from Autodock4.2 do not contain aliphatic protons, we use Open Babel [52] to protonate those atoms as in the original database (Prestwick or Maybridge). The PROPKA [53] module from the PDB2PQR software package [54, 55] was used to determine the protonation state of all ionizable groups at pH 7.0. The final models were solvated with a dodecahedral water box, centered at the geometric center of the complex. To neutralize the systems, Na<sup>+</sup> ions were added when necessary. The AMBER99SB-ILDN [56] force field was used to model the protein with the TIP3P water model [57]. The GAFF force field [58] parameters were obtained for the compounds using Antechamber [58, 59]. ACPYPE [60] was used to change the topology files from amber to GROMACS [61, 62], which was used for all the MD simulations. The systems were minimized until the maximum force was  $\leq 1000$  kJ/mol-nm with the steepest descent algorithm. MD simulations were carried out with periodic boundary conditions. A spherical cutoff of 1.2 nm for the non-bonded interactions was applied together with a switch function acting between 1.0 and 1.2 nm. The non-bonded pair list was updated every 20 steps. The particle mesh Ewald method was used to compute long-range electrostatic force terms, and the leapfrog algorithm to propagate the equations of motion. All bond lengths and angles involving hydrogen atoms were constrained using the LINCS algorithm [63]. Equilibration consisted of 100 ps of NVT followed by 100 ps of NPT simulation at 310 K, with a time step of 2 fs. During equilibration the coordinates of protein and of ligand heavy atoms were restrained using a constant force of 100 kJ/mol-nm. Finally, MD simulations between 5–15 ns were carried out using the GROMACS 5.1.3 program [61, 62] with a time step of 2 fs, without restraints, in an isothermal-isobaric (NPT) ensemble at 310.15 K and 1 atm.

**Exponential consensus ranking.** A consensus methodology was used to combine the results from different scoring functions both for the docking and MD VS stages. We used an exponential consensus ranking (ECR) methodology [43]. This method assigns a score  $p(r_i^j)$  to each molecule  $i$  for each scoring function  $j$  using an exponential function  $p(r_i^j) = \exp\left(\frac{-r_i^j}{\alpha}\right)/\alpha$ , which depends on the rank of the molecule ( $r_i^j$ ) given by each individual docking program.  $\alpha$  is the expected value of the exponential distribution, which we have set to 50% of the total molecules at each stage. The final score  $P(i)$  is defined as the sum of the exponential functions for all of the programs,  $P(i) = \sum_j p(r_i^j) = \frac{1}{\alpha} \sum_j \exp\left(\frac{-r_i^j}{\alpha}\right)$ .

**Validation metrics.** The enrichment factor (EF<sub>x</sub>%) is a measure of the change on the ligand/decoys proportion in a molecular dataset, after filtering it to the x%. EF<sub>x</sub>% is defined as the ratio between ligands (Hits) found at a certain threshold (x%) of the best ranked compounds and the number of compounds at that threshold (N<sub>x</sub>%) normalized by the ratio between the hits contained in the entire dataset (Hits<sub>100%</sub>) and the total number of compounds N<sub>100%</sub>:

$$EF_x = \frac{Hits^{x\%}}{N^{x\%}} \times \frac{N^{100\%}}{Hits^{100\%}}. \quad (1)$$

Values of EF<sub>x</sub>% higher than 1 indicate an enrichment of the compound library.

The enrichment plot (EP) measures the performance of a filtering method at different levels of a compound library reduction. In an EP, the percentage of ligands found in the top x% of ranked compounds vs the top x% of filtered compounds is plotted [64].

To assess the error of the flexi-pharma EPs, a bootstrapping analysis with replacement was used. The selected MD frames were iteratively re-sampled with replacement 100 times. Thus, 100 EPs were obtained for each trajectory. From these the average and the error of the EPs were calculated (similarly as in ref. [31]).

## Experimental methods

**Chemicals.** The selected compounds were acquired from Molport and dissolved in 100% DMSO to prepare stock solutions at 50 mM and 10 mM. According to the manufacturer indications, the purity of the compounds was >95%, and had been determined by high performance liquid chromatography (HPLC), thin layer chromatography (TLC), NMR, IR or basic titration.

**Protein purification and quantification.** CaFADS was produced as a recombinant protein in *Escherichia coli* BL21(DE3) and purified as previously described in ref. [40]. Protein purity was tested by 15% SDS-PAGE. Protein content in pure samples (in 20 mM PIPES, pH 7.0) was quantified using the theoretical extinction coefficient ( $\epsilon$ ) 279 nm = 27.8 mM<sup>-1</sup>·cm<sup>-1</sup>.

**Differential scanning fluorescence.** Interaction of compounds with CaFADS was evaluated using fluorescence thermal denaturation, on the bases of the shifts in denaturation mid-points of thermal curves of the protein [65]. Denaturations were performed in a Stratagene Agilent Mx3005p qPCR instrument (Santa Clara, US) following SYPR Orange (ThermoFisher Scientific) emission fluorescence (excitation at 492 nm and emission at 610 nm), which greatly increases when this probe binds to protein hydrophobic regions becoming solvent exposed upon thermal unfolding. Solutions containing 2 μM CaFADS with the studied compound in an increasing 5-250 μM concentration range (2% residual final concentration of DMSO) and 5xSYPR Orange in 20 mM PIPES pH 7.0, 10 mM MgCl<sub>2</sub>, with a 100 μL total volume were dispensed into 96-well microplates (BRAND 96-well plates pure grade™). After an initial 1 min incubation at 25 °C within the equipment, unfolding curves were registered from 25 to 100 °C

at  $1\text{ }^{\circ}\text{C}\cdot\text{min}^{-1}$ . Control experiments with *CaFADS* samples with/without DMSO were routinely performed in each microplate. For those compounds shifting midpoint denaturation temperature,  $T_m$ , the dissociation constant,  $K_d$ , was predicted by fitting the data to the equation [66]

$$\frac{\Delta T_m}{T_m} = \frac{NRT_m^0}{\Delta H_0} \ln \left( 1 + \frac{[L]}{K_d} \right), \quad (2)$$

which estimates the extent of the ligand-induced protein stabilization/destabilization.  $\Delta T_m = |T_m - T_m^0|$  with  $T_m^0$  and  $T_m$  being the midpoint denaturation temperatures in the absence and the presence of ligand, respectively, and  $\Delta H_0$  the unfolding enthalpy of the protein in the absence of ligand.

**Evaluation of the compound's ability to inhibit the *CaFADS* enzymatic activity.** To determine the compound's ability to inhibit the RFK and/or the FMNAT activities of *CaFADS*, both enzymatic activities were quantitatively measured in the absence and presence of the compounds following previously described protocols [41]. Reaction mixtures contained  $50\text{ }\mu\text{M}$  ATP,  $5\text{ }\mu\text{M}$  RF in  $20\text{ mM}$  PIPES, pH 7.0,  $0.8\text{ mM}$   $\text{MgCl}_2$ , when assaying the RFK activity, and  $50\text{ }\mu\text{M}$  ATP,  $10\text{ }\mu\text{M}$  FMN in  $20\text{ mM}$  PIPES, pH 7.0,  $10\text{ mM}$   $\text{MgCl}_2$  when measuring the FMNAT reaction. Each compound was tested at  $250\text{ }\mu\text{M}$  ( $0.5\%$  residual final concentration of DMSO) for each of the two enzymatic reactions. The samples were pre-incubated at  $25\text{ }^{\circ}\text{C}$ , the reaction was then initiated by the addition of  $\sim 40\text{ nM}$  *CaFADS* (final concentration) and allowed for 1 min. Finally, the reaction was stopped by boiling the samples for 5 min and the denatured protein was eliminated through centrifugation. The transformation of RF into FMN and FAD (RFK activity) and of FMN into FAD (FMNAT activity) was evaluated through flavins separation by HPLC (Waters), as previously described [37]. All the experiments were performed in triplicate. To evaluate the potency of compounds as inhibitors, we took advantage of the decrease in quantum yield of fluorescence when FMN is transformed into FAD, which allows to follow such transformation in a continuous system. Measurements were carried out using a microplate reader Synergy HT multimode plate reader (Biotek) with BRAND 96-well plates pure Grade. Reaction mixtures contained  $5\text{ }\mu\text{M}$  RF or FMN, and  $50\text{ }\mu\text{M}$  ATP in  $20\text{ mM}$  PIPES, pH 7.0,  $10\text{ mM}$   $\text{MgCl}_2$ , and the inhibitor compound in a  $5\text{-}250\text{ }\mu\text{M}$  concentration range ( $2\%$  residual final concentration of DMSO). Reactions were initiated through addition of  $0.4\text{ }\mu\text{M}$  *CaFADS*, being the final reaction volume  $100\text{ }\mu\text{L}$ . Flavin fluorescence (excitation at  $440\text{ nm}$  and emission at  $530\text{ nm}$ ) was registered at  $25\text{ }^{\circ}\text{C}$ , every  $50\text{ s}$  during 15 min. The fluorescence change per time unit ( $\Delta F/\Delta t$ ) was calculated as the slope of the resulting fluorescence decays recorded between 0 and 6 min (linear decay of the fluorescence). Controls which contained the reaction mixture without the enzyme and without any potential *CaFADS* inhibitory compound were included in the assay and referred as the  $0\%$  and  $100\%$  of enzymatic activity, respectively.  $\text{IC}_{50}$  was calculated as the concentration of compound required for a  $50\%$  inhibition of the enzymatic activity.

**Determination of the antibacterial activity of the compounds.** The minimum inhibitory concentration (MIC) of the inhibitors was determined by the resazurin serial broth microdilution method [67] according to the Clinical and Laboratory Standards Institute guidelines. Compounds were tested against a panel of bacterial strains including Gram positives, Gram negatives and acid fast bacteria (see S3 Table). Serial 2-fold dilutions of the inhibitors were performed in cation-adjusted Mueller-Hinton broth (Difco) in 96-well polypropylene flat-bottom plates, with a final volume of  $100\text{ }\mu\text{L}$  per well. Subsequently, liquid cultures of the bacterial strains in logarithmic phase were adjusted to  $10^6\text{ CFU/ml}$  in Mueller-Hinton broth, and  $100\text{ }\mu\text{L}$  of this suspension were added to each well, resulting in a final inoculum of  $5\cdot 10^5\text{ CFU/ml}$ .



Plates were incubated for 18 hours at 37 °C. Then, 30  $\mu$ L of 0.4 mM filter-sterilized resazurin (Sigma-Aldrich) was added to each well, and results were revealed after 4 h of further incubation at 37 °C. When testing the compounds against mycobacteria, Middlebrook 7H9 (Difco) supplemented with 10% ADC (0.2% dextrose, 0.5% V fraction BSA and 0.0003% bovine catalase) (BD Difco) and with 0.5% glycerol (Scharlau) was used as culture media, and plates were incubated 4 days for *Mycobacterium smegmatis* and 7 days for *M. tuberculosis*. Resazurin (blue) is an indicator of bacterial growth, since metabolic activity of bacteria reduces it to resorufin (pink). The minimum inhibitory concentration (MIC) is the lowest concentration of compound that does not change the resazurin colour from blue to pink.

**Evaluation of the cytotoxicity of the compounds in eukaryotic cell lines.** The (4,5-dimethylthiazol-2-yl)-2,5-diphenyl tetrazolium bromide (MTT) assay was used to determine the effect of the compounds in cell growth and viability of HeLa (ATCC CCL-2) and A549 (ATCC CCL-185) eukaryotic cell lines. Both cell lines were routinely cultured in high-glucose DMEM (Lonza) supplemented with 10% fetal bovine serum, 4 mM glutamine GlutaMAX™ (Gibco) and 1x non-essential amino acids (Gibco), under 5% CO<sub>2</sub> at 37 °C in a humidified atmosphere. For the MTT assay, cells were initially seeded in 96-well flat-bottom plates at a density of 10<sup>4</sup> cells per well and cultured for 24 h. Cultures were routinely tested for mycoplasma presence. The compounds were dissolved in fresh culture medium, added in a 4-512  $\mu$ M concentration range (1% DMSO final concentration), and incubated with the cells for 24 h. Finally, formazan crystals were dissolved with pure DMSO and MTT absorbance was measured at 570 and 650 nm. Untreated cells were included as control of 100% viability. Assays were done in quadruplicate.

## Results and discussion

### Virtual screening protocol

The VS protocol aims to find active compounds, from large compound libraries, towards receptors for which little or no information about ligands or ligand-receptor structures is available. This is the case of the CaFADS. To achieve this goal, we implemented a funnel-like protocol with four filtering stages (Fig 1). It includes three main VS stages plus an experimental stage. In the following, we present the principal ideas for the integrative VS protocol.

#### **Flexi-Pharma: Pharmacophore filtering from ligand-free receptor conformations.**

Pharmacophore-based VS strategies are computationally efficient. These strategies are able to explore large compound libraries using pharmacophores: an ensemble of physico-chemical features that ensure the optimal interactions within the active site of a specific biological target [16]. Therefore, the first stage of the protocol implements a pharmacophore-based VS strategy [31]. The method flexi-pharma defines pharmacophores from ligand-free receptor conformations from MD simulations. It implements a rank-by-vote strategy, assigning a vote to each compound that matches an MD conformation. The use of multiple conformations allows for a better exploration of the pharmacophoric space. The voting strategy enables the filtering of the molecules at any percentage of the dataset. Details for the flexi-pharma strategy are presented in the Methods and in ref. [31].

**ECR-docking: Exponential consensus ranking of docking VS.** The second stage of the protocol consists of a docking-based VS. Molecular docking aims to find the most favorable binding conformation of a molecule (*i.e.*, pose) upon binding to a pocket of a protein target [68, 69], and assigns a docking score to each molecule. The docking score is an empirical or physics-based estimation of the affinity of the molecule towards the biological target. Therefore, with molecular docking, it is possible to screen and rank molecules from compound libraries. However, it has been shown that the docking results might be system or structure

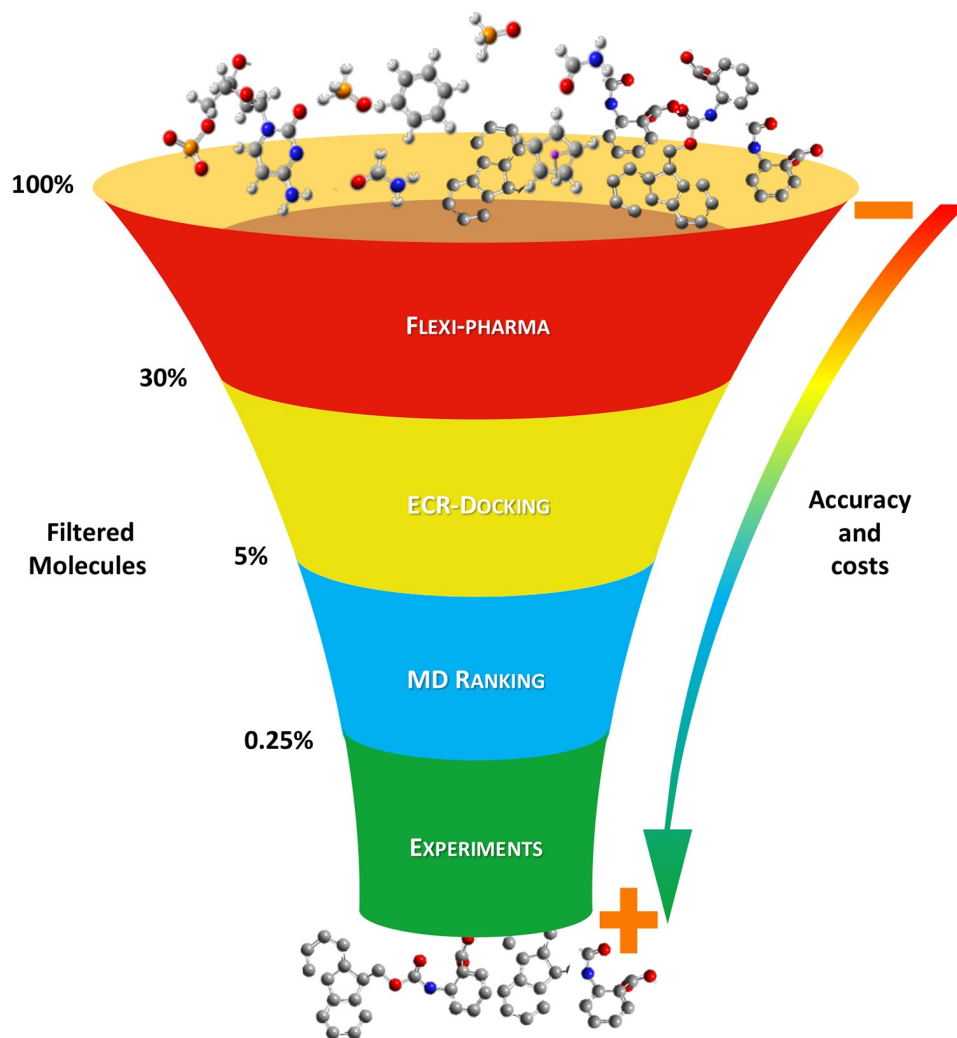


**Fig 1. Main stages of the funnel-like VS protocol.** The protocol consists of four stages: *i*) flexible pharmacophore-based VS (flexi-pharma) [31], *ii*) docking and exponential consensus ranking (ECR-docking) [43], *iii*) MD simulations with consensus ranking -that includes a new Morse-based ligand-flexibility score-, and *iv*) biological experimental binding and activity assays. At each stage, the compound library was filtered. The protocol was optimized and validated over a library of 1993 compounds, which was previously tested over CaFADS [41]. On the left, we show an example of the reduction of this library going from 100% to 0.25% through the successive steps.

<https://doi.org/10.1371/journal.pcbi.1007898.g001>

dependent [43, 70], possibly due to algorithm-parameterization biases, which are trained over particular benchmark systems. To overcome this limitation, we use a consensus strategy that combines the results from different docking programs to obtain a consensus rank using a sum of exponential functions (ECR method) [43]. Below, in the S1 Text and S2 Fig, we describe the different docking-scoring alternatives that we used to find the optimal enrichment for the FMNAT-FADS ligand screening.

**MD-ranking VS.** MD simulations were used to estimate the compound affinities and the stability of the predicted complexes filtered from the docking stage. The MD starting configuration was selected from the best pose obtained with Autodock4.2 [44, 46, 47] in the previous stage. Inspired by conformational-prediction tools that take into account flexibility [71, 72], we used two measures for the stability and affinity of the ligand bound to the receptor in the MD ensemble. The first measure generates a consensus rank using multiple scoring functions

over the MD conformations. We called this scoring function-based rank (see below for details). The second measure is based on the root mean square deviation (RMSD) of the ligand's atomic positions along the MD trajectory. This is used with a Morse potential to define a score that measures the ligand's flexibility (see below for details). Finally, the scoring function-based rank and the Morse-based rank are combined using the ECR method. We use this analysis to select the percentage of best-ranked molecules for the activities assays. In the following, we describe the scoring function-based rank and the Morse-based rank.

**Scoring function-based rank.** We used four scoring functions: Autodock4.2 [44, 46, 47], Vina [48], Vinardo [51] and CY score [73], which were calculated over each MD conformation. For each scoring function, an average score over all the conformations is calculated for each molecule. This can then be used to rank the molecules. The ranks from the four scoring functions are used with the ECR method [43] to obtain a consensus rank by combining their individual ranks.

**Morse-based rank.** We used the standard deviation of the RMSD of the ligand's atomic positions around the binding site as an indicator of the ligand's flexibility. Those ligands showing a small standard deviation of the RMSD at the binding site indicate a very rigid complex, which leads to a conformational penalization. On the other hand, molecules with high RMSD standard deviation, indicate a dissociation tendency, which leads to an affinity penalization. These behaviors can be characterized using a Morse potential (Eq 3 and Fig 2)

$$V_M(r) = \omega(1 - \exp^{-a(r-r_0)})^2, \quad (3)$$

where  $\omega$  is the depth of the well,  $r_0$  is the position of the minimum,  $a = \sqrt{\frac{k}{2\omega}}$  and  $k$  is a constant that defines the width of the well. For the Morse-base score, we used  $V_M(r)$  from Eq 3, where the dependent variable  $r$  is the standard deviation of the RMSD along the MD trajectory, and  $r_0$  is the standard deviation corresponding to a normal distribution with null entropy (i.e.,  $r_0 = 0.242 \text{ \AA}$ ). The Morse potential was implemented with a force constant  $k = 1 \text{ kcal/mol.nm}^2$  and a depth of the well  $\omega = 1 \text{ kcal/mol}$ . Thus, RMSD values lower or higher than  $0.242 \text{ \AA}$  are penalized with Morse-based score. We used this to rank the molecules according to the  $V_M(r)$  score. We note that most molecules have a RMSD standard deviation greater than  $0.242 \text{ \AA}$ , therefore, the parameters  $k$  and  $\omega$  used in the score do not have a great impact in the final Morse-based rank.

**VS parameter dependence.** Although the presented VS protocol is sufficiently general to be applied over any receptor target, there are several parameters and setups that can be optimized. Moreover, because -in its complete form- it has not been tested, we considered it necessary to first validate and optimize the VS protocol over a benchmark library with known inhibitors of the CaFADS—FMNAT activity [41]. The results are presented in the following section.

## VS protocol FADS validation: Prestwick Chemical Library

To validate and optimize the VS protocol for screening potential ligands of CaFADS, a molecular library (Prestwick Chemical Library) was used. A previous study showed that 39 of its 1993 compounds are able to bind to the CaFADS with FMNAT inhibitory activity [41]. To study the performance, we measure the enrichment factor (EF) and the enrichment plots (EP) [64] (see the Methods). In the following, we present the results for each stage of the VS protocol applied over the Prestwick Chemical Library.

**Flexi-pharma FADS optimization and validation.** In Fig 3, we present the EP obtained after the application of the flexi-pharma stage over the Prestwick compound library. Since the

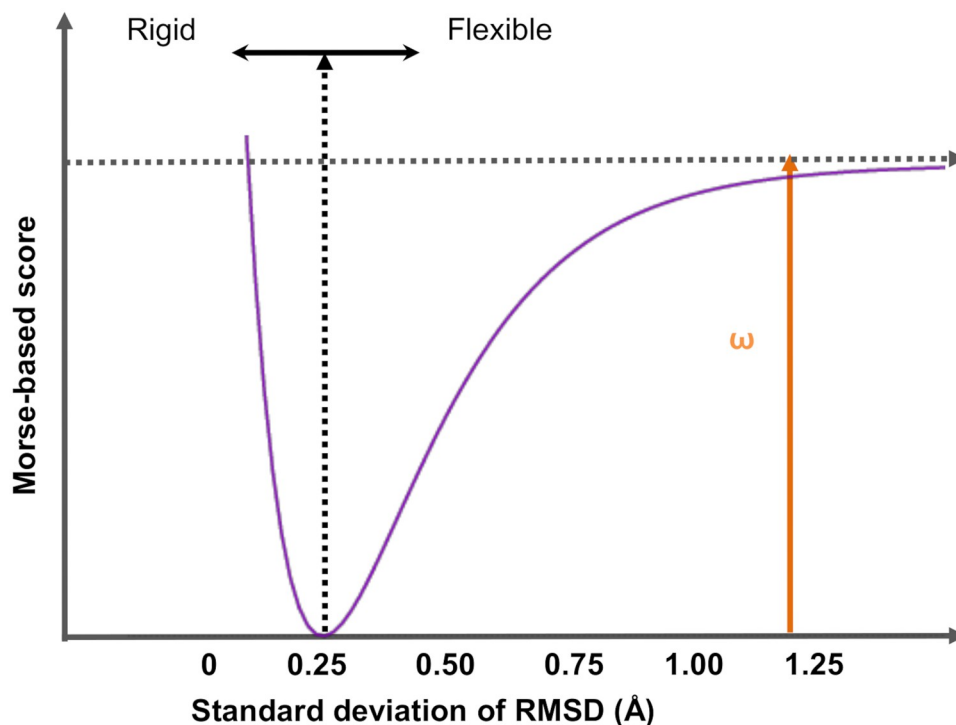


**Fig 2. Morse-based score.** A score that uses a Morse potential (Eq 3) was implemented for scoring the flexibility of the ligand inside the pocket using MD simulations. The input variable is the standard deviation of the RMSD of the ligand's atomic positions around the binding site. Ligands that show large RMSD variations are considered very flexible -with dissociation tendencies (*i.e.*, unstable)- and their behavior is penalized (right of vertical black dashed arrow). Ligands with small RMSD fluctuations are considered rigid leading to a conformational penalization (left of black vertical dashed arrow). The Morse potential was implemented with a force constant  $k = 1 \text{ kcal/mol.nm}^2$ , a depth of the well of  $\omega = 1 \text{ kcal/mol}$ , and the minimum is localized at  $r_0 = 0.242 \text{ \AA}$ .

<https://doi.org/10.1371/journal.pcbi.1007898.g002>

flexi-pharma method uses MD conformations of the ligand-free receptor, we used 600 equidistant frames from 60 ns of MD of the ligand-free CaFADS, which was carried out in a previous study [42]. We applied the flexi-pharma VS as described in the Methods. We find an enrichment of the compound library, showing that the data (black line) are better than a random EP (red line). The vertical violet line shows the percentage of molecules selected to pass to the next stage. The selected list of compounds consists of 600 potential ligands ( $\approx 30\%$  of the initial compound library) with 24 actual ligands, resulting in a EF of 2.0 for this stage. These results support the usefulness of flexi-pharma to enrich the Prestwick compound library.

The EPs showed in the Fig 3 involved several parameters, such as the affinity grid threshold value (*i.e.*, percentage of grid points with lowest grid energies), the active spaces and the number of features used to define the pharmacophores (see ref. [31]). In that work, it was shown that the results are almost independent of the affinity-grid threshold. However, a large threshold implies a large number of features, which increases the pharmacophore set and the computational time to carry out the VS. Therefore, a good computational efficiency is obtained with small threshold values, while maintaining the performance. For this study, the threshold value of 0.1% is used. Because of the large size of the FMNAT active site, the pharmacophores were obtained from 7 active spaces (centered at NE2-H31, NE2-H57, CA-E108, CG-L110, ND2-N125, OG-S164 and CZ-R168 [50]).

**ECR-docking FADS optimization and validation.** The second stage of the VS protocol uses a docking-based strategy. Docking generates an optimal molecule-bound conformation

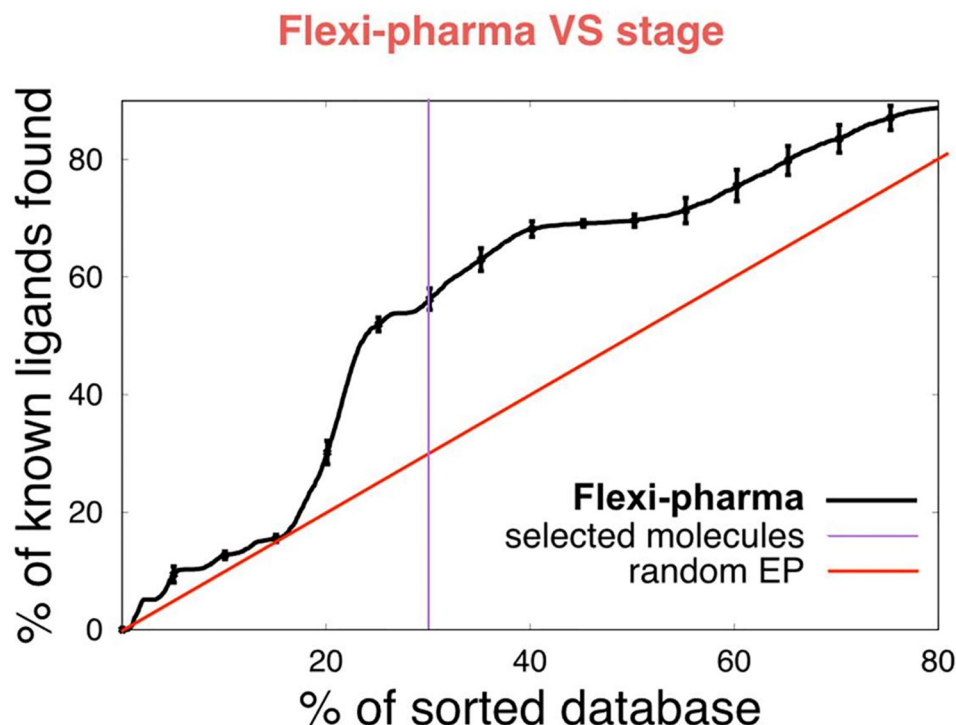


**Fig 3. Flexi-pharma VS stage over the Pretswick library.** Average enrichment plot of the Pretswick library using the flexi-pharma stage over MD conformations of ligand-free CaFADS. The affinity-grid threshold value is 0.1% and 600 equidistant frames obtained from an MD of 60 ns were used [42]. The flexi-pharma number of votes for each molecule was used as a score to calculate the EPs. Bootstrapping analysis was performed by sampling with replacement 100 times to obtain the average EP and its standard deviation. The violet line shows the screening threshold ( $\approx 30\%$ ) for the selection of molecules to be filtered and passed onto the second stage.

<https://doi.org/10.1371/journal.pcbi.1007898.g003>

with a corresponding score. However, some docking-program outcomes depend on the system of study [43, 70]. Thus, a particular docking software can show good results for a receptor, however, it can show bad results for other receptors. For an untested receptor it is impossible to know, in advance, which docking software generates the best outcome. To overcome this limitation, we implement a modified version of the exponential consensus rank (ECR) strategy [43] using several docking programs.

The top 600 molecules of the Pretswick library filtered from the flexi-pharma stage were docked, using several programs, to the FMNAT module using the crystallographic structure (PDB 2X0K) of CaFADS. After several attempts (see the S1 Text), we found that the best EP was obtained by using the best pose from Autodock4.2 and re-scoring it with Autodock4.2 [44, 46, 47], Vina [48], Vinardo [51] (a function scoring implemented in Smina [49]) and Cyscore [73] scoring functions. The molecules that did not have the best Autodock4.2 pose within the FMNAT-FADS active site (less than 5 Å of H31 and N125) [50] were discarded, reducing the list to 467 molecules (including 23 confirmed inhibitors). The ranks from each scoring function were combined in using an ECR methodology to obtain a consensus rank. The enrichment plot after this analysis is shown in the Fig 4 and S2 Fig. The top 100 molecules from this analysis contained 9 confirmed ligands, which represents a global EF% (*i.e.*, the EF% normalized to the initial compound library) of 4.6, showing a clear enrichment.

**MD-ranking FADS optimization and validation.** MD simulations of potential ligand-receptor complexes allows for a more accurate sampling of their conformational space. The

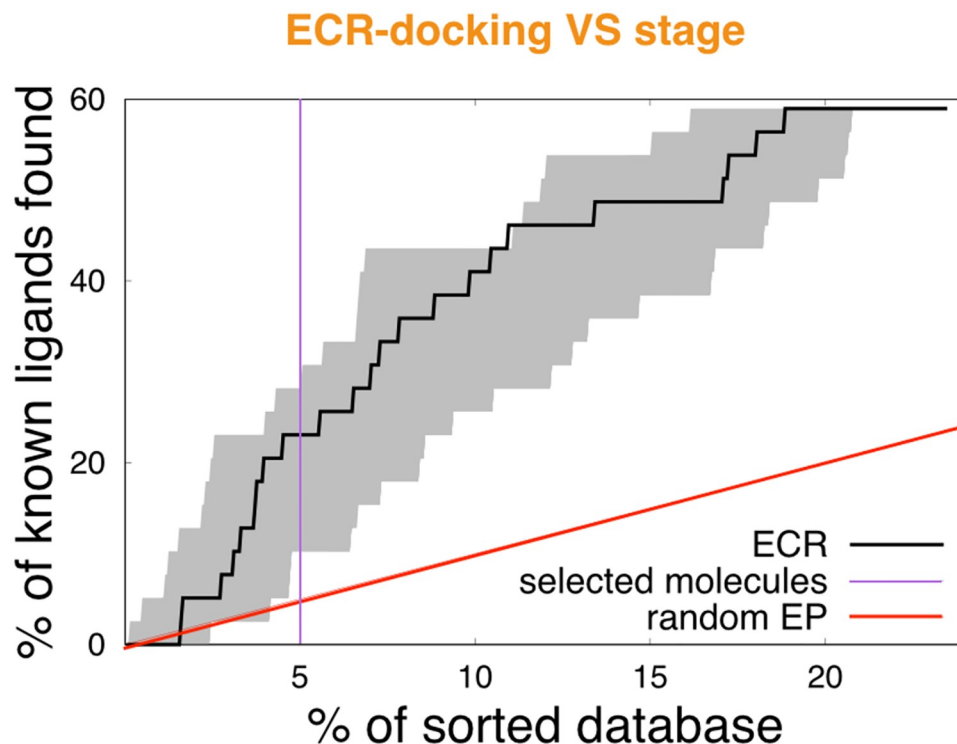


**Fig 4. ECR-docking VS stage over the Pretswick library.** Enrichment plot using the ECR (black line) from the best Autodock4.2 pose that is re-scored with four scoring functions (Autodock4.2, Vina, Vinardo and CYScore). The shaded area encloses the best and worst behaviors for the individual scoring functions. The enrichment plot is normalized by the initial database values (39-ligands and 1993 compounds). The violet line shows the threshold for the selection of molecules for the third VS stage.

<https://doi.org/10.1371/journal.pcbi.1007898.g004>

stability of these conformations should give an estimate of the affinity of the potential ligand towards the receptor. As mentioned previously, the starting conformation was chosen from the best docking pose from Autodock4.2 obtained from the previous stage. For the Pretswick library, we found that by dividing the MD stage into two substages according to the simulation time (MD-ranking 1 and MD-ranking 2), there is a good trade-off between computational costs and performance. In the MD-ranking 1, we ran 5 ns for all the compounds filtered from the docking stage. We used the two measures over the MD conformations, scoring function-based and Morse-based, to rank of the potential ligands to the *CaFADS*. The two results were combined using an ECR to obtain the EPs shown in Fig 5 (black line). Our results indicate that it is possible to obtain an enrichment of the library compound using MD and combining the two measures using an ECR methodology. We note that, although the EP from the Morse-base rank shows better outcome than the EP from the ECR scoring functions-based (ECR-SF) (blue and green lines, respectively, in Fig 5), the use of both measures is relevant. The logic behind combining the two stability measures, lies in that the Morse-based rank gives only information about the conformational stability of the ligand but it does not contain direct information about any physico-chemical interactions. Whereas the scoring functions, *e.g.*, Autodock4.2 or Vina, include physics-based interactions which are relevant. Therefore, the scoring functions-based rank supplies an empirical contribution to the enthalpy and global entropy in the binding process. Thus, the two strategies should complement each other.

We selected the top 50 molecules to be screened in the MD-ranking 2 stage. For this filtered set, we extended the MD time to 15 ns for each complex. These new conformations are scored

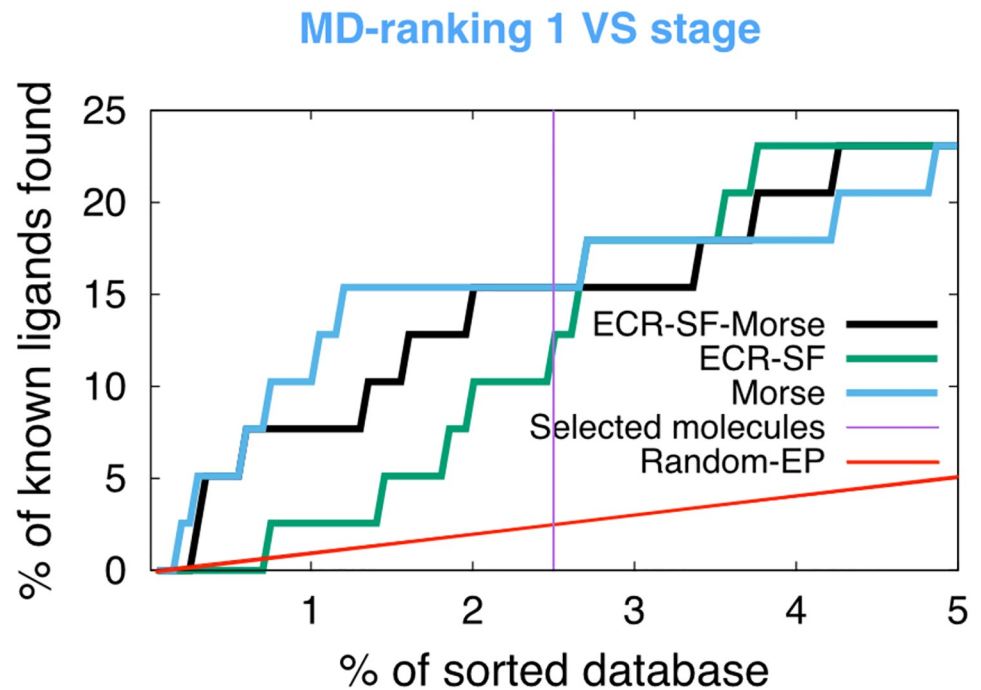


**Fig 5. MD-ranking 1 VS stage over the Prestwick library.** Enrichment plot obtained using an ECR methodology (black) from the combination of the ECR scoring function-based rank (ECR-SF) (green) and Morse-based rank (blue). 5 ns of MD for 100 complexes were carried out. We used 200 equidistant frames from the last 2 ns of MD simulation. The enrichment plot is normalized to the initial database (39-ligands and 1993 compounds). The violet line shows the threshold for the molecule selection for the MD-ranking 2 stage.

<https://doi.org/10.1371/journal.pcbi.1007898.g005>

similarly as before (*i.e.*, ECR combined scoring function-based and Morse-based ranking) and we select the top 5 molecules. The EFs for all the stages of the protocol are shown in [Table 1](#). These results confirm that all stages of the VS protocol increase the enrichment while saving computational resources.

### VS protocol FADS application: Maybridge database

Once the efficiency of the VS protocol was optimized with the Prestwick library, the protocol was implemented over the Maybridge compound library that contains 14000 molecules. A description of the VS protocol for this library is shown in [S3 Fig](#). For the flexi-pharma filtering we selected 3000 molecules. Then, the best 600 were selected using the ECR-docking stage. For the second MD-ranking VS stage, we tested the best 300 molecules. In [S4 Fig](#), we present the

**Table 1. EFs obtained for each VS stages using the Prestwick library.**

| Stage        | Stage EF | Global EF | Ligands | Molecules filtered |
|--------------|----------|-----------|---------|--------------------|
| Flexi-pharma | 2.0      | 2.0       | 24      | 600                |
| ECR-Docking  | 2.3      | 4.6       | 9       | 100                |
| MD-ranking 1 | 1.3      | 6.1       | 6       | 50                 |
| MD-ranking 2 | 1.7      | 10.2      | 1       | 5                  |

Stage EF is the enrichment factor relative to the previous step, while the Global EF is the enrichment factor normalized to the initial database (39-ligands and 1993 compounds).

<https://doi.org/10.1371/journal.pcbi.1007898.t001>

rank obtained from each individual scoring function in comparison to the ECR, which was used to select the top 30 molecules. We note that the difference in the screening between the Maybridge library with respect to the Prestwick library is the percentage of molecules selected at each step. These numbers were changed to optimize the computational efficiency, since for just the MD-ranking stages 6  $\mu$ s of MD simulation time were used.

### Experimental evaluation of the affinity and the inhibitory activity of selected molecules

Considering a range of properties for the 30 best VS-ranked compounds that relate to their potential drug-likeness, shown in S1 Table [74, 75], as well as their commercial availability, 17 compounds were chosen as virtual screening hits (VSH) to experimentally evaluate their performance. From the experimental assays 5 compounds were found as true ligands of CaFADS. Table 2 and Fig 6 show the dissociation constant ( $K_d$ ) values in the range of 1.7–41  $\mu$ M.

Since binding of small molecules to a protein usually alters its thermal conformational stability, shifting the midpoint temperatures ( $T_m$ ) of thermal denaturation curves [65], displacements in  $T_m$  induced by the different VSH appeared as a feasible approach to experimentally identify those binding CaFADS [76]. 5 compounds, out of the 17 selected, produced a dose-response  $T_m$  shift,  $\Delta T_m$ , indicative of interaction with CaFADS (Fig 6A). Compounds C6 and C9 increased  $T_m$  by more than 3 degrees, indicating binding to the protein. In addition, C3, C5 and C18 shifted it to lower values (up to 2 and 6 degrees, respectively), suggesting that they produced a ligand-induced perturbation consistent with binding and destabilization of CaFADS. Fitting of the corresponding dose-response data to Eq 2 that relates them to the binding affinity, allowed to estimate the corresponding  $K_d$  values (Fig 6B, second column in Table 2). The data pointed to C5, C9 and C18 as the stronger binders. In addition, postulated the C5 > C18 > C9 > C3 > C6 affinity ranking with  $K_d$  values in the 1.7–41  $\mu$ M range. The previous results support that compounds C5, C6, C9, C18 and C3 are actual ligands of CaFADS, highlighting the capacity of the VS protocol to find protein ligands for receptor targets.

As our VS was directed towards the FMNAT active site of CaFADS, we then rated the power of the 17 VSHs as inhibitors of CaFADS ability to transform FMN into FAD. Hits were evaluated in terms of concentration of compounds causing 50% enzyme inhibition ( $IC_{50}$ ), as

**Table 2. In vitro performance of VS hits over the FMNAT and RFK+FMNAT CaFADS activities.**

| Compound | $K_d$ ( $\mu$ M) <sup>a</sup> | FMNAT $IC_{50}$ ( $\mu$ M) <sup>b</sup> | FMNAT % Res. act. 250 $\mu$ M | RFK+FMNAT $IC_{50}$ ( $\mu$ M) <sup>b</sup> | RFK+FMNAT % Res. act. 250 $\mu$ M |
|----------|-------------------------------|---|-------------------------------|---|-----------------------------------|
| C2       |                               |   | >95                           |   | 88 ± 2                            |
| C3       | 18 ± 8                        | 238 ± 7                                 | 48 ± 3                        | 248 ± 3                                     | 48 ± 5                            |
| C5       | 1.7 ± 0.7                     | 53 ± 1                                  | 6.0 ± 1.4                     | 83 ± 2                                      | 14 ± 1.3                          |
| C6       | 41 ± 3                        | 96 ± 6                                  | 48 ± 6                        |   | 57 ± 3                            |
| C7       |                               |   | >95                           |   | 82 ± 7                            |
| C9       | 6.4 ± 1.2                     |   | 56 ± 6                        |   | 76 ± 3                            |
| C18      | 3.0 ± 0.9                     | 143 ± 4                                 | 35 ± 4                        | 147 ± 4                                     | 35 ± 4                            |
| C26      |                               |   | 72 ± 6                        |   | 84 ± 4                            |

The table includes dissociation constant ( $K_d$ ) for the compounds altering thermal stability of CaFADS, concentration of compound causing 50% enzyme inhibition ( $IC_{50}$ ) and residual activity at 250  $\mu$ M of compound for the FMNAT and RFK+FMNAT activities of CaFADS. Thermal stability and activity experiments were carried out in 20 mM PIPES, pH 7.0, 10 mM MgCl<sub>2</sub>. CaFADS activities were assayed at 25 °C. All samples contained 2% DMSO. (n = 3, mean ± SD).

<sup>a</sup> Obtained from differential scanning fluorescence data and

<sup>b</sup> kinetic measurements. For details see the Methods.

<https://doi.org/10.1371/journal.pcbi.1007898.t002>



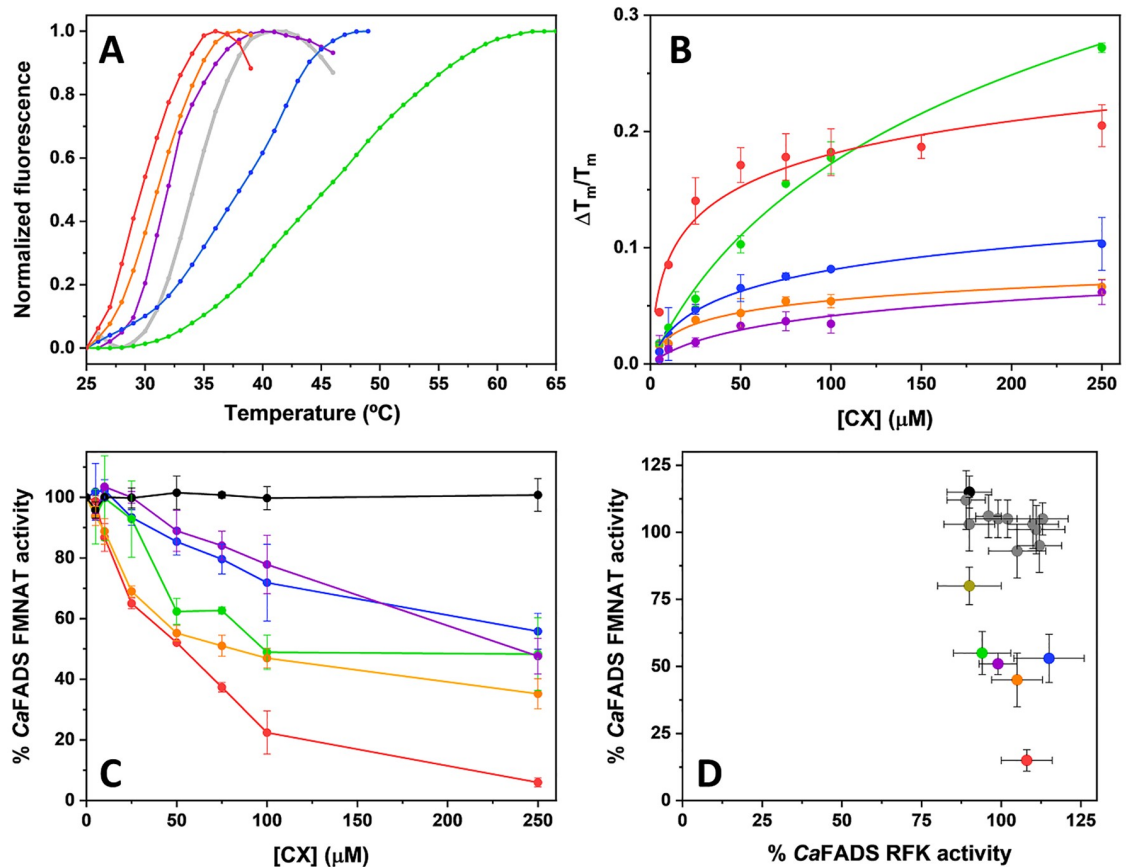


**Fig 6. In vitro assessment of VSHs ability to bind and to inhibit CaFADS.** A) Thermal denaturation curve for CaFADS (2  $\mu\text{M}$ ) observed by differential scanning fluorescence and  $T_m$  shifts observed in the presence of the compounds at 250  $\mu\text{M}$ . Thermal stability curves are plotted against the normalized fluorescence signal. Experiments were carried out in 20 mM PIPES, pH 7.0, 10 mM  $\text{MgCl}_2$ , 2% DMSO. B) Dependence of  $\Delta T_m/T_m$  on the VSH concentration and data fit to Eq 2. C) Dose-response curves for the FMNAT activity of CaFADS in the presence of representative VSHs. Experiments performed at 25  $^\circ\text{C}$  in 20 mM PIPES, pH 7.0, 10 mM  $\text{MgCl}_2$ , 2% DMSO, with 5  $\mu\text{M}$  FMN and 50  $\mu\text{M}$  ATP. Values derived from these representations are included in Table 2, such as the  $\text{IC}_{50}$  and % of remaining activity at 250  $\mu\text{M}$  of the VSH. D) Comparison of the effects of the VSHs on the RFK and FMNAT activities of CaFADS. All the experiments were carried out at 25  $^\circ\text{C}$ , in 20 mM PIPES pH 7.0,  $\text{MgCl}_2$  (10 mM when assaying FMNAT activity and 0.8 mM when assaying RFK activity) at saturating concentrations substrates and in the presence of 250  $\mu\text{M}$  of the VSH (2% DMSO, final concentration). Compound color code: Protein in the absence of VSH is shown in light gray, C3 is violet, C5 is red, C6 is green, C9 is blue, C12 is black (shown as control, neither binder nor inhibitor) and C18 is orange. Note that not all molecules are shown in all panels. In panel D, compounds different from the above mentioned are indicated in dark gray and calculated activity percentages are relative to the corresponding ones in absence of compounds. (n = 3, mean  $\pm$  SD).

<https://doi.org/10.1371/journal.pcbi.1007898.g006>

well as of the percentage of remaining activity at the highest compound concentration assayed (250  $\mu\text{M}$ ) (Fig 6C, third and fourth columns in Table 2). 6 out of the 17 VSHs produced some inhibitory effect on the FMNAT activity. These were compounds C3, C5, C6, C9, C18 and C26. Among them, C5 and C6 yielded  $\text{IC}_{50}$  values below 100  $\mu\text{M}$ , C5  $\text{IC}_{50} = 53 \pm 1 \mu\text{M}$  and C6  $\text{IC}_{50} = 96 \pm 6 \mu\text{M}$ , with C5 inhibiting over 90% the FMNAT activity of CaFADS at the maximal compound concentration assayed. The structure of these compounds is shown in S5 Fig.

CaFADS is a bifunctional enzyme that in addition to the FMNAT N-terminal module holds an RFK C-terminal module that transforms riboflavin (RF) into FMN, producing the substrate of the FMNAT activity. The presence of this second module was not considered in our VS protocol, where only the ATP/FMN binding pocket of the FMNAT module was used as the active site. Nonetheless, since the RFK module also comprises an active site binding adenine and

Table 3. In vivo performance of VS hits.

| Compound | MIC ( $\mu\text{M}$ )<br><i>C. ammoniagenes</i> | MIC ( $\mu\text{M}$ )<br><i>M. tuberculosis</i> |
|----------|---|---|
| C2       | 128   | 256   |
| C3       | >256  | 256   |
| C5       | 32  | 128   |
| C6       | 128   | 128   |
| C27      | 128   | 256   |

VSHs which minimal inhibitory concentration (MIC) against *C. ammoniagenes* and *M. tuberculosis* is lower than 256  $\mu\text{M}$ .

<https://doi.org/10.1371/journal.pcbi.1007898.t003>

flavin nucleotides, its RFK activity might also be affected by the VSHs. Therefore, we also evaluated the ability of *CaFADS* to transform RF into FMN and subsequently into FAD. Fig 6D, compares the effect of the VSHs on both individual activities of *CaFADS*, RFK and FMNAT, showing that, under the assay conditions, the 17 hits produced minor effects on the RFK activity. In agreement, when evaluating the overall *CaFADS* activity the effect of the VSHs follows a similar trend to that when individually evaluating the FMNAT activity.

To assess the effect of VSHs on the growth of different bacteria, we determined their MIC (Table 3 and S2 Table). Bacterial cells of *C. ammoniagenes*, *Corynebacterium glutamicum*, *Corynebacterium diphtheriae*, *M. tuberculosis*, *M. smegmatis*, *S. pneumoniae*, *E. coli*, *Listeria monocytogenes*, *Pseudomonas aeruginosa*, *Salmonella thyphimurium*, *Staphylococcus aureus* and *Bacillus spp.* were grown in the presence of increasing concentrations of the selected VSHs. Among the VSHs, C2, C5, C6, C18 and C27 produced a detectable inhibition in the growth of *C. ammoniagenes*, being C5 (MIC = 32  $\mu\text{M}$ ) the compound producing the largest antibacterial effect followed by C2 (MIC = 64  $\mu\text{M}$ ). Interestingly, C5 is also the hit exhibiting the lowest  $\text{IC}_{50}$  for the FMNAT activity of *CaFADS* (Table 2). The five VSHs exhibiting antibacterial activity against *C. ammoniagenes* also had activity on the other *Corynebacterium* species analyzed, being particularly relevant the effects of C1 and C5 on *C. glutamicum* as well as of C5 and C18 on *C. diphtheriae*. Four of these five compounds, C2, C5, C6 and C27, as well as C3, had also antibacterial effect in the growth of *Mycobacterium* species, although they were in general less potent. In addition, C18 and C27 produced moderate MIC values (64  $\mu\text{M}$ ) for *L. monocytogenes* growth, C6 for *S. pneumoniae*, and C27 for *S. aureus*. It is also worth to note the inhibition of *Bacillus spp.* growth caused by C5 and C27 (MIC = 32  $\mu\text{M}$ ).

In general, we observed that the VSHs showing inhibitory activity against *CaFADS* also inhibit the growing of *Corynebacterium* species. Thus, we can hypothesize that the growing inhibition effect should be caused by the *CaFADS* inhibition. In addition, those VSHs also inhibit the growing of the *Mycobacterium* species, supporting *CaFADS* as a representative model of the FADS of *M. tuberculosis*. The fact that the compounds identified through VS have demonstrated some antimicrobial activity is an important result, even when this antimicrobial activity is moderate; historically, potential enzyme inhibitors identified through *in silico* or *in vitro* protein-binding assays are mostly devoted of any antimicrobial activity, due to their inability to cross the high permeability barrier posed by the bacterial envelope [77].

Finally, we evaluated for the effect of VSHs on eukaryotic cell growth and viability. Compounds C2, C5 and C6 were not cytotoxic in HeLa and A549 cell lines, with  $\text{IC}_{50}$  (concentration of compounds causing the 50% inhibition of the cellular viability) above the maximal concentration evaluated (512  $\mu\text{M}$ ). In contrast, C18 and C27 showed moderate cytotoxicity in both cell lines but only in the 256-512  $\mu\text{M}$  range, with complete viability being retained at

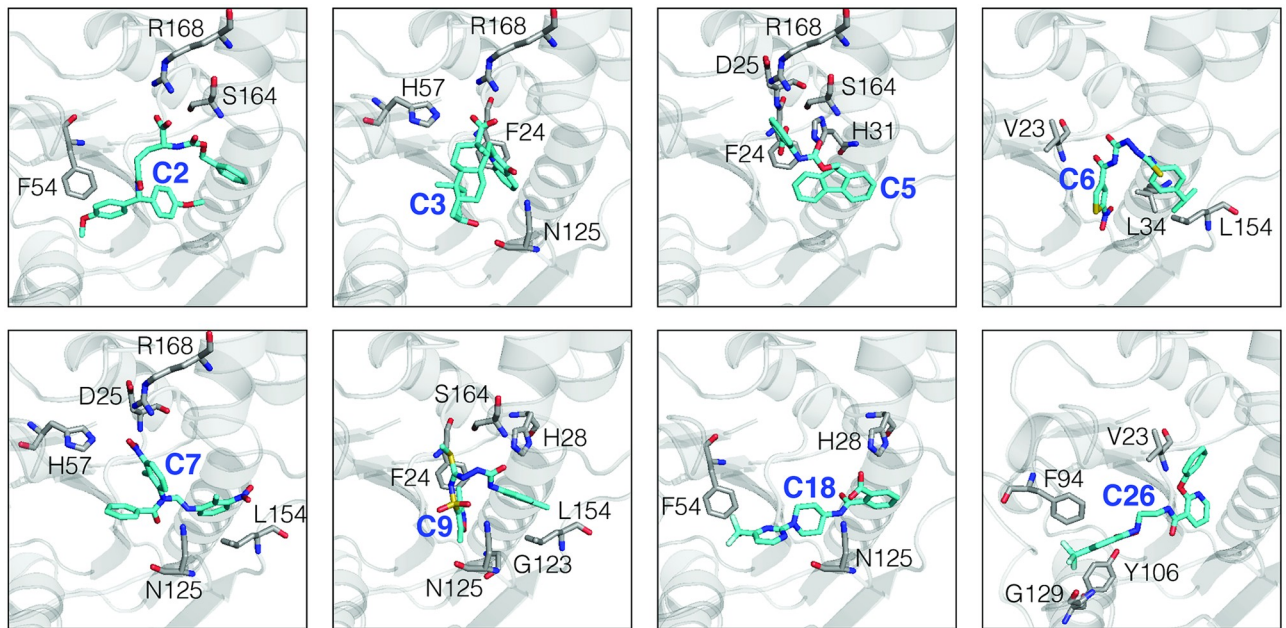


**Fig 7. Docking poses showing the main interactions of the VSHs and *CaFADS*.** These were obtained with Autodock4.2 and were used as the starting conformation for the MD stage.

<https://doi.org/10.1371/journal.pcbi.1007898.g007>

lower concentrations. Thus, the compounds do not show high cytotoxic effects against eukaryotic cells, highlighting their potential use against prokaryotic pathogens.

### Binding pocket VSHs interactions

Fig 7 shows the main interactions between the VSHs (from Table 2) and *CaFADS*. According to the simulations, most hits interact with the ATP binding site (C2, C3, C5, C6, C7 and C9). Only two compounds (C18 and C26) interact with the binding site of both natural substrates (ATP and FMN). Detailed interactions between the VSHs and the *CaFADS* are represented in S6 Fig. A global view of the VSHs inside the binding pocket is shown in S7 Fig. It is worth to note that all the ligands show direct interactions with key residues in the FMAT binding pocket. Compounds C2, C3, C5, C6, C7, C9 and C18 interact with N125, which is considered the key catalytic residue for the FMNAT activity. In addition, all compounds show direct interactions with highly conserved residues, particularly those responsible for the stabilization of the phosphates of the ATP (H28, H31, H57, S164 and R168).

### Conclusion

We developed a VS protocol that is able to find ligands of an enzyme which does not require previous knowledge of ligands or ligand-receptor structures. The protocol is computationally efficient allowing for the screening of large compound libraries with moderate computational resources. The protocol was implemented over *CaFADS*, an enzyme that is considered a good model for FADSs of bacterial species that cause tuberculosis and pneumonia [40, 41].

The VS protocol involves a funnel-like strategy with filtering stages that increase in accuracy. In the first stage, we used the flexi-pharma method [31], a pharmacophore filtering strategy with ligand-free receptor conformations from MD. In the second stage, we used a consensus docking strategy to combine the results from different docking programs using the exponential consensus ranking (ECR) method [43]. In the third stage of MD-ranking, we

developed a new score for the ligand's flexibility using a Morse potential. This score is combined with other scoring functions using the ECR method over the MD ensemble.

The protocol was optimized and validated over an experimentally-tested compound library with known ligands of the *CaFADS*. We implemented the VS strategy over a unexplored compound library, resulting in a list of 17 compounds that were tested experimentally. Notably, we discovered five compounds able to bind to the *CaFADS*. One of these compounds shows significant inhibition of the FMNAT activity of *CaFADS*. In comparison to previous work [41], the computational protocol gives an enrichment of around 8 for the experimental stage. In addition, some of the new compounds show growth inhibitory activity against *Corynebacterium*, *Mycobacterium* or *Streptococcus* species, supporting the use of the integrative VS protocol for the initial stages of drug discovery.

Although our final results show a good experimental enrichment, we note that the generalization of the entire protocol (shown in Fig 1) is still to be optimized, and validated for multiple systems with diverse active sites.

## Supporting information

**S1 Fig. Example of the Flexi-pharma pharmacophore mapping.** The green, red and gray spheres represent hydrogen-bond acceptor, negatively charged and aromatic features, respectively.

(TIF)

**S2 Fig. Enrichment plot for the different ECR-docking strategies.** The violet line shows the EP from ECR combination of Autodock4.2, Vina and Smina docking results using the best pose from each program (as was done in ref. [43]). We also studied the outcome when using the best pose for each molecule from the different programs: from Autodock4.2 (black), Vina (green) and Smina (blue), then re-scored it with Autodock4.2, Vina, Vinardo and CYscore, and these new scores were combined using an ECR methodology. We find that using the Autodock4.2 pose and re-scoring it with the other programs produces the best outcome.

(TIF)

**S3 Fig. Funnel-like protocol implemented for the Maybridge compound library.** The number of filtered molecules is shown on the left. The computational protocol has several stages: first, a pharmacophore-based VS (flexi-pharma), then ECR-Docking, afterwards two MD stages (that depended on the simulation time) were used for ranking the compounds with a Morse-based score and an ECR combination of scoring functions. In the physico-chemical stage, we assessed a range of properties for the 30 best VS-ranked compounds that relate to their potential drug-likeness (S1 Table), as well as their commercial availability, selecting 17 compounds for the experimental assays. 5 compounds were found to be ligands of *CaFADS*.

(TIF)

**S4 Fig. Ranks for the individual scoring functions and the ECR method for the MD-ranking stage 2 using 300 molecules filtered from the Maybridge compound library.** The best ranked molecules by the ECR are also well ranked for the majority of the programs but not necessarily for all. The top 30 molecules given by the ECR are selected for the following stage.

(TIF)

**S5 Fig. Structure of the active VSHs towards *CaFADS* or the organisms tested.** C3, C5, C6, C9 and C18 are able to bind to *CaFADS*. C3, C5, C6 and C18 cause 50% of FMNAT activity inhibition ( $IC_{50}$ ) at concentration lower than 250  $\mu$ M. C3, C5 and C18 cause 50% RFK-

FMNAT activity inhibition ( $IC_{50}$  at concentration lower than 250  $\mu$ M. C3, C5, C6, C9, C18 and C26 have FMNAT residual activity < 95% at 250  $\mu$ M of compound. C2, C3, C5, C6, C7, C9, C18 and C26 have RFK+FMNAT residual activity < 95% at 250  $\mu$ M of compound. C2, C5, C6 and C27 have MIC values lower than 256  $\mu$ M against *C. ammoniagenes*, and or C2, C3, C5, C6 and C27 *Mycobacterium* species.

(TIF)

**S6 Fig. 2D representation of interactions between VSHs and CaFADS found in the docking stage.** The Autodock pose obtained in the docking stage was used to observe the interactions with CaFADS. Compounds C2, C3, C5, C6, C7 and C9 interact with the ATP binding site and compounds C18 and C26 show interactions with the binding site of both ATP and FMN. Almost all compounds interact with key residues in the binding pocket: H28, H31, H57, N125, S164 and R168.

(TIF)

**S7 Fig. Global view of the CaFADS receptor with VSHs.** A global view of the receptor structure with the superposition of the Autodock poses of the VSHs compounds. The docked compounds cover a wide range of the receptor binding pocket.

(TIF)

**S1 Text. Description of the different ECR-docking FADS optimization strategies.**

(PDF)

**S1 Table. Summary of properties for the CaFADS best ranked VS compounds.** The table shows the VS rank, the Zinc and Maybridge Codes, the names and summary of physico-chemical criteria (values at pH 7.0) to evaluate their potential drug-likeness. Preferred criteria values are indicated on the top in green. Favorable criteria for each compound are highlighted in a green background, those in the limit are in a yellow background and those violating the criteria are in a red background. Compounds selected for experimental evaluation as virtual screening hits (VSH) are highlighted in red font in the first four columns.

(PDF)

**S2 Table. Minimal Inhibitory Concentration (MIC) of VSHs against different microorganisms.** Compounds were, in most cases, assayed in the 0-256  $\mu$ M concentration range. In some cases, they were assayed only in the 0-64  $\mu$ M concentration range, and if no effect was observed in these cases > 64 is shown. Best performing compounds are colored from red, orange, yellow to green.

(PDF)

**S3 Table. Bacterial strains tested for VSH antibacterial activity.**

(PDF)

## Acknowledgments

The authors would like to acknowledge the use of Servicios Generales de Apoyo a la Investigación-SAI, Universidad de Zaragoza. We thank M. Minjarez and M. Martinez-Júlvez for their collaboration in evaluating physico-chemical properties of VS hits. The authors would also like to acknowledge Dr. Claudio Cavasotto for insightful discussions about the Flexi-pharma method. Some computations were performed in a local server with an NVIDIA Titan X GPU. P.C. gratefully acknowledges the support of NVIDIA Corporation for the donation of this GPU.

## Author Contributions

**Conceptualization:** Isaias Lans, Ernesto Anoz-Carbonell, José Antonio Aínsa, Milagros Medina, Pilar Cossio.

**Data curation:** Isaias Lans, Ernesto Anoz-Carbonell, Karen Palacio-Rodríguez, José Antonio Aínsa, Milagros Medina, Pilar Cossio.

**Formal analysis:** Isaias Lans, Ernesto Anoz-Carbonell.

**Funding acquisition:** José Antonio Aínsa, Milagros Medina, Pilar Cossio.

**Investigation:** Isaias Lans, Ernesto Anoz-Carbonell, Karen Palacio-Rodríguez, José Antonio Aínsa, Milagros Medina, Pilar Cossio.

**Methodology:** Isaias Lans, Ernesto Anoz-Carbonell, Karen Palacio-Rodríguez.

**Resources:** José Antonio Aínsa, Milagros Medina, Pilar Cossio.

**Software:** Isaias Lans.

**Supervision:** José Antonio Aínsa, Milagros Medina, Pilar Cossio.

**Validation:** Isaias Lans, Ernesto Anoz-Carbonell, Karen Palacio-Rodríguez, José Antonio Aínsa, Milagros Medina, Pilar Cossio.

**Visualization:** Isaias Lans, Ernesto Anoz-Carbonell, Karen Palacio-Rodríguez.

**Writing – original draft:** Isaias Lans, Ernesto Anoz-Carbonell, Karen Palacio-Rodríguez, José Antonio Aínsa, Milagros Medina, Pilar Cossio.

**Writing – review & editing:** Isaias Lans, Ernesto Anoz-Carbonell, Karen Palacio-Rodríguez, José Antonio Aínsa, Milagros Medina, Pilar Cossio.

## References

1. Tacconelli E, Carrara E, Savoldi A, Harbarth S, Mendelson M, Monnet DL, et al. Discovery, research, and development of new antibiotics: the WHO priority list of antibiotic-resistant bacteria and tuberculosis. *Lancet Infect Dis*. 2018; 18(3):318–327. [https://doi.org/10.1016/S1473-3099\(17\)30753-3](https://doi.org/10.1016/S1473-3099(17)30753-3) PMID: 29276051
2. Rognan D. The impact of *in silico* screening in the discovery of novel and safer drug candidates. *Pharmacol Therapeut*. 2017; 175:47–66. <https://doi.org/10.1016/j.pharmthera.2017.02.034>
3. Walters WP, Stahl MT, Murcko MA. Virtual screening—an overview. *Drug Discov Today*. 1998; 3(4):160–178. [https://doi.org/10.1016/S1359-6446\(97\)01163-X](https://doi.org/10.1016/S1359-6446(97)01163-X)
4. Leelananda SP, Lindert S. Computational methods in drug discovery. *Beilstein J Org Chem*. 2016; 12(1):2694–2718. <https://doi.org/10.3762/bjoc.12.267> PMID: 28144341
5. Fradera X, Babaoglu K. Overview of methods and strategies for conducting virtual small molecule screening. *Curr Protoc Chem Biol*. 2017; 9(3):196–212. <https://doi.org/10.1002/cpch.27> PMID: 28910858
6. Schneider G. Automating drug discovery. *Nat Rev Drug Discov*. 2017; 17(2):97–113. <https://doi.org/10.1038/nrd.2017.232> PMID: 29242609
7. Sliwoski G, Kothiwale S, Meiler J, Lowe EW. Computational methods in drug discovery. *Pharmacol Rev*. 2014; 66(1):334–395. <https://doi.org/10.1124/pr.112.007336> PMID: 24381236
8. Kalyanamoorthy S, Chen YPP. Structure-based drug design to augment hit discovery. *Drug discov today*. 2011; 16(17-18):831–839. <https://doi.org/10.1016/j.drudis.2011.07.006> PMID: 21810482
9. Spyraakis F, Cavasotto CN. Open challenges in structure-based virtual screening: Receptor modeling, target flexibility consideration and active site water molecules description. *Arch Biochem Biophys*. 2015; 583:105–119. <https://doi.org/10.1016/j.abb.2015.08.002> PMID: 26271444
10. Kitchen DB, Decornez H, Furr JR, Bajorath J. Docking and scoring in virtual screening for drug discovery: methods and applications. *Nat Rev Drug Discov*. 2004; 3(11):935–949. <https://doi.org/10.1038/nrd1549> PMID: 15520816

11. Bajorath J. Integration of virtual and high-throughput screening. *Nat Rev Drug Discov*. 2002; 1(11):882–894. <https://doi.org/10.1038/nrd941> PMID: 12415248
12. Lyne PD. Structure-based virtual screening: an overview. *Drug Discov Today*. 2002; 7(20):1047–1055. [https://doi.org/10.1016/S1359-6446\(02\)02483-2](https://doi.org/10.1016/S1359-6446(02)02483-2) PMID: 12546894
13. Tanrikulu Y, Krüger B, Proschak E. The holistic integration of virtual screening in drug discovery. *Drug Discov Today*. 2013; 18(7–8):358–364. <https://doi.org/10.1016/j.drudis.2013.01.007> PMID: 23340112
14. Kumar A, Zhang KY. Hierarchical virtual screening approaches in small molecule drug discovery. *Meth-ods*. 2015; 71:26–37. <https://doi.org/10.1016/j.ymeth.2014.07.007> PMID: 25072167
15. Bresso E, Furlan A, Noel P, Leroux V, Maina F, Dono R, et al. Large-Scale Virtual Screening Against the MET Kinase Domain Identifies a New Putative Inhibitor Type. *Molecules*. 2020; 25(4):938. <https://doi.org/10.3390/molecules25040938>
16. Mortier J, Dhakal P, Volkamer A. Truly Target-Focused Pharmacophore Modeling: A Novel Tool for Mapping Intermolecular Surfaces. *Molecules*. 2018; 23(8). <https://doi.org/10.3390/molecules23081959> PMID: 30082611
17. Wang X, Shen Y, Wang S, Li S, Zhang W, Liu X, et al. PharmMapper 2017 update: a web server for potential drug target identification with a comprehensive target pharmacophore database. *Nucleic Acids Res*. 2017; 45(W1):W356–W360. <https://doi.org/10.1093/nar/gkx374> PMID: 28472422
18. Rohini K, Agarwal P, Preethi B, Shanthi V, Ramanathan K. Exploring the Lead Compounds for Zika Virus NS2B-NS3 Protein: an e-Pharmacophore-Based Approach. *Appl Biochem Biotechnol*. 2019; 187(1):194–210. <https://doi.org/10.1007/s12010-018-2814-3> PMID: 29911269
19. Stumpfe D, Ripphausen P, Bajorath J. Virtual compound screening in drug discovery. *Future Med Chem*. 2012; 4(5):593–602. <https://doi.org/10.4155/fmc.12.19> PMID: 22458679
20. Chen L, Du-Cuny L, Moses S, Dumas S, Song Z, Rezaeian AH, et al. Novel inhibitors induce large conformational changes of GAB1 pleckstrin homology domain and kill breast cancer cells. *PLoS Comput Biol*. 2015; 11(1). <https://doi.org/10.1371/journal.pcbi.1004021>
21. De Vivo M, Masetti M, Bottegoni G, Cavalli A. Role of molecular dynamics and related methods in drug discovery. *J Med Chem*. 2016; 59(9):4035–4061. <https://doi.org/10.1021/acs.jmedchem.5b01684> PMID: 26807648
22. Zhao H, Caffisch A. Molecular dynamics in drug design. *European J Med Chem*. 2015; 91:4–14. <https://doi.org/10.1016/j.ejmech.2014.08.004>
23. Śledź P, Caffisch A. Protein structure-based drug design: from docking to molecular dynamics. *Curr Opin Struc Biol*. 2018; 48:93–102. <https://doi.org/10.1016/j.sbi.2017.10.010>
24. Mortier J, Rakers C, Bermudez M, Murgueitio MS, Riniker S, Wolber G. The impact of molecular dynamics on drug design: applications for the characterization of ligand–macromolecule complexes. *Drug Discov Today*. 2015; 20(6):686–702. <https://doi.org/10.1016/j.drudis.2015.01.003> PMID: 25615716
25. Durrant JD, McCammon JA. Molecular dynamics simulations and drug discovery. *BMC Biol*. 2011; 9(1):71. <https://doi.org/10.1186/1741-7007-9-71> PMID: 22035460
26. Duan L, Liu X, Zhang JZ. Interaction entropy: a new paradigm for highly efficient and reliable computation of protein–ligand binding free energy. *J Am Chem Soc*. 2016; 138(17):5722–5728. <https://doi.org/10.1021/jacs.6b02682> PMID: 27058988
27. Cavasotto CN, Orry AJ. Ligand Docking and Structure-based Virtual Screening in Drug Discovery. *Curr Top Med Chem*. 2007; 7(10):1006–1014. <https://doi.org/10.2174/156802607780906753> PMID: 17508934
28. Carlson HA, Masukawa KM, Rubins K, Bushman FD, Jorgensen WL, Lins RD, et al. Developing a dynamic pharmacophore model for HIV-1 integrase. *J Med Chem*. 2000; 43(11):2100–2114. <https://doi.org/10.1021/jm990322h> PMID: 10841789
29. Wieder M, Garon A, Perricone U, Boresch S, Seidel T, Almerico AM, et al. Common Hits Approach: Combining Pharmacophore Modeling and Molecular Dynamics Simulations. *J Chem Inf Model*. 2017; 57(2):365–385. <https://doi.org/10.1021/acs.jcim.6b00674> PMID: 28072524
30. Polishchuk P, Kutlushina A, Bashirova D, Mokshyna O, Madzhidov T. Virtual screening using pharmacophore models retrieved from molecular dynamic simulations. *Int J Mol Sci*. 2019; 20(23). <https://doi.org/10.3390/ijms20235834> PMID: 31757043
31. Lans I, Palacio-Rodriguez K, Cavasotto CN, Cossio P. Flexi-pharma: a molecule-ranking strategy for virtual screening using pharmacophores from ligand-free conformational ensembles. *J Comput Aid Mol Des*. 2020;. <https://doi.org/10.1007/s10822-020-00329-7>
32. Mayhew SG, Ludwig ML. 2 Flavodoxins and Electron-Transferring Flavoproteins. vol. 12; 1975. p. 57–118.

33. Mayhew SG, Tollin G. General properties of flavodoxins. *Chemistry and biochemistry of flavoenzymes*. 1992; 3:389–426.
34. Lans I, Frago S, Medina M. Understanding the FMN cofactor chemistry within the Anabaena Flavodoxin environment. *Biochim Biophys Acta*. 2012; 1817(12):2118–2127. <https://doi.org/10.1016/j.bbabi.2012.08.008> PMID: 22982476
35. Herguedas B, Martínez-Júlvez M, Frago S, Medina M, Hermoso JA. Oligomeric State in the Crystal Structure of Modular FAD Synthetase Provides Insights into Its Sequential Catalysis in Prokaryotes. *J Mol Biol*. 2010; 400(2):218–230. <https://doi.org/10.1016/j.jmb.2010.05.018> PMID: 20471397
36. Herguedas B, Lans I, Sebastián M, Hermoso JA, Martínez-Júlvez M, Medina M. Structural insights into the synthesis of FMN in prokaryotic organisms. *Acta Crystallogr, Sect D: Biol Crystallogr*. 2015; 71. <https://doi.org/10.1107/S1399004715019641>
37. Serrano A, Ferreira P, Martínez-Júlvez M, Medina M. The prokaryotic FAD synthetase family: a potential drug target. *Curr Pharm Des*. 2013; 19(14):2637–48. <https://doi.org/10.2174/1381612811319140013> PMID: 23116401
38. Serrano A, Sebastián M, Arilla-Luna S, Baquedano S, Pallarés MC, Lostao A, et al. Quaternary organization in a bifunctional prokaryotic FAD synthetase: Involvement of an arginine at its adenylyltransferase module on the riboflavin kinase activity. *Biochim Biophys Acta*. 2015; 1854(8):897–906. <https://doi.org/10.1016/j.bbapap.2015.03.005> PMID: 25801930
39. Krupa A, Sandhya K, Srinivasan N, Jonnalagadda S. A conserved domain in prokaryotic bifunctional FAD synthetases can potentially catalyze nucleotide transfer. *Trends Biochem Sci*. 2003; 28(1):9–12. [https://doi.org/10.1016/S0968-0004\(02\)00009-9](https://doi.org/10.1016/S0968-0004(02)00009-9) PMID: 12517446
40. Frago S, Martínez-Júlvez M, Serrano A, Medina M. Structural analysis of FAD synthetase from *Corynebacterium ammoniagenes*. *BMC Microbiol*. 2008; 8(1):160. <https://doi.org/10.1186/1471-2180-8-160> PMID: 18811972
41. Sebastián M, Anoz-Carbonell E, Gracia B, Cossio P, Aínsa JA, Lans I, et al. Discovery of antimicrobial compounds targeting bacterial type FAD synthetases. *J Enzyme Inhib Med Chem*. 2018; 33(1):241–254. <https://doi.org/10.1080/14756366.2017.1411910> PMID: 29258359
42. Lans I, Seco J, Serrano A, Burbano R, Cossio P, Daza MC, et al. The Dimer-of-Trimers Assembly Prevents Catalysis at the Transferase Site of Prokaryotic FAD Synthase. *Biophys J*. 2018; 115(6):988–995. <https://doi.org/10.1016/j.bpj.2018.08.011> PMID: 30177440
43. Palacio-Rodríguez K, Lans I, Cavasotto CN, Cossio P. Exponential consensus ranking improves the outcome in docking and receptor ensemble docking. *Sci Rep*. 2019; 9(1):5142. <https://doi.org/10.1038/s41598-019-41594-3> PMID: 30914702
44. Morris GM, Huey R, Lindstrom W, Sanner MF, Belew RK, Goodsell DS, et al. AutoDock4 and AutoDockTools4: Automated docking with selective receptor flexibility. *J Comput Chem*. 2009; 30(16):2785–91. <https://doi.org/10.1002/jcc.21256> PMID: 19399780
45. Koes DR, Camacho CJ. Pharmer: Efficient and Exact Pharmacophore Search. *J Chem Inf Model*. 2011; 51(6):1307–1314. <https://doi.org/10.1021/ci200097m> PMID: 21604800
46. Cosconati S, Forli S, Perryman AL, Harris R, Goodsell DS, Olson AJ. Virtual Screening with AutoDock: Theory and Practice. *Expert Opin Drug Discov*. 2010; 5(6):597–607. <https://doi.org/10.1517/17460441.2010.484460> PMID: 21532931
47. Forli S, Olson AJ. A Force Field with Discrete Displaceable Waters and Desolvation Entropy for Hydrated Ligand Docking. *J Med Chem*. 2012; 55(2):623–638. <https://doi.org/10.1021/jm2005145> PMID: 22148468
48. Trott O, Olson AJ. AutoDock Vina: Improving the speed and accuracy of docking with a new scoring function, efficient optimization, and multithreading. *J Comput Chem*. 2009; 31(2).
49. Koes DR, Baumgartner MP, Camacho CJ. Lessons learned in empirical scoring with smina from the CSAR 2011 benchmarking exercise. *J Chem Inf Model*. 2013; 53(8):1893–1904. <https://doi.org/10.1021/ci300604z> PMID: 23379370
50. Serrano A, Frago S, Velázquez-Campoy A, Medina M. Role of key residues at the flavin mononucleotide (FMN): adenylyltransferase catalytic site of the bifunctional riboflavin kinase/flavin adenine dinucleotide (FAD) Synthetase from *Corynebacterium ammoniagenes*. *Int J Mol Sci*. 2012; 13(11):14492–14517. <https://doi.org/10.3390/ijms131114492> PMID: 23203077
51. Quiroga R, Villarreal MA, Ballester P, Wong MH, Allain N, Laguerre M, et al. Vinardo: A Scoring Function Based on Autodock Vina Improves Scoring, Docking, and Virtual Screening. *PLoS One*. 2016; 11(5):e0155183. <https://doi.org/10.1371/journal.pone.0155183> PMID: 27171006
52. O'Boyle NM, Banck M, James CA, Morley C, Vandermeersch T, Hutchison GR. Open Babel: An open chemical toolbox. *J Cheminformatics*. 2011; 3(1):33. <https://doi.org/10.1186/1758-2946-3-33>



53. Olsson MHM, S ndergaard CR, Rostkowski M, Jensen JH. PROPKA3: Consistent Treatment of Internal and Surface Residues in Empirical pKa Predictions. *J Chem Theory Comput.* 2011; 7(2):525–537. <https://doi.org/10.1021/ct100578z> PMID: 26596171
54. Dolinsky TJ, Nielsen JE, McCammon JA, Baker NA. PDB2PQR: an automated pipeline for the setup of Poisson-Boltzmann electrostatics calculations. *Nucleic Acids Res.* 2004; 32:W665–W667. <https://doi.org/10.1093/nar/gkh381> PMID: 15215472
55. Dolinsky TJ, Czodrowski P, Li H, Nielsen JE, Jensen JH, Klebe G, et al. PDB2PQR: expanding and upgrading automated preparation of biomolecular structures for molecular simulations. *Nucleic Acids Res.* 2007; 35(Web Server issue):W522–5. <https://doi.org/10.1093/nar/gkm276> PMID: 17488841
56. Lindorff-Larsen K, Piana S, Palmo K, Maragakis P, Klepeis JL, Dror RO, et al. Improved side-chain torsion potentials for the Amber ff99SB protein force field. *Proteins.* 2010; 78(8):1950–8. <https://doi.org/10.1002/prot.22711> PMID: 20408171
57. Jorgensen WL, Chandrasekhar J, Madura JD, Impey RW, Klein ML. Comparison of simple potential functions for simulating liquid water. *J Chem Phys.* 1983; 79(926).
58. Wang J, Wolf RM, Caldwell JW, Kollman PA, Case DA. Development and testing of a general amber force field. *J Comput Chem.* 2004; 25(9):1157–1174. <https://doi.org/10.1002/jcc.20035> PMID: 15116359
59. Wang J, Wang W, Kollman P, Case D. Antechamber, An Accessory Software Package For Molecular Mechanical Calculations; 2000. Available from: <http://ambermd.org/antechamber/antechamber.pdf>.
60. Sousa Da Silva AW, Vranken WF. ACPYPE—AnteChamber PYthon Parser interfacE. *BMC Res Notes.* 2012; 5. <https://doi.org/10.1186/1756-0500-5-367> PMID: 22824207
61. Berendsen HJC, van der Spoel D, van Drunen R. GROMACS: A message-passing parallel molecular dynamics implementation. *Comput Phys Commun.* 1995; 91(1-3):43–56. [https://doi.org/10.1016/0010-4655\(95\)00042-E](https://doi.org/10.1016/0010-4655(95)00042-E)
62. Abraham MJ, Murtola T, Schulz R, P  ll S, Smith JC, Hess B, et al. GROMACS: High performance molecular simulations through multi-level parallelism from laptops to supercomputers. *SoftwareX.* 2015; 1:19–25. <https://doi.org/10.1016/j.softx.2015.06.001>
63. Hess B, Bekker H, Berendsen HJC, Fraaije JGEM. LINCS: A linear constraint solver for molecular simulations. *J Comput Chem.* 1997; 18(12):1463–1472. [https://doi.org/10.1002/\(SICI\)1096-987X\(199709\)18:12%3C1463::AID-JCC4%3E3.0.CO;2-H](https://doi.org/10.1002/(SICI)1096-987X(199709)18:12%3C1463::AID-JCC4%3E3.0.CO;2-H)
64. Jain AN. Bias, reporting, and sharing: computational evaluations of docking methods. *J Comput Aided Mol Des.* 2008; 22(3-4):201–212. <https://doi.org/10.1007/s10822-007-9151-x> PMID: 18075713
65. Velazquez-Campoy A, Sancho J, Abian O, Vega S. Biophysical Screening for Identifying Pharmacological Chaperones and Inhibitors Against Conformational and Infectious Diseases. *Curr Drug Targets.* 2016; 17(13):1492–1505. <https://doi.org/10.2174/1389450117666160201110449> PMID: 26844568
66. Cooper A, McAuley-Hecht KE. Microcalorimetry and the molecular recognition of peptides and proteins. *Philos Trans R Soc A.* 1993; 345(1674):23–35.
67. Palomino JC, Martin A, Camacho M, Guerra H, Swings J, Portaels F. Resazurin microtiter assay plate: Simple and inexpensive method for detection of drug resistance in *Mycobacterium tuberculosis*. *Antimicrob Agents Chemother.* 2002; 46(8):2720–2722. <https://doi.org/10.1128/AAC.46.8.2720-2722.2002> PMID: 12121966
68. Sousa SF, Ribeiro AJM, Coimbra JTS, Neves RPP, Martins SA, Moorthy NSHN, et al. Protein-Ligand Docking in the New Millennium—A Retrospective of 10 Years in the Field. *Curr Med Chem.* 2013; 20(18):2296–2314. <https://doi.org/10.2174/0929867311320180002> PMID: 23531220
69. Yuriev E, Holien J, Ramsland PA. Improvements, trends, and new ideas in molecular docking: 2012–2013 in review. *J Mol Recognit.* 2015; 28(10):581–604. <https://doi.org/10.1002/jmr.2471> PMID: 25808539
70. Cavasotto CN, Abagyan RA. Protein Flexibility in Ligand Docking and Virtual Screening to Protein Kinases. *J Mol Biol.* 2004; <https://doi.org/10.1016/j.jmb.2004.01.003> PMID: 15001363
71. Sarti E, Zamuner S, Cossio P, Laio A, Seno F, Trovato A. BACHSCORE. A Tool for Evaluating Efficiently and Reliably the Quality of Large Sets of Protein Structures. *Comput Phys Commun.* 2013; 184(12):2860–2865. <https://doi.org/10.1016/j.cpc.2013.07.019>
72. Cossio P, Granata D, Laio A, Seno F, Trovato A. A simple and efficient statistical potential for scoring ensembles of protein structures. *Sci Rep.* 2012; 2:1–8. <https://doi.org/10.1038/srep00351>
73. Cao Y, Li L. Improved protein-ligand binding affinity prediction by using a curvature-dependent surface-area model. *Bioinformatics.* 2014; 30(12):1674–1680. <https://doi.org/10.1093/bioinformatics/btu104> PMID: 24563257
74. Lipinski CA. Lead-and drug-like compounds: the rule-of-five revolution. *Drug Discov Today.* 2004; 1(4):337–341. <https://doi.org/10.1016/j.ddtec.2004.11.007>

75. Ghose AK, Viswanadhan VN, Wendoloski JJ. A knowledge-based approach in designing combinatorial or medicinal chemistry libraries for drug discovery. 1. A qualitative and quantitative characterization of known drug databases. *J Comb Chem.* 1999; 1(1):55–68. <https://doi.org/10.1021/cc9800071> PMID: [10746014](https://pubmed.ncbi.nlm.nih.gov/10746014/)
76. Villanueva R, Romero-Tamayo S, Laplaza R, Martínez-Olivan J, Velázquez-Campoy A, Sancho J, et al. Redox-and Ligand Binding-Dependent Conformational Ensembles in the Human Apoptosis-Inducing Factor Regulate Its Pro-Life and Cell Death Functions. *Antioxid Redox Sign.* 2019; 30(18):2013–2029.
77. Lewis K. The Science of Antibiotic Discovery. *Cell.* 2020; 181:29–45. <https://doi.org/10.1016/j.cell.2020.02.056> PMID: [32197064](https://pubmed.ncbi.nlm.nih.gov/32197064/)

## Supporting Information

*In silico* discovery and biological validation of ligands of FAD synthase, a promising antimicrobial target

Isaias Lans<sup>1</sup>, Ernesto Anoz-Carbonell<sup>2,3,4</sup>, Karen Palacio-Rodríguez<sup>1</sup>, José Antonio Aínsa<sup>3,4,5</sup>, Milagros Medina<sup>2,3</sup> and Pilar Cossio<sup>1,6\*</sup>.

<sup>1</sup>Biophysics of Tropical Diseases Max Planck Tandem Group, University of Antioquia, Medellín, Colombia

<sup>2</sup>Departamento de Bioquímica y Biología Molecular y Celular, Facultad de Ciencias, Universidad de Zaragoza, Spain

<sup>3</sup>Instituto de Biocomputación y Física de Sistemas Complejos (Unidades Asociadas BIFI-IQFR y CBsC-CSIC), Universidad de Zaragoza, Spain

<sup>4</sup>Grupo de Genética de Micobacterias, Departamento de Microbiología, Pediatría, Radiología y Salud Pública. Facultad de Medicina, Universidad de Zaragoza, Zaragoza, Spain.

<sup>5</sup>CIBER Enfermedades Respiratorias (CIBERES), Instituto de Salud Carlos III, Spain.

<sup>6</sup>Department of Theoretical Biophysics, Max Planck Institute of Biophysics, 60438, Frankfurt am Main, Germany

\* picossio@biophys.mpg.de

## SUPPORTING TEXT

### **SI 1 Text. Description of the different ECR-docking FADS optimization strategies.**

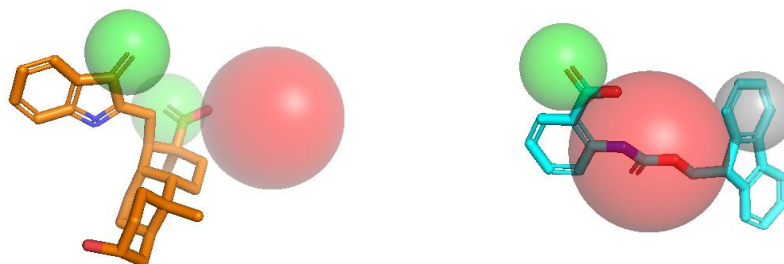
The ECR-docking was implemented using two strategies:

1) The best ranked molecules from the step 1 were docked to the FMNAT-FADS active site using the Autodock4.2 [1–3], Vina [4] and Smina [5] programs. The scores of the best poses from each docking program (evaluated with its own scoring function) were used to obtain 3 ranks (one for each docking program). The three ranks were combined using ECR to obtain a consensus rank (violet line in Figure SI 2).

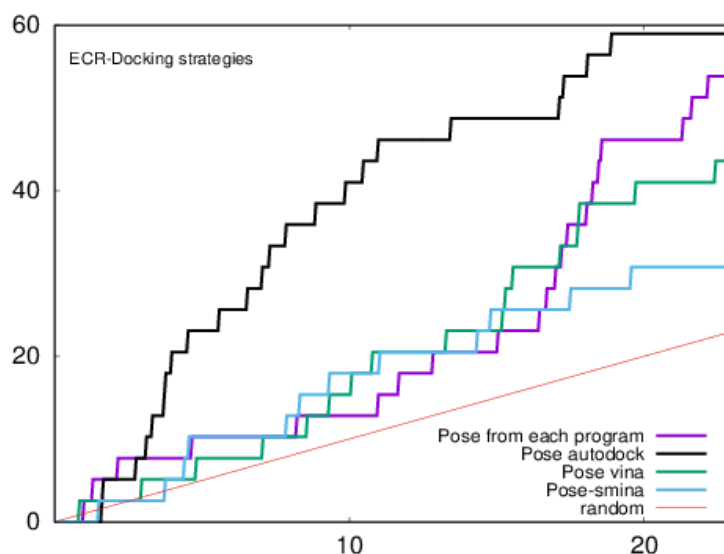
2) In the second strategy, we extracted the best pose from each program and re-evaluated it with Autodock4.2 [1–3], Vina [4], Vinardo [6] and CYScore [7] scoring functions. Then, the 4 obtained ranks were combined using an ECR strategy to obtain a consensus rank (black, green and blue lines in Figure SI 2).

We found that the best EP was obtained with the second strategy using the best pose from Autodock4.2 (black line in Figure SI 2).

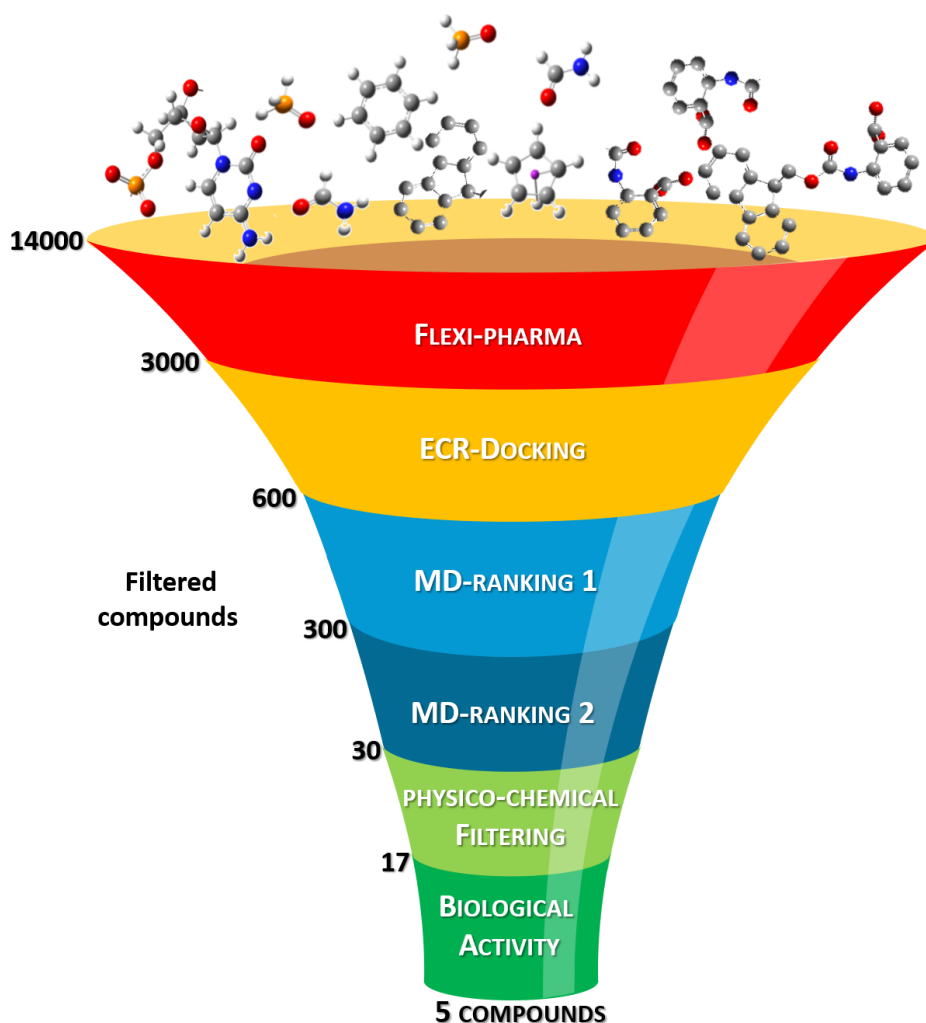
## SUPPORTING FIGURES



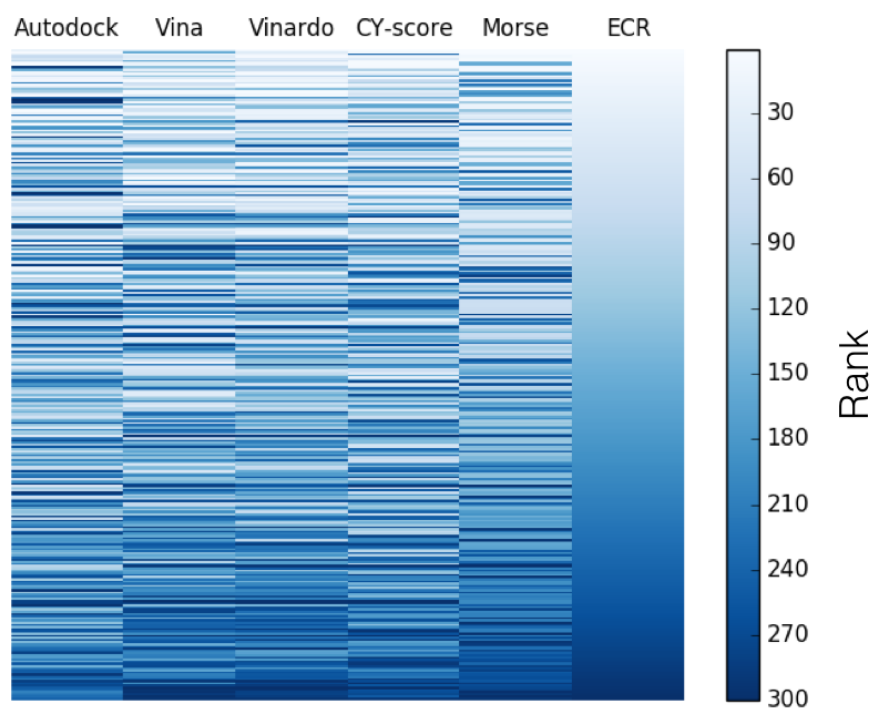
**SI 1 Fig. Example of the Flexi-pharma pharmacophore mapping.** The green, red and gray spheres represent hydrogen-bond acceptors, negatively charged and aromatic features, respectively.



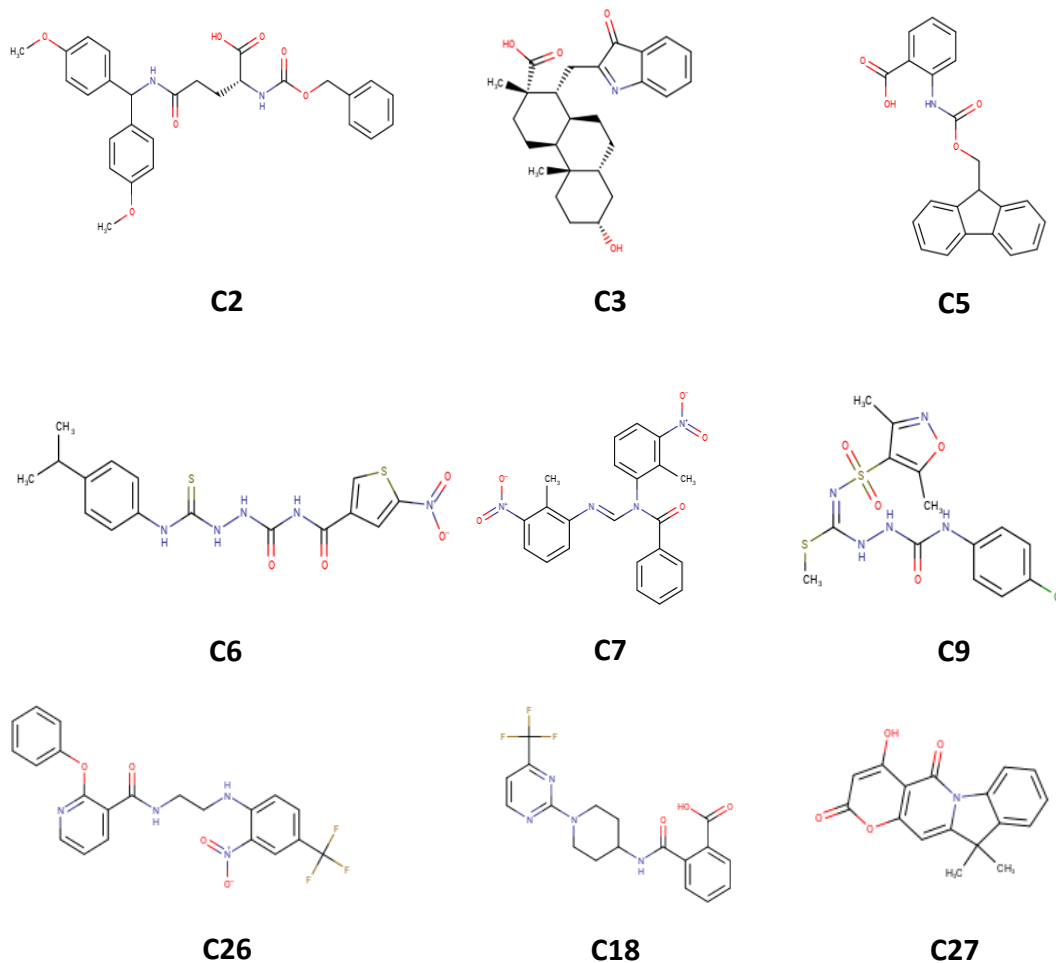
**SI 2 Fig. Enrichment plot for the different ECR-docking strategies.** The violet line shows the EP from ECR combination of Autodock4.2, Vina and Smina docking results using the best pose from each program (as was done in ref. [8]). We also studied the outcome when using the best pose for each molecule from the different programs: from Autodock4.2 (black), Vina (green) and Smina (blue), then re-scored it with Autodock4.2, Vina, Vinardo and CYscore, and these new scores were combined using an ECR methodology. We find that using the Autodock4.2 pose and re-scoring it with the other programs produces the best outcome.



**SI 3 Fig. Funnel-like protocol implemented for the Maybridge compound library.** The number of filtered molecules is shown on the left. The computational protocol had several stages: first a pharmacophore-based VS (Flexi-pharma), then ECR-Docking, afterwards two stages (that depended on the simulation time) were used for ranking the compounds with a Morse-based score and an ECR combination of scoring functions. In the physico-chemical stage, we assessed a range of properties for the 30 best VS-ranked compounds that relate to their potential drug-likeness (SI 1 Table), as well as their commercial availability, selecting 17 compounds for the experimental assays. 5 compounds were found to be ligands of *CaFADS*.

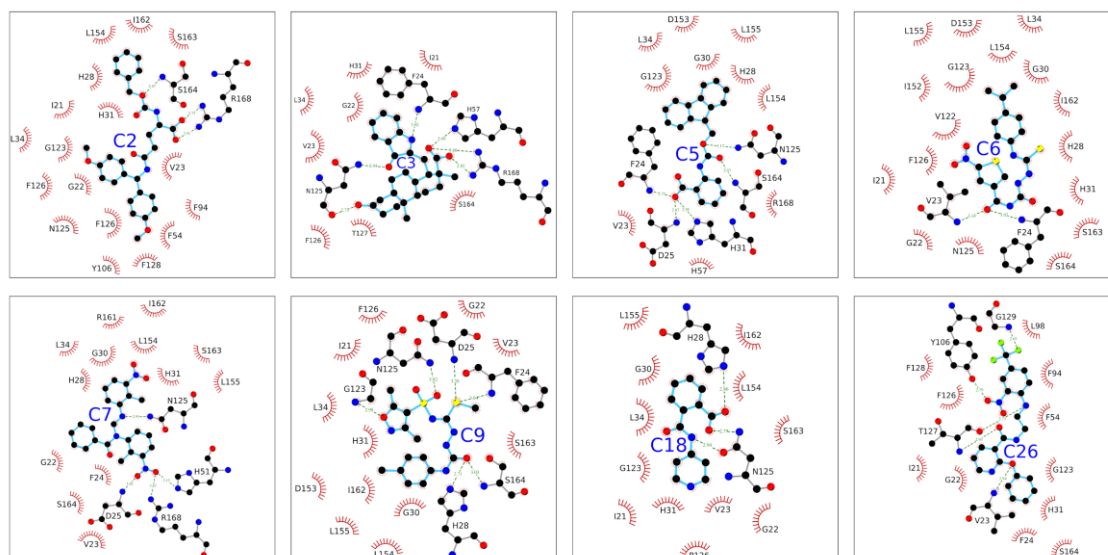


**SI 4 Fig. Ranks for the individual scoring functions and the ECR method** for the MD-ranking stage 2 using 300 molecules filtered from the Maybridge compound library. The best ranked molecules by the ECR are also well ranked for the majority of the programs but not necessarily for all. The top 30 molecules given by the ECR are selected for the following stage.

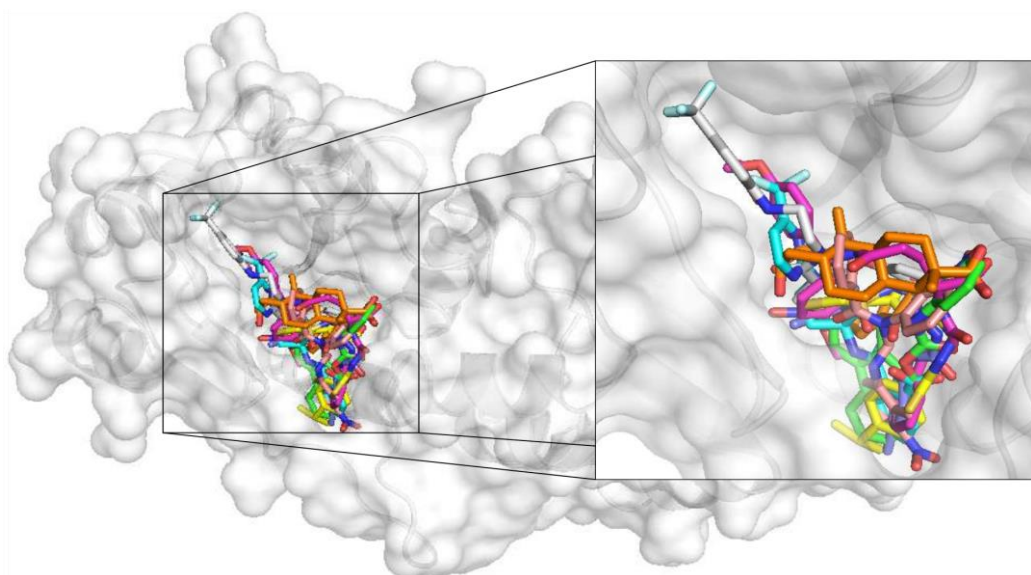


**SI 5 Fig. Structure of the active VSHs towards *Ca*FADS or the microorganisms tested.** Compounds C3, C5, C6, C9 and C18 can bind to *Ca*FADS. Compounds C3, C5, C6 and C18 cause 50% of FMNAT activity inhibition ( $IC_{50}$ ) at concentration lower than 250  $\mu$ M. Compounds C3, C5 and C18 cause 50% RFK-FMNAT activity inhibition ( $IC_{50}$ ) at concentration lower than 250  $\mu$ M. Compounds C3, C5, C6, C9, C18 and C26 have FMNAT residual activity < 95% at 250  $\mu$ M of compound. Compounds C2, C3, C5, C6, C7, C9, C18 and C26 have RFK+FMNAT residual activity < 95% at 250  $\mu$ M of compound. Compounds C2, C5, C6 and C27 have minimal inhibitory concentration (MIC) lower than 256  $\mu$ M against *C. ammoniagenes*, and so do compounds C2, C3, C5, C6 and C27 against *M. tuberculosis*.





**SI 6 Fig. 2D representation of interactions between VSHs and *CaFADS* found in the docking stage.** The Autodock4.2 pose obtained in the docking stage was used to observe the interactions with the FMNAT module of *CaFADS*. Compounds C2, C3, C5, C6, C7 and C9 interact with the ATP binding site and compounds C18 and C26 show interactions with the binding site of both ATP and FMN. Almost all compounds interact with key residues in the binding pocket: H28, H31, H57, N125, S164 and R168.



**SI 7 Fig. Global view of the FMNAT module of the *CaFADS* receptor with VSHs.** A global view of the receptor structure with the superposition of the Autodock poses of the VSHs compounds. The docked compounds cover a wide range of the receptor binding pocket.

## SUPPORTING TABLES

**SI 1 Table. Summary of properties for the CaFADS best ranked VS compounds.** The table shows the VS rank, the Zinc and Maybridge Codes, the names and summary of physicochemical criteria (values at pH 7.0) to evaluate their potential drug-likeness. Preferred criteria values are indicated on the top in green. Favorable criteria for each compound are highlighted in a green background, those in the limit are in a yellow background, and those violating the criteria are in a red background. The 17 compounds selected for experimental evaluation as virtual screening hits (VSH) are highlighted in red font in the first four columns. <sup>a</sup> n.a., not available.

| Rank      | Rank virtual screening | Zinc code    | Maybridge code | Compound name  | <5    | <500                  | <5            | <12              | <10             | <140                   |
|-----------|------------------------|--------------|----------------|--|-------|-----------------------|---------------|------------------|-----------------|------------------------|
|           |                        |              |                |  | xlogP | Molecular Weight (Da) | H-bond Donors | H-bond Acceptors | Rotatable Bonds | Polar Surface Area (Å) |
| <b>C1</b> | 56.16                  | ZINC12339395 | BTB10088       | 6-(tert-butyl)-1,1-dimethyl-4-((4-nitrobenzoyl)oxy)ethanimidoylindane  | 7.0   | 409                   | 0             | 6                | 6               | 84                     |
| <b>C2</b> | 47.52                  | ZINC08626845 | BTB13323       | 2-(((benzyloxy)carbonyl)amino)-5-((di(4-methoxyphenyl)methyl)amino)-5-oxopentanoic acid                        | 4.1   | 505                   | 2             | 9                | 13              | 126                    |
| <b>C3</b> | 42.55                  | ZINC20421376 | DSHS00507      | 7-hydroxy-2,4b-dimethyl-1-((3-oxo-2,3-dihydro-1H-2-indolylidene)methyl)perhydro-2-phenanthrene-carboxylic acid | 4.6   | 424                   | 1             | 5                | 3               | 90                     |
| <b>C4</b> | 36.72                  | ZINC00152822 | HTS06058       | 5-oxo-3-phenyl-5-(2-quinolinylamino)pentanoic acid   | 1.5   | 333                   | 1             | 5                | 6               | 82                     |
| <b>C5</b> | 34.71                  | ZINC00622112 | JFD02331       | 2-(((9H-9-fluorenyl)methoxy)carbonyl)amino)benzoic acid  | 5.0   | 358                   | 1             | 5                | 5               | 78                     |
| <b>C6</b> | 31.90                  | ZINC08628159 | DFP00196       | N-((2-((4-isopropylanilino)carbothioyl)hydrazino)carbonyl)-5-nitrothiophene-3-carboxamide                      | 3.0   | 407                   | 4             | 9                | 7               | 128                    |
| <b>C7</b> | 29.18                  | ZINC08647954 | RJC01786       | N1-(2-methyl-3-nitrophenyl)-N1-(((2-methyl-3-nitrophenyl)imino)methyl)benzamide                                | 5.2   | 418                   | 0             | 9                | 6               | 124                    |

|     |       |              |                             |  |       |     |   |    |    |     |
|-----|-------|--------------|-----------------------------|--|-------|-----|---|----|----|-----|
| C8  | 28.27 | ZINC12339036 | BTB02392                    | 3-[1-cyano-2-(3-nitrophenyl)vinyl]-1-phenyl-5-(1H-pyrrol-1-yl)-1H-pyrazole-4-carbonitrile                      | 4.2   | 406 | 0 | 8  | 5  | 116 |
| C9  | 27.97 | ZINC13464706 | CD10652                     | N1-(4-chlorophenyl)-2-[[[(3,5-dimethylisoxazol-4-yl)sulfonyl]imino]o(methylthio)methyl]hydrazine-1-carboxamide | 4.3   | 418 | 3 | 9  | 6  | 126 |
| C10 | 27.41 | ZINC01027823 | GK03621                     | N'-[[4-cyanophenyl]methylene]-1-(4-nitrophenyl)-5-(trifluoromethyl)-1H-pyrazole-4-carbohydrazide               | 3.6   | 428 | 1 | 9  | 6  | 129 |
| C11 | 26.33 | ZINC04377491 | S08597                      | 5-(4-methoxyanilino)-5-oxo-3-(3,4,5-trimethoxyphenyl)pentanoic acid  | 0.9   | 402 | 1 | 8  | 10 | 106 |
| C12 | 26.33 | ZINC04381325 | PD00681                     | 6-[[4-(4-chlorophenoxy)anilino]carbonyl]-3,4-dimethylcyclohex-3-ene-1-carboxylic acid                          | 5.5   | 399 | 1 | 5  | 5  | 78  |
| C13 | 25.13 | ZINC01047279 | SPB00790                    | 2-[[5-[4-(tert-butyl)phenyl]-4-(2-furylmethyl)-4H-1,2,4-triazol-3-yl]thio]-3-nitropyridine                     | 5.8   | 435 | 0 | 8  | 7  | 103 |
| C14 | 24.60 | ZINC04698082 | RDR00756                    | 3-(1,3-benzodioxol-5-yl)-2-(benzoylamino)acrylic acid  | 2.7   | 310 | 1 | 6  | 4  | 87  |
| C15 | 24.58 | ZINC08636642 | HTS07543                    | 3-(4-methylphenyl)-7,9-diphenylpyrido[3',2':4,5]furo[3,2-d]pyrimidine-2,4(1H,3H)-dione                         | 6.0   | 444 | 0 | 6  | 3  | 80  |
| C16 | 23.85 | ZINC03128794 | BTB02953 (n.a) <sup>a</sup> | 5-[[[1-(2,4-dimethylphenyl)-1H-1,2,3,4-tetraazol-5-yl]thio]methyl]-3-(3-nitrophenyl)-1,2,4-oxadiazole          | 4.2   | 409 | 0 | 10 | 6  | 128 |
| C17 | 23.77 | ZINC01033276 | HTS06059                    | 5-[4-(aminosulfonyl)anilino]-5-oxo-3-phenylpentanoic acid  | -0.13 | 361 | 3 | 7  | 7  | 129 |
| C18 | 23.63 | ZINC01048374 | AW00987                     | 2-[[[1-[4-(trifluoromethyl)pyrimidin-2-yl]piperidin-4-yl]amino]carbonyl]benzoic acid                           | 2.8   | 393 | 1 | 7  | 5  | 98  |
| C19 | 22.38 | ZINC08629386 | BTB08256                    | 1-(2-methoxyphenyl)-5,5-dimethyl-2-[[2-nitro-4-(trifluoromethyl)phenyl]thio]-1,4,5,6-tetrahydropyrimidin-4-one | 5.1   | 453 | 0 | 7  | 6  | 88  |

|     |       |              |           |   |     |     |   |    |   |     |
|-----|-------|--------------|-----------|---|-----|-----|---|----|---|-----|
| C20 | 22.32 | ZINC31723536 | DSHS00186 | 2-(1-naphthylmethylidene)-1,2,3,4-tetrahydronaphthalen-1-one 1-(2,4-dinitrophenyl)hydrazone                     | 8.4 | 464 | 1 | 8  | 5 | 116 |
| C21 | 21.53 | ZINC04381326 | PD00681   | 6-([4-(4-chlorophenoxy)anilino]carbonyl)-3,4-dimethylcyclohex-3-ene-1-carboxylic acid                           | 5.5 | 399 | 1 | 5  | 5 | 78  |
| C22 | 20.91 | ZINC08636573 | HTS06857  | 3,7-bis(4-methylphenyl)-2-(4-nitrophenyl)-7-oxo-5-phenyl-2,4-heptadienenitrile                                  | 7.4 | 498 | 0 | 5  | 8 | 86  |
| C23 | 20.12 | ZINC33380709 | BLT00007  | methyl 4-[2-(2,4-dinitrophenyl)hydrazono]-4-(4-methylphenyl)butanoate   | 5.2 | 386 | 1 | 10 | 9 | 142 |
| C24 | 19.93 | ZINC01042691 | RF01303   | [3-(2,6-dichlorophenyl)-5-methylisoxazol-4-yl]methyl 4-nitrobenzoate  | 5.2 | 407 | 0 | 7  | 6 | 98  |
| C25 | 19.63 | ZINC08618071 | FM00297   | [3-(2,6-dichlorophenyl)-5-methylisoxazol-4-yl]{2-[(4-methyl-2-nitrophenoxy)methyl]-1,3-thiazolan-3-yl}methanone | 4.8 | 508 | 0 | 8  | 6 | 101 |
| C26 | 19.61 | ZINC08649294 | RH01964   | N-[2-[2-nitro-4-(trifluoromethyl)anilino]ethyl]-2-phenoxynicotinamide   | 4.2 | 446 | 2 | 8  | 9 | 109 |
| C27 | 19.03 | ZINC15923715 | NRB05091  | 4-hydroxy-11,11-dimethyl-5,11-dihydro-2H-pyrano[2',3':4,5]pyrido[1,2-a]indole-2,5-dione                         | 2.7 | 294 | 0 | 5  | 0 | 75  |

**Table SI 2. Minimal Inhibitory Concentration (MIC) of VSHs against different microorganisms.** Compounds were, in most cases, assayed in the 0-256  $\mu$ M concentration range. In some cases, they were assayed only in the 0-64  $\mu$ M concentration range, and if no effect was observed in these cases >64 is shown. Best performing compounds are colored from green, yellow, orange to red.

| Bacteria                | Media <sup>a</sup> | Virtual Screening Hit MIC ( $\mu$ M) |      |      |       |      |      |      |      |      |      |      |      |      |         |      |      |      |      |
|-------------------------|--------------------|--------------------------------------|------|------|-------|------|------|------|------|------|------|------|------|------|---------|------|------|------|------|
|                         |                    | C2                                   | C3   | C4   | C5    | C6   | C7   | C8   | C9   | C10  | C11  | C12  | C14  | C17  | C18     | C25  | C26  | C27  |      |
|                         | BHI                | 64                                   | >64  | >64  | >64   | >64  | >64  | >64  | >64  | >64  | >64  | >64  | >64  | >64  |         |      |      |      |      |
|                         | MH                 | 128                                  | >256 | >256 | 32    | 128  | >256 | >256 | >256 | >256 | >256 | >256 | >256 | >256 | >256    | >256 | >256 | >256 | 128  |
|                         | MH+DIP             | 128                                  | >256 | >256 | 32    | 128  | >256 | >256 | >256 | >256 | >256 | >256 | >256 | >256 | >256    | >256 | >256 | >256 | 64   |
|                         | MH+DFO             | 128                                  | >256 | >256 | 32    | 128  | >256 | >256 | >256 | >256 | >256 | >256 | >256 | >256 | 128-256 | >256 | >256 | >256 | 128  |
| <i>C. ammonia</i>       | MH+DIP+DFO         | 64                                   | >256 | >256 | 32    | 128  | >256 | >256 | >256 | >256 | >256 | >256 | >256 | >256 | 256     | >256 | >256 | >256 | 128  |
| <i>C. glutamicum</i>    | BHI                | 16                                   | >64  | >64  | 32    | >64  | >256 | >64  | >64  | >64  | >64  | >64  | >64  | >64  | >256    | >256 | >256 | >256 | 64   |
|                         | BHI                | 64                                   | >64  | >64  | 64    | >64  | >64  | >64  | >64  | >64  | >64  | >64  | >64  | >64  |         |      |      |      |      |
|                         | MH                 | 128                                  | >256 | >256 | 32    | 128  | >256 | >256 | >256 | >256 | >256 | >256 | >256 | >256 | 32      | >256 | >256 | >256 | 64   |
| <i>M. tuberculosis</i>  | 7H9G-ADC           | 256                                  | 256  | >256 | 128   | 128  | >256 | >256 | >256 | >256 | >256 | >256 | >256 | >256 | >256    | >256 | >256 | >256 | 256  |
| <i>M. smegmatis</i>     | 7H9G-ADC           | 256                                  | >256 | >256 | >256  | >256 | >256 | >256 | >256 | >256 | >256 | >256 | >256 | >256 |         |      |      |      |      |
|                         | BHI                | 256                                  | 256  | >256 | 128   | >256 | >256 | >256 | >256 | >256 | >256 | >256 | >256 | >256 |         |      |      |      |      |
|                         | MH                 | >256                                 | 256  | >256 | 256   | 64   | >256 | >256 | >256 | >256 | >256 | >256 | >256 | >256 |         |      |      |      |      |
| <i>S. pneumoniae</i>    |                    | >256                                 | >64  | >64  | >64   | >64  | >64  | >64  | >64  | >64  | >64  | >64  | >64  | >64  | >256    | >256 | >256 | >256 | >256 |
| <i>E. coli</i>          | LB                 | >64                                  | >64  | >64  | >64   | >64  | >64  | >64  | >64  | >64  | >64  | >64  | >64  | >64  | >256    | >256 | >256 | >256 | >256 |
| <i>L. monocytogenes</i> | BHI                | >64                                  | >64  | >64  | >64   | >64  | >64  | >64  | >64  | >64  | >64  | >64  | >64  | >64  | 64      | >256 | >256 | >256 | 64   |
| <i>P. aeruginosa</i>    | MH                 | >256                                 | >256 | >256 | >256  | >256 | >256 | >256 | >256 | >256 | >256 | >256 | >256 | >256 | >256    | >256 | >256 | >256 | >256 |
| <i>S. thyphimurium</i>  | MH                 | >256                                 | >256 | >256 | >256  | >256 | >256 | >256 | >256 | >256 | >256 | >256 | >256 | >256 | >256    | >256 | >256 | >256 | >256 |
| <i>S. aureus</i>        | MH                 | 128                                  | >256 | >256 | 32-64 | >256 | >256 | >256 | >256 | >256 | >256 | >256 | >256 | >256 | 256     | >256 | >256 | >256 | 64   |
| <i>Bacillus spp.</i>    | MH                 | 128                                  | 256  | >256 | 32    | >256 | >256 | >256 | >256 | >256 | >256 | >256 | >256 | >256 | 256     | >256 | >256 | >256 | 32   |

<sup>a</sup>BHI, brain heart infusion broth; MH, Cation-adjusted Mueller-Hinton broth; DIP, 2,2'-bipyridine; DFO, deferoxamine; 7H9G, Middlebrook 7H9 broth supplemented with glycerol; ADC, albumin dextrose catalase supplement.

**Table SI 3. Bacterial strains tested for VSH antibacterial activity.**

| <b>Bacterial strain</b>  | <b>Features</b>   | <b>Source</b> |
|--|---|---------------|
| <i>Corynebacterium ammoniagenes</i> ATCC 7862                  | Reference strain  | ATCC          |
| <i>Corynebacterium glutamicum</i> ATCC 13032                   | Reference strain  | ATCC          |
| <i>Corynebacterium diphtheriae</i> ATCC 39255                  | Strain lacking diphtheria toxin                                 | ATCC          |
| <i>Mycobacterium tuberculosis</i> H37Rv                        | Reference laboratory strain (virulent)                          | ATCC          |
| <i>Mycobacterium smegmatis</i> mc <sup>2</sup> 155 ATCC 700084 | High-efficiency strain for DNA transformation                   | ATCC          |
| <i>Streptococcus pneumoniae</i> ATCC 49619                     | Clinical isolated   | ATCC          |
| <i>Escherichia coli</i> ATCC 10536                             | Reference strain to test bactericidal activity of disinfectants | ATCC          |
| <i>Listeria monocytogenes</i> EDGe ATCC BAA-679                | Clinical isolate  | ATCC          |
| <i>Pseudomonas aeruginosa</i> ATCC 15442                       | Reference strain to test bactericidal activity of disinfectants | ATCC          |
| <i>Salmonella thyphimurium</i> SV5015                          | <i>Salmonella thyphimurium</i> SL1344 <i>his</i> <sup>+</sup>   | [9]           |
| <i>Staphylococcus aureus</i> CECT 794 (ATCC 29213)             | Reference strain to test antimicrobial susceptibility           | CECT          |
| <i>Bacillus sp.</i> CECT 40                                    | Environmental isolate   | CECT          |

ATCC, American Type Culture Collection

CECT, Spanish Type Culture Collection

## REFERENCES

1. Morris GM, Huey R, Lindstrom W, Sanner MF, Belew RK, Goodsell DS, et al. AutoDock4 and AutoDockTools4: Automated docking with selective receptor flexibility. *J Comput Chem.* 2009;30: 2785–91. doi:10.1002/jcc.21256
2. Cosconati S, Forli S, Perryman AL, Harris R, Goodsell DS, Olson AJ. Virtual Screening with AutoDock: Theory and Practice. *Expert Opin Drug Discov.* 2010;5: 597–607. doi:10.1517/17460441.2010.484460
3. Forli S, Olson AJ. A Force Field with Discrete Displaceable Waters and Desolvation Entropy for Hydrated Ligand Docking. *J Med Chem.* 2012;55: 623–638. doi:10.1021/jm2005145
4. Trott O, Olson AJ. AutoDock Vina: Improving the speed and accuracy of docking with a new scoring function, efficient optimization, and multithreading. *J Comput Chem.* 2009;31: NA-NA. doi:10.1002/jcc.21334
5. Koes DR, Baumgartner MP, Camacho CJ. Lessons Learned in Empirical Scoring with smina from the CSAR 2011 Benchmarking Exercise. *J Chem Inf Model.* 2013;53: 1893–1904. doi:10.1021/ci300604z
6. Quiroga R, Villarreal MA, Ballester P, Wong M-H, Allain N, Laguerre M, et al. Vinardo: A Scoring Function Based on Autodock Vina Improves Scoring, Docking, and Virtual Screening. Sticht H, editor. *PLoS One.* 2016;11: e0155183. doi:10.1371/journal.pone.0155183
7. Cao Y, Li L. Improved protein-ligand binding affinity prediction by using a curvature-dependent surface-area model. *Bioinformatics.* 2014;30: 1674–1680. doi:10.1093/bioinformatics/btu104
8. Palacio-Rodríguez K, Lans I, Cavasotto CN, Cossio P. Exponential consensus ranking improves the outcome in docking and receptor ensemble docking. *Sci Rep.* 2019;9: 5142. doi:10.1038/s41598-019-41594-3
9. Qi SY, Moir A, David O'Connor C. Proteome of *Salmonella typhimurium* SL1344: Identification of novel abundant cell envelope proteins and assignment to a two-dimensional reference map. *J Bacteriol.* 1996;178: 5032–5038. doi:10.1128/jb.178.16.5032-5038.1996





# General discussion



## I. Species-specific strategies regulate the biosynthesis of flavin cofactors.

The flavin cofactors are essential in cell bioenergetics because they act as cofactors of a plethora of flavoproteins and flavoenzymes (Macheroux *et al.*, 2011). Hence, its production should be thoroughly regulated to maintain the cellular and flavoproteome homeostasis. In general, eukaryotes and most archaea synthesize FMN and FAD through two independent monofunctional enzymes; whereas most prokaryotic organisms depend on a single bifunctional enzyme, the FAD synthase (FADS) (Serrano *et al.*, 2013a)

The eukaryotic monofunctional RFKs and the C-terminal modules of prokaryotic FADSs show high overall structural similarity. However, species-specific features have been reported regarding the conformation of several structural elements, such as loops FlapI and FlapII and the catalytic PTAN motif (Frago *et al.*, 2008; Herguedas *et al.*, 2010; Karthikeyan *et al.*, 2003a; Sebastián *et al.*, 2017a; Wang *et al.*, 2003). These variations modulate conformational reorganizations occurring upon ligand binding and catalysis, and result in a variety of species-specific strategies to regulate FMN biosynthesis; as demonstrated for the RFK cycles of the prokaryotic FADSs of *Corynebacterium ammoniagenes* and *Streptococcus pneumoniae* (Sebastián *et al.*, 2017c, 2018a). The results in **Publication I** (Anoz-Carbonell *et al.*, 2020a) further reinforce our hypothesis and extend it to monofunctional RFKs.

The inhibition of the RFK activity by the products of the reaction seems to be a common regulatory mechanism, although inhibition potency and mechanism varies with the enzyme. Hence, FMN and ADP inhibit the RFK reaction through the formation of non-productive ternary complexes that kinetically and thermodynamically competes with the catalytically competent complex (**Publication I**) (Anoz-Carbonell *et al.*, 2020a; Sebastián *et al.*, 2017c, 2018a). However, the inhibition by RF substrate seems to be a species-specific mechanism, since it has been observed just for the RFK activity of *CaFADS* but not for other prokaryotic FADS or eukaryotic RFKs so far studied (Herguedas *et al.*, 2015; Sebastián *et al.*, 2017c). Other significant differences are observed in ligand binding cooperativity, which might exacerbate the inhibitory effect of substrates and/or products, as observed in *CaFADS* but with modest contribution in *SpnFADS* and *HsRFK*. Altogether, our data reflect noteworthy differences in the RFK catalytic mechanism of the characterized prokaryotic FADS and eukaryotic RFKs: *HsRFK* and *SpnFADS* follow a random sequential binding of the RFK substrates, while substrates binding to *CaFADS* is concerted

**(Publication I)** (Anoz-Carbonell *et al.*, 2020a; Sebastián *et al.*, 2017c, 2018a). Additionally, for all these three RFK proteins, the release of FMN and ADP products might be the rate-limiting step of the whole catalytic cycle. Hence, this seems to be a prevailing regulatory mechanism of the RFK activity, as well as a potential strategy to control the delivery of FMN to their respective FMNATs (FMNAT modules of prokaryotic FADS or eukaryotic FMNATs) or to the FMN client apo-flavoproteins.

The FMNAT module of prokaryotic FADSs differ from eukaryotic FMNATs (or FADSs) both in sequence and structure. Although both adopt a Rossmann  $\alpha/\beta/\alpha$  topology, they belong to two different proteins superfamilies, the *nucleotidyl-transferase* and the *adenine nucleotide  $\alpha$ -hydroxylase-like* superfamilies, respectively (Herguedas *et al.*, 2010; Huerta *et al.*, 2009; Leulliot *et al.*, 2010; Sebastián *et al.*, 2017a; Wang *et al.*, 2003). Thus, FAD biosynthesis is regulated through several mechanisms that, depending on the species, can include the inhibition of the FMNAT reaction by the substrates and/or products, the redox state of the FMN substrate, the stabilization of quaternary assemblies coupled to catalysis (Bowers-Komro *et al.*, 1989; Sebastián *et al.*, 2017a; Serrano *et al.*, 2015; Torchetti *et al.*, 2011). Moreover, the release of the FAD product is the rate-limiting step in the FMNAT catalysis both in the prokaryotic and eukaryotic enzymes (Arilla-Luna *et al.*, 2019; Huerta *et al.*, 2013; Lans *et al.*, 2018; Park *et al.*, 2012), as observed for RFKs. In the case of the human *hFADS*, this regulatory feature was also hypothesized (Giancaspero *et al.*, 2015b; Torchetti *et al.*, 2011), and has been further confirmed with the D238A *hFADS6* mutant, in which the enzymatic activity increases as a result of a lower affinity for the flavin ligand, and thus a higher product release as reported in **Publication II** (Leone *et al.*, 2019).

The detailed characterization of the catalytic cycles of the enzymes implicated on the flavin cofactor biosynthesis in *Homo sapiens* might contribute to the better understanding of the molecular bases of flavin-related pathologies, such as lipid storage myopathy due to FLAD1 deficiency, amyotrophic lateral sclerosis or certain types of cancers (Hirano *et al.*, 2011; Hu *et al.*, 2020; Olsen *et al.*, 2016; Tolomeo *et al.*, 2020). Furthermore, it might provide a framework to new therapeutic strategies and to the design and developpe selective compounds targeting these enzymes.

## II. The two active sites of the NQO1 homodimer of *Homo sapiens* are non-equivalent during catalysis.

Flavoenzymes and flavoproteins execute crucial roles in energetic metabolism as well as in other cellular processes, such as cell signaling, protein folding, or nucleotide synthesis (Joosten and van Berkel, 2007; Macheroux *et al.*, 2011). Nonetheless, in the human being, most flavin-dependent enzymes catalyze oxidation–reduction processes in primary metabolic pathways, and approximately two thirds of them are associated with disorders caused by allelic variants affecting protein function (Lienhart *et al.*, 2013).

Human NQO1 is a dimeric FAD-dependent flavoprotein involved in the antioxidant defense, the activation of cancer prodrugs and the stabilization of oncosuppressors (Beaver *et al.*, 2019; Oh *et al.*, 2016; Ross and Siegel, 2018). Furthermore, changes in the activity of this enzyme have been associated to different pathologies, including cancer and cardiovascular and neurological diseases (Ross *et al.*, 2000). The enzymatic cycle of NQO1 follows a bi-bi mechanism divided in two half reactions, each of them comprising ligand binding/release events and the hydride transfer reaction (Bianchet *et al.*, 2004; Hosoda *et al.*, 1974). Early studies with rat NQO1 pointed to the existence of functional non-equivalent active sites within the protein dimer and negative cooperativity towards some inhibitors (Rase *et al.*, 1976).

Our work (**Publication III**) further reinforces the mechanism of rat *r*NQO1, and extends it to human *h*NQO1 (Anoz-Carbonell *et al.*, 2020b). In *h*NQO1, the hydride transfer from NAD(P)H to the flavin cofactor occurs with a 20-fold difference in rate constants between active sites. Therefore, the *fast* pathway might dominate the observed steady-state kinetics, representing a sort of half-of-sites activity. This kinetic difference between both active sites was also observed in the hydride transfer of the oxidative half-reaction. Moreover, the HT of both active sites is slowed down by the inhibitor dicoumarol in both the reductive and oxidative half-reactions. Analysis of KIEs and their temperature dependence also supports our proposal of two non-equivalent active sites, since they show significant different contributions from quantum tunneling, structural dynamics and reorganizations to the HT process.

A deep understanding of the catalytic mechanism of this disease-related enzyme would allow us to rationalize the effects of missense variants (such as

the polymorphisms p.P187S or p.R139W), as well as to design more selective modulators/inhibitors of NQO1 activity and pro-drugs which are activated by NQO1 as chemotherapeutics.

### III. Exploring prokaryotic FADSs as antimicrobial targets.

The emergence during the last decades of drug-resistant microorganisms reveals the need to develop new antimicrobial drugs, focusing on the discovery of new druggable targets and processes in prokaryotes. In our group, we propose prokaryotic FADSs as potential antimicrobial targets. These bifunctional proteins synthesize the essential flavin cofactors FMN and FAD, and hence they have a crucial role in flavin homeostasis and in the maintenance of flavoprotein and flavoenzyme function (Frago *et al.*, 2008). Indeed, FADS are highly conserved among prokaryotes and have been described as essential for numerous microorganisms (Goodall *et al.*, 2018; Kobayashi *et al.*, 2003; Liu *et al.*, 2017; Minato *et al.*, 2019). Furthermore, FMNAT modules of prokaryotic FADS and eukaryotic FMNATs differ both in sequence, structure and biochemical features (Herguedas *et al.*, 2010; Huerta *et al.*, 2009; Leulliot *et al.*, 2010; Wang *et al.*, 2003), so potential inhibitors that specifically target the FMNAT module of FADS are likely to be selective to bacteria without affecting the eukaryotic host enzymes.

In our group, we decided to explore the potentiality of FADSs as antimicrobial targets through the high-throughput screening against the FADS of *Corynebacterium ammoniagenes*. CaFADS is hitherto the best characterized prokaryotic FADS and a good representative model for the FADS of *Mycobacterium tuberculosis* (Frago *et al.*, 2008, 2009; Herguedas *et al.*, 2010; Marcuello *et al.*, 2013). For that, we have followed two different but complementary approaches: a wet-laboratory activity-based HTS (**Publication IV**) (Sebastián *et al.*, 2018b) and a docking-based virtual screening (**Publication V**) (Lans *et al.*, 2020)¶.

In the activity-based HTS against CaFADS (**Publication IV**) (Sebastián *et al.*, 2018b), we identified 37 compounds inhibiting its enzymatic activities (RFK and/or FMNAT), three of which are selective and potent inhibitors of the FMNAT activity. Additionally, the species-specificity of HTS hits was confirmed, since only a third of the compounds have moderate inhibitory effects on SpnFADS, another member of the prokaryotic FADS family.

Additionally, a virtual screening was used to find new *Ca*FADS ligands from a larger compound library (**Publication V**) (Lans *et al.*, 2020). With this *in silico* approach, we have identified 5 compounds from the 17 best-scored hits that are *in vitro* ligands of *Ca*FADS and inhibit its FMNAT enzymatic activity.

We also tested the antimicrobial activity of both HTS hits against several bacterial strains, including *C. ammoniagenes*, *S. pneumoniae* and *M. tuberculosis*; as well as their cytotoxic activity in eukaryotic cell lines (**Publications IV and V**) (Lans *et al.*, 2020; Sebastián *et al.*, 2018b). The selective FMNAT inhibitors from the HTS had mild or no antimicrobial effect against the tested strains, and those compounds targeting the both the RFK and FMNAT activity (non-selective HTS hits) had strong effect on microbial growth. In contrast, the compounds identified in the virtual screening are active but at high concentrations. Furthermore, all the identified FMNAT inhibitors do not show significant cytotoxic effect at the concentrations required for the antimicrobial activity, highlighting their potential use against prokaryotic pathogens. However, derivatization of this compounds into second generation hits, the utilization of vehiculation systems or the combination with synergistic antimicrobial partners are some strategies to further increase the efficacy of these inhibitors.

In these studies, we have focused on compounds targeting the FMNAT modules of prokaryotic FADSs, because of the lack of sequence and structural similarity with eukaryotic FMNATs/FADSs. To date, antimicrobials targeting the RFK modules of FADS have not been exploited, since their structural homology with the eukaryotic RFKs envisaged the potential compromise of the specificity of these inhibitors, resulting in deleterious effects to the host (Serrano *et al.*, 2013a). However, our results in **Publication I** (Anoz-Carbonell *et al.*, 2020a) demonstrate species-specific mechanisms in RFKs (associated with significant differences in secondary structure elements and their conformational changes upon ligand binding and catalysis), hence re-opening the door to antimicrobials against RFK modules of bacterial FADSs.





# Conclusions



**PUBLICATION I. Human riboflavin kinase: Species-specific traits in the biosynthesis of the FMN cofactor.**

- Inhibition of the HsRFK activity provides with an intricate regulatory mechanism that might contribute to flavins production according to the cellular needs.
- Binding of the substrates and products into non-competent complexes act as kinetic and thermodynamic traps for the formation of the catalytically competent complex.
- HsRFK catalytic and regulatory mechanisms differ from those of the so far evaluated bacterial counterparts, reinforcing the idea of species-specific mechanisms in RFK catalysis and opening the door to antimicrobials against this enzymatic activity of prokaryotic FADS.

**PUBLICATION II. Mutation of aspartate 238 in FAD synthase isoform 6 increasing the specific activity by weakening the FAD binding.**

- The D238A *hFADS6* mutant, as the D181A *CgFMNAT* “supermutant” (mutant in the orthologous residue), has higher turn-over number and catalytic efficiency than the WT protein.
- The D238A substitution in *hFADS* drastically lowers the affinity for the flavin ligands, favoring FAD product release after catalysis, and therefore increasing the specific activity.
- Our data is consistent with the proposed mechanism for FAD biosynthesis by *hFADS*, in which the limiting step of the overall catalytic process is the FAD releasing step.

**PUBLICATION III. The catalytic cycle of the antioxidant and cancer-associated human NQO1 enzyme: hydride transfer, conformational dynamics and functional cooperativity.**

- *hNQO1* has two non-equivalent active sites in the protein dimer that differ significantly in the rate for hydride transfer from NAD(P)H to the flavin cofactor.

- The inhibitor dicoumarol slows down the reductive and oxidative half-reactions at both active sites within the protein dimer.
- Analysis of KIEs and their temperature dependence shows different contributions from quantum tunneling, structural dynamics and reorganizations to catalysis at the two active sites of a *hNQO1* dimer.

**PUBLICATION IV. Discovery of antimicrobial compounds targeting bacterial type FAD synthases.**

- 37 compounds of the Prestwick Chemical Library® (1240 compounds) inhibit *CaFADS* enzymatic activities (RFK and/or FMNAT), three of which are specific and potent inhibitors of the FMNAT activity.
- Two of these three hits are not species-selective, since they inhibit both *CaFADS* and *SpnFADS*.
- No antimicrobial effect against *C. ammoniagenes* and *S. pneumoniae* was detected for these three FMNAT inhibitors. However, compounds affecting both RFK and FMNAT activities show the best antimicrobial properties.
- Prokaryotic FADSs are promising species-selective antimicrobial targets.

**PUBLICATION V. *In silico* discovery and biological validation of ligands of FAD synthase, a promising new antimicrobial target.**

- The applied virtual screening protocol is able to computationally screen large compound libraries to find ligands/binders of *CaFADS*.
- 5 compounds out of the 17 best-scored from the VS of the Maybridge Chemical Library® (14000 compounds) against *CaFADS*, are *in vitro* ligands of this protein and inhibit its FMNAT activity.
- These *bona fide* hits have antimicrobial activity against *C. ammoniagenes* and *M. tuberculosis*, without showing significant cytotoxicity in eukaryotic cell lines.

# Conclusiones



**PUBLICACIÓN I. Human riboflavin kinase: Species-specific traits in the biosynthesis of the FMN cofactor.**

- La inhibición de la actividad de *HsRFK* proporciona un intrincado mecanismo regulatorio que podría contribuir a la producción de flavinas de acuerdo con las necesidades intracelulares.
- La unión de los sustratos y productos en complejos no-competentes actúa a modo de trampas cinéticas y termodinámicas a la formación del complejo catalítico competente.
- Los mecanismos catalíticos y regulatorios de *HsRFK* difieren de los observados en las RFKs bacterianas, lo que refuerza la idea de mecanismos especie-específicos en la catálisis RFK y abre la puerta al desarrollo de antimicrobianos frente a esta actividad enzimática de las FADS procariontas.

**PUBLICACIÓN II. Mutation of aspartate 238 in FAD synthase isoform 6 increasing the specific activity by weakening the FAD binding.**

- El mutante D238A *hFADS6*, de forma similar al “supermutante” D181A *CgFMNAT* (mutante en el residuo ortólogo), tiene mayor número de recambio y eficiencia catalítica que la proteína silvestre.
- La sustitución D238A en *hFADS* reduce drásticamente la afinidad por el ligando flavínico, favoreciendo la liberación del producto tras la catálisis y, con ello, incrementando la actividad específica.
- Nuestros datos son consistentes con el mecanismo propuesto para la biosíntesis de FAD por *hFADS*, en el que la etapa limitante del proceso catalítico es la liberación del FAD.

**PUBLICACIÓN III. The catalytic cycle of the antioxidant and cancer-associated human NQO1 enzyme: hydride transfer, conformational dynamics and functional cooperativity.**

- El dímero de *hNQO1* tiene dos centros activos no idénticos que difieren significativamente en la velocidad de transferencia de hidruro del NAD(P)H al cofactor flavínico.
- El inhibidor dicumarol ralentiza las semi-reacciones de reducción y oxidación de ambos centros activos del dímero.
- El análisis de los efectos isotópicos cinéticos y su dependencia con la temperatura muestra diferentes contribuciones del efecto túnel, dinámicas conformacionales y reorganizaciones moleculares en la catálisis de ambos centros activos del dímero de *hNQO1*.

**PUBLICACIÓN IV. Discovery of antimicrobial compounds targeting bacterial type FAD synthases.**

- 37 compuestos de la quimoteca Prestwick Chemical Library® (1240 compuestos) inhiben las actividades enzimáticas de *CaFADS* (RFK y/o FMNAT), tres de los cuales son inhibidores específicos y potentes de la actividad FMNAT.
- Dos de estos tres compuestos no son selectivos de especie, ya que inhiben tanto *CaFADS* como *SpnFADS*.
- No se detecta efecto antimicrobiano frente a *C. ammoniagenes* y *S. pneumoniae* para estos tres inhibidores de la actividad FMNAT. Sin embargo, los compuestos que afectan simultáneamente a las actividades RFK y FMNAT presentan mejores propiedades antimicrobianas.
- Las FADSs procariotas son prometedoras dianas de antimicrobianos.



**PUBLICACIÓN V. *In silico* discovery and biological validation of ligands of FAD synthase, a promising new antimicrobial target.**

- El protocolo de cribado virtual empleado permite identificar de forma computacional compuestos que unan *CaFADS*.
- 5 compuestos de los 17 mejor clasificados del cribado virtual de la quimioteca Maybridge Chemical Library® (14000 compuestos) frente a *CaFADS*, son ligandos *in vitro* de esta proteína e inhiben su actividad FMNAT.
- Estos inhibidores tienen actividad antimicrobiana frente a *C. ammoniagenes* y *M. tuberculosis*, sin presentar citotoxicidad en líneas celulares eucariotas.



# Participation in other related publications



Apart from those included in this Doctoral Thesis, Ernesto Anoz Carbonell has contributed to the following publications:

- Pérez-Amigot D, Taleb V, Boneta S, **Anoz-Carbonell E**, Sebastián M, Velázquez-Campoy A, Polo V, Martínez-Júlvez M, Medina M. 2019. Towards the competent conformation for catalysis in the ferredoxin-NADP<sup>+</sup> reductase from the *Brucella ovis* pathogen. *Biochimica et Biophysica Acta (BBA) – Bioenergetics*, 1860(10):148058.

JCR Impact Factor 2019: 3.465. Rank: Q2 (125/297) Biochemistry and Molecular Biology; Q2 (18/71) Biophysics.

- Sanz-García F‡, **Anoz-Carbonell E‡**, Pérez-Herran E, Martín C, Lucía A, Rodrigues L, Aínsa JA. 2019 Mycobacterial aminoglycoside acetyltransferases: a little of drug resistance, and a lot of other roles. *Frontiers in Microbiology*, 10:46.

JCR Impact Factor 2019: 4.235. Rank: Q2 (34/135) Microbiology.  
‡Both authors have contributed equally to this work.

**Ernesto Anoz Carbonell contributions:** Experimental work: protein purification, spectroscopic characterization, and isothermal titration calorimetry experiments. Data analysis. Manuscript writing, review and editing.



## Towards the competent conformation for catalysis in the ferredoxin-NADP<sup>+</sup> reductase from the *Brucella ovis* pathogen

Daniel Pérez-Amigot<sup>a,b,1</sup>, Víctor Taleb<sup>a,b,1</sup>, Sergio Boneta<sup>b,c</sup>, Ernesto Anoz-Carbonell<sup>a,b</sup>,  
María Sebastián<sup>a,b</sup>, Adrián Velázquez-Campoy<sup>a,b,d,e,f</sup>, Víctor Polo<sup>b,c</sup>, Marta Martínez-Júlvez<sup>a,b,\*</sup>,  
Milagros Medina<sup>a,b,\*</sup>

<sup>a</sup> Departamento de Bioquímica y Biología Molecular y Celular, Facultad de Ciencias, Universidad de Zaragoza, 50009 Zaragoza, Spain

<sup>b</sup> Instituto de Biocomputación y Física de Sistemas Complejos (Joint Units: BIFI-IQFR and GBSC-CSIC), Universidad de Zaragoza, 50018 Zaragoza, Spain

<sup>c</sup> Departamento de Química Física, Universidad de Zaragoza, 50009 Zaragoza, Spain

<sup>d</sup> Aragon Institute for Health Research (IIS-Aragon), Zaragoza 50009, Spain

<sup>e</sup> Biomedical Research Networking Center in Digestive and Hepatic Diseases (CIBERehd), Madrid, Spain

<sup>f</sup> Fundación ARAID, Government of Aragon, Zaragoza 50018, Spain

### ARTICLE INFO

#### Keywords:

Bacterial ferredoxin-NADP(H) reductase  
Hydride transfer  
Charge-transfer complex  
Active site geometry  
Stopped-flow  
X-ray diffraction  
Molecular dynamics

### ABSTRACT

*Brucella ovis* encodes a bacterial subclass 1 ferredoxin-NADP(H) reductase (BoFPR) that, by similarity with other FPRs, is expected either to deliver electrons from NADPH to the redox-based metabolism and/or to oxidize NADPH to regulate the soxRS regulon that protects bacteria against oxidative damage. Such potential roles for the pathogen survival under infection conditions make of interest to understand and to act on the BoFPR mechanism. Here, we investigate the NADP<sup>+</sup>/H interaction and NADPH oxidation by hydride transfer (HT) to BoFPR. Crystal structures of BoFPR in free and in complex with NADP<sup>+</sup> hardly differ. The latter shows binding of the NADP<sup>+</sup> adenosine moiety, while its redox-reactive nicotinamide protrudes towards the solvent. Nonetheless, pre-steady-state kinetics show formation of a charge-transfer complex (CTC-1) prior to the hydride transfer, as well as conversion of CTC-1 into a second charge-transfer complex (CTC-2) concomitantly with the HT event. Thus, during catalysis nicotinamide and flavin reacting rings stack. Kinetic data also identify the HT itself as the rate limiting step in the reduction of BoFPR by NADPH, as well as product release limiting the overall reaction. Using all-atom molecular dynamics simulations with a thermal effect approach we are able to visualise a potential transient catalytically competent interaction of the reacting rings. Simulations indicate that the architecture of the FAD folded conformation in BoFPR might be key in catalysis, pointing to its adenine as an element to orient the reactive atoms in conformations competent for HT.

### 1. Introduction

Plant-type ferredoxin-NADP<sup>+</sup> reductases are FAD-dependent enzymes structurally and functionally subdivided in two groups known as plastidic-type FNRs and bacterial-type FPRs [1,2]. The main function of FNRs in photosynthetic cells is the electron transfer from Photosystem I

to NADP<sup>+</sup>, via ferredoxin, to produce reducing power in the form of NADPH [2,3]. This reaction can be physiologically reversible and, thus, FNRs can also oxidize NADPH to provide reducing power to various metabolic processes in photosynthetic cells as well as in non-photosynthetic tissues and in some bacteria [4–6]. FPRs in general work in the NADPH oxidation sense of the reaction. In heterotrophic bacteria

**Abbreviations:** CHES, 2-(cyclohexylamino)ethanesulfonic acid; CTC, charge transfer complex; DCPIP, 2,6-dichlorophenolindophenol; DMSO, dimethyl sulfoxide; *E. coli*, *Escherichia coli*; FAD, flavin adenine dinucleotide; FNR, plastidic type ferredoxin-NADP<sup>+</sup> reductase; FPR, bacterial type ferredoxin-NADP<sup>+</sup> reductase; HEPES, 4-(2-hydroxyethyl)-1-piperazineethanesulfonic acid; HT, hydride transfer; IPTG, isopropyl β-D-1-thiogalactopyranoside; ITC, isothermal titration calorimetry; MD, molecular dynamics; MES, 2-(N-morpholino)ethanesulfonic acid; NADP<sup>+</sup> and NADPH, oxidized and reduced forms of the nicotinamide adenine dinucleotide phosphate; PEG, polyethylene glycol; PIPES, piperazine-*N,N'*-bis(2-ethanesulfonic acid); ROS, reactive oxygen species; SDS-PAGE, sodium dodecyl sulfate polyacrylamide gel electrophoresis; Tris, tris(hydroxymethyl) aminomethane

\* Corresponding authors at: Departamento de Bioquímica y Biología Molecular y Celular, Facultad de Ciencias, Universidad de Zaragoza, Pedro Cerbuna, 12, 50009 Zaragoza, Spain.

E-mail addresses: [mmartine@unizar.es](mailto:mmartine@unizar.es) (M. Martínez-Júlvez), [mmedina@unizar.es](mailto:mmedina@unizar.es) (M. Medina).

<sup>1</sup> These two authors have equally contributed to the study and must both be considered as first authors.

<https://doi.org/10.1016/j.bbabio.2019.148058>

Received 16 June 2019; Received in revised form 19 July 2019; Accepted 2 August 2019

Available online 05 August 2019

0005-2728/ © 2019 Elsevier B.V. All rights reserved.

they usually provide electrons, via ferredoxin or flavodoxin, to processes such as nitrogen, hydrogen, methane or CO<sub>2</sub> assimilation and fixation, activation of anaerobic enzymes, fatty acid desaturation or  $\beta$ -carotene hydroxylation [1,2]. A key antioxidant role in the protection of Gram negative bacteria against changing environments is also related to their NADPH oxidase activity [7–9]. Thus, FPRs are reported as a component of the soxRS regulon system that protects bacteria against superoxide and nitric oxide damage. In this context, at least five loci involved in the superoxide response of *Escherichia coli* are related to redox processes including the *fpr* gene, with NADPH formation and FPR protein levels stimulated when bacteria are exposed to oxidative environments [10–13]. Therefore, some bacteria finely regulate the NADPH (H) pool homeostasis, and its deployment to the oxidized state, by the FPR action to produce the oxidation of the soxRS sensor. This later fact in turn activates the protective bacterial response under oxidative environments [14].

Both FNRs and FPRs fold in two domains, the N-terminal being the main responsible for FAD binding while the C-terminal domain binds NADP<sup>+</sup>/H [1–3,9,15]. Despite overall FAD binding is similar, differences are found in its conformation that is respectively extended and folded. The extended FAD in FNRs is favoured by a  $\beta$ -hairpin structure that is replaced by a short loop in FPRs (Fig. SP1A). On its side, the folded FAD in FPRs is stabilised by the stacking of its adenosine to an aromatic residue found in a C-terminal tail present in FPRs but absent in FNRs. A key dissimilarity among FNRs and some FPRs also occurs at the active site. The isoalloxazine ring of FNRs stacks between two aromatic residues, being the one facing its *Re*-face a highly conserved C-terminal Tyr that controls substrates/products access/release as well as the optimal catalytic competent conformation for catalysis [2,16–18]. Subclass II FPRs conserve this aromatic residue, but subclass I members lack it (Fig. SP1A). Such traits are claimed as the causes for differences in catalytic efficiencies described between FNRs and FPRs.

The Gram negative  $\alpha$ -proteobacterium *Brucella ovis* has a *fpr* gene (coding for BoFPR) whose immediate downstream *sodr* gene codifies for a superoxide dismutase (SOD). SOD enzymes are directly involved in the process of reactive oxygen species (ROS) elimination, and its overexpression in some *Brucella* genus inhibits bacterial intracellular growth [19]. Noticeably, *sodr* genes are found immediately upstream of *fpr* in some highly related Rhizobiales (which share more than 80% of sequence identity). In most bacteria the *fpr* genomic context lacks *sodr* genes, but contains genes for ferredoxins and/or flavoproteins (Fig. SP1B). As chromosomal proximity in prokaryotes can relate to gene co-regulation [20], a functional association might be envisaged between BoFPR and BoSOD. Bacteria from the genus *Brucella* are facultative intracellular pathogens that cause brucellosis in humans and many animals, including cows, goats, sheep, dogs, and pigs. *B. ovis* is the causative agent of this zoonosis in sheep, causing genital injuries, placentitis, perinatal mortality increase and a lack of fertility [21–23]. The host tries to cope with the infection through phagocytosis involving the activation of neutrophils which undergo the respiratory burst releasing of ROS intended to target foreign pathogens [24]. Since in Gram negative bacteria FPR might perform an important function in ROS response, processes involving BoFPR might be of utmost importance for the survival of *B. ovis* under infection conditions.

Better understanding of the proteins that support *Brucella* intracellular growth is critical to design safe and effective vaccines and treatments of brucellosis. In this context, we present here the isolation of BoFPR, as well as a study of its mechanism for NADPH oxidation. Our combined spectroscopic, kinetic and structural (both experimental and theoretical) approaches provide an insight into the molecular mechanism for NADPH oxidation by BoFPR. In addition, we present structural details on the contribution of the FAD folded conformation and of the C-terminal tail of FPRs to the formation of a geometry that allocates the N5 of the isoalloxazine of FAD and the C4 of the nicotinamide from NADPH in close proximity. We consider that knowledge about these facts in the context of what is known about other members

of this family is of interest both from the mechanistic point of view in FPRs and to consider BoFPR a potential therapeutic target.

## 2. Materials and methods

### 2.1. Protein production

The BOV-0348 gene of *B. ovis* ATCC 25840 was synthesized and cloned into the *Nco*I/*Bam*HI sites of the pET-28a(+) plasmid by GenScript. In this way the coding fragment contains the BoFPR gene preceded by an extension coding for a His<sub>6</sub>-Tag plus a PreScission protease cleavage sequence. PET28a-BoFPR was used to transform *E. coli* BL21 (DE3) competent cells. Transformed cells were selected on LB/agar with 30  $\mu$ g/mL kanamycin and then grown in LB media. BoFPR expression was induced by overnight incubation with 200  $\mu$ M IPTG at 37 °C. Cells were harvested by centrifugation and stored at –20 °C. To purify BoFPR, cells were thawed, resuspended in cell disruption buffer (20 mM potassium phosphate, pH 7.4, 10 mM imidazole, 0.5 M NaCl, and 1  $\mu$ M phenylmethanesulfonyl fluoride) and broken by ultrasonic treatment at 4 °C (12 cycles of 30 s) in a DRH UP200 DR sonicator (Hielscher). The cell debris was removed by centrifugation and the supernatant was loaded onto a His-Trap HP column (GE Healthcare) equilibrated with cell disruption buffer. The column was washed with the same buffer. His<sub>6</sub>-BoFPR was then eluted by using a 10 → 500 mM imidazole gradient and collected in aliquots while recording absorbance at 280 nm. Fractions being yellow were analysed by SDS-PAGE. Those containing BoFPR were pooled and dialysed against 25 mM Tris/HCl, pH 7.4. To remove the His<sub>6</sub>-Tag, the protein was incubated with the PreScission Protease and then loaded in tandem His-Trap and GST-Trap columns (GE Healthcare) to eliminate both the His<sub>6</sub>-tag and the protease. Purification was completed using a HiPrep™ 26/60 Sephacryl® S-200 HR chromatography (GE Healthcare). Pure BoFPR fractions were pooled and stored at –20 °C.

### 2.2. Spectroscopic analyses

UV–visible absorption spectra were recorded in an UV–Vis Cary 100 spectrophotometer (Agilent Technologies) at 25 °C. CD spectra were obtained in a Chirascan spectropolarimeter (Applied Photophysics Ltd.) at 25 °C with 5  $\mu$ M protein for the far-UV region and 20  $\mu$ M for the near-UV and visible regions, with 0.1 and 1 cm path length cuvettes, respectively. Fluorescence spectra were monitored using a Cary Eclipse fluorimeter (Agilent Technologies) with 20  $\mu$ M protein solutions. The molar absorption coefficient for BoFPR at 451 nm was spectrophotometrically determined by thermal denaturation of the protein for 10 min at 90 °C, followed by centrifugation, separation of the precipitated apoprotein, and spectroscopic quantification of the FAD released to the supernatant as previously described [25]. Spectral evolution upon stepwise reduction of BoFPR (20  $\mu$ M) was achieved by photoreduction in the presence of 5-diazariboflavin (4  $\mu$ M) and 3 mM EDTA under anaerobic conditions [26]. Unless otherwise stated samples were in 25 mM Tris/HCl, pH 7.4.

### 2.3. Isothermal titration calorimetry

Interaction of BoFPR<sub>ox</sub> with NADP<sup>+</sup> was evaluated by isothermal titration calorimetry (ITC) using a high precision Auto-ITC200 calorimeter (MicroCal-Malvern Panalytical) thermostated at 25 °C. Interaction parameters were obtained by direct titration of BoFPR<sub>ox</sub> (10  $\mu$ M in the cell) with NADP<sup>+</sup> solutions (150 or 250  $\mu$ M in the syringe) in 25 mM Tris/HCl, pH 7.4, following procedures described previously [27,28]. A home-derived model for one binding site implemented in Origin 7.0 (OriginLab) was used to determine the binding stoichiometry (N), the association constant ( $K_a$ ), and the binding enthalpy ( $\Delta H$ ) [27,28]. The values of the dissociation constant ( $K_d$ ), the free energy of binding ( $\Delta G$ ) and the enthalpic contribution to the



binding ( $-T\Delta S$ ) were derived from basic thermodynamic relationships.

#### 2.4. Evaluation of BoFPR thermal stability

The increase in the FAD cofactor fluorescence by its dissociation from the holoprotein upon thermal unfolding was used to evaluate BoFPR stability through assessing the midpoint temperature for flavin release ( $T_{mFAD}$ ). Denaturation curves were recorded in 25 mM Tris/HCl, pH 7.4, using a Varian Cary Eclipse fluorimeter (Agilent Technologies Ltd.) from 20 to 85 °C with scan rates of 1.5 °C/min and 2 μM protein, both in the absence and presence of a 50-fold excess of NADP<sup>+</sup>. Samples were excited at 450 nm and fluorescence was recorded at 530 nm.  $T_{mFAD}$  values were determined by analysing thermal FAD release curves as one-transition (i.e., a two-state process, native ↔ unfolded or FAD bound ↔ unbound, N ↔ U) by applying the following equations [29]:

$$S_{obs} = \frac{S_N + S_U e^{-(\Delta G/RT)}}{1 + e^{-(\Delta G/RT)}} = \frac{S_{N,0} + m_N T + (S_{U,0} + m_U T) e^{-(\Delta G/RT)}}{1 + e^{-(\Delta G/RT)}} \quad (1)$$

where  $S_{obs}$  is the measured protein signal at a given temperature ( $T$ ),  $S_N$  and  $S_U$  are the intrinsic fluorescent signals corresponding to protein-bound FAD and protein-free FAD, respectively, and considered linear functions of the temperature ( $S_{N,0}$  and  $S_{U,0}$  are the y-axis intercepts, and  $m_N$  and  $m_U$  are the slopes). On the other hand, the free energy difference in Eq. (1) follows,  $\Delta G_i = \Delta H_i \left(1 - \frac{1}{T_{mFADi}}\right) + \Delta C_{Pi} \left(T - T_{mFADi} - T \ln \frac{T}{T_{mFADi}}\right)$ , where  $\Delta H_i$  is the van't Hoff enthalpy for each FAD release transition,  $T_{mFADi}$  is the mid-transition temperature for FAD release,  $\Delta C_{Pi}$  is the heat capacity change for the unfolding transition associated with FAD release, and  $R$  is the ideal gas constant.

The heat capacity of BoFPR<sub>ox</sub> and BoFPR<sub>ox</sub>:NADP<sup>+</sup> samples was measured as a function of temperature ( $\Delta C_p(T)$ ) using a High-sensitivity differential scanning PEAQ-DSC automated microcalorimeter (MicroCal-Malvern Analytical). Thermal denaturation scans were performed with 20 μM degassed BoFPR<sub>ox</sub> solutions, both in the absence and presence of a 5-fold excess of NADP<sup>+</sup> at a scanning rate of 1 °C/min from 10 to 95 °C. Reference solutions (containing buffers but lacking BoFPR and NADP<sup>+</sup>) were treated similarly to record the baseline of the instrument before experiments. No precipitation/aggregation occurred during thermal denaturation. Thermograms were baseline-corrected and analysed using a home-derived routine implemented in Origin 7 (OriginLab).

#### 2.5. Steady-state enzymatic assays and evaluation of the inhibitory effects

The BoFPR NADPH-dependent diaphorase activity was determined by following the 2,6-dichlorophenolindophenol (DCPIP) reduction (95 μM) at 620 nm ( $\epsilon_{620} = 21 \text{ mM}^{-1} \text{ cm}^{-1}$ ) in samples containing 20 nM BoFPR and a 0–50 μM NADPH range [30]. Kinetic measurements were carried out at 25 °C, in 25 mM Tris/HCl, pH 7.4.  $k_{cat}$  and  $K_m^{NADPH}$  values were calculated by data fitting to the Michaelis-Menten equation considering inhibition by excess of NADPH,

$$\frac{v}{[BoFPR]} = \frac{k_{cat} [NADPH]}{K_m^{NADPH} + [S](1 + [S]/K_i)} \quad (2)$$

which also provided the corresponding inhibition constant,  $K_i$ . NADPH consumption when using oxygen and superoxide as potential BoFPR electron acceptors was quantified by monitoring the decrease in absorbance at 340 nm. Superoxide was added as a potassium 18-crown-6 salt (Sigma-Aldrich) dissolved in dimethyl sulfoxide (DMSO).

The diaphorase activity was also assayed at different pH values using as buffers 25 mM MES in the pH 5.5–6.0 range, 25 mM PIPES in the pH 6.3–6.7 range, 25 mM Tris/HCl in the pH 7.0–8.4 range, and 25 mM CHES in the pH 8.7–9.2 range, all of them containing 150 mM NaCl. The relative activities obtained were fitted to a three-state model using the following equation:

$$F = \frac{F_A + F_N 10^a + F_B 10^{(a+b)}}{1 + 10^a + 10^{(a+b)}} \quad (3)$$

where  $F_A$ ,  $F_N$  and  $F_B$  are the activities (%) at acidic, neutral and basic pH values respectively, and  $a = m(\text{pH} - \text{p}K_{a1})$  and  $b = n(\text{pH} - \text{p}K_{a2})$ , being  $m$  and  $n$  the number of protons exchanged in each of the two transitions [31].

The inhibitory effect of small molecules (Table SP1) on the BoFPR diaphorase activity was evaluated, in 25 mM Tris/HCl, 2% DMSO, pH 7.4, at 25 °C, using 20 nM BoFPR, saturating DCPIP (95 μM) and NADPH (50 μM), and varying the concentration of the compounds. These data were used to determine the concentration of the compound causing 50% enzyme inhibition ( $IC_{50}$ ) and maximal inhibition ( $IC_{max}$ ), as well as the BoFPR residual activity at  $IC_{max}$  [30].

#### 2.6. Stopped-flow kinetic measurements

Fast reduction of BoFPR<sub>ox</sub> by NADPH was evaluated by using a SX.18MV stopped-flow spectrophotometer (Applied Photophysics Ltd.) with a photodiode array detector following settled down procedures [32]. All samples were made anaerobic before introduction into the stopped-flow syringes. BoFPR (~20 μM) was mixed with a range of NADPH concentrations at ratios from 1:1 to 1:20 in 25 mM Tris/HCl, pH 7.4 at both 6 and 25 °C. Multiple wavelength absorption data (400–1000 nm) were collected and processed using the X-Scan software (Applied Photophysics Ltd.). Time spectral deconvolution was performed by global analysis and numerical integration methods using Pro-Kineticist (Applied Photophysics Ltd.). Collected data were fitted to either single ( $A \rightarrow B$  or  $B \rightarrow C$ ) or two ( $A \rightarrow B \rightarrow C$ ) steps model allowing estimation of the corresponding observed conversion rate constants ( $k_{A \rightarrow B}$ ,  $k_{B \rightarrow C}$ ) at each NADPH concentration, as well as obtaining spectral information of intermediate and final species [32,33]. A, B and C are spectral species, reflecting a distribution of enzyme intermediates (reactants, charge-transfer complexes (CTCs), products, Michaelis complex) at any certain time along the course of the enzyme:coenzyme interaction and HT or reorganization processes and do not necessarily represent a single distinct enzyme intermediate. Moreover, none of them represents individual species and, their spectra cannot be included as fixed in the global-fitting.  $k_{A \rightarrow B}$  or  $k_{B \rightarrow C}$  showing hyperbolic dependence profiles on the NADPH concentration was fitted to the equation describing binding at a single site followed by reorganization processes or a HT, allowing determination of the corresponding interaction constant ( $K_d$ ) as well as rate constants for the subsequent process ( $k$ ) [33].

$$k_{obs} = k_{A \rightarrow B} = k_{B \rightarrow C} = \frac{k \cdot [NADPH]}{[NADPH] + K_d} \quad (4)$$

where, depending on  $k_{A \rightarrow B}$  or  $k_{B \rightarrow C}$  processes,  $k$  might respectively account for the kinetic limiting rate for BoFPR:NADPH complex formation,  $k_{on}$ , or for the HT rate constant,  $k_{HT}$ ; while  $K_d$  might respectively account for the BoFPR:NADPH complex dissociation constant,  $K_d^{NADPH}$ , or for a reorganization constant related to the transformation between reaction intermediate species,  $K_d^{reg}$ .

#### 2.7. Protein crystallization and X-ray diffraction

Crystals of BoFPR, alone and complexed with NADP<sup>+</sup>, were obtained using either the hanging-drop or sitting-drop vapour-diffusion methods at 291 K. A typical drop consisted of 0.33 μl of BoFPR (9.5 mg/ml) in Tris/HCl 25 mM, NaCl 150 mM, pH 7.4 and 0.33 μl of reservoir solution, set up by a NANODROP II (Innovadyne Technologies, Inc. USA). Drops were equilibrated against 60 μl of reservoir solution. Adequate crystals for X-ray diffraction were obtained in the condition 25% PEG 4K, 0.1 M MES, pH 6.5 and 0.2 mM MgCl<sub>2</sub> (C7 of Classic screen from Jena Bioscience). Crystals reached maximum size in one week and were cryoprotected with 20% of glycerol before diffraction.

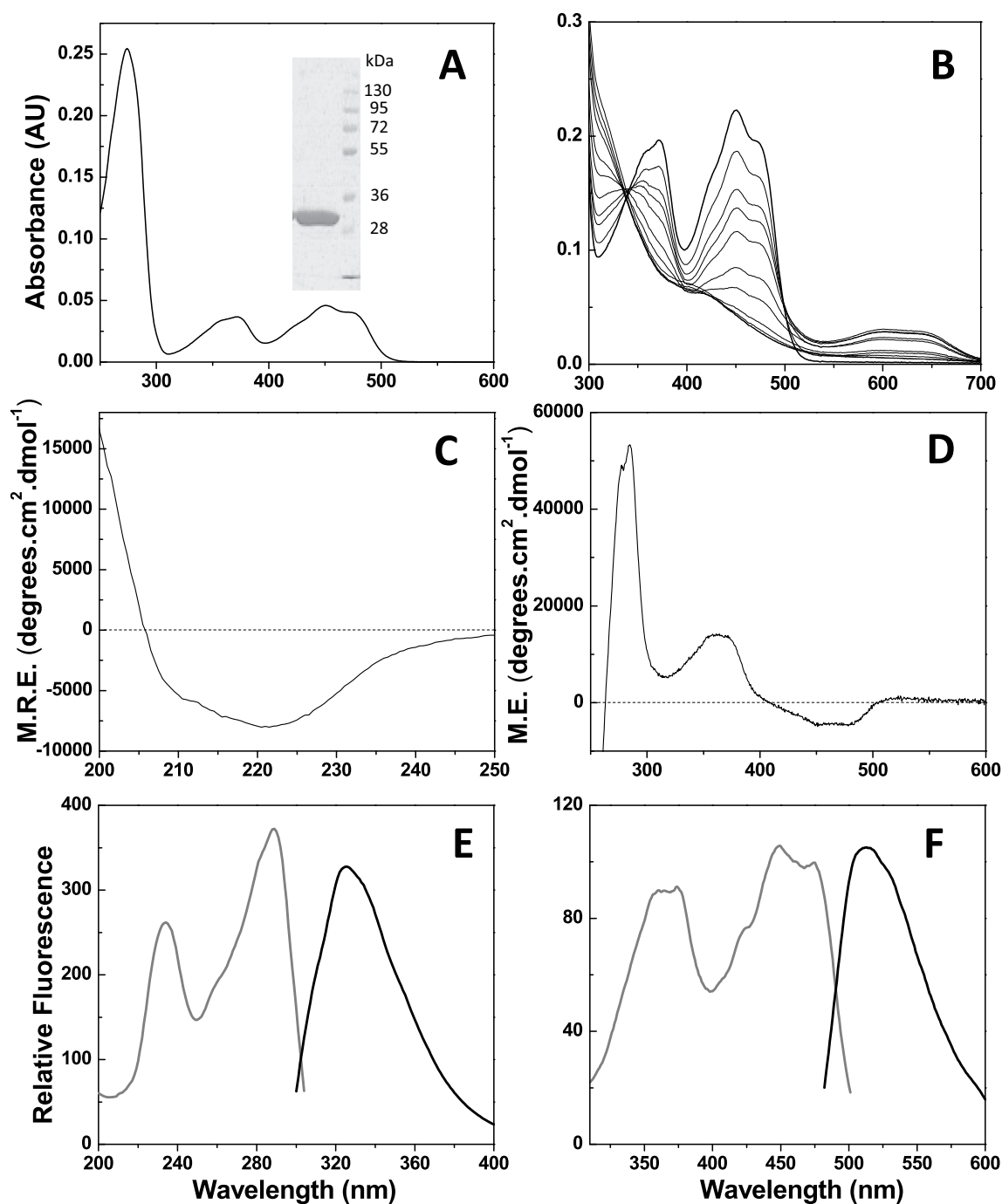


**Fig. 1.** Spectroscopic properties of BoFPR. (A) UV/Vis absorption spectrum of BoFPR (4 μM). The inset shows the SDS-PAGE of the purified sample (lane 1) and of several Molecular Weight Markers (lane 2). (B) Spectra evolution for the photoreduction of BoFPR (20 μM) under anaerobic conditions and in the presence of 4 μM 5-deazariboflavin and 3 mM EDTA. (C) far-UV and (D) near-UV/Vis CD spectra of BoFPR. Spectra obtained with 5 μM (0.1 cm path-length cuvette) and 20 μM (1 cm path-length cuvette) protein respectively. (E) Far UV and (F) visible fluorescence spectra of BoFPR (20 μM). Black lines show the fluorescence emission spectra when exciting at 280 (E) and 450 (F) nm, whereas grey lines correspond to excitation spectra when collecting fluorescence at 326 (E) and 514 (F) nm. All spectra were recorded in Tris/HCl 25 mM, pH 7.4 at 25 °C.

Crystals of BoFPR<sub>ox</sub>:NADP<sup>+</sup> complex were obtained adding NADP<sup>+</sup> in powder on drops containing crystals of BoFPR, previously grown in 2% PEG 400, 0.1 M HEPES, pH 7.5 and 2 M ammonium sulfate, and incubating that mixture for 25 min. Crystals were cryoprotected with a solution containing 85% of mother liquor and 15% of glycerol with 10 mM NADP<sup>+</sup>. Data were collected from a single crystal of BoFPR<sub>ox</sub> using the synchrotron source DLS beamline I24 and a Pilatus3 6M detector with a wavelength of 0.968620 Å, to a maximum resolution of 1.69 Å. Crystals belonged to P4<sub>1</sub> tetragonal space group with one

molecule in the asymmetric unit and unit cell dimensions shown in Table SP2. BoFPR<sub>ox</sub>:NADP<sup>+</sup> diffraction data were collected in the B13 (XALOC) beamline at ALBA synchrotron with a Dectris Pilatus 6M detector and a wavelength of 0.979260 Å, to a maximum resolution of 1.4 Å. Crystals belonged to the P2<sub>1</sub>2<sub>1</sub>2<sub>1</sub> group (Table SP2). All data sets were processed, scaled and reduced with XDS [34] and SCALA [35] from the CCP4 package [36]. The structures were solved by molecular replacement using the MOLREP [37] program from CCP4 [36] and the structure of *P. aeruginosa* FPR (PDB ID: 2QDX) as search model.

Automatic refinement was performed by Refmac5 [38] from the CCP4 package and alternating manual model building by WinCOOT [39]. Final models comprised residues 2–258 and one FAD for both structures and 166 and 257 water molecules for BoFPR<sub>ox</sub> and BoFPR<sub>ox</sub>:NADP<sup>+</sup>, respectively. Additionally, one SO<sub>4</sub><sup>2-</sup> and one NADP<sup>+</sup> molecules were refined in the complex structure. PROCHECK [40] was used to assess the final structure quality. Relevant data collection statistics and refinement parameters are presented in Table SP2. The coordinates and structure factors for BoFPR<sub>ox</sub> and BoFPR<sub>ox</sub>:NADP<sup>+</sup> have been deposited in the Protein Data Bank with PDB IDs 6RR3 and 6RRA, respectively.

## 2.8. Molecular dynamics simulations

An initial model of BoFPR<sub>ox</sub>, including the FAD cofactor, was built using the *A. vinelandii* FPR crystallographic structure (PDB ID: 1A8P) [41] as template and Prime [42,43] after a Needleman-Wunsch sequence alignment ([zhanglab.ccmb.med.umich.edu/NW-align](http://zhanglab.ccmb.med.umich.edu/NW-align)). Protonation states were adjusted to pH 7.0. To produce a BoFPR<sub>ox</sub>:NADPH complex model, the NADPH coenzyme was manually introduced in the BoFPR<sub>ox</sub> model and allocated using as models the BoFPR:NADP<sup>+</sup> (PDB ID: 6RRA) and *P. aeruginosa* FPR:NADP<sup>+</sup> (PDB ID: 3CRZ) complexes [44]. PyMOL was used for structural manipulations and figures production [45]. All-atom molecular dynamics (MD) simulations were performed using GROMACS 5.1.5 [46]. AMBER ff03 [47] parameters were applied to the amino acids while ligands were parameterised using GAFF [48] and density functional theory (DFT). Atomic charges were calculated with the Gaussian09 package [49] at the B3LYP/6-31G level of theory and used with Antechamber [50] through ACPYPE [51]. Oxidized FAD and NADPH redox states for the cofactor and coenzyme have been used respectively in all simulations. Each system was placed in the centre of a rhombic dodecahedron box, solvated with a TIP3P water model and neutralised by adding sodium ions. Final systems consisted in 37,456 and 37,410 total atoms for BoFPR<sub>ox</sub> and BoFPR<sub>ox</sub>:NADPH, respectively. A steepest descent minimization was performed to avoid close contacts or clashes. Desired conditions were achieved after a 100 ps simulation with NVT ensemble and the generation of random initial velocities, and a 100 ps simulation with NPT ensemble, both restraining the movement of atoms of protein and ligands with a 1000 kJ·mol<sup>-1</sup>·nm<sup>-1</sup> harmonic potential. Longer NPT simulations with positions unrestrained were then performed, collecting the data every 10 ps. A time step of 2 fs and leap-frog integrator, periodic boundary conditions, Particle Mesh Ewald method for long range electrostatic interaction, Parrinello-Rahman method for pressure control, modified Berendsen method for temperature equilibration and LINCS to restrain bonds including hydrogen atoms were used. Trajectories were analysed using VMD [52] and GROMACS package tools [46]. PROPKA software was used to assign pK<sub>a</sub> values to X-ray and model structures [53].

## 3. Results and discussion

### 3.1. BoFPR has the typical spectroscopic features of a member of the plant FNR family

After purification BoFPR shows a single band in SDS-PAGE that corresponds to a molecular weight of ~30 kDa, as well as an absorption spectrum with maxima at 274, 371 and 451 nm and a shoulder at 490 nm, with Abs<sub>274</sub>/Abs<sub>451</sub> ratio of 5.5 (Fig. 1A). Thermal denaturation confirms that BoFPR has FAD as cofactor, allowing also to determine a molar extinction coefficient of 11.5 ± 0.4 mM<sup>-1</sup> cm<sup>-1</sup> at 451 nm in 25 mM Tris/HCl, pH 7.4. Upon stepwise photoreduction the BoFPR spectrum shows absorption decrease at 450 nm concomitant with the initial appearance of a new band with a maximum at 584 nm and its subsequent bleaching (Fig. 1B). Such spectral observations relate to transformation of the oxidized (ox) FAD state to the fully

reduced state (hq) through the transient stabilisation of a neutral semiquinone (sq) state. Isosbestic points are detected at 340 nm and 260 nm for the ox/hq transition, and at 500 nm for the ox/sq transition. Nonetheless, maximal sq stabilisation is estimated below 25%, suggesting a lower midpoint reduction potential for the ox/sq one-electron transfer step,  $E_{ox/sq}$ , than for the sq/hq one-electron step. This later trait is typical in FNR family members that need to exchange electrons between obligatory two-electron transfer substrates, such as pyridine nucleotides, and obligatory one-electron transfer redox centres, such as iron-sulfur clusters [54].

The BoFPR far-UV CD spectrum has minima at 221.5 and at 208 nm (Fig. 1C), suggestive of folding in  $\alpha$ -helices and  $\beta$ -sheets. The 277.5 nm maximum in the near-UV CD suggests at least one Tryptophan internalized within the folded protein, while the Vis CD features relate to the FAD (maximum at 358 nm and minima at 451 and 478.5 nm) (Fig. 1D). When excited in the near-UV (280 nm) BoFPR emission is centred at 326 nm (Fig. 1E), suggestive of at least one tryptophan in a folded protein environment. In agreement, the corresponding excitation spectrum (Fig. 1E) has a maximum at 290 nm. The BoFPR Vis emission spectrum shows typical features of a strongly quenched flavin, in agreement with its excitation and absorption spectra (Fig. 1F and A). Altogether these data indicate that the purified BoFPR is correctly folded and contains one molecule of FAD per molecule of protein.

### 3.2. BoFPR binds the NADP<sup>+</sup>/H and exhibits NADPH oxidoreductase activity

To evaluate the BoFPR<sub>ox</sub> ability to bind the expected product of its catalytic reaction, NADP<sup>+</sup>, we first used differential spectroscopy in the flavin absorption region. Nonetheless, NADP<sup>+</sup> addition induces no spectral changes, suggesting that either NADP<sup>+</sup> does not bind to BoFPR<sub>ox</sub> or its binding does not affect the isoalloxazine electronic properties. Such behaviour differs from that reported for other FPRs and FNRs, where characteristic and species specific difference spectra have been reported [55,56]. The profiles for thermal release of the FAD from BoFPR<sub>ox</sub> also show that the presence of NADP<sup>+</sup> hardly affects  $T_{mFAD}$  ( $T_{mFAD}^{BoFPRox} = 328.3 \pm 0.3$  K,  $T_{mFAD}^{BoFPRox:NADP^+} = 328.9 \pm 0.3$  K) and the related unfolding enthalpy ( $\Delta H^{BoFPRox} = 100 \pm 5$  kcal/mol,  $\Delta H^{BoFPRox:NADP^+} = 120 \pm 5$  kcal/mol) (Fig. 2A). Similarly, DSC shows two partially overlapping transitions of similar temperatures ( $T_{m1}^{BoFPRox} = 326.4 \pm 0.5$  K,  $T_{m2}^{BoFPRox} = 328.6 \pm 0.5$  K,  $T_{m1}^{BoFPRox:NADP^+} = 326.3 \pm 0.5$  K, and  $T_{m2}^{BoFPRox:NADP^+} = 328.6 \pm 0.5$  K) and unfolding enthalpies ( $\Delta H_1^{BoFPRox} = 138 \pm 2$  kcal/mol,  $\Delta H_2^{BoFPRox} = 70 \pm 3$  kcal/mol,  $\Delta H_1^{BoFPRox:NADP^+} = 140 \pm 2$  kcal/mol and  $\Delta H_2^{BoFPRox:NADP^+} = 62 \pm 2$  kcal/mol) for BoFPR<sub>ox</sub> and BoFPR<sub>ox</sub>:NADP<sup>+</sup> complex (Fig. 2B). Thus, NADP<sup>+</sup> does not induce BoFPR thermal stabilisation, contrary to that found in other FNRs [57]. Moreover, these analyses suggest that the BoFPR<sub>ox</sub> unfolding process of the FAD-binding and NADP<sup>+</sup>-binding domains are not fully cooperative, with the FAD domain being just slightly more stable, and the presence of NADP<sup>+</sup> not having impact on the thermal stability of BoFPR<sub>ox</sub>.

To further evaluate NADP<sup>+</sup> binding to BoFPR<sub>ox</sub> we used ITC. Fig. 2C provides a thermogram consistent with binding of a molecule per BoFPR<sub>ox</sub> molecule with  $K_d^{BoFPRox:NADP^+} = 3.7 \pm 0.2$   $\mu$ M,  $\Delta G = -7.4 \pm 0.3$  kcal/mol,  $\Delta H = -32 \pm 1$  kcal/mol, and  $-T\Delta S = 24.6$  kcal/mol. Therefore, NADP<sup>+</sup> binding to BoFPR<sub>ox</sub> under our experimental conditions is apparently enthalpically driven with an opposing entropic contribution. Binding affinity is in the range of plastidic FNRs, but changes are observed when comparing the enthalpic/entropic contributions ratio to the binding [27,28,57,58]. Altogether these data show that despite BoFPR<sub>ox</sub> is able to bind its NADP<sup>+</sup> product, the binding mode might differ from other family members. Thus, despite binding of the NADP<sup>+</sup> to BoFPR<sub>ox</sub> occurs, the nicotinamide moiety of the NADP<sup>+</sup> hardly influences the flavin environment and the protein thermal stability.

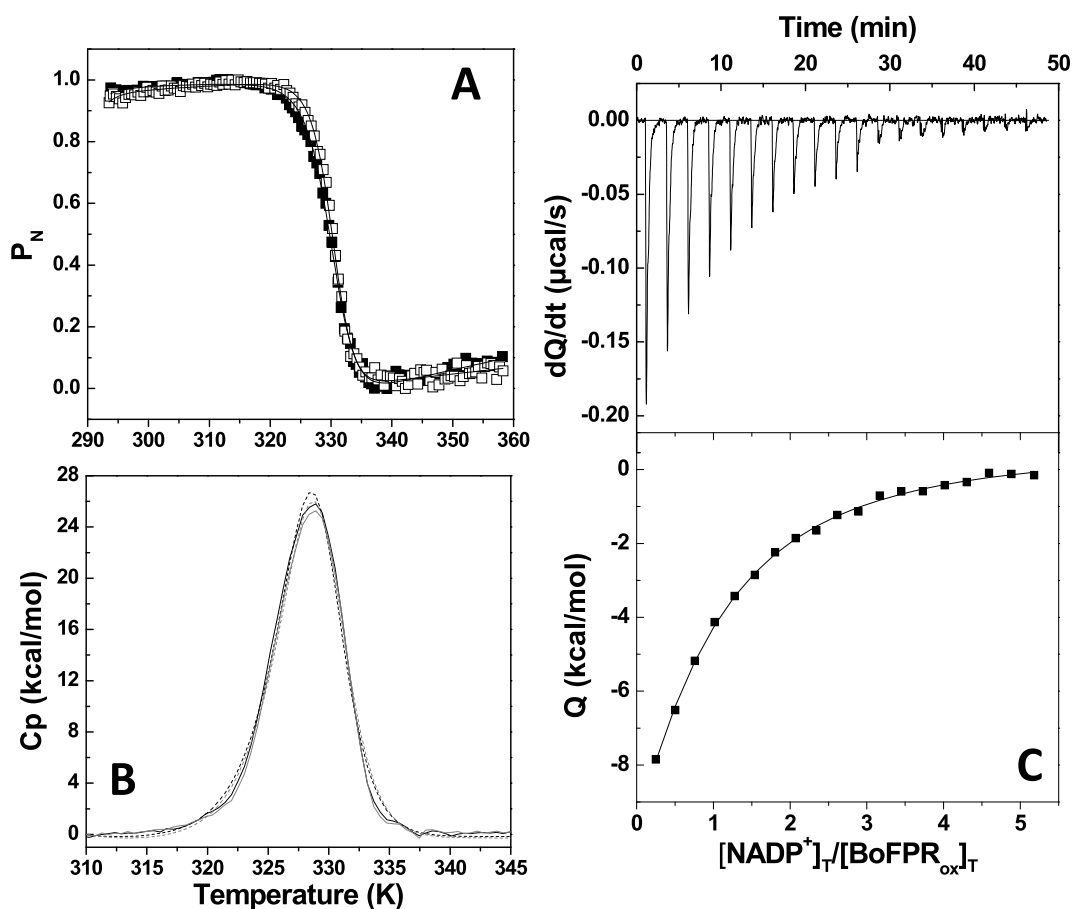


**Fig. 2.** The interaction of BoFPR with NADP<sup>+</sup>. (A) Thermal denaturation curves of BoFPR<sub>ox</sub> (2 µM, closed squares) and BoFPR<sub>ox</sub>:NADP<sup>+</sup> (2 µM:100 µM, open squares) roughly normalized to the fluorescence of the FAD bound fraction ( $P_N$ , from 1 to 0), with their global fits to a one-transition model represented by continuous lines. Decrease in FAD bound fraction was experimentally followed by increase in the FAD fluorescence upon its release from the holoprotein along a 20 to 85 °C temperature ramp. (B) DSC thermogram for solutions of BoFPR<sub>ox</sub> (20 µM, black) and BoFPR<sub>ox</sub>:NADP<sup>+</sup> complex (20 µM:100 µM, grey). Fittings to a two-transition unfolding process are shown in dashed lines. (C) Thermogram (top panel) for the calorimetric titration of BoFPR<sub>ox</sub> (10 µM) in calorimetric cell with NADP<sup>+</sup> (250 µM in syringe) at 25 °C and corresponding binding isotherm with ligand-normalized integrated heats (bottom panel). All experiments were performed in Tris/HCl 25 mM, pH 7.4.

We have then explored the ability of BoFPR to oxidize NADPH, by evaluating its diaphorase activity to transfer electrons from NADPH to the artificial electron acceptor DCPIP. Our data indicate an oxido-reductase activity that depends on the NADPH concentration with inhibition by its excess (Fig. 3A). Data fitting to the Michaelis-Menten equation that takes into account such inhibition (Eq. (2)) allows to determine  $k_{cat}$ ,  $K_M^{NADPH}$  and  $K_i$  for BoFPR in the values of  $14.3 \pm 0.7 \text{ s}^{-1}$ ,  $3.7 \pm 0.2 \text{ µM}$ , and  $52 \pm 8 \text{ µM}$ , respectively.  $K_M^{NADPH}$

is in the range described for both FNRs and FPRs, while  $k_{cat}$ , following the trait of other FPRs, is considerably lower than that found in FNRs [56,58,59]. Such traits have been claimed as the causes for differences in catalytic efficiency so far described between FNRs and FPRs. Nonetheless, it is remarkable the strong deleterious effect of the NADPH excess on BoFPR activity, while in other family members considerably more modest deleterious effects are observed [60]. Finally, NADPH oxidation is not detected when using either molecular oxygen or

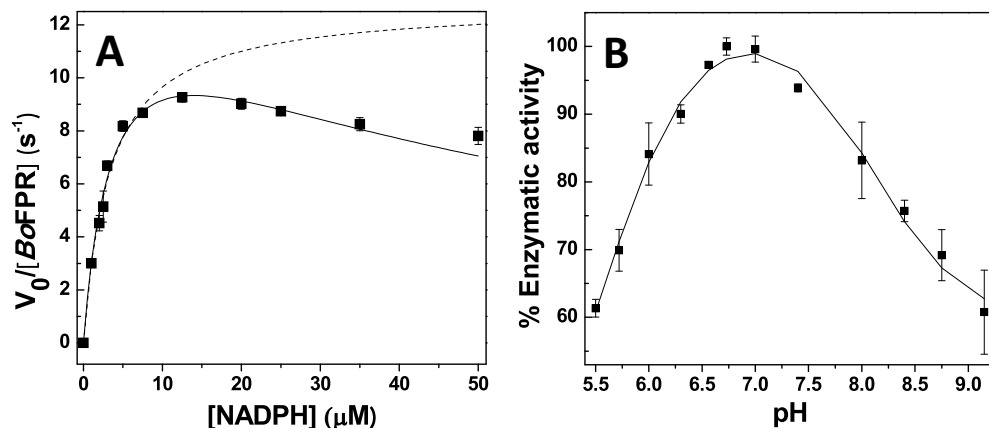


**Fig. 3.** Steady-state catalytic activity of BoFPR. (A) Steady-state kinetic profile for the diaphorase activity of BoFPR. Experimental data were fitted to the Michaelis-Menten equation when considering inhibition by excess of substrate (solid line) or in the absence of inhibition (dotted line). Measurements were recorded with 20 nM BoFPR in Tris/HCl 25 mM, pH 7.4, using 95 µM DCPIP and a 0–50 µM range of NADPH at 25 °C. (B) Effect of pH on the apparent rate constant at 12.5 µM NADPH as a function of pH. Line shows data fitting to Eq. (3).

superoxide as BoFPR electron acceptors, suggesting that the enzyme has neither oxidase nor superoxide reductase activities.

The BoFPR DCPIP diaphorase activity is highly dependent on the pH, with maximal activity at pH 6.7 and two inflection points at  $5.5 \pm 0.7$  and  $8.1 \pm 0.1$  (Fig. 3B). The first fits well with the theoretical isoelectric point of the protein sequence,  $pI \sim 5.6$ , indicating that the activity decrease when lowering the pH from 6.7 to 5.5 might relate to the enzyme change in charge. The second  $pK_a$  suggests a deprotonation at the active site over pH 8.0. Since in the structures below described no residue around the active site is predicted to have a  $pK_a$  close to 8, this protonation might be related to a change in the protonation state of the flavin isoalloxazine ring [61].

As the chemical compound 1-[5-(4-Chloro-benzylsulfanyl)-[1,3,4]thiadiazol-2-yl]-3-(4-chloro-phenyl)-urea (named D5) was recently shown as inhibitor of XacFPR [30], we have here evaluated also its potential, as well as that of four analogues (Table SP1), as BoFPR inhibitors. All five compounds show high  $IC_{50}$  values on the NADPH-

dependent BoFPR diaphorase activity (160–1900  $\mu M$  range) (Table SP1), and the more efficient one, D5, is only able to decrease the enzyme activity over 80% at  $IC_{max}$ . As a consequence, D5 appears species specific for XacFPR versus BoFPR, and none of the here studied compounds turns out to be good inhibitors of BoFPR.

### 3.3. Hydride transfer from NADPH to BoFPR is the reaction limiting step and occurs through formation of two charge transfer complexes between the donor and acceptor rings

We then used stopped-flow with photodiode array detection to evaluate the reductive half-reaction conducting to NADPH oxidation (Fig. 4). Anaerobic fast mixing of NADPH with BoFPR<sub>ox</sub> courses with fast stabilisation of a band centred in the 580–600 nm region compatible with the formation of a CTC between the oxidized isoalloxazine and the reduced nicotinamide rings, FPR<sub>ox</sub>:NADPH, labelled before as CTC-1 in other FNRs and FPRs [32,33,58] (Fig. 4A). Stepwise formation

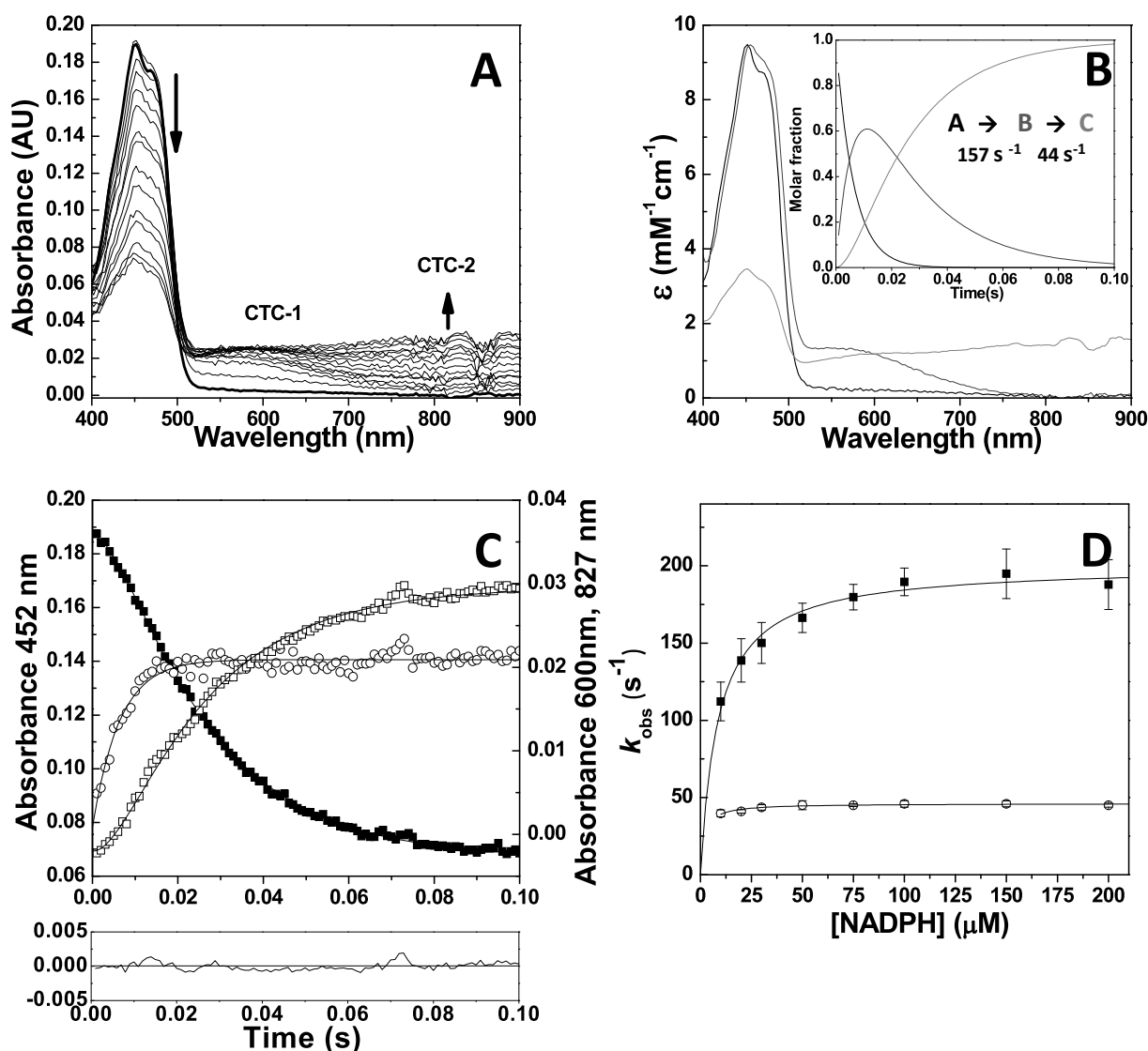


**Fig. 4.** Pre-steady-state activity of BoFPR. Kinetic evaluation of the NADPH oxidation by BoFPR<sub>ox</sub> as followed by stopped-flow spectrophotometry. (A) Spectral evolution for the mixing of BoFPR (20  $\mu M$ ) with NADPH (60  $\mu M$ ) in 25 mM Tris/HCl, pH 7.4, at 6  $^{\circ}C$  in a 100 ms timescale. The bold line represents the BoFPR spectrum before mixing. Formation of two CTCs at 580–600 nm (CTC-1) and 820–860 nm (CTC-2) are detected. (B) Spectral deconvolution of intermediate species observed during the reaction of BoFPR<sub>ox</sub> with NADPH when using a three states fitting model ( $A \rightarrow B \rightarrow C$ ); species A, B and C are shown in black, dark grey and grey continuous lines, respectively. The inset shows their evolution profile. (C) Kinetic traces at 452 nm (closed squares), 600 nm (open circles) and 827 nm (open squares). The residual of the fit at 827 nm is shown at the bottom. (D) Dependence of  $k_{A \rightarrow B}$  (closed squares) and  $k_{B \rightarrow C}$  (open circles) on the NADPH concentration. Data fitting to Eq. (4) are presented.

of this band is detected in experiments at 6 °C, but this process becomes too fast at 25 °C to be detected (not shown). Subsequent spectroscopic changes bring about the decrease of the 452 nm flavin band-I, indicative of isoalloxazine reduction by hydride transfer (HT) from NADPH, and the appearance of a second broad charge transfer band centred around 840 nm that agrees with a  $\text{FPR}_{\text{hq}}:\text{NADP}^+$  CTC species (CTC-2) (Fig. 4A). Global analysis of spectral evolution at 6 °C best fits to a three species model,  $A \rightarrow B \rightarrow C$ . The initial identified spectroscopic species (A) closely relates to  $\text{BoFPR}_{\text{ox}}$ . Features of the intermediate species (B) are suggestive of the binding of the NADPH substrate and the formation of a CTC-1 species. The final species (C) is mainly contributed by a CTC-2 spectrum, indicating that HT has already taken place (Fig. 4B–C). Thus, data at 6 °C allow estimation of observed conversion rate constants for NADPH binding and CTC-1 formation ( $k_{A \rightarrow B}$ ), as well as those ( $k_{B \rightarrow C}$ ) consistent with transformation of CTC-1 into CTC-2 that include the HT process.  $k_{A \rightarrow B}$  values show a hyperbolic dependence on the NADPH concentration (Fig. 4D), allowing to determine a dissociation constant for NADPH binding to  $\text{BoFPR}_{\text{ox}}$  ( $K_d^{\text{CTC-1}}$ ) of  $8.7 \pm 0.9 \mu\text{M}$  and limiting rate for this CTC-1 formation of  $200 \pm 3 \text{ s}^{-1}$ . On the contrary  $k_{B \rightarrow C}$  values hardly showed concentration dependence in the over 1:1 protein:NADPH ratio assayed, suggesting that they nearly correspond to the limiting rate for the HT ( $k_{\text{HT}}$ ),

being in this case of  $48 \pm 1 \text{ s}^{-1}$ . To the best of our knowledge this is the first report of parameters for CTC-1 and CTC-2 formation obtained independently for a FNR/FPR family member. In addition, these data identify the HT itself as the limiting step in the semi-reductive half reduction where  $\text{BoFPR}$  is reduced by NADPH. Moreover, when compared with the steady-state parameters they also envisage product release from the CTC-2 complex as limiting the overall  $\text{BoFPR}$  turnover. Nonetheless, in experiments at 25 °C, CTC-1 formation occurs within the instrumental dead-time and a single step mechanism applies, being this what was so far described for FNRs and FPRs [32,33]. At this temperature  $k_{\text{obs}}$  also depends hyperbolically on the NADPH concentration, but in this case it will account for NADPH binding, for reorganization of the Michaelis complex into the CTC-1 and for the HT process itself, allowing to determine a  ${}^{\text{app}}K_d^{\text{NADPH}}$  of  $31 \pm 5 \mu\text{M}$ , and  ${}^{\text{app}}k_{\text{HT}}$  of  $167 \pm 5 \text{ s}^{-1}$ . These values are in the range of those reported for other FPRs, particularly of subclass I, while are consistently higher and lower respectively than those in FNRs [32,58]. In addition,  $\text{BoFPR}$  behaves similarly to other subclass I FPRs regarding spectroscopic stabilisation of CTC-1 and, particularly, of CTC-2 during catalysis, while only CTC-1 stabilisation has been reported for subclass II FPRs [32,58].

Therefore, in  $\text{BoFPR}$ , as in the other bacterial FPRs, formation of these CTCs during HT from NADPH is suggestive of stacking of the

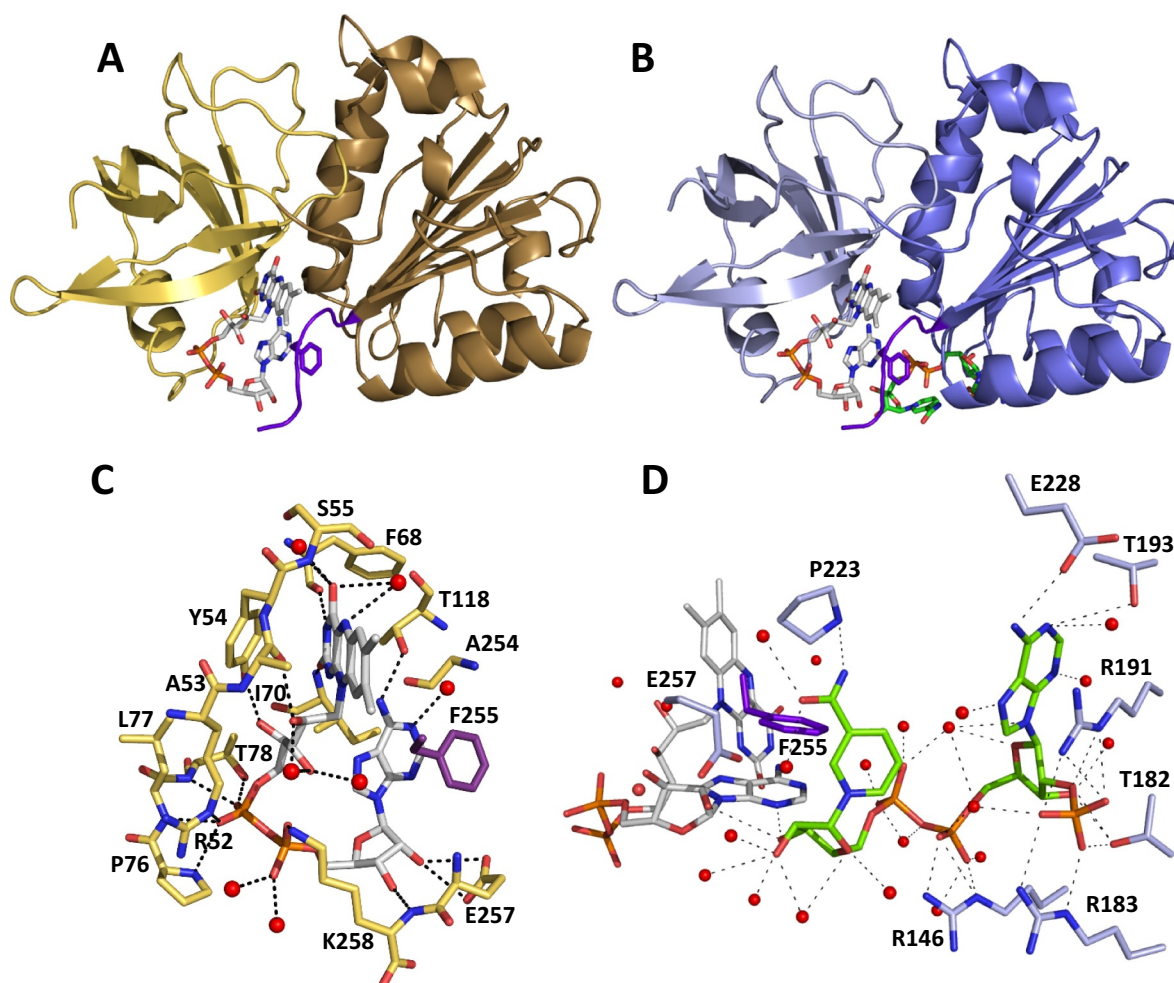


Fig. 5. Crystal structures for  $\text{BoFPR}_{\text{ox}}$  and  $\text{BoFPR}_{\text{ox}}:\text{NADP}^+$  complex. (A) Cartoon representation of  $\text{BoFPR}_{\text{ox}}$  (PDB ID: 6RR3). N-terminal and C-terminal domains are shown in wheat and brown respectively. (B) Cartoon representation of  $\text{BoFPR}_{\text{ox}}:\text{NADP}^+$  complex (PDB ID: 6RRA). N-terminal and C-terminal domains are shown in pale and dark blue respectively. In (A) and (B) the C-terminal tail is coloured in purple with the F255 side-chain (stacking the adenine of FAD) shown in sticks. (C) H-bond network stabilising the FAD folded conformation of  $\text{BoFPR}$  and detail of the stacking of F255 (violet) to its adenine. (D) H-bond network stabilising  $\text{NADP}^+$  binding in the  $\text{BoFPR}:\text{NADP}^+$  complex. Parallel- and T-stacking of F255 (violet) to the FAD adenine moiety and the nicotinamide of  $\text{NADP}^+$  is observed. In (C) and (D) water molecules are represented as red spheres. In all panels FAD is shown in sticks with carbon atoms in white, while in (B) and (D)  $\text{NADP}^+$  is in sticks with green carbon atoms.

reactive isoalloxazine and nicotinamide rings to encounter their respective N5 and C4 atoms to allow direct HT, as also proposed in FNRs [16,32,62]. Differences in the side-chain stacking against the isoalloxazine suggest dissimilarities in competent active site geometries within FPR subclasses, where it is suggested that the initial pre-organization of CTC-1 situates the N5 of FAD and the C4 of NADPH reacting atoms at optimal tunnel distance in a stiff competent active site [32]. In addition, the C-terminal tail in FPRs suggests an overall more complex mechanism than in FNRs. Thus, the higher reorganization energy to attain the catalytically competent state and the minimization of gating contribution in tunnelling ready conformations in FPRs makes them less efficient in the HT processes than FNRs [32,63].

### 3.4. Crystal structures of *B. ovis* FPR<sub>ox</sub> do not envisage the coupling of reactant rings

To evaluate coupling of BoFPR<sub>ox</sub> and the coenzyme at the atomic level, we have solved the 3D structure of BoFPR<sub>ox</sub> in the absence (Fig. 5A) and presence of NADP<sup>+</sup> (Fig. 5B). BoFPR<sub>ox</sub> consist of an N-terminal domain (residues 3–98) that folds into a six-stranded anti-parallel  $\beta$ -barrel and a short  $\alpha$ -helix, and of a C-terminal domain (residues 99–258) built of a Rossmann nucleotide binding fold (Fig. 5A). Such overall folding resembles those of other bacterial FPRs, as the subtype Ia from *Xanthomonas citri* subsp. *citri* (XacFPR), the subtype Ib from *Rhodobacter capsulatus* (RcFPR) and the subtype II from *Escherichia coli* (EcFPR) (Table SP3). As other FPRs, BoFPR lacks of the large FAD-binding domain loop that interacts with the adenylate moiety of the cofactor in plastidic FNRs. This is one of the reasons why its FAD adopts a folded conformation (Fig. 5A) [15,58]. Folded FAD is stabilised by the stacking of the adenine ring to Phe255 at the C-terminal tail (Fig. 5C), while the adenine ribose interacts with the C-terminal Glu257 and Lys258. Arg52, Pro76, Leu77, Thr78 and Lys258 H-bond the FAD pyrophosphate, while Tyr54 and Ile70 H-bond the flavin ribityl chain (Fig. 5C). Ser55, Ile70 and Phe68 H-bond the isoalloxazine, and Tyr54 and Ala254 respectively stack at its *Si*- and *Re*-face. Seven water molecules complete this H-bonds network. The Ala at the *Re*-face of the isoalloxazine and the residue properties at the C-terminal sequence (Fig. SP1) fit BoFPR<sub>ox</sub> in the subclass Ia. As expected, BoFPR also conserves, in sequence and spatial conformation (Figs. SP1 and SP2), the catalytic triad (S55, C220 and E252 in BoFPR) directly involved in the interaction with the NADP<sup>+</sup> nicotinamide ring in the FNR family [1].

The BoFPR<sub>ox</sub>:NADP<sup>+</sup> structure keeps the overall protein folding and active site features, showing very minor changes to accommodate NADP<sup>+</sup> (RMSD 0.23 Å for 229 C $\alpha$ ) (Fig. 5B). NADP<sup>+</sup> binds through its 2'-AMP moiety while its redox reactive nicotinamide nucleotide (NMN) moiety orients out of the active site and barely interacts with the protein (Fig. 5D), as so far reported in all experimental FPR and FNR structures in complex with NADP<sup>+</sup> [44,55,64–66]. Binding of the 2'-AMP moiety displaces Arg146 and Arg191 side-chains (by ~4.5 Å) and reduces their mobility (Fig. SP2A and B). Arg146 contributes to the NADP<sup>+</sup> pyrophosphate binding, Arg191, Thr182 and Arg183 stabilise the ribose 2'-P charge, and Thr193 and Glu228 the adenine base. On the contrary, the NMN moiety is largely accessible to the solvent, with one of the nicotinamide ring sides in front of Pro223 and the C-tail residues Phe255 and Glu257. Interestingly, soaking of NADP<sup>+</sup> does not influence the Phe255 position that maintains its stacking to the adenine of FAD and favours T-stacking of the nicotinamide ring against them (Fig. 5D). B-factor values of FAD in BoFPR<sub>ox</sub> envisage some flexibility for the ribose and the pyrophosphate cofactor moieties facing the solvent, while FAD overall decreases in BoFPR<sub>ox</sub>:NADP<sup>+</sup> (Fig. SP2C and D).

Therefore, the nicotinamide conformation observed in our BoFPR<sub>ox</sub>:NADP<sup>+</sup> structure is far from envisaging the competent flavin-nicotinamide coupling for catalysis foreseen by our kinetic studies. Nonetheless, our structural observations agree with the in solution

structural data that indicate no coupling of rings when, as in this case, both are in the oxidized state.

### 3.5. Thermal effects on molecular simulations allow to envisage formation of a catalytic competent organization

According to the formation of CTCs during HT, we would expect that displacement of the adenine moiety of FAD and of the C-terminal tail of bacterial FPRs would contribute to coupling of reacting flavin and nicotinamide rings. As there are not experimental data supporting a nicotinamide active site entrance path, we have here used a MD approach to simulate a potential BoFPR<sub>ox</sub>:NADPH catalytically competent complex architecture. Our initial MD simulations at 27 °C show slightly faster stabilisation of the BoFPR<sub>ox</sub>:NADPH model than that of the BoFPR<sub>ox</sub>, with the complex exhibiting lower RMSD values and both maintaining overall crystallographic folding (Figs. SP3 and SP4). Root mean square fluctuations (RMSF) indicate that the FAD keeps position along simulation time, nonetheless, its adenine nucleotide moiety results much more flexible than its isoalloxazine moiety (Fig. SP3B). In the BoFPR<sub>ox</sub>:NADPH model, RMSFs suggest stable coupling of the 2'-AMP moiety of the NADPH, while its NMN moiety is more flexible, solvent exposed and hardly in contact with the protein chain. RMSFs for BoFPR<sub>ox</sub> and BoFPR<sub>ox</sub>:NADPH C $\alpha$  atoms agree with the protein core around the active site having very low flexibility (Fig. SP3B). Therefore, these simulations indicate a packed isoalloxazine environment and do not envisage access of the nicotinamide ring to the FPR active site, in agreement with crystal structures and biochemical characterizations in other FPRs [44,55,58].

In this context, production of a HT competent conformation bringing together the flavin and nicotinamide rings can be considered as an infrequent event that might be explored by applying a Temperature Accelerated MD method [67]. We have run short MD simulations of the BoFPR<sub>ox</sub>:NADPH model at increasing temperatures (Fig. SP5). RMSD and radius of gyration at 150 °C suggest protein unfolding, while at 100 °C uncoupling of NADPH is observed. No changes in these parameters are however detected at lower temperatures. Longer MD simulations at 50 °C show a stable complex, with low RMSD and a nearly constant isoalloxazine interaction network (Fig. SP6). Nonetheless, some fluctuations in the radius of gyration are observed, and in some replicas the FAD transiently populates an extended conformation where its adenine moiety opens towards the solvent (maximum isoalloxazine:adenine distance at 8.2 ns in Fig. 6A) as a consequence of the C-terminal tail displacement and uncoupling the adenine:F255 stacking. Such displacement allows approaching of the NADPH nicotinamide ring towards the active site, decreasing the distance between the N5 and C4 reacting atoms up to 8 Å (Fig. SP6B). It is worth to note that our approach treating the transient displacement towards the solvent of the adenine of FAD as an infrequent event assisted by the C-terminal tail, agrees with experimental data on shortened RcFPR variants which despite leaving FAD in a more exposed situation do not promote significant changes in its folded conformation [58].

We then selected one of the snapshots showing the FAD extended conformation and the shortened reacting atoms distance (8.2 ns in Fig. 6A) as starting structure of longer MDs at physiological temperature (37 °C). The new simulations show transient snapshots characterized by N5-C4 distances which might be short enough (up to only 4.8 Å) for a direct HT (Fig. 6B). In these snapshots fully parallel stacking of the isoalloxazine and nicotinamide reacting rings is prevented by the adenine ring of FAD, particularly by its amide group, that keeps the corresponding N10-C2 distances larger than the N5-C4 ones (Fig. 6B).

### 3.6. The adenine moiety of FAD in FPRs might mimic the C-terminal aromatic in FNRs during HT catalysis

Mutational and theoretical analysis to the C-terminal Tyr residue

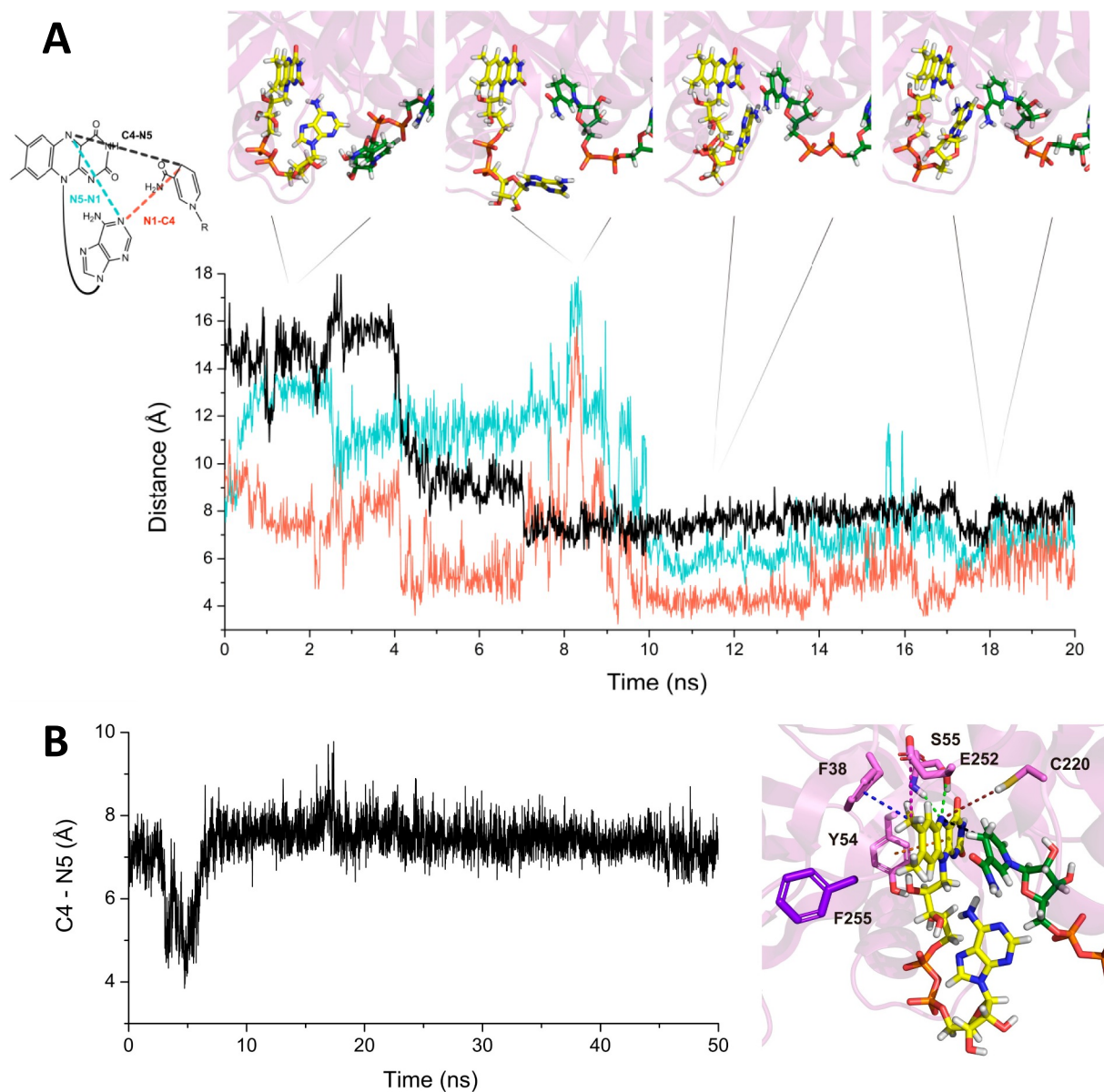


**Fig. 6.** Simulation of the coupling of the FAD and NADPH redox active rings. (A) Time evolution of the relative position of the nicotinamide of NADPH regarding the isoalloxazine and adenine moieties of the FAD in a temperature accelerated MD run at 50 °C for the BoFPR<sub>ox</sub>:NADPH complex. Figure shows evolution of distances from the reactive C4 atom of the nicotinamide regarding two FAD positions, N5 isoalloxazine and N1 adenine, as well as between these two FAD positions. Top panels show relative dispositions of FAD (carbons in yellow) and NADPH (carbons in green) in representative frames at 2, 8.2, 10.5 and 18.5 ns of the MD simulation. (B) Time evolution of the reactant atoms distance (C4 nicotinamide and N5 FAD) along a MD simulation at 37 °C when using as starting structure the snapshot than minimizes such distance whereas maximizing distances to the N1 adenine in the temperature accelerated MD simulation (8.2 ns structure in the 50 °C MD). On the right it is shown the structural model for the snapshot (4.74 ns) showing the minimum distance, with FAD, NADPH and some active site residues shown in sticks (colour code as in A, and as in SP5B for lines).

stacking at the *Re*-face of the isoalloxazine ring in plastidic FNRs pointed to this residue having a critical role in HT between the N5 of the FAD(H<sup>-</sup>) and the C4 of the nicotinamide ring of NADP<sup>+</sup>(H). Though the presence of this Tyr was not obligatory for HT, it was shown to be crucial for the high catalytic efficiency of FNRs by i) modulating the FAD midpoint reduction potential, ii) avoiding a too strong interaction between the reacting rings that would be incompatible with product release, iii) contributing to the optimal geometry between the N5 and C4 reacting atoms for HT, and iv) providing flexibility at the active site for the HT step to occur through tunnelling [16,17,68,69]. FNRs have a short C-terminal tail, 1 to 6 residues long, beyond the residue in front of the isoalloxazine *Re*-face. Moreover, in subclass I this residue is not aromatic anymore and it is usually replaced by an Ala (Fig. SP1). Thus, in FNRs the C-terminal tail together with the adenosine

moiety of the folded FAD occludes access of the nicotinamide to the active site (Fig. 5B and D) [44,55]. So far, we have no structural details about a potential arrangement for the coupling of reacting rings in FPRs, but CTC formation during catalysis is reported in several species [32], including BoFPR (Fig. 4), pointing to their stacking. Contrary to that observed in plastidic FNRs (where NADP<sup>+</sup>/H binding at the 2'-P-AMP has a key impact in the relative disposition of the reacting rings), structural, binding and dynamic kinetic studies point to low contributions of NADPH binding at the 2'-P-AMP site to attain the catalytic complex in FPRs. Instead, these studies suggest fluctuations at the C-terminal tail as potential promoters to increase the probability of competent nicotinamide:isoalloxazine couplings [32,44,55,70,71]. In addition, while pre-organization motions to accommodate the NADPH in the active site, including active site compression, favour overall



catalytic enhancement in FNRs, those effects have been shown to contribute much less to catalysis in FPRs [32,66,72].

Our simulations suggest that, facilitated by the C-terminal tail dynamics, the adenine moiety of the BoFPR FAD can transiently move towards the solvent, moment in which the nicotinamide of the NADPH can make its way towards the active site (Figs. 6 and SP6). The data also suggest that the direct and parallel stacking of the nicotinamide ring to the isoalloxazine ring is avoided by the adenine moiety of FAD (Fig. 6B). Noticeably, such snapshots of the dynamics resemble the competent catalytic conformation suggested for plastidic FNRs during catalysis, where it is the key C-terminal Tyr residue above mentioned the one avoiding parallel stacking of reacting rings [17,62]. This will suggest that in subclass I FPRs, the adenine of FAD will contribute to attain an optimal geometry during catalysis that avoids a strong interaction between the reacting rings. On its side, the C-terminal tail, despite not being directly involved in the catalytic event, will rather modulate the strength of molecular links to expedite the entry and exit of  $\text{NADP}^+/\text{H}$ .

In conclusion, BoFPR is a bacterial subclass I FPR that oxidizes NADPH through the formation of two CTCs, occurring before and after the HT event. Therefore, during catalysis binding of NADPH takes place with stacking of the nicotinamide and flavin reacting rings. However, as reported for other FPRs, x-ray diffraction, at least from BoFPR<sub>ox</sub>:NADP<sup>+</sup> crystals generated in aerobic conditions, does not allow envisaging neither a catalytic competent geometry nor how it is attained. The use of all-atom MD simulations with a thermal effect approach allows producing potential competent isoalloxazine:nicotinamide interactions envisage a potential role to facilitate catalysis for the folded FAD in FPRs. In the BoFPR models the FAD folded conformation places its adenine moiety among the reacting rings, suggesting that during catalysis the adenine of FAD might have some of the roles claimed for the C-terminal Tyr in the plastidic family members.

### Transparency document

The [Transparency document](#) associated with this article can be found, in online version.

### Declaration of competing interest

No competing financial interests exist.

### Acknowledgements

This work has been supported by the Spanish Ministry of Economy, Industry and Competitiveness (MINECO) [BIO2016-75183-P AEI/FEDER, UE to M.M.], and the Gobierno de Aragón-FEDER [Grupo de Referencia Biología Estructural (E35\_17R to M.M.)]. The authors acknowledge Diamond Light Source and ALBA synchrotrons for beam-times (proposal mx14739 and 2018072896, respectively), and their staff of beamlines I24 (DLS) and BL13 (XALOC) for assistance. Authors would like to acknowledge the use of Servicio General de Apoyo a la Investigación-SAI, Universidad de Zaragoza.

### Authors' contributions

M.M.-J. and M.M., conceptualization, funding acquisition, project administration, supervision, writing-review and editing. D.P.-A., V.-T., S.B., E.A.-C., M.S., A.V.-C., and V.P., investigation, formal analysis, writing-original draft.

### Appendix A. Supplementary data

Supplementary data to this article can be found online at <https://doi.org/10.1016/j.bbabo.2019.148058>.

### References

- [1] A. Aliverti, V. Pandini, A. Pennati, M. de Rosa, G. Zanetti, Structural and functional diversity of ferredoxin-NADP<sup>+</sup> reductases, *Arch. Biochem. Biophys.* 474 (2008) 283–291.
- [2] E.A. Ceccarelli, A.K. Arakaki, N. Cortez, N. Carrillo, Functional plasticity and catalytic efficiency in plant and bacterial ferredoxin-NADP(H) reductases, *Biochim. Biophys. Acta* 1698 (2004) 155–165.
- [3] P. Mulo, M. Medina, Interaction and electron transfer between ferredoxin-NADP<sup>+</sup> (+) oxidoreductase and its partners: structural, functional, and physiological implications, *Photosynth. Res.* 134 (2017) 265–280.
- [4] G. Hanke, P. Mulo, Plant type ferredoxins and ferredoxin-dependent metabolism, *Plant Cell Environ.* 36 (2013) 1071–1084.
- [5] A.S. López Rivero, M.A. Rossi, E.A. Ceccarelli, D.L. Catalano-Dupuy, A bacterial 2[4Fe4S] ferredoxin as redox partner of the plastidic-type ferredoxin-NADP, *Biochim. Biophys. Acta Gen. Subj.* 1863 (2019), 651–660.
- [6] X. Guan, S. Chen, C.P. Voon, K.B. Wong, M. Tikkanen, B.L. Lim, FdC1 and leaf-type ferredoxins channel electrons from photosystem I to different downstream electron acceptors, *Front. Plant Sci.* 9 (2018) 410.
- [7] C. Bittel, L.C. Tabares, M. Armesto, N. Carrillo, N. Cortez, The oxidant-responsive diaphorase of *Rhodobacter capsulatus* is a ferredoxin (flavodoxin)-NADP(H) reductase, *FEBS Lett.* 553 (2003) 408–412.
- [8] P.J. Pomposiello, B. Demple, Identification of SoxS-regulated genes in *Salmonella enterica* serovar typhimurium, *J. Bacteriol.* 182 (2000) 23–29.
- [9] M.L. Tondo, M.A. Musumeci, M.L. Delprato, E.A. Ceccarelli, E.G. Orellano, Structural-functional characterization and physiological significance of ferredoxin-NADP<sup>+</sup> reductase from *Xanthomonas axonopodis* pv. citri, *PLoS One* 6 (2011) e27124.
- [10] A.R. Krapp, R.E. Rodriguez, H.O. Poli, D.H. Paladini, J.F. Palatnik, N. Carrillo, The flavoenzyme ferredoxin (flavodoxin)-NADP(H) reductase modulates NADP(H) homeostasis during the soxRS response of *Escherichia coli*, *J. Bacteriol.* 184 (2002) 1474–1480.
- [11] P.J. Pomposiello, M.H. Bennik, B. Demple, Genome-wide transcriptional profiling of the *Escherichia coli* responses to superoxide stress and sodium salicylate, *J. Bacteriol.* 183 (2001) 3890–3902.
- [12] J.L. Brumaghim, Y. Li, E. Henle, S. Linn, Effects of hydrogen peroxide upon nicotinamide nucleotide metabolism in *Escherichia coli*: changes in enzyme levels and nicotinamide nucleotide pools and studies of the oxidation of NAD(P)H by Fe(III), *J. Biol. Chem.* 278 (2003) 42495–42504.
- [13] E. Sevilla, M.T. Bes, A. González, M.L. Peleato, M.F. Fillat, Redox-based transcriptional regulation in prokaryotes: revisiting model mechanisms, *Antioxid. Redox Signal.* 30 (2019) 1651–1696.
- [14] A.R. Krapp, M.V. Humbert, N. Carrillo, The soxRS response of *Escherichia coli* can be induced in the absence of oxidative stress and oxygen by modulation of NADPH content, *Microbiology.* 157 (2011) 957–965.
- [15] L. Serre, F.M. Vellieux, M. Medina, C. Gómez-Moreno, J.C. Fontecilla-Camps, M. Frey, X-ray structure of the ferredoxin:NADP<sup>+</sup> reductase from the cyanobacterium *Anabaena* PCC 7119 at 1.8 Å resolution, and crystallographic studies of NADP<sup>+</sup> binding at 2.25 Å resolution, *J. Mol. Biol.* 263 (1996) 20–39.
- [16] I. Lans, M. Medina, E. Rosta, G. Hummer, M. García-Viloca, J.M. Lluch, et al., Theoretical study of the mechanism of the hydride transfer between ferredoxin-NADP<sup>+</sup> reductase and NADP<sup>+</sup>: the role of Tyr303, *J. Am. Chem. Soc.* 134 (2012) 20544–20553.
- [17] I. Lans, J.R. Peregrina, M. Medina, M. García-Viloca, A. González-Lafont, J.M. Lluch, Mechanism of the hydride transfer between *Anabaena* Tyr303Ser FNRrd/FNRox and NADP<sup>+</sup>/H. A combined pre-steady-state kinetic/ensemble-averaged transition-state theory with multidimensional tunneling study, *J. Phys. Chem. B* 114 (2010) 3368–3379.
- [18] D.H. Paladini, M.A. Musumeci, N. Carrillo, E.A. Ceccarelli, Induced fit and equilibrium dynamics for high catalytic efficiency in ferredoxin-NADP(H) reductases, *Biochemistry.* 48 (2009) 5760–5768.
- [19] X. Liu, M. Zhou, Y. Yang, J. Wu, Q. Peng, Overexpression of Cu-Zn SOD in *Brucella abortus* suppresses bacterial intracellular replication via down-regulation of Sar1 activity, *Oncotarget.* 9 (2018) 9596–9607.
- [20] J.O. Korbil, L.J. Jensen, C. von Mering, P. Bork, Analysis of genomic context: prediction of functional associations from conserved bidirectionally transcribed gene pairs, *Nat. Biotechnol.* 22 (2004) 911–917.
- [21] A.L. Ridler, D.M. West, Control of *Brucella ovis* infection in sheep, *Vet. Clin. North Am. Food Anim. Pract.* 27 (2011) 61–66.
- [22] N. Picard-Hagen, X. Berthelot, J.L. Champion, L. Eon, F. Lyazrhi, M. Marois, et al., Contagious epididymitis due to *Brucella ovis*: relationship between sexual function, serology and bacterial shedding in semen, *BMC Vet. Res.* 11 (2015) 125.
- [23] F. De Massis, K. Zilli, G. Di Donato, R. Nuvoloni, S. Pelini, L. Sacchini, et al., Distribution of *Brucella* field strains isolated from livestock, wildlife populations, and humans in Italy from 2007 to 2015, *PLoS One* 14 (2019) e0213689.
- [24] J. Lykkesfeldt, O. Svendsen, Oxidants and antioxidants in disease: oxidative stress in farm animals, *Vet. J.* 173 (2007) 502–511.
- [25] P. Macheroux, UV-visible spectroscopy as a tool to study flavoproteins, *Methods Mol. Biol.* 131 (1999) 1–7.
- [26] S. Frago, I. Lans, J.A. Navarro, M. Hervás, D.E. Edmondson, M.A. De la Rosa, et al., Dual role of FMN in flavodoxin function: electron transfer cofactor and modulation of the protein-protein interaction surface, *Biochim. Biophys. Acta* 2010 (1797) 262–271.
- [27] M. Martínez-Júlvez, M. Medina, A. Velázquez-Campoy, Binding thermodynamics of ferredoxin:NADP<sup>+</sup> reductase: two different protein substrates and one energetics,

- Biophys. J. 96 (2009) 4966–4975.
- [28] A. Velázquez-Campoy, G. Goñi, J.R. Peregrina, M. Medina, Exact analysis of heterotropic interactions in proteins: characterization of cooperative ligand binding by isothermal titration calorimetry, *Biophys. J.* 91 (2006) 1887–1904.
- [29] J. Sancho, The stability of 2-state, 3-state and more-state proteins from simple spectroscopic techniques... plus the structure of the equilibrium intermediates at the same time, *Arch. Biochem. Biophys.* 531 (2013) 4–13.
- [30] M. Martínez-Júlvez, G. Goñi, D. Pérez-Amigot, R. Laplaza, I.A. Ionescu, S. Petrocelli, et al., Identification of inhibitors targeting ferredoxin-NADP<sup>+</sup> reductase from the *Xanthomonas citri* subsp. *citri* phytopathogenic bacteria, *Molecules.* 23 (2017).
- [31] P. Ferreira, M. Medina, F. Guillen, M. Martínez, W. Van Berkel, A. Martínez, Spectral and catalytic properties of aryl-alcohol oxidase, a fungal flavoenzyme acting on polyunsaturated alcohols, *Biochem. J.* 389 (2005) 731–738.
- [32] A. Sánchez-Azqueta, D.L. Catalano-Dupuy, A. López-Rivero, M.L. Tondo, E.G. Orellano, E.A. Ceccarelli, et al., Dynamics of the active site architecture in plant-type Ferredoxin-NADP(+) reductases catalytic complexes, *Biochim. Biophys. Acta* 1837 (2014) 1730–1738.
- [33] J. Tejero, J.R. Peregrina, M. Martínez-Júlvez, A. Gutiérrez, C. Gómez-Moreno, N.S. Scrutton, et al., Catalytic mechanism of hydride transfer between NADP<sup>+</sup>/H and ferredoxin-NADP<sup>+</sup> reductase from *Anabaena* PCC 7119, *Arch. Biochem. Biophys.* 459 (2007) 79–90.
- [34] W. Kabsch, *Xds. Acta Crystallogr. D Biol. Crystallogr.* 66 (2010) 125–132.
- [35] P. Evans, Scaling and assessment of data quality, *Acta Crystallogr. D Biol. Crystallogr.* 62 (2006) 72–82.
- [36] M.D. Winn, C.C. Ballard, K.D. Cowtan, E.J. Dodson, P. Emsley, P.R. Evans, et al., Overview of the CCP4 suite and current developments, *Acta Crystallogr. D Biol. Crystallogr.* 67 (2011) 235–242.
- [37] A. Vagin, A. Teplyakov, MOLREP: an automated program for molecular replacement, *J. Appl. Crystallogr.* 30 (1997) 1022–1025.
- [38] G.N. Murshudov, A.A. Vagin, E.J. Dodson, Refinement of macromolecular structures by the maximum-likelihood method, *Acta Crystallogr. D Biol. Crystallogr.* 53 (1997) 240–255.
- [39] P. Emsley, B. Lohkamp, W.G. Scott, K. Cowtan, Features and development of Coot, *Acta Crystallogr. D Biol. Crystallogr.* 66 (2010) 486–501.
- [40] R.A. Laskowski, M.W. MacArthur, D.S. Moss, J.M. Thornton, PROCHECK: a program to check the stereochemical quality of protein structures, *J. Appl. Crystallogr.* 26 (1993) 283–291.
- [41] G. Sridhar Prasad, N. Kresge, A.B. Muhlberg, A. Shaw, Y.S. Jung, B.K. Burgess, et al., The crystal structure of NADPH:ferredoxin reductase from *Azotobacter vinelandii*, *Protein Sci.* 7 (1998) 2541–2549.
- [42] M.P. Jacobson, D.L. Pincus, C.S. Rapp, T.J. Day, B. Honig, D.E. Shaw, et al., A hierarchical approach to all-atom protein loop prediction, *Proteins.* 55 (2004) 351–367.
- [43] Schrödinger. Schrödinger Release 2017-1. New York, NY.: Schrödinger LLC; 2017.
- [44] A. Wang, J.C. Rodríguez, H. Han, E. Schönbrunn, M. Rivera, X-ray crystallographic and solution state nuclear magnetic resonance spectroscopic investigations of NADP<sup>+</sup> binding to ferredoxin NADP reductase from *Pseudomonas aeruginosa*, *Biochemistry.* 47 (2008) 8080–8093.
- [45] Delano WL. The PyMOL molecular graphics system. DeLano Scientific, San Carlos, CA, USA. 2002:<http://www.pymol.org>.
- [46] Abraham MJ, Murtola T, Schulz R, Páll S, Smith JC, Hess B, et al. GROMACS: high performance molecular simulations through multi-level parallelism from laptops to supercomputers. *SoftwareX.* 2015;1-2:19–25.
- [47] Y. Duan, C. Wu, S. Chowdhury, M.C. Lee, G. Xiong, W. Zhang, et al., A point-charge force field for molecular mechanics simulations of proteins based on condensed-phase quantum mechanical calculations, *J. Comput. Chem.* 24 (2003) 1999–2012.
- [48] J. Wang, R.M. Wolf, J.W. Caldwell, P.A. Kollman, D.A. Case, Development and testing of a general amber force field, *J. Comput. Chem.* 25 (2004) 1157–1174.
- [49] Frisch MJ, Trucks GW, H., Schlegel B, G. E. Scuseria, M. A. Robb, et al. *Gaussian 09, Revision D.01.* Wallingford CT: Gaussian, Inc.; 2016.
- [50] J. Wang, W. Wang, P.A. Kollman, D.A. Case, Automatic atom type and bond type perception in molecular mechanical calculations, *J. Mol. Graph. Model.* 25 (2006) 247–260.
- [51] Sousa da Silva AW, Vranken WF. ACPYPE - AnteChamber PYthon Parser interfacE. *BMC Res Notes.* 2012;5:367.
- [52] W. Humphrey, A. Dalke, K. Schulten, VMD: visual molecular dynamics, *J. Mol. Graph.* 14 (1996) 33–38 (27-8).
- [53] M.H.M. Olsson, C.R. Søndergaard, M. Rostkowski, J.H. Jensen, PROPKA3: consistent treatment of internal and surface residues in empirical pKa predictions, *J. Chem. Theory Comput.* 7 (2011) 525–537.
- [54] A. Sánchez-Azqueta, B. Herguedas, R. Hurtado-Guerrero, M. Hervás, J.A. Navarro, M. Martínez-Júlvez, et al., A hydrogen bond network in the active site of *Anabaena* ferredoxin-NADP(+) reductase modulates its catalytic efficiency, *Biochim. Biophys. Acta* 2014 (1837) 251–263.
- [55] A. Bortolotti, I. Pérez-Dorado, G. Goñi, M. Medina, J.A. Hermoso, N. Carrillo, et al., Coenzyme binding and hydride transfer in *Rhodobacter capsulatus* ferredoxin/flavodoxin NADP(H) oxidoreductase, *Biochim. Biophys. Acta* 2009 (1794) 199–210.
- [56] M. Medina, M. Martínez-Júlvez, J.K. Hurley, G. Tollin, C. Gómez-Moreno, Involvement of glutamic acid 301 in the catalytic mechanism of ferredoxin-NADP<sup>+</sup> reductase from *Anabaena* PCC 7119, *Biochemistry.* 37 (1998) 2715–2728.
- [57] M.M. Koskela, K.M. Dahlström, G. Goñi, N. Lehtimäki, M. Nurmi, A. Velázquez-Campoy, et al., Arabidopsis FNRL protein is an NADPH-dependent chloroplast oxidoreductase resembling bacterial ferredoxin-NADP, *Physiol. Plant.* 162 (2018) 177–190.
- [58] A. Bortolotti, A. Sánchez-Azqueta, C.M. Maya, A. Velázquez-Campoy, J.A. Hermoso, M. Medina, et al., The C-terminal extension of bacterial flavodoxin-reductases: involvement in the hydride transfer mechanism from the coenzyme, *Biochim. Biophys. Acta* 2014 (1837) 33–43.
- [59] M. Martínez-Júlvez, G. Goñi, D. Pérez-Amigot, R. Laplaza, I.A. Ionescu, S. Petrocelli, et al., Identification of inhibitors targeting ferredoxin-NADP<sup>+</sup> reductase from the *Xanthomonas citri* subsp. *citri* phytopathogenic bacteria, *Molecules.* 23 (2018) 29.
- [60] N. Carrillo, E.A. Ceccarelli, Open questions in ferredoxin-NADP<sup>+</sup> reductase catalytic mechanism, *Eur. J. Biochem.* 270 (2003) 1900–1915.
- [61] F. Müller, Free flavins: synthesis, chemical and physical properties, in: F. Müller (Ed.), *Chemistry and Biochemistry of Flavoenzymes*: Boca Raton, CRC Press, FL, 1991, pp. 1–71.
- [62] J.R. Peregrina, I. Lans, M. Medina, The transient catalytically competent coenzyme allocation into the active site of *Anabaena* ferredoxin NADP<sup>+</sup>-reductase, *Eur. Biophys. J.* 41 (2012) 117–128.
- [63] C.R. Pudney, A. Guerriero, N.J. Baxter, L.O. Johannissen, J.P. Waltho, S. Hay, et al., Fast protein motions are coupled to enzyme H-transfer reactions, *J. Am. Chem. Soc.* 135 (2013) 2512–2517.
- [64] M.A. Musumeci, H. Botti, A. Buschiazzi, E.A. Ceccarelli, Swapping FAD binding motifs between plastidic and bacterial ferredoxin-NADP(H) reductases, *Biochemistry.* 50 (2011) 2111–2122.
- [65] A.S. Nascimento, D.L. Catalano-Dupuy, A. Bernardes, O. Neto Mde, M.A. Santos, E.A. Ceccarelli, et al., Crystal structures of *Leptospira interrogans* FAD-containing ferredoxin-NADP<sup>+</sup> reductase and its complex with NADP<sup>+</sup>, *BMC Struct. Biol.* 7 (2007) 69.
- [66] J.A. Hermoso, T. Mayoral, M. Faro, C. Gomez-Moreno, J. Sanz-Aparicio, M. Medina, Mechanism of coenzyme recognition and binding revealed by crystal structure analysis of ferredoxin-NADP<sup>+</sup> reductase complexed with NADP<sup>+</sup>, *J. Mol. Biol.* 319 (2002) 1133–1142.
- [67] M.R. Sorensen, A.F. Voter, Temperature-accelerated dynamics for simulation of infrequent events, *J. Chem. Phys.* 112 (2000) 9599–9606.
- [68] J. Tejero, I. Pérez-Dorado, C. Maya, M. Martínez-Júlvez, J. Sanz-Aparicio, C. Gómez-Moreno, et al., C-terminal tyrosine of ferredoxin-NADP<sup>+</sup> reductase in hydride transfer processes with NAD(P)<sup>+</sup>/H, *Biochemistry.* 44 (2005) 13477–13490.
- [69] L. Piubelli, A. Aliverti, A.K. Arakaki, N. Carrillo, E.A. Ceccarelli, P.A. Karplus, et al., Competition between C-terminal tyrosine and nicotinamide modulates pyridine nucleotide affinity and specificity in plant ferredoxin-NADP<sup>+</sup> reductase, *J. Biol. Chem.* 275 (2000) 10472–10476.
- [70] I. Nogués, I. Pérez-Dorado, S. Frago, C. Bittel, S.G. Mayhew, C. Gómez-Moreno, et al., The ferredoxin-NADP(H) reductase from *Rhodobacter capsulatus*: molecular structure and catalytic mechanism, *Biochemistry.* 44 (2005) 11730–11740.
- [71] J.T. Wan, J.T. Jarrett, Electron acceptor specificity of ferredoxin (flavodoxin):NADP<sup>+</sup> oxidoreductase from *Escherichia coli*, *Arch. Biochem. Biophys.* 406 (2002) 116–126.
- [72] K.M. Kean, R.A. Carpenter, V. Pandini, G. Zanetti, A.R. Hall, R. Faber, et al., High-resolution studies of hydride transfer in the ferredoxin:NADP, *FEBS J.* 284 (2017) 3302–3319.

## Supplementary Material

### Towards the competent conformation for catalysis in the ferredoxin-NADP<sup>+</sup> reductase from the *Brucella ovis* pathogen

Daniel Pérez-Amigot<sup>1,2,&</sup>, Víctor Taleb<sup>1,2,&</sup>, Sergio Boneta<sup>2,3</sup>, Ernesto Anoz-Carbonell<sup>1,2</sup>, María Sebastián<sup>1,2</sup>, Adrián Velázquez-Campoy<sup>1,2,4,5,6</sup>, Víctor Polo<sup>2,3</sup>, Marta Martínez-Júlvez<sup>1,2,\*</sup>, and Milagros Medina<sup>1,2,\*</sup>

<sup>1</sup>Departamento de Bioquímica y Biología Molecular y Celular, Facultad de Ciencias, Universidad de Zaragoza, 50009 Zaragoza, Spain.

<sup>2</sup>Instituto de Biocomputación y Física de Sistemas Complejos (Joint Units: BIFI-IQFR and GBsC-CSIC), Universidad de Zaragoza, 50018 Zaragoza, Spain.

<sup>3</sup>Departamento de Química Física, Universidad de Zaragoza, 50009 Zaragoza, Spain.

<sup>4</sup>Aragon Institute for Health Research (IIS-Aragon), Zaragoza 50009, Spain

<sup>5</sup>Biomedical Research Networking Center in Digestive and Hepatic Diseases (CIBERehd), Madrid, Spain

<sup>6</sup>Fundacion ARAID, Government of Aragon, Zaragoza 50018, Spain

## SUPPLEMENTARY FIGURES

**A**

|        |     |  |     |
|--------|-----|--|-----|
| BoFPR  | 51  | TRAYSIASSLyE-----DGLEFFSIKVP-----NGPLTSKLQHLKKG        | 87  |
| XacFPR | 51  | LRAYSIASANwe-----EHLEFFSIKVP-----DGPLTSRLQHIQPG        | 87  |
| AvFPR  | 50  | MRAYSIASPNyE-----EHLEFFSIKVP-----NGPLTSRLQHLKEG        | 86  |
| RcFPR  | 63  | MRAYSIASPAwD-----EELFFYSIKVP-----DGPLTSRLQHIKVG        | 99  |
| EcFPR  | 49  | QRAYSIVNSPdN-----PDLEFYLVTV-----DGKLSPLLAALKPG         | 85  |
| AnFNR  | 77  | LRLYSIASTRhGddv-ddKTISLCVRQLEykhpesgetvYGVCSTYLTHIEPG  | 127 |
| PsfNR  | 86  | LRLYSIASSA-IgdfgdsKTVSLCVKRLVytnda-gevvKGVCNFLCDLKP    | 136 |
|        |     |  |     |
| BoFPR  | 215 | DRMMLCGSPEMLAETKQILEER-G-----F-TEGSqs-ePgeFVIKafvek    | 258 |
| XacFPR | 215 | DRFMI CGSPQMLADLRSLDSR-G-----F-QTSPrigtPghYVFERafvek   | 259 |
| AvFPR  | 214 | DRAMICGSPMLDESCEVLDGF-G-----L-KISPrmgePgDYLIERafvek    | 258 |
| RcFPR  | 227 | DRAMVCGSLAFNVDVMKVLESY-G-----L-REGAns-ePreFVVERafvgegi | 272 |
| EcFPR  | 207 | SHVMLCGNPQMRDTQQLKetrQ-----M-TKHLrr-rPghMTAERHYw       | 248 |
| AnFNR  | 251 | THTYICGLRGMEEGIDAALSAA-AakegvtwsdyQkDLKka--gR--WHVETy  | 303 |
| PsfNR  | 261 | TFVVMCGLKGMEKGIDDIMVSL-AakgidwiewKrTLKka--eQ--WNVEVY   | 308 |

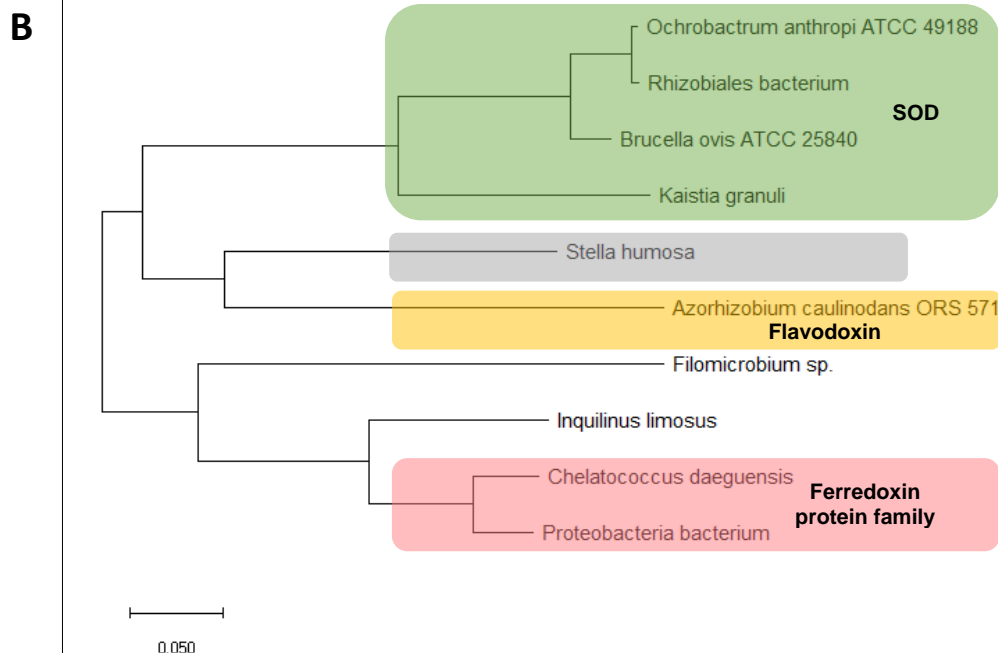


**Figure SP1.** (A) Selected fragments of a multiple sequence structural alignment including the bacterial FPRs, BoFPR and FPRs from *Xanthomonas citri subsp citri* (XacFPR), *Azotobacter vinelandii* (AvFPR), *Rodhobacter capsulatus* (RcFPR) and *Escherichia coli* (EcFPR), and the plastidic FNRs from *Anabaena* (AnFNR) and *Pisum sativum* (PsfNR). Highly conserved identical and similar residues are shadowed in dark and light gray respectively, residues of the structural conserved catalytic triad are highlighted in red, and residue stacking at the *Re*-face of the isoalloxazine is highlighted in blue. Regions highly differing between both enzyme types are shown in lower case and the region corresponding to the FAD binding loop in plastidic FNRs is underlined. Alignments were generated using the PDBeFOLD server (<http://www.ebi.ac.uk/msd-srv/ssm/>) and graphically visualized using BioEdit (<http://www.mbio.ncsu.edu/BioEdit/bioedit.html>). (B) Phylogenetic tree of several bacterial FPRs sequences identified in a Blast search (NCBI) starting with the BoFPR sequence. Selected sequences identities are in the range of 94.96 to 65.62 % relative to BoFPR. Organisms from *Brucellaceae* (taxid:118882) and *Brucella* (taxid:234) were excluded during the search. Evolutionary analyses were conducted in MEGA X [1] using Clustal W, Maximum Likelihood and JTT matrix-based model [2]. The tree with the highest log likelihood is shown. Initial tree(s) were obtained automatically by applying Neighbor-Join and BioNJ algorithms to a matrix of pairwise distances estimated using a JTT model, and then selecting the topology with superior log likelihood value. Regions shaded the same color contain proteins codified in genes located in the close genomic context of *fpr* and which might be related with the potential FPR function.

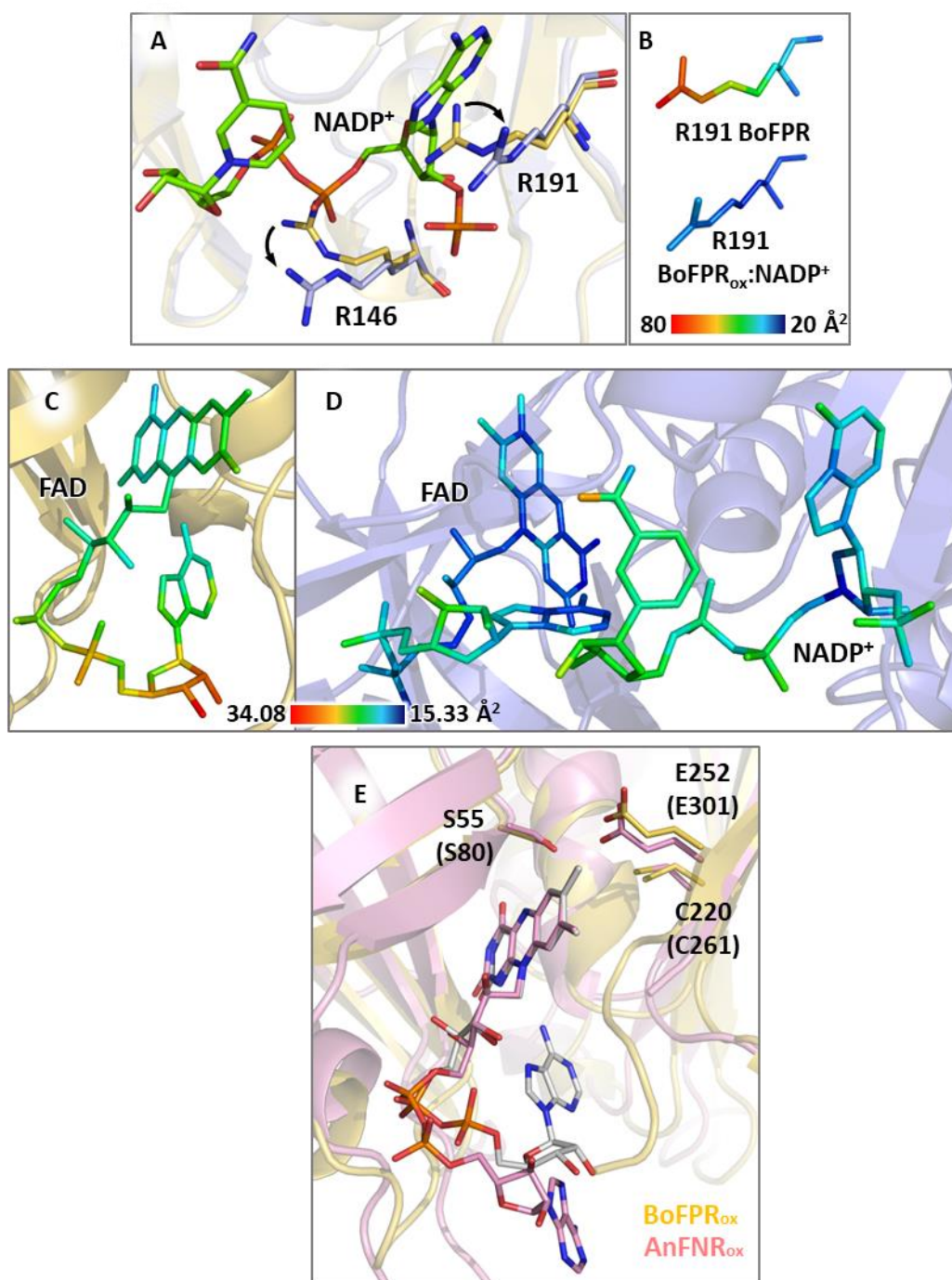


**Figure SP2.** Detail of the NADP<sup>+</sup> binding site in the crystallographic structures. (A) Position of R146 and R191 side-chains in BoFPR (yellow C atoms) and in BoFPR<sub>ox</sub>:NADP<sup>+</sup> (grey C atoms). Arrows indicate the outwards displacement of these residues when the coenzyme binds. NADP<sup>+</sup> is represented as sticks with green C atoms. B-factor representation of (B) R191 in BoFPR<sub>ox</sub> and BoFPR<sub>ox</sub>:NADP<sup>+</sup>; (C) FAD in BoFPR<sub>ox</sub> (yellow) and (D) FAD and NADP<sup>+</sup> in BoFPR<sub>ox</sub>:NADP<sup>+</sup> (blue). (E) Detail of residues of the conserved catalytic triad in stick representation in BoFPR (yellow) and AnFNR (light pink). Residue numbers correspond to the BoFPR (in brackets, AnFNR numbering).

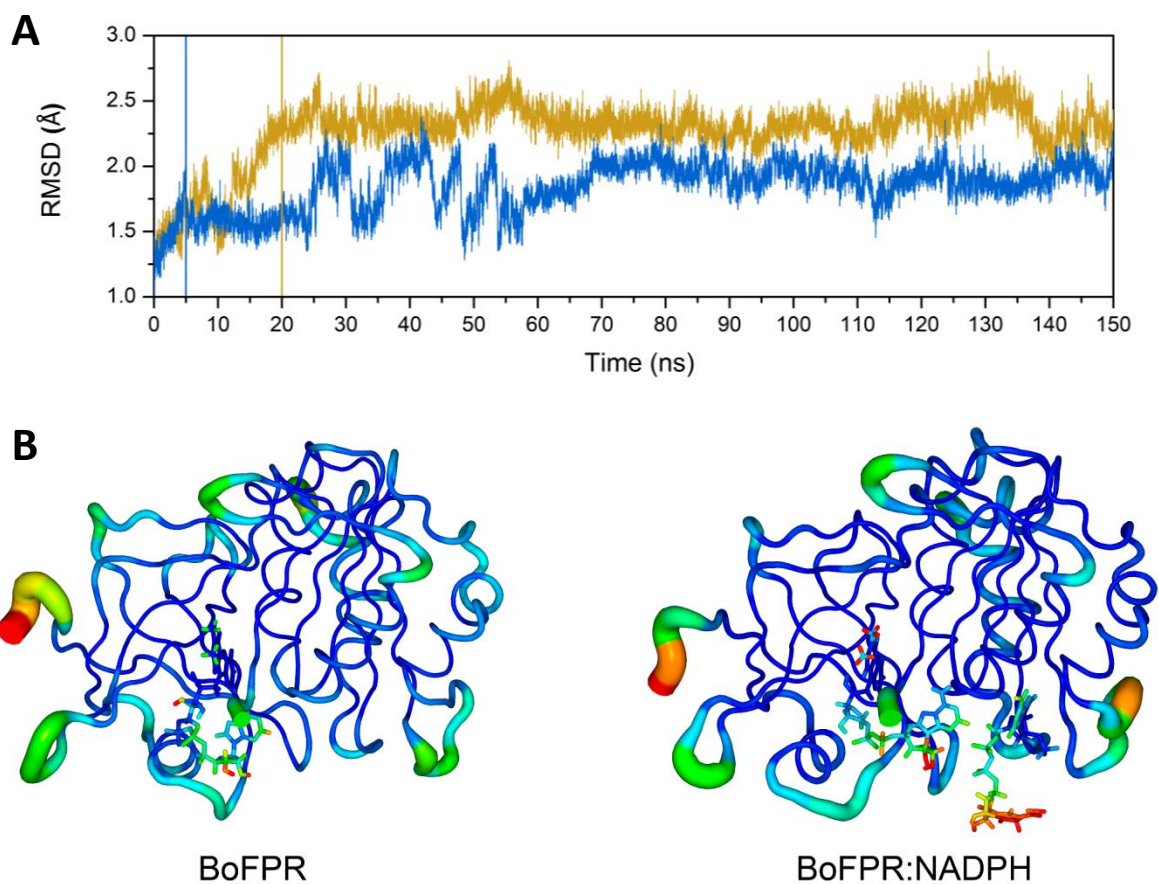


**Figure SP3.** Starting MD simulations at 27 °C. (A) Root mean square deviation (RMSD) against the starting structure along MD simulations of BoFPR<sub>ox</sub> (gold) and BoFPR<sub>ox</sub>:NADPH (blue) models. Vertical lines indicate apparent ranges for the equilibration phase end (coenzyme favours reaching of the equilibrium). (B) Equivalent B-factors as calculated from root mean square fluctuation (RMSF) in the MD simulations of BoFPR<sub>ox</sub> and BoFPR<sub>ox</sub>:NADPH.

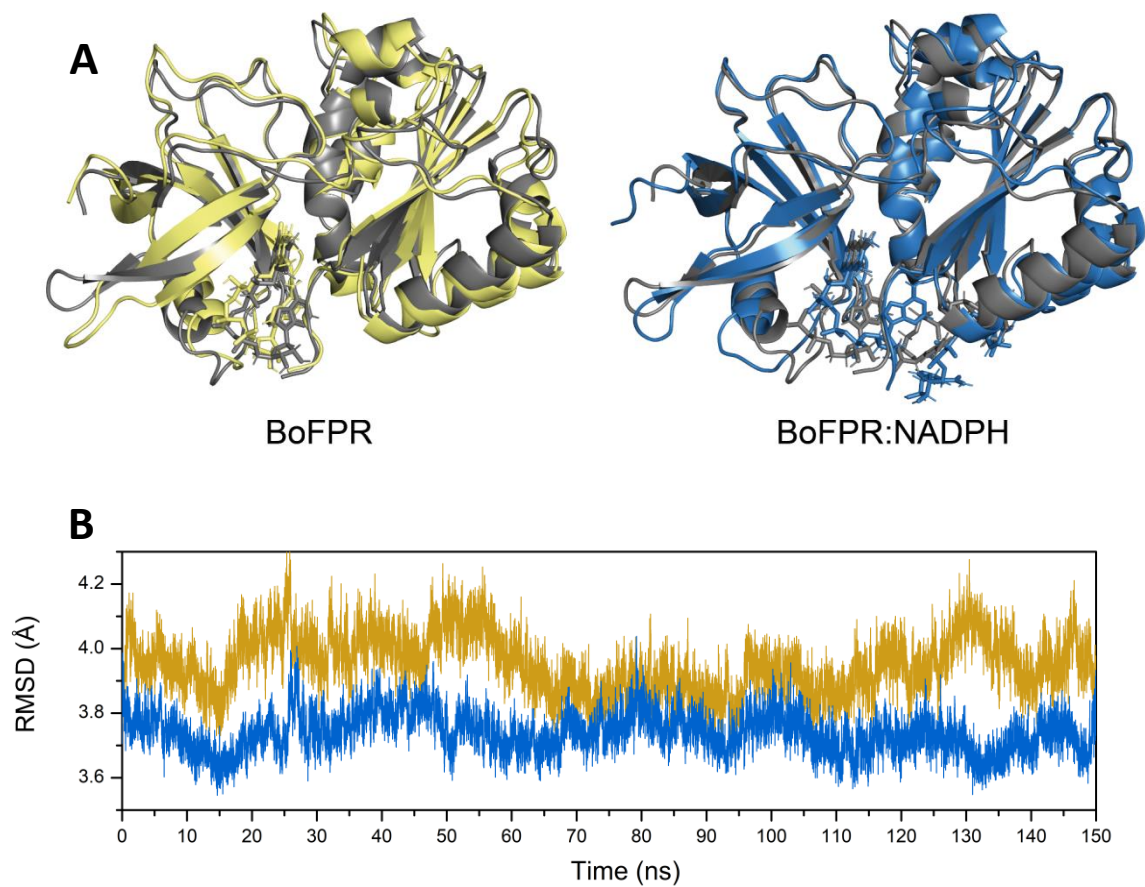


**Figure SP4.** (A) Model structures at the end of the MD simulation for BoFPR<sub>ox</sub> (gold) and (B) BoFPR<sub>ox</sub>:NADPH (blue) aligned on the corresponding crystallographic structures (PDB 6RR3 and 6RRA), in grey). (B) RMSD of the BoFPR<sub>ox</sub> (gold) and BoFPR<sub>ox</sub>:NADPH (blue) structures along the MD simulation at 27 °C regarding the corresponding crystallographic structures.

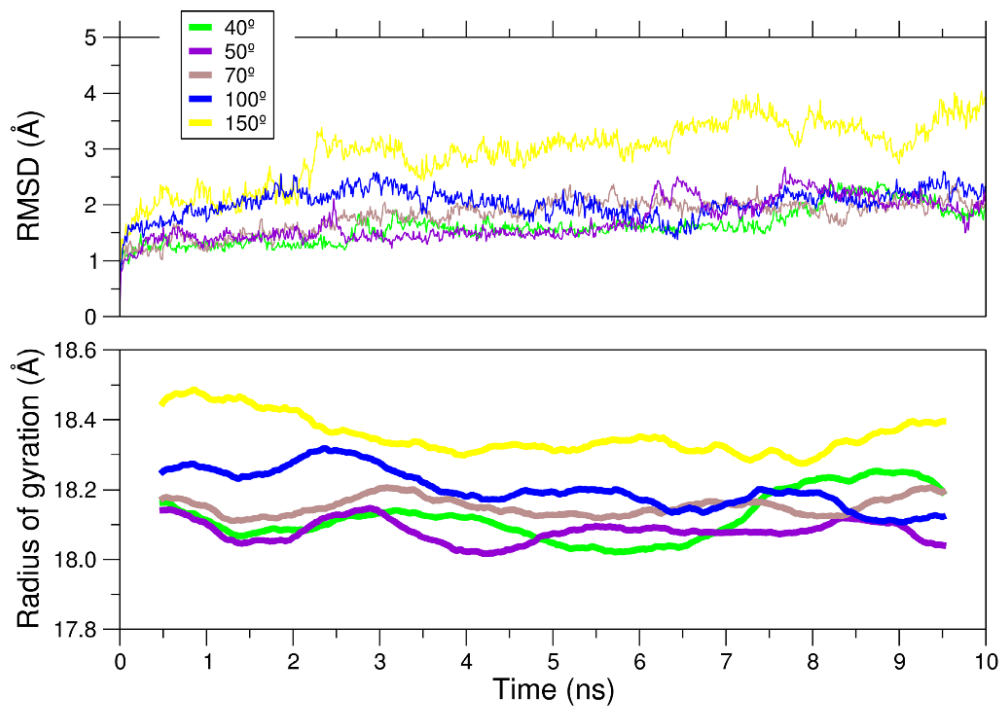


**Figure SP5.** Effect of temperature on RMSD and radius of gyration along MD simulations of the BoFPR<sub>ox</sub>:NADPH model.



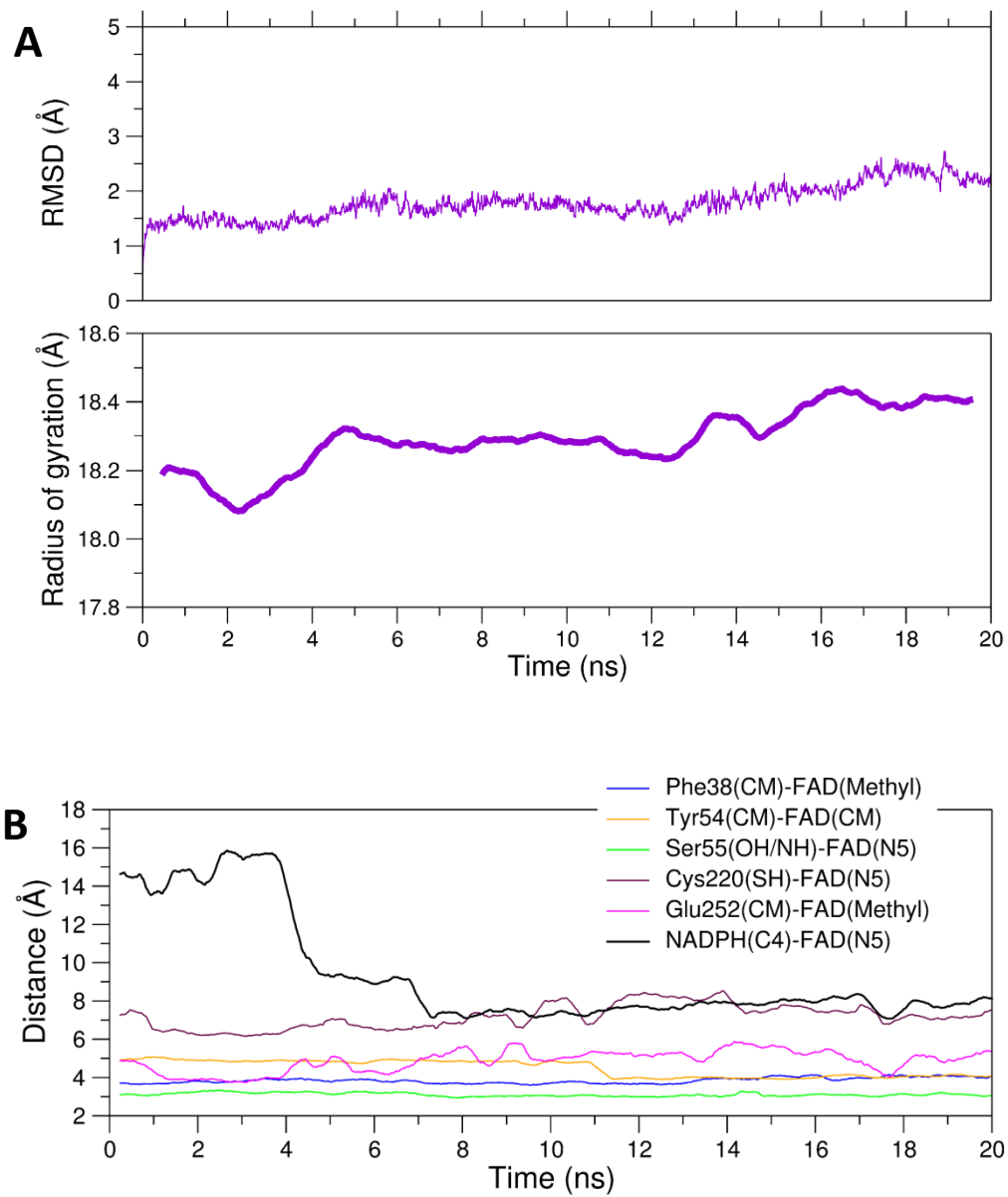


**Figure SP6.** Temperature accelerated MD simulation of BoFPR<sub>ox</sub>:NADPH at 50 °C. (A) Evolution of RMSD and radius of gyration in a replica of interest. (B) Evolution of selected distances.

**SUPPLEMENTAL TABLES**

**Table SP1. Compounds evaluated on the NADPH-dependent DCPIP diaphorase activity of BoFPR**

| HIT | IUPAC name  | Structure | cLog P | Mw     | IC <sub>50</sub> (μM) | IC <sub>max</sub> (μM) | Inhibition % at IC <sub>max</sub> |
|-----|---|-----------|--------|--------|-----------------------|------------------------|-----------------------------------|
| D5  | 1-[5-(4-Chlorobenzylsulfanyl)-[1,3,4]thiadiazol-2-yl]-3-(4-chlorophenyl)-urea             |           | 5.781  | 411.32 | 160±10                | 500±4                  | 88±2                              |
| E1  | 2-[(5-[(4-fluorophenyl)carbamoyl]amino)-1,3,4-thiadiazol-2-yl)sulfanyl]-N-methylacetamide |           | 2.159  | 341.38 | 320±10                | >>>> <sup>a</sup>      | <2                                |
| E2  | 1-(4-fluorophenyl)-3-{5-[(2-oxopropyl)sulfanyl]-1,3,4-thiadiazol-2-yl}urea                |           | 3.002  | 326.36 | 430±10                | >1000 <sup>a</sup>     | 25±10                             |
| E3  | 2-[(5-[(4-chlorophenyl)carbamoyl]amino)-1,3,4-thiadiazol-2-yl)sulfanyl]acetic acid        |           | 3.012  | 344.79 | 1900±20               | >>>> <sup>a</sup>      | <4.5                              |
| E4  | 1-(4-chlorophenyl)-3-[5-(methylsulfanyl)-1,3,4-thiadiazol-2-yl]urea                       |           | 3.557  | 300.78 | 150±10                | 370±10                 | 64±5                              |

<sup>a</sup> Not reached in the assayed range.

percentages in sequence identity ( $\%_{\text{seq}} = N_{\text{ident}} / N_{\text{align}}$ ) and RMSD values ( $\text{\AA}^2$ ; in brackets) after the pairwise comparison and 3D structural alignment of sequences included in Figure SP1 as calculated by the PDBeFold server (<http://www.ebi.ac.uk/msd-srv/ssm/>).

|                  | BoFPR           | XacFPR<br>(4B4D) | AvFPR<br>(1A8P) | RcFPR<br>(2BGI) | EcFPR<br>(1FDR) | AnFNR<br>(1QUE) | PsFNR<br>(1QG0) |
|------------------|-----------------|------------------|-----------------|-----------------|-----------------|-----------------|-----------------|
| BoFPR            |                 | 59.8<br>(0.841)  | 65.0<br>(0.893) | 55.1<br>(1.106) | 36.9<br>(1.694) | 16.8<br>(2.704) | 19.2<br>(2.672) |
| XacFPR<br>(4B4D) | 59.8<br>(0.841) |                  | 63.6<br>(0.737) | 49.5<br>(1.079) | 33.6<br>(1.687) | 20.6<br>(2.616) | 21.5<br>(2.572) |
| AvFPR<br>(1A8P)  | 65.0<br>(0.893) | 63.6<br>(0.737)  |                 | 54.2<br>(0.926) | 33.2<br>(1.653) | 19.2<br>(2.464) | 19.6<br>(2.471) |
| RcFPR<br>(2BGI)  | 55.1<br>(1.106) | 49.5<br>(1.079)  | 54.2<br>(0.926) |                 | 36.0<br>(1.831) | 19.2<br>(2.631) | 16.8<br>(2.664) |
| EcFPR<br>(1FDR)  | 36.9<br>(1.694) | 33.6<br>(1.687)  | 33.2<br>(1.653) | 36.0<br>(1.831) |                 | 20.1<br>(2.622) | 22.0<br>(2.560) |
| AnFNR<br>(1QUE)  | 16.8<br>(2.704) | 20.6<br>(2.616)  | 19.2<br>(2.464) | 19.2<br>(2.631) | 20.1<br>(2.622) |                 | 55.6<br>(1.273) |
| PsFNR<br>(1QG0)  | 19.2<br>(2.672) | 21.5<br>(2.572)  | 19.6<br>(2.471) | 16.8<br>(2.664) | 22.0<br>(2.560) | 55.6<br>(1.273) |                 |

**Table SP3.** Data collection and refinement statistics for Bo<sub>ox</sub>FPR and the Bo<sub>ox</sub>FPR:NADP<sup>+</sup> complex.

|                                    | Bo <sub>ox</sub> FPR   | Bo <sub>ox</sub> FPR:NADP <sup>+</sup><br>(soaking)   |
|------------------------------------|--|---|
| Crystallization conditions         | 25% PEG4K, 0.1 M MES<br>pH 6.5 and 0.2 mM<br>MgCl <sub>2</sub> | 2% PEG400, 0.1 M HEPES pH 7.5 and 2M<br>ammonium sulphate. NADP <sup>+</sup> in powder<br>onto crystals |
| Data collection statistics         |  |   |
| Space group                        | P4 <sub>1</sub>  | P 2 <sub>1</sub> 2 <sub>1</sub> 2 <sub>1</sub>  |
| Unit cell parameters               |  |   |
| a, Å                               | 39.07  | 58.64   |
| b, Å                               | 39.07  | 70.75   |
| c, Å                               | 164.91   | 84.24   |
| Wavelength, Å                      | 0.968620   | 0.979260  |
| Resolution, Å                      | 41.23-1.69<br>(1.78-1.69)                                      | 84.24-1.40<br>(1.48-1.40)   |
| No. of unique reflections          | 26843 ( 3432)  | 69102(9824)   |
| Redundancy                         | 4.1 (2.0)  | 4.5 (3.6)   |
| Completeness, %                    | 97.4 (85.1)  | 99.3 (97.9)   |
| Mn(I)/sd                           | 12.2 (2.0)   | 12.7 (2.1)  |
| R <sub>merge</sub> <sup>a</sup>    | 0.059 (0.347)  | 0.056 (0.515)   |
| Refinement statistics              |  |   |
| Resolution range, Å                | 41.23-1.69   | 54.18-1.40  |
| Protein non-hydrogen atoms         | 2071   | 2071  |
| Ligand non-hydrogen atoms          | 53   | 106   |
| Solvent non-hydrogen atoms         | 166  | 257   |
| R <sub>work</sub> (%)              | 16.8   | 17.99   |
| R <sub>free</sub> <sup>b</sup> (%) | 21.0   | 20.24   |
| rmsd bond length, Å                | 0.010  | 0.028   |
| rmsd bond angles, °                | 1.640  | 2.620   |
| Average B-factor, Å <sup>2</sup>   | 25.61  | 24.85   |

Values in parentheses correspond to the highest resolution shell.

<sup>a</sup>  $R_{sym} = \sum |I - I_{av}| / \sum I$ , where the summation is over symmetry equivalent reflections.

<sup>b</sup> R calculated for 5% of data excluded from the refinement



**Ernesto Anoz Carbonell contributions:** Experimental work: plasmid construction, mycobacteria genetic modification, and antimicrobial activity assays. Data analysis. Manuscript writing, review and editing.



# Mycobacterial Aminoglycoside Acetyltransferases: A Little of Drug Resistance, and a Lot of Other Roles

OPEN ACCESS

**Edited by:**

Silvia Buroni,  
University of Pavia, Italy

**Reviewed by:**

Peter Sander,  
University of Zurich, Switzerland  
Roland Brosch,  
Institut Pasteur, France

**\*Correspondence:**

José A. Ainsa  
ainsa@unizar.es

**† Present address:**

Fernando Sanz-García,  
Departamento de Biotecnología  
Microbiana, Centro Nacional  
de Biotecnología, Consejo Superior  
de Investigaciones Científicas,  
Madrid, Spain  
Esther Pérez-Herrán,  
GlaxoSmithKline, Tres Cantos  
Medicines Development Campus,  
Tres Cantos, Spain  
Liliana Rodrigues,  
Unit of Medical Microbiology, Global  
Health and Tropical Medicine, Instituto  
de Higiene e Medicina Tropical,  
Universidade Nova de Lisboa, Lisbon,  
Portugal

‡ These authors have contributed  
equally to this work

**Specialty section:**

This article was submitted to  
Evolutionary and Genomic  
Microbiology,  
a section of the journal  
Frontiers in Microbiology

**Received:** 05 October 2018

**Accepted:** 11 January 2019

**Published:** 30 January 2019

**Citation:**

Sanz-García F, Anoz-Carbonell E,  
Pérez-Herrán E, Martín C, Lucía A,  
Rodrigues L and Ainsa JA (2019)  
Mycobacterial Aminoglycoside  
Acetyltransferases: A Little of Drug  
Resistance, and a Lot of Other Roles.  
Front. Microbiol. 10:46.  
doi: 10.3389/fmicb.2019.00046

**Fernando Sanz-García<sup>1††</sup>, Ernesto Anoz-Carbonell<sup>1,2†</sup>, Esther Pérez-Herrán<sup>1†</sup>,  
Carlos Martín<sup>1,3</sup>, Ainhoa Lucía<sup>1,3</sup>, Liliana Rodrigues<sup>1,3,4†</sup> and José A. Ainsa<sup>1,3\*</sup>**

<sup>1</sup> Departamento de Microbiología, Facultad de Medicina – Instituto Universitario de Investigación de Biocomputación y Física de Sistemas Complejos, Instituto de Investigación Sanitaria Aragón, Universidad de Zaragoza, Zaragoza, Spain,

<sup>2</sup> Departamento de Bioquímica y Biología Molecular y Celular, Facultad de Ciencias – Instituto Universitario de Investigación de Biocomputación y Física de Sistemas Complejos, Universidad de Zaragoza, Zaragoza, Spain, <sup>3</sup> Centro de Investigación Biomédica en Red Enfermedades Respiratorias, Instituto de Salud Carlos III, Madrid, Spain, <sup>4</sup> Fundación Agencia Aragonesa para la Investigación y el Desarrollo, Zaragoza, Spain

Aminoglycoside acetyltransferases are important determinants of resistance to aminoglycoside antibiotics in most bacterial genera. In mycobacteria, however, aminoglycoside acetyltransferases contribute only partially to aminoglycoside susceptibility since they are related with low level resistance to these antibiotics (while high level aminoglycoside resistance is due to mutations in the ribosome). Instead, aminoglycoside acetyltransferases contribute to other bacterial functions, and this can explain its widespread presence along species of genus *Mycobacterium*. This review is focused on two mycobacterial aminoglycoside acetyltransferase enzymes. First, the aminoglycoside 2'-N-acetyltransferase [AAC(2')], which was identified as a determinant of weak aminoglycoside resistance in *M. fortuitum*, and later found to be widespread in most mycobacterial species; AAC(2') enzymes have been associated with resistance to cell wall degradative enzymes, and bactericidal mode of action of aminoglycosides. Second, the Eis aminoglycoside acetyltransferase, which was identified originally as a virulence determinant in *M. tuberculosis* (enhanced intracellular survival); Eis protein in fact controls production of pro-inflammatory cytokines and other pathways. The relation of Eis with aminoglycoside susceptibility was found after the years, and reaches clinical significance only in *M. tuberculosis* isolates resistant to the second-line drug kanamycin. Given the role of AAC(2') and Eis proteins in mycobacterial biology, inhibitory molecules have been identified, more abundantly in case of Eis. In conclusion, AAC(2') and Eis have evolved from a marginal role as potential drug resistance mechanisms into a promising future as drug targets.

**Keywords:** mycobacteria, aminoglycoside antibiotics, aminoglycoside acetyltransferase, drug target, pathogenicity, aminoglycoside resistance

## BACTERIAL RESISTANCE TO AMINOGLYCOSIDE ANTIBIOTICS

Aminoglycoside (AG) antibiotics (**Box 1**) have not been an exception to the fact that after their introduction in clinical practice, resistance has been recorded (Waglechner and Wright, 2017). In fact, the three classes of aminoglycoside-modifying enzymes, aminoglycoside acetyltransferases (AACs), aminoglycoside phosphotransferases (APHs), and aminoglycoside nucleotidyltransferases

(ANTs), have been widely detected in most pathogenic bacteria as a major determinant of resistance; in these bacteria the presence of aminoglycoside-modifying enzymes correlated with patterns of AG susceptibility (Smith and Baker, 2002). The modified AG (either by acetylation, phosphorylation or nucleotidylation) fails to inhibit their bacterial target, the 30S ribosomal subunit (Smith and Baker, 2002). Most genes encoding aminoglycoside-modifying enzymes are plasmid-located (indicative of a potential acquisition by horizontal gene transfer processes) and confer the bacterial hosts with high levels of AG resistance (Davies and Wright, 1997).

In mycobacteria, however, resistance to AGs resulted mainly from mutations of the ribosome components that prevent the drugs from inhibiting its function (Jugheli et al., 2009; Zhang and Yew, 2009; Shcherbakov et al., 2010). This is due to the fact that most mycobacterial species have either one (like *Mycobacterium tuberculosis*) or two (like *Mycobacterium fortuitum*) ribosomal operons, hence making dominant those mutations acquired in their components (Magnet and Blanchard, 2005; Shi et al., 2013). The presence of aminoglycoside-modifying enzymes, mostly AAC, in mycobacterial species has been reported over the years (as detailed in the following sections), and the role of such AACs has been explored, originally for their contribution to AG resistance, and more recently for their role in other bacterial processes, which has resulted in the interest of developing inhibitors of these enzymes (Jana and Deb, 2005; Labby and Garneau-Tsodikova, 2013). In this review, we will summarize major findings on two mycobacterial AACs, the AAC(2')-I and Eis enzymes, that have resulted in a Copernican turn for AACs in mycobacteria, from being putative drug resistance mechanisms, to reach the status of novel drug targets.

## AACs IN NON-TUBERCULOUS MYCOBACTERIA

The first detection of AACs in mycobacteria (Hull et al., 1984) was reported in a group of *M. fortuitum* isolates, an opportunistic fast-growing mycobacteria. Biochemical assays of crude extracts from *M. fortuitum* strains revealed the presence of AAC activity, strongly acetylating gentamicin and kanamycin A, along with other AGs. This substrate profile was consistent with that of AAC(3) enzymes that had been previously described in *Pseudomonas* and *Enterobacteriaceae* (Angelatou et al., 1982), although confirmation at the genetic or molecular levels were not done at that time. Surprisingly, the AG susceptibility profile of *M. fortuitum* could not be correlated with the activity of AACs, indicating that in this species AACs were not the major responsible for AG resistance; it was neither correlated with the presence of plasmids, hence suggesting a chromosomal location (Hull et al., 1984). In fact, the frequency of resistant mutants to kanamycin and amikacin in *M. fortuitum* and the related species *Mycobacterium chelonae* ranged between  $10^{-4}$  and  $10^{-7}$  (Wallace et al., 1985). This relatively high frequency of mutations, along with the fact that AAC activity was detected at similar levels between susceptible and resistant strains, led the authors to suggest that ribosome alterations were the main

factor responsible of AG resistance in these species (Wallace et al., 1985). In another study (Udou et al., 1986), altered transport or permeability of AGs was identified as a contributor to AG resistance in *M. fortuitum*, since ribosomes from a clinical isolate were inhibited by one tenth of the MIC of AGs: for example, the MIC of kanamycin for *M. fortuitum* was 50  $\mu\text{g/ml}$ , and in cell-free systems, 5  $\mu\text{g/ml}$  of kanamycin reduced the activity of ribosomes to 13% in comparison with drug-free controls; similar results were obtained when using gentamicin or paromomycin (Udou et al., 1986).

The biochemical analysis of crude extracts from other non-tuberculous mycobacteria such as *Mycobacterium smegmatis*, *Mycobacterium phlei*, *Mycobacterium vaccae*, and *Mycobacterium kansasii*, from both clinical and environmental origins, revealed similar characteristics to those found in *M. fortuitum*: crude extracts from all strains contained AAC enzymatic activity, but no correlation with AG susceptibility profile could be established (Udou et al., 1987; Ho et al., 2000). In other mycobacterial species such as *Mycobacterium avium* and *Mycobacterium intracellulare*, however, AAC activity could not be detected (Ho et al., 2000). In a recent study, using cell-free translation assays, ribosomes of *Mycobacterium abscessus* and *M. smegmatis* were inhibited by both AGs having a 2'-amino group (tobramycin, dibekacin, and kanamycin B) and by those having a 2'-hydroxyl group (amikacin, and kanamycin A). However, in *M. abscessus*, those AGs having a 2'-amino group (tobramycin, dibekacin, and kanamycin B) were less efficient in killing the cells and inhibiting its ribosomes, which is consistent with the presence of a highly active AAC(2') activity in this species. These findings suggested that in *M. abscessus*, AACs could somewhat mitigate the bactericidal effect of its AGs substrates (Maurer et al., 2015).

Interestingly, when characterizing the enzymatic activity of crude extracts, early reports detected that substrates such as amino sugars, malonyl-CoA, propionyl-CoA or butyryl-CoA inhibited the enzymatic activity of AACs from mycobacterial species. Such effect of non-acetyl CoA donors had never been described for the AAC(3) enzymes from other bacteria (Udou et al., 1987). Altogether, these findings strongly suggested for the very first time that, in mycobacteria, AACs could have important metabolic functions, and their contribution to AG resistance could be marginal (Udou et al., 1989).

## AAC(2'), A NEW ENZYME COMES INTO SCENE

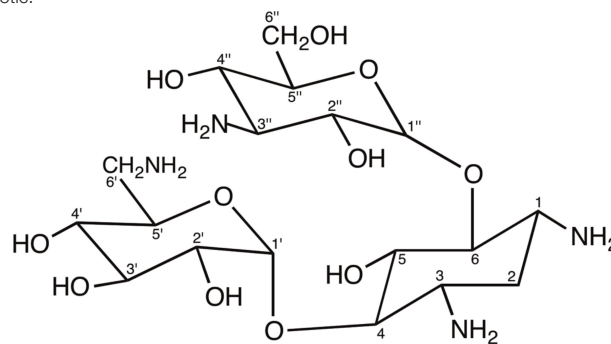
In *Providencia stuartii*, a Gram-negative species, phylogenetically distant from mycobacteria, a novel class of AAC was identified as AAC(2'), because of its acetylating activity against gentamicin and lack of enzymatic activity against kanamycin A. The gene encoding AAC(2')-Ia was cloned from *P. stuartii* (Rather et al., 1993) and found to be present in the chromosome of all isolates of this bacteria. In *P. stuartii*, the expression of the *aac(2')-Ia* gene was controlled by several transcriptional regulators (Macinga and Rather, 1999), suggesting that this enzyme could play an important role, beyond its contribution to drug resistance (Franklin and Clarke, 2001). In fact, AAC(2')-Ia contributes to



**BOX 1 | Aminoglycosides: origins, structure, mode of action, resistance and clinical use.**

Most aminoglycoside antibiotics are produced by bacterial species of the genus *Streptomyces*, such as the antitubercular streptomycin that is produced by *S. griseus* being the first antibiotic identified from bacteria. Other genera producing aminoglycosides are *Micromonospora* and *Bacillus*. Many semi-synthetic aminoglycosides, such as amikacin, have also been produced (Mingeot-Leclercq et al., 1999; Magnet and Blanchard, 2005; Shi et al., 2013).

Structurally, aminoglycosides are formed by an aminocyclitol (commonly, 2-deoxystreptamine) with additional amino sugars bound by glycosidic bonds. There are two large families of 2-deoxystreptamine aminoglycosides, those carrying substitutions at positions 4 and 5 of the 2-deoxystreptamine ring (including neomycin, paromomycin, lividomycin, ribostamycin and butirosin) and those being substituted at positions 4 and 6 of the 2-deoxystreptamine ring (including kanamycin, amikacin, tobramycin, dibekacin, arbekacin, gentamicin, isepamicin, sisomicin, and netilmicin). The carbon atoms in the sugar bound to position 4 of the 2-deoxystreptamine ring are named with primed numbers ('), and those in the sugar bound to positions 5 or 6 of the 2-deoxystreptamine ring are named with double-primed numbers (''). Other aminoglycosides contain aminocyclitols distinct to 2-deoxystreptamine (this is the case of streptomycin or apramycin) or are formed by fused amino sugar rings (i.e., spectinomycin) (Magnet and Blanchard, 2005; Shi et al., 2013). The following figure shows the structure of kanamycin A, an example of 4,6 di-substituted 2-deoxystreptamine aminoglycoside antibiotic.



The bacterial target of aminoglycosides is the 30S small ribosomal subunit, and their global effect is the interference with protein synthesis. In bacterial cells, translation is initiated when the 30S ribosomal subunit binds the Shine-Dalgarno sequence (because of sequence complementarity between the Shine-Dalgarno sequence and the 16S rRNA molecule of the 30S ribosomal subunit), which is normally present in the 5' untranslated region of mRNAs. Next, initiation factors and fMet-tRNA will join the complex that finally will recruit the 50S ribosomal subunit in order to start translation. Aminoglycoside binding to the 30S subunit does not affect the binding of mRNA and the large 50S subunit, so translation can proceed. However, aminoglycosides differ in their binding site at the 30S subunit, hence affecting the protein production at different levels. Whereas spectinomycin blocks translocation (hence being bacteriostatic), streptomycin and most 2-deoxystreptamine aminoglycosides lock the ribosome in a conformation that is prone to introducing erroneous aminoacyl-tRNAs. The accumulation of aberrant proteins in the bacteria results in cell death (Davies and Wright, 1997; Magnet and Blanchard, 2005; Shell et al., 2015).

Resistance to aminoglycosides may be due to several mechanisms (Davies and Wright, 1997; Magnet and Blanchard, 2005). Reduced uptake (which can be a consequence of alterations in the composition of bacterial membrane or to metabolic conditions like anaerobiosis) or the action of efflux pumps can lead to limited intracellular concentration of aminoglycosides, hence causing resistance. Mutations in 16S ribosomal RNA or certain ribosomal proteins such as S12 (encoded by *rpsL* gene) lead to aminoglycoside resistance through target modification; this is also achieved after the action of methyltransferases, which introduce methyl groups in guanine or adenine nucleotides of 16S ribosomal RNA. The presence of aminoglycoside-modifying enzymes is, however, the most prevalent mechanism of aminoglycoside resistance; there are three types of aminoglycoside-modifying enzymes: aminoglycoside *N*-acetyltransferases (AAC), *O*-phosphotransferases (APH), and *O*-nucleotidyltransferases (ANT). Aminoglycoside-modifying enzymes are named by using the aforementioned abbreviations, followed by a number in brackets indicating the site of modification in the aminoglycoside molecule (as explained above), a Roman numeral related with substrate profile, and a lower-case letter for differentiating isoenzymes, i.e., AAC(2')-Ib.

Clinically, due to their oto- and nephrotoxicity and the rising prevalence of resistance, aminoglycosides are commonly reserved as a second line of treatment of serious infections. Due to their low absorption when given orally, aminoglycosides need to be administered through injections. Streptomycin was a first-line drug in the treatment of tuberculosis, and in our days, kanamycin and amikacin are listed as second line drugs against this disease. Spectinomycin is used against *Neisseria gonorrhoeae* infections (Suay-García and Perez-Gracia, 2018). *Pseudomonas aeruginosa* infections in cystic fibrosis patients, septicemia, endocarditis and several other infections caused by non-tuberculous mycobacteria, Gram-positive or Gram-negative bacteria can be treated efficiently by using aminoglycosides, either alone or in combinations with other antibacterials such as the beta-lactam antibiotics (Mingeot-Leclercq et al., 1999; Magnet and Blanchard, 2005; Bassetti et al., 2018).

*O*-acetylation of peptidoglycan affecting cell morphology and the expression of autolysins, and can use acetylated peptidoglycan precursors as donors of acetyl groups, another indication about the role of this enzyme beyond resistance (Payie et al., 1995, 1996; Clarke et al., 1996; Payie and Clarke, 1997).

## AAC(2') in Mycobacteria

Given the high AG acetylating activity against gentamicin, tobramycin, netilmicin and its derivatives 2'-*N*-ethyl- and 6'-*N*-ethyl-netilmicin, kanamycin A and kanamycin B found in *M. fortuitum* (Hull et al., 1984; Ainsa et al., 1996), we launched a molecular approach aimed at characterizing the determinant of AG resistance in this species. A genomic library of *M. fortuitum* was transformed in *M. smegmatis*, and characterization of AG

resistant clones allowed the identification of a *M. fortuitum* gene showing sequence similarity to *aac(2')-Ia* of *P. stuartii*. The enzyme of *M. fortuitum* was named AAC(2')-Ib (Ainsa et al., 1996) and was capable of acetylating gentamicin, but not kanamycin A, hence indicating that another AAC enzyme should be present in *M. fortuitum*. Similarly to *P. stuartii*, the *aac(2')-Ib* gene was found in all strains of *M. fortuitum* regardless of the phenotype of AG resistance, suggesting other roles for the AAC(2')-Ib in this species. Further studies (done by database searching or by southern blot analysis using the probe of *aac(2')-Ib* gene) demonstrated the presence of *aac(2')-I* genes in other mycobacterial species, including *M. tuberculosis* (the major pathogenic species in this genus), *Mycobacterium leprae*, and *M. smegmatis*, indicating thus that the presence

of *aac(2′)-I* genes in mycobacteria could be universal (Ainsa et al., 1997). Interestingly, the expression of the *aac(2′)-Id* gene in *M. smegmatis* was driven from two promoters, and the strongest one produced a leaderless transcript having a GTG translation start codon at its 5′ end (Mick et al., 2008). Leaderless transcripts are those in which the transcription start site coincides with the translation start codon; although representing a rather unusual feature in the model organism *E. coli*, they are quite common in mycobacteria, where 25% of all transcripts are predicted to be leaderless (Shell et al., 2015); in fact, *eis* gene of *M. tuberculosis* (see the section “The Eis Protein Becomes a Novel Aminoglycoside Acetyltransferase,” below) is transcribed also as a leaderless mRNA (Zaunbrecher et al., 2009). In leaderless mRNAs, there is no Shine-Dalgarno sequence, and 70S ribosomes bind directly to the 5′-end of the mRNA in order to initiate translation (Shell et al., 2015).

## New Roles for AAC(2′) in Mycobacteria

Two major evidences supported that in mycobacteria, AAC(2′)-I enzymes could have additional roles other than acetylation of AGs containing 2′-amino group: first, the capability of amino sugars and diverse acyl-CoA molecules to inhibit the acetylating activity of mycobacterial crude extracts (Udou et al., 1989); and second, the implication of AAC(2′)-Ia (an enzyme of the same class) in acetylation of cell wall substrates in *P. stuartii*. In a series of laboratory mutants of *P. stuartii* expressing *aac(2′)-Ia* gene at different levels, it was found that the extent of peptidoglycan acetylation correlated with the activity of AAC(2′)-Ia, hence suggesting a partial contribution of this enzyme (along with other enzymes) to peptidoglycan acetylation. Many bacterial pathogens acetylate their peptidoglycan as a way to resist the action of muramidase enzymes. Under *in vitro* conditions, AAC(2′)-Ia was able to acetylate tobramycin having acetylated peptidoglycan as donor of acetyl groups (Payie et al., 1995, 1996; Payie and Clarke, 1997).

We investigated the hypothesis of mycobacterial AAC(2′)-I enzymes having also a role in cell wall metabolism, and a gene knock-out mutant of *M. smegmatis* deleted in *aac(2′)-Id* gene was constructed. This mutant (named EP-10) defective in AAC(2′)-I activity was more susceptible to gentamicin, tobramycin, dibekacin, and netilmicin than the parental wild-type strain, and crude extracts of *M. smegmatis* EP-10 failed to acetylate 2′-amino group containing AGs, whereas wild-type strains of *M. smegmatis* readily acetylated such AGs (Ainsa et al., 1997; Maurer et al., 2015). *M. smegmatis* EP-10 was also twofold more susceptible to lysozyme, a feature that has been associated with the extent of peptidoglycan acetylation (Ainsa et al., 1997). Hence, we concluded that in *M. smegmatis*, AAC(2′)-Id enzyme could also contribute to acetylation of peptidoglycan, since a less extensively acetylated peptidoglycan in the knock-out strain would be more susceptible to lysozyme degradation affecting cell viability.

## Biochemical Analysis of Mycobacterial AAC(2′)-I Enzymes

The presence of an AG (2′)-N-acetyltransferase gene in the genome of *M. tuberculosis* was intriguing. In this species, AAC

activity had never been reported (Mitsuhashi et al., 1977) and the expression of the *aac(2′)-Ic* gene [annotated as Rv1258c gene in the *M. tuberculosis* H37Rv genome (Cole et al., 1998)] in the surrogate host *M. smegmatis* could not be associated with any change in the levels of susceptibility to AGs (Ainsa et al., 1997). We constructed a knock-out mutant of *M. tuberculosis* H37Rv deleted in the *aac(2′)-Ic* gene and observed that the mutant (named *M. tuberculosis* B1) was twofold more susceptible than the original wild-type strain to AGs containing a 2′-amino group such as gentamicin, tobramycin and dibekacin, and fourfold more susceptible to 6′-N-ethyl-netilmicin. This indicated that the *aac(2′)-Ic* gene was being expressed in *M. tuberculosis* although at a very low level, and that the AAC(2′)-Ic enzyme in *M. tuberculosis* would acetylate all these four AGs in the wild type strain; hence, acetylated AGs would bind less efficiently to the ribosome, and the AAC(2′)-Ic enzyme would contribute to basal AG resistance in this species.

In order to find the physiological role of this enzyme in *M. tuberculosis*, recombinant *E. coli*-produced AAC(2′)-Ic enzyme from *M. tuberculosis* was studied and found to efficiently acetylate AG antibiotics containing an amino group at the 2′ position (as expected; for example,  $K_m$  for kanamycin B was 1.4  $\mu\text{M}$ ), and surprisingly, it was also capable of acetylating (although to a much lesser extent) other AGs such as kanamycin A ( $K_m$  320  $\mu\text{M}$ ) and amikacin ( $K_m$  968  $\mu\text{M}$ ) that have a hydroxyl group in the 2′ position, hence suggesting this enzyme to be capable of both N- and O-acetylation (Hegde et al., 2001; Draker et al., 2003). This residual activity of AAC(2′)-Ic against kanamycin A and amikacin does not affect their bactericidal activity, and these two antibiotics are used as second line drugs against drug resistant *M. tuberculosis* (World Health Organization [WHO], 2010). The activity of *M. tuberculosis* AAC(2′)-Ic is dependent on metal ions, being inhibited by  $\text{Cu}^{2+}$  and  $\text{Au}^{3+}$  (Li et al., 2015).

Another study consisted in binding covalently the AGs kanamycin A, tobramycin, neamine and neomycin B to an agarose matrix in order to quantify the extent of AG acetylation by AAC enzymes and their subsequent ability to bind an artificial probe mimicking the A-site of the ribosome (Barrett et al., 2008). In such experimental model system, the AGs acetylated by *M. tuberculosis* AAC(2′)-Ic enzyme (only tobramycin, neamine and neomycin B) maintained their binding affinity with the probe mimicking A-site of the ribosome at detectable levels, maybe because the percent of AG acetylation by AAC(2′)-Ic was low. In contrast, these AGs were very efficiently acetylated by *E. coli* AAC(3) (at a different amino group) and had readily lost their affinity for binding this artificial probe. These experiments suggested that subtle differences in the structure of modified AGs (i.e., acetylation at the amino group in 2′ or 3 position) are sufficient to drastically affect their capability of binding to the A-site probe, and this would be expected to correlate with their activity as ribosome inhibitors. In consequence, in mycobacteria, AAC(2′)-I enzymes would not play a major role in resistance to these drugs (Barrett et al., 2008). High resolution crystal structures of AAC(2′)-Ic complexed with AGs demonstrated that this enzyme is a member of the GNC5 acetyltransferase superfamily and suggested a role in the synthesis of mycothiol,

a metabolite that has a key role in regulating redox potential in mycobacteria (Vetting et al., 2002, 2003).

In agreement with the preferential *N*-acetylating activity over the *O*-acetylating activity that was found in the *M. tuberculosis* enzyme (Hegde et al., 2001; Draker et al., 2003), *M. abscessus* clinical isolates were found to be more susceptible to AGs containing a hydroxyl group at the 2' position (such as amikacin and kanamycin A) than to AGs with a 2'-amino group (such as tobramycin, dibekacin and kanamycin B), as the latter group would be substrates of *M. abscessus* AAC(2')-I enzyme (Maurer et al., 2015). In fact, crude extracts of *M. abscessus* efficiently acetylated kanamycin B, whereas kanamycin A was not acetylated at detectable levels. In this species, deletion of the *aac(2')-I* gene resulted in increased susceptibility to kanamycin B, tobramycin, dibekacin and gentamicin C (all of them containing a 2'-amino group) (Rominski et al., 2017). These two reports demonstrate that in *M. abscessus*, the presence of an AAC(2')-I enzyme contributes to decreased innate susceptibility to AGs containing a 2'-amino group (Luthra et al., 2018).

## Becoming a Drug Target: Developing Inhibitors of AAC(2')-I

The interest in developing inhibitors against AAC(2')-I enzymes came from a study in the non-tuberculous species *M. abscessus* (Maurer et al., 2014). It was found that AGs such as amikacin, gentamicin or tobramycin, which are normally bactericidal against *E. coli*, do not have such activity against *M. abscessus* or *M. smegmatis*. However, disruption of the chromosomally encoded *aac(2')-I* gene in these species restored the bactericidal activity of these AGs (Maurer et al., 2014). Given that AGs are used as second-line drugs in treatment of multidrug resistant (MDR) tuberculosis infections, and also in the treatment of other infections caused by non-tuberculous mycobacteria, the possibility of developing compounds that could enhance bactericidal activity of current antimycobacterial treatments became an interesting approach.

To date, the only putative inhibitor of *M. tuberculosis* AAC(2')-Ic is andrographolide, a natural product that was identified in methanolic extracts of a plant that were capable of inhibiting growth of *M. tuberculosis* strains (Prabu et al., 2015). *In silico* analysis predicted that this compound could potentially bind with a high affinity the AAC(2')-Ic enzyme, as well as isocitrate lyase (a metabolic enzyme of the glyoxylate shunt, involved in persistence and virulence of *M. tuberculosis*) and other *M. tuberculosis* proteins (Prabu et al., 2015). However, the specificity of this binding and the ability to really inhibit such putative target proteins were not tested. Given that the gene encoding AAC(2')-Ic is not essential in *M. tuberculosis*, a direct link between AAC(2')-Ic inhibition and bacterial growth inhibition could be discarded. Hence, the ability of plant extracts containing andrographolide to inhibit growth of *M. tuberculosis* could be due to the presence of additional compounds in the extract, or to multiple effects on *M. tuberculosis* cells. Other *in silico* analysis revealed that AAC(2')-Ic enzyme from *M. tuberculosis* could interact with ten other proteins (including a protein of a putative RND-like efflux pump), suggesting that

inhibition of AAC(2')-Ic could also impact many other metabolic processes, hence conferring this enzyme with a relevant role in drug discovery of antituberculosis agents (Joshi et al., 2013).

## THE Eis PROTEIN BECOMES A NOVEL AMINOGLYCOSIDE ACETYLTRANSFERASE

Investigation of *M. tuberculosis* virulence factors lead to the identification of a protein, that was required for infecting and survival in human macrophages; this protein was named Eis for enhanced intracellular survival (**Box 2**) (Wei et al., 2000). Bioinformatic analysis revealed that Eis protein of *M. tuberculosis* was an acetyltransferase of the GCN-5 family (Samuel et al., 2007).

Later on, the analysis of kanamycin resistant *M. tuberculosis* laboratory and clinical strains revealed mutations in the -10 and -35 regions of the *eis* gene promoter, which resulted in increased levels of *eis* mRNA and Eis protein. These mutations were related to low-level resistance to kanamycin (MIC 25 µg/ml), but not to amikacin (MIC < 4 µg/ml), whereas 16S rRNA mutations confer higher levels of resistance to kanamycin (MIC > 80 µg/ml) and frequently cross-resistance to amikacin. These *eis* mutants also displayed increased levels of AAC activity, hence demonstrating that Eis was a novel class of AAC, highly divergent from all other previously known AACs. Eis is capable of acetylating kanamycin more efficiently than amikacin, and streptomycin was not found to be a substrate of Eis (Zaunbrecher et al., 2009). From then on, detection of mutations in *eis* promoter has become a relevant assay in clinical microbiology laboratories for determining susceptibility to kanamycin (Georghiou et al., 2012); the diagnostic and clinical implications of these tests are beyond the scope of this review.

Formation of stable hexamers by Eis is required for its AAC activity (Ganaie et al., 2011; Anand and Sharma, 2018), which can acetylate multiple amine groups of different AG antibiotics, including netilmicin, sisomicin, neamine, ribostamycin, paromomycin, neomycin B, kanamycin, amikacin, tobramycin and hygromycin, resulting in mono-, di-, tri-, and tetraacetylated products (Chen et al., 2011; Houghton et al., 2013a), being able to use not only acetyl-CoA but also other acyl-CoA derivatives (Chen et al., 2012a). The Eis protein works by a random-sequential bisubstrate mechanism of acetylation (Tsodikov et al., 2014). Interestingly, Eis is also able to acetylate capreomycin, a polypeptide second-line antituberculosis drug commonly used in the treatment of MDR tuberculosis infections (Reeves et al., 2013). Several metal ions such as Au<sup>3+</sup>, Cd<sup>2+</sup> and Zn<sup>2+</sup> inhibited Eis activity *in vitro* (Li et al., 2015).

Other mycobacterial species such as *M. smegmatis* and *M. abscessus* have ortholog (and even paralog) *eis* genes, although the Eis proteins have distinct biochemical features and impact on AG susceptibility in comparison with Eis of *M. tuberculosis* (Chen et al., 2012b; Rominski et al., 2017). For example, *M. abscessus* has two *eis* genes, and the deletion of one (but not the other one) resulted in altered AG susceptibility (Rominski et al., 2017; Luthra et al., 2018). Consistently with these findings, mutational

**BOX 2 |** Discovery and characterization of enhanced intracellular survival (Eis) protein of *M. tuberculosis*.

A genome wide investigation of the ability of *M. tuberculosis* for infecting macrophages resulted in the identification of a coding sequence that, once cloned in the non-pathogenic *M. smegmatis* species, conferred capacity for infecting the human macrophage-like cell line U937. This gene was named *eis* (Rv2416c in the *M. tuberculosis* genome; Cole et al., 1998) for enhanced intracellular survival (Wei et al., 2000), and was detected only in pathogenic species of mycobacteria. The promoter of the *eis* gene is similar to consensus *E. coli* sigma-70 dependent promoters (Roberts et al., 2004) and it is recognized by *M. tuberculosis* SigA sigma factor (Wu et al., 2009). The Eis protein was found to be mostly hydrophilic, but having a hydrophobic N-terminal end, so that it could be found in the cytosolic but also in other cell fractions such as the membrane, cell wall or among the secreted proteins of *M. tuberculosis* (Dahl et al., 2001). In fact, antibodies against Eis could detect this protein in the sera of tuberculosis patients (Dahl et al., 2001) and in the cytoplasm of infected macrophages (Samuel et al., 2007). Also, it was found that Eis protein, directly added to cultures of human monocytes, modulated the secretion of pro-inflammatory cytokines in a similar way to that found in *M. tuberculosis* infected cells (Samuel et al., 2007), hence suggesting a role of Eis as an effector protein. Further studies demonstrated that Eis inhibits the extra-cellular signal-regulated kinase 1/2 (ERK1/2) and JAK pathways, and in consequence it inhibited the production of TNF-alpha and IL-4, and stimulated the production of IFN-gamma and IL-10 (Lella and Sharma, 2007). The effect of Eis in increasing production of IL-10 was found to be related to Eis-mediated acetylation of histone H3, which binds the promoter of the human IL-10 gene (Duan et al., 2016). Hence, by disturbing cross-regulation of T-cells and impairing TH1 and TH2 response, Eis could mediate *M. tuberculosis* pathogenicity (Lella and Sharma, 2007). In fact, an isolate of the Beijing family (which are more transmissible and virulent than other *M. tuberculosis* genetic lineages (Hanekom et al., 2011) was found to contain elevated levels of Eis protein, mediated by increased expression of SigA (Wu et al., 2009). Other key factors in host immune response to tuberculosis are also mediated by Eis, which increased production of ROS and consequently modulated processes such as autophagy, inflammation, and cell death (Shin et al., 2010). These processes are started by Eis-dependent acetylation of dual-specificity phosphatase-16 (DUSP16)-mitogen-activated protein kinase phosphatase-7 (MKP-7), which dephosphorylates the JNK protein leading to its inactivation (Kim et al., 2012; Yoon et al., 2013). Other studies have revealed the activity of Eis for acetylating arylalkylamines such as histamine, octopamine, or tyramine, suggesting novel roles for this protein in *M. tuberculosis* pathogenicity (Pan et al., 2018).

changes in the amino acid residues lining the substrate binding site of *M. tuberculosis* Eis altered its substrate specificity (Jennings et al., 2013).

It is important to note that in *M. tuberculosis*, transcription of the *eis* gene is activated by the regulator WhiB7 (Reeves et al., 2013). Mutations in the promoter of *whiB7* gene that led to increase in the mRNA of this gene resulted in increased expression of *eis* gene, along with other genes such as *rv1258c* (encoding the Tap efflux pump; Ainsa et al., 1998), hence resulting in cross resistance to several drugs including kanamycin (mediated by Eis protein) or streptomycin (mediated by Tap efflux pump). Similarly, in *M. abscessus*, WhiB7 controlled the expression of one of the two *eis* genes in this species and also that of the *erm(41)* gene, which encodes a ribosomal methyltransferase that by altering target structure is associated with resistance to macrolide antibiotics (Pryjma et al., 2017; Luthra et al., 2018). Subinhibitory concentrations of clarithromycin induced the *whiB7* gene and consequently decreased Eis-mediated susceptibility to AGs, such as amikacin that is currently used in the treatment of *M. abscessus* infections (Pryjma et al., 2017).

## Aminoglycosides and Beyond . . .

The unusual properties of Eis acetyltransferase include its capability for acetylating peptides and proteins (Kim et al., 2012; Houghton et al., 2013b; Yoon et al., 2013), in contrast with other AACs. The *M. tuberculosis* nucleoid-associated protein HU (encoded by Rv2986c gene) can be acetylated by Eis on multiple lysine residues, hence decreasing its ability to interact with DNA, and altering its DNA compaction activity (Ghosh et al., 2016; Green et al., 2018). Overexpression of Eis led to a hyperacetylation of HU protein, and consequently, to a decompaction of the genome (Ghosh et al., 2016). The reverse effect (condensation of relaxed DNA) could be reached through the deacetylation of HU protein, which is mediated by a Sir2 family protein from *M. tuberculosis* encoded by the Rv1155c gene (Anand et al., 2017; Green et al., 2018). Controlling the architecture of DNA is a key process in any bacteria, and so, the

HU protein is essential for *M. tuberculosis*. In fact, inhibitors of HU have been discovered (Bhowmick et al., 2014), which could act in synergy with potential inhibitors of Eis, as described in the next section.

## Finding Inhibitors of Eis Protein

The crystal structure of *M. tuberculosis* Eis protein was determined by several groups (Chen et al., 2011; Kim et al., 2012), which has been useful for determining docking properties of potential inhibitory compounds; also, its comparison with the crystal structure of *M. smegmatis* Eis protein revealed several distinct structural features that may account for the biochemical and substrate differences between the two proteins (Kim et al., 2014). A first screening of potential inhibitors of Eis from *M. tuberculosis* resulted in the identification of 25 molecules (including the antiseptic chlorhexidine) that inhibited Eis with IC<sub>50</sub> values in the low micromolar range. In addition, this inhibition was specific to the *M. tuberculosis* Eis protein, since these molecules could not inhibit significantly AACs from AAC(2'), AAC(3), and AAC(6') families (Green et al., 2012), nor Eis protein from *Bacillus anthracis* (Green et al., 2015a). Later studies revealed the presence of *eis*-like genes in many pathogenic and non-pathogenic bacteria (remarkably, many mycobacterial species have two or even three paralogs of the *eis* gene), and chlorhexidine was capable of inhibiting (to different levels) all Eis proteins that were capable of acetylating AGs (Green et al., 2015b).

A second screening of a larger collection of small-molecule compounds resulted in the identification of several families of compounds capable of inhibiting Eis activity. These contained diverse chemical scaffolds (Garzan et al., 2016a,b, 2017; Willby et al., 2016; Ngo et al., 2018). Besides, these inhibitors were highly selective for Eis, and did not inhibited AACs from other families (Garzan et al., 2016b). More importantly, as these inhibitors bound in the AG pocket of the Eis protein, they were able to reverse kanamycin resistance of a *M. tuberculosis* isolate (Garzan et al., 2016b; Willby et al., 2016; Ngo et al., 2018).

Some of these inhibitors, such as those based on a pyrrolo[1,5-a]pyrazine scaffold, also lacked any toxicity on mammalian cell lines (Garzan et al., 2017).

## OTHER AMINOGLYCOSIDE-MODIFYING ENZYMES IN MYCOBACTERIA

Genome-wide analysis of *M. tuberculosis* genome identified only one other potential AAC (encoded by the Rv1347c gene), although such enzymatic activity could not be detected on the recombinant protein (Draker et al., 2003). Later studies related the product of the Rv1347c gene with a role in the synthesis of mycobactin, the mycobacterial siderophore (Card et al., 2005).

Leaving apart AACs, only a few reports of other classes of aminoglycoside-modifying enzymes have been done in mycobacteria. An APH enzyme of the APH(3'') family, conferring resistance to the AG streptomycin only, has been characterized in *M. fortuitum* (Ramon-Garcia et al., 2006) and *M. abscessus* (Dal Molin et al., 2018; Luthra et al., 2018); the latter species encodes up to 11 additional putative APH enzymes (Ripoll et al., 2009). Furthermore, a putative APH of the APH(3') class, encoded by the Rv3168 gene of *M. tuberculosis*, was identified and expressed as a recombinant enzyme in *E. coli*, being related to kanamycin phosphotransferase activity (Ahn and Kim, 2013).

## BACK TO THE START POINT: Eis IN *M. fortuitum*

We started this review referring to previous work that has shown that crude extracts of *M. fortuitum* harbored AAC activity having gentamicin, tobramycin, netilmicin and its derivatives 2'-N-ethyl- and 6'-N-ethyl-netilmicin, kanamycin A and kanamycin B as substrates. So far, the only AG acetyltransferase identified in this species has been AAC(2')-Ib (Ainsa et al., 1996), which cannot explain the acetyltransferase activity against kanamycin A and 2'-N-ethyl-netilmicin detected in *M. fortuitum* crude extracts. Later studies characterized Eis AAC in diverse mycobacterial species, but no report were been done on a putative Eis protein in *M. fortuitum*. In view of the universal presence of Eis proteins in mycobacteria, and its activity as AAC, we hypothesized that *M. fortuitum* could also have a putative Eis protein that would be responsible for the acetyltransferase activity against kanamycin A and 2'-N-ethyl-netilmicin detected in crude extracts of this species, as it was reported earlier (Hull et al., 1984; Ainsa et al., 1996).

Thus, we first ascertained the existence of an *eis* gene in the genome of *M. fortuitum* (Ho et al., 2012), which presented a 94% of identity with respect to the one reported in *M. tuberculosis*; the sequence of both Eis proteins from *M. tuberculosis* and *M. fortuitum* also presented high levels of identity (Figure 1). We designed two oligonucleotides for amplifying specifically a DNA fragment from *M. fortuitum* genome containing *eis* gene. This DNA fragment was subsequently cloned in pMV261 vector (Stover et al., 1991), which expresses genes constitutively under

the control of the *hsp60* gene promoter, resulting in plasmid pFS2. Given that this plasmid still contains the Tn903-derived aminoglycoside-3'-phosphotransferase (*aph*) gene (present in the original pMV261 cloning vector) conferring kanamycin resistance as selection marker, we anticipated that *M. smegmatis* strains harboring pMV261 vector or its derivatives would be intrinsically resistant to kanamycin A; this would prevent from determining whether this antibiotic is a substrate of the *M. fortuitum* Eis protein. Additionally, the selection marker could have cross-effect with other AGs and thus interfering with the resistance phenotype conferred by *eis* gene. To circumvent these problems, we generated a derivative of pFS2 through the disruption of the *aph* gene with the ampicillin resistance cassette (*bla* gene) from pGEM®-T easy (Promega). The resistance to 2'-N-ethylnetilmicin conferred by *eis* gene, as demonstrated for the parental plasmid pFS2 (see Table 1) was used as resistance marker for transformant selection and plasmid maintenance. This process resulted in plasmid pEAC which contains the *M. fortuitum eis* gene and no other determinant of AG resistance.

The three plasmids [original empty vector pMV261 as a control, and the two plasmids (pFS2 and pEAC) containing *M. fortuitum eis* gene] were introduced in *M. smegmatis* mc<sup>2</sup> 155 in order to over-express the ortholog *eis* gene from *M. fortuitum* and to elucidate its hypothetical implication in AG susceptibility. The antibiotic susceptibility assay was made, based on a double dilution protocol with the addition of resazurin dye (Palomino et al., 2002).

We observed that plasmids pFS2 and pEAC produced detectable changes in AG susceptibility of *M. smegmatis* mc<sup>2</sup> 155, which can be attributed to the expression of the plasmid-borne *M. fortuitum eis* gene. The major shift in the MICs was detected for 2'-N-ethylnetilmicin (Table 1), since the MIC increased from 3.12 to 6.25 µg/ml in the control strains to 50–100 µg/ml in the strains containing *M. fortuitum* Eis, accounting for a 8- to 32-fold increase; similar changes were observed for 6'-N-ethylnetilmicin (8-fold increase in the MIC). A moderate decrease in the susceptibility to kanamycin A (fivefold), hygromycin (twofold to fourfold) and gentamicin (twofold to fourfold) was also observed. Finally, slight changes (twofold) in the MICs were detected for kanamycin B and capreomycin; this finding is consistent with previous reports on the activity of *M. tuberculosis* Eis against capreomycin (Reeves et al., 2013). The levels of susceptibility to the AGs amikacin, streptomycin and spectinomycin, and to other non-AG compounds tested (isoniazid, rifampicin, ethambutol, ciprofloxacin, tetracycline, chloramphenicol) were not altered significantly by the presence of the plasmid-encoded *eis* gene (Table 1 and data not shown), suggesting that either these antimicrobials are not substrates of the Eis enzyme or the corresponding acetylations (if any) might just not affect antibacterial activity.

## CONCLUDING REMARKS

The presence and activity of AAC(2')-I and Eis AACs in mycobacteria have clearly demonstrated that their primary role is little related with susceptibility to AGs.



**TABLE 1 |** MICs (μg/ml) of antibiotics of different structural families in the *M. smegmatis* mc<sup>2</sup> 155 strains that overexpress *eis* gene from *M. fortuitum*.

| Strain                       | <i>M. smegmatis</i> mc <sup>2</sup> 155 |            |            |            |
|------------------------------|---|------------|------------|------------|
|                              | None                                    | pMV261     | pFS2       | pEAC       |
| Plasmid                      | None                                    | pMV261     | pFS2       | pEAC       |
| Marker gene on plasmid       | None                                    | <i>aph</i> | <i>aph</i> | <i>bla</i> |
| <i>M. fortuitum eis</i> gene | —                                       | —          | +          | +          |
| Gentamicin                   | 0.78-1.56                               | 0.78       | 3.12       | 3.12       |
| 2'-N-ethyl netilmicin        | 6.25                                    | 3.12-6.25  | 50-100     | 50         |
| 6'-N-ethyl netilmicin        | 3.12                                    | 3.12       | 3.12-6.25  | 25         |
| Kanamycin A                  | 1.56                                    | >100       | >100       | 7.8        |
| Kanamycin B                  | 6.25                                    | >100       | >100       | 12.5       |
| Hygromycin                   | 15.6                                    | 15.6       | 31.2-62.5  | 62.5       |
| Amikacin                     | 0.39                                    | 0.39       | 0.39       | 0.39       |
| Capreomycin                  | 1.95                                    | 1.95       | 3.9        | 3.9        |
| Streptomycin                 | 0.25                                    | 0.25       | 0.25       | 0.25       |
| Spectinomycin                | 62.5                                    | 31.2-62.5  | 62.5       | 62.5       |

The values separated by a dash indicate that growth was detected in both concentrations. The range of antibiotic concentrations spanned from 0.78 μg/ml to 100 μg/ml, and from 0.25 μg/ml to 125 μg/ml; a twofold difference in the MIC was not considered as significant. *aph*: aminoglycoside 3'-phosphotransferase from Tn903; *bla*: beta-lactamase.

In the case of AAC(2')-I enzymes, its presence in phylogenetically distant genera as *Providencia* and *Mycobacterium* remains to be an evolutionary mystery.

In contrast with this restricted distribution of AAC(2')-I enzymes among bacteria, Eis enzymes seem to be more widely distributed, being present even in non-pathogenic and environmental species, which suggest a general function of Eis-like enzymes in bacterial metabolism, and virtually excludes any potential selection of *eis* genes due to the use of AGs, or its horizontal transfer from other species.

It is clear that in mycobacteria ribosomal modifications constitute the major mechanism of AG resistance, given that only one or two copies of ribosomal RNA operons are present in these species, hence making likely the acquisition of mutations conferring high levels of AG resistance. Then, AAC(2')-I enzymes only contribute modestly to innate low level susceptibility to AGs, and despite other roles have been suggested in the literature for mycobacterial AAC(2')-I enzymes, their relevance as potential drug targets is still modest, especially in comparison with Eis acetyltransferase. The contribution of Eis acetyltransferase to virulence of *M. tuberculosis*, and the finding that Eis is related with resistance to kanamycin (a second line drug for the treatment of tuberculosis) in clinical isolates has greatly attracted the attention and promoted the interest in developing Eis inhibitors. In some way, Eis inhibitors would fall into the class of anti-virulence and anti-resistance mechanisms compounds, which is a trending topic

in the age of antimicrobial resistance. Globally, antimicrobial resistance is a major public health threat, and multi and extensively drug resistant (MDR, XDR) tuberculosis is a case of particular concern, so progress and major advances that can be expected from the coming years will be greatly welcomed.

## AUTHOR CONTRIBUTIONS

JA, LR, and CM contributed to the conception and design of the study. FS-G, EA-C, AL, LR, and EP-H carried out the experimental work. FS-G, EA-C, and JA wrote the manuscript. All authors contributed to manuscript revision, read and approved the submitted version.

## REFERENCES

- Ahn, J. W., and Kim, K. J. (2013). Rv3168 phosphotransferase activity mediates kanamycin resistance in *Mycobacterium tuberculosis*. *J. Microbiol. Biotechnol.* 23, 1529–1535. doi: 10.4014/jmb.1306.06048
- Ainsa, J. A., Blokpoel, M. C., Otal, I., Young, D. B., De Smet, K. A., and Martin, C. (1998). Molecular cloning and characterization of Tap, a putative multidrug efflux pump present in *Mycobacterium fortuitum* and *Mycobacterium tuberculosis*. *J. Bacteriol.* 180, 5836–5843.
- Ainsa, J. A., Martin, C., Gicquel, B., and Gomez-Lus, R. (1996). Characterization of the chromosomal aminoglycoside 2'-N-acetyltransferase gene from *Mycobacterium fortuitum*. *Antimicrob. Agents Chemother.* 40, 2350–2355. doi: 10.1128/AAC.40.10.2350
- Ainsa, J. A., Perez, E., Pelicic, V., Berthet, F. X., Gicquel, B., and Martin, C. (1997). Aminoglycoside 2'-N-acetyltransferase genes are universally present in mycobacteria: characterization of the aac(2')-Ic gene from *Mycobacterium tuberculosis* and the aac(2')-Id gene from *Mycobacterium smegmatis*. *Mol. Microbiol.* 24, 431–441. doi: 10.1046/j.1365-2958.1997.3471717.x
- Anand, C., Garg, R., Ghosh, S., and Nagaraja, V. (2017). A Sir2 family protein Rv1151c deacetylates HU to alter its DNA binding mode in *Mycobacterium tuberculosis*. *Biochem. Biophys. Res. Commun.* 493, 1204–1209. doi: 10.1016/j.bbrc.2017.09.087
- Anand, S., and Sharma, C. (2018). Glycine-rich loop encompassing active site at interface of hexameric *M. tuberculosis* Eis protein contributes to its structural stability and activity. *Int. J. Biol. Macromol.* 109, 124–135. doi: 10.1016/j.ijbiomac.2017.12.058
- Angelatou, F., Litsas, S. B., and Kontomichalou, P. (1982). Purification and properties of two gentamicin-modifying enzymes, coded by a single plasmid pPK237 originating from *Pseudomonas aeruginosa*. *J. Antibiot.* 35, 235–244. doi: 10.7164/antibiotics.35.235
- Barrett, O. J., Pushechnikov, A., Wu, M., and Disney, M. D. (2008). Studying aminoglycoside modification by the acetyltransferase class of resistance-causing enzymes via microarray. *Carbohydr. Res.* 343, 2924–2931. doi: 10.1016/j.carres.2008.08.018
- Bassetti, M., Vena, A., Croxatto, A., Righi, E., and Guery, B. (2018). How to manage *Pseudomonas aeruginosa* infections. *Drugs Context* 7:212527. doi: 10.7573/dic.212527
- Bhowmick, T., Ghosh, S., Dixit, K., Ganesan, V., Ramagopal, U. A., Dey, D., et al. (2014). Targeting *Mycobacterium tuberculosis* nucleoid-associated protein HU with structure-based inhibitors. *Nat. Commun.* 5:4124. doi: 10.1038/ncomms5124
- Carrd, G. L., Peterson, N. A., Smith, C. A., Rupp, B., Schick, B. M., and Baker, E. N. (2005). The crystal structure of Rv1347c, a putative antibiotic resistance protein from *Mycobacterium tuberculosis*, reveals a GCN5-related fold and suggests an alternative function in siderophore biosynthesis. *J. Biol. Chem.* 280, 13978–13986. doi: 10.1074/jbc.M413904200
- Chen, W., Biswas, T., Porter, V. R., Tsodikov, O. V., and Garneau-Tsodikova, S. (2011). Unusual regioversatility of acetyltransferase Eis, a cause of drug resistance in XDR-TB. *Proc. Natl. Acad. Sci. U.S.A.* 108, 9804–9808. doi: 10.1073/pnas.1105379108
- Chen, W., Green, K. D., and Garneau-Tsodikova, S. (2012a). Cosubstrate tolerance of the aminoglycoside resistance enzyme Eis from *Mycobacterium tuberculosis*. *Antimicrob. Agents Chemother.* 56, 5831–5838. doi: 10.1128/AAC.00932-12
- Chen, W., Green, K. D., Tsodikov, O. V., and Garneau-Tsodikova, S. (2012b). Aminoglycoside multiacetylating activity of the enhanced intracellular survival protein from *Mycobacterium smegmatis* and its inhibition. *Biochemistry* 51, 4959–4967. doi: 10.1021/bi3004473
- Clarke, A. J., Francis, D., and Keenleyside, W. J. (1996). The prevalence of gentamicin 2'-N-acetyltransferase in the Proteaceae and its role in the O-acetylation of peptidoglycan. *FEMS Microbiol. Lett.* 145, 201–207.
- Cole, S. T., Brosch, R., Parkhill, J., Garnier, T., Churcher, C., Harris, D., et al. (1998). Deciphering the biology of *Mycobacterium tuberculosis* from the complete genome sequence. *Nature* 393, 537–544. doi: 10.1038/31159
- Dahl, J. L., Wei, J., Moulder, J. W., Laal, S., and Friedman, R. L. (2001). Subcellular localization of the intracellular survival-enhancing Eis protein of *Mycobacterium tuberculosis*. *Infect. Immun.* 69, 4295–4302. doi: 10.1128/IAI.69.7.4295-4302.2001
- Dal Molin, M., Gut, M., Rominski, A., Haldimann, K., Becker, K., and Sander, P. (2018). Molecular mechanisms of intrinsic streptomycin resistance in *Mycobacterium abscessus*. *Antimicrob. Agents Chemother.* 62:e001427-17. doi: 10.1128/AAC.01427-17
- Davies, J., and Wright, G. D. (1997). Bacterial resistance to aminoglycoside antibiotics. *Trends Microbiol.* 5, 234–240. doi: 10.1016/S0966-842X(97)01033-0
- Draker, K. A., Boehr, D. D., Elowe, N. H., Noga, T. J., and Wright, G. D. (2003). Functional annotation of putative aminoglycoside antibiotic modifying proteins in *Mycobacterium tuberculosis* H37Rv. *J. Antibiot.* 56, 135–142. doi: 10.7164/antibiotics.56.135
- Duan, L., Yi, M., Chen, J., Li, S., and Chen, W. (2016). *Mycobacterium tuberculosis* EIS gene inhibits macrophage autophagy through up-regulation of IL-10 by increasing the acetylation of histone H3. *Biochem. Biophys. Res. Commun.* 473, 1229–1234. doi: 10.1016/j.bbrc.2016.04.045
- Franklin, K., and Clarke, A. J. (2001). Overexpression and characterization of the chromosomal aminoglycoside 2'-N-acetyltransferase of *Providencia stuartii*. *Antimicrob. Agents Chemother.* 45, 2238–2244. doi: 10.1128/AAC.45.8.2238-2244.2001
- Ganaie, A. A., Lella, R. K., Solanki, R., and Sharma, C. (2011). Thermostable hexameric form of Eis (Rv2416c) protein of *M. tuberculosis* plays an important role for enhanced intracellular survival within macrophages. *PLoS One* 6:e27590. doi: 10.1371/journal.pone.0027590
- Garzan, A., Willby, M. J., Green, K. D., Gajadeera, C. S., Hou, C., Tsodikov, O. V., et al. (2016a). Sulfonamide-based inhibitors of aminoglycoside acetyltransferase Eis abolish resistance to kanamycin in *Mycobacterium tuberculosis*. *J. Med. Chem.* 59, 10619–10628. doi: 10.1021/acs.jmedchem.6b01161
- Garzan, A., Willby, M. J., Green, K. D., Tsodikov, O. V., Posey, J. E., and Garneau-Tsodikova, S. (2016b). Discovery and optimization of two Eis inhibitor families

## FUNDING

FS-G and EA-C are recipients of FPU fellowships from the Spanish Ministry of Economy and Competitiveness. JA acknowledges funding from the European Commission [More Medicines for Tuberculosis (MM4TB) grant 260872] and the Spanish Ministry of Economy and Competitiveness (grants SAF-2013-48971-C2-2-R and SAF2017-84839-C2-1-R).

## ACKNOWLEDGMENTS

Dessi Marinova was acknowledged for critical reading of the manuscript.

- as kanamycin adjuvants against drug-resistant *M. tuberculosis*. *ACS Med. Chem. Lett.* 7, 1219–1221. doi: 10.1021/acsmchemlett.6b00261
- Garzan, A., Willby, M. J., Ngo, H. X., Gajadeera, C. S., Green, K. D., Holbrook, S. Y., et al. (2017). Combating enhanced intracellular survival (Eis)-mediated kanamycin resistance of *Mycobacterium tuberculosis* by novel pyrrolo[1,5-a]pyrazine-based Eis inhibitors. *ACS Infect. Dis.* 3, 302–309. doi: 10.1021/acsinfectdis.6b00193
- Georghiou, S. B., Magana, M., Garfein, R. S., Catanzaro, D. G., Catanzaro, A., and Rodwell, T. C. (2012). Evaluation of genetic mutations associated with *Mycobacterium tuberculosis* resistance to amikacin, kanamycin and capreomycin: a systematic review. *PLoS One* 7:e33275. doi: 10.1371/journal.pone.0033275
- Ghosh, S., Padmanabhan, B., Anand, C., and Nagaraja, V. (2016). Lysine acetylation of the *Mycobacterium tuberculosis* HU protein modulates its DNA binding and genome organization. *Mol. Microbiol.* 100, 577–588. doi: 10.1111/mmi.13339
- Green, K. D., Biswas, T., Chang, C., Wu, R., Chen, W., Janes, B. K., et al. (2015a). Biochemical and structural analysis of an Eis family aminoglycoside acetyltransferase from bacillus anthracis. *Biochemistry* 54, 3197–3206. doi: 10.1021/acs.biochem.5b00244
- Green, K. D., Pricer, R. E., Stewart, M. N., and Garneau-Tsodikova, S. (2015b). Comparative study of Eis-like enzymes from pathogenic and nonpathogenic bacteria. *ACS Infect. Dis.* 1, 272–283. doi: 10.1021/acsinfectdis.5b00036
- Green, K. D., Biswas, T., Pang, A. H., Willby, M. J., Reed, M. S., Stuchlik, O., et al. (2018). Acetylation by Eis and deacetylation by Rv1151c of *Mycobacterium tuberculosis* HupB: biochemical and structural insight. *Biochemistry* 57, 781–790. doi: 10.1021/acs.biochem.7b01089
- Green, K. D., Chen, W., and Garneau-Tsodikova, S. (2012). Identification and characterization of inhibitors of the aminoglycoside resistance acetyltransferase Eis from *Mycobacterium tuberculosis*. *ChemMedChem* 7, 73–77. doi: 10.1002/cmdc.201100332
- Hanekom, M., Gey van Pittius, N. C., McEvoy, C., Victor, T. C., Van Helden, P. D., and Warren, R. M. (2011). *Mycobacterium tuberculosis* Beijing genotype: a template for success. *Tuberculosis* 91, 510–523. doi: 10.1016/j.tube.2011.07.005
- Hegde, S. S., Javid-Majid, F., and Blanchard, J. S. (2001). Overexpression and mechanistic analysis of chromosomally encoded aminoglycoside 2'-N-acetyltransferase (AAC(2')-Ic) from *Mycobacterium tuberculosis*. *J. Biol. Chem.* 276, 45876–45881. doi: 10.1074/jbc.M108810200
- Ho, I. I., Chan, C. Y., and Cheng, A. F. (2000). Aminoglycoside resistance in *Mycobacterium kansasii*, *Mycobacterium avium-M. intracellulare*, and *Mycobacterium fortuitum*: are aminoglycoside-modifying enzymes responsible? *Antimicrob. Agents Chemother.* 44, 39–42. doi: 10.1128/AAC.44.1.39-42.2000
- Ho, Y. S., Adroub, S. A., Aleisa, F., Mahmood, H., Othoum, G., Rashid, F., et al. (2012). Complete genome sequence of *Mycobacterium fortuitum* subsp. *fortuitum* type strain DSM46621. *J. Bacteriol.* 194, 6337–6338. doi: 10.1128/JB.01461-12
- Houghton, J. L., Biswas, T., Chen, W., Tsodikov, O. V., and Garneau-Tsodikova, S. (2013a). Chemical and structural insights into the regioversatility of the aminoglycoside acetyltransferase Eis. *Chembiochem* 14, 2127–2135. doi: 10.1002/cbic.201300359
- Houghton, J. L., Green, K. D., Pricer, R. E., Mayhoub, A. S., and Garneau-Tsodikova, S. (2013b). Unexpected N-acetylation of capreomycin by mycobacterial Eis enzymes. *J. Antimicrob. Chemother.* 68, 800–805. doi: 10.1093/jac/dks497
- Hull, S. I., Wallace, R. J. Jr., Bobey, D. G., Price, K. E., Goodhines, R. A., Swenson, J. M., et al. (1984). Presence of aminoglycoside acetyltransferase and plasmids in *Mycobacterium fortuitum*. Lack of correlation with intrinsic aminoglycoside resistance. *Am. Rev. Respir. Dis.* 129, 614–618.
- Jana, S., and Deb, J. K. (2005). Molecular targets for design of novel inhibitors to circumvent aminoglycoside resistance. *Curr. Drug Targets* 6, 353–361. doi: 10.2174/1389450053765860
- Jennings, B. C., Labby, K. J., Green, K. D., and Garneau-Tsodikova, S. (2013). Redesign of substrate specificity and identification of the aminoglycoside binding residues of Eis from *Mycobacterium tuberculosis*. *Biochemistry* 52, 5125–5132. doi: 10.1021/bi4002985
- Joshi, R. S., Jamdhade, M. D., Sonawane, M. S., and Giri, A. P. (2013). Resistome analysis of *Mycobacterium tuberculosis*: identification of aminoglycoside 2'-N-acetyltransferase (AAC) as co-target for drug designing. *Bioinformation* 9, 174–181. doi: 10.6026/97320630009174
- Jugheli, L., Bzekalava, N., de Rijk, P., Fissette, K., Portaels, F., and Rigouts, L. (2009). High level of cross-resistance between kanamycin, amikacin, and capreomycin among *Mycobacterium tuberculosis* isolates from Georgia and a close relation with mutations in the *rrs* gene. *Antimicrob. Agents Chemother.* 53, 5064–5068. doi: 10.1128/AAC.00851-09
- Kim, K. H., An, D. R., Song, J., Yoon, J. Y., Kim, H. S., Yoon, H. J., et al. (2012). *Mycobacterium tuberculosis* Eis protein initiates suppression of host immune responses by acetylation of DUSP16/MKP-7. *Proc. Natl. Acad. Sci. U.S.A.* 109, 7729–7734. doi: 10.1073/pnas.1120251109
- Kim, K. H., An, D. R., Yoon, H. J., Yang, J. K., and Suh, S. W. (2014). Structure of *Mycobacterium smegmatis* Eis in complex with paromomycin. *Acta Crystallogr. F Struct. Biol. Commun.* 70(Pt 9), 1173–1179. doi: 10.1107/S2053230X14017385
- Labby, K. J., and Garneau-Tsodikova, S. (2013). Strategies to overcome the action of aminoglycoside-modifying enzymes for treating resistant bacterial infections. *Future Med. Chem.* 5, 1285–1309. doi: 10.4155/fmc.13.80
- Lella, R. K., and Sharma, C. (2007). Eis (enhanced intracellular survival) protein of *Mycobacterium tuberculosis* disturbs the cross regulation of T-cells. *J. Biol. Chem.* 282, 18671–18675. doi: 10.1074/jbc.C600280200
- Li, Y., Green, K. D., Johnson, B. R., and Garneau-Tsodikova, S. (2015). Inhibition of aminoglycoside acetyltransferase resistance enzymes by metal salts. *Antimicrob. Agents Chemother.* 59, 4148–4156. doi: 10.1128/AAC.00885-15
- Luthra, S., Rominski, A., and Sander, P. (2018). The role of antibiotic-target-modifying and antibiotic-modifying enzymes in *Mycobacterium abscessus* drug resistance. *Front. Microbiol.* 9:2179. doi: 10.3389/fmicb.2018.02179
- Macinga, D. R., and Rather, P. N. (1999). The chromosomal 2'-N-acetyltransferase of *Providencia stuartii*: physiological functions and genetic regulation. *Front. Biosci.* 4, D132–D140. doi: 10.2741/Macinga
- Magnet, S., and Blanchard, J. S. (2005). Molecular insights into aminoglycoside action and resistance. *Chem. Rev.* 105, 477–498. doi: 10.1021/cr0301088
- Maurer, F. P., Bruderer, V. L., Castelberg, C., Ritter, C., Scherbakov, D., Bloemberg, G. V., et al. (2015). Aminoglycoside-modifying enzymes determine the innate susceptibility to aminoglycoside antibiotics in rapidly growing mycobacteria. *J. Antimicrob. Chemother.* 70, 1412–1419. doi: 10.1093/jac/dku550
- Maurer, F. P., Bruderer, V. L., Ritter, C., Castelberg, C., Bloemberg, G. V., and Bottger, E. C. (2014). Lack of antimicrobial bactericidal activity in *Mycobacterium abscessus*. *Antimicrob. Agents Chemother.* 58, 3828–3836. doi: 10.1128/AAC.02448-14
- Mick, V., Rebollo, M. J., Lucia, A., Garcia, M. J., Martin, C., and Ainsa, J. A. (2008). Transcriptional analysis of and resistance level conferred by the aminoglycoside acetyltransferase gene *aac(2')-Id* from *Mycobacterium smegmatis*. *J. Antimicrob. Chemother.* 61, 39–45. doi: 10.1093/jac/dkm440
- Minget-Leclercq, M. P., Glupczynski, Y., and Tulkens, P. M. (1999). Aminoglycosides: activity and resistance. *Antimicrob. Agents Chemother.* 43, 727–737. doi: 10.1128/AAC.43.4.727
- Mitsuhashi, S., Tanaka, T., Kawabe, H., and Umezawa, H. (1977). Biochemical mechanism of kanamycin resistance in *Mycobacterium tuberculosis*. *Microbiol. Immunol.* 21, 325–327. doi: 10.1111/j.1348-0421.1977.tb00294.x
- Ngo, H. X., Green, K. D., Gajadeera, C. S., Willby, M. J., Holbrook, S. Y. L., Hou, C., et al. (2018). Potent 1,2,4-triazino[5,6 b]indole-3-thioether inhibitors of the kanamycin resistance enzyme Eis from *Mycobacterium tuberculosis*. *ACS Infect. Dis.* 4, 1030–1040. doi: 10.1021/acsinfectdis.8b00074
- Palomino, J. C., Martin, A., Camacho, M., Guerra, H., Swings, J., and Portaels, F. (2002). Resazurin microtiter assay plate: simple and inexpensive method for detection of drug resistance in *Mycobacterium tuberculosis*. *Antimicrob. Agents Chemother.* 46, 2720–2722. doi: 10.1128/AAC.46.8.2720-2722.2002
- Pan, Q., Zhao, F. L., and Ye, B. C. (2018). Eis, a novel family of arylalkylamine N-acetyltransferase (EC 2.3.1.87). *Sci. Rep.* 8:2435. doi: 10.1038/s41598-018-20802-6
- Payie, K. G., and Clarke, A. J. (1997). Characterization of gentamicin 2'-N-acetyltransferase from *Providencia stuartii*: its use of peptidoglycan metabolites for acetylation of both aminoglycosides and peptidoglycan. *J. Bacteriol.* 179, 4106–4114. doi: 10.1128/jb.179.13.4106-4114.1997



- Paye, K. G., Rather, P. N., and Clarke, A. J. (1995). Contribution of gentamicin 2'-N-acetyltransferase to the O acetylation of peptidoglycan in *Providencia stuartii*. *J. Bacteriol.* 177, 4303–4310. doi: 10.1128/jb.177.15.4303-4310.1995
- Paye, K. G., Strating, H., and Clarke, A. J. (1996). The role of O-acetylation in the metabolism of peptidoglycan in *Providencia stuartii*. *Microb. Drug Resist.* 2, 135–140. doi: 10.1089/mdr.1996.2.135
- Prabu, A., Hassan, S., Prabuseenivasan, Shainaba, A. S., Hanna, L. E., and Kumar, V. (2015). Andrographolide: a potent antituberculosis compound that targets Aminoglycoside 2'-N-acetyltransferase in *Mycobacterium tuberculosis*. *J. Mol. Graph. Model.* 61, 133–140. doi: 10.1016/j.jmgm.2015.07.001
- Pryjma, M., Burian, J., Kuchinski, K., and Thompson, C. J. (2017). Antagonism between front-line antibiotics clarithromycin and amikacin in the treatment of *Mycobacterium abscessus* infections is mediated by the *whiB7* gene. *Antimicrob. Agents Chemother.* 61:e01353-17. doi: 10.1128/AAC.01353-17
- Ramon-Garcia, S., Otal, I., Martin, C., Gomez-Lus, R., and Ainsa, J. A. (2006). Novel streptomycin resistance gene from *Mycobacterium fortuitum*. *Antimicrob. Agents Chemother.* 50, 3920–3922. doi: 10.1128/AAC.00223-06
- Rather, P. N., Orosz, E., Shaw, K. J., Hare, R., and Miller, G. (1993). Characterization and transcriptional regulation of the 2'-N-acetyltransferase gene from *Providencia stuartii*. *J. Bacteriol.* 175, 6492–6498. doi: 10.1128/jb.175.20.6492-6498.1993
- Reeves, A. Z., Campbell, P. J., Sultana, R., Malik, S., Murray, M., Plikaytis, B. B., et al. (2013). Aminoglycoside cross-resistance in *Mycobacterium tuberculosis* due to mutations in the 5' untranslated region of *whiB7*. *Antimicrob. Agents Chemother.* 57, 1857–1865. doi: 10.1128/AAC.02191-12
- Ripoll, F., Pasek, S., Schenowitz, C., Dossat, C., Barbe, V., Rottman, M., et al. (2009). Non mycobacterial virulence genes in the genome of the emerging pathogen *Mycobacterium abscessus*. *PLoS One* 4:e5660. doi: 10.1371/journal.pone.0005660
- Roberts, E. A., Clark, A., McBeth, S., and Friedman, R. L. (2004). Molecular characterization of the Eis promoter of *Mycobacterium tuberculosis*. *J. Bacteriol.* 186, 5410–5417. doi: 10.1128/JB.186.16.5410-5417.2004
- Rominski, A., Selchow, P., Becker, K., Brulle, J. K., Dal Molin, M., and Sander, P. (2017). Elucidation of *Mycobacterium abscessus* aminoglycoside and capreomycin resistance by targeted deletion of three putative resistance genes. *J. Antimicrob. Chemother.* 72, 2191–2200. doi: 10.1093/jac/dkx125
- Samuel, L. P., Song, C. H., Wei, J., Roberts, E. A., Dahl, J. L., Barry, C. E., et al. (2007). Expression, production and release of the Eis protein by *Mycobacterium tuberculosis* during infection of macrophages and its effect on cytokine secretion. *Microbiology* 153(Pt 2), 529–540. doi: 10.1099/mic.0.2006/002642-0
- Shcherbakov, D., Akbergenov, R., Matt, T., Sander, P., Andersson, D. I., and Botzger, E. C. (2010). Directed mutagenesis of *Mycobacterium smegmatis* 16S rRNA to reconstruct the in vivo evolution of aminoglycoside resistance in *Mycobacterium tuberculosis*. *Mol. Microbiol.* 77, 830–840. doi: 10.1111/j.1365-2958.2010.07218.x
- Shell, S. S., Wang, J., Lapierre, P., Mir, M., Chase, M. R., Pyle, M. M., et al. (2015). Leaderless transcripts and small proteins are common features of the mycobacterial translational landscape. *PLoS Genet.* 11:e1005641. doi: 10.1371/journal.pgen.1005641
- Shi, K., Caldwell, S. J., Fong, D. H., and Berghuis, A. M. (2013). Prospects for circumventing aminoglycoside kinase mediated antibiotic resistance. *Front. Cell. Infect. Microbiol.* 3:22. doi: 10.3389/fcimb.2013.00022
- Shin, D. M., Jeon, B. Y., Lee, H. M., Jin, H. S., Yuk, J. M., Song, C. H., et al. (2010). *Mycobacterium tuberculosis* Eis regulates autophagy, inflammation, and cell death through redox-dependent signaling. *PLoS Pathog.* 6:e1001230. doi: 10.1371/journal.ppat.1001230
- Smith, C. A., and Baker, E. N. (2002). Aminoglycoside antibiotic resistance by enzymatic deactivation. *Curr. Drug Targets Infect. Disord.* 2, 143–160. doi: 10.2174/1568005023342533
- Stover, C. K., de la Cruz, V. F., Fuerst, T. R., Burlein, J. E., Benson, L. A., Bennett, L. T., et al. (1991). New use of BCG for recombinant vaccines. *Nature* 351, 456–460. doi: 10.1038/351456a0
- Suay-Garcia, B., and Perez-Gracia, M. T. (2018). Future prospects for *Neisseria gonorrhoeae* treatment. *Antibiotics* 7:E49. doi: 10.3390/antibiotics7020049
- Tsodikov, O. V., Green, K. D., and Garneau-Tsodikova, S. (2014). A random sequential mechanism of aminoglycoside acetylation by *Mycobacterium tuberculosis* Eis protein. *PLoS One* 9:e92370. doi: 10.1371/journal.pone.0092370
- Udou, T., Mizuguchi, Y., and Wallace, R. J. Jr. (1987). Patterns and distribution of aminoglycoside-acetylating enzymes in rapidly growing mycobacteria. *Am. Rev. Respir. Dis.* 136, 338–343. doi: 10.1164/ajrccm/136.2.338
- Udou, T., Mizuguchi, Y., and Wallace, R. J. Jr. (1989). Does aminoglycoside-acetyltransferase in rapidly growing mycobacteria have a metabolic function in addition to aminoglycoside inactivation? *FEMS Microbiol. Lett.* 48, 227–230. doi: 10.1111/j.1574-6968.1989.tb03304.x
- Udou, T., Mizuguchi, Y., and Yamada, T. (1986). Biochemical mechanisms of antibiotic resistance in a clinical isolate of *Mycobacterium fortuitum*. Presence of beta-lactamase and aminoglycoside-acetyltransferase and possible participation of altered drug transport on the resistance mechanism. *Am. Rev. Respir. Dis.* 133, 653–657. doi: 10.1164/arrd.1986.133.4.653
- Vetting, M., Roderick, S. L., Hegde, S., Magnet, S., and Blanchard, J. S. (2003). What can structure tell us about in vivo function? The case of aminoglycoside-resistance genes. *Biochem. Soc. Trans.* 31(Pt 3), 520–522. doi: 10.1042/bst0310520
- Vetting, M. W., Hegde, S. S., Javid-Majid, F., Blanchard, J. S., and Roderick, S. L. (2002). Aminoglycoside 2'-N-acetyltransferase from *Mycobacterium tuberculosis* in complex with coenzyme A and aminoglycoside substrates. *Nat. Struct. Biol.* 9, 653–658. doi: 10.1038/nsb830
- Waglechner, N., and Wright, G. D. (2017). Antibiotic resistance: it's bad, but why isn't it worse? *BMC Biol.* 15:84. doi: 10.1186/s12915-017-0423-1
- Wallace, R. J. Jr., Hull, S. I., Bobey, D. G., Price, K. E., Swenson, J. M., Steele, L. C., et al. (1985). Mutational resistance as the mechanism of acquired drug resistance to aminoglycosides and antibacterial agents in *Mycobacterium fortuitum* and *Mycobacterium chelonae*. Evidence is based on plasmid analysis, mutational frequencies, and aminoglycoside-modifying enzyme assays. *Am. Rev. Respir. Dis.* 132, 409–416. doi: 10.1164/arrd.1985.132.2.409
- Wei, J., Dahl, J. L., Moulder, J. W., Roberts, E. A., O'Gaora, P., Young, D. B., et al. (2000). Identification of a *Mycobacterium tuberculosis* gene that enhances mycobacterial survival in macrophages. *J. Bacteriol.* 182, 377–384. doi: 10.1128/JB.182.2.377-384.2000
- Wilby, M. J., Green, K. D., Gajadeera, C. S., Hou, C., Tsodikov, O. V., Posey, J. E., et al. (2016). Potent inhibitors of acetyltransferase Eis overcome kanamycin resistance in *Mycobacterium tuberculosis*. *ACS Chem. Biol.* 11, 1639–1646. doi: 10.1021/acscchembio.6b00110
- World Health Organization [WHO] (2010). *Treatment of Tuberculosis Guidelines*. Geneva: World Health Organization. doi: 10.1099/mic.0.024638-0
- Wu, S., Barnes, P. F., Samten, B., Pang, X., Rodrigue, S., Ghanny, S., et al. (2009). Activation of the Eis gene in a W-Beijing strain of *Mycobacterium tuberculosis* correlates with increased SigA levels and enhanced intracellular growth. *Microbiology* 155(Pt 4), 1272–1281. doi: 10.1099/mic.0.024638-0
- Yoon, H. J., Kim, K. H., Yang, J. K., Suh, S. W., Kim, H., and Jang, S. (2013). A docking study of enhanced intracellular survival protein from *Mycobacterium tuberculosis* with human DUSP16/MKP-7. *J. Synchrotron Radiat.* 20(Pt 6), 929–932. doi: 10.1107/S0909049513021341
- Zaunbrecher, M. A., Sikes, R. D. Jr., Metchock, B., Shinnick, T. M., and Posey, J. E. (2009). Overexpression of the chromosomally encoded aminoglycoside acetyltransferase Eis confers kanamycin resistance in *Mycobacterium tuberculosis*. *Proc. Natl. Acad. Sci. U.S.A.* 106, 20004–20009. doi: 10.1073/pnas.0907925106
- Zhang, Y., and Yew, W. W. (2009). Mechanisms of drug resistance in *Mycobacterium tuberculosis*. *Int. J. Tuberc. Lung Dis.* 13, 1320–1330.

**Conflict of Interest Statement:** The authors declare that the research was conducted in the absence of any commercial or financial relationships that could be construed as a potential conflict of interest.

Copyright © 2019 Sanz-García, Anoz-Carbonell, Pérez-Herrán, Martín, Lucía, Rodrigues and Ainsa. This is an open-access article distributed under the terms of the Creative Commons Attribution License (CC BY). The use, distribution or reproduction in other forums is permitted, provided the original author(s) and the copyright owner(s) are credited and that the original publication in this journal is cited, in accordance with accepted academic practice. No use, distribution or reproduction is permitted which does not comply with these terms.



# Bibliography



- Abbas, C.A., and Sibirny, A.A. (2011). Genetic control of biosynthesis and transport of riboflavin and flavin nucleotides and construction of robust biotechnological producers. *Microbiol. Mol. Biol. Rev.* *75*, 321–360.
- Adamovich, Y., Shlomai, A., Tsvetkov, P., Umansky, K.B., Reuven, N., Estall, J.L., Spiegelman, B.M., and Shaul, Y. (2013). The Protein Level of PGC-1, a Key Metabolic Regulator, Is Controlled by NADH-NQO1. *Mol. Cell. Biol.* *33*, 2603–2613.
- Ammelburg, M., Hartmann, M.D., Djuranovic, S., Alva, V., Koretke, K.K., Martin, J., Sauer, G., Truffault, V., Zeth, K., Lupas, A.N., et al. (2007). A CTP-Dependent Archaeal Riboflavin Kinase Forms a Bridge in the Evolution of Cradle-Loop Barrels. *Structure* *15*, 1577–1590.
- Anoz-Carbonell, E., Rivero, M., Polo, V., Velázquez-Campoy, A., and Medina, M. (2020a). Human riboflavin kinase: Species-specific traits in the biosynthesis of the FMN cofactor. *FASEB J.* *34*, 10871–10886.
- Anoz-Carbonell, E., Timson, D.J., Pey, A.L., and Medina, M. (2020b). The Catalytic Cycle of the Antioxidant and Cancer-Associated Human NQO1 Enzyme: Hydride Transfer, Conformational Dynamics and Functional Cooperativity. *Antioxidants* *9*.
- Anusevičius, Ž., Šarlauskas, J., and Čenas, N. (2002). Two-electron reduction of quinones by rat liver NAD(P)H:quinone oxidoreductase: Quantitative structure-activity relationships. *Arch. Biochem. Biophys.* *404*, 254–262.
- Arilla-Luna, S., Serrano, A., and Medina, M. (2019). Specific Features for the Competent Binding of Substrates at the FMN Adenylyltransferase Site of FAD Synthase from *Corynebacterium ammoniagenes*. *Int. J. Mol. Sci.* *20*, 5083.
- Asher, G., Lotem, J., Cohen, B., Sachs, L., and Shaul, Y. (2001). Regulation of p53 stability and p53-dependent apoptosis by NADH quinone oxidoreductase 1. *Proc. Natl. Acad. Sci. U. S. A.* *98*, 1188–1193.
- Asher, G., Tsvetkov, P., Kahana, C., and Shaul, Y. (2005). A mechanism of ubiquitin-independent proteasomal degradation of the tumor suppressors p53 and p73. *Genes Dev.* *19*, 316–321.
- Asher, G., Dym, O., Tsvetkov, P., Adler, J., and Shaul, Y. (2006). The crystal structure of NAD(P)H quinone oxidoreductase 1 in complex with its potent inhibitor dicoumarol. *Biochemistry* *45*, 6372–6378.
- Bafunno, V., Giancaspero, T.A., Brizio, C., Bufano, D., Passarella, S., Boles, E., and Barile, M. (2004). Riboflavin uptake and FAD synthesis in *Saccharomyces cerevisiae* mitochondria: involvement of the Flx1p carrier in FAD export. *J. Biol. Chem.* *279*, 95–102.
- Barile, M., Brizio, C., De Virgilio, C., Delfino, S., Quagliariello, E., and Passarella, S. (1997). Flavin Adenine Dinucleotide and Flavin Mononucleotide Metabolism in Rat Liver. *Eur. J. Biochem.* *249*, 777–785.
- Barile, M., Brizio, C., Valenti, D., De Virgilio, C., and Passarella, S. (2000). The riboflavin/FAD cycle in rat liver mitochondria. *Eur. J. Biochem.* *267*, 4888–4900.
- Barile, M., Giancaspero, T.A., Leone, P., Galluccio, M., and Indiveri, C. (2016). Riboflavin transport and metabolism in humans. *J. Inherit. Metab. Dis.* *39*, 545–557.
- Bauer, A.K., Faiola, B., Abernethy, D.J., Marchan, R., Pluta, L.J., Wong, V.A., Roberts, K., Jaiswal, A.K., Gonzalez, F.J., Butterworth, B.E., et al. (2003a). Genetic susceptibility to benzene-induced toxicity: role of NADPH: quinone oxidoreductase-1. *Cancer Res.* *63*, 929–935.

- Bauer, S., Kemter, K., Bacher, A., Huber, R., Fischer, M., and Steinbacher, S. (2003b). Crystal structure of *Schizosaccharomyces pombe* riboflavin kinase reveals a novel ATP and riboflavin-binding fold. *J. Mol. Biol.* 326, 1463–1473.
- Beaver, S.K., Mesa-Torres, N., Pey, A.L., and Timson, D.J. (2019). NQO1: A target for the treatment of cancer and neurological diseases, and a model to understand loss of function disease mechanisms. *Biochim. Biophys. Acta - Proteins Proteomics* 1867, 663–676.
- Becker, K., Christopherson, R.I., Cowden, W.B., Hunt, N.H., and Schirmer, R.H. (1990). Flavin analogs with antimalarial activity as glutathione reductase inhibitors. *Biochem. Pharmacol.* 39, 59–65.
- van den Berg, P.A., Widengren, J., Hink, M.A., Rigler, R., and Visser, A.J. (2001). Fluorescence correlation spectroscopy of flavins and flavoenzymes: photochemical and photophysical aspects. *Spectrochim Acta A Mol Biomol Spectrosc* 57, 2135–2144.
- van den Berg, P.A.W., Feenstra, K.A., Mark, A.E., Berendsen, H.J.C., and Visser, A.J.W.G. (2002). Dynamic Conformations of Flavin Adenine Dinucleotide: Simulated Molecular Dynamics of the Flavin Cofactor Related to the Time-Resolved Fluorescence Characteristics. *J. Phys. Chem. B* 106, 8858–8869.
- Bertagnolli, B.L., and Hager, L.P. (1993). Role of flavin in acetoin production by two bacterial pyruvate oxidases. *Arch. Biochem. Biophys.* 300, 364–371.
- Beyer, R.E., Segura-Aguilar, J., Di Bernardo, S., Cavazzoni, M., Fato, R., Fiorentini, D., Galli, M.C., Setti, M., Landi, L., and Lenaz, G. (1996). The role of DT-diaphorase in the maintenance of the reduced antioxidant form of coenzyme Q in membrane systems. *Proc. Natl. Acad. Sci. U. S. A.* 93, 2528–2532.
- Bianchet, M.A., Faig, M., and Amzel, L.M. (2004). Structure and Mechanism of NAD[P]H:Quinone Acceptor Oxidoreductases (NQO). *Methods Enzymol.* 382, 144–174.
- Bowers-Komro, D.M., Yamada, Y., and McCormick, D.B. (1989). Substrate specificity and variables affecting efficiency of mammalian flavin adenine dinucleotide synthetase. *Biochemistry* 28, 8439–8446.
- Briggs, W.R., Christie, J.M., and Salomon, M. (2001). Phototropins: A new family of flavin-binding blue light receptors in plants. *Antioxidants Redox Signal.* 3, 775–788.
- Brizio, C., Galluccio, M., Wait, R., Torchetti, E.M., Bafunno, V., Accardi, R., Gianazza, E., Indiveri, C., and Barile, M. (2006). Over-expression in *Escherichia coli* and characterization of two recombinant isoforms of human FAD synthetase. *Biochem. Biophys. Res. Commun.* 344, 1008–1016.
- Cheek, S., Ginalski, K., Zhang, H., and Grishin, N. V. (2005). A comprehensive update of the sequence and structure classification of kinases. *BMC Struct. Biol.* 5.
- Chen, Y., Jie, W., Yan, W., Zhou, K., and Xiao, Y. (2012). Lysine-specific histone demethylase 1 (LSD1): A potential molecular target for tumor therapy. *Crit. Rev. Eukaryot. Gene Expr.* 22, 53–59.
- Chernyshev, A., Fleischmann, T., and Kohen, A. (2007). Thymidyl biosynthesis enzymes as antibiotic targets. *Appl. Microbiol. Biotechnol.* 74, 282–289.
- Christen, B., Abeliuk, E., Collier, J.M., Kalogeraki, V.S., Passarelli, B., Collier, J.A., Fero, M.J., McAdams, H.H., and Shapiro, L. (2011). The essential genome of a bacterium. *Mol. Syst. Biol.* 7, 528.

- Cialabrini, L., Ruggieri, S., Kazanov, M.D., Sorci, L., Mazzola, F., Orsomando, G., Osterman, A.L., and Raffaelli, N. (2013). Genomics-Guided Analysis of NAD Recycling Yields Functional Elucidation of COG1058 as a New Family of Pyrophosphatases. *PLoS One* 8, e65595.
- Clark, W.M., and Lowe, H.J. (1956). Studies on oxidation-reduction. XXIV. Oxidation-reduction potentials of flavin adenine dinucleotide. *J Biol Chem* 221, 983–992.
- Colucci, M.A., Couch, G.D., and Moody, C.J. (2008). Natural and synthetic quinones and their reduction by the quinone reductase enzyme NQO1: From synthetic organic chemistry to compounds with anticancer potential. *Org. Biomol. Chem.* 6, 637–656.
- Crooks, G.E., Hon, G., Chandonia, J.M., and Brenner, S.E. (2004). WebLogo: a sequence logo generator. *Genome Res* 14, 1188–1190.
- Crossley, R.A., Gaskin, D.J.H., Holmes, K., Mulholland, F., Wells, J.M., Kelly, D.J., van Vliet, A.H.M., and Walton, N.J. (2007). Riboflavin biosynthesis is associated with assimilatory ferric reduction and iron acquisition by *Campylobacter jejuni*. *Appl. Environ. Microbiol.* 73, 7819–7825.
- Cushman, M., Mihalic, J.T., Kis, K., and Bacher, A. (1999). Design and synthesis of 6-(6-d-ribitylamino-2,4-dihydroxypyrimidin-5-yl)-1-hexylphosphonic acid, a potent inhibitor of lumazine synthase. *Bioorganic Med. Chem. Lett.* 9, 39–42.
- Dagley, S. (1987). Lessons From Biodegradation. *Annu. Rev. Microbiol.* 41, 1–24.
- Daniels, L., Bakhiet, N., and Harmon, K. (1985). Widespread distribution of a 5-deazaflavin cofactor in actinomyces and related bacteria. *Syst. Appl. Microbiol.* 6, 12–17.
- Danson, S., Ward, T.H., Butler, J., and Ranson, M. (2004). DT-diaphorase: A target for new anticancer drugs. *Cancer Treat. Rev.* 30, 437–449.
- Duan, Y., Chen, T., Chen, X., Jingyu, W., and Zhao, X. (2010). Enhanced riboflavin production by expressing heterologous riboflavin operon from *B. cereus* ATCC14579 in *Bacillus subtilis*. *Chinese J. Chem. Eng.* 18, 129–136.
- Dym, O., and Eisenberg, D. (2001). Sequence-structure analysis of FAD-containing proteins. *Protein Sci* 10, 1712–1728.
- Edwards, A.M. (2006). Chapter 1. General Properties of Flavins. In *Flavins: Photochemistry and Photobiology*, E. Silva, and A.M. Edwards, eds. (The Royal Society of Chemistry), pp. 1–11.
- Efimov, I., Kuusk, V., Zhang, X., and McIntire, W.S. (1998). Proposed steady-state kinetic mechanism for *Corynebacterium ammoniagenes* FAD synthetase produced by *Escherichia coli*. *Biochemistry* 37, 9716–9723.
- Ernster, L., Danielson, L., and Ljunggren, M. (1962). DT diaphorase I. Purification from the soluble fraction of rat-liver cytoplasm, and properties. *BBA - Biochim. Biophys. Acta* 58, 171–188.
- Fagerholm, R., Hofstetter, B., Tommiska, J., Aaltonen, K., Vrtel, R., Syrjäkoski, K., Kallioniemi, A., Kilpivaara, O., Mannermaa, A., Kosma, V.M., et al. (2008). NAD(P)H:quinone oxidoreductase 1 NQO1\*2 genotype (P187S) is a strong prognostic and predictive factor in breast cancer. *Nat. Genet.* 40, 844–853.
- Faig, M., Bianchet, M.A., Talalay, P., Chen, S., Winski, S., Ross, D., and Amzel, L.M. (2000). Structures of recombinant human and mouse NAD(P)H:quinone oxidoreductases: Species comparison and structural changes with substrate binding and release. *Proc. Natl. Acad. Sci.* 97, 3177–3182.

- Faig, M., Bianchet, M.A., Winski, S., Hargreaves, R., Moody, C.J., Hudnott, A.R., Ross, D., and Amzel, L.M. (2001). Structure-based development of anticancer drugs: Complexes of NAD(P)H:quinone oxidoreductase 1 with chemotherapeutic quinones. *Structure* 9, 659–667.
- Fedorovich, D., Protchenko, O., and Lesuisse, E. (1999). Iron uptake by the yeast *Pichia guilliermondii*. Flavinogenesis and reductive iron assimilation are co-regulated processes. *Biometals an Int. J. Role Met. Ions Biol. Biochem. Med.* 12, 295–300.
- Fischer, M., and Bacher, A. (2006). Biosynthesis of vitamin B2 in plants. *Physiol. Plant.* 126, 304–318.
- Fisher, J., Spencer, R., and Walsh, C. (1976). Enzyme-catalyzed redox reactions with the flavin analogues 5-deazariboflavin, 5-deazariboflavin 5'-phosphate, and 5-deazariboflavin 5'-diphosphate, 5'→5'-adenosine ester. *Biochemistry* 15, 1054–1064.
- Forneris, F., Binda, C., Vanoni, M.A., Mattevi, A., and Battaglioli, E. (2005). Histone demethylation catalysed by LSD1 is a flavin-dependent oxidative process. *FEBS Lett.* 579, 2203–2207.
- Foster, C.E., Bianchet, M.A., Talalay, P., Zhao, Q., and Amzel, L.M. (1999). Crystal structure of human quinone reductase type 2, a metalloflavoprotein. *Biochemistry* 38, 9881–9886.
- Fraaije, M.W., and Mattevi, A. (2000). Flavoenzymes: Diverse catalysts with recurrent features. *Trends Biochem. Sci.* 25, 126–132.
- Frago, S., Martínez-Júlvez, M., Serrano, A., and Medina, M. (2008). Structural analysis of FAD synthetase from *Corynebacterium ammoniagenes*. *BMC Microbiol.* 8, 160.
- Frago, S., Velázquez-Campoy, A., and Medina, M. (2009). The puzzle of ligand binding to *Corynebacterium ammoniagenes* FAD synthetase. *J. Biol. Chem.* 284, 6610–6619.
- Frago, S., Lans, I., Navarro, J.A., Hervás, M., Edmondson, D.E., De la Rosa, M.A., Gómez-Moreno, C., Mayhew, S.G., and Medina, M. (2010). Dual role of FMN in flavodoxin function: electron transfer cofactor and modulation of the protein-protein interaction surface. *Biochim Biophys Acta* 1797, 262–271.
- Di Francesco, A., Di Germanio, C., Panda, A.C., Huynh, P., Peadar, R., Navas-Enamorado, I., Bastian, P., Lehrmann, E., Diaz-Ruiz, A., Ross, D., et al. (2016). Novel RNA-binding activity of NQO1 promotes SERPINA1 mRNA translation. *Free Radic. Biol. Med.* 99, 225–233.
- Fuchs, K.R., Shekels, L.L., and Bernlohr, D.A. (1992). Analysis of the ACP1 gene product: classification as an FMN phosphatase. *Biochem Biophys Res Commun* 189, 1598–1605.
- Gaedigk, A., Tyndale, R.F., Jurima-Romet, M., Sellers, E.M., Grant, D.M., and Leeder, J.S. (1998). NAD(P)H:quinone oxidoreductase: polymorphisms and allele frequencies in Caucasian, Chinese and Canadian Native Indian and Inuit populations. *Pharmacogenetics* 8, 305–313.
- Galluccio, M., Brizio, C., Torchetti, E.M., Ferranti, P., Gianazza, E., Indiveri, C., and Barile, M. (2007). Over-expression in *Escherichia coli*, purification and characterization of isoform 2 of human FAD synthetase. *Protein Expr. Purif.* 52, 175–181.
- García-Angulo, V.A. (2017). Overlapping riboflavin supply pathways in bacteria. *Crit. Rev. Microbiol.* 43, 196–209.
- García, J.I., Medina, M., Sancho, J., Alonso, P.J., Gomez-Moreno, C., Mayoral, J.A., and Martínez, J.I. (2002). Theoretical analysis of the electron spin density distribution of the flavin semiquinone isoalloxazine ring within model protein environments. *J. Phys. Chem. A* 106, 4729–4735.



- Gasdaska, P.Y., Fisher, H., and Powis, G. (1995). An Alternatively Spliced Form of NQO1 (DT-Diaphorase) Messenger RNA Lacking the Putative Quinone Substrate Binding Site Is Present in Human Normal and Tumor Tissues. *Cancer Res.* 55, 2542 LP – 2547.
- Ghisla, S., and Hemmerich, P. (1971). Synthesis of the flavocoenzyme of monoamine oxidase. *FEBS Lett.* 16, 229–232.
- Ghisla, S., and Massey, V. (1986). New flavins for old: artificial flavins as active site probes of flavoproteins. *Biochem J* 239, 1–12.
- Ghisla, S., and Massey, V. (1989). Mechanisms of flavoprotein-catalyzed reactions. *Eur J Biochem* 181, 1–17.
- Giancaspero, T.A., Locato, V., de Pinto, M.C., De Gara, L., and Barile, M. (2009). The occurrence of riboflavin kinase and FAD synthetase ensures FAD synthesis in tobacco mitochondria and maintenance of cellular redox status. *FEBS J.* 276, 219–231.
- Giancaspero, T.A., Busco, G., Panebianco, C., Carmone, C., Miccolis, A., Liuzzi, G.M., Colella, M., and Barile, M. (2013). FAD synthesis and degradation in the nucleus create a local flavin cofactor pool. *J. Biol. Chem.* 288, 29069–29080.
- Giancaspero, T.A., Galluccio, M., Miccolis, A., Leone, P., Eberini, I., Iametti, S., Indiveri, C., and Barile, M. (2015a). Human FAD synthase is a bi-functional enzyme with a FAD hydrolase activity in the molybdopterin binding domain. *Biochem. Biophys. Res. Commun.* 465, 443–449.
- Giancaspero, T.A., Colella, M., Brizio, C., Difonzo, G., Fiorino, G.M., Leone, P., Brandsch, R., Bonomi, F., Iametti, S., and Barile, M. (2015b). Remaining challenges in cellular flavin cofactor homeostasis and flavoprotein biogenesis. *Front Chem* 3, 30.
- Gomes, B., and McCormick, D.B. (1983). Purification and general characterization of FAD synthetase from rat liver. *Proc. Soc. Exp. Biol. Med. Soc. Exp. Biol. Med. (New York, N.Y.)* 172, 250–254.
- Gong, M., Hay, S., Marshall, K.R., Munro, A.W., and Scrutton, N.S. (2007). DNA binding suppresses human AIF-M2 activity and provides a connection between redox chemistry, reactive oxygen species, and apoptosis. *J. Biol. Chem.* 282, 30331–30340.
- Goodall, E.C.A., Robinson, A., Johnston, I.G., Jabbari, S., Turner, K.A., Cunningham, A.F., Lund, P.A., Cole, J.A., and Henderson, I.R. (2018). The essential genome of *Escherichia coli* K-12. *MBio* 9, 1–18.
- Granjeiro, J.M., Ferreira, C. V, Juca, M.B., Taga, E.M., and Aoyama, H. (1997). Bovine kidney low molecular weight acid phosphatase: FMN-dependent kinetics. *Biochem Mol Biol Int* 41, 1201–1208.
- Griffin, J.E., Gawronski, J.D., Dejesus, M.A., Ioerger, T.R., Akerley, B.J., and Sasseti, C.M. (2011). High-resolution phenotypic profiling defines genes essential for mycobacterial growth and cholesterol catabolism. *PLoS Pathog* 7, e1002251.
- Grill, S., Busenbender, S., Pfeiffer, M., Köhler, U., and Mack, M. (2008). The bifunctional flavokinase/flavin adenine dinucleotide synthetase from *Streptomyces davawensis* produces inactive flavin cofactors and is not involved in resistance to the antibiotic roseoflavin. *J. Bacteriol.* 190, 1546–1553.
- Grininger, M., Staudt, H., Johansson, P., Wachtveitl, J., and Oesterhelt, D. (2009). Dodecin is the key player in flavin homeostasis of archaea. *J. Biol. Chem.* 284, 13068–13076.

- Gromer, S., Urig, S., and Becker, K. (2004). The Thioredoxin System - From Science to Clinic. *Med. Res. Rev.* 24, 40–89.
- Gross, E., Kastner, D.B., Kaiser, C.A., and Fass, D. (2004). Structure of Ero1p, source of disulfide bonds for oxidative protein folding in the cell. *Cell* 117, 601–610.
- Gudipati, V., Koch, K., Lienhart, W.D., and Macheroux, P. (2014). The flavoproteome of the yeast *Saccharomyces cerevisiae*. *Biochim Biophys Acta* 1844, 535–544.
- Gutiérrez-Preciado, A., Torres, A.G., Merino, E., Bonomi, H.R., Goldbaum, F.A., and García-Angulo, V.A. (2015). Extensive Identification of Bacterial Riboflavin Transporters and Their Distribution across Bacterial Species. *PLoS One* 10, e0126124.
- Hagihara, T., Fujio, T., and Aisaka, K. (1995). Cloning of FAD synthetase gene from *Corynebacterium ammoniagenes* and its application to FAD and FMN production. *Appl. Microbiol. Biotechnol.* 42, 724–729.
- Herguedas, B., Martínez-Júlvez, M., Frago, S., Medina, M., and Hermoso, J.A. (2009). Crystallization and preliminary X-ray diffraction studies of FAD synthetase from *Corynebacterium ammoniagenes*. *Acta Crystallogr. Sect. F* 65, 1285–1288.
- Herguedas, B., Martínez-Júlvez, M., Frago, S., Medina, M., Hermoso, J. a., Martínez-Júlvez, M., Frago, S., Medina, M., Hermoso, J. a., Martínez-Júlvez, M., et al. (2010). Oligomeric State in the Crystal Structure of Modular FAD Synthetase Provides Insights into Its Sequential Catalysis in Prokaryotes. *J. Mol. Biol.* 400, 218–230.
- Herguedas, B., Lans, I., Sebastián, M., Hermoso, J.A., Martínez-Júlvez, M., and Medina, M. (2015). Structural insights into the synthesis of FMN in prokaryotic organisms. *Acta Crystallogr. Sect. D Biol. Crystallogr.* 71, 2526–2542.
- Heuts, D.P.H.M., Scrutton, N.S., McIntire, W.S., and Fraaije, M.W. (2009). What's in a covalent bond? *FEBS J.* 276, 3405–3427.
- Hirano, G., Izumi, H., Yasuniwa, Y., Shimajiri, S., Ke-Yong, W., Sasagiri, Y., Kusaba, H., Matsumoto, K., Hasegawa, T., Akimoto, M., et al. (2011). Involvement of riboflavin kinase expression in cellular sensitivity against cisplatin. *Int J Oncol* 38, 893–902.
- Hosoda, S., Nakamura, W., and Hayashi, K. (1974). Properties and reaction mechanism of DT diaphorase from rat liver. *J. Biol. Chem.* 249, 6416–6423.
- Howe, J. a., Wang, H., Fischmann, T.O., Balibar, C.J., Xiao, L., Galgoci, A.M., Malinverni, J.C., Mayhood, T., Villafania, A., Nahvi, A., et al. (2015). Selective small-molecule inhibition of an RNA structural element. *Nature* 526, 672–677.
- Hu, L.T., Stamberg, J., and Pan, S. (1996). The NAD(P)H:quinone oxidoreductase locus in human colon carcinoma HCT 116 cells resistant to mitomycin C. *Cancer Res.* 56, 5253–5259.
- Hu, P., Pan, Y., Wang, C., Zhang, W., Huang, H., Wang, J., and Zhang, N. (2020). FLAD1 is up-regulated in Gastric Cancer and is a potential prediction of prognosis. *Int. J. Med. Sci.* 17, 1763–1772.
- Huerta, C., Borek, D., Machius, M., Grishin, N. V, and Zhang, H. (2009). Structure and mechanism of a eukaryotic FMN adenylyltransferase. *J Mol Biol* 389, 388–400.
- Huerta, C., Grishin, N. V, and Zhang, H. (2013). The “super mutant” of yeast FMN adenylyltransferase enhances the enzyme turnover rate by attenuating product inhibition. *Biochemistry* 52, 3615–3617.

- Hümbelin, M., Griesser, V., Keller, T., Schurter, W., Haiker, M., Hohmann, H.P., Ritz, H., Richter, G., Bacher, A., and Van Loon, A.P.G.M. (1999). GTP cyclohydrolase II and 3,4-dihydroxy-2-butanone 4-phosphate synthase are rate-limiting enzymes in riboflavin synthesis of an industrial *Bacillus subtilis* strain used for riboflavin production. *J. Ind. Microbiol. Biotechnol.* *22*, 1–7.
- Hutchison, C.A., Chuang, R.Y., Noskov, V.N., Assad-Garcia, N., Deerinck, T.J., Ellisman, M.H., Gill, J., Kannan, K., Karas, B.J., Ma, L., et al. (2016). Design and synthesis of a minimal bacterial genome. *Science* *351*.
- Iamurri, S.M., Daugherty, A.B., Edmondson, D.E., and Lutz, S. (2013). Truncated FAD synthetase for direct biocatalytic conversion of riboflavin and analogs to their corresponding flavin mononucleotides. *Protein Eng. Des. Sel.* *26*, 791–795.
- Igarashi, K., Verhagen, M.F., Samejima, M., Schüle, M., Eriksson, K.E., and Nishino, T. (1999). Cellobiose dehydrogenase from the fungi *Phanerochaete chrysosporium* and *Humicola insolens*. A flavohemoprotein from *Humicola insolens* contains 6-hydroxy-FAD as the dominant active cofactor. *J. Biol. Chem.* *274*, 3338–3344.
- Ingram, B.O., Turbyfill, J.L., Bledsoe, P.J., Jaiswal, A.K., and Stafford, D.W. (2013). Assessment of the contribution of NAD(P)H-dependent quinone oxidoreductase 1 (NQO1) to the reduction of vitamin K in wild-type and NQO1-deficient mice. *Biochem. J.* *456*, 47–54.
- Jaiswal, A.K., Burnett, P., Adesnik, M., and McBride, O.W. (1990). Nucleotide and Deduced Amino Acid Sequence of a Human cDNA (NQO2) Corresponding to a Second Member of the NAD(P)H:Quinone Oxidoreductase Gene Family. Extensive Polymorphism at the NQO2 Gene Locus on Chromosome 6. *Biochemistry* *29*, 1899–1906.
- Joosten, V., and van Berkel, W.J. (2007). Flavoenzymes. *Curr Opin Chem Biol* *11*, 195–202.
- Jorns, M.S., Baldwin, E.T., Sancar, G.B., and Sancar, A. (1987). Action mechanism of Escherichia coli DNA photolyase. II. Role of the chromophores in catalysis. *J Biol Chem* *262*, 486–491.
- Karthikeyan, S., Zhou, Q., Mseeh, F., Grishin, N. V., Osterman, A.L., and Zhang, H. (2003a). Crystal Structure of Human Riboflavin Kinase Reveals a  $\beta$  Barrel Fold and a Novel Active Site. *Arch. Structure* *11*, 265–273.
- Karthikeyan, S., Zhou, Q., Osterman, A.L., and Zhang, H. (2003b). Ligand Binding-Induced Conformational Changes in Riboflavin Kinase: Structural Basis for the Ordered Mechanism. *Biochemistry* *42*, 12532–12538.
- Kasai, S., Nakano, H., Maeda, K., and Matsui, K. (1990). Purification, properties, and function of flavokinase from rat intestinal mucosa. *J Biochem* *107*, 298–303.
- Kashchenko, V.E., and Shavlovsky, G.M. (1976). Purification and properties of riboflavin kinase from yeast *Pichia guilliermondii* (Russian). *Biokhimiya* *41*, 376–383.
- Kearney, E.B. (1952). The interaction of yeast flavokinase with riboflavin analogues. *J. Biol. Chem.* *194*, 747–754.
- Kearney, E.B., Goldenberg, J., Lipsick, J., and Perl, M. (1979). Flavokinase and FAD synthetase from *Bacillus subtilis* specific for reduced flavins. *J. Biol. Chem.* *254*, 9551–9557.
- Keilin, D., and Hartree, E.F. (1946). Prosthetic group of glucose oxidase (notatin). *Nature* *157*, 801.
- Kobayashi, K., Ehrlich, S.D., Albertini, A., Amati, G., Andersen, K.K., Arnaud, M., Asai, K., Ashikaga, S., Aymerich, S., Bessieres, P., et al. (2003). Essential *Bacillus subtilis* genes. *Proc. Natl. Acad. Sci. U. S. A.* *100*, 4678–4683.

- Krupa, A., Sandhya, K., Srinivasan, N., and Jonnalagadda, S. (2003). A conserved domain in prokaryotic bifunctional FAD synthetases can potentially catalyze nucleotide transfer. *Trends Biochem Sci* 28, 9–12.
- Langer, S., Hashimoto, M., Hobl, B., Mathes, T., and Mack, M. (2013). Flavoproteins are potential targets for the antibiotic roseoflavin in *Escherichia coli*. *J Bacteriol* 195, 4037–4045.
- Lans, I., Seco, J., Serrano, A., Burbano, R., Cossio, P., Daza, M.C., and Medina, M. (2018). The dimer-of-trimers assembly prevents catalysis at the transferase site of prokaryotic FAD synthase. *Biophys. J.* 115, 988–995.
- Lee, R.S., and Ford, H.C. (1997). Purification and characterization of 5'-nucleotidase/FAD pyrophosphatase from human placenta. *Methods Enzym.* 280, 424–436.
- Lee, C.P., Simard-Duquesne, N., Ernster, L., and Hoberman, H.D. (1965). Stereochemistry of hydrogen-transfer in the energy-linked pyridine nucleotide transhydrogenase and related reactions. *Biochim. Biophys. Acta* 105, 397–409.
- Lee, E.R., Blount, K.F., and Breaker, R.R. (2009). Roseoflavin is a natural antibacterial compound that binds to FMN riboswitches and regulates gene expression. *RNA Biol* 6, 187–194.
- Lee, J., Kim, K.S., Lee, M.H., Kim, Y.S., Lee, M.H., Lee, S.E., Kim, Y.K., Ryu, M.J., Kim, S.J., Choi, M.J., et al. (2013). NAD(P)H: Quinone Oxidoreductase 1 and NRH: Quinone Oxidoreductase 2 polymorphisms in papillary thyroid microcarcinoma: Correlation with phenotype. *Yonsei Med. J.* 54, 1158–1167.
- Leone, P., Galluccio, M., Barbiroli, A., Eberini, I., Tolomeo, M., Vrenna, F., Gianazza, E., Iametti, S., Bonomi, F., Indiveri, C., et al. (2018). Bacterial Production, Characterization and Protein Modeling of a Novel Monofunctional Isoform of FAD Synthase in Humans: An Emergency Protein? *Molecules* 23, 116.
- Leone, P., Galluccio, M., Quarta, S., Anoz-Carbonell, E., Medina, M., Indiveri, C., and Barile, M. (2019). Mutation of Aspartate 238 in FAD Synthase Isoform 6 Increases the Specific Activity by Weakening the FAD Binding. *Int. J. Mol. Sci.* 20.
- Leulliot, N., Blondeau, K., Keller, J., Ulryck, N., Quevillon-Cheruel, S., and van Tilbeurgh, H. (2010). Crystal structure of yeast FAD synthetase (Fad1) in complex with FAD. *J Mol Biol* 398, 641–646.
- Lewis, K. (2013). Platforms for antibiotic discovery. *Nat. Rev. Drug Discov.* 12, 371–387.
- Leyes, D., and Scrutton, N.S. (2016). Sweating the assets of flavin cofactors: New insight of chemical versatility from knowledge of structure and mechanism. *Curr. Opin. Struct. Biol.* 41, 19–26.
- Li, R., Bianchet, M.A., Talalay, P., and Amzel, L.M. (1995). The three-dimensional structure of NAD(P)H:quinone reductase a flavoprotein involved in cancer chemoprotection and chemotherapy: Mechanism of the two-electron reduction. *Proc. Natl. Acad. Sci. U. S. A.* 92, 8846–8850.
- Li, Z., Zhang, Y., Jin, T., Men, J., Lin, Z., Qi, P., Piao, Y., and Yan, G. (2015). NQO1 protein expression predicts poor prognosis of non-small cell lung cancers. *BMC Cancer* 15, 207.
- Lienhart, W.-D., Strandback, E., Gudipati, V., Koch, K., Binter, A., Uhl, M.K., Rantasa, D.M., Bourgeois, B., Madl, T., Zangger, K., et al. (2017). Catalytic competence, structure and stability of the cancer-associated R139W variant of the human NAD(P)H:quinone oxidoreductase 1 (NQO1). *FEBS J.* 284, 1233–1245.

- Lienhart, W.D., Gudipati, V., and MacHeroux, P. (2013). The human flavoproteome. *Arch Biochem Biophys* 535, 150–162.
- Lienhart, W.D., Gudipati, V., Uhl, M.K., Binter, A., Pulido, S.A., Saf, R., Zangger, K., Gruber, K., and Macheroux, P. (2014). Collapse of the native structure caused by a single amino acid exchange in human NAD(P)H:Quinone oxidoreductase. *FEBS J.* 281, 4691–4704.
- Lind, C., Hochstein, P., and Ernster, L. (1982). DT-diaphorase as a quinone reductase: A cellular control device against semiquinone and superoxide radical formation. *Arch. Biochem. Biophys.* 216, 178–185.
- Lind, C., Cadenas, E., Hochstein, P., and Ernster, L. (1990). DT-diaphorase: Purification, properties, and function. *Methods Enzymol.* 186, 287–301.
- Liu, B., Liu, H., Zhong, D., and Lin, C. (2010). Searching for a photocycle of the cryptochrome photoreceptors. *Curr Opin Plant Biol* 13, 578–586.
- Liu, X., Gallay, C., Kjos, M., Domenech, A., Slager, J., van Kessel, S.P., Knoop, K., Sorg, R.A., Zhang, J.-R., and Veening, J.-W. (2017). High-throughput CRISPRi phenotyping identifies new essential genes in *Streptococcus pneumoniae*. *Mol. Syst. Biol.* 13, 931.
- Logvinenko, E., Shavlovskii, G., Trach, V., and Sibirnyĭ, V. (1973). Role of flavins in regulating riboflavin synthetase synthesis in *Pichia guilliermondii* and *Candida utilis*. *Mikrobiologiya* 42.
- Long, D.J. 2nd, Gaikwad, A., Multani, A., Pathak, S., Montgomery, C.A., Gonzalez, F.J., and Jaiswal, A.K. (2002). Disruption of the NAD(P)H:quinone oxidoreductase 1 (NQO1) gene in mice causes myelogenous hyperplasia. *Cancer Res.* 62, 3030–3036.
- Ludwig, M.L., Patridge, K.A., Metzger, A.L., Dixon, M.M., Eren, M., Feng, Y., and Swenson, R.P. (1997). Control of oxidation-reduction potentials in flavodoxin from *Clostridium beijerinckii*: the role of conformation changes. *Biochemistry* 36, 1259–1280.
- Ma, Y., Kong, J., Yan, G., Ren, X., Jin, D., Jin, T., Lin, L., and Lin, Z. (2014). NQO1 overexpression is associated with poor prognosis in squamous cell carcinoma of the uterine cervix. *BMC Cancer* 14, 414.
- Macheroux, P., Kappes, B., and Ealick, S.E. (2011). Flavogenomics - A genomic and structural view of flavin-dependent proteins. *FEBS J.* 278, 2625–2634.
- Mack, M., and Grill, S. (2006). Riboflavin analogs and inhibitors of riboflavin biosynthesis. *Appl. Microbiol. Biotechnol.* 71, 265–275.
- Manstein, D.J., and Pai, E.F. (1986). Purification and characterization of FAD synthetase from *Brevibacterium ammoniagenes*. *J. Biol. Chem.* 261, 16169–16173.
- Marcuello, C., Arilla-Luna, S., Medina, M., and Lostao, A. (2013). Detection of a quaternary organization into dimer of trimers of *Corynebacterium ammoniagenes* FAD synthetase at the single-molecule level and at the in cell level. *Biochim. Biophys. Acta - Proteins Proteomics* 1834, 665–676.
- Marshall, K.R., Gong, M., Wodke, L., Lamb, J.H., Jones, D.J.L., Farmer, P.B., Scrutton, N.S., and Munro, A.W. (2005). The human apoptosis-inducing protein AMID is an oxidoreductase with a modified flavin cofactor and DNA binding activity. *J. Biol. Chem.* 280, 30735–30740.
- Marsili, E., Baron, D.B., Shikhare, I.D., Coursolle, D., Gralnick, J.A., and Bond, D.R. (2008). *Shewanella* secretes flavins that mediate extracellular electron transfer. *Proc. Natl. Acad. Sci. U. S. A.* 105, 3968–3973.

- Martínez, J.I., Frago, S., Lans, I., Alonso, P.J., García-Rubio, I., and Medina, M. (2016). Spin Densities in Flavin Analogs within a Flavoprotein. *Biophys. J.* 110, 561–571.
- Mashhadi, Z., Zhang, H., Xu, H., and White, R.H. (2008). Identification and characterization of an archaeon-specific riboflavin kinase. *J Bacteriol* 190, 2615–2618.
- Massey, V. (2000). The chemical and biological versatility of riboflavin. *Biochem Soc Trans* 28, 283–296.
- Matern, A., Pedrolli, D., Großhennig, S., Johansson, J., and Mack, M. (2016). Uptake and metabolism of the antibiotics roseoflavin and 8-demethyl-8-aminoriboflavin in riboflavin auxotrophic *Listeria monocytogenes*. *J. Bacteriol.* JB.00388-16.
- Matsui, K. (1965). Nekoflavin, a new flavin compound, in the choroid of cat's eye. *J. Biochem.* 57, 201–206.
- Mayhew, S.G. (1971). Studies on flavin binding in flavodoxins. *BBA - Enzymol.* 235, 289–302.
- Mayhew, S.G. (1999a). The effects of pH and semiquinone formation on the oxidation-reduction potentials of flavin mononucleotide. A reappraisal. *Eur J Biochem* 265, 698–702.
- Mayhew, S.G. (1999b). Potentiometric measurement of oxidation-reduction potentials. *Methods Mol Biol* 131, 49–59.
- Mayhew, S.G., and Ludwig, M.L. (1975). Flavodoxins and electron-transferring flavoproteins. *Enzymes* 12, 57–118.
- McCormick, D.B., and Butler, R.C. (1962). Substrate specificity of liver flavokinase. *BBA - Biochim. Biophys. Acta* 65, 326–332.
- McCormick, D.B., Oka, M., Bowers-Komro, D.M., Yamada, Y., and Hartman, H.A. (1997). Purification and properties of FAD synthetase from liver. *Methods Enzymol.* 280, 407–413.
- Medina-Carmona, E., Neira, J.L., Salido, E., Fuchs, J.E., Palomino-Morales, R., Timson, D.J., and Pey, A.L. (2017). Site-to-site interdomain communication may mediate different loss-of-function mechanisms in a cancer-associated NQO1 polymorphism. *Sci. Rep.* 7, 1–18.
- Medina, M. (2012). Enzymes of FMN and FAD metabolism. In *Handbook of Flavoproteins*, R. Hille, S. Miller, and B. Palfey, eds. (Berlin: Walter de Gruyter publishers.), pp. 71–100.
- Medina Carmona, E., Palomino-Morales, R.J., Fuchs, J.E., Esperanza, P.G., Noel, M.T., Salido, E., Timson, D.J., and Pey, A.L. (2016). Conformational dynamics is key to understanding loss-of-function of NQO1 cancer-associated polymorphisms and its correction by pharmacological ligands. *Sci. Rep.* 6, 1–14.
- Megarity, C.F., and Timson, D.J. (2019). Cancer-associated variants of human NQO1: impacts on inhibitor binding and cooperativity. *Biosci. Rep.* 39.
- Mehta-Kolte, M.G., and Bond, D.R. (2012). *Geothrix fermentans* secretes two different redox-active compounds to utilize electron acceptors across a wide range of redox potentials. *Appl. Environ. Microbiol.* 78, 6987–6995.
- Meighen, E.A. (1991). Molecular biology of bacterial bioluminescence. *Microbiol. Rev.* 55, 123–142.
- Merrill, A.H., and McCormick, D.B. (1980). Affinity chromatographic purification and properties of flavokinase (ATP:riboflavin 5'-phosphotransferase) from rat liver. *J. Biol. Chem.* 255, 1335–1338.

- Merrill Jr., A.H., and McCormick, D.B. (1980). Affinity chromatographic purification and properties of flavokinase (ATP:riboflavin 5'-phosphotransferase) from rat liver. *J Biol Chem* 255, 1335–1338.
- Miccolis, A., Galluccio, M., Giancaspero, T.A., Indiveri, C., and Barile, M. (2012). Bacterial over-expression and purification of the 3'phosphoadenosine 5'phosphosulfate (PAPS) reductase domain of human FAD synthase: functional characterization and homology modeling. *Int. J. Mol. Sci.* 13, 16880–16898.
- Miccolis, A., Galluccio, M., Nitride, C., Giancaspero, T.A., Ferranti, P., Iametti, S., Indiveri, C., Bonomi, F., and Barile, M. (2014). Significance of redox-active cysteines in human FAD synthase isoform 2. *Biochim. Biophys. Acta* 1844, 2086–2095.
- Michaelis, L., and Schwarzenbach, G. (1938). The intermediate forms of oxidation-reduction of the flavins. *J. Biol. Chem.* 123, 527–542.
- Miller, J.R., and Edmondson, D.E. (1999). Influence of flavin analogue structure on the catalytic activities and flavinylation reactions of recombinant human liver monoamine oxidases A and B. *J. Biol. Chem.* 274, 23515–23525.
- Minato, Y., Gohl, D.M., Thiede, J.M., Chacón, J.M., Harcombe, W.R., Maruyama, F., and Baughn, A.D. (2019). Genomewide Assessment of *Mycobacterium tuberculosis* Conditionally Essential Metabolic Pathways . *MSystems* 4.
- Misevičiene, L., Anusevičius, Ž., Šarlauskas, J., and Čenas, N. (2006). Reduction of nitroaromatic compounds by NAD(P)H:quinone oxidoreductase (NQO1): The role of electron-accepting potency and structural parameters in the substrate specificity. *Acta Biochim. Pol.* 53, 569–576.
- Mitsuda, H., Tsuge, H., Tomozawa, Y., and Kawai, F. (1970). Multiplicity of acid phosphatase catalyzing FMN hydrolysis in spinach leaves. *J. Vitaminol. (Kyoto).* 16, 52–57.
- Miura, R. (2001). Versatility and specificity in flavoenzymes: control mechanisms of flavin reactivity. *Chem. Rec.* 1, 183–194.
- Monaco, H.L. (1997). Crystal structure of chicken riboflavin-binding protein. *EMBO J.* 16, 1475–1483.
- Morgunova, E., Meining, W., Illarionov, B., Haase, I., Jin, G., Bacher, A., Cushman, M., Fischer, M., and Ladenstein, R. (2005). Crystal Structure of Lumazine Synthase from *Mycobacterium tuberculosis* as a Target for Rational Drug Design: Binding Mode of a New Class of Purinetrione Inhibitors<sup>†</sup>. *Biochemistry* 44, 2746–2758.
- Moscovitz, O., Tsvetkov, P., Hazan, N., Michaelevski, I., Keisar, H., Ben-Nissan, G., Shaul, Y., and Sharon, M. (2012). A Mutually Inhibitory Feedback Loop between the 20S Proteasome and Its Regulator, NQO1. *Mol. Cell* 47, 76–86.
- Muller, F., and Edmondson, D.E. (2018). Structure, synthesis, and physical properties of covalently bound flavins and 6- and 8-hydroxyflavins. In *Chemistry and Biochemistry of Flavoenzymes*, (CRC Press), pp. 73–103.
- Müller, F. (1991). Free Flavins: Synthesis, Chemical and Physical Properties. In *Chemistry and Biochemistry of Flavoenzymes*, F. Müller, ed. (Boca Raton, FL, CRC Press), pp. 1–71.
- Murthy, Y.V.S.N., and Massey, V. (1997). Synthesis and applications of flavin analogs as active site probes for flavoproteins. *Methods Enzymol.* 280, 436–460.
- Murty, C.V.R., and Adiga, P.R. (1982). Pregnancy suppression by active immunization against gestation-specific riboflavin carrier protein. *Science* (80-. ). 216, 191–193.

- Muru, K., Reinson, K., Künnapas, K., Lilleväli, H., Nochi, Z., Mosegaard, S., Pajusalu, S., Olsen, R.K.J., and Öunap, K. (2019). FLAD1-associated multiple acyl-CoA dehydrogenase deficiency identified by newborn screening. *Mol. Genet. Genomic Med.* 7, e915.
- Myllykallio, H., Lipowski, G., Leduc, D., Filee, J., Forterre, P., and Liebl, U. (2002). An alternative flavin-dependent mechanism for thymidylate synthesis. *Science* (80-. ). 297, 105–107.
- Myllykallio, H., Leduc, D., Filee, J., and Liebl, U. (2003). Life without dihydrofolate reductase FoaA. *Trends Microbiol.* 11, 220–223.
- Myllykallio, H., Sournia, P., Heliou, A., and Liebl, U. (2018). Unique features and anti-microbial targeting of folate- and flavin-dependent methyltransferases required for accurate maintenance of genetic information. *Front. Microbiol.* 9.
- Nakagawa, S., Hagihara, T., Fujio, T., and Aisaka, K. (1995). Metaphosphate-dependent phosphorylation of riboflavin to FMN by *Corynebacterium ammoniagenes*. *Appl. Microbiol. Biotechnol.* 43, 325–329.
- Nakano, H., and McCormick, D.B. (1991). Stereospecificity of the metal.ATP complex in flavokinase from rat small intestine. *J. Biol. Chem.* 266, 22125–22128.
- Natarajan, S.K., and Becker, D.F. (2012). Role of apoptosis-inducing factor, proline dehydrogenase, and NADPH oxidase in apoptosis and oxidative stress. *Cell Heal. Cytoskelet* 2012, 11–27.
- Nebert, D.W., Roe, A.L., Vandale, S.E., Bingham, E., and Oakley, G.G. (2002). NAD(P)H:quinone oxidoreductase (NQO1) polymorphism, exposure to benzene, and predisposition to disease: a HuGE review. *Genet. Med.* 4, 62–70.
- Negri, A., Massey, V., and Williams, C.H. (1987). D-aspartate oxidase from beef kidney. Purification and properties. *J. Biol. Chem.* 262, 10026–10034.
- Nemeikaitė-Čėnienė, A., Šarlauskas, J., Jonušienė, V., Marozienė, A., Misevičienė, L., Yantsevich, A. V., and Čėnas, N. (2019). Kinetics of flavoenzyme-catalyzed reduction of tirapazamine derivatives: Implications for their prooxidant cytotoxicity. *Int. J. Mol. Sci.* 20.
- Newsome, J.J., Colucci, M.A., Hassani, M., Beall, H.D., and Moody, C.J. (2007). Benzimidazole- and benzothiazole-quinones: Excellent substrates for NAD(P)H:quinone oxidoreductase 1. *Org. Biomol. Chem.* 5, 3665–3673.
- Nishimasu, H., Ishitani, R., Yamashita, K., Iwashita, C., Hirata, A., Hori, H., and Nureki, O. (2009). Atomic structure of a folate/FAD-dependent tRNA T54 methyltransferase. *Proc. Natl. Acad. Sci. U. S. A.* 106, 8180–8185.
- Nolan, K.A., Zhao, H., Faulder, P.F., Frenkel, A.D., Timson, D.J., Siegel, D., Ross, D., Burke, T.R., Stratford, I.J., and Bryce, R.A. (2007). Coumarin-based inhibitors of human NAD(P)H:Quinone oxidoreductase-1. Identification, structure-activity, off-target effects and in vitro human pancreatic cancer toxicity. *J. Med. Chem.* 50, 6316–6325.
- Nolan, K.A., Doncaster, J.R., Dunstan, M.S., Scott, K.A., Frenkel, A.D., Siegel, D., Ross, D., Barnes, J., Levy, C., Leys, D., et al. (2009). Synthesis and Biological Evaluation of Coumarin-Based Inhibitors of NAD(P)H: Quinone Oxidoreductase-1 (NQO1) †. *J. Med. Chem.* 52, 7142–7156.
- Nolan, K.A., Scott, K.A., Barnes, J., Doncaster, J., Whitehead, R.C., and Stratford, I.J. (2010). Pharmacological inhibitors of NAD(P)H quinone oxidoreductase, NQO1: Structure/activity relationships and functional activity in tumour cells. *Biochem. Pharmacol.* 80, 977–981.



- Novo, N., Ferreira, P., and Medina, M. (2020). The apoptosis-inducing factor family: Moonlighting proteins in the crosstalk between mitochondria and nuclei. *IUBMB Life*.
- Oh, E.-T., Kim, J., Kim, J.M., Kim, S.J., Lee, J.-S., Hong, S.-S., Goodwin, J., Ruthenborg, R.J., Jung, M.G., Lee, H.-J., et al. (2016). NQO1 inhibits proteasome-mediated degradation of HIF-1 $\alpha$ . *Nat. Commun.* 7, 13593.
- Oka, M., and McCormick, D.B. (1987). Complete purification and general characterization of FAD synthetase from rat liver. *J Biol Chem* 262, 7418–7422.
- Olin-Sandoval, V., Moreno-Sanchez, R., and Saavedra, E. (2012). Targeting Trypanothione Metabolism in Trypanosomatid Human Parasites. *Curr. Drug Targets* 11, 1614–1630.
- Olsen, R.K.J., Koňářiková, E., Giancaspero, T.A., Mosegaard, S., Boczonadi, V., Mataković, L., Veauville-Merllié, A., Terrile, C., Schwarzmayr, T., Haack, T.B., et al. (2016). Riboflavin-Responsive and -Non-responsive Mutations in FAD Synthase Cause Multiple Acyl-CoA Dehydrogenase and Combined Respiratory-Chain Deficiency. *Am. J. Hum. Genet.* 98, 1130–1145.
- Pallotta, M.L. (2011). Evidence for the presence of a FAD pyrophosphatase and a FMN phosphohydrolase in yeast mitochondria: a possible role in flavin homeostasis. *Yeast* 28, 693–705.
- Pan, S.-S., Han, Y., Farabaugh, P., and Xia, H. (2002). Implication of alternative splicing for expression of a variant NAD(P)H:quinone oxidoreductase-1 with a single nucleotide polymorphism at 465C>T. *Pharmacogenetics* 12, 479–488.
- Pan, S.S., Forrest, G.L., Akman, S.A., and Hu, L.T. (1995). NAD(P)H:quinone oxidoreductase expression and mitomycin C resistance developed by human colon cancer HCT 116 cells. *Cancer Res.* 55, 330–335.
- Papatheodorou, I., Fonseca, N.A., Keays, M., Tang, Y.A., Barrera, E., Bazant, W., Burke, M., Füllgrabe, A., Fuentes, A.M.-P., George, N., et al. (2018). Expression Atlas: gene and protein expression across multiple studies and organisms. *Nucleic Acids Res.* 46, D246–D251.
- Park, K.J., Lee, C.H., Kim, A., Jeong, K.J., Kim, C.H., and Kim, Y.S. (2012). Death receptors 4 and 5 activate Nox1 NADPH oxidase through riboflavin kinase to induce reactive oxygen species-mediated apoptotic cell death. *J Biol Chem* 287, 3313–3325.
- Payne, K.A.P., White, M.D., Fisher, K., Khara, B., Bailey, S.S., Parker, D., Rattray, N.J.W., Trivedi, D.K., Goodacre, R., Beveridge, R., et al. (2015). New cofactor supports  $\alpha,\beta$ -unsaturated acid decarboxylation via 1,3-dipolar cycloaddition. *Nature* 522, 497–501.
- Peng, Q., Lu, Y., Lao, X., Chen, Z., Li, R., Sui, J., Qin, X., and Li, S. (2014). The NQO1 Pro187Ser polymorphism and breast cancer susceptibility: Evidence from an updated meta-analysis. *Diagn. Pathol.* 9, 100.
- Pey, A.L., Megarity, C.F., and Timson, D.J. (2014). FAD binding overcomes defects in activity and stability displayed by cancer-associated variants of human NQO1. *Biochim. Biophys. Acta - Mol. Basis Dis.* 1842, 2163–2173.
- Pey, A.L., Megarity, C.F., Medina-Carmona, E., and Timson, D.J. (2016). Natural small molecules as stabilizers and activators of cancer-associated NQO1 polymorphisms. *Curr. Drug Targets* 17, 1506–1514.
- Piano, V., Palfey, B.A., and Mattevi, A. (2017). Flavins as Covalent Catalysts: New Mechanisms Emerge. *Trends Biochem. Sci.* 42, 457–469.

- Pidugu, L.S.M., Mbimba, J.C.E., Ahmad, M., Pozharski, E., Sausville, E.A., Emadi, A., and Toth, E.A. (2016). A direct interaction between NQO1 and a chemotherapeutic dimeric naphthoquinone. *BMC Struct. Biol.* 16, 1.
- Pink, J.J., Planchon, S.M., Tagliarino, C., Varnes, M.E., Siegel, D., and Boothman, D.A. (2000). NAD(P)H:quinone oxidoreductase activity is the principal determinant of  $\beta$ -lapachone cytotoxicity. *J. Biol. Chem.* 275, 5416–5424.
- Prochaska, H.J., Santamaria, A.B., and Talalay, P. (1992). Rapid detection of inducers of enzymes that protect against carcinogens. *Proc. Natl. Acad. Sci. U. S. A.* 89, 2394–2398.
- Rase, B., Bartfai, T., and Ernster, L. (1976). Purification of DT-diaphorase by affinity chromatography: Occurrence of two subunits and nonlinear dixon and scatchard plots of the inhibition by anticoagulants. *Arch. Biochem. Biophys.* 172, 380–386.
- Reyes, P., Rathod, P.K., Sanchez, D.J., Mrema, J.E.K., Rieckmann, K.H., and Heidrich, H.G. (1982). Enzymes of purine and pyrimidine metabolism from the human malaria parasite, *Plasmodium falciparum*. *Mol. Biochem. Parasitol.* 5, 275–290.
- Ritsert, K., Huber, R., Turk, D., Ladenstein, R., Schmidt-Bäse, K., and Bacher, A. (1995). Studies on the lumazine synthase/riboflavin synthase complex of *Bacillus subtilis*: Crystal structure analysis of reconstituted, icosahedral  $\beta$ -subunit capsids with bound substrate analogue inhibitor at 2.4 Å resolution. *J. Mol. Biol.* 253, 151–167.
- Ross, D., and Siegel, D. (2018). NQO1 in protection against oxidative stress. *Curr. Opin. Toxicol.* 7, 67–72.
- Ross, D., Kepa, J.K., Winski, S.L., Beall, H.D., Anwar, A., and Siegel, D. (2000). NAD(P)H:quinone oxidoreductase 1 (NQO1): chemoprotection, bioactivation, gene regulation and genetic polymorphisms. *Chem. Biol. Interact.* 129, 77–97.
- Rossmann, M.G., Moras, D., and Olsen, K.W. (1974). Chemical and biological evolution of a nucleotide-binding protein. *Nature* 250, 194–199.
- Rothman, N., Smith, M.T., Hayes, R.B., Traver, R.D., Hoener, B., Campleman, S., Li, G.L., Dosemeci, M., Linet, M., Zhang, L., et al. (1997). Benzene poisoning, a risk factor for hematological malignancy, is associated with the NQO1 609C->T mutation and rapid fractional excretion of chlorzoxazone. *Cancer Res.* 57, 2839–2842.
- Ryan, A., Kaplan, E., Nebel, J.-C., Polycarpou, E., Crescente, V., Lowe, E., Preston, G.M., and Sim, E. (2014). Identification of NAD(P)H Quinone Oxidoreductase Activity in Azoreductases from *P. aeruginosa*: Azoreductases and NAD(P)H Quinone Oxidoreductases Belong to the Same FMN-Dependent Superfamily of Enzymes. *PLoS One* 9, e98551.
- Ryder, B., Tolomeo, M., Nochi, Z., Colella, M., Barile, M., Olsen, R.K., and Inbar-Feigenberg, M. (2019). A Novel Truncating FLAD1 Variant, Causing Multiple Acyl-CoA Dehydrogenase Deficiency (MADD) in an 8-Year-Old Boy. *JIMD Rep.* 45, 37–44.
- Sandoval, F.J., and Roje, S. (2005). An FMN hydrolase is fused to a riboflavin kinase homolog in plants. *J. Biol. Chem.* 280, 38337–38345.
- Sandoval, F.J., Zhang, Y., and Roje, S. (2008). Flavin nucleotide metabolism in plants: Monofunctional enzymes synthesize FAD in plastids. *J. Biol. Chem.* 283, 30890–30900.
- Santos, M.A., Jimenez, A., and Revuelta, J.L. (2000). Molecular characterization of FMN1, the structural gene for the monofunctional flavokinase of *Saccharomyces cerevisiae*. *J. Biol. Chem.* 275, 28618–28624.

- Sanyal, S., Ryk, C., De Verdier, P.J., Steineck, G., Larsson, P., Onelöv, E., Hemminki, K., and Kumar, R. (2007). Polymorphisms in NQO1 and the clinical course of urinary bladder neoplasms. *Scand. J. Urol. Nephrol.* *41*, 182–190.
- Sarlauskas, J., Nemeikaite-Ceniene, A., Anusevicius, Z., Miseviciene, L., Julvez, M.M., Medina, M., Gomez-Moreno, C., and Cenas, N. (2004). Flavoenzyme-catalyzed redox cycling of hydroxylamino and amino metabolites of 2,4,6-trinitrotoluene: implications for their cytotoxicity. *Arch. Biochem. Biophys.* *425*, 184–192.
- Šarlauskas, J., Dičkancaite, E., Nemeikaite, A., Anusevičius, Ž., Nivinskas, H., Segura-Aguilar, J., and Čenas, N. (1997). Nitrobenzimidazoles as substrates for DT-diaphorase and redox cycling compounds: Their enzymatic reactions and cytotoxicity. *Arch. Biochem. Biophys.* *346*, 219–229.
- Sassetti, C.M., Boyd, D.H., and Rubin, E.J. (2003). Genes required for mycobacterial growth defined by high density mutagenesis. *Mol Microbiol* *48*, 77–84.
- Schrecker, A.W., and Kornberg, A. (1950). Reversible enzymatic synthesis of flavin-adenine dinucleotide. *J Biol Chem* *182*, 795–803.
- Scott, K.A., Barnes, J., Whitehead, R.C., Stratford, I.J., and Nolan, K.A. (2011). Inhibitors of NQO1: Identification of compounds more potent than dicoumarol without associated off-target effects. *Biochem. Pharmacol.* *81*, 355–363.
- Sebastián, M., Lira-Navarrete, E., Serrano, A., Marcuello, C., Velázquez-Campoy, A., Lostao, A., Hurtado-Guerrero, R., Medina, M., and Martínez-Júlvez, M. (2017a). The FAD synthetase from the human pathogen *Streptococcus pneumoniae*: A bifunctional enzyme exhibiting activity-dependent redox requirements. *Sci. Rep.* *7*.
- Sebastián, M., Serrano, A., Velázquez-Campoy, A., and Medina, M. (2017b). Kinetics and thermodynamics of the protein-ligand interactions in the riboflavin kinase activity of the FAD synthetase from *Corynebacterium ammoniagenes*. *Sci Rep* *7*, 7281.
- Sebastián, M., Velázquez-Campoy, A., and Medina, M. (2018a). The RFK catalytic cycle of the pathogen *Streptococcus pneumoniae* shows species-specific features in prokaryotic FMN synthesis. *J. Enzyme Inhib. Med. Chem.* *33*, 842–849.
- Sebastián, M., Anoz-Carbonell, E., Gracia, B., Cossio, P., Aínsa, J.A., Lans, I., and Medina, M. (2018b). Discovery of antimicrobial compounds targeting bacterial type FAD synthetases. *J. Enzyme Inhib. Med. Chem.* *33*, 241–254.
- Sebastián, M., Arilla-Luna, S., Bellalou, J., Yruela, I., and Medina, M. (2019). The biosynthesis of flavin cofactors in *Listeria monocytogenes*. *J. Mol. Biol.* *431*, 2762–2776.
- Sepúlveda Cisternas, I., Salazar, J.C., and García-Angulo, V.A. (2018). Overview on the bacterial iron-riboflavin metabolic axis. *Front. Microbiol.* *9*.
- Serrano, A., Frago, S., Velázquez-Campoy, A., and Medina, M. (2012). Role of key residues at the flavin mononucleotide (FMN):adenylyltransferase catalytic site of the bifunctional riboflavin kinase/flavin adenine dinucleotide (FAD) Synthetase from *Corynebacterium ammoniagenes*. *Int. J. Mol. Sci.* *13*, 14492–14517.
- Serrano, A., Frago, S., Herguedas, B., Martínez-Júlvez, M., Velázquez-Campoy, A., and Medina, M. (2013a). Key Residues at the Riboflavin Kinase Catalytic Site of the Bifunctional Riboflavin Kinase/FMN Adenylyltransferase From *Corynebacterium ammoniagenes*. *Cell Biochem. Biophys.* *65*, 57–68.

- Serrano, A., Ferreira, P., Martínez-Júlvez, M., and Medina, M. (2013b). The prokaryotic FAD synthetase family: a potential drug target. *Curr. Pharm. Des.* 19, 2637–2648.
- Serrano, A., Sebastián, M., Arilla-Luna, S., Baquedano, S., Pallarés, M.C., Lostao, A., Herguedas, B., Velázquez-Campoy, A., Martínez-Júlvez, M., and Medina, M. (2015). Quaternary organization in a bifunctional prokaryotic FAD synthetase: Involvement of an arginine at its adenylyltransferase module on the riboflavin kinase activity. *Biochim. Biophys. Acta - Proteins Proteomics* 1854, 897–906.
- Serrano, A., Sebastián, M., Arilla-Luna, S., Baquedano, S., Herguedas, B., Velázquez-Campoy, A., Martínez-Júlvez, M., and Medina, M. (2017). The trimer interface in the quaternary structure of the bifunctional prokaryotic FAD synthetase from *Corynebacterium ammoniagenes*. *Sci. Rep.* 7, 404.
- Shaw, P.M., Reiss, A., Adesnik, M., Nebert, D.W., Schembri, J., and Jaiswal, A.K. (1991). The human dioxin-inducible NAD(P)H:quinone oxidoreductase cDNA-encoded protein expressed in COS-1 cells is identical to diaphorase 4. *Eur. J. Biochem.* 195, 171–176.
- Siegel, D., and Ross, D. (2000). Immunodetection of NAD(P)H:quinone oxidoreductase 1 (NQO1) in human tissues. *Free Radic. Biol. Med.* 29, 246–253.
- Siegel, D., Beall, H., Senekowitsch, C., Ross, D., Kasai, M., Arai, H., and Gibson, N.W. (1992). Bioreductive Activation of Mitomycin C by DT-Diaphorase. *Biochemistry* 31, 7879–7885.
- Siegel, D., Bolton, E.M., Burr, J.A., Liebler, D.C., and Ross, D. (1997). The reduction of  $\alpha$ -tocopherolquinone by human NAD(P)H: Quinone oxidoreductase: The role of  $\alpha$ -tocopherolhydroquinone as a cellular antioxidant. *Mol. Pharmacol.* 52, 300–305.
- Siegel, D., Anwar, A., Winski, S.L., Kepa, J.K., Zolman, K.L., and Ross, D. (2001). Rapid polyubiquitination and proteasomal degradation of a mutant form of NAD(P)H:quinone oxidoreductase 1. *Mol. Pharmacol.* 59, 263–268.
- Siegel, D., Gustafson, D.L., Dehn, D.L., Han, J.Y., Boonchoong, P., Berliner, L.J., and Ross, D. (2004). NAD(P)H:quinone oxidoreductase 1: Role as a superoxide scavenger. *Mol. Pharmacol.* 65, 1238–1247.
- Siegel, D., Kepa, J.K., and Ross, D. (2012). NAD(P)H:Quinone Oxidoreductase 1 (NQO1) Localizes to the Mitotic Spindle in Human Cells. *PLoS One* 7, e44861.
- Siegel, D., Dehn, D.D., Bokatzian, S.S., Quinn, K., Backos, D.S., Francesco, A. Di, Bernier, M., Reisdorph, N., De Cabo, R., and Ross, D. (2018). Redox modulation of NQO1. *PLoS One* 13.
- Singer, T.P., and McIntire, W.S. (1984). Covalent Attachment of Flavin to Flavoproteins: Occurrence, Assay, and Synthesis. *Methods Enzymol.* 106, 369–378.
- Skelly, J. V., Sanderson, M.R., Suter, D.A., Baumann, U., Read, M.A., Gregory, D.S.J., Bennett, M., Hobbs, S.M., and Neidle, S. (1999). Crystal Structure of Human DT-diaphorase: A Model for Interaction with the Cytotoxic Prodrug 5-(Aziridin-1-yl)-2,4-dinitrobenzamide (CB1954). *J. Med. Chem.* 42, 4325–4330.
- Smith, W.W., Burnett, R.M., Darling, G.D., and Ludwig, M.L. (1977). Structure of the semiquinone form of flavodoxin from *Clostridium* MP. Extension of 1.8 Å resolution and some comparisons with the oxidized state. *J. Mol. Biol.* 117, 195–225.
- Solovieva, I.M., Kreneva, R.A., Leak, D.J., and Perumov, D.A. (1999). The ribR gene encodes a monofunctional riboflavin kinase which is involved in regulation of the *Bacillus subtilis* riboflavin operon. *Microbiology* 145, 67–73.

- Spaan, A.N., Ijlst, L., Van Roermund, C.W.T., Wijburg, F.A., Wanders, R.J.A., and Waterham, H.R. (2005). Identification of the human mitochondrial FAD transporter and its potential role in multiple acyl-CoA dehydrogenase deficiency. *Mol. Genet. Metab.* *86*, 441–447.
- Spencer, R., Fisher, J., and Walsh, C. (1976). Preparation, characterization, and chemical properties of the flavin coenzyme analogues 5-deazariboflavin, 5-deazariboflavin 5'-phosphate, and 5-deazariboflavin 5'-diphosphate, 5' leads to 5'-adenosine ester. *Biochemistry* *15*, 1043–1053.
- Stanulla, M., Dnynybil, C., Bartels, D.B., Dördelmann, M., Löning, L., Claviez, A., and Schrappe, M. (2007). The NQO1 C609T polymorphism is associated with risk of secondary malignant neoplasms after treatment for childhood acute lymphoblastic leukemia: A matched-pair analysis from the ALL-BFM study group. *Haematologica* *92*, 1581–1582.
- Stoehr, C.G., Nolte, E., Wach, S., Wieland, W.F., Hofstaedter, F., Hartmann, A., and Stoehr, R. (2012). NAD(P)H:quinone oxidoreductase 1 (NQO1) P187S polymorphism and prostate cancer risk in Caucasians. *Int. J. Mol. Sci.* *13*, 10959–10969.
- Strandback, E., Lienhart, W., Hromic-Jahjefendic, A., Bourgeois, B., Högler, A., Waltenstorfer, D., Winkler, A., Zangger, K., Madl, T., Gruber, K., et al. (2019). A small molecule chaperone rescues the stability and activity of a cancer-associated variant of NAD(P)H:quinone oxidoreductase 1 *in vitro*. *FEBS Lett.* 1873-3468.13636.
- Straub, F.B. (1939). Isolation and properties of a flavoprotein from heart muscle tissue. *Biochem. J.* *33*, 787–792.
- Subbayya, I.N., Ray, S.S., Balaram, P., and Balaram, H. (1997). Metabolic enzymes as potential drug targets in *Plasmodium falciparum*. *Indian J. Med. Res.* *106*, 79–94.
- Sun, M., Moore, T.A., and Song, P.S. (1972). Molecular luminescence studies of flavins. I. The excited states of flavins. *J Am Chem Soc* *94*, 1730–1740.
- Susin, S.A., Lorenzo, H.K., Zamzami, N., Marzo, I., Snow, B.E., Brothers, G.M., Mangion, J., Jacotot, E., Costantini, P., Loeffler, M., et al. (1999). Molecular characterization of mitochondrial apoptosis-inducing factor. *Nature* *397*, 441–446.
- Tachibana, S., and Murakami, T. (1975). The isolation and some properties of new flavins ("schizoflavin") formed by *Schizophyllum commune*. *J. Nutr. Sci. Vitaminol. (Tokyo)*. *21*, 61–63.
- Talalay, P., and Dinkova-Kostova, A.T. (2004). Role of Nicotinamide Quinone Oxidoreductase 1 (NQO1) in Protection against Toxicity of Electrophiles and Reactive Oxygen Intermediates. *Methods Enzymol.* *382*, 355–364.
- Tedeschi, G., Negri, A., Ceciliani, F., Ronchi, S., Vetere, A., D'Aniello, G., and D'Aniello, A. (1994). Properties of the flavoenzyme d-aspartate oxidase from *Octopus vulgaris*. *Biochim. Biophys. Acta (BBA)/Protein Struct. Mol.* *1207*, 217–222.
- Tolomeo, M., Nisco, A., Leone, P., and Barile, M. (2020). Development of Novel Experimental Models to Study Flavoproteome Alterations in Human Neuromuscular Diseases: The Effect of Rf Therapy. *Int. J. Mol. Sci.* *21*.
- Torchetti, E.M., Brizio, C., Colella, M., Galluccio, M., Giancaspero, T.A., Indiveri, C., Roberti, M., and Barile, M. (2010). Mitochondrial localization of human FAD synthetase isoform 1. *Mitochondrion* *10*, 263–273.

- Torchetti, E.M., Bonomi, F., Galluccio, M., Gianazza, E., Giancaspero, T.A., Iametti, S., Indiveri, C., and Barile, M. (2011). Human FAD synthase (isoform 2): a component of the machinery that delivers FAD to apo-flavoproteins. *FEBS J.* 278, 4434–4449.
- Traver, R.D., Horikoshi, T., Danenberg, K.D., Stadlbauer, T.H., Danenberg, P. V, Ross, D., and Gibson, N.W. (1992). NAD(P)H:quinone oxidoreductase gene expression in human colon carcinoma cells: characterization of a mutation which modulates DT-diaphorase activity and mitomycin sensitivity. *Cancer Res.* 52, 797–802.
- Venugopal, A., Bryk, R., Shi, S., Rhee, K., Rath, P., Schnappinger, D., Ehrhart, S., and Nathan, C. (2011). Virulence of mycobacterium tuberculosis depends on lipoamide dehydrogenase, a member of three multienzyme complexes. *Cell Host Microbe* 9, 21–31.
- Villanueva, R., Romero-Tamayo, S., Laplaza, R., Martínez-Olivan, J., Velázquez-Campoy, A., Sancho, J., Ferreira, P., and Medina, M. (2019). Redox- and Ligand Binding-Dependent Conformational Ensembles in the Human Apoptosis-Inducing Factor Regulate Its Pro-Life and Cell Death Functions. *Antioxid Redox Signal* 30.
- Vitreschak, A.G., Rodionov, D.A., Mironov, A.A., and Gelfand, M.S. (2002). Regulation of riboflavin biosynthesis and transport genes in bacteria by transcriptional and translational attenuation. *Nucleic Acids Res.* 30, 3141–3151.
- Walker, W.H., Singer, T.P., Ghisla, S., and Hemmerich, P. (1972). Studies on succinate dehydrogenase. 8-Histidyl-FAD as the active center of succinate dehydrogenase. *Eur. J. Biochem.* 26, 279–289.
- Walsh, C.T., and Wencewicz, T.A. (2013). Flavoenzymes: Versatile catalysts in biosynthetic pathways. *Nat. Prod. Rep.* 30, 175–200.
- Walsh, C.T., and Wencewicz, T.A. (2014). Prospects for new antibiotics: a molecule-centered perspective. *J Antibiot* 67, 7–22.
- Walsh, C., Fisher, J., Spencer, R., Graham, D.W., Ashton, W.T., Brown, J.E., Brown, R.D., and Rogers, E.F. (1978). Chemical and enzymic properties of riboflavin analogs. *Biochemistry* 17, 1942–1951.
- Wang, G., and Maier, R.J. (2004). An NADPH quinone reductase of *Helicobacter pylori* plays an important role in oxidative stress resistance and host colonization. *Infect Immun* 72, 1391–1396.
- Wang, W., Kim, R., Jancarik, J., Yokota, H., and Kim, S.H. (2003). Crystal structure of a flavin-binding protein from *Thermotoga maritima*. *Proteins Struct. Funct. Genet.* 52, 633–635.
- Wang, W., Kim, R., Yokota, H., and Kim, S.-H.H. (2004). Crystal structure of flavin binding to FAD synthetase of *Thermotoga maritima*. *Proteins Struct. Funct. Bioinforma.* 58, 246–248.
- Weber, G. (1950). Fluorescence of riboflavin and flavin-adenine dinucleotide. *Biochem J* 47, 114–121.
- Wegrzyn, A.B., Stolle, S., Rienksma, R.A., Martins dos Santos, V.A.P., Bakker, B.M., and Suarez-Diez, M. (2019). Cofactors revisited – Predicting the impact of flavoprotein-related diseases on a genome scale. *Biochim. Biophys. Acta - Mol. Basis Dis.* 1865, 360–370.
- Welkie, G.W., and Miller, G.W. (1960). Iron Nutrition of *Nicotiana tabacum* in Relation to Riboflavin, Riboflavin-5-phosphate, and Flavin Adenine Dinucleotide Content. *Plant Physiol.* 35, 516–520.

- Winkler, W.C., Cohen-Chalamish, S., and Breaker, R.R. (2002). An mRNA structure that controls gene expression by binding FMN. *Proc. Natl. Acad. Sci. U. S. A.* *99*, 15908–15913.
- Winski, S.L., Faig, M., Bianchet, M.A., Siegel, D., Swann, E., Fung, K., Duncan, M.W., Moody, C.J., Amzel, L.M., and Ross, D. (2001). Characterization of a mechanism-based inhibitor of NAD(P)H:Quinone oxidoreductase 1 by biochemical, x-ray crystallographic, and mass spectrometric approaches. *Biochemistry* *40*, 15135–15142.
- World Health Organization (2014). Antimicrobial resistance. Global Report of Surveillance. Retrieved from <https://www.who.int/medicines/publications/global-priority-list-antibiotic-resistant-bacteria/en/>
- World Health Organization (2017). Global priority list of antibiotic-resistant bacteria to guide research, discovery, and development of new antibiotics. Retrieved from <https://www.who.int/medicines/publications/global-priority-list-antibiotic-resistant-bacteria/>
- Wu, K., Knox, R., Sun, X.Z., Joseph, P., Jaiswal, A.K., Zhang, D., Deng, P.S.K., and Chen, S. (1997). Catalytic properties of NAD(P)H:quinone oxidoreductase-2 (NQO2), a dihydronicotinamide riboside dependent oxidoreductase. *Arch. Biochem. Biophys.* *347*, 221–228.
- Wu, M., Repetto, B., Glerum, D.M., and Tzagoloff, A. (1995). Cloning and characterization of FAD1, the structural gene for flavin adenine dinucleotide synthetase of *Saccharomyces cerevisiae*. *Mol. Cell. Biol.* *15*, 264–271.
- Xu, L.L., Wain, J.C., Miller, D.P., Thurston, S.W., Su, L., Lynch, T.J., and Christiani, D.C. (2001). The NAD(P)H:quinone Oxidoreductase 1 Gene Polymorphism and Lung Cancer. *Cancer Epidemiol. Prev. Biomarkers* *10*.
- Yamada, Y., Merrill, A.H., and McCormick, D.B. (1990). Probable reaction mechanisms of flavokinase and FAD synthetase from rat liver. *Arch. Biochem. Biophys.* *278*, 125–130.
- Yonezawa, A., and Inui, K.I. (2013). Novel riboflavin transporter family RFVT/SLC52: Identification, nomenclature, functional characterization and genetic diseases of RFVT/SLC52. *Mol. Aspects Med.* *34*, 693–701.
- Yruela, I., Arilla-Luna, S., Medina, M., and Contreras-Moreira, B. (2010). Evolutionary divergence of chloroplast FAD synthetase proteins. *BMC Evol. Biol.* *10*, 311.
- Yurgel, S.N., Rice, J., Domreis, E., Lynch, J., Sa, N., Qamar, Z., Rajamani, S., Gao, M., Roje, S., and Bauer, W.D. (2014). *Sinorhizobium meliloti* flavin secretion and bacteria-host interaction: Role of the bifunctional RibBA protein. *Mol. Plant-Microbe Interact.* *27*, 437–445





# Abbreviations



|                 |  |
|-----------------|--|
| $\alpha$        | Cooperativity constant                                       |
| $\Delta$        | Increment / deletion   |
| $\varepsilon$   | Molar extinction coefficient                                 |
| $\lambda$       | Wavelength   |
| $[\theta]_{mr}$ | Molar ellipticity per residue                                |
| 3D              | Three-dimensional  |
| A               | Arrhenius pre-exponential factor                             |
| Å               | Angstrom   |
| Abs             | Absorbance   |
| $A_D$           | Arrhenius pre-exponential factor for DT                      |
| ADP             | Adenosine 5'-diphosphate                                     |
| $A_H$           | Arrhenius pre-exponential factor for HT                      |
| AMP             | Adenosine 5'-monophosphate                                   |
| ANP             | Adenine nucleotide (denotes for either ADP or ATP)           |
| $^{app}k_{cat}$ | Apparent catalytic constant                                  |
| ATP             | Adenosine 5'-triphosphate                                    |
| AU              | Absorbance units   |
| CaFADS          | FAD synthetase from <i>Corynebacterium ammoniagenes</i>      |
| cal             | Calorie  |
| CD              | Circular Dichroism   |
| CgFMNAT         | FMNAT of <i>Candida glabrata</i>                             |
| CPK             | Corey, Pauling, Koltun, colors code for atoms                |
| CSB             | Chicago Sky Blue   |
| CTC             | Charge transfer complex                                      |
| CTP             | Cytosine 5'-triphosphate                                     |
| Da              | Dalton   |
| DAD             | Donor-acceptor distance                                      |
| DCPIP           | 2,6-Dichlorophenolindophenol                                 |
| DEAE            | Diethylaminoethyl  |
| Dic             | Dicoumarol   |
| DMSO            | Dimethylsulfoxide  |
| DT              | Deuteride transfer   |
| DTT             | Dithiothreitol   |
| $E_a$           | Activation energy  |
| EC              | Enzyme commission  |
| ECR             | Exponential consensus ranking                                |
| EDTA            | Ethylenediaminetetraacetic acid                              |
| $E_{ox/sq}$     | Redox potential for the oxidized and the semiquinone species |
| Eqn             | Equation   |
| $E_{sq/hq}$     | Redox potential for the semiquinone and the reduced species  |
| <i>et. al.</i>  | <i>Et alia</i> (and collaborators)                           |
| FAD             | Flavin adenine dinucleotide                                  |
| FADasa          | FAD hydrolase  |
| FADpp           | FAD pyrophosphorilase  |
| FADS            | FAD synthase   |
| FDA             | Food and Drug Administration                                 |
| FHy             | FMN hydrolase  |
| Fig             | Figure   |
| FLV             | Flavins (denotes for either RF or FMN)                       |
| FMN             | Flavin mononucleotide / Riboflavin 5'-monophosphate          |
| FMNAT           | FMN adenylyltransferase                                      |

|                                  |   |
|----------------------------------|---|
| FPLC                             | Fast Protein Liquid Chromatography  |
| G                                | Gibbs free energy   |
| GST                              | Glutathione transferase   |
| GTP                              | Guanosin 5'-triphosphate  |
| H                                | Enthalpy  |
| HEPES                            | 4-(2-hydroxyethyl)-1-piperazineethanesulfonic acid                                  |
| hFADS                            | Human FAD synthase  |
| hFADS6                           | Isoform 6 of human FADS   |
| hNQO1                            | NQO1 from <i>Homo sapiens</i>   |
| HPLC                             | High Performance Liquid Chromatography  |
| hq                               | Hydroquinone  |
| HsRFK                            | Riboflavin kinase from <i>Homo sapiens</i>  |
| HSS                              | High Strength Silica  |
| HT                               | Hydride transfer  |
| HTS                              | High-throughput screening   |
| IC <sub>50</sub>                 | Concentration causing 50% of inhibition (cellular viability, enzymatic activity...) |
| IPTG                             | Isopropyl β-D-1-thiogalactopyranoside   |
| ITC                              | Isothermal Titration Calorimetry  |
| K <sub>a</sub>                   | Association constant  |
| K <sub>a</sub> <i>app.</i> , ANP | Apparent association constant for ANP ligands                                       |
| k <sub>cat</sub>                 | Catalytic constant  |
| K <sub>D</sub>                   | Dissociation constant   |
| K <sub>i</sub>                   | Inhibition constant   |
| KIE                              | Kinetic isotope effect  |
| K <sub>m</sub>                   | Michaelis-Menten constant   |
| KSVE                             | Kinetic solvent viscosity effects   |
| LB                               | Lysogeny-Broth  |
| Lm1FADS                          | Type I-FAD synthetase from <i>Listeria monocytogenes</i>                            |
| Lm2FADS                          | Type II-FAD synthetase from <i>Listeria monocytogenes</i>                           |
| MBTb                             | Molybdopterin-binding domain  |
| MD                               | Molecular dynamic   |
| MIC                              | Minimal inhibitory concentration  |
| MRE                              | Molar residue ellipticity   |
| Mt                               | <i>Mycobacterium tuberculosis</i>   |
| MtFADS                           | FAD synthetase from <i>Mycobacterium tuberculosis</i>                               |
| MW                               | Molecular weight  |
| N                                | Stoichiometry for an interaction  |
| NAD(P) <sup>+</sup>              | Oxidized nicotinamide adenine dinucleotide (phosphate)                              |
| NAD(P)H                          | Reduced nicotinamide adenine dinucleotide (phosphate)                               |
| NADD                             | Nicotinamide adenine dinucleotide, deuterated at A-face of C4                       |
| NQO1                             | NAD(P)H:quinone oxidoreductase 1  |
| O.D.                             | Optical density   |
| O.N                              | Over night  |
| ox                               | Oxidized  |
| PAIN                             | Pan-assay Interference Compound   |
| PAPS                             | Phosphoadenosine 5-phosphosulfate   |
| PDB                              | Protein Data Bank   |
| pH                               | Potential of Hydrogen   |
| PIPES                            | 1,4-Piperazine diethane sulfonic acid   |
| PMSF                             | Phenylmethylsulfonyl Fluoride   |
| PP <sub>i</sub>                  | Pyrophosphate   |

|                        |   |
|------------------------|---|
| rd                     | Reduced   |
| RF                     | Riboflavin  |
| RFK                    | Riboflavin kinase                                       |
| RMSD                   | Root Mean Square Deviation                              |
| <i>r</i> NQO1          | NQO1 from <i>Rattus norvegicus</i>                      |
| rpm                    | Revolutions per minute                                  |
| <i>S</i>               | Entropy   |
| <i>Sc</i> FMNAT        | FMNAT of <i>Saccharomyces cerevisiae</i>                |
| SDS                    | Sodium Dodecyl Sulphate                                 |
| SDS-PAGE               | Denaturing electrophoresis with SDS                     |
| SNP                    | Single nucleotide polymorphism                          |
| <i>Sp</i> FADS         | FAD Synthetase from <i>Streptococcus pneumoniae</i>     |
| <i>Sp</i> RFK          | Riboflavin kinase from <i>Schizosaccharomyces pombe</i> |
| <i>T<sub>m</sub></i>   | Melting Temperature                                     |
| <i>Tm</i> FADS         | FAD Synthetase from <i>Thermotoga maritima</i>          |
| Tris                   | Tris(hydroxymethyl)aminomethane                         |
| TTP                    | Thymidine 5'-triphosphate                               |
| UV                     | Ultraviolet   |
| UV-vis                 | Ultraviolet-visible                                     |
| <i>V<sub>max</sub></i> | Maximum reaction velocity                               |
| VS                     | Virtual screening                                       |
| WHO                    | World Health Organization                               |
| WT                     | Wild Type   |